Lecture Notes in Bioengineering

Moumita Mukherjee · J. K. Mandal ·
Siddhartha Bhattacharyya ·
Christian Huck · Satarupa Biswas *Editors*

Advances in Medical Physics and Healthcare Engineering

Proceedings of AMPHE 2020

Springer

Lecture Notes in Bioengineering

Lecture Notes in Bioengineering (LNBE) publishes the latest developments in bioengineering. It covers a wide range of topics, including (but not limited to):

- Bio-inspired Technology & Biomimetics
- Biosensors
- Bionanomaterials
- Biomedical Instrumentation
- Biological Signal Processing
- Medical Robotics and Assistive Technology
- Computational Medicine, Computational Pharmacology and Computational Biology
- Personalized Medicine
- Data Analysis in Bioengineering
- Neuroengineering
- Bioengineering Ethics

Original research reported in proceedings and edited books are at the core of LNBE. Monographs presenting cutting-edge findings, new perspectives on classical fields or reviewing the state-of-the art in a certain subfield of bioengineering may exceptionally be considered for publication. Alternatively, they may be redirected to more specific book series. The series' target audience includes advanced level students, researchers, and industry professionals working at the forefront of their fields.

Indexed by SCOPUS, EI Compendex, INSPEC, zbMATH, SCImago.

More information about this series at http://www.springer.com/series/11564

Moumita Mukherjee · J. K. Mandal ·
Siddhartha Bhattacharyya · Christian Huck ·
Satarupa Biswas
Editors

Advances in Medical Physics and Healthcare Engineering

Proceedings of AMPHE 2020

Springer

Editors
Moumita Mukherjee
Adamas University
Kolkata, India

J. K. Mandal
Kalyani University
Kolkata, India

Siddhartha Bhattacharyya
Christ University
Bengaluru, India

Christian Huck
University Innsbruck
Innsbruck, Tirol, Austria

Satarupa Biswas
Adamas University
Kolkata, India

ISSN 2195-271X ISSN 2195-2728 (electronic)
Lecture Notes in Bioengineering
ISBN 978-981-33-6914-6 ISBN 978-981-33-6915-3 (eBook)
https://doi.org/10.1007/978-981-33-6915-3

This Springer imprint is published by the registered company Springer Nature Singapore Pte Ltd.
The registered company address is: 152 Beach Road, #21-01/04 Gateway East, Singapore 189721, Singapore

Preface

Healthcare technology is a marriage between medical science and technology to offer humanity better health. With increasing life expectancy, there is a constant demand and scope of improvement in the healthcare industry around the world. With this idea, the Department of Physics, Adamas University, in collaboration with the School of Engineering and Technology, has organised the 1st International Conference—Advances in Medical Physics and Healthcare Technology—AMPHE 2020, to create a platform for global professional development in terms of scientific research for the healthcare providing community. The theme of the conference being interdisciplinary in nature has created considerable interest amongst students, researchers, and faculty members from biomedical engineering, biotechnology, medical physics, life sciences, material science, and also from electrical, electronics, and mechanical engineering backgrounds nurturing applications in biomedical domain. The conference had special sessions along with regular technical sessions to discuss emerging trends of applications in healthcare technology. AMPHE 2020 has been conducted in technical co-sponsorship with IEEE—Kolkata Section and IEEE—ED section.

Original contributions from the academicians, researchers, consultants as well as practising engineers associated with advances and recent trends in medical physics and healthcare engineering are presented in the conference. All the submitted papers have gone through the peer-review process by the technical program committee, and accepted papers (acceptance rate: 60%) are considered for publication in the proceedings. The tracks for invited talks and contributory papers are:

Electron devices, systems, and circuits for health care
Biomedical sensors and transducers
Biomedical signal processing, radar signal and data processing, speech, image, and video processing, information theory and coding, antennas and propagation, sensor networks, big data analytics
Spectroscopy, medical imaging, and image processing techniques
Biomaterials, tissue engineering, and drug delivery systems
Biophysical modelling and simulation
Bio-robotics and biomechanics

Machine learning, machine intelligence, IoT, IoHT, and AI in diagnostic and therapeutic systems
Neural and rehabilitation engineering
VLSI, nano-technology, nano-science, and nano-medicine
Medical physics and electronics, materials
Control systems, robotics, automation and vision
Modelling/simulation of devices
Communication, networking, biotelemetry
Photonics, optical technology in bio-engineering
Bio-informatics, bio-engineering
Innovative intelligent systems and applications.

The conference committee wish to acknowledge Springer Nature, for their support to publish the full-refereed proceedings in the Lecture Notes in Bioengineering. Special thanks to Editor Shri Aninda Bose for his technical support and guidance to organise the conference and in publication.

Kolkata, India

Prof. (Dr.) Moumita Mukherjee
Convener, IEEE AMPHE 2020

Contents

About the Editors

Dr. Moumita Mukherjee is an alumnus of Presidency College (Kolkata) and Calcutta University. Dr. Mukherjee received M.Sc. (Physics) degree with specialization in Electronics and Communication, M.Tech. degree in Biomedical Engineering and Ph.D. (Tech.) degree in Radio Physics and Electronics (2009), University of Calcutta, India. She has worked as DRDO-Scientist under DRDO, Ministry of Defence, Government of India, till 2015. She obtained 'Visiting Scientist' position from Newcastle University, UK (2009–2011). She obtained PDF position from Technical University, Darmstadt, Germany (2010). Dr. Mukherjee is Visiting/Adjunct Professor and a member of Board of Studies of the Joint Academic program on Biomedical Instrumentation under Calcutta University and the West Bengal University of Health Sciences. In continuation of her position at DRDO, she joined Adamas University in 2015 and presently working as Professor—Department of Physics (Pure & Applied Science)—and Dean (Research & Development). She has guided more than 30 postgraduate thesis under Calcutta University & West Bengal University of Health Sciences, West Bengal University of Technology (WBUT) and Adamas University. She is presently guiding/completed 11 (Eleven) Ph.D. theses under Adamas University and WBUT as Supervisor/Jt. Supervisor. Her research interest is focused on THz electronics, semiconductor devices based on wide-band-gap semiconductors, graphene electronics, photosensors, nano-biosensors and medical electronics & instruments, and biomedical imaging. She has published more than 150 peer-reviewed research papers on THz electronics, semiconductor devices, biomedical electronics & instrumentation and photonics in reputed international refereed journals including IEEE, SPIE, Elsevier, Springer and reviewed conference proceedings with more than 850 citations globally with h-index 16. She is Principal Investigator of five industry funded research projects and one Government of India reserach project of worth ~ 65 Lakhs. She is a reviewer of a number of international peer-reviewed journals and editorial board member of international journals. She has worked as Volume Editor of ISBN numbered books published from UK and India. She has delivered a number of invited talks and presented several research articles in IEEE International Conferences in India and abroad.

Dr. Mukherjee has received National Merit Scholarship award from Government of India and was enlisted in ‘Marques Who’s Who in Science and Engineering’ and ‘Marques Who’s Who in the World.’ She has received ‘IEEE best paper award’ three times in 2009, 2010 and 2019, prestigious ‘Best Scientist Award,’ ‘Bharat Gaurav Award’ in 2015, Best paper award in Science and Technology Congress, India, in 2012, Best paper award in International Conference MICRO 2019.

Dr. Mukherjee is a member of IEEE (USA), IEEE-ED society (USA), and a life member of Biomedical Society of India, Indian Science News Association and Indian Science Congress.

Prof. J. K. Mandal M.Tech. (Computer Science, University of Calcutta), Ph.D. (Engg., Jadavpur University) in the field of Data Compression and Error Correction Techniques, and is Professor in Computer Science and Engineering, University of Kalyani, India. He is Former Dean Faculty of Engineering, Technology and Management 2008–2012 (two consecutive terms) and has 29 years of teaching and research experiences.

He served as Professor, Computer Applications, Kalyani Government Engineering College for two years. He served as Associate and Assistant Professor at the University of North Bengal for sixteen years. He is a life member of Computer Society of India since 1992 and a life member of Cryptology Research Society of India. He is a member of AIRCC. He is Honorary Chairman of CSI Kolkata Chapter 2016–2017. He is working in the field of network security, steganography, remote sensing & GIS application, image processing, wireless and sensor networks. He is Domain Expert of Uttar Banga Krishi Viswavidyalaya, Bidhan Chandra Krishi Viswavidyalaya, for planning and integration of public domain networks. He is Chief Editor, Advanced Computing: An International Journal, Associate Editor (Guest), Microsystem Technologies, Springer, Chief Editor, CSI Journal of Computing and Editor of Proceedings of ETCS 2012, NIDS-98 and ERC-95 of CSI. Seventeen Scholars awarded Ph.D., one submitted till January 2017, and eight scholars are pursuing their Ph.D. degree. He published five books from LAP—Lambert Academic Publishing, Germany, and one book from IGI Global publishers, Indexed by Thomson Reuters. Total number of publications is 359 including 146 publications in various international journals. He edited fifteen volumes as Volume Editor from Science Direct, Springer, CSI etc., organizing various international conferences of Springer and Science Direct. He is Director, IQAC, University of Kalyani, and Chairman, Center for Information Resource Management (CIRM), Kalyani University. He has successfully executed five research projects funded by AICTE, Ministry of IT Government of West Bengal.

Dr. Siddhartha Bhattacharyya (LFOSI, LFISRD, FIETE, FIEI, SMIEEE, SMIETI, SMACM, LMCRSI, LMCSI, LMISTE, LMIUPRAI, LMCEGR, LMICCI, LMALI, MIET, MIRSS, MIAENG, MCSTA, MIAASSE, MIDES, MISSIP, MSDIWC) is currently serving as Professor in the Department of Computer Science and Engineering of Christ University, Bangalore. He is a co-author of five books and co-editor of 54 books and has more than 280 research publications in international journals and conference proceedings to his credit. He has got two PCTs to his credit. He is Associate Editor of Applied Soft Computing, IEEE Access, Evolutionary Intelligence and IET Quantum Communications. He is Founding Editor-in-Chief of International Journal of Hybrid Intelligence, Inderscience. He is serving as Book Series Editor of IGI Global, De Gruyter, CRC Press, John Wiley & Sons, Elsevier and Springer. His research interests include hybrid intelligence, pattern recognition, multimedia data processing, social networks and quantum computing.

Christian Huck obtained his doctorate in chemistry in 1998 from the University in Innsbruck, Austria, where he continued to work as Assistant Professor until the habilitation in 2006. In 2013, he received a call as Full Professor at the University of Stuttgart, Germany, and in 2015, another call back to the University of Innsbruck, where he is currently Vice-Head of the Institute of Analytical Chemistry and Radiochemistry and Head of the spectroscopy unit. From 2014 until 2017, he was Visiting Professor at Kwansei-Gakuin University in Sanda, Japan, in the laboratory of Professor Yukihiro Ozaki. Christian has published more than 300 peer-reviewed manuscripts resulting in an h-index of 49 based on more than 8500 citations. Besides several numerous awards, he was also the receiver of 2018 Tomas Hirschfeld Award. In his research, he is mainly focusing on vibrational spectroscopic technologies (NIR, MIR, Raman) for life and material science. Currently, he is Editor-in-Chief for Spectrochimica Acta A (Elsevier) and NIR news (Sage).

Dr. Satarupa Biswas is Assistant Professor in the Department of Physics at Adamas University since February 2019. She completed her doctoral studies from Indian Institute of Technology Kharagpur on Retinal prosthesis. She earned her B.Tech. and M.Tech. degrees, both in Biomedical Engineering, from West Bengal University of Technology and Jadavpur University, respectively. Her area of specialization includes neural rehabilitation, microdevice fabrication, simulation of medical devices, electrophysiology and biomedical instrumentation. She has authored 15 articles in reputed peer-reviewed international journals and national and international conferences. She is a reviewer for IET Micro & Nano Letters. She has received certification in Neural Networks and Deep Learning, Healthcare Innovations, Healthcare Organizations and Health Systems, and Fundamental Neuroscience for Neuroimaging. She is a member of IEEE Kolkata section. As an executive committee member of IEEE EMBS student club of IIT Kharagpur section, she actively participated in organizing various academic events and activities.

Indian Sign Language Recognition Using Combined Feature Extraction

R. Itkarkar Rajeshri, Anil Kumar V. Nandi, and Vaishali B. Mungurwadi

Abstract This research paper aims for the recognition of Indian sign language (ISL). Sign language is a language commonly used by deaf and dumb people to communicate with each other and rest of the world. There is an extensive research carried out for American sign language (ASL), but due to the lack of standard dataset, research for Indian sign language recognition is hampered a lot. This research work focuses on the use of a combined feature extraction technique so as to improve the accuracy and reduce complexity. Histogram of orientation gradient (HOG) and Gabor features are combined and classified using support vector machine (SVM) and K-Nearest neighbor (KNN) with accuracy of 83.92% and 84.92%, respectively.

Keywords Indian sign language (ISL) · HOG · Gabor · SVM

1 Introduction

Vision-based hand gesture recognition is appealing more nowadays as it provides the most natural way to interact for human-machine interaction. The vision base method is widely adopted for research due to low computational complexity. This paper work presents research carried out for the recognition of Indian sign language (ISL). ISL is one of the sign languages which is more complex than American Sign Language as it consists of complex signs (most signs are two hand signs). The typical processes performed for sign language recognition are preprocessing, feature extraction, and classification. Preprocessing consists of converting a color image into gray. Feature extraction is a technique where features such as shape, geometric features, statistical features, texture features, etc. for an image can be extracted. The shape of the hand can be used to identify the gesture termed as shape identification. The contour of the hand identifies the shape. Extracting the contour of hand gives more information in shape detection. Classification techniques such linear classifiers KNN, SVM, and

R. Itkarkar Rajeshri (✉) · A. K. V. Nandi
BVB Hubali, Hubli, Karnataka, India

V. B. Mungurwadi
Aavishkar Technologies, Hubli, Karnataka, India

M. Mukherjee et al. (eds.), *Advances in Medical Physics and Healthcare Engineering*, Lecture Notes in Bioengineering, https://doi.org/10.1007/978-981-33-6915-3_1

neural network can be applied for recognition. This paper focuses on creation of own database with use of a simple web camera, feature extraction by combining Histogram of orientation gradient (HOG) and Gabor features and classified using support vector machine (SVM) and K-Nearest neighbor (KNN). Gabor filters are used in image processing due to its mathematical and biological properties (Guptaa et al. 2012). The feature dimension generated depends on the selection of parameters for the Gabor filter. The Gabor filter is designed by selecting parameters such as orientation, bandwidth, and frequency. The HOG features give the spatial distribution of local intensity gradients. These features well describe the hand gestures as they describe the edge features. Thus the shape feature of the hand gestures can be extracted by using HOG.

2 Related Work

Hand gesture recognition is one form of interaction between human and computer to achieve typical application. A real-time hand gesture recognition system implemented (Kishore and Rajesh Kumar 2012) with an accuracy of 96% using a combination of color and texture features and fuzzy logic for classification (Nandy et al. 2010). Indian sign language recognition was implemented by evaluating mean feature of histogram gradient and Euclidean distance for recognition and used for controlling a humanoid robot. Gabor is a linear filter that gives best localization characteristics by changing, bandwidth, frequency, and orientation (Huang et al. 2010). In (Zhao et al. 2010) extracted HOG features were converted into low-dimensional subspace using PCA-LDA. It was classified using the nearest neighbor classifier to achieve a recognizing accuracy of 91% in real-time. While in (Teoh and Branunl 2015) the authors used both HOG and Gabor for vehicle detection with three different classifiers SVM, Multi perceptron neural network, and distance classifier. They obtained best performance with HOG and SVM with less processing time. The authors in (Sheenu et al. 2015) have used HOG method followed by sequential minimal optimization with a recognition rate of 93.12%.

3 Methodology

The methodology proposed is a novel method for ISL recognition, where the Gabor features and HOG features combined to form a feature vector. The obtained feature vector is of a higher dimension, and hence PCA is used further to reduce the dimension and then applied to the classifier for recognition. The classifier used is SVM and KNN. Figure 1 shows the proposed methodology for ISL recognition.

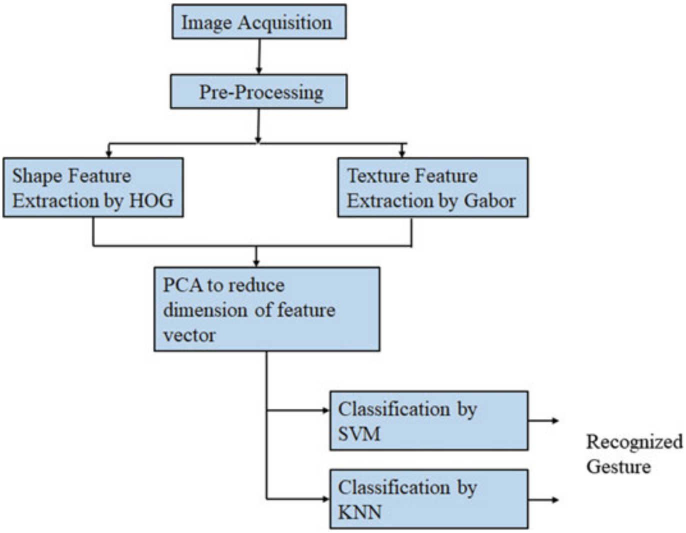

Fig. 1 Proposed methodology for ISL recognition

3.1 Feature Extraction by HOG

The HOG features are widely used for object detection. The image is divided into small square cells, the histogram of oriented gradients is computed for each cell, normalizes the result using a block-wise pattern, and return descriptors for each cell. Histogram of Oriented Gradient descriptor assumes that the local object appearance and shape within an image can be described by the distribution of intensity gradients or edge directions. The implementation of these descriptors can be achieved by dividing the image into small connected regions called cells, and for each cell computing a histogram of gradient directions i.e. edge orientations for the pixels within the cell. The combination of these histograms then represents the descriptor (Savaris and von Wagenheim 2010). The shape features are evaluated by applying color normalization on the input image, then evaluate the horizontal and vertical gradients, next is the formation of spatial blocks and then calculate orientation bin-wise and then forming a feature vector. The gradient magnitude and its orientation are calculated as in Eqs. (1) and (2) respectively, where *gx* and *gy* are horizontal and vertical gradients.

$$G = \sqrt{gx^2 + gy^2} \quad (1)$$

$$\theta = \tan^{-1} \frac{gy}{gx} \quad (2)$$

3.2 Feature Extraction by Gabor Filter

Gabor filter is a linear filter used for object edge detection. Gabor transform has strong frequency and orientation selectivity so that the edge features can be extracted. Gabor gives the best resolution in time and frequency domain and hence recognized as a very useful tool in computer vision and image processing (Huang et al. 2010). The parameters such as bandwidth, frequency, and orientation are changed to achieve best local features as Gabor is a linear filter. The features are extracted by convolution of the Gaussian kernel with the input image. A 2-D Gabor filter kernel over the image (x, y) is defined as per Eq. 3

$$G(x, y, \theta, \lambda, \varphi, \sigma, \gamma) = \exp -\frac{1}{2}\left\{\frac{x'^2}{\sigma x'^2} + \frac{y'^2}{\sigma y'^2}\right\}\cos\left(\frac{2\pi}{\lambda x'} + \varphi\right) \quad (3)$$

where $x' = x\sin\theta + y\cos\theta$ and $y' = x\cos\theta - y\sin\theta$, $G(x, y, \theta, \lambda, \varphi, \sigma, \gamma)$ kernel is a function of various parameters $\theta, \lambda, \varphi, \sigma, \gamma$ of the wavelet. θ is the orientation of the Gabor function, varied between 0 and 360. λ is the wavelength of the cosine factor of the Gabor kernel referred to as the wavelength of the filter. φ, it is the phase shift of the Gabor function in degrees which specifies the elasticity of the Gabor function. The features are extracted by convolution of the image with Gabor kernel represented as in Eq. 4

$$G(x, y, \theta, \lambda, \varphi, \sigma, \gamma)(x, y) = I(x, y) * G(x, y, \theta, \lambda, \varphi, \sigma, \gamma) \quad (4)$$

where $I(x, y)$ is the image.

The HOG features and Gabor features are finally combined together to form feature vector. The features are concatenated and the length of the feature vector.

4 Results

4.1 Results of HOG and Gabor

For implementation, Matlab is used. The final HOG vector Obtained is a vector of $2 \times 2 \times 9$ vector i.e. 36×1. Here as the block overlap is of 2 there are 9 matrices of 2×2 size. Thus 8×8 cell finally reduced to 2×2 of 2 block overlap. Therefore 9 bins contain gradients of each cell. The final feature vector evaluated is the combination of both HOG and Gabor. This combination provides a perfect feature matrix which represents signs of Indian sign language. The HOG extraction method applied to a grayscale resized image of 130×130 resolution results in a feature vector of size 2700×1. The cell size selected 8, the block size is 2, and bin size is 3 for HOG extraction. The Gabor coefficients obtained after convolution of the Gaussian kernel

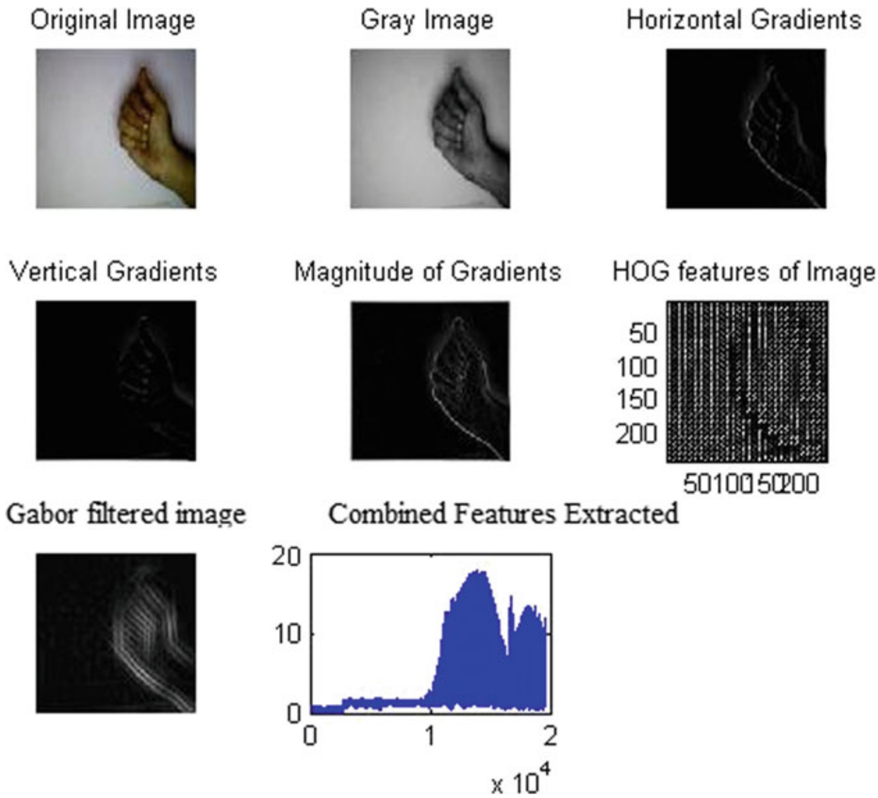

Fig. 2 Results of combined features of HOG and Gabor gestures for sign "0"

with the sign image are of size 16,900 × 1. Figures 2 and 3 shows the results for sign "0" and "*A*".

The performance of the classifier algorithm is stated by evaluating the accuracy from confusion matrix. The confusion matrix is as shown in Table 1 is for SVM and Table 2 is for KNN. The average accuracy obtained with SVM 83.92% and with KNN is 84.92% for $K = 3$. As there is very less research carried on ISL and no method used based on combined recognition comparison with existing work cannot be obtained.

5 Conclusion

The combined feature extraction by HOG and Gabor technique is obtained to increase the accuracy and reduce complexity of the system, though average accuracy obtained is just 83.92 and 84.92%. Gabor though is a robust technique accuracy decreases as filter output depends on many parameters. The recognition for ISL is a challenging

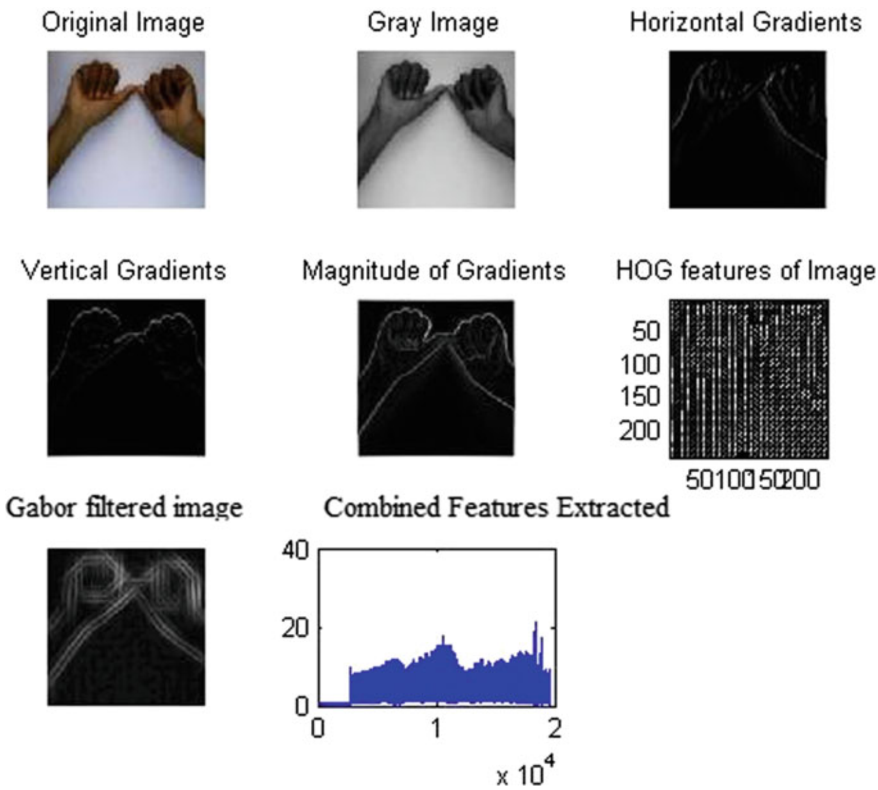

Fig. 3 Results of combined features of HOG and Gabor gestures for Sign "*A*"

Table 1 Confusion matrix by combined hog and Gabor features with SVM

Sign	*A*	*B*	*C*	*D*	1	2	3	4
A	**71**	0	0	0	0	0	0	0
B	0	**50**	0	0	0	0	0	0
C	0	0	**80**	0	0	5	0	0
D	0	0	0	**75**	0	0	0	25
1	0	0	0	0	**100**	0	0	0
2	0	0	0	0	0	**100**	0	0
3	0	0	0	0	0	0	**100**	0
4	0	0	0	0	0	0	0	**95**

Table 2 Confusion matrix by combined hog and Gabor features with KNN

Sign	*A*	*B*	*C*	*D*	1	2	3	4
A	**71**	0	0	0	0	0	0	0
B	0	**75**	5	0	0	0	20	0
C	0	0	**65**	0	15	5	0	0
D	0	0	0	**75**	0	0	0	25
1	0	0	0	0	**100**	0	0	0
2	0	0	0	0	0	**100**	0	0
3	0	0	0	0	0	2	**98**	0
4	0	0	0	0	0	0	0	**95**

task as the signs in ISL are complex. Further, the technique can be extended to recognize sentences and generate audio output for the recognized gestures.

Acknowledgements The Author Rajeshri Itkarkar, presently working with AISSMSCOE would like to thank Hon. Secretory Shri Maloji Raje Chatrapati and Principal Dr. D. S. Bormane of AISSMS College of Engineering Pune for their guidance and support.

References

Chen Q, et al (2008) Hand gesture recognition using Haar-like features and a stochastic context-free grammar. IEEE Trans Instrum Measure 57:9

Geetha M, Manjusha UC (2013) A vision based recognition of Indian sign language alphabets and numerals using B-spline approximation. Int J Comput Sci Eng (IJCSE)

Guptaa S, Jaafar J, Ahmad WFW (2012) Static hand gesture recognition using local gabor filter. In: International symposium on robotics and intelligent sensors

Huang Z, Jiang D, Zhao W (2010) Study of sign language recognition based on gabor wavelet transforms. In: International conference on computer design and applications (ICCDA 2010). IEEE

Kishore PVV, Rajesh Kumar P (2012) A model for real time sign language recognition system. Int J Adv Res Comput Sci Softw Eng 2(6):30–35

Nandy A, Mondal S, Prasad JS, Chakraborty P, Nandi GC (2010) Recognizing and interpreting Indian sign language gesture for human robot interaction. In: International conference on computer and communication technology, ICCCT'10, pp 712–717

Savaris A, von Wagenheim A (2010) Comparative evaluation of static gesture recognition techniques based on nearest neighbor, neural networks and support vector machines. J Braz Comput Soc 16:147–162

Sheenu, Joshi G, Vig R (2015) A multi-class hand gesture recognition in complex background using sequential minimal optimization. In: International conference on signal processing, computing and control

Teoh SS, Branunl T (2015) Performance evaluation of HOG and Gabor features for vision based vehicle detection. In: IEEE international conference on control system, computing and Engineering 27–29 Nov 2015

Zhao Y, Wang W, Wang Y (2011) A real-time hand gesture recognition method. 978-1-4577-0321-8/11 ©2011 IEEE

Creating Sleep-Health Awareness and Developing of a Sleep-Apnea Screening Tool for People of Developing/Under-Developed Countries

Jyoti S. Bali, Anilkumar V. Nandi, P. S. Hiremath, Prabha C. Nissimagoudar, and Poornima G. Patil

Abstract The socio-economic development of a nation depends on the health of the citizens, who contribute towards it. Sleep-health is an essential indicator of the well-being of a person. There are many ailments related to heart and brain reported that are caused by problems of lack of sleep, interrupted sleep, and unhygienic sleep conditions. Several sleep-related disorders are affecting people of various age groups, which reduce the quality of life as well as the physical and mental health of the affected person drastically. Awareness about the problem among medical experts and the general public is poor in countries of lower economy, like India. The Polysomnography (PSG), a gold-standard and a popular test is used to detect sleep-related disorders. PSG requires a sophisticated Sleep-Lab facility and proves costly and hence not affordable by lower sections of society. Under the proposed work, the focus is on the need for creating awareness on the up-keeping of sleep-health and developing a convenient screening tool for sleep apnea. The development issues of an intelligent and cost-efficient screening tool as an alternative to PSG and the feasibility of using the tool at smaller clinical setups are discussed.

Keywords Sleep-health · Sleep-related disorders · Quality of life · Polysomnography(PSG) · Sleep lab facility · Cost-efficient screening tool

---

J. S. Bali (✉) · A. V. Nandi · P. S. Hiremath · P. C. Nissimagoudar
KLE Technological University, Hubballi, Karnataka 580031, India
e-mail: Jyoti_bali@kletech.ac.in

A. V. Nandi
e-mail: anilnandy@bvb.edu

P. C. Nissimagoudar
e-mail: pcnissimagoudar@kletech.ac.in

P. G. Patil
Visvesvaraya Technological University, Belagavi, Karnataka, India

M. Mukherjee et al. (eds.), *Advances in Medical Physics and Healthcare Engineering*, Lecture Notes in Bioengineering, https://doi.org/10.1007/978-981-33-6915-3_2

1 Introduction

Sleep apnea is a type of breathing disorder resulting in interruptions in breathing or causing shallow breathing during night sleep. The disorder can occur in three different forms, namely, Obstructive Sleep Apnea (OSA), Central Sleep apnea (CSA), and Mixed Sleep Apnea (MSA), among which OSA is the most prevalent. In all these three forms of sleep apnea, the interrupted breathing activity leads to the problem of oxygen deficiency leading to chronic cardiac-related ailments, namely stroke, hypertension, atrial fibrillation, etc. Only a close relative of the patient can identify the problem as it occurs during night sleep. In most cases, the problem goes unnoticed in the preliminary stage. Earlier detection of sleep apnea can save a patient from severe life risk. The delay of diagnosis can prove fatal (Campbell et al. 2017; Thomas et al. 2017; Elgendi et al. 2014). The awareness toward sleep apnea is very poor across the globe. Even in developed countries like the US, only 15–20% of the affected population is screened for sleep apnea as per a survey report. The problem occurs among people of all economic sections and age groups. The health care cost towards the treatment of heart-related ailments is very high, many times not affordable by some sections of society. The need for creating awareness about sleep disorder is very critical. Even the medical experts do not insist cardiac patients to undergo sleep test, as it can provide information on the root cause as sleep apnea many times. Even the experts in the medical community fail to educate people about sleep health, and the need for screening in case of heart-related problems (Campbell et al. 2017; Thomas et al. 2017; Elgendi et al. 2014; Bali and Nandi 2016, 2017a, b; Stuart 2010; https://www.resmed.com).

2 Sleep Apnea Diagnosis and Treatment Methods

Polysomnography (PSG) is a well-established gold-standard test, conducted overnight on the patient to detect the presence of sleep-related disorders. PSG test is conducted in a sophisticated sleep lab facility with instrumentation systems, and monitoring equipment, under the supervision of a trained technician. PSG test involves monitoring of several physiological parameters gathered from the set of electrodes put on the patient's body during the entire sleep time. The test proves to be very cumbersome and expensive involving complex analysis and is available at tertiary level health care facilities. The facility is not affordable by poorer sections of society in countries of the lower economy. The affected people are advised to visit the sleep lab facility, only after undergoing heart stroke or any other heart-related ailment. There are several standard guidelines released from various internationally renowned organizations, namely, American Academy of Sleep Medicine (AASM), Indian Society for Sleep Research (ISSR), All India Institute of Medical Sciences (AIIMS), New Delhi, and other international bodies. They provide guidelines for therapists and experts responsible for creating awareness and promoting research in the area of sleep and sleep medicine. There are different home-based portable monitoring devices used as screening tools that simplify the diagnosis of OSA before the affected person is referred for Polysomnography (PSG) test by an expert. The devices can be used for sleep evaluation program that provides access to sleep lab facility, PSG test, and specialists. CPAP method provides an effective treatment for diagnosed OSA (Bali and Nandi 2017a, b; Stuart 2010; https://www.resmed.com).

The sleep apnea detection methodologies have evolved over years, from study of various physiological parameters in single or as a combination. Some of the important physiological parameters used are, namely, breathing pattern, nasal airflow, EEG, ECG, Saturated Oxygen (SaO_2) and limb movements gathered from the human being through sophisticated instrumentation systems. EEG provides information on the mental activity of the brain from the fully active state, engaged in cognitive efforts to sleepiness. The effect of sleep apnea causes the shifting of EEG from the delta wave to theta and alpha waves. EEG needs pre-processing to free it from artifacts before analysis. Saturated blood oxygen (SpO_2) is measured by a pulse oximetry sensor, and the sleep apnea event is accompanied by a reduction in SpO_2 level. The analysis of ECG and SpO_2 in combination can provide information on the de-saturated oxygen level as well the Heart rate variability parameters caused by sleep apnea events. The physiological parameters used for sleep apnea study along with the respective features are listed in Table 1.

Analysis of recording of the tracheal sound during sleep can provide information on estimated respiratory flow and changes in the breathing pattern caused by the occurrence of an apnea event. The analysis of ECG and SpO_2 in combination can provide information on the de-saturated oxygen level as well the Heart rate variability parameters. They are implemented using a combination of classifiers. Whenever the sleep apnea event occurs, the de-saturation of blood oxygen sensed by SpO_2 sensor level initiates the sympathetic nervous system by monitoring EEG to act in order to restore the blood oxygen level. The analysis of power spectral features of EEG and ECG in sleep conditions are used in detecting the OSA events during night sleep (Campbell et al. 2017; Thomas et al. 2017; Elgendi et al. 2014; Bali and Nandi 2016,

Table 1 Physiological parameters used for sleep apnea study

Physiological parameters	Feature extraction
EEG	Measure of the shift from Delta waves to Theta and Alpha waves
ECG	Cyclic variation patterns in heart rate and RR interval duration
SpO_2	Oxygen De-saturation level, spectral and non-linear features
Snoring	Estimation of Formant frequency
Body movement	Analysis of video of captured body movements in different angles
EEG + ECG	Power spectral features of EEG and ECG in sleep conditions
ECG + SpO_2	Heart rate variability parameters with De-saturated oxygen level
Tracheal sound	Estimation of Respiratory flow and changes in the breathing pattern
Airflow	Spectral features

2017a, b; Stuart 2010; https://www.resmed.com; https://www.usa.philips.com/healthcare/product/HC1109289).

3 Sleep Apnea Detection Systems for Home Use

Apart from Polysomnography (PSG) test, the home-testing devices can be of help in testing of a patient for sleep apnea conditions. AASM (2009) standard approves the use of such sleep monitoring devices as screening tools. Home sleep test (HST) devices are user-friendly to be used by experts for monitoring their patients at ease. With the advancement of technology in developing systems as per standard, dealing with Sleep apnea is not so difficult. There is a good demand for cost-effective portable recording systems as screening tools for sleep apnea before the patient is advised for costly and cumbersome PSG test. Thus sleep apnea patients and normal subjects can be clearly separated with a more convenient and cost-effective system. The various diagnostic devices used for Sleep apnea are, namely, Clinical PSG devices, ambulatory PSG devices. Among the HST Devices, Oximeter, Actigraphy Devices, and Sleep Screening Devices are popularly used. The physicians, expert in the area, need to use specialized software for analyzing as per their requirements. Some of the real-time monitors are equipped to gather and transmit data as well as do real-time analysis of apnea events that occur and alert the patient or the attendant immediately and give analysis as feedback (Elgendi et al. 2014; Bali and Nandi 2016, 2017a, b; Stuart 2010; https://www.resmed.com; https://www.usa.philips.com/healthcare/product/HC1109289). Table 2 provides a summary of real-time sleep apnea monitoring devices.

The studies are carried out by several researchers to suggest alternative means of sleep apnea detection in a home environment with a reduced number of physiological parameters required for analysis. There is no such proven screening device yet, and experts can use that at the primary and secondary clinical setups. The respiration function and heart function are inter-dependent. The changes in the heart function, caused by sleep disorder can be captured using the Electrocardiography (ECG), a well-established diagnostic modality. Similarly, during the sleep apnea condition, the physiological signals like EEG, blood oxygen, body position, temperature, EMG characteristics change and deviate from their normal characteristics. The medical experts in sleep lab facility observe such changes in characteristics of physiological signals and infer about the sleep apnea conditions. Several researchers have proposed to automate sleep apnea diagnostics with intelligent assistive technology. However, they have not reached the acceptable accuracy and efficiency. Hence there is a need for an efficient, cost-effective and portable facility that can be used at primary and secondary-level health-care facilities (Satija et al. 2018; Krishnan and Athavale 2018; Bali et al. 2018a, b, c; Lyon et al. 2018; Altay and Kremlev 2018; Liu et al. 2018; Dey et al. 2017; Bali et al. 2020; https://www.resmed.com; https://www.usa.philips.com/healthcare/product/HC1109289; https://physionet.org/

Table 2 Real-time sleep apnea monitoring devices

Parameters	System features
Multi-parameter input	ApneaLink™ Plus using respiratory action, pulse rate, oxygen saturation, and nasal airflow (off-line)
	The SleepStrip™ uses thermistors for oral and nasal airflow(Off-line)
	WM ARES, monitors heart rate, airflow, respiratory action, pulse rate, oxygen saturation (off-line)
	Alice Night One from Philips, Respironics, gathers data on airflow, snore, thorax effort, SpO_2, pulse rate, body position(on-line)
	Transmitter for body position, nasal airflow, abdomen/chest efforts, oxygen saturation (on-line)
Body movement	Body movement captured in 10 videos of 3 different angles with two SONY infrared camcorders
SpO_2 only	Wearable system using PPG signal from SpO_2 sensor (on-line)
	HealthGear, a blood oximeter for the blood oxygen level (on-line)
	Medical, Inc., 4100 Digital Pulse Oximeter, decision tree classifier, ADTree (on-line)
ECG only	Apnea MedAssist, with Android operating system based smartphone using single lead ECG sensor (on-line)

physiobank/database/slpdb/; https://sleepdata.org/datasets/shhs; https://www.physionet.org/physiobank/database/apnea-ecg/).

Design of optimized hardware and efficient algorithms is very important to develop a wearable device to gather the required physiological parameters. The system needs to be user-friendly, cost-effective with optimized battery life. The offline processing of captured information can be done for analysis and automated decision making on the condition of sleep disorder and advise timely medication. In the process, medical experts need to be trained on the use of smart screening tools for sleep apnea for earlier identification, to avoid life threats. There is a need for a cost-effective screening tool with a lesser number of sensors. In order to support the development of the screening tool, there is a need for developing reliable Indian data sets for sleep apnea testing and validation by domain experts. The need for government initiatives on creating awareness on the sleep apnea problem among common people is very crucial and is to be conducted through the government health-care facilities and Non-Government Organizations (NGO's). In this direction, ECG signal forms an important source of information for studying sleep apnea conditions (Campbell et al. 2017; Thomas et al. 2017; Elgendi et al. 2014; Bali and Nandi 2016, 2017a, b; Stuart 2010; Satija et al. 2018; Krishnan and Athavale 2018; Bali et al. 2018a; https://www.resmed.com; https://www.usa.philips.com/healthcare/product/HC1109289). ECG signal is a reliable diagnostic modality used for study and diagnosis of heart health. ECG signal can be analyzed using which the signatures due to sleep apnea disorder can be tracked. But the ECG signal needs to be pre-processed for separating it from the undesired inherent noise present in it as baseline wander noise, motion artifact noise, and the power-line interference noise. Efficient analysis of the ECG signal to detect the deviations caused in its parameters due to sleep apnea effect needs to be ensured. There are several ECG signal preprocessing techniques developed over the years to improve the Signal to Noise Ratio (SNR) of the signal. The survey of automated ECG processing and analysis algorithms that evolved from derivative methods in time domain and transform domain has been carried out. The QRS detection process is a very critical step, for extraction of important parameters from the ECG signal. Several research studies are carried out to compare the various QRS detection methods with regard to the three assessment criteria, namely, robustness to noise, choice of parameters and the attained numerical efficiency for battery-enabled, portable applications involving large ECG databases (Satija et al. 2018; Krishnan and Athavale 2018; Bali et al. 2018a, b, c; Lyon et al. 2018; Altay and Kremlev 2018; Liu et al. 2018; Dey et al. 2017; Bali et al. 2020; https://physionet.org/physiobank/database/slpdb/; https://sleepdata.org/datasets/shhs; https://www.physionet.org/physiobank/database/apnea-ecg/).

The experimentation of working with sleep apnea problems requires a wide variety of ECG datasets of normal subjects as well sleep apnea affected subjects for study. The databases can be got from hospitals with Sleep lab facility or use benchmark databases from standard sources. The estimated performance measures of analysis algorithms depend on the datasets used. There are publicly available databases for study, namely, *The MIT-BIH Polysomnography Database,* Sleep Laboratory, Boston's Beth Israel Hospital for chronic OSA syndrome and the effect of CPAP treatment, Sleep Heart Health Study (SHHS) housing recordings of EEG, EOG, EMG, airflow, thoracic and abdominal excursions, ECG, body position, ECG Apnea database from physionet.org (PNDB) comprising of 70 night time ECG recordings. Once the ECG signal features are extracted, there is a need to analyze the significant features depicting sleep apnea conditions using an intelligent decision-making algorithm (Lyon et al. 2018; Altay and Kremlev 2018; Liu et al. 2018; Dey et al. 2017; Bali et al. 2020; https://physionet.org/physiobank/database/slpdb/; https://sleepdata.org/datasets/shhs; https://www.physionet.org/physiobank/database/apnea-ecg/). Hence the proposed work aims at throwing light on the available methods, technologies, devices for sleep apnea detection and monitoring. Also, the need for a useful screening tool that can be used by experts at smaller clinical setups is emphasized.

4 Conclusion

There is a critical need for creating awareness of sleep health, sleep hygiene, and the impact of sleep disorders on cardiac health among the people of the countries of the lower economy. The proposed tool can prove a boon to the people of developing and under-developed countries, where the health care facility is not easily affordable by lower-income groups of society. The local clinical setups can be equipped with the screening tool to make affected people be aware of the problem early and undergo preventive measures to avoid future damage to the health of the individual. Hence there is a need for simplified and reliable screening tool that can be used by experts as a supplementary facility to PSG at the primary and secondary health care facilities, so that the detection can happen at an earlier time. Later the patient can be referred for a sleep lab test for detailed analysis and finalize the medication accordingly, thus improving the quality of life.

References

Altay YA, Kremlev AS (2018) Comparative analysis of ECG signals processing methods in the time-frequency domain. In: 2018 IEEE conference of Russian young researchers in electrical and electronic engineering (EIConRus), pp 1058–1062

ApneaLink™. https://www.resmed.com

Bali JS, Nandi A (2016) An experience, using software based tools for teaching and learning mathematically intensive signal processing theory concepts. In: 2016 IEEE 4th international conference on MOOCs, Innovation and Technology in Education (MITE), Madurai, pp 100–104. https://doi.org/10.1109/MITE.2016.029

Bali JS, Nandi A (2017a) ECG signal based power aware system for obstructive sleep apnea detection. In: 2017 international conference on recent trends in electrical, electronics and computing technologies. 978-1-5090-6266-9/17 $31.00 © 2017 IEEE. https://doi.org/10.1109/ICRTEECT.2017.43

Bali JS, Nandi A (2017b) Simplified process of obstructive sleep apnea detection using ECG signal based analysis with data flow programming. In: ICTIS 2017 , Ahmadabad 25th and 26th March 2017, Information and communication technology for intelligent systems (ICTIS 2017), smart innovation, systems and technologies, vol 84. Springer, Cham. https://doi.org/10.1007/978-3-319-63645-0_18

Bali JS, Nandi A, Hiremath PS (2018a) Performance comparison of ANN classifiers for sleep apnea detection based on ECG signal analysis using Hilbert Transform. Int J Comput Technol 17(2):7312–7325. https://doi.org/10.24297/ijct.v17i2.7616

Bali JS, Nandi AV, Hiremath PS, Patil PG (2018b) Detection of sleep apnea in ECG signal using Pan-Tompkins algorithm and ANN classifiers. COMPUSOFT 7(11):2852–2861

Bali JS, Nandi AV, Hiremath PS, Patil PG (2018c) Detection of sleep apnea from ECG signals using WT and ANN classifiers. IPASJ Int J Electr Eng (IIJEE) 6(11):1–14

Bali J, Nandi A, Hiremath PS (2020) Efficient ANN algorithms for sleep apnea detection using transform methods. In: Verma O, Roy S, Pandey S, Mittal M (eds) Advancement of machine intelligence in interactive medical image analysis. Algorithms for intelligent systems. Springer, Singapore. Print ISBN 978-981-15-1099-1. Online ISBN 978-981-15-1100-4. https://doi.org/10.1007/978-981-15-1100-4_5

Campbell B, Richley D, Ross C, Eggett CJ (2017) Clinical guidelines by consensus: recording a standard 12-lead electrocardiogram. An approved method by the Society for Cardiological Science and Technology (SCST). https://www.scst.org.uk/resources/SCST_ECG_Recording_Guidelines_2017

Dey D, Chaudhuri S, Munshi S (2017) Obstructive sleep apnoea detection using convolutional neural network based deep learning framework. Biomed Eng Lett 8. https://doi.org/10.1007/s13534-017-0055-y

Elgendi M, Eskofier B, Doko S, Abbott D (2014) Revisiting QRS detection methodologies for portable, wearable battery operated and wireless ECG systems. PLoS ONE 9(1):e84018

https://physionet.org/physiobank/database/slpdb/

https://sleepdata.org/datasets/shhs

https://www.physionet.org/physiobank/database/apnea-ecg/

Krishnan S, Athavale Y (2018) Trends in biomedical signal feature extraction. Biomed Signal Process Control 43:41–63

Liu F, Liu C, Jiang X, Zhang Z, Zhang Y, Li J, Wei S (2018) Performance analysis of ten common QRS detectors on different ECG application cases. Feife J Healthc Eng (Article ID 9050812)

Lyon A, Mincholé A, Martínez JP, Laguna P, Rodriguez B (2018) Computational techniques for ECG analysis and interpretation in light of their contribution to medical advances. J R Soc Interface 15(138):20170821

Philips Alice Night One. https://www.usa.philips.com/healthcare/product/HC1109289

Satija U, Ramkumar B, Manikandan MS (2018) A review of signal processing techniques for electrocardiogram signal quality assessment. IEEE Rev Biomed Eng 11:36–52

Stuart M (2010) Sleep apnea devices: the changing of the guard. STARTUP J 15(10):1–8

Thomas RJ, Shin C, Bianchi MT, Kushida C, Yun C-H (2017) Distinct polysomnographic and ECG spectograpic phenotypes embedded within Obstructive Sleep Apnea. Sleep Sci Pract 1:11

Robust Detection of Atrial Arrhythmias Using Sub-modules of Different Feature Predictors

Nabanita Sinha and Arpita Das

Abstract Incorporation of robust electrocardiogram (ECG) diagnosis model in health monitoring applications is crucial for early-stage prediction of cardiac arrhythmias. This work introduces a model to discriminate atrial fibrillation and congestive heart failure from normal sinus rhythm by employing three parallel sub-modules. The discrete wavelet transform (DWT) is applied for decomposition of ECG signal. Various feature predictors are extracted to evaluate the fundamental characteristics of decomposed RR interval signal. Different sets of significant feature predictors are constructed for three sub-modules. The individual decision of sub-module classifiers is processed to produce final outcome of the model based on proposed decision-making rule. The decision mapping approach may either specify a valid detection of atrial fibrillation/congestive heart failure/normal sinus rhythm or predict the misleading outcomes of three sub-modules. The main impact of this work is the prediction of misleading outcomes by analyzing the proposed decision mapping rules followed by a rechecking option with other segments of ECG signals of same patient. The assessment of the model is done using open MIT-BIH database. Experimental result shows that the prediction accuracy of the model is improved for final decision-making approach.

Keywords ECG classification · Parallel submodules · Cardiac arrhythmia · RR interval signal · DWT

1 Introduction

Atrial arrhythmias occur above the ventricles or upper chamber of heart called atria due to irregular function in the heart's electrical system (Sinha and Das 2020). Atrial arrhythmias are of different types -supraventricular, atrial fibrillation, atrial flutter,

N. Sinha (✉) · A. Das
Department of Radio Physics and Electronics, University of Calcutta, Rajabazar Science College Campus, Kolkata, India

A. Das
e-mail: adrpe@caluniv.ac.in

M. Mukherjee et al. (eds.), *Advances in Medical Physics and Healthcare Engineering*, Lecture Notes in Bioengineering, https://doi.org/10.1007/978-981-33-6915-3_3

and so on. CHF is a heart disease that prevents the heart from pumping blood properly into the body's organs (Murberg and Furze 2004). Atrial fibrillation (AF) and congestive heart failure (CHF) are prevalent disposing conditions of heart that share risk of morbidity and mortality factors. In the assessment of Framingham Heart Study, AF and CHF were found to be associated with each other. The existence of either raises the danger of creating the other and shares the risk of mortality connected with other (Lubitz et al. 2010).

CHF is also classified as systolic or diastolic heart failure. Globally there are more than 25 million people suffer from congestive heart disease (Ponikowski et al. 2014). There are different conditions for heart failure growth. Today as a consequence of fast lifestyle and inappropriate diets, this disease has become very prevalent throughout the world. Hypertension, myocardial infarction, diabetes, obesity, anemia, kidney failure, heart valve defects, and depression can cause the danger of developing CHF (Pazos-Lopez et al. 2011). Although cardiac failure is a major medical condition, the heart does not just suddenly stop working. Different drugs are used for treating CHF patients. Other most prevalent cardiac disorder is AF (Feinberg et al. 1995). Although it is not deemed a life-threatening arrhythmia, but due to AF the quality of life may be significantly affected and the risk of stroke may be increased. Approximately 15% of strokes happen in AF individuals (Go et al. 2001). AF appears in various forms. It often begins as paroxysmal (self-terminating) and with time becomes more persistent. Paroxysmal AF is defined as an AF attack that lasts for 2 min to less than 7 days and returns to normal sinus rhythm spontaneously. Permanent AF lasts more than 7 days and the rhythm of the sinus can't be restored. Approximately 18% of paroxysmal AF can evolve years into permanent AF over 4 years (Al-Khatib et al. 2000). The precise prediction of paroxysmal AF is clinically essential due to the increase likelihood of stabilization and prevention of atrial disorder with distinct atrial pacing method (Prakash et al. 1997). The therapeutic objective of AF detection is to prevent the possibilities of stroke and regenerate the sinus rhythm. Hence, early-phase diagnosis of AF and CHF is essential to determine the prognosis of the disease and prescribe essential medications for the patients.

The electrical activity of the human heart reflects the situation of the cardiovascular system. Accordingly, the measurement of the cardiac activity in form of electrocardiogram (ECG) signals is the significant empirical aid for the diagnosis of heart diseases. Any heart illness such as CHF/AF triggers unique alteration to the electrical activity of the human core and these alterations can be detected by the analysis of ECG signal. However, due to the inner complexity of ECG recording, which is transient in nature interpretation and analysis of different kinds of cardiac disorder, becomes difficult (Shiyovich et al. 2010). The researches have suggested that the use of computer-based algorithms may improve the diagnostic accuracy. In this view, computer aided diagnosis (CAD) system has been developed as an alternative for automatic detection of heart diseases. The CAD system has been used to extract significant information from ECG signals to diagnose the patients with heart disease (Acharya et al. 2004).

Over the past few years, several techniques have been proposed based on the analysis of RR interval of ECG signal. Cerutti et al. (1997) have extracted useful features by applying auto-regressive model on RR signal. Nonlinear techniques are also used for the analysis of ECG signal. Lee et al. (2013) has developed AF detection techniques using entropy measurement approach. In other study fractal dimension has been evaluated for AF detection (Martis et al. 2012a). The QRS-complex analysis strategy has also been employed to evaluate the ECG signals of atrial activity. Few techniques are applied to extract ECG beat characteristics to discriminate AF and normal sinus Rhythm (Annavarapu and Kora 2016). Martis et al. (2013) combined independent component analysis and Bayesian paradigm method together to detect AF. Tripathy et al. (2017) applied two-stage variational mode decomposition approach to classify AF and normal ECG signal. In this study, they developed an index for AF diagnosis (Martis et al. 2012b). For prediction of CHF many works analyzed the heart rate variability (HRV) and the characteristics of ECG signals (Liu et al. 2014). Several methods have been applied for evaluating the features in time-domain (Pecchia et al. 2011b; Yu and Lee 2012) as well as frequency-domain (Pecchia et al. 2011a; Khaled et al. 2006). Various nonlinear features like entropy-based analysis (Narin et al. 2014; Acharya et al. 2016), Poincare plot (Khaled et al. 2006; Thakre and Smith 2006), and fractal scaling exponents (Kamath 2015) have been estimated from HRV and ECG signal to discriminate normal heart and CHF conditions.

Although many contributions have been reported in the detection of AF and CHF, but there is a need to improve the precision of the CAD diagnosis to identify AF and CHF at early stage. In this work, our objective is to develop an efficient and robust model for mobile-based cardiac health monitoring system to recognize both AF and CHF from the normal sinus rhythm (NSR). In this view, we have proposed a composite model with three parallel sub-modules to detect serious heart conditions. We have applied discrete wavelet transform (DWT) to decompose the RR interval of ECG signal into five different subbands and then various features are extracted. Depending on the proposed selection principle, three category feature set is produced and fed to the respective sub-modules for prediction of AF and CHF from NSR. Finally, the support vector machine (SVM) classifier discriminates the test ECG patterns. The classification results of three sub-modules are fed into the decision mapping level to make a unified valid decision to detect the class of ECG signals and predict the misleading outcomes if any. The main contributions of the proposed work are summarized below

1. Selection of three sub category feature sets based on the statistical p-values.
2. Introduction of three parallel sub-modules to identify NSR, AF, and CHF.
3. Introduction of final decision-level mapping to predict misleading detection of ECG signals.

The rest of the paper is organized in the following way. Section 2 presents the detailed descriptions of the proposed model including the materials used for the electrocardiogram dataset. Section 3 explains the classification results in terms of different performance indices. In Sect. 4 a brief discussion of the experimental results are described. Finally Sect. 5 draws the conclusion of the proposed work.

2 Proposed Model

In this study, we have proposed a new approach of ECG signal diagnosis system to categorize NSR, AF, and CHF. Our proposed model consists of three parallel sub-modules to identify the RR interval of ECG Signals. The schematic diagram of the proposed model is illustrated in Fig. 1.

Initially, the signal is preprocessed for reduction of baseline wondering and power line interference noises. Hence DWT is performed to decompose the input RR interval into five different levels of sub-bands. The feature predictors such as Mean (ME), Standard deviation (SD), Skewness (SKW), Kurtosis (KUT) and Detrended fluctuation analysis (DFA) are extracted from each level of sub band coefficients. Following

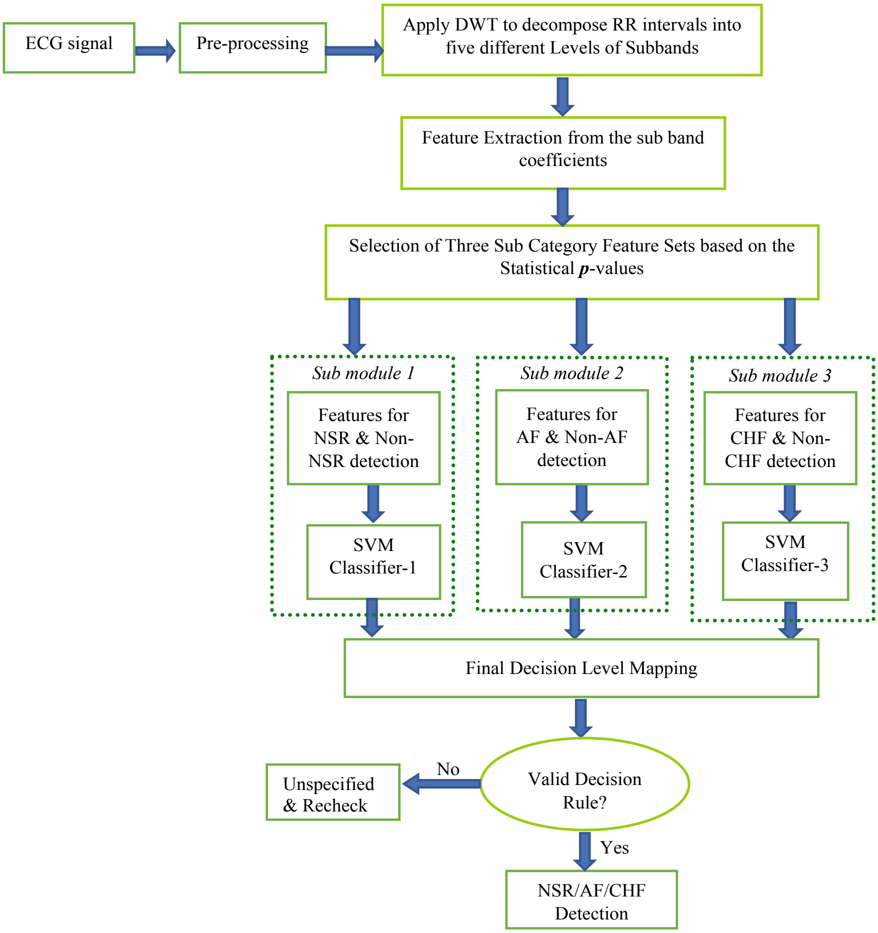

Fig. 1 Schematic diagram of the proposed model

this, statistical *p*-value of each feature is computed to cluster them into three subcategories based on the proposed selection principle. These subcategory features are grouped to identify NSR, AF, and CHF. As shown in Fig. 1, *sub-module-1* categorizes the test ECG patterns as NSR/Non-NSR, *sub-module-2* categorizes the ECG signals as AF/Non-AF and *sub-module-3* categorizes the ECG signal as CHF/Non-CHF respectively.

The SVM classifier of each sub-module discriminates the test ECG patterns. The last level is the decision mapping approach for assessing the valid class of the input ECG signals. Outcomes of three classifiers may produce at most eight combinations. Among them, three combinations are able to determine the valid decision mapping rules as stated below

1. If classifier-1 predicts the ECG pattern as *NSR*, classifier-2 predicts the ECG signal as *Non-AF* and classifier-3 predicts the ECG pattern as *Non-CHF*—Final decision is *Normal Heart Condition.*
2. If classifier-1 predicts the ECG pattern as *Non-NSR*, classifier-2 predicts the ECG signal as *AF* and classifier-3 predicts the ECG pattern as *Non-CHF*—Final decision is *AF type Arrhythmia Suspected*.
3. If classifier-1 predicts the ECG pattern as *Non-NSR*, classifier-2 predicts the ECG signal as Non-*AF* and classifier-3 predicts the ECG pattern as *CHF*—Final decision is *CHF Suspected*.

Any other combinations of classifier-1, classifier-2, and classifier-3 are labeled as *Unspecified* and they go for *Rechecking State.* Each of the processing block of the proposed model and the materials used for this work are discussed in the following sections.

2.1 Material

For the evaluation of our proposed model the open-access database of physio.net (Goldberger 1982) provider has been employed in this work. Three types of ECG database those are used for this research are described below:

(i) MIT-BIH Atrial Fibrillation database, containing 23 one-hour duration two lead ECG signals sampled at 250 Hz,
(ii) BIDMC Congestive Heart Failure RR interval database includes 15 ECG recordings, digitized at 250 samples per second
(iii) MIT-BIT Normal Sinus Rhythm database including 18 long-term ECG recordings digitized at 128 samples per second.

2.2 Preprocessing

In this work, preprocessing of raw ECG signals taken from Physio.net database is decomposed into three steps. In the first step, uniform sampling rate is maintained for all three ECG datasets and the Pan-Tompkins algorithm (Ponikowski et al. 2014) has been used for the detection of R peaks. Then RR signal is constructed by measuring the time interval of successive R peaks (Pan and Tompkins 1985). The last step is the segmentation of the ECG signal. Each frame of RR signals contains 1000 non-overlapping samples.

2.3 Application of DWT

In this work, RR interval signals are first subjected to DWT-db6 (Rajendra Acharya et al. 2015). The DWT decomposes any signals into a set of wavelet coefficient spectrum. The wavelet coefficients are independent to the translations and scaling of the signal and carry the significant information of that signal (Christianini and Taylor 2000). The input signals are evaluated by passing through both the high pass and low pass filter in DWT-db6. Then low pass filter coefficients are again subjected to the low pass filter and the high pass filter. This process is repeated for different levels of decomposition. In this work, five-level decomposition of RR signal is computed to obtain different sub-band coefficients (a_5, d_5, d_4, d_3, d_2, d_1), where a_5 is the approximation coefficient and d_1–d_5 corresponds to detail coefficients in five levels.

2.4 Feature Extraction

For automated diagnosis of ECG signals, the following five feature parameters are extracted from each of the six sub-band coefficients ($a_5, d_5, d_4, d_3, d_2, d_1$) to produce a set of 30 feature characteristics. This feature set expresses the crucial dynamics of RR interval of ECG signal.

Detrended Fluctuation Analysis (DFA): This method has been employed to quantify the scaling property of nonstationary time series data (Peng 1995). This robust technique is addressed to realize the correlation behavior of ECG signal by calculating the scaling exponent from RR signal. Moreover, the scaling exponent evaluates the short-term and long-term correlation present in RR signals that can be useful to recognize the types of heart condition.

Mean (ME): It is estimated to measure the average by computing sum of all the observed outcomes from the given samples divided by the total number of samples. It is expressed as,

$$\overline{y} = 1/n \sum_{i=1}^{n} y_i \tag{1}$$

where n is the no of samples and y corresponds to the observed value. In this work, sample mean has been calculated to analyze the characteristics of RR signal for different cardiac conditions.

Standard Deviation (SD): It is calculated to measure the amount of variation of a given set of values.

Low value of SD indicates close to mean of the set and high SD indicates that the values are spread over a wider range. It is expressed as

$$s = \sqrt{\sum_{i=1}^{n} \frac{(y_i - y_i)^2}{n - 1}} \tag{2}$$

where $\{y_1, y_2, \ldots y_n\}$ are observed values of given sample. $\overline{y}$ is the mean value and n is the sample size. SD has been used to distinguish different states of physiologic conditions from ECG signals.

Skewness (SKW) and Kurtosis (KUT): These two techniques are used to evaluate the probability distribution of the signal (Masetic and Subasi 2013)

$$\text{KUT} = \frac{E\left\{(Y - \mu)^4\right\}}{\sigma^4} \tag{3}$$

$$\text{SKW} = \frac{E\left\{(Y - \mu)^3\right\}}{\sigma^3} \tag{4}$$

where Y denotes the probability distribution of signal and μ and σ represents mean value and standard deviation of data set. These techniques can be used as an efficient tool to identify heart abnormalities from the analysis of RR signal.

2.5 Feature Selection Principle

Feature selection process categorizes the set of 30 feature characteristics into three subsets of feature based on the selection principle proposed in (Sinha and Das 2020). These three subsets of feature are responsible for detection of (a) NSR/Non-NSR; (b) AF/Non-AF; (c) CHF/Non-CHF.

Widely used t-test method is applied to compute the statistical p-value of each feature. The selection principle for grouping of feature set into three subcategories is stated below:

1. Features are grouped having p-value < 0.005 for identifying NSR/AF and NSR/CHF. These features are selected for discrimination of NSR from AF and CHF. Hence, they are used for detection of NSR and Non-NSR signals.
2. Similarly features having p-value < 0.005 for identifying AF/CHF and NSR/AF. Features are exploited to discriminate AF and Non-AF patterns.
3. Finally, features are selected to detect CHF and Non-CHF patterns by grouping those features having p-value < 0.005 for identifying AF/CHF and NSR/CHF.

Other features possessing p-value > 0.005 for identifying any of AF/CHF or NSR/CHF or NSR/AF are labeled as insignificant features and discarded from the detection pipeline.

2.6 Classifier

In this study, SVM is used for the classification of RR episodes from the extracted features. SVM is a widely used powerful classifier developed on the basis of identifying the optimum hyperplane between two classes (Ratnakar et al. 2009). In SVM, kernel function is used to covert the nonseparable nonlinear signals to higher dimensional feature space. The performance of SVM depends on the types of kernel used. In this work, we have used Radial Basis Function (RBF) as kernel transformation function for discriminating different types of ECG signals to achieve higher classification accuracy.

2.7 Decision Level Mapping

In the proposed approach, outcomes of three classifiers may produce at most eight combinations as they produce two possible states—Yes/No. Among these outcomes, three combinations are valid for correct decision mapping rules and rest of the combinations give rise to ambiguous decisions. For example, if the classification result the classer 1 is NSR and other two classifier shows Non-AF and Non-CHF, respectively, the final prediction decision level will be Normal ECG class. Hence, misleading outcome from any one of the classifiers addresses the ambiguity and prescribe the rechecking option of the ECG signals with other timing segments of same patient. As a result, possibility of incorrect prediction of arrhythmia is less for the proposed approach.

Table 1 Prediction of misleading outcomes by the proposed model

	Classifier-1	Classifier-2	Classifier-3	Decision level result
Initial outcomes	Non-NSR	AF	CHF	Unspecified (misleading result)
After rechecking	Non-NSR	AF	Non-CHF	AF
Initial outcomes	Non-NSR	Non-AF	Non-CHF	Unspecified (misleading result)
After rechecking	NSR	Non-AF	Non-CHF	Normal
Initial outcomes	NSR	AF	Non-CHF	Unspecified (misleading result)
After rechecking	NSR	Non-AF	Non-CHF	Normal
Initial outcomes	Non-NSR	AF	CHF	Unspecified (misleading result)
After rechecking	Non-NSR	Non-AF	CHF	CHF
Initial outcomes	NSR	AF	CHF	Unspecified (misleading result)
After rechecking	NSR	Non-AF	Non-CHF	Normal

3 Experimental Result

In this work, our proposed model is designed to discriminate two severe abnormal cardiac conditions such as AF and CHF from the NSR signals. For validating the proposed approach, ECG signals are taken from Physio.net database. In the proposed model, following the fundamental preprocessing stages, DWT is applied to decompose RR intervals into five different levels of sub bands. Hence various features are extracted to characterize the nonstationary features of RR signal such as long-term memory effect, fractality, complex dynamics, scaling behaviors, and so on. Categorization of extracted features into three clusters initiates the parallel analysis scheme of ECG signal. Furthermore, decision level mapping approach predicts the misleading results to improve the reliability of the proposed model. According to the proposed decision mapping rule, if the outcomes of three classifiers are labeled as unspecified, this model prescribes rechecking state by another segment of ECG data for the same patient.

Table 1 describes some of the unspecified conditions appeared in the experiments and final valid results after rechecking state. This improvement in detection accuracy can be achieved by the prediction of misleading outcomes (Fig. 2).

4 Discussion

In this study, a new model has been proposed to discriminate two severe heart diseases AF and CHF from normal heart conditions. We have designed a robust, automated diagnostic system to classify ECG signals by analyzing the features of multilevel decomposed RR signals. Many studies have been found to identify normal sinus rhythm and AF patients by analysis of ECG signal. In this study, our main objective is to discriminate both AF and CHF categories from NSR signals by analyzing the

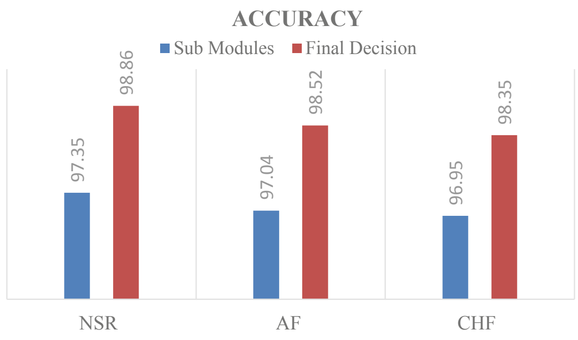

Fig. 2 Overall accuracy of the proposed model

Table 2 Summary of the classification performances of the proposed model with other research works

S. No.	Work	Year	ECG class	Classifier	Accuracy (%)
1	Liao et al. (2015)	2015	NSR, CHF	SVM	97.27
2	Kamath et al. (2015)	2015	NSR, CHF	ROC	98.2
3	Masetic et al. (2013)	2013	NSR, CHF	DT	99.86
4	Maryam and Hassan (2012a)	2012	NSR, AF	SVM	96.3
5	Martis et. al (2012)	2013	NSR, AF	KNN Classifier	97.65
6	Tripathy et al. (2017)	2017	NSR, AF	KNN Classifier	98.67
7(a)	Proposed model	–	NSR	SVM	98.86
7(b)	Proposed model	–	AF	SVM	98.52
7(c)	Proposed model	–	CHF	SVM	98.35

HRV signal. Also, parallel sub-modules are introduced to predict the misleading outcome to distinguish NSR, AF, and CHF patients.

Table 2 shows the comparison of experimental results of the proposed model with current scientific research works. From the performance point of view, our proposed model produces encouraging results and predicts the misleading outcomes efficiently.

5 Conclusion

This work presents a new model for detection of AF and CHF at early stages to reduce the risk of mortality related to each other. Novelty of this model is prediction of misleading outcomes by addressing the concept of decision level mapping approach. However, the classification accuracies of different sub-modules may be further improved by extracting new feature combinations. Further improvement in feature selection strategy may also refine the classification performances. In a future study, we shall consider the mentioned aspects of improvements.

Acknowledgements This work is supported by the Center of Excellence (CoE) in Systems Biology and Biomedical Engineering, TEQIP Phase-III, University of Calcutta funded by the World Bank, MHRD India.

References

Acharya UR, Kannathal N, Krishnan SM (2004) Comprehensive analysis of cardiac health using heart rate signals. Physiol Meas 25(5):1139–1151

Acharya UR, Fujita H, Sudarshan VK, Oh SL, Muhammad A, Koh JEW, Tan JH, Chua KC, Chua KP, Tan RS (2016) Application of empirical mode decomposition (EMD) for automated identification of congestive heart failure using heart rate signals. Neural Comput Appl 1–22

Al-Khatib SM, Wilkinson WE, Sanders LL, McCarthy EA, Pritchett ELC (2000) Observations on the transition from intermittent to permanent atrial fibrillation. Am Heart J 140(1):142–145

Annavarapu A, Kora P (2016) Ecg-based atrial fibrillation detection using different orderings of conjugate symmetric–complex hadamard transform. Int J Cardiovasc Acad 2(3):151–154

Cerutti S, Mainardi L, Porta A, Bianchi A (1997) Analysis of the dynamics of RR interval series for the detection of atrial fibrillation episodes. Comput Cardiol 77–80

Christianini N, Taylor JS (2000) An introduction to support vector machines and other kernel-base

Feinberg WM, Blackshear JL, Laupacis A, Kronmal R, Hart RG (1995) Prevalence, age distribution, and gender of patients with atrial fibrillation. Arch Intern Med 155(5):469–473

Go AS, Hylek EM, Phillips KA, Chang Y, Henault LE, Selby JV, Singer DE (2001) Prevalence of diagnosed atrial fibrillation in adults. J Am Med Assoc 285(18):2370–2375

Goldberger AL (1982) A specific ECG triad associated with congestive heart failure. Pacing Clin Electro Physio l 5:593–599

Kamath C (2015) A new approach to detect congestive heart failure using detrended fluctuation analysis of electrocardiogram signals. J Eng Sci Technol 10:145–159

Khaled AS, Owis MI, Mohamed ASA (2006) Employing time-domain methods and poincare plot of heart rate variability signals to detect congestive heart failure. BIME J 1:35–41

Lee J, Reyes BA, McManus DD, Maitas O, Chon KH (2013) Atrial fibrillation detection using an iphone 4s. IEEE Trans Biomed Eng 60(1):203–206

Liao KYK, Chiu CC, Yeh SJ (2012) A novel approach for classification of congestive heart failure using relatively short-term ECG waveforms and SVM classifier. In: Proceedings of international multi conference of engineers and computer scientists, Hong Kong

Liu G, Wang L, Wang Q, Zhou G, Wang Y, Jiang Q (2014) A new approach to detect congestive heart failure using short-term heart rate variability measures. PLOS one 9:93399

Lubitz SA, Benjamin EJ, Ellinor PT (2010) Atrial fibrillation in congestive heart failure. Heart Fail Clin 6(2):187–200

Martis RJ, Prasad H, Chakraborty C, Ray AK (2012a) Automated detection of atrial flutter and fibrillation using ECG signals in wavelet framework. J Mech Med Biol 12(5):1240023

Martis RJ, Acharya UR, Mandana K, Ray A, Chakraborty C (2012b) Application of principal component analysis to ECG signals for automated diagnosis of cardiac health. Expert Syst Appl 39(14):11792–11800

Martis RJ, Acharya UR, Prasad H, Chua CK, Lim CM (2013) Automated detection of atrial fibrillation using Bayesian paradigm. Knowl-Based Syst 54:269–275

Maryam M, Hassan G (2012) Prediction of paroxysmal atrial fibrillation based on non-linear analysis and spectrum and bispectrum features of the heart rate variability signal. Comput Methods Programs Biomed 105:40–49

Masetic Z, Subasi A (2013) Detection of congestive heart failures using C4.5 Decision Tree. Southeast Eur J Soft Comput 2:74–77

Murberg TA, Furze G (2004) Depressive symptoms and mortality in patients with congestive heart failure: a six-year follow-up study. Med Sci Monit 10(12):CR643–CR648

Narin A, Isler Y, Ozer M (2014) Investigating the performance improvement of HRV indices in CHF using feature selection methods based on backward elimination and statistical significance. Comput Biol Med 45:72–79

Pan J, Tompkins WJ (1985) A real-time QRS detection algorithm. IEEE Trans Biomed Eng 32(3):230–236

Pazos-Lopez P, Peteiro-Vazquez J, Carcía-Campos A, García-Bueno L, de Torres JPA, Castro-Beiras A (2011) The causes, consequences, and treatment of left or right heart failure. Vasc Health Risk Manage 7:237

Pecchia L, Melillo P, Sansone M, Bracale M (2011a) Discrimination power of short-term heart rate variability measures for CHF assessment. IEEE Trans Inf Technol Biomed 15(1):40–46

Pecchia L, Melillo P, Bracale M (2011b) Remote health monitoring of heart failure with data mining via CART method on HRV features. IEEE Trans Biomed Eng 58: 800–804

Peng CK (1995) Quantification of scaling exponents and crossover phenomena in nonstationary heartbeat time series. Chaos 5(1):82–87. https://doi.org/10.1063/1.166141

Ponikowski P, Anker SD, AlHabib KF, Cowie MR, Force TL, Hu S, Jaarsma T, Krum H, Rastogi V, Rohde LE, Samal UC, Shimokawa H, Siswanto BB, Silwa K, Filippatos G (2014) Heart failure: preventing disease and death worldwide, ESC Heart Fail 1(1):4–25

Prakash A, Saksena S, Hill M, Krol RB, Munsif AN, Giorgberidze I, Mathew P, Mehra R (1997) Acute effects of dual site right atrial pacing in patients with spontaneous and inducible atrial flutter and fibrillation. J Am Coll Cardiol 29(5):1007–1014

Rajendra Acharya U et al (2015) Computer-aided diagnosis of diabetic subjects by heart rate variability signals using discrete wavelet transform method. Knowl Based Syst. https://doi.org/10.1016/j.knosys.2015.02.005

Ratnakar M, Sunil KS, Nitisha J (2009) Signal filtering using discrete wavelet transform. Int J Recent Trends Eng

Shiyovich A, Wolak A, Yacobovich L, Grosbard A, Katz A (2010) Accuracy of diagnosing atrial flutter and atrial fibrillation from a surface electrocardiogram by hospital physicians: analysis of data from internal medicine departments. Am J Med Sci 340(4):271–275

Sinha N, Das A (2020) Automatic diagnosis of cardiac arrhythmias based on three stage feature fusion and classification model using DWT. Biomed Signal Process Control. https://doi.org/10.1016/j.bspc.2020.102066

Thakre TP, Smith ML (2006) Loss of lag-response curvilinearity of indices of heart rate variability in congestive heart failure. BMC Cardiovasc Disorders 6:27

Tripathy RK, Mario R, Paternina A, Jung GA, Pattanaik P (2017) Automated detection of atrial fibrillation ECG signals using two stage VMD and atrial fibrillation index. Mech Med Biol 17(7):1740044

Yu SN, Lee MY (2012) Bispectral analysis and genetic algorithm for congestive heart failure recognition based on heart rate variability. Comput Biol Med 42:816–825

Normalized Average Gradient-Based Fusion Method in Shearlet Domain for Studying the Prognosis of Alzheimer's Disease

Suranjana Mukherjee and Arpita Das

Abstract In the present study, functional and anatomical information is merged to analyze the prognosis of *Alzheimer's disease (AD).* The shift-invariant *non-subsampled shearlet transform (NSST)* based decomposition technique is employed to restore all possible directional information of the source images. Then maximum *root mean square of local absolute energy (RMLAE)* based selection and *normalized average gradient (NAG)* scheme is applied for *lower frequency subband (LFSB)* and *higher frequency subbands (HFSBs)*, respectively, to combine multimodal information in a single frame. The proposed fusion rule is able to combine the utmost information of *LFSB* and every finer texture related to edges and notches. The fused component has been generated by inverse *NSST*. Efficiency of the proposed fusion scheme has been reflected in the experimental results.

Keywords MRI · MST · PET

1 Introduction

In medical diagnosis, a single imaging procedure cannot provide all the information alone. For example, *magnetic resonance imaging (MRI)* provides the anatomical information like soft tissue regions. On the other hand, from *positron emitted tomography (PET),* functional information like blood flow, food activity and metabolism of affected organ is obtained (Wang et al. 2014; Das and Bhattacharya 2017). Hence, the fused image of different modalities in one composite frame saves valuable time of a doctor in diagnostic procedure.

Multi-scale transform (MST) is widely used in combining multimodal information (Liu et al. 2015; Pajares and Cruz 2004; Singh et al. 2012; Miao et al. 2011). The wavelet (WT) based methods like discrete wavelet transform (DWT), stationary wavelet transform (SWT), dual tree complex wavelet transform (DTCWT) consider the only three directional information namely horizontal, vertical and diagonal. Hence, the finer features are lost in the fused images.

S. Mukherjee (✉) · A. Das
Department of Radio Physics and Electronics, University of Calcutta, Kolkata, India

M. Mukherjee et al. (eds.), *Advances in Medical Physics and Healthcare Engineering*, Lecture Notes in Bioengineering, https://doi.org/10.1007/978-981-33-6915-3_4

The pseudo-Gibbs phenomenon distorts the original information during up- and down-sampling process of WT. NSST (Easley et al. 2008) is preferred in the present work to overcome the problems like lack of directionality and down-up-sampling. The fusion rule plays a crucial role in combining multimodal information after decomposition. The conventional *simple averaging process (SAP)* and *max* rule for merging *LFSB* and *HFSB* may lose the salient features and degrade the contrast severely (Singh et al. 2012; Miao et al. 2011). In many of the recent works, *local average energy* (*LAE)* techniques are employed popularly for improving clarity and contrast (Srivastava et al. 2016; Yang et al. 2016; Yin et al. 2018). Srivastava et al. have combined both subband and coefficients by employing *LAE* (Srivastava et al. 2016). Yang et al. has combined *LFSB* and *HFSBs* images by *LAE* based on the maximum coefficient strength and the maximum of local type-2 fuzzy-entropy rule, respectively (Yang et al. 2016). Yin et al. presented a fusion model in *NSST* domain in which *LFSB* are fused by multiplying *LAE* with weighted sum of eight neighborhood-based modified Laplacian operator (Yin et al. 2018). On the other hand, *HFSBs* are combined using a pulse adaptive pulse coupled neural network model. The fused images have improved clarity in these approaches (Srivastava et al. 2016; Yang et al. 2016; Yin et al. 2018). It has been seen in one of our earlier works (Mukherjee and Das 2020) *RMLAE* servers better than conventional *LAE*. Thus, selection of maximum of *RMLAE* is preferred in the present work along with *NAG* scheme for merging *HFSBs.*

The rest of the article is organized as follows. Section 2 describes the proposed methodology. Experimental evaluation and its comparative analysis are presented in Sect. 3. The subjective and objective evaluations are discussed in this section and some conclusions have been drawn in Sect. 4.

2 Proposed Method

The YUV plane is preferred color plane in this approach for the *PET* image to preserve the proper color detail which may blur in conventional *red (R), green (G), blue (B)* plane. *Y* is the luminance component and *U, V* are the two chrominance parts in the *YUV*-color plane. The sub-images are fused according to the proposed fusion rules. Basic framework of the proposed approach is described in Fig. 1.

The fusion steps are as follows.

(a) Extract *R, G, B* plane of *PET* and convert to *YUV*-color space.
(b) Decompose the *MRI* image, and the *Y*-plane of *PET*, to three levels in *NSST* domain.
(c) Combine the *LFSB* and *HFSB* according to the proposed fusion rules.
(d) Reconstruct the fused components by applying inverse *NSST*.
(e) Integrate fused *Y*-plane with *U*, *V* components.
(f) Convert *YUV* plane to *RGB* plane to obtain fused image.

Every relevant block of Fig. 1 is described in the following section.

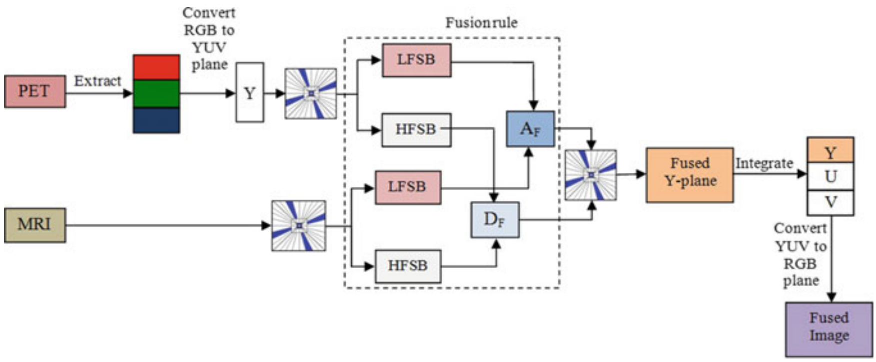

Fig. 1 Block diagram of proposed scheme

2.1 Non-subsampled Shearlet Transform

The shift invariance in *NSST* is achieved by the non-subsampled Laplacian pyramidal filter bank scheme, in which pseudo-Gibbs phenomenon is suppressed properly because downsamplers are replaced with convolutions. The 'maxflat' is used as pyramidal filter in NSST analysis and images are decomposed into 3 levels. In the directional localization, the frequency plane is decomposed into a *LFSB* and several numbers of trapezoidal *HFSBs* utilizing shift-invariant shearing filter as a result edge/color information of source images are preserved in the fused images. For j level of decomposition, a pair of trapezoids known as shearlets of size $2^{2j} \times 2^{j}$ (approx) is produced which are oriented along the line slope $l \times 2^{-j}$, where l is any integer value and it is described in Fig. 2. Inverse NSST is obtained by the summation of shearing filter (Easley et al. 2008).

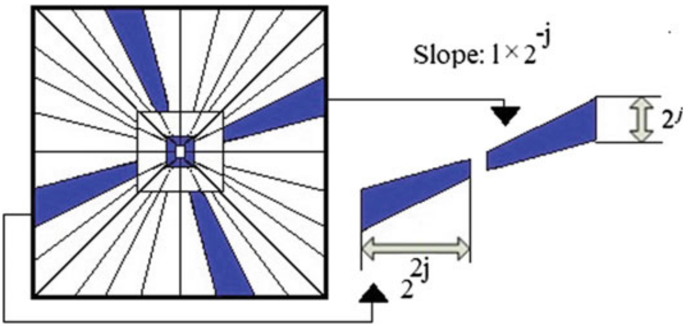

Fig. 2 Representation of shearlets

2.2 Combination of LFSB and HFSB by Proposed Method

The *RMLAE* is estimated by placing a 3×3 sliding window around the pixel locations to incorporate the salient features of a significant region. The mathematical representation is as follows-

$$A_A(i, j) = \left[\frac{1}{3 \times 3} \sum_{m=1}^{3} \sum_{n=1}^{3} LFSB_A(i + m, j + m) \right] \text{ and}$$
$$A_B(i, j) = \left[\frac{1}{3 \times 3} \sum_{m=1}^{3} \sum_{n=1}^{3} LFSB_B(i + m, j + m) \right] \quad (1)$$

The *LFSB* are merged by utilizing maximum *of RMLAE* selection rule which is very simple and computationally efficient. The decision mapping is as follows-

$$\begin{aligned} LFSB_{F,k,l}(i, j) &= A_{A,k} \text{ for } A_{A,k} \geq A_{B,k}(i, j) \\ &= A_{B,k} \text{ for } A_{A,k} < A_{B,k}(i, j) \end{aligned} \quad (2)$$

where $A_{A,k}$ and $A_{B,k}$ are the *RMLAE* of *LFSB* of image *A* and *B* with *k*th decomposition level at (i, j) spatial location.

The average gradient (*AG*) of *X* and *Y*-direction are estimated for better representation of spatial structures related to edges, contours, textural variations of *HFSBs*. The mathematical representation for estimation of *AG* for the *HFSBs* is as follows-

$$AG_A = \frac{1}{M \times N} \sum_{i=0}^{M-1} \sum_{j=0}^{N-1} \sqrt{\frac{1}{2}\left(I_{X,A}^2 + I_{Y,A}^2\right)} \text{ and}$$
$$AG_B = \frac{1}{M \times N} \sum_{i=0}^{M-1} \sum_{j=0}^{N-1} \sqrt{\frac{1}{2}\left(I_{X,B}^2 + I_{Y,B}^2\right)} \quad (3)$$

where I_X and I_Y denotes the gradient of the *HFSBs* in *X*- and *Y*-direction, respectively.

The, *NAG* is there to highlight the detail information of both modalities. The relevant factor is calculated as follows-

$$Q_A = \frac{AG_A}{AG_A + AG_B} \text{ and } Q_B = \frac{AG_B}{AG_A + AG_B} \quad (4)$$

Now *HFSBs* are merged as follows-

$$HFSB_{F,k} = Q_A * HFSB_{A,k} + Q_B * HFSB_{B,k} \quad (5)$$

3 Experimental Result

3.1 Dataset Preparation

The entire fusion scheme has been implemented on different sagittal slices of brain *MRI* and *PET* images of a 70-year old man, who is suffering from mild *AD* as described by Havard University (Johnson and Becker 2003). The proposed method is compared with *SAP-max* rule in DWT and SWT domain. The three levels of decomposition is performed for every case to obtain a fair comparison.

3.2 Analyses of Fusion Result

It is evident that DWT and SWT techniques are suffering from poor contrast and lack of visual clarity. The fusion scheme using DWT suffers from Gibbs phenomenon severely. It is suppressed moderately in case of SWT as down- and up-sampling is avoided by inserting zeros in between the filter coefficients. But SWT captures information of only three directions like DWT. Hence, some of the directional information of source images is lost in the fused images while *NSST* with the proposed rule is well enough to restore the color/edge information.

There are some parameters like entropy, standard deviation (STD) and AG to evaluate the information content, visual clarity and sharpness of the fused images (Mukherjee and Das 2020). The quantitative evaluation in Table 1 shows that the fused image is information rich with improved visual clarity and good texture distribution.

There is presence of artifacts for fusion in DWT domain during up- and down-sampling. So, that entropy and AG is more than that of SWT. The superiority of the proposed scheme is reflected in quantitative evaluation also. All the parameters have the highest value in comparison with the other methods.

Table 1 Quantitative evaluation

Image set	Evaluation parameter	DWT	SWT	Proposed
Set1 of Fig. 3	Entropy	4.8227	4.7916	4.9520
	STD	0.2272	0.2339	0.2448
	AG	0.0085	0.0068	0.0175
Set2 of Fig. 3	Entropy	4.9239	4.9094	5.1556
	STD	0.2457	0.2530	0.2673
	AG	0.0093	0.0071	0.0185
Set3 of Fig. 3	Entropy	5.0216	5.0139	5.2393
	STD	0.2404	0.2420	0.2557
	AG	0.0102	0.0091	0.0184

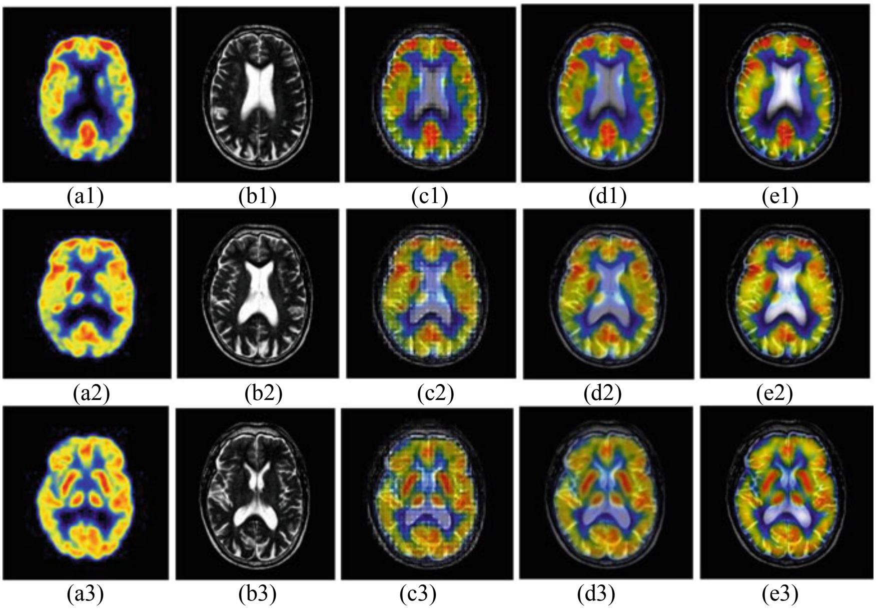

Fig. 3 Fusion of multimodal images **a1**–**a3** PET **b1**–**b3** MRI **c1**–**c3** DWT **d1**–**d3** SWT **e1**–**e3** proposed

4 Conclusion

The proposed approach overcomes the limitations of widely used sap-max rule. The NSST-based decomposition serves best in restoring directional detail. The maximum of *RMLAE* selection serves excellently in preserving information and clarity. The *NAG*-based combination prominently highlights the significant directional detail of both modalities of images. The present scheme is able to restore every salient detail related to edges, curvatures and notches with enhanced information restoration and clarity. The integrated image may help in accurate diagnosis as well as reduce the storage space of preserving multiple images.

Acknowledgements This work is financially supported by the Center of Excellence (CoE), University of Calcutta, funded by the World Bank, MHRD India. The authors are grateful to the radiologist Dr. Soumitra Halder of Metiabruz Super Speciality Hospital for providing us valuable comments on the subjective evaluation of the proposed scheme.

References

Das A, Bhattacharya M (2017) Study on neurodegeneration at different stages using MR images: computational approach to registration process with optimisation techniques. Comput Methods Biomech Biomed Eng Imag Vis 5(3):165–182

Easley G, Labate D, Lim W (2008) Sparse directional image representations using the discrete shearlet transform. Appl Comput Harmon Anal 25(1):25–46

Johnson KA, Becker JA (2003) The whole brain atlas. Available on line at: https://www.med.harvard.edu/aanlib/home.html.

Liu Y, Liu S, Wang Z (2015) A general framework for image fusion based on multi-scale transform and sparse representation. Inf Fusion 24(1):147–164

Miao QG, Shi C, Xu PF, Yang M, Shi YB (2011) A novel algorithm of image fusion using shearlets. Opt Commun 284(6):1540–1547

Mukherjee S, Das A (2020) Vague set theory based segmented image fusion technique for analysis of anatomical and functional images. Exp Syst Appl 113592

Pajares G, Cruz JM (2004) A wavelet-based image fusion tutorial. Pattern Recogn 37(9):1855–1872

Singh R, Srivastava R, Prakash O, Khare A, Srivastava R (2012) Multi-modal medical image fusion in dual tree complex wavelet transform domain using maximum and average fusion rules. J Med Imaging Health Inf 2(2):168–173

Srivastava R, Prakash O, Khare A (2016) Local energy-based multimodal medical image fusion in curvelet domain. IET Comput Vis 10(6):513–527

Wang L, Li B, Tian L (2014) Multimodal medical volumetric data fusion using 3-D discrete shearlet transform and global-to-local rule. IEEE Trans Biomed Eng 61(1):197–206

Yang Y, Que Y, Huang S, Lin P (2016) Multimodal sensor medical image fusion based on type-2 fuzzy logic in NSCT domain. IEEE Sens J 16(10):3735–3745

Yin M, Liu X, Liu Y, Chen X (2018) Medical image fusion with parameter-adaptive pulse coupled neural network in nonsubsampled shearlet transform domain. IEEE Trans Instrum Measure 68(1):49–64

In Vitro Biocompatibility Study on Implantable Crystalline Silica-Aluminium Metal-Based Hybrid Composites

Sourav Debnath and Akshay Kumar Pramanick

Abstract Attempt has been taken towards carrying out detailed investigation about the relevance of using fabricated crystalline silica-aluminium metal-based hybrid composite as biomedical implants, in vitro. In vitro corrosion study has carried out into simulated body fluid (SBF), and corresponding changes of surface morphology have found out and reported. In addition, bactericidal analysis and cytotoxicity study have carried out and reported for the same fabricated metal matrix composites as per available standards.

Keywords Crystalline silica-aluminium metal matrix hybrid composite · Surface roughness · In vitro corrosion · Optical microscopy · Bactericidal · Cytotoxicity

1 Introduction

Replacement of natural bone with implants is sometimes essential after severe accident, bone-related diseases, or major tumour removal. Moreover, after a certain age, human are suffering from various joint-related pain and nowadays joint replacement is most common thing. Replacement with artificial implants can relieve the affected patients and improves the quality of living (Learmonth et al. 2007). The used biomedical implants should be biocompatible in nature and will not create any adverse reactions with host tissues. Successful surgery not only depends upon the knowledge of surgeon but also the materials used as implants (Learmonth et al. 2007; Mizuno 2014).

After implantation, implants should direct contact with body fluids and blood tissues. Hence, it is a useful practice to study the behaviour of implantable biomaterials into simulated body fluid, in vitro. In this regard, corrosion test into body fluids (Yang et al. 2006; Abidin et al. 2010; Bidhendi and Pouranvari 2011) is very feasible because corrosion not only the cause of mechanical failure of implantable biomaterials but also may cause tissue inflammations. Hence, corrosion directly hampers the biocompatibility and materials properties.

S. Debnath (✉) · A. K. Pramanick
Metallurgical and Material Engineering Department, Jadavpur University, Kolkata 700032, India

M. Mukherjee et al. (eds.), *Advances in Medical Physics and Healthcare Engineering*, Lecture Notes in Bioengineering, https://doi.org/10.1007/978-981-33-6915-3_5

Implants should proceed under cytotoxicity and bactericidal analysis for safety assessments (Mizuno 2014; Radu et al. 2008). During last few years, considerable focus has been concentrated on fabricating "tissue trilored" biocompatible implants (Wang et al. 2010; Yamamoto et al. 2007; Tsuchiya et al. 1993; Liu et al. 2015; Vergaro et al. 2010; Nie et al. 2010). This research takes care of this by carrying out cytotoxicity and bactericidal analysis separately.

Present study focused towards fabricating in vitro biocompatible crystalline silica-aluminium metal-based hybrid composites. Several research have carried out on various grads of Mg/Mg-based alloys, Co–Cr alloys, zirconia, titanium, stainless steel or polymer-based implants (Learmonth et al. 2007; Mizuno 2014; Yang et al. 2006; Abidin et al. 2010; Bidhendi and Pouranvari 2011; Radu et al. 2008; Wang et al. 2010; Yamamoto et al. 2007; Tsuchiya et al. 1993; Liu et al. 2015; Vergaro et al. 2010; Nie et al. 2010; Takamori et al. 2008) but little efforts have seen for composites, especially aluminium metal matrix composites with such compositions.

2 Materials and Methods

2.1 Fabrication of Crystalline Silica-Aluminium Metal-Based Hybrid Composite

Crystalline silica-aluminium metal-based hybrid composites have fabricated through "Powder Metallurgy" technique maintaining the steps of milling and mixing, pressing and finally sintering conducted at 600 °C temperature for an hour. In fabricated composites, aluminium matrix is reinforced with crystalline silica by 20 wt% and beta-tricalcium phosphate by 10 wt%. Mentioned that sintering was carried out separately into inert muffle furnace and hot press as described elsewhere (Debnath and Pramanick 2019). Any reaction has not addressed between matrix and hybrid reinforcements for the composite fabricated into hot press (Debnath and Pramanick 2019,2016; Debnath et al. 2016). The prepared metal matrix composite fabricated through hot pressing has preferable physical, mechanical as well as some evaluated in vitro biological properties like bioactivity, haemocompatibility along with satisfactory clot test which is already been demonstrated in our previous study (Debnath and Pramanick 2019).

2.2 Characterization and Biological Evaluations

Characterization and biological evaluations have discussed below.

2.2.1 Microstructure

Crystalline silica-aluminium metal-based hybrid composite was considered for surface morphology analysis before and after in vitro corrosion study, using "LEICA Optical Microscopy, model DM-2700M Image Analyzer."

2.2.2 Surface Roughness

Fabricated crystalline silica-aluminium metal-based hybrid composite was considered for surface roughness measurement as surface roughness has great influence on biocompatibility of implants. Roughness value has measured as per ISO 5436-2 standards employing surface roughness tester, model "Taylor Hobson instrument/Sutronic 3+."

2.2.3 In Vitro Corrosion Test

SBF was prepared followed by "Kokubo's method" (Mizuno 2014; Kokubo et al. 1990). In vitro corrosion study has performed into this SBF medium at identical physiological temperature (36–37 °C), employing "POTENTIOSTAT GALVANOSTAT Super-PG 1000."

2.2.4 Bactericidal Study

Distilled water treated "Nutrient agar media" was autoclaved at temperature 121 °C for the period of 20 min for making it sterile. Mixing with "*Staphylococcus aureus*" has carried out and distributed in the petri dish. Time has provided for solidifying the medium. Fabricated composite under study has considered and poured into the porcelain bit. Due to capillary action, sample has come out into the bit. Used two bits have different concentrations, 2 mg/10 mL and mg/10 mL, which were kept into the same petri dish. At last, the petri dish, carrying the sample under study, has incubated for 24 h, maintaining temperature 30–35 °C.

2.2.5 Cytotoxicity Study

Crystalline silica-aluminium metal-based hybrid composites fabricated into inert muffle furnace and hot press were considered separately for cytotoxicity study. "Prepared peripheral blood mononuclear cells" (PBMC) have incubated with the samples for 24 h. MTT has added and again incubated for four hours. Addition of MTT kills the cells and consequently formation of crystals was found out. "Dimethyl sulfoxide" (DMSO) was used after withdrawn the media. Solution has become purple colour depending upon the amount of formed crystal. Optical density was noted against

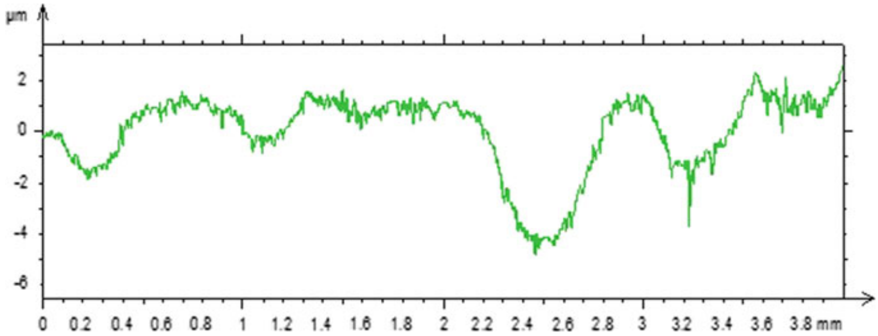

Fig. 1 Surface roughness of crystalline silica-aluminium metal-based hybrid composite

blank when cells are died. Experiment was conducted number of times for each sample under study to get more accuracy.

3 Results and Discussion

Acquired results and consequent discussion are elaborated below.

3.1 Surface Roughness

Figure 1 shows the roughness of fabricated crystalline silica-aluminium metal-based hybrid composite in which arithmetic mean roughness (Ra) was found out 0.405 µm and rms value of surface roughness (Rq) was recorded 0.472 µm. This surface has classified as moderately smooth and useful to proceed biocompatibility evaluations as per ISO/FDIS 23317, Implants for surgery (Mizuno 2014).

3.2 Analysis on In Vitro Corrosion

In vitro corrosion test has performed on fabricated metal matrix composite as shown in Fig. 2 and corresponding I_{corr} and E_{corr} values are recorded in Table 1. It has found out that the value of corrosion is typically low under such test environments.

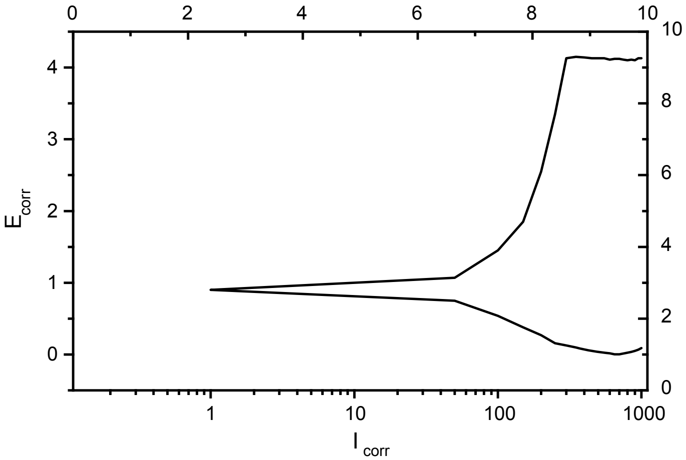

Fig. 2 In vitro corrosion for fabricated crystalline silica-aluminium metal-based hybrid composite into SBF solution

Table 1 In vitro corrosion

Composition	Corrosion current density (I_{corr})	Corrosion voltage (E_{corr})
Crystalline silica-aluminium metal-based hybrid composite	36.808 mA/cm^2	0.885 mV/cm^2

3.2.1 Corroded Surface Evaluation

Figure 3 shows the surface morphology of crystalline silica-aluminium metal-based hybrid composite at different magnifications. In this surface structure, it has observed that reinforcing phases are distributed systematically into aluminium metal matrix.

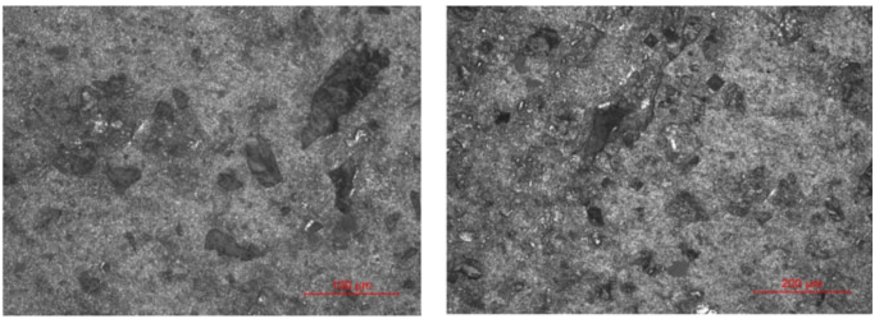

Fig. 3 Surface morphology of crystalline silica-aluminium metal-based hybrid composite

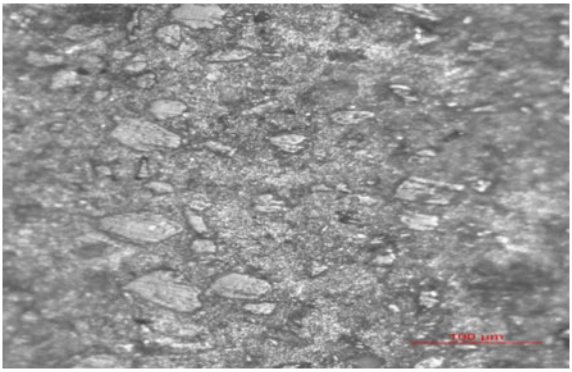

Fig. 4 Crystalline silica-aluminium metal-based hybrid composite after in vitro corrosion test

Figure 4 shows the surface after corrosion test. Crystalline silica-aluminium meta-based hybrid composite makes constructive reaction towards formation of apatite layer under this test environment.

3.3 Bactericidal Study

Antimicrobial activities of candidate metal matrix composite have tested with the degree of growth inhibition of microorganisms and corresponding petri dish has shown in Fig. 5. No zone of inhibition has found out during 24 h of observations as seen in Fig. 5.

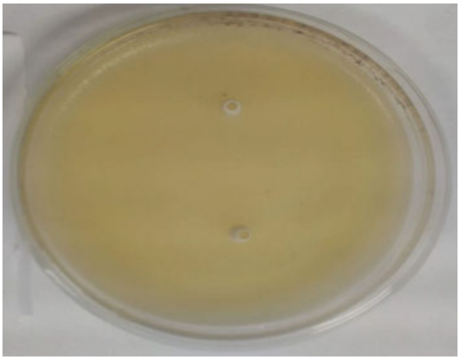

Fig. 5 Bactericidal analysis on crystalline silica-aluminium metal-based hybrid composite

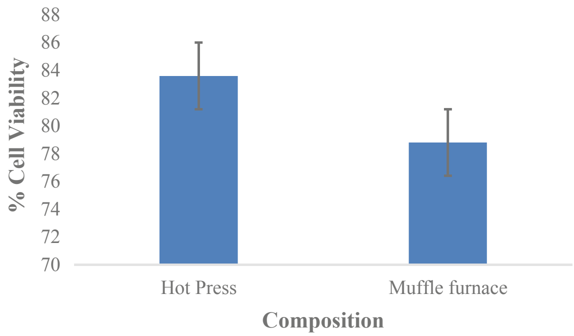

Fig. 6 Cytotoxicity study on crystalline silica-aluminium metal-based hybrid composite

3.4 Cytotoxicity

Figure 6 shows the result obtained from cytotoxicity study based on crystalline silica-aluminium metal-based hybrid composites. Crystalline silica-aluminium metal-based hybrid composite fabricated into hot press shows more than 80% cell viability and hence, considered as non-cytotoxic as per ISO 10993-5 standards.

4 Conclusion

Significant conclusions based on in vitro biocompatibility studies on fabricated crystalline silica-aluminium metal-based hybrid composites are as follows.

- Crystalline silica-aluminium metal-based hybrid composite fabricated into hot press has satisfactory in vitro corrosion properties.
- Crystalline silica-aluminium metal-based hybrid composite possesses practically no bactericidal property. Hence, this fabricated metal matrix composite will not able to kill the existing tissues and not make any adverse reactions to human body after implantation.
- Based on the results on cytotoxicity study, the crystalline silica-aluminium metal-based hybrid composite fabricated into hot press can be classified as non-cytotoxic in nature.

References

Abidin NIZ, Martin D, Atrens A (2010) Corrosion of high purity Mg, AZ91, ZE41 and Mg2Zn0.2Mn in Hank's solution at room temperature. Corros Sci 53:862–872

Bidhendi HRA, Pouranvari M (2011) Corrosion study of metallic biomaterials in simulated body fluid. Assoc Metal Eng Serbia (AMES), Metal MJoM 17(1):13–22

Debnath S, Pramanick AK (2016) Development and evaluation of various properties of crystalline silica-aluminium metal based composites. IJERGS 4(2):236–245

Debnath S, Pramanick AK (2019) Fabrication of beta-tricalcium phosphate/crystalline silicaaluminium metal matrix composites: physical, mechanical, and in vitro biological evaluations. Biotechnol Biol Sci 48–54

Debnath S, Basu S, Pramanick AK (2016) Development and study on various properties of titanium oxide-tri calcium phosphate composites through powder metallurgy technique. IOSR J 2(Special issue 2K16):1–6

Kokubo T, Kushitani H, Sakka S, Kitsugi T, Yamamoto T (1990) Solutions able to reproduce in vivo surface-structure changes in bioactive glass-ceramic A-W. J Biomed Mater Res 24:721–734

Learmonth ID, Young C, Rorabeck C (2007) The operation of the century: total hip replacement. Lancet 370(9597):1508–1519

Liu HY, Du L, Zhao YT, Tian WQ (2015) In vitro hemocompatibility and cytotoxicity evaluation of halloysite nanotubes for biomedical application. J Nanomater 2015(article ID 685323):1–9

Mizuno M (2014) Implants for surgery: in vitro evaluation for apatite-forming ability of implant materials, ISO/DIS 23317. International Organization for Standardization (ISO), Geneva, Switzerland

Nie FL, Zheng YF, Wei HC, Yang G (2010) In vitro corrosion, cytotoxicity and hemocompatibility of bulk nanocrystalline pure iron. Biomed Mater 5:1–10

Radu A, Eleonora C, Lucian A, Georgeta C, Virginia V, Cristiana T (2008) In vitro biocompatibility testing of implantable biomaterials. Roumanian Biotechnol Lett 13(4):3863–3872

Takamori ER, Cruz R, Goncalvez F, Zanetti RV, Zanetti A, Granjeiro JM (2008) Effect of roughness of zirconia and titanium on fibroblast adhesion. Artif Organs 32:305

Tsuchiya T, Ikarashi Y, Hata H, Toyoda K, Takahashi M, Uchima T, Tanaka N, Sasaki T, Nakamura A (1993) Comparative studies of the toxicity of standard reference materials in various cytotoxicity tests and in vivo implantation tests. J Appl Biomater 4:153

Vergaro V, Abdullayev E, Lvov YM (2010) Cytocompatibility and uptake of halloysite clay nanotubes. Biomacromolecules 11(3):820–826

Wang BL, Li L, Zheng YF (2010) In vitro cytotoxicity and hemocompatibility studies of Ti-Nb, Ti-Nb-Zr and Ti-Nb-Hf biomedical shape memory alloys. Biomed Mater 5:1–7

Yamamoto A, Kohyama Y, Hosoda H, Miyazaki S, Hanawa T (2007) Cytocompatibility evaluation of Ti-Ni and Ti-Mo-Al system shape memory alloys Mater. Trans. 48:361

Yang H, Yang K, Zhang B (2006) Pitting corrosion resistance of La added 316L stainless steel in simulated body fluids. Mater Lett 61(2007):1154–1157

Segmentation of Brain Tumor Using Cluster Validity Index-Based Fuzzy C-Means Algorithm

Kaustav Das and Arpita Das

Abstract The present work introduces a novel segmentation approach for detection of brain tumor in presence of surrounding obscured tissues. In this view, kernel-based fuzzy clustering algorithm is employed to capture the clear boundary of the tumors. Proposed method also considers two significant features of brain MRI for segmentation; one is regional entropy and the other regional brightness. The most important issue of fuzzy clustering algorithm is the selection of optimal number of clusters prior to the clustering. This work determines the optimal cluster number by introducing the concept of cluster validity indices. Employing five different cluster validity indices, the optimal cluster number is obtained for both of the features. Then, these two features are integrated using principal component analysis method. Following this, shape characteristics of the segmented tumors are extracted for grading the benignancy/malignancy of the tumors. Finally, the superiority of the proposed segmentation approach is compared with similar research works in this field and its efficiency is studied in terms of the classification indices.

Keywords Brain tumors · Regional features · Cluster validity indices · Fuzzy c-means algorithm · Benignancy/malignancy

1 Introduction

Cancer is a life-threatening disease, and one of the most frightening among them is the brain cancer. The survival rate for people with brain cancer decreases with age (American Society of Clinical Oncology (ASCO) 2020). More than a million cases of brain tumor are diagnosed per year in India. A popular and effective technique, Magnetic Resonance Imaging (MRI) provides exquisite detail of the brain, to detect the prognosis of tumor, but sometimes the presence of surrounding soft tissues obscures the tumor outline. In this view, image segmentation is one of the most crucial

K. Das (✉) · A. Das
Department of Radiophysics and Electronics, University of Calcutta, Kolkata, India

A. Das
e-mail: adrpe@caluniv.ac.in

M. Mukherjee et al. (eds.), *Advances in Medical Physics and Healthcare Engineering*, Lecture Notes in Bioengineering, https://doi.org/10.1007/978-981-33-6915-3_6

steps in tumor analysis. There are several popular image segmentation techniques applied in medical imaging but a single approach is not applicable for all types of brain MRI. Hence, there is a need for more advanced and automated approach, which would mostly eliminate the inconveniences present in the conventional techniques and would provide better result for diagnosis of brain tumor.

Based on these, present work introduces a novel cluster validity index-based fuzzy c-means (FCM) clustering algorithm for segmentation of brain MRI. FCM is one of the most popular and widely used algorithms due to its robustness in presence of ambiguity and impreciseness. Two significant regional features of MRI; local entropy and brightness captured by appropriate kernel are utilized as the data of FCM model which accurately detects the prognosis of brain tumors. To combat the problem of manual selection of cluster numbers in FCM algorithm, this work employs five cluster validity indices for prediction of appropriate cluster numbers. Following this segmentation approach, discrimination of benignancy/malignancy of tumors also produces encouraging results.

The proposed method is discussed in Sect. 2. Section 3 provides the experimental results using the proposed detection model and finally Sect. 4, Sect. 5 draws some discussion and conclusion of this work.

2 Proposed Methodology

To resolve high degrees of inhomogeneity present in brain MRI, a novel cluster validity index-based FCM algorithm has been proposed using two significant spatial characteristics of MRI. The framework of the proposed approach, consisting of different blocks is shown in Fig. 1. To abide by the principles of medical ethics, multimodal brain MRIs ($T1$-weighted, $T2$-weighted, Gad, and PD) have been used from benchmarked databases from '*The Whole Brain Atlas-Harvard Medical School*' (Johnson and Becker 2003) and '*The Multimodal Brain Tumor Image Segmentation Benchmark (BRATS)*' (Lastname et al. 2015).

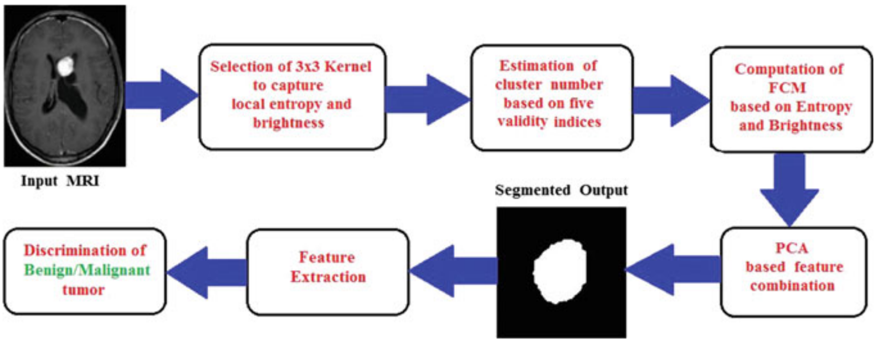

Fig. 1 Framework of the proposed approach

In the following sections, the different blocks of the proposed methodology have been further discussed in detail.

2.1 Significant Feature Selection

From several research works, it has been observed that statistical features like local entropy, brightness, homogeneity, relative variances have been individually used to resolve the impreciseness in edge detection (Despotovic et al. 2015). On the contrary, Das et al. (2019) studied that, the combination of local entropy and local brightness is an effective pair to model the impreciseness present in mammograms. Sometimes, in brain MRI, the presence of overlapped soft tissues flattens the brightness of tumor and hence leads to over/under segmentation problems. As local entropy of a region estimates the information carried by it, surrounding soft tissues occupy different grade of entropy compared to the tumors. Following this, the present study shows that the combinations of local entropy (E) and brightness (B) efficiently resolve the uncertainties present in the process of tumor segmentation.

Regional entropy (E) and brightness (B) are mathematically expressed by the following two equations

$$E = -\sum_{i=1}^{n} p(x_i) \log p(x_i) \tag{1}$$

$$B = \frac{1}{n} \sum_{i=1}^{n} I(x_i) \tag{2}$$

where $X = \{x_1, x_{2,} \ldots, x_i, \ldots, x_n\}$ denotes the set of image pixels and $p(x_i)$ is the probability of occurrence of pixel intensity $I(x_i)$ inside the kernel.

A kernel of size 3×3 ($n = 9$) has been moved across the entire image to fetch different characteristics of E and B, which in turn are used as the data for the proposed approach.

2.2 Cluster Number Selection

A conventional clustering algorithm Fuzzy c-means (FCM) has a great advantage of being more flexible than hard clustering techniques and provides better result in case of overlapped imprecise data. In spite of being advantageous, the most important challenge in FCM algorithm is to predict the optimal number of clusters (Gueorguieva et al. 2017). In this view, present work addresses optimal cluster number selection in terms of various cluster validity indices, prior to the segmentation using FCM algorithm.

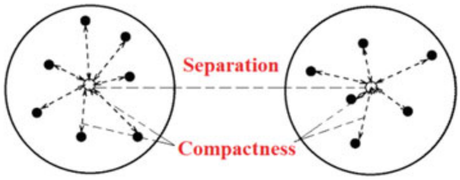

Fig. 2 Compactness and separation within two clusters

Cluster Validity Indices

Cluster validation approach evaluates the obtained results and finds the best partitioning of the given data (Gueorguieva et al. 2017). The two important criteria for selection of the cluster number are *compactness* and *separation* of the underlying data which has been clearly shown in Fig. 2.

Compactness refers to the closeness of the members in each cluster, measured by the variance of cluster members and it should be minimized for better clustering. *Separation* refers to the distance between two different clusters, the inter-cluster distance (Wang and Zhang 2007). In the present work, five effective cluster validation indices have been employed for evaluating the cluster numbers (Wang and Zhang 2007; Bataineh et al. 2011; Pakhira et al. 2004). The validation indices and their mathematical formulations are described below

(i) **Partition Coefficient (*PC*)**: It measures the overlapping between the clusters and its value lies in the range of $[1/K_C, 1]$, where K_C is the number of clusters (Capitaine and Frelicot 2011). Closer the value of PC to unity, more crisp the clustering would be (Gueorguieva et al. 2017).

$$\mathrm{PC} = \frac{1}{n}\sum_{i=1}^{K_c}\sum_{j=1}^{n}\left(\mu_{ij}^2\right) \tag{3}$$

where n is the size of the data matrix, μ_{ij} is the membership value of jth data point in ith cluster.

(ii) **Classification Entropy (*CE*)**: *CE* measures the fuzziness of a given cluster (Capitaine and Frelicot 2011). Hence, CE estimates the effectiveness of partitioning and its value lies between the intervals $[0, \log K_c]$. Lower value of CE reflects better partitioning of dataset Z.

$$\mathrm{CE} = -\frac{1}{n}\sum_{i=1}^{K_c}\sum_{j=1}^{n}\mu_{ij}\log\mu_{ij} \tag{4}$$

(iii) **Separation Coefficient (*SC*)**: *SC* computes the ratio of sum of the separation and compactness of clusters (Gueorguieva et al. 2017). Minimum value of SC indicates the better separation between the clusters.

$$SC = \sum_{i=1}^{K_c} \frac{\sum_{j=1}^{n} \left(\mu_{ij}\right)^x \left\| z_j - c_i^2 \right\|}{n_i \quad \sum_k^{K_c} \left\| c_k - c_i^2 \right\|} \tag{5}$$

where x is the fuzzifier index taken as 2, $\left\| z_j - c_i \right\|$ is the Euclidean distance for jth data point and ith cluster.

(iv) **Separation Index (*SI*)**: *SI* utilizes the minimum distance of separation for the partition validity (Gueorguieva et al. 2017). Lower value of SI indicates better separation.

$$\mathrm{SI} = \frac{\sum_{i=1}^{K_c} \sum_{j=1}^{n} \left(\mu_{ij}\right)^2 \left\| z_j - c_i \right\|^2}{n \ \min_{ik} \| c_k - c_i \|^2} \tag{6}$$

(v) **Xie-Beni's Validation (*XB*)**: *XB* estimates the ratio of total variation within the given clusters and the separation between clusters and its smaller value indicates that the clusters are compact as well as well separated (Xie and Beni 1991).

$$\mathrm{XB} = \frac{\sum_{i=1}^{K_c} \sum_{j=1}^{n} \left(\mu_{ij}\right)^x \left\| z_j - c_i \right\|^2}{n \ \min_{ik} \left\| z_j - c_i \right\|^2} \tag{7}$$

The optimal number of clusters has been selected by the following selection rule—"*For optimal cluster number, the majority of cluster validity indices (PC, CE, SC, SI, XB) must satisfy their respective criteria*".

2.3 FCM Algorithm

FCM is an objective function-based algorithm in which the membership values are assigned to each of the data point (*E*/*B*) corresponding to a cluster depending on the Euclidean distance between the data point and the cluster center (Bezdek et al. 1984; Kang et al. 2009; Adhikari et al. 2015). Higher degrees of membership are assigned to those data points which are close to the cluster center, and hence, the objective function gets minimized accordingly. The objective function of the FCM algorithm has been shown below

$$J^{\mathrm{FCM}}(U, Z, \{D_i\}) = \sum_{i=1}^{K_c} \sum_{k=1}^{M} (\mu_{ik})^m \cdot d_{ik}^2 D_i \tag{8}$$

where $U = [\mu_{ij}]$ denotes the matrix of membership values, Z is the given 'q' dimensional data of 'n' objects, D_i is the local norm inducing matrix which is used as an optimization variable in $U = [\mu_{ij}]$, K_c denotes the center of the clusters, d_{ik}^2 is the

Euclidean metrics which depends on the corresponding Euclidean distance d_{ij}^2 and m denotes the fuzzifier index usually taken as 2 for best results.

The degree of membership value of given dataset Z in the cluster K_c, satisfies the equation below,

$$\sum_{i=1}^{K_c} \mu_{ij} = 1 \text{ for, } 0 \le \mu_{ij} \le 1 \text{ and } K_c = 1, 2, \ldots, n \tag{9}$$

where $\mu_{ij} = \frac{1}{\sum_{t=1}^{K_c} \left(\frac{d_{ij}}{d_{it}}\right)^{\frac{2}{m-1}}}$.

Also, the equations for the cluster center (c_i) and the Euclidean metric (d_{ik}^2) has been stated below-

$$c_i = \frac{\sum_{j=1}^{n} \mu_{ij}^m z_j}{\sum_{j=1}^{n} \mu_{ij}^m} \text{ for } \forall_j = 1, 2, \ldots, n \tag{10}$$

$$d_{ik}^2 = \sum_{j=1}^{K_c} d_{ij}^2 = \sum_{j=1}^{K_c} \left\| z_j - c_i \right\|^2 \text{ for } \forall_j = 1, 2, \ldots, K_c \tag{11}$$

where K_c denotes the cluster number, ${d_{ij}}^2$ is the Euclidean distance between jth data point and the ith cluster center.

2.4 Feature Combination Using Principal Component Analysis

To measure the contributions of each of the statistical features that is, regional entropy and brightness, a popular and extensively used computational technique known as principal component analysis (PCA) has been employed in this work. PCA is an useful approach to find out the principal component of the datasets for both of the features and henceforth, determines the respective weight factors for them (Mukherjee and Das 2020). It works on the principle of computing the covariance matrix created from the datasets of both of the regional features. Hence, it makes the segmentation approach automated and robust.

2.5 Shape-Based Feature Extraction

Several research works have been conducted, to extract information of the region of interest (ROI). The aim of this work is to determine the better feature extraction technique, in case of a particular scenario. From several studies, it has been observed that the malignant tumors consist of uneven shape irregularities in comparison with benign tumors as shown in Fig. 3. Hence, the characterization of tumors in terms of its shape has been the main focus to capture these shape irregularities.

In this view, the proposed method addresses a combination of some conventional shape metrics with a radius vector (r) based shape descriptor (Kurtosis) to study the tumor characteristics of brain MRI. The radius vector-based feature is insensitive to image orientation and alignments (Kobayashi et al. 2008). The mathematical formulations are as follows

$$\text{Kurtosis} = \frac{\frac{1}{N}\sum_{n=1}^{N}[r(n)-m]^4}{\left(\frac{1}{N}\sum_{n=1}^{N}[r(n)-m]^2\right)^2} \tag{12}$$

where N is the total number of contour pixels and mean $m = \frac{1}{N}\sum_{n=1}^{N}[r(n)]$

$$\text{Area Mismatch Ratio(AMR)} = \frac{|\text{CA} - A|}{A} \tag{13}$$

$$\text{Compactness} = \frac{P^2}{4\pi A} \tag{14}$$

$$\text{Solidity} = \frac{A}{\text{CA}} \tag{15}$$

$$\text{Eccentricity} = \frac{W}{L} \tag{16}$$

where W, L, A, P, CA denotes width, length, area, perimeter and convex area of the tumor, respectively.

Based on these extracted feature characteristics, the segmented tumors have been categorized into malignant/benign groups.

Fig. 3 Variation in shape of a tumor

2.6 Classification

In this work, a conventional k nearest neighbor (KNN) classifier has been chosen, to classify the brain tumors into malignant/benign classes. KNN is a supervised classification algorithm which classifies a data point based on its neighboring data points. From known training datasets, KNN classifies the test data based on a similarity measure. The parameter 'k' in KNN algorithm refers to the number of *nearest neighbors* which are determined based on some distance parameters (Zhang et al. 2018). In this work, Euclidean distance measures between the known and the unknown data points have been considered. The performance of the KNN classifier on the proposed FCM model has been evaluated based on some statistical measures and the performance indices such as sensitivity, specificity and accuracy have been estimated by the following mathematical formulations

Sensitivity: It estimates how correctly the classifier can predict the malignant tumors.

$$\text{Sensitivity}(\%) = \frac{\text{TP}}{\text{TP} + \text{FN}} \times 100 \tag{17}$$

Specificity: It estimates how correctly the classifier can predict the benign tumors.

$$\text{Specificity}(\%) = \frac{\text{TN}}{\text{TN} + \text{FP}} \times 100 \tag{18}$$

Accuracy: It estimates the total correctly predicted malignant and benign tumors.

$$\text{Accuracy}(\%) = \frac{\text{TP} + \text{TN}}{\text{TP} + \text{FP} + \text{FN} + \text{TN}} \times 100 \tag{19}$$

where (TP): number of previously known malignant tumors correctly identified as malignant; (TN): number of previously known benign tumors correctly identified as benign; (FP): number of previously known benign tumors incorrectly identified as malignant; (FN): number of previously known malignant tumors incorrectly identified as benign.

Further, this classifier has been validated using a popular technique, k-fold cross-validation. Specifically, fivefold cross-validation approach has been employed here which estimates the performance of the KNN classifier. The entire dataset is divided into $\boldsymbol{k}$-subsets, such that every time each of the $\boldsymbol{k}$ subset is considered as test set and the remaining $(\boldsymbol{k} - 1)$ subsets as training sets, to validate the performance. The average estimation of total $\boldsymbol{k}$ number of trials provides the total effectiveness of the model.

3 Experimental Results

The dataset in the present work consists of 50 randomly chosen brain MRIs (31 benign and 19 malignant samples) specified by expert radiologists, taken from the benchmarked sources as mentioned in Sect. 2. To detect brain tumor using the proposed segmentation approach, following steps have been executed.

3.1 Cluster Number Selection Procedure

The following Tables 1 and 2 present the dataset of five validity indices computed by varying the cluster numbers (K_C) from 3 to 9 with respect to the features; regional entropy and regional brightness, respectively. By thorough analysis of the datasets and following the selection rule—“*For optimal cluster number, the majority of cluster validity indices (PC, CE, SC, SI, XB) must satisfy their respective criteria*”, the cluster selection procedure has been carried out.

Table 1 Computation of validity indices for regional entropy

Cluster No (K_C)	PC	CE	SC	SI	XB
3	0.8135	0.3405	0.2482	5.2044e−06	14.6713
4	0.7830	0.4130	0.1722	3.3804e−06	4.6505
5	0.7752	0.4479	0.1277	2.5341e−06	18.2617
6	0.7702	0.4708	0.1084	2.0773e−06	22.9741
7	0.7821	0.4507	0.0858	1.5667e−06	**3.4409**
8	0.8299	0.3670	0.0710	1.2960e−06	6.2280
9	**0.8874**	**0.2603**	**0.0551**	**9.9248e−07**	6.8446

Source: Bold-face values indicate the best results of validity indices

Table 2 Computation of validity indices for regional brightness

Cluster No (K_C)	PC	CE	SC	SI	XB
3	**0.8986**	**0.1965**	0.4660	**1.0535e−06**	844.047
4	0.8724	0.2603	0.5575	9.5907e−06	354.710
5	0.8025	0.3776	0.4516	8.9937e−06	213.899
6	0.7941	0.4076	0.4641	8.6859e−06	533.602
7	0.7964	0.4111	0.3572	7.0682e−06	175.245
8	0.7926	0.4274	0.3572	7.1218e−06	577.251
9	0.7779	0.4639	**0.3141**	6.1569e−06	**160.554**

Source: Bold-face values indicate the best results of validity indices

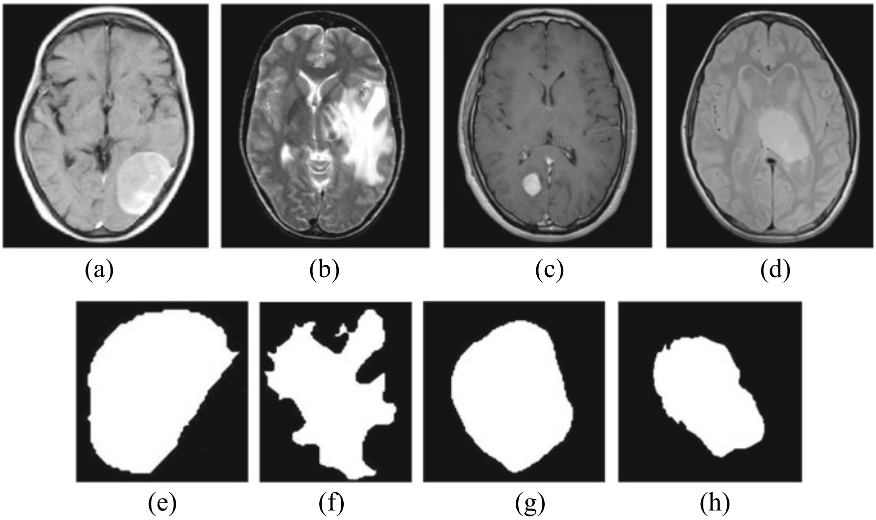

Fig. 4 Different brain MRI modalities (from the database) with their segmented outputs using validity index-based FCM algorithm; **a** MRI T1; **b** MRI T2; **c** MRI T1 GAD; **d** MRI PD; **e**–**h** shows the corresponding segmented outputs of a, b, c and d, respectively

By analyzing from Tables 1 and 2, it can be observed that $\boldsymbol{K_C = 9}$ and $\boldsymbol{K_C = 3}$ has been selected as the optimal cluster numbers, following the above-mentioned selection rule for both the features regional entropy (E) and regional brightness (B), respectively.

3.2 Data of the Proposed Segmentation Approach

The segmentation results of brain MRIs with various illumination and contrast, obtained after successful execution of the proposed approach, are shown in Fig. 4.

By varying the nearest neighbor ‘k’ of the KNN classifier, it has been found empirically that for k = 7, the maximum average accuracy of **96.0%;** sensitivity of **96.42%** and specificity of **95.45%** have been obtained.

4 Discussion

The efficiency of the proposed segmentation approach is estimated in terms of classification accuracy. Table 3, shows a brief comparison of overall classification accuracy, of the proposed approach with other related research works. It is found that

Table 3 A brief comparative study of the proposed model with other related research works

S. No.	Authors	Features	Classifiers	Accuracy(%)
1	Sachdeva et al. (2016)	Gray-level co-occurrence Matrix (GLCM) based features	Support Vector Machine (SVM), Artificial Neural Net. (ANN)	89.0 (SVM) 94.1(ANN)
2	Nabizadeh et al. (2015)	Gabor wavelet (GW) and statistical features (SF)	Linear SVM	92.2 (GW) 95.1 (SF)
3	Amin et al. (2020)	DWT fusion on MRI	Convolutional neural net. (CNN)	96.0
4	Jothi et al. (2016)	GLCM, gray-level difference method-based features	Decision tree-based classifier, instance-based learner	93.5
5	**Proposed model**	**Shape describing features**	**KNN**	**96.0**

Source: Bold-face values indicate the best results of validity indices

the present work shows superior/comparable performances with respect to recent studies.

5 Conclusion

The present work has addressed an automated, robust and efficient segmentation technique based on five effective cluster validity indices to estimate the optimal cluster numbers in an automated manner. The combination of two significant regional features makes the proposed segmentation method more efficient. Moreover, following the detection procedure, the shape describing feature set makes the classification easier and the results also show the superiority of the proposed approach with other related studies. As the cluster number selection procedure takes a significant time frame hence, further investigation of more sophisticated segmentation model may lead to more robust and cost-effective diagnostic system for real-time use.

Acknowledgements The present work is partially supported by the Center of Excellence (CoE) in Systems Biology and Biomedical Engineering, University of Calcutta, funded by the World Bank, MHRD India. Authors would also like to thank Dr. S. K. Sharma of EKO X-ray and Imaging Institute, Kolkata for providing the valuable comments on the subjective evaluation.

References

Adhikari SK, Sing JK, Basu DK, Nasipuri M (2015) Conditional spatial fuzzy C-means clustering algorithm for segmentation of MRI images. Appl Soft Comput 34:758–769

American Society of Clinical Oncology (ASCO) (2020) Brain tumor: statistics. https://www.cancer.net/cancer-types/brain-tumor/statistics. Last accessed Apr 2020

Amin J, Sharif M, Gul N, Yasmin M, Shad SA (2020) Brain tumor classification based on DWT fusion of MRI sequences using convolutional neural network. Pattern Recogn Lett 129:115–122

Bataineh KM, Naji M, Saqer M (2011) A comparison study between various fuzzy clustering algorithms. Jordan J Mech Industr Eng 5(4):335–343

Bezdek JC, Ehrlich R, Full W (1984) FCM: the fuzzy c-means clustering algorithm. Comput Geosci 10(2–3):191–203

Capitaine HL, Frelicot C (2011) A cluster-validity index combining an overlap measure and a separation measure based on fuzzy-aggregation operators. IEEE Trans Fuzzy Syst 19(3):580–588

Das P, Das A (2019) A fast and automated segmentation method for detection of masses using folded kernel based fuzzy c-means clustering algorithm. Appl Soft Comput 85(105775)

Despotovic I, Goossens B, Philips W (2015) MRI segmentation of the human brain: challenges, methods and applications. Comput Math Methods Med 23(450341)

Gueorguieva N, Valova I, Georgiev G (2017) M&MFCM: fuzzy C-means clustering with Mahalanobis and Minkowski distance metrics. Procedia Comput Sci 114:224–233

Johnson KA, Becker JA (2003) The whole brain atlas (Media). Lippincott Williams and Wilkins. https://www.med.harvard.edu/AANLIB/

Jothi G, Inbarani HH (2016) Hybrid tolerance rough set-firefly based supervised feature selection for MRI brain tumor image classification. Appl Soft Comput 46:639–651

Kang J, Min L, Luan Q, Li X, Liu J (2009) Novel modified fuzzy c-means algorithm with applications. Dig Signal Process 19(2):309–319

Kobayashi T, Otsu N (2008) Image feature extraction using gradient local auto-correlations. In: Forsyth D, Torr P, Zisserman A (eds) Computer vision-ECCV 2008. Lecture notes in computer science, vol 5302. Springer, Berlin, pp 346–358

Menze et al (2015) The multimodal brain tumor image segmentation benchmark (BRATS). IEEE Trans Med Imag 34(10)

Mukherjee S, Das A (2020) Effective fusion technique using FCM based segmentation approach to analyze Alzheimer's disease. In: Pattnaik P, Mohanty S, Mohanty S (eds) Smart healthcare analytics in Iot enabled environment. Intelligent Systems Reference Library, vol 178. Springer, Cham, pp 91–107

Nabizadeh N, Kubat M (2015) Brain tumors detection and segmentation in MR images: Gabor wavelet versus statistical features. Comput Electr Eng 45:286–301

Pakhira MK, Bandyopadhyay S, Maulik U (2004) Validity index for crisp and fuzzy clusters. Pattern Recogn 37(3):487–501

Sachdeva J, Kumar V, Gupta I, Khandelwal N, Ahuja CK (2016) A package-SFERCB-"Segmentation, feature extraction, reduction and classification analysis by both SVM and ANN for brain tumors." Appl Soft Comput 47:151–167

Wang W, Zhang Y (2007) On fuzzy cluster validity indices. Fuzzy Sets Syst 158(19):2095–2117

Xie XL, Beni G (1991) A validity measure for fuzzy clustering. IEEE Trans Pattern Anal Mach Intel 13:841–847

Zhang S, Li X, Zong M, Zhu X, Wang R (2018) Efficient kNN classification with different numbers of nearest neighbors. IEEE Trans Neural Netw Learn Syst 29(5):1774–1785

Biomarkers and Heart Rate Variability in the Prognosis of Cardiovascular Disease: A Perspective

Rahul Kumar, Yogender Aggarwal, and Vinod Kumar Nigam

Abstract The cholesterol level, risk factors, cellular events including calcification and inflammation lead to the formation of atherosclerosis plaque. The deposited plaque leads to baroreflex impairment that narrows the blood vessels resulted in catastrophic clinical manifestation of cardiovascular diseases (CVDs). The severity of plaque is influenced by the risk factors. In the prognosis of atherosclerosis events, various biomarkers play an important role such as interleukin-6 (IL-6), C-reactive protein (CRP), low-density lipoprotein (LDL) levels and tumor necrosis factor-α (TNF-α), and many more. C-reactive protein (CRP) has suggested predicting cardiovascular events. The atherosclerosis progression has also been associated with an elevated heart rate (HR) with the relationship between heart rate and arterial stiffness. However, the exact role of the CRP assay for treatment decisions has not been fully established and the identification of such biomarkers is the ongoing quest that can predict the cardiovascular risk. Further, there has been little evidence of an association between HR and its variability with coronary atherosclerosis. Thus, measurement of heart rate variability (HRV) indexed to biomarker as an established measure of autonomic function, may offer additive predictive information and identify the risk factors of CVDs progression.

Keywords Atherosclerosis · Biomarker · Cardiovascular disease · Heart rate variability

1 Introduction

Atherosclerosis is a common form of cardiovascular diseases (CVDs) and the major causes of morbidity and mortality worldwide (Vroman et al. 2019; Santos and Umpierre 2020). Cholesterol is found to be playing an important role in the pathogenesis of atherosclerosis. The severity of plaque triggers the thrombosis in the arteries and causes the several cardiovascular diseases (CVDs) such as coronary

R. Kumar · Y. Aggarwal (✉) · V. K. Nigam
Department of Bio-Engineering, Birla Institute of Technology Mesra, Ranchi 835215, India
e-mail: yaggarwal@bitmesra.ac.in

M. Mukherjee et al. (eds.), *Advances in Medical Physics and Healthcare Engineering*, Lecture Notes in Bioengineering, https://doi.org/10.1007/978-981-33-6915-3_7

artery diseases (CAD), peripheral vascular diseases, and myocardial infarction (MI) (Chen et al. 2019). Atherosclerosis is more common at progressively older ages with approximately tripling of its risk with each decade of life. Previous studies suggested that cholesterol is a key mediator of the plaque deposition for the pathogenesis of atherosclerosis. Willams et al. and Tabas et al. demonstrated that the elevated levels of LDL cholesterol and apolipoprotein B (apo B) 100 directly affect the inner layer of the arterial wall (intima), sparks an inflammatory response that associated with atherosclerotic events (Williams and Tabas 1998; Tabas et al. 2007). Several risk factors that cause the special unhealthy diet are the bases of arterial injury that lead to the dysfunction of endothelial the modify the app lipoprotein and help the access of monocytes into the subendothelial space. As soon as apoB lipoprotein gets internalized by macrophages this lipoprotein stimulates the formation of foam cells. As the time-lapse, this foam cell or fatty streak (Linton et al. 2019) releases the growth factor from the deposited fatty streak, consequent proliferation of smooth muscle cell (SMC). The development of thrombus and predispose of generalized and systemic factors take place, these factors help in the progression of atherosclerosis (Virmani et al. 2002). The deposition of plaque also influences the baroreceptor. Various studies have been done for the establishment of the relationship between atherosclerosis and baroreflex function, that atherosclerosis can lead to baroreflex dysfunction. Angell-James (1974) first described a reduced afferent baroreceptor activity in atherosclerotic animals than Vlachakis et al. also highlights the role of atherosclerosis that reduced the baroreceptor activity in hypertensive patients (Vlachakis et al. 1976). Baroreflex arises from arterial and cardiac baroreceptor that expresses through the vagus nerve. This arterial baroreceptor help to inhibit the heartbeat in the transient rise of blood pressure (Rovere et al. 1988). Further, Mortara et al. demonstrated that impaired baroreflex was linked with poor prognosis of chronic heart failure (Mortara et al. 1997). Moreover, the impairment of the baroreflex receptor was identified after myocardial infarction (Ferrari et al. 2007). The function of baroreflex and effectiveness of cardiac parasympathetic regulation is measured by Baroreflex sensitivity (BRS) (Rovere et al. 1988). A recent study suggested that activated baroreflex can be used for the treatment of hypertensive patients (Heusser et al. 2010; Scheffers et al. 2010).

Recent studies highlight the role of risk factors, inflammation, and lipid accumulation that mediate baroreflex dysfunction and the different stages of CAD. Moreover, the different stages of atherogenesis could be related to different biomarkers such as endothelial cells (CD40L, E-selectin), platelets, growth factors (IGF-1), inflammation (C-reactive protein) CRP, cytokines (IL-6, IL-8), accumulation of cholesterol, enzymes (Squalene synthase, acyl-coenzyme A: cholesterol acyltransferases (ACAT), proprotein convertase subtilisin/Kexin type 9 (PCSK9), glutathione peroxidase, NADPH oxidase, and catalases), chemokines (IP-10, TNF-α), reduced concentrations of high-density lipoprotein (HDL) and increased triglycerides (Stamellos et al. 1993; Stary et al. 1994; Miyazaki et al. 1998; Benjannet et al. 2004; Wang et al. 2004; Manea et al. 2015).

Heart rate variability (HRV) is the measurement of the R-R successive interval between heartbeats (Berntson et al. 1997). The activity of the autonomic nervous system (ANS) and its sympathetic and parasympathetic branches, control almost all visceral, vascular, and metabolic functions (Vinik et al. 2013). The autonomic dysfunction reflects the cardiovascular risk that, measured using HRV analysis (Aggarwal et al. 2020). The diminished HRV is a strong predictor of mortality including hypertension and obesity (Stein et al. 2005; Thayer et al. 2010). Further, the strong relationship between HR and arterial stiffness was revealed but there has been little evidence of any association between HR, or its variability with human coronary atherosclerosis. The relationship between low HRV and sudden cardiac death in post-MI and heart failure patients has also suggested but was lightly characterized (Galinier et al. 2000). Disturbances in autonomic equilibrium (sympathetic and parasympathetic tone) have been implicated in several cardiovascular conditions including MI, heart failure, and sudden cardiac death (Malik et al. 1996). However, the relationship between atherosclerosis, baroreflex dysfunction, and biomarkers an open quest? The relationship between various biomarkers and HRV as a biomarker for the development of atherosclerosis research is going on. Thus, the present review aimed to examine and discuss literature that different biomarkers and the utility of HRV parameters as biomarkers have been studied extensively to enlighten for complications and functionality of different stages of atherosclerosis such as CAD and MI risk prediction.

2 Risk Factors and Atherosclerosis

Atherosclerosis is one of the causes of cardiovascular outcomes and identification of risk factors that arose from the Framings heart study and seven-country study (Wilson et al. 1998). The major modifiable risk such as behavioral, tobacco use, unhealthy diet and obesity, physical inactivity, high serum lipid level, alcohol intake, hypertension, diabetes mellitus, and hyperlipidemia cause CVDs and enable to identify patients at particularly high stroke risk (Wolf et al. 1991). Several studies have shown that Autonomic dysfunction has been implicated in the development of hypertension, increased inflammation, and endothelial dysfunction to acute clinical events and later largely thrombotic lesion of atherosclerosis. Studies suggested that reducing these factors reduces the atherosclerosis events (Hackam and Anand 2003; Arnett et al. 2019). However, these risk factors have been suggested being associated with increased levels of inflammatory mediators, raised blood pressure, blood glucose, and blood lipids with altered autonomic function with the progression of CAD (Minami et al. 1999; Roach et al. 2004; Kasapis and Thompson 2005). Other risk factors such as polymorphisms within genes suggested being responsible for the wide range of atherosclerotic diseases that underlying cause most of the deaths worldwide (Chen et al. 2007).

Moreover, individual or population risk of atherosclerosis, major risk factors have been studied for the prediction but it is difficult to distinguish those individuals with modern risk factors who may be benefited from the aggressive risk factors.

3 Pathophysiology of Atherosclerosis

Mechanical and molecular stimuli activate signaling pathways leading to a dysfunctional endothelium lining that likely to occur at arterial intima (Gimbrone and Garcia-Cardena 2013). Endothelial cell dysfunction is an initial step in an atherosclerotic lesion that is subjected to low shear stress and disturbed blood flow (atherosclerosis prone areas) (Davies 1995; Gimbrone et al. 2000). Activated endothelial causes monocyte recruitment and promote nitric oxide (NO) (Galkina and Ley 2007). The increased production of (NO) promotes endothelial cell migration and (Lei et al. 2013), while the expression of superoxide dismutase (SOD) is increased to reduce cellular oxidative stress (Topper et al. 1996). The reduced expression of eNOS and SOD leads to increased accumulation and retention of subendothelial atherogenic apolipoprotein B (apoB)-containing lipoproteins (low-density lipoproteins (LDL)) and very-low-density lipoproteins (VLDL) and chylomicrons) (Gerrity et al. 1979; Schwenke and Carew 1989). The monocyte-derived macrophages internalize the retained apoB-containing lipoproteins from extracellular space, get oxidized and uptake via phagocytosis (Gerl et al. 2006; Torzewski et al. 2004). In the macrophages, unesterified cholesterol molecules lead to foam cell formation, a hallmark of atherosclerosis via several apoE receptors (LRP1 and VLDLR) (Schwartz and Reaven 2012; Fujioka et al. 1998). Also, macrophage-derived chemoattractants (matrix metalloproteinase (MMP)) cause tunica media smooth muscle cells to migrate into the intima and proliferate (Newby 2007). However, HDL prevents smooth muscle cell chemokine production and proliferation. In the lumen, SMC cells accumulated and vascular remodeling takes place resulting in the advanced lesion. The advanced lesion is a type of non-resolving inflammatory condition that leads to the formation of vulnerable plaque and increases the risk of plaque rupture. The rupture of plaque established the exposure of procoagulant and prothrombotic factors from the lesion to platelet that helps in the development of thrombus formation. Thrombus formation at sites of plaque rupture causes the majority of clinical events with the help of acute occlusive luminal thrombosis that lead to myocardial infarction, unstable angina, sudden cardiac death, and stroke (Virmani et al. 2002; Libby 2013). The detailed mechanism of atherosclerosis events elaborated in Fig. 1.

4 Atherosclerosis and Biomarkers

The review of the literature suggested endothelial denudation, the release of growth factor from the deposited fatty streak, consequent proliferation of smooth muscles cell (SMC), development of thrombus, and predispose of generalized and systemic factors as key factors in the development of atherosclerosis (Libby et al. 1988; Turunen et al. 1999). The literature on signaling pathways linking these factors in CAD development has been sparsely understood. Several proinflammatory biomarkers, plaque

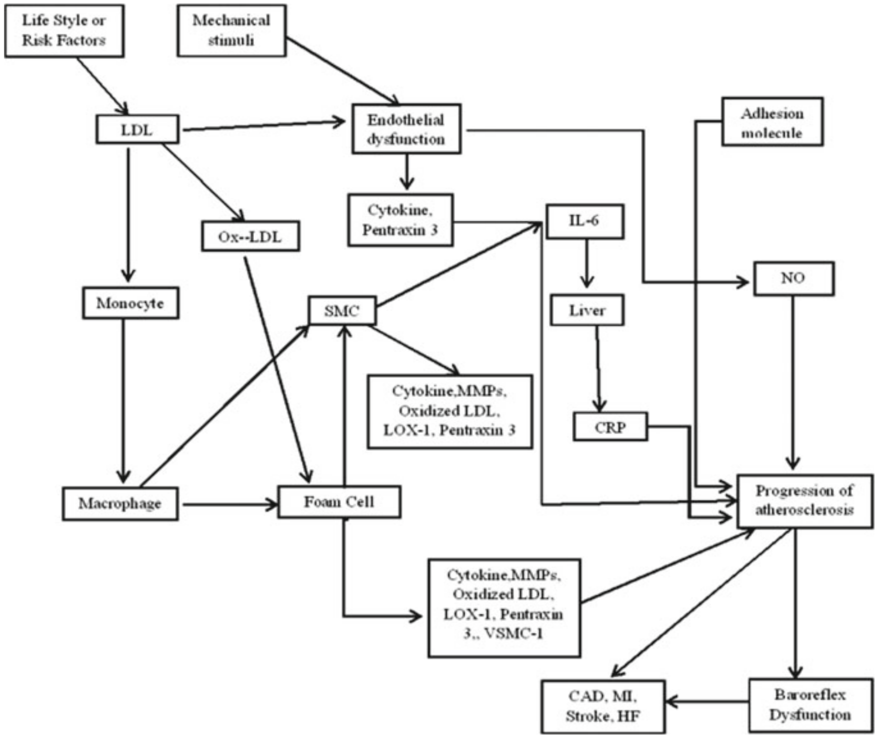

Fig. 1 Pathogenesis of atherosclerosis and expression of inflammatory biomarkers via atherosclerosis lesion. Principal proinflammatory markers such as cytokines, pentraxin-3, MMPs, and LOX-1 produced via macrophages, endothelial cells, and vascular smooth muscle cells in the atherosclerotic lesion, while CRP produced through the messenger cytokine IL-6 and released and circulated at different stages in atherosclerosis from different mechanisms. CRP indicates C-reactive protein; IL-6, interleukin-6; LDL, low-density lipoprotein; LOX-1, lectin-like oxidized LDL receptor-1; and MMP, matrix metalloproteinase, LDL-low-density lipoprotein, Ox-LDL-low-density lipoprotein, SMC-smooth muscle cells, VSMC-vascular smooth muscle cells, NO-nitric oxide, CAD-coronary artery disease, MI-myocardial infraction, HF-heart failure

destabilization, and plaque rupture had been revealed to predict the future cardiovascular (CV) events and identification of such biomarkers is the ongoing quest that can predict the cardiovascular risk (Libby and King 2015). IL-6, TNF-α, and CRP are members of the inflammatory cytokine that is released from vascular smooth muscle cells, endothelial cells, monocytes, macrophages, and involved in atherosclerosis progression. The increased concentration of blood IL-6 is associated with MI as compared to normal subjects. Further, at an older age, IL-6 is more significantly associated with the incidences of ischemic cardiac disease, stroke, and heart failure events (Ridker et al. 2000). C-reactive protein (CRP) is produced in the liver and colocalized with modified LDL and macrophages, at atherosclerotic lesions in both humans and experimental animals (Sun et al. 2005; Agrawal et al. 2010). However, the exact role of the high-sensitive CRP assay for treatment decisions has not been fully established in the prediction of plaque rupture (Yousuf et al. 2013). Further, Hs-CRP was used to detect small amount of inflammatory marker but high levels were affected by the infection and tissue damage, as well as obesity, old age, hypertension, diabetes mellitus, smoking, and other cardiovascular risks (Soeki and Sata 2016). Furthermore, other biomarkers such as lectin-like oxidized LDL receptor-1 LOX-1 that mediate plaque destabilization via apoptotic smooth muscle cells and enhancement of MMP secretion by mature foam cells (Pirillo and Norata 2013). LOX-1 shows its activity earlier with the beginning of acute coronary syndrome. Pentraxin 3 (PTX3) is an acute-phase response protein that is associated with CRP and became a more specific marker that is involved in atherosclerotic lesions. Recently, Garlanda et al. and Bonacina et al. detected the PTX3 in the human carotid atherosclerotic lesion and acute myocardial infarction (AMI) (Garlanda et al. 2005; Bonacina et al. 2013). Platelets are early players in the acceleration of atherogenesis (Massberg et al. 2002; Badrnya et al. 2014). The Amplification of inflammatory cascade (cytokine IL-6) directs the proatherogenic effects in the arterial wall (Huber et al. 1999). Further, Rogacev et al. (2012) suggested monocyte subtype $CD14^{++}CD16^{+}$ in plaque instability and prediction of cardiovascular disorders.

The increased expression of matrix metalloprotein (MMPs) acts as a potent mediator of plaque destabilization and vulnerability in atherosclerosis (Gerdes et al. 2002; Nold et al. 2003; Ishida et al. 2004). Augmented reactive oxygen species (ROS) have also been suggested in deteriorating the vascular function of atherosclerosis in vascular tissues (Satoh et al. 2012). It mediates various signaling pathway that induces the inflammation in atherogenesis from the initiation of fatty streak development through lesion progress to ultimate plaque rupture. Examination of CVDs risk in individuals has been explored the possibility of using different biomarkers in addition to traditional risk factors (Kaptoge et al. 2012).

5 Heart Rate Variability and Cardiovascular Disorder

Altered heart rate (HR) and reduced heart rate variability (HRV) has suggested being associated with increased risk of CVDs (Kanne et al. 1987; Filipovsky et al. 1992). However, the literature on the pathophysiological link between these associations is still obscured. Few studies demonstrated a relationship between resting HR and progression of coronary atherosclerosis in monkeys (Beere et al. 1984; Kaplan et al. 1987). Further, the strong relationship between HR and arterial stiffness was revealed but there has been little evidence of any association between HR, or its variability with human coronary atherosclerosis. The relationship between low HRV and sudden cardiac death in post-MI and heart failure patients has also suggested but was lightly characterized (Bilchick et al. 2002; Galinier et al. 2000). Disturbances in autonomic equilibrium (sympathetic and parasympathetic tone) have been implicated in several cardiovascular conditions including myocardial infarction (MI), heart failure, and sudden cardiac death (Malik et al. 1996).

An increase in vascular oxidative stress, endothelial dysfunction, and atherosclerosis progression has been demonstrated to be associated with an elevated HR. Resting HR influences plaque disruption through shear and circumferential tensile stress (Custodis et al. 2010). Increased HR leads to enhanced cardiac activity with higher oxygen consumption. This creates an imbalance between oxygen demand and supply, which leads to the progression of MI and directly proportional to the developing ischemia. Also, MI accelerates glycolysis and lactate production with decreased mitochondrial function in the artery. Myocardial infarction has also been suggested to be associated with CAD with reduced coronary blood flow and diastolic filling time (Andrews et al. 1993; Lang et al. 2010). The congestive heart failure and acute coronary syndromes patients exhibited a relation between HRV and inflammation, as measured by serum markers such as interleukin-6 (IL-6) and CRP (Aronson et al. 2001; Lanza et al. 2006). C-reactive protein, IL-6, and other inflammatory cytokines were strongly associated with decreased HRV (Libby 2001).

6 Current Status of Inflammatory Biomarkers for Atherosclerosis

Among the biomarkers reported to date, serum amyloid A (SAA), it expresses in cell forming atherosclerosis lesion, and elevated level of SAA is associated with CAD, its severity, and indicates early mortality (Johnson et al. 2004). ICAM-1(Intracellular adhesion molecule-1) Expression of ICAM-1 on smooth muscle cells in humans found in human aorta and coronary vessels. Increased plasma baseline concentration of ICAM-1 was associated with a greater incidence of future cardiovascular patients with Known CVD (Haim et al. 2002). IL-18 Found in plaque macrophage (Gerdes et al. 2002). TNF-α levels are markedly elevated in advanced heart failure and indicators of recurrent non-fatal MI or fatal cardiovascular disease events. TNF-α predicts short-term CVDs events in contrast to CRP and seems to be involved in earlier pathogenesis than CRP (Haddy et al. 2003). IL-6 is a predictor of peripheral atherosclerosis, IL-6 response to ischemia, and further tissue inhibitors of metalloproteinases by the fibroblasts IL-6 and CRP are associated with the development of atherosclerosis (Ridker et al. 2000). IL-6 is produced via TNF-α (Ng et al. 1994). Furthermore, the role of TNF-α is to influence the lipid metabolism (Jovinge et al. 1998) and is associated with cardiovascular disease events (Ferrari 1999).

However, previous study demonstrated that (Lundberg and Hansson 2010) inflammatory component of atherosclerosis interplay between the immunologically active endothelium and other tissues (liver and endothelial receptor). The CRP is mostly used for the detection of vascular inflammation. However, the blood concentration of CRP produced due to vascular inflammation is very low. So, high-sensitivity CRP (hs-CRP) assay techniques have been utilized for the detection of small changes in CRP concentrations.

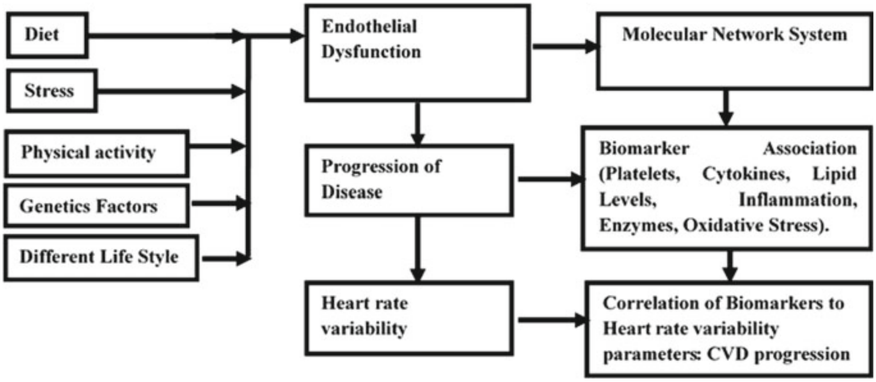

Fig. 2 Block diagram for identification of cardiovascular diseases through biomarkers indexed heart rate variability technique

7 Proposed Signaling Pathway Under Atherosclerosis

Risk factor, impaired baroreflex, and endothelial dysfunction cause the pathogenesis of atherosclerosis. Triggered by accumulated cholesterol levels and changes in blood pressure by adjusting the heart rate (vagal) and peripheral vascular tone (sympathetic) and secrete vascular cell adhesion molecular-1 (VCAM-1) and monocyte chemotactic protein-1 (MCP-1). This cytokine and autonomic dysfunction (vagus) together play an important role in the inflammatory reaction and create C-reactive protein (CRP) and interleukin (IL-6). Heart Rate Variability (HRV) predicts cardiovascular events and is associated with higher levels of CRP, IL-6, and fibrinogen. Thus, the modulation of ANS and higher levels of cholesterol will affect the inflammatory biomarker that is associated with atherosclerosis. The proposed signaling model will help the indexing of HRV to inflammatory biomarkers that are associated with the different stages of atherosclerosis The schematic flow chart represents the correlation of biomarkers and HRV in progression of atherosclerosis (Fig. 2).

8 Future Direction

CVDs is a major health problem to the worldwide and risk factor are preventable with early diagnosis and proper treatment (Wang 2011**).** The balance of the autonomic nervous system (ANS) is associated with different cardiovascular risk factors and is considered as a predictor of cardiovascular events (Gerritsen et al. 2001**).** Thus, the measurement of HRV indexed to biomarker may offer additive predictive information and identify the risk factors of CVDs progression.

Acknowledgements The authors are thankful to Dr. Prabin Kumar Shrivastava of Rajendra Institute of Medical Sciences, Ranchi for his valuable suggestion for the proposed signaling pathway.

References

Agrawal A, Hammond DJ Jr, Singh SK (2010) Atherosclerosis-related functions of C-reactive protein. Cardiovasc Haematol Disord Drug Targets 10:235–240

Aggarwal Y, Das J, Mazumder PM, Kumar R, Sinha RK (2020) Heart rate variability features from nonlinear cardiac dynamics in identification of diabetes using artificial neural network and support vector machine. Biocybern Biomed Eng

Andrews TC, Fenton T, Toyosaki N, Glasser SP, Young PM, MacCallum G, Gibson RS, Shook TL, Stone PH (1993) Subsets of ambulatory myocardial ischemia based on heart rate activity. Circadian distribution and response to anti-ischemic medication. The Angina and Silent Ischemia Study Group (ASIS). Circulation 88:92–100

Angell-James JE (1974) Arterial baroreceptor activity in rabbits with experimental atherosclerosis. Circ Res 34:27–39

Arnett DK, Blumenthal RS, Albert MA, Buroker AB, Goldberger ZD, Hahn EJ, Himmelfarb CD, Khera A, Lloyd-Jones D, McEvoy JW, Michos ED (2019) ACC/AHA guideline on the primary prevention of cardiovascular disease: a report of the American College of Cardiology/American Heart Association task force on clinical practice guidelines. J Am Coll Cardiol 74(10):1043–1044

Aronson D, Mittleman MA, Burger AJ (2001) Interleukin-6 levels are inversely correlated with heart rate variability in patients with decompensated heart failure. J Cardiovasc Electrophysiol 12:294–300

Badrnya S, Schrottmaier WC, Kral JB, Yaiw KC, Volf I, Schabbauer G, Söderberg-Nauclér C, Assinger A (2014) Platelets mediate oxidized low-density lipoprotein–induced monocyte extravasation and foam cell formation. Arter Thromb Vasc Bio 34:571–580

Beere PA, Glagov S, Zarins CK (1984) Retarding effect of lowered heart rate on coronary atherosclerosis. Science 226:180–182

Benjannet S, Rhainds D, Essalmani R, Mayne J, Wickham L, Jin W, Asselin MC, Hamelin J, Varret M, Allard D, Trillard M, Abifadel M, Tebon A, Attie AD, Rader DJ, Boileau C, Brissette L, Chretien M, Prat A, Seidah NG (2004) NARC-1/PCSK9 and its natural mutants: zymogen cleavage and effects on the low-density lipoprotein (LDL) receptor and LDL cholesterol. J Biol Chem 279:48865–48875

Berntson GG, Thomas Bigger J, Eckberg DL et al (1997) Heart rate variability: origins, methods, and interpretive caveats. Psychophysiology 34:623–648

Bilchick KC, Fetics B, Djoukeng R, Fisher SG, Fletcher RD, Singh SN, Nevo E, Berger RD (2002) Prognostic value of heart rate variability in chronic congestive heart failure (Veterans affairs' survival trial of antiarrhythmic therapy in congestive heart failure). Am J Cardiol 90:24–28

Bonacina F, Baragetti A, Catapano AL, Norata GD (2013) Long pentraxin 3: experimental and clinical relevance in cardiovascular diseases. Mediators Inflamm 2013:725102

Chen W, Li S, Srinivasan SR, Boerwinkle E, Berenson GS (2007) A genome scan for loci influencing levels and trends of lipoprotein lipid-related traits since childhood: the Bogalusa heart study. Atherosclerosis 190:248–255

Chen PY, Qin L, Li G, Wang Z, Dahlman JE, Malagon-Lopez J, Gujjar S, Cilfone NA, Kauffman KJ, Sun L, Sun H (2019) Endothelial TGF-β signaling drives vascular inflammation and atherosclerosis. Nat Met 1(9):912–926

Custodis F, Schirmer SH, Baumhakel M, Heusch G, Bohm M, Laufs U (2010) Vascular pathophysiology in response to increased heart rate. J Am Coll Cardiol 56:1973–1983

Davies PF (1995) Flow-mediated endothelial mechano transduction. Physiol Rev 75:519–560

De Ferrari GM, Sanzo A, Bertoletti A, SpecchiaG, Vanoli E, Schwarz PJ (2007) Baroreflex sensitivity predicts long-term cardiovascular mortality after myocardial infarction even in patients with preserved left ventricular function. J Am Coll Cardiol 50:2285–2290

Ferrari R (1999) The role of TNF in cardiovascular disease. Pharmacol Res 40:97–105

Filipovsky J, Ducimetiere P, Safar ME (1992) Prognostic significance of exercise blood pressure and heart rate in middle-aged men. Hypertension 20:333–339

Fujioka Y, Cooper A, Fong L (1998) Multiple processes are involved in the uptake of chylomicron remnants by mouse peritoneal macrophages. J Lipid Res 39:2339–2349

Galinier M, Pathak A, Fourcade J, Androdias C, Curnier D, Varnous S, Boveda S, Massabuau P, Fauvel M, Senard JM, Bounhoure JP (2000) Depressed low frequency power of heart rate variability as an independent predictor of sudden death in chronic heart failure. Eur Heart J 21:475–448

Galinier M, Pathak A, Fourcade J, Androdias C, Curnier D, Varnous S, Boveda S, Massabuau P, Fauvel M, Senard JM, Bounhoure JP (2000) Depressed low frequency power of heart rate variability as an independent predictor of sudden death in chronic heart failure. Eur Heart J 21:475–482

Galkina E, Ley K (2007) Vascular adhesion molecules in atherosclerosis. Arterioscler Thromb Vasc Biol 27, 2292–2301

Garlanda C, Bottazzi B, Bastone A, Mantovani A (2005) Pentraxins at the crossroads between innate immunity, inflammation, matrix deposition, and female fertility. Annu Rev Immunol 23:337–366

Gerdes N, Sukhova GK, Libby P, Reynolds RS, Young JL, Schonbeck U (2002) Expression of interleukin (IL)-18 and functional IL-18 receptor on human vascular endothelial cells, smooth muscle cells, and macrophages: implications for atherogenesis. J Exp Med 195:245–257

Gerdes N, Sukhova GK, Libby P, Reynolds RS, Young JL, Schönbeck U (2002) Expression of interleukin (IL)-18 and functional IL-18 receptor on human vascular endothelial cells, smooth muscle cells, and macrophages: implications for atherogenesis. J Exp Med 195(2):245–257

Gerl VB, Bhakdi S, Lackner KJ (2006) Enzymatic modification of low-density lipoprotein. In: Torzewski M, Lackner KJ (eds) Initiation and progression of atherosclerosis—enzymatic or oxidative modification of low-density lipoprotein? Clin Chem Lab Med 44:1389–1394

Gerritsen J, Dekker JM, TenVoorde BJ, Kostense PJ, Heine RJ, Bouter LM, Stehouwer CD (2001) Impaired autonomic function is associated with increased mortality, especially in subjects with diabetes, hypertension, or a history of cardiovascular disease: the Hoorn Study. Diab Care 24(10):1793–1798

Gerrity RG, Naito HK, Richardson M, Schwartz CJ (1979) Dietary induced atherogenesis in swine. Morphology of the intima in prelesion stages. Am J Clin Pathol 95:775–792

Gimbrone MA Jr, Garcia-Cardena G (2013) Vascular endothelium, hemodynamics, and the pathobiology of atherosclerosis. Cardio Pathol 22:9–15

Gimbrone MA Jr, Topper JN, Nagel T, Anderson KR, Garcia-Cardena G (2000) Endothelial dysfunction, hemodynamic forces, and atherogenesis. Ann N Y Acad Sci 902:230–239

Hackam DG, Anand SS (2003) Emerging risk factors for atherosclerotic vascular disease: a critical review of the evidence. JAMA 290(7):932–940

Haddy N, Sass C, Droesch S, Zaiou M, Siest G, Ponthieux A, Lambert D, Visvikis S (2003) IL-6, TNF-α and atherosclerosis risk indicators in a healthy family population: the STANISLAS cohort. Atherosclerosis 170(2):277–283

Haim M, Tanne D, Boyko V, Reshef T, Goldbourt U, Leor J, Mekori YA, Behar S (2002) Soluble intercellular adhesion molecule-1 and long-term risk of acute coronary events in patients with chronic coronary heart disease: data from the Bezafibrate Infarction Prevention (BIP) Study. J Am Coll Cardiol 39(7):1133–1138

Heusser K, Tank J, Engeli S, Diedrich A, Menne J, Eckert S, Peters T, Sweep FC, Haller H, Pichmlmaier AM, Luft FC, Jordan J (2010) Carotid baroreceptor stimulation, sympathetic activity, baroreflex function and blood pressure in hypertensive patients. Hypertension 55319–55626

Huber SA, Sakkinen P, Conze D, Hardin N, Tracy R (1999) Interleukin-6 exacerbates early atherosclerosis in mice. Arter Thromb Vasc Biol 19:2364–2367

Ishida Y, Migita K, Izumi Y, Nakao K, Ida H, Kawakami A, Abiru S, Ishibashi H, Eguchi K, Ishii N (2004) The role of IL-18 in the modulation of matrix metalloproteinases and migration of human natural killer (NK) cells. FEBS Lett 569:156–160

Johnson BD, Kip KE, Marroquin OC, Ridker PM, Kelsey SF, Shaw LJ, Pepine CJ, Sharaf B, Bairey Merz CN, Sopko G, Olson MB (2004) Serum amyloid A as a predictor of coronary artery disease

and cardiovascular outcome in women: the National Heart, Lung, and Blood Institute–Sponsored Women's Ischemia Syndrome Evaluation (WISE). Circulation 109(6):726–732
Jovinge S, Hamsten A, Tornvall P et al (1998) Evidence for a role of tumor necrosis factor alpha in disturbances of triglyceride and glucose metabolism predisposing to coronary heart disease. Metabolism 47:113–118
Kanne WB, Kannel C, Paffenbarger Jr RS, Cupples LA (1987) Heart rate and cardiovascular mortality: the Framingham Study. Am Heart J 113:1489–1494
Kaplan JR, Manuck SB, Adams MR, Weingand KW, Clarkson TB (1987) Inhibition of coronary atherosclerosis by propranolol in behaviorally predisposed monkeys fed an atherogenic diet. Circulation 76:1364–1372
Kaptoge S, Di Angelantonio E, Pennells L (2012) Emerging risk factors collaboration. C-reactive protein, fibrinogen, and cardiovascular disease prediction. N Engl J Med 367:1310–1320
Kasapis C, Thompson PD (2005) The effects of physical activity on serum C-reactive protein and inflammatory markers: a systematic review. J Am Coll Cardiol 45:1563–1569
La Rovere MT, Specchia G, Mortara A, Schwartz PJ (1988) Baroreflex sensitivity, clinical correlates, and cardiovascular mortality among patients with a first myocardial infarction: a prospective study. Circulation 78:816–824
Lang CC, Gupta S, Kalra P, Keavney B, Menown I, Morley C, Padmanabhan S (2010) Elevated heart rate and cardiovascular outcomes in patients with coronary artery disease: clinical evidence and pathophysiological mechanisms. Atherosclerosis 212:1–8
Lanza GA, Sgueglia GA, Cianflone D, Rebuzzi AG, Angeloni G, Sestito A, Infusino F, Crea F, Maseri A (2006) Relation of heart rate variability to serum levels of C-reactive protein in patients with unstable angina pectoris. Am J Cardiol 97:1702–1706
Lei J, Vodovotz Y, Tzeng E, Billiar TR (2013) Nitric oxide, a protective molecule in the cardiovascular system. Nitric Oxide-Biol Ch 35:175–185
Libby P (2001) Inflammation in atherosclerosis. Arter Thromb Vasc Biol 3:2045–2051
Libby P (2013) Mechanisms of acute coronary syndromes and their implications for therapy. N Engl 368:2004–2013
Libby P, King K (2015) Biomarkers: a challenging conundrum in cardiovascular disease. Arter Thromb Vasc Biol 35:2491–2495
Libby P, Mach F, Selwyn AP, Ganz P (1988) Current concepts in cardiovascular pathology: the role of LDL cholesterol in plaque rupture and stabilization. Am J Med 104:14S–18S
Linton MF, Yancey PG, Davies SS, Jerome WG, Linton EF, Song WL, Doran AC, Vickers KC (2019) The role of lipids and lipoproteins in atherosclerosis. InEndotext [Internet]
Lundberg AM, Hansson GK (2010) Innate immune signals in atherosclerosis. Clin Immunol 134(1):5–24
Malik M, Camm AJ, Bigger JT, Breithardt G, Cerutti S, Cohen RJ, Coumel P, Fallen EL, Kennedy HL, Kleiger RE, Lombardi F, Malliani A, Moss AJ, Rottman JN, Schmidt G, Schwartz PJ, Singer DH (1996) Heart rate variability standards of measurement, physiological interpretation, and clinical use. Eur Heart J 17:354–381
Manea A, Manea SA, Gan AM, Constantin A, Fenyo IM, Raicu M, Muresian H, Simionescu M (2015) Human monocytes, and macrophages express NADPH oxidase 5; a potential source of reactive oxygen species in atherosclerosis. Biochem Biophys Res Commun 461:172–179
Massberg S, Brand K, Grüner S, Page S, Müller E, Müller I, Bergmeier W, Richter T, Lorenz M, Konrad I, Nieswandt B (2002) A critical role of platelet adhesion in the initiation of atherosclerotic lesion formation. J Exp Med 196:887–896
Minami J, Ishimitsu T, Matsuoka H (1999) Effects of smoking cessation on blood pressure and heart rate variability in habitual smokers. Hypertension 33:586–590
Miyazaki A, Sakashita N, Lee O, Takahashi K, Horiuchi S, Hakamata H, Morganelli PM, Chang CC, Chang TY (1998) Expression of ACAT-1 protein in human atherosclerotic lesions and cultured human monocytes-macrophages. Arter Thromb Vasc Biol 18:1568–1574

Mortara A, La Rovere MT, Pinna GD, Prpa A, Maestri R, Febo O, Pozzoli M, Opasich C, Tavazzi L (1997) Arterial baroreflex modulation of heart rate in chronic heart failure: clinical and hemodynamic correlates and prognostic implications. Circulation 96:3450–3458

Newby AC (2007) Metalloproteinases and vulnerable atherosclerotic plaques. Trends Cardiovasc Med 17:253–258

Ng SB, Tan YH, Guy GR (1994) Differential induction of the interleukin-6 gene by tumor necrosis factor and interleukin-1. J Biol Chem 269:19021–19027

Nold M, Goede A, Eberhardt W, Pfeilschifter J, Mühl H (2003) IL-18 initiates release of matrix metalloproteinase-9 from peripheral blood mononuclear cells without affecting tissue inhibitor of matrix metalloproteinases-1: suppression by TNFα blockage and modulation by IL-10. Naunyn-Schmiedeberg's Arch Pharmacol 367:68–75

Pirillo A, Norata GD, Catapano AL (2013) LOX-1, OxLDL, and atherosclerosis. Mediators Inflamm 2013

Ridker PM, Rifai N, Stampfer MJ, Hennekens CH (2000) Plasma concentration of interleukin-6 and the risk of future myocardial infarction among apparently healthy men. Circulation 101:1767–1772

Roach D, Wilson W, Ritchie D, Sheldon R (2004) Dissection of long-range heart rate variability: controlled induction of prognostic measures by activity in the laboratory. J Am Coll Cardiol 43:2271–2277

Rogacev KS, Cremers B, Zawada AM, Seiler S, Binder N, Ege P, Große-Dunker G, Heisel I, Hornof F, Jeken J, Rebling NM (2012) CD14++ CD16+ monocytes independently predict cardiovascular events: a cohort study of 951 patients referred for elective coronary angiography. J Am Coll Cardiol 60:1512–1520

Santos LP, Umpierre D (2020) Exercise, cardiovascular health, and risk factors for atherosclerosis: a narrative review on these complex relationships and caveats of literature. Front Physio 11

Satoh K, Fukumoto Y, Sugimura K, Miura Y, Aoki T, Nochioka K, Tatebe S, Miyamichi-Yamamoto S, Shimizu T, Osaki S, Takagi Y (2012) Plasma cyclophilin A is a novel biomarker for coronary artery disease. Circulation 77:447–455

Scheffers IJ, Kroon AA, Schmidli J, Jordan J, Tordoir JJ, Mohaupt MG, Luft FC, Haller H, Menne J, Engeli S, Ceral J, Eckert S, Erglis A, Narkiewicz K, Philipp T, de Leeuw PW (2010) Novel baroreflex activation therapy in resistant hypertension: results of a European multi-center feasibility study. J Am Coll Cardiol 56:1254–1258

Schwartz EA, Reaven PD (2012) Lipolysis of triglyceride-rich lipoproteins, vascular inflammation, and atherosclerosis. Biochimica et Biophys Acta 1821:858–866

Schwenke DC, Carew TE (1989) Initiation of atherosclerotic lesions in cholesterol-fed rabbits. II. Selective retention of LDL versus selective increases in LDL permeability in susceptible sites of arteries. Arteriosclerosis 9:908–918

Soeki T, Sata M (2016) Inflammatory biomarkers and atherosclerosis. Inte Heart J 15:346

Stamellos KD, Shackelford JE, Shechter, I, Jiang, G, Conrad, D, Keller GA, Krisans SK (1993) Subcellular localization of squalene synthase in rat hepatic cells. Biochemical and immunochemical evidence. J Biol Chem 268:12825–12836

Stary HC, Chandler AB, Glagov S, Guyton J, Insull W, Jr Rosenfeld ME, Schaffer SA, Schwartz CJ, Wagner, WD, Wissler RW (1994) A definition of initial, fatty streak, and intermediate lesions of atherosclerosis. A report from the Committee on Vascular Lesions of the Council on Arteriosclerosis, American Heart Association. Circulation 89:2462–2478

Stein PK, Domitrovich PP, Huikuri HV, Kleiger RE (2005) Traditional and nonlinear heart rate variability are each independently associated with mortality after myocardial infraction. J cardiovasc Electrophysio 26:13–20

Sun H, Koike T, Ichikawa T, Hatakeyama K, Shiomi M, Zhang B, Kitajima S, Morimoto M, Watanabe T, Asada Y, Chen YE (2005) C-reactive protein in atherosclerotic lesions: its origin and pathophysiological significance. Am J Pathol 167:1139–1148

Tabas I, Williams KJ, Boren J (2007) Subendothelial lipoprotein retention as the initiating process in atherosclerosis: update and therapeutic implications. Circulation 116:1832–1844

Thayer JF, Yamamoto SS, Brosschot JF (2010) The relationship of autonomic imbalance, heart rate variability and cardiovascular disease risk factors. Int J Cardiol 141:122–131
Topper JN, Cai J, Falb D, Gimbrone MA Jr (1996) Identification of vascular endothelial genes differentially responsive to fluid mechanical stimuli: cyclooxygenase-2, manganese superoxide dismutase, and endothelial cell nitric oxide synthase are selectively up-regulated by steady laminar shear stress. Proc Natl Acad Sci USA 93:10417–10422
Torzewski M, Suriyaphol P, Paprotka K, Spath L, Ochsenhirt V, Schmitt A, Han SR, Husmann M (2004) In the arterial wall: a new role for plasmin and matrix metalloproteinases in atherogenesis. Arteriscl Throm Vas 24:2130–2136
Turunen MP, Hiltunen MO, Yla-Herttuala S (1999) Gene therapy for angiography, restenosis and related diseases. Exp Gerontol 34:564–574
Vinik AI, Erbas T, Casellini CM (2013) Diabetic cardiac autonomic neuropathy, inflammation and cardiovascular disease. J Diabet Investigat 4:4–18
Virmani R, Burke AP, Kolodgie FD, Farb A (2002) Vulnerable plaque: the pathology of unstable coronary lesions. J Inter cardio 15:439–446
Vlachakis ND, Mendlowitz M, DeGusman DD (1976) Diminished baroreceptor sensitivity in elderly hypertensives: possible role of atherosclerosis. Atherosclerosis 24:243–249
Vroman A, Ruvkun V, Shvartz E, Wojtkiewicz G, Santos Masson G, Tesmenitsky Y, Folco E, Gram H, Nahrendorf M, Swirski FK, Sukhova GK (2019) Stage-dependent differential effects of interleukin-1 isoforms on experimental atherosclerosis. Eur Heart J 40(30):2482–2491
Wang TJ (2011) Assessing the role of circulating, genetic, and imaging biomarkers in cardiovascular risk prediction. Circulation 123(5):551–565
Wang HH, Hung TM, Wei J, Chiang AN (2004) Fish oil increases antioxidant enzyme activities in macrophages and reduces atherosclerotic lesions in apoE-knockout mice. Cardiovasc Res 61:169–176
Williams KJ, Tabas I (1998) The response- to-retention hypothesis of atherogenesis reinforced. Curr Opin Lipidol 9:471–474
Wilson PW, D'Agostino RB, Levy D, Belanger AM, Silbershatz H, Kannel WB (1998) Prediction of coronary heart disease using risk factor categories. Circulation 97(18):1837–1847
Wolf PA, D'Agostino RB, Belanger AJ, Kannel WB (1991) Probability of stroke: a risk profile from the Framingham Study. Stroke 22:312–318
Yousuf O, Mohanty BD, Martin SS, Joshi PH, Blaha MJ, Nasir K, Blumenthal RS, Budoff MJ (2013) High-sensitivity C-reactive protein and cardiovascular disease: a resolute belief or an elusive link? Am Coll Cardiol 62:397–408

Gabor Filter Based Automated Enhancement of Brain Tumors

Debapriya Mukherjee and Arpita Das

Abstract Present work introduces 2D Gabor filtering technique for enhancement of brain tumors in presence of obscuring tissue in the surrounding and low illumination. Since Gabor filter can capture the edge information from different orientations, filter response is strong in all directions of edges. Enhanced tumor is completely segmented using fuzzy *c*-means clustering (FCM) algorithm and subjected to shape-based feature extraction employing the concept of extrema. Feature values obtained are used to train a classifier to determine the class (benign/malignant) of the tumor.

Keywords Brain tumors · Enhancement · Gabor filtering · Fuzzy *c*-means clustering algorithm · Feature extraction · Extrema · Classifier

1 Introduction

Cancer is a disease that leads to uncontrolled growth and division of cells. Among different types of cancers brain cancer is one of the deadliest that put people of all ages and genders in a perilous state (Brain Tumor 2019; Central Brain Tumor Registry of the United States (CBTRUS) Fact Sheet 2020). Some brain tumors may be slow-growing and benign but malignant tumors exhibit fast growth and therefore cause rapid deterioration. That is why it is important to get a thorough and accurate diagnosis of a brain tumor as early as possible. The choice of treatment for brain tumors depends on a variety of factors like type, location, and size of the tumor along with the patient's age and general health. The effectiveness of the various treatments largely depends upon the time of detection and the accuracy of the acquired information about the tumor under investigation. Early detection has been found to increase the chances of complete recovery. Also, the detailed description of the regions of interest and their accurate interpretation enables physicians to properly diagnose the disease and determine the treatment procedure. From various studies it

D. Mukherjee (✉) · A. Das
Department of Radio Physics and Electronics, University of Calcutta, Kolkata, India

A. Das
e-mail: adrpe@caluniv.ac.in

M. Mukherjee et al. (eds.), *Advances in Medical Physics and Healthcare Engineering*, Lecture Notes in Bioengineering, https://doi.org/10.1007/978-981-33-6915-3_8

Fig. 1 Changes in tumor shape

has been found that the malignant and benign tumors in the brain are morphologically different (Das and Das 2020). Figure 1 shows that malignant tumors tend to show more irregularity along the edges than benign ones. These changes in the shape of tumors are considered by many medical practitioners to be evidential in determining malignancy.

As the quality of the images affects their interpretation, medical images should have maximum clarity and thus be maximally enhanced for better visualization and accurate interpretation. **Image enhancement** techniques have been widely adopted in many applications of image processing where improvement in the quality of images is necessary. For example, one can remove noise, sharpen, or brighten an image, making it easier to identify key features like edges, corners, and curvatures. The more general methods of image enhancement are filtering with morphological operators (Kimori 2011), Histogram equalization (Singh and Dixit 2015), Noise removal using a Wiener filter (King et al. 1983), Linear contrast adjustment (Tsai and Yeh 2008), Median filtering (Tong and Neuvo 1994), Unsharp mask filtering (Levi 1974), Contrast-limited adaptive histogram equalization (CLAHE) (Stark 2000), Decorrelation stretch. Among the methods mentioned so far, over the last decade, enhancement using Gabor filter (Mehrotra et al. 1992; Rangayyan, et al. 2008), log Gabor filter (Wang et al. 2008; Yao et al. 2006) have yielded the most promising results. The enhancement procedure is followed by the process of **image segmentation** which aims at segregating the region under suspicion from its imprecise surrounding. Many effective segmentation techniques have been introduced by researchers among which K-means clustering technique (Zalik 2008), Fuzzy *C* means algorithm (Cai et al. 2007; Gueorguieva et al. 2017) are widely used. Since our primary concern is to determine the class of the tumor post-detection, so the segmented image of the brain tumor is fed to a classifier that utilizes certain feature values extracted from the segmented image to classify it into benign or malignant classes.

In this regard, present work describes a way to integrate Gabor filtering with FCM algorithm to generate a highly enhanced and precisely segmented image of a brain tumor or lesion from an input MRI or CT scan. This image is then classified to determine the class of the tumor with the help of shape-based features extracted from the segmented image.

In the rest of the work, proposed approach is discussed in Sect. 2. Section 3 shows some experimental results. Finally Sect. 4 draws some conclusion of the work.

2 Proposed Approach

We have implemented ***Gabor filters*** on MRI (T1, T2, GAD, PD) and CT images of the brain and made an attempt at enhancing the different features such as the boundaries of the affected regions by employing the characteristics of this filter. This is followed by complete segregation of the ROI from its ambiguous surroundings using ***FCM algorithm***. The segmented images thus obtained show precisely the contour of the tumor that is to be further studied by implementing the process of ***feature extraction***. The resulting feature values are then employed to train a classifier to complete the task of ***classification*** of the tumor into benign or malignant classes.

2.1 Image Enhancement

Over decades research has been done to discover and improve ways of enhancing the affected area since eventually, it increases the accuracy in its segmentation. While doing so, attention was drawn by the significance of the different frequency components of an image. It has been observed that in an image, the low frequencies are related to slowly varying intensity components and the high frequencies are caused by sharp transitions in intensity, such as edges and noise (Gonzalez and Woods 2008). Thus an attempt at smoothing or sharpening an image introduced the mechanism of filtering which has become a preliminary part of image processing ever since. A lowpass filter that allows only the low frequencies to pass through causes blurring of the image, whereas a highpass filter allowing only the high frequencies enhance the sharpness of the image but at the cost of the noise that may get incorporated. However, extensive studies indicated that an efficient way of acquiring an image with sharp distinct edges (suppressed low frequencies) and reduced noise (suppressed high frequencies) is to implement a ***bandpass*** filter. ***Gabor filters*** are basically orientation and frequency-sensitive bandpass filters, used for edge and texture analysis. One of the reasons for which Gabor filters (Mehrotra et al. 1992; Rangayyan, et al. 2008) have gained popularity is their ability to detect edges having various orientations. The response of the Gabor filter is strong if the orientation of the filter matches the orientations of the edges that are to be detected in an image. The IRF of a 2-D Gabor real valued filter is given by:

$$g_{\lambda\theta\psi\sigma\gamma}(x, y) = \exp\left(-\frac{-x'^2 + \gamma^2 y'^2}{2\sigma^2}\right)\cos\left(\frac{2\pi x'}{\lambda} + \psi\right) \tag{1}$$

$$x' = x\cos(\theta) + y\sin(\theta) \tag{2}$$

$$y' = y\cos(\theta) - x\sin(\theta) \tag{3}$$

where the arguments x and y specify the position of a light impulse in the visual field and σ, γ, λ, θ and ψ are the parameters defined below:

$\boldsymbol{\sigma}$ = specifies the standard deviation of the Gaussian function which controls the width of the Gaussian function.
$\boldsymbol{\gamma}$ = known to be the aspect ratio, that specifies the ellipticity of the Gaussian factor. The typical values lie between 0.2 and 1. The kernel takes the shape of a circle when the value is 1.
$\boldsymbol{\lambda}$ = specifies the wavelength of the cosine factor of the Gabor function. The wavelength is given in pixels. Valid values are real numbers between 2 and 256.
$\boldsymbol{\theta}$ = specifies the orientation of the normal to the parallel stripes of the Gabor function. The orientation is specified in degrees. Valid values are real numbers between 0 and 180.
$\boldsymbol{\psi}$ = specifies the phase offset of the cosine factor of the Gabor function. It is specified in degrees. Valid values are real numbers between −180 and 180.

The Gabor filters are applied in the same manner as other conventional filters. There is usually an array of pixels (usually 2D array since 2D images are involved) known as '***mask***' or a '***convolutional kernel***' that represents the filter. In this array, each pixel is assigned a value and a convolution operation is performed between the kernel and the image as the kernel slides over every pixel of the image. At the output, we get an image whose edges and boundaries are more distinct, thus helping in better analysis of the region of interest. In practice, to analyze texture or obtain features from an image, a bank of Gabor filters with a number of different orientations can be used. In the present work, we have implemented a bank of 16 Gabor filters to generate highly enhanced images of the brain tumors by capturing their outlines precisely from 16 different orientations. Figure 2 shows the image of a brain tumor when seen through a Gabor filter from 16 different orientations ($\boldsymbol{\theta} = \mathbf{0}°, \mathbf{11.25}°, \mathbf{22.50}°, \mathbf{33.75}°, \mathbf{45}°, \mathbf{56.25}°, \mathbf{67.5}°, \mathbf{78.5}°, \mathbf{90}°, \mathbf{101.25}°, \mathbf{112.5}°, \mathbf{123.75}°, \mathbf{135}°, \mathbf{146.25}°, \mathbf{157.5}°, \mathbf{168.75}°$).

2.2 Image Segmentation

In the second stage of our proposed methodology, we have applied the most widely used ***fuzzy c-means (FCM) algorithm*** to complete the task of separating the suspected region from its imprecise background. FCM is an unsupervised soft-clustering technique that transforms the crisp boundary concept into a degree of membership function (Gueorguieva et al. 2017). Membership value (varying between 0 and 1) is found by calculating the distance between the cluster centre and each data point. The membership value is higher for the data point that is closer to the cluster centre indicating a higher probability of it belonging to that cluster. Following the selection of suitable cluster numbers empirically, FCM algorithm preserves the target cluster (representative of suspected region) appropriately and suppresses others for separating it from the imprecise surrounding regions.

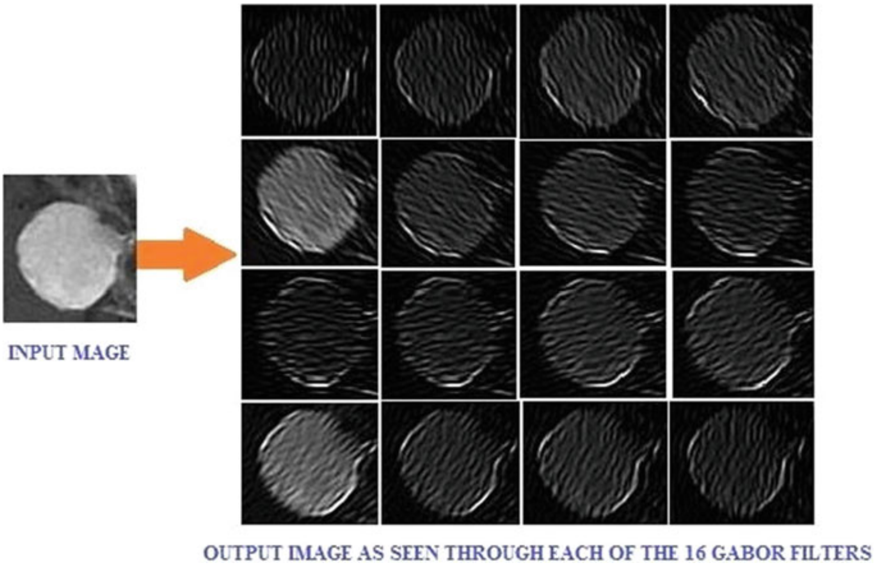

Fig. 2 Output of filtering through 16 Gabor filters

2.3 Feature Extraction

The complete segmentation of the tumor is followed by the process of extraction of various features of the suspected region based on which the tumor can be classified into either benign or malignant groups. Feature extraction is a critical step in image processing since different features from an image provide a better description of the ROI and thereby make the identification of the affected region highly accurate. The morphological changes that have been seen to occur in a tumor as it tends toward malignancy have encouraged researchers to study the various shape-based features like ***compactness***, ***eccentricity***, ***perimeter***, ***area***, ***solidity***, ***convex area***, etc. Other than these conventional features, one of the most widely used approaches is ***Extrema*** based characterization (Das and Das 2020) In the present study we have emphasized the implementation of ***extrema*** based features for characterization of brain tumors. As mentioned earlier, the contours of malignant tumors have more irregularities than benign ones, and the extrema (e) determines the extent of concavity/convexity of the tumor profile. Figure 3 shows that in a benign tumor the length of the radius vectors varies negligibly because of its smooth boundary. But in case of a malignant tumor, the variation in the lengths of radius vectors are quite significant due to the spiculations present along its boundary. Extrema refers to the radius vector of maximum or minimum length. The concept of extrema (e) is applied in the development of various shape-dependent features which on implementation led to successful detection of malignancy in a tumor.

Fig. 3 Variation in radius vector lengths in **a** benign and **b** malignant tumor

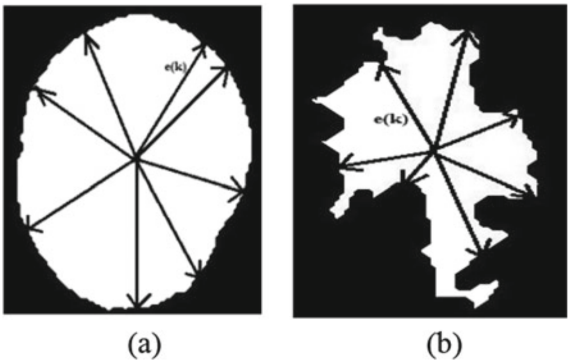

Given below are various characterization of ***e*** such as ***extrema count***, ***extrema diff.***, ***extrema entropy***, ***extrema variance***, ***extrema acutance***, ***r.m.s. value of extremea*** (Das and Das 2020) that enable us to distinguish between a benign and malignant tumor.

$$\text{Total extrema count } (\boldsymbol{e_{count}}) = K \tag{4}$$

$$\text{Extrema difference } \left(\boldsymbol{e_{diff}}\right) = e_{\max} - e_{\min} \tag{5}$$

$$\text{Extrema entropy } (\boldsymbol{e_{ent}}) = -\sum_{k-1}^{K} e(k) \log e(k) \tag{6}$$

where K is the total number of extrema count

$$\text{Extrema variation } (\boldsymbol{e_{var}}) = \frac{1}{K}\sum_{k-1}^{K} [e(k) - e_m]^2 \tag{7}$$

where

$$e_m = \text{extrema mean} = \frac{1}{K}\sum_{k-1}^{K} [e(k)]$$

$$\text{Extrema acutance } (\boldsymbol{e_{ac}}) = \frac{e_{\max} - e_{\min}}{K}\sum_{k-1}^{K} [e(k)] \tag{8}$$

$$\text{Extrema r.m.s. value } (\boldsymbol{e_{r.m.s.}}) = \sqrt{\frac{1}{K}\sum_{k-1}^{K-1} [e(k) - e(k+1)]^2} \tag{9}$$

Unlike benign tumors with smooth boundary, malignant tumors having higher number of marginal spiculations tend to elevate the feature values that we have applied.

2.4 Classification

The process of classification of the segmented tumor into benign/malignant category is an essential task which concludes our proposed methodology. In the present work, for classification we have implemented ***K-NN algorithm*** (Zhang 2018) that uses '***feature similarity***' to predict the class (benign/malignant) of a new test sample based on how closely it matches the feature values in the training set. The selection of the ***number of nearest neighbors*** (***K***) is crucial as it determines the accuracy of classification. The classifier measures the distance between the test sample and each of the nearest training samples, the number is decided by the value of K. The distance functions commonly used are Euclidean, Hamming, Manhattan, although present study employs the Euclidean distance metric to locate the nearest neighbor. The neighbors having the least distance from the test sample ultimately decide the class to which the test sample gets assigned by the rule of majority. For example, if $K = 4$, then the test sample is allocated to that class to which majority of the 4 nearest neighbors belong.

One of the approaches for assessing the efficiency of the classification algorithm is ***k-fold cross-validation*** (Wong 2015). In this approach, initially, the dataset is randomly divided into 'k' subsets or folds of equal sizes. The classification model is run k times and each time one of the k groups is used as test-set/validation-set while the other $(k - 1)$ groups form the training set. The error estimation is averaged overall k-trials to obtain total effectiveness of the model. Although there is no rule for choosing the value of k, but $k = 5$ or 10 is found to be very common in the field of applied machine learning as these values have been found to result in a model skill estimate with low bias and modest variance.

In the present study, we have divided the entire dataset into 5 groups ($k = 5$) and each time out of 5 trials one of the 5 groups become the validation-set whereas the other 4 groups are used to train the classifier model. The performance of the classifier is evaluated in terms of parameters like **Sensitivity (*Sen*), Specificity (*Sp*), Accuracy (*Acc*)** which have been described below:

- **Sensitivity (*Sen*)**: It estimates how correctly the classifier can predict the benign tumors.

$$\mathrm{Sen}(\%) = \frac{\mathrm{TP}}{\mathrm{TP} + \mathrm{FN}} \times 100 \tag{10}$$

- **Specificity (*Sp*)**: It estimates how correctly the classifier can predict the malignant tumors.

$$\mathrm{Sp}\,(\%) = \frac{\mathrm{TN}}{\mathrm{TN} + \mathrm{FP}} \times 100 \tag{11}$$

- **Accuracy (*Acc*)**: It estimates the overall correct prediction of benign and malignant tumors.

$$\mathrm{Acc}\,(\%) = \frac{\mathrm{TP} + \mathrm{TN}}{\mathrm{TP} + \mathrm{FP} + \mathrm{FN} + \mathrm{TN}} \times 100 \tag{12}$$

where the number of previously known malignant tumors correctly predicted as malignant (TN); the number of previously known benign tumors correctly predicted as benign (TP); the number of previously known benign tumors incorrectly predicted as malignant (FN); the number of previously known malignant tumors incorrectly predicted as benign (FP).

3 Experimental Results

Proposed enhancement and segmentation techniques are applied on the brain MRI and CT images from the benchmark database of "*The Whole Brain Atlas—Harvard Medical School*" (Johnson and Becker 1999) and "*The Multimodal Brain Tumor Image Segmentation Benchmark* (*BRATS*)" (Menze 2015).

Some of the results of enhancement and segmentation have been shown in Fig. 4.

In the proposed approach, we have selected **fivefold** cross-validation technique and varied the number of neighbors (**K**) to observe the corresponding variation in the parameters like Sensitivity, Specificity and Accuracy. In doing so, we obtained the best results for $\mathbf{K = 4}$ which implies that the test sample is allocated to that class to which majority of the 4 nearest neighbors belong.

Using a K-NN classifier with **4 nearest neighbors** and **fivefold cross-validation** to estimate the classifier efficiency we acquired a **Sensitivity of 100%, Specificity of 94.11%, and Accuracy of 96.67%**.

4 Conclusion

Present work suggests the design of an efficient model for tumor detection using the method of enhancement followed by segmentation of the brain tumor before it can be classified into benign/malignant class. In this regard, a bank 16 Gabor filters are implemented to precisely identify the tumor boundary. Following this, the tumor is successfully segmented from its inhomogeneous background by employing fuzzy c-means clustering algorithm. The segmented image of the tumor is further studied through the process of feature extraction where various shape-based features help the classifier to finally determine the class of the tumor accurately.

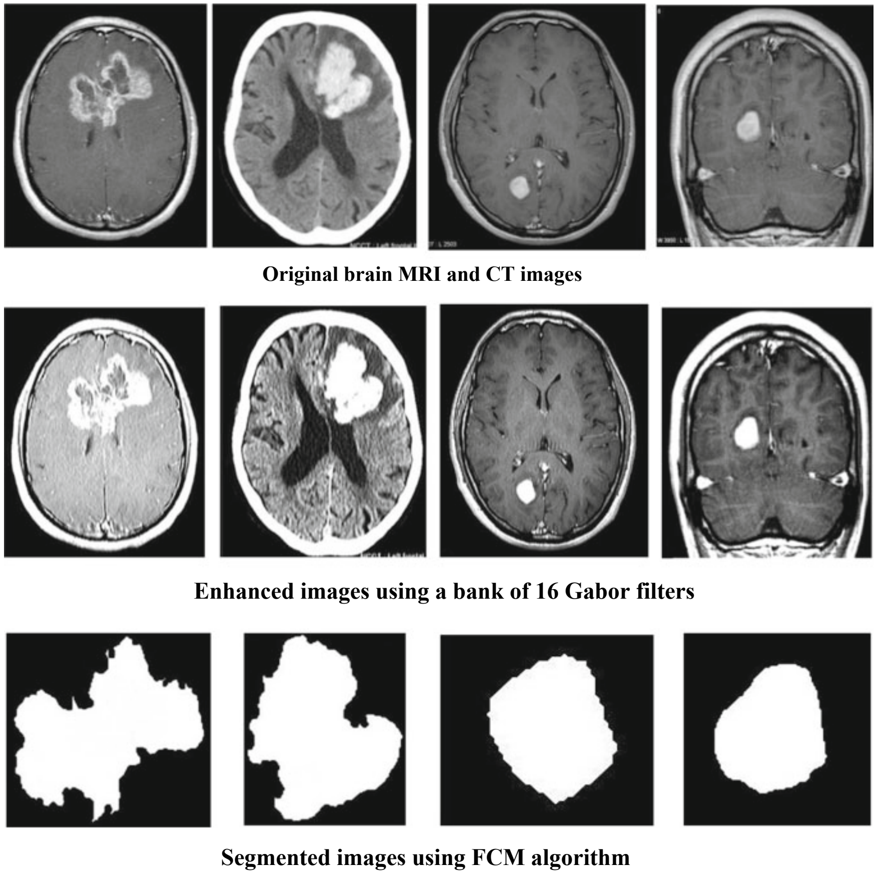

Fig. 4 Enhancement and segmentation results using the proposed techniques

In future, some modifications in the proposed approach can be introduced with the aim of improving the performance of the model. In this respect, Gabor filter can be replaced with Log-Gabor filter to overcome its limitations. The maximum bandwidth of a Gabor filter used in image enhancement is limited to approximately one octave and thus they are not optimal if one is seeking broad spectral information with maximal spatial localization. Log-Gabor filters, on the other hand, can be constructed with arbitrary bandwidth and the bandwidth can be optimized to produce a filter with minimal spatial extent. Also, these filters have an extended tail at high frequencies which results in the preservation of image details. Apart from that, the number and type of features that have been employed greatly determine the classifier performance and the present work with the features already discussed resulted in an accuracy of 96.67%. However, introduction of more complex features may increase the accuracy of classification further as they would enable the classifier to comprehensively analyze the tumor.

Acknowledgements This work is partially supported by the Center of Excellence (CoE) in Systems Biology and Biomedical Engineering, University of Calcutta, funded by the World Bank, MHRD India. The authors would also like to thank the radiologist Dr. Soumitra Halder of Metiabruz Super Speciality Hospital for providing valuable comments on subjective evaluation of the MRIs.

References

Brain Tumor: Statistics, Cancer.net, https://www.cancer.net/cancer-types/brain-tumor/statistics. Last accessed 08 Dec 2019

Cai W, Chen S, Zhang D (2007) Fast and robust fuzzy *C*-means clustering algorithms incorporating local information for image segmentation. Pattern Recogn 40(3):825–838

Central Brain Tumor Registry of the United States (CBTRUS) Fact Sheet, https://www.cbtrus.org/cbtrus-fact-sheet/. Last accessed 15 Apr 2020

Das P, Das A (2020) Shift invariant extrema based feature analysis scheme to discriminate the spiculation nature of mammograms. ISA Trans 103:156–165

Gonzalez RC, Woods RE (2008) Digital image processing, 3rd edn. Pearson Education

Gueorguieva N, Valova I, Georgiev G (2017) M&MFCM: fuzzy *c*-means clustering with Mahalanobis and Minkowski distance metrics. Proc Comput Sci 114:224–233

Johnson KA, Becker JA (1999) The whole brain Atlas (media). Lippincott Williams and Wilkins. https://www.med.harvard.edu/AANLIB/

Kimori Y (2011) Mathematical morphology-based approach to the enhancement of morphological features in medical images. J Clin Bioinform 1–33 (2011)

King MA, Doherty PW, Schwinger RB, Penney BC (1983) A Wiener filter for nuclear medicine images. Med Phys 10(6):876–880

Levi L (1974) Unsharp Masking and related image enhancement techniques. Comput Graph Image Process 3(2):163–177

Mehrotra R, Namuduri KR, Ranganathan N (1992) Gabor filter based edge detection. Pattern Recogn 25(12):1479–1494

Menze BH et al (2015) The multimodal brain tumor image segmentation Benchmark (BRATS). IEEE Trans Med Imag 34(10):1993–2024

Rangayyan RM et al (2008) Detection of blood vessels in the retina with multiscale Gabor filters. J Electron Imag 17(2):023018 (2008)

Singh RP, Dixit M (2015) Histogram Equalization: a strong technique for image enhancement. Int J Sig Process Image Process Pattern Recogn 8(8):345–352

Stark JA (2000) Adaptive image contrast enhancement using generalizations of histogram equalization. IEEE Trans Image Process 9(5):889–896

Tong S, Neuvo Y (1994) Detail-preserving median based filters in image processing. Pattern Recogn Lett 15(4):341–347

Tsai CM, Yeh ZM (2008) Contrast enhancement by automatic and parameter-free piecewise linear transformation for color images. IEEE Trans Consum Electron 54(2):213–219

Wang W, Li J, Huang F, Feng H (2008) Design and implementation of Log-Gabor filter in fingerprint image enhancement. Pattern Recogn Lett 29(3):301–308

Wong T-T (2015) Performance evaluation of classification algorithms by *k*-fold and leave-one-out cross validation. Pattern Recogn 48(9):2839–2846

Yao P, Li J, Ye X, Zhuang Z, Li B (2006) Iris recognition algorithm using modified log-gabor filters. In: 18th international conference on pattern recognition (ICPR’06). IEEE

Zalik KR (2008) An efficient *k*-means clustering algorithm. Pattern Recogn Lett 29(9):1385–1391

Zhang S et al (2018) Efficient *k*-NN classification with different numbers of nearest neighbours. IEEE Trans Neural Netw Learn Syst 29(5):1774–1785

Green Synthesis of Magnetite (Fe_3O_4) Nanoparticles Using *Azadirachta indica* Leaf Extract and Their Characterization

Ruhana Pervin, K. A. Khan, N. I. Khan, A. K. M. Atique Ullah, and S. M. Zian Reza

Abstract Magnetite (Fe_3O_4) nanoparticles (NPs) were prepared through green synthesis route using *Azadirachta indica* leaf extract that acted as an efficient stabilizer and capping agent of the NPs. Two types of magnetite NPs were synthesized using 5 and 10 mL *Azadirachta indica* leaf extract of the same concentration. The X-ray diffraction (XRD) analysis showed that the particles were crystalline with cubic inverse spinel structure and the crystallite size was found to be about 5.73 nm and 6.34 nm, respectively. The surface morphology of the NPs was investigated by field emission scanning electron microscopy (FESEM) which showed that NPs were spherical in shape. The Fourier transform infrared spectroscopy (FT-IR) analysis showed that the capping agents of the NPs contained the functional groups alcohol, alkane, amine, alkyne, etc. The thermal stability of Fe_3O_4 NPs was investigated using differential scanning calorimetry (DSC) and thermogravimetric analysis (TGA). DSC showed endothermic and exothermic peaks. The percentage of weight loss was about 55% and 40%, respectively, as found from TGA. The NPs were superparamagnetic in nature with zero coercivity and zero reminance magnetization which was observed using a vibrating sample magnetometer (VSM). On the treatment of aqueous solutions of ferrous and ferric salts in alkaline medium with *Azadirachta indica* leaf extract, the rapid formation of stable iron oxide nanoparticles (Fe_3O_4-NPs) is observed to occur. The average crystallite size was determined by Scherer formula which showed that the crystallite size of the NPs gets increased with the increasing amount of *Azadirachta indica* extract used. Which support and show a good agreement with XRD and VSM analysis.

R. Pervin · K. A. Khan (✉)
Department of Physics, Jagannath University, Dhaka 1100, Bangladesh

N. I. Khan
Nanoscience and Technology Research Laboratory, Atomic Energy Centre, Bangladesh Atomic Energy Commission, Dhaka 1000, Bangladesh

A. K. M. Atique Ullah
Chemistry Division, Nanoscience and Technology Research Laboratory, Atomic Energy Centre, Bangladesh Atomic Energy Commission, Dhaka 1000, Bangladesh

S. M. Zian Reza
Department of Physics, Uttara University, Dhaka, Bangladesh

M. Mukherjee et al. (eds.), *Advances in Medical Physics and Healthcare Engineering*, Lecture Notes in Bioengineering, https://doi.org/10.1007/978-981-33-6915-3_9

Keywords Green synthesis · NPs · Magnetic properties · Thermal analysis · Crystal structure analysis

1 Introduction

Nanoparticles have excellent recognition and acceptance due to their desirable characteristic features some of which include catalytic, optical, magnetic and electrical properties (Payman and Allan 2009; Fazlzadeh et al. 2016; Lu et al. 2010; Klokkenburg et al. 2007). These particles possess remarkably new properties when compared to their bulk counterpart. This means that nanoparticles do not necessarily behave in the same manner as larger particles in chemical reactions, but tend to be much more reactive (Sulistyaningsih et al. 2013; Davor 1993; Nicolae et al. 2014). The particles possess an enormous amount of energy in their high surface-to-volume ratio, which changes their reactivity (Parker et al. 1993; Bashar et al. 2013; Khan 1998; Ruhane et al. 2017a). Nanoparticles have a general tendency to adsorb species very readily, which has obvious kinetic advantages. Due to environmental concerns, the green route methods have become increasingly popular to synthesize nanoparticles as they are well known to be environmentally friendly and help to reduce harmful effects on environment (Ruhane et al. 2017b; Mehedi and Khan 2018; Khan et al. 2019a). Nanoparticle is a particle in the nanometer scale which usually in the range of 1–100 nm (Khan et al. 2019b; Mehedi and Khan 2019; Hassan and Khan 2020). There are a lot of applications of NPs nowadays. Our main motto to use our produced NPs for electricity generation from different leaf extracts (Khan et al. 2019c; Hazrat Ali et al. 2019).

1.1 Methods and Materials

The chemicals and reagents used in this work are of analytical grade and are used without further purification. De-ionized (DI) water with resistivity 18 MΩ-cm is used as solvent in order to prepare the solutions required in this work. The chemicals and reagents used in this work are listed here: Ferric chloride anhydrous ($FeCl_3$) (Merck, India), Ferrous chloride tetra hydrates ($FeCl_2 \cdot 4H_2O$) (Merck, India), Sodium hydroxide (NaOH) (Merck, India), Citrus limon peel extract, Acetone (CH_3COCH_3) (Merck, India), Ethanol (CH_3OH) (Merck, India), Dichloromethane (CH_2Cl_2) (Merck, India), HeLA Cell line (a human cervical carcinoma cell line), Vero Cell line (a kidney epithelial cell extracted from an African green monkey), DMEM (Dulbecco's Modified Eagle's medium), 1% penicillin streptomycin, 0.2% gentamycin, 10% fetal bovine serum, DI water, etc. Furthermore, the equipments and instruments were used for the synthesis, characterization and antibacterial application of the Fe_3O_4 NPs: Ceramic mortar, Digital balance (AB 265/S/SACT METTLER, Toleto, Switzerland), Magnetic stirrer with thermostat hotplate (GALLTMKAMP,

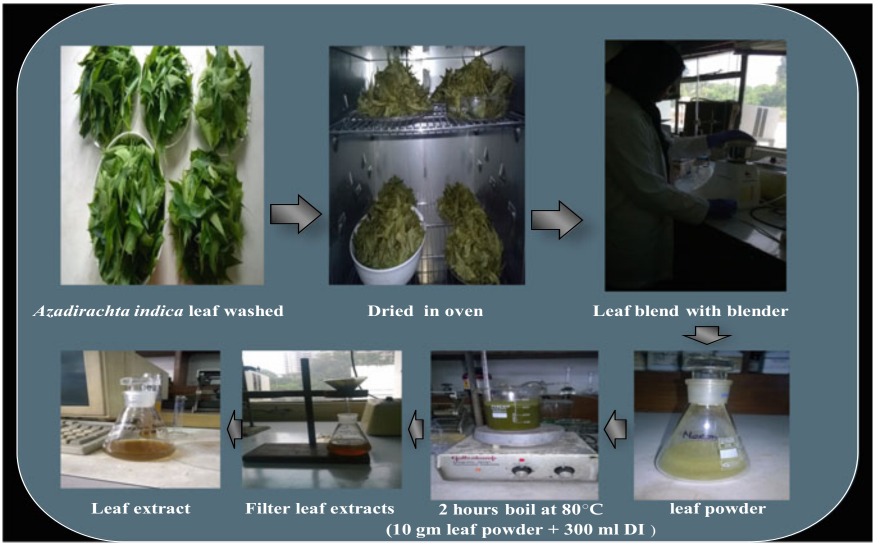

Fig. 1 Methods of *Azadirachta indica* leaf extract preparation

England), Incubator (115 V) RI 115, Electric oven (Binder), Bath sonicator (Decon FS minor), X-ray diffractometer (Philips, Expert Pro, Holland), Fourier transform infrared spectrophotometer (Jasco-FT-IR-6300), Field emission scanning electron microscopy (JSM-7600F, Tokyo, Japan), TGA machine (TA instrument, SDT Q-600) and Vibrating sample magnetometer (EV-9 Micro Sense, Germany).

Figure 1 shows the preparation of *Azadirachta indica* leaf extract preparation. Firstly, it has been taken washed *Azadirachta indica* leaf then it was dried, then the leaf was blended by a blender and then it was made leaf powder. After that this powder was mixed with DI water and heated at 80 °C for two hours, then it was filtered and we got leaf extract.

Figure 2 shows the preparation of iron oxide nanoparticles (Fe_3O_4-NPs) from *Azadirachta indica* leaf extract. It is shown that it needs seven different steps to get iron oxide nanoparticles (Fe_3O_4-NPs) from *Azadirachta indica* leaf extract.

1.2 Synthesis of Fe_3O_4 NPs

Fe_3O_4 NPs were synthesized via a facile green synthesis route where $FeCl_3$ and $FeCl_2 \cdot 4H_2O$ were used as precursor and *Azadirachta indica* leaf extract was used as a source of reducing and capping agents. To synthesize Fe_3O_4, the *Azadirachta indica* leaf extract was added to an aqueous mixture of Fe^{3+} and Fe^{2+} chloride at a 2:1 M ratio (Khan et al. 2018a, b). The chemical reaction of Fe_3O_4 precipitation is given below:

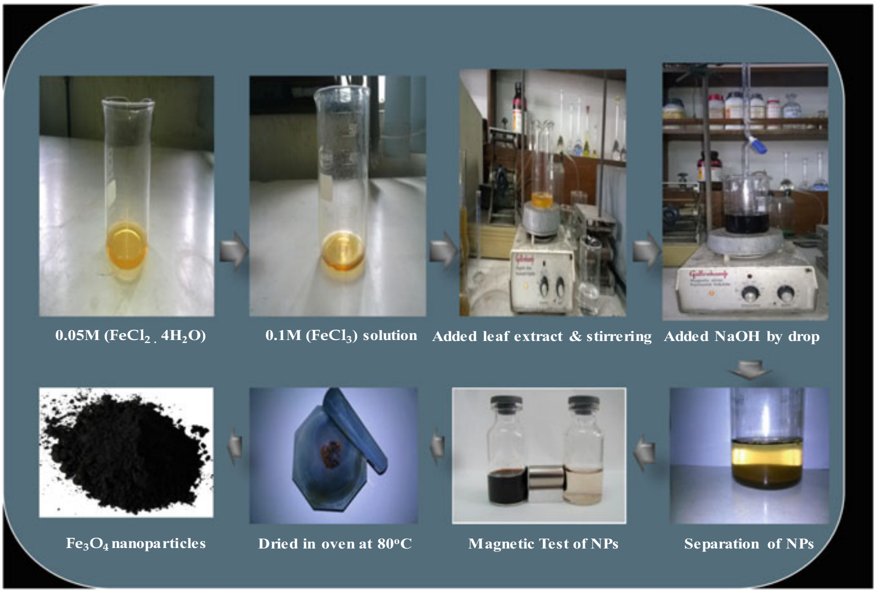

Fig. 2 Methods of NPs preparation from *Azadirachta indica*

$$\text{Azadirachta indica} + H_2O + Fe^{2+}(aq) + Fe^{3+}(aq) + OH^- \\ \rightarrow [\text{Azadirachta indica}/Fe_3O_4]$$

2 Results and Discussion

2.1 Structural Analysis of XRD

The diffraction peaks of synthesized Fe_3O_4 NPs are assigned to the crystal planes of (220), (311), (400), (440), respectively. The analyzed diffraction peaks were matched well with the standard magnetite XRD patterns with JCPDS file no: 89.0691 which declared the crystallographic system of spherical structure (Fig. 3).

Debye–Scherrer's Formula
Equation for calculating structural parameters.

Debye–Scherrer's Formula

$$D = \frac{k\lambda}{\beta_{hkl}\cos\theta} \tag{1}$$

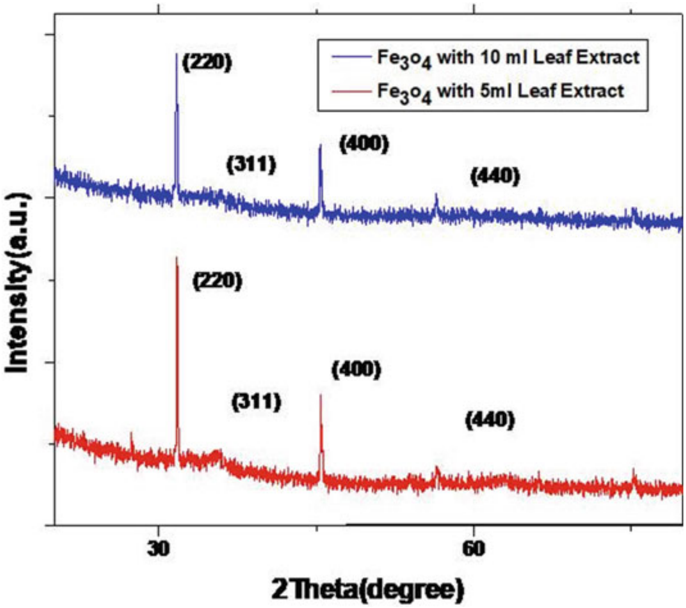

Fig. 3 Structural analysis of XRD

Table 1 Structural analysis for XRD

Leaf extract in Ml	Crystallite size *D* in (Nm) line/Nm	Micros-train (*E*) × 10^{-3}
5	5.73	2.90
10	6.34	1.46

where β is the full width at half maxima (FWHM), λ is the wavelength (λ = 0.15406 Å), D the average crystallite size and θ is Bragg's angle.

Table 1 shows the crystallite size and structural parameter for different capping and stabilizing agents presentation (Fig. 4).

The crystallite size is increasing, respectively, according to the leaf extract increasing and the estimated crystallite size are 5.73 and 6.34 nm (Fig. 5).

2.2 Fourier Transform Infrared Spectroscopy (FT-IR) Analysis

The Fourier transform infrared spectroscopy (FT-IR) analysis showed that the capping agents of the NPs contained the functional groups alcohol, alkane, amine, alkyne, etc. (Table 2).

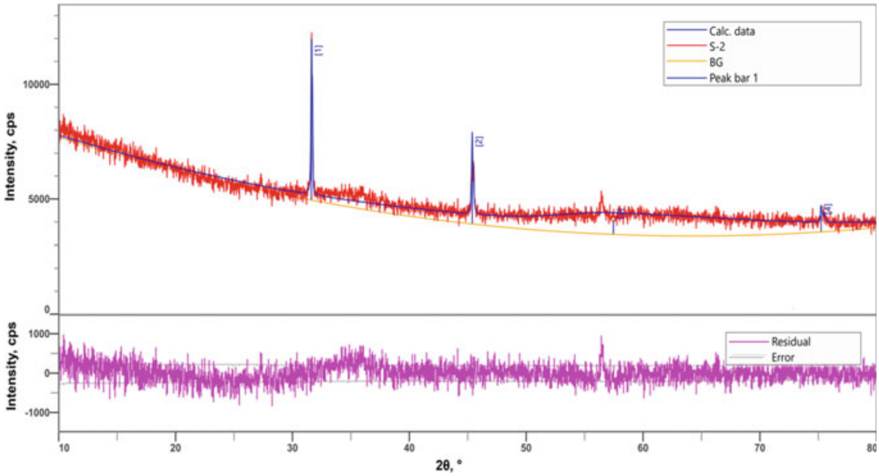

Fig. 4 Variation of intensity with 2θ

Fig. 5 Variation of transmittance (a.u.) with 2θ

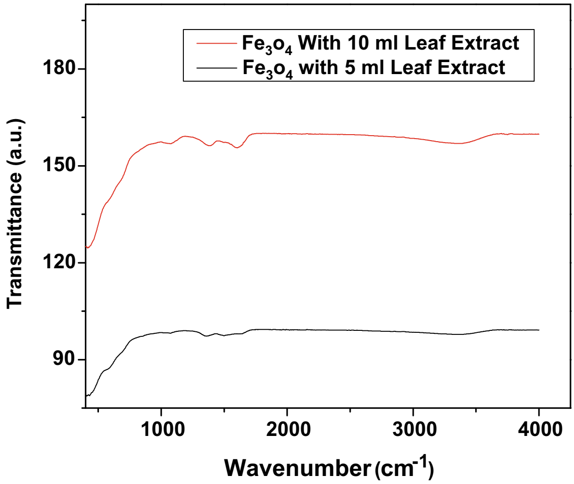

2.3 Surface Morphology of the NPs

The surface morphology of the NPs was investigated by field emission scanning electron microscopy (FESEM) which showed that NPs were spherical in shape (Fig. 6).

Table 2 Table for Fourier transform infrared spectroscopy (FT-IR) analysis

Functional group	Peak position (sample-1)	Peak position (sample-2)	Attribution
– OH	3450.29	3456.65	Stretching vibration of –OH functional group
N–H	3324.09	3327.92	N–H stretching and bending vibration of amine group NH_2
Azadirachta indica	3415.29	3416.05	The involvement of functional groups of *Azadirachta indica* in the reduction process
– C≡C–	2424.78	2429.65	Alkyne group presents in phytoconstituents of extracts
Fe–0	1623.85	1622.13	Stretching vibration of Fe–O bond
– CH_3	1370.72	1375.01	Bending alkanes
C–O	1076.06	1133.44	Stretching carbonyl
– O–H	939.21	942.88	Bending hydroxyl

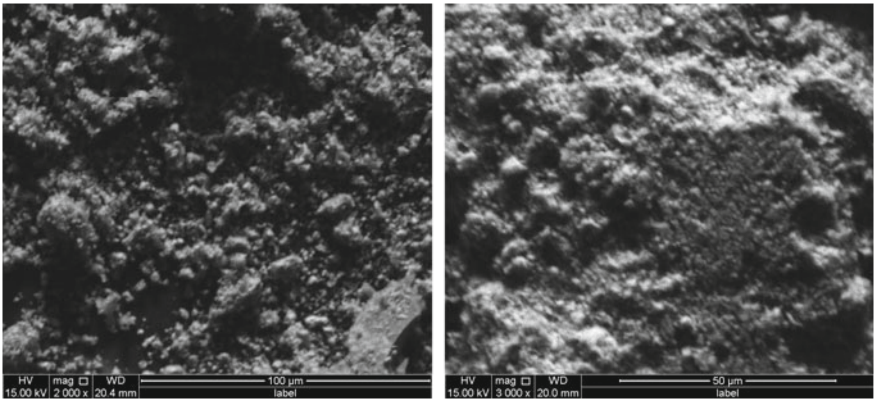

Fig. 6 Surface morphology of the NPs

2.4 VSM Analysis of NPs

The NPs were superparamagnetic in nature with zero coercivity and zero reminance magnetization which was observed (Figs. 7 and 8).

Finally, we can say that the saturation magnetization (Ms) of the Fe_3O_4 indicates the presence of non-magnetic surface layers resulting from the strong chemical

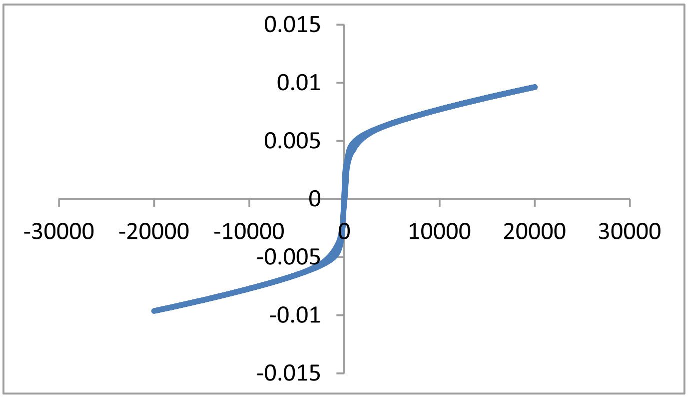

Magnetization Vs Applied field (Oe) graph

Fig. 7 Magnetization curve of Fe_3O_4 NPs of sample-1 as a function of applied field

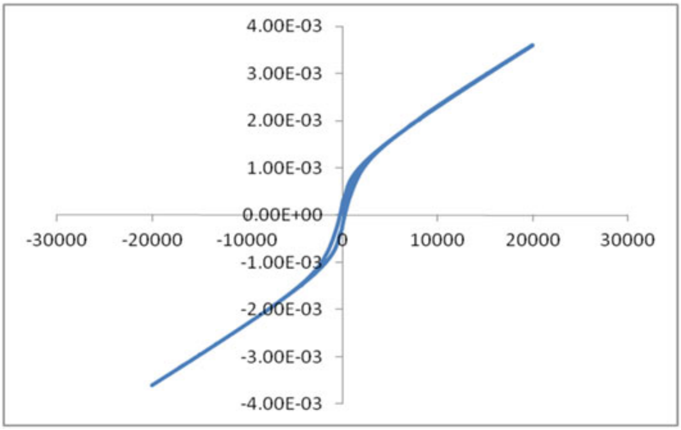

Magnetization Vs Applied field (Oe) graph

Fig. 8 Magnetization curve of Fe_3O_4 NPs of sample-2 as a function of applied field

attachment of the stabilizing agent of *Azadirachta indica* leaf extract to the Fe_3O_4s surface which also observed by FT-IR spectroscopy.

2.5 DSC Analysis of NPs

In DSC curve, exothermic and endothermic peak are observed, and the sharp exothermic peak occurred in between 800 to 840 °C due to the physical state change

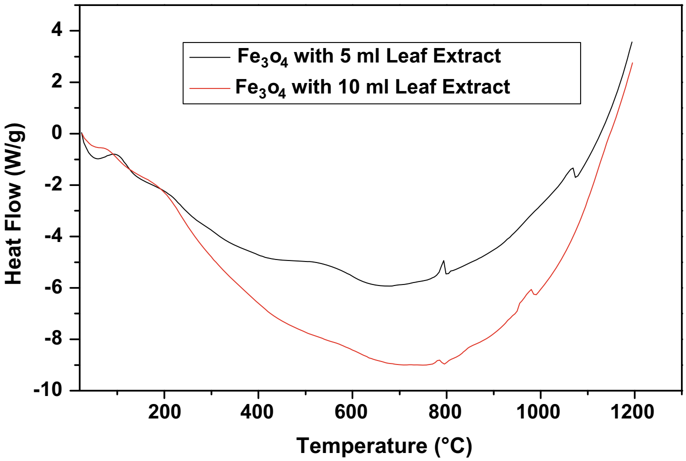

Fig. 9 DSC plot as a function of temperature of Fe_3O_4 NPs

of water. The result of DSC demonstrated that the magnetite is unstable at high temperature and it gets transferred to hematite at high temperature (Fig. 9).

3 Conclusions

Magnetite NPs were successfully synthesized through green synthesis method using *Azadirachta indica* leaf extract. Leaf extract acts as capping and stabilizing agent that prevents the conglomerated of magnetite NPs formed during synthesis. Crystallinity, surface morphology, magnetic property and thermal properties are analyzed here. From the XRD, FT-IR, FESEM, TGA, DSC and VSM analysis, it can be concluded that we have successfully synthesized crystalline Fe_3O_4 NPs.

Acknowledgements The authors are grateful to the GARE (Grant of Advanced Research in Education) project, Ministry of Education, GoB for financing during the research work (Project/User ID: PS2019949).

References

Bashar I, Ihab MO, Borhan AA, Yousef H (2013) Magnetic nanoparticles: surface effects and properties related to biomedicine applications. Int J Mol Sci 14:266–305

Davor B (1993) X-ray diffraction line broadening: modelling and applications to high-T_c superconductors. J Res Natl Inst Stand Technol 98:321–353

Fazlzadeh M, Rahmani K, Zarei A, Abdoallahzadeh H, Nasiri F, Khosravi R (2016) A novel green synthesis of zero valent iron nanoparticles (NZVI) using three plant extracts and their efficient application for removal of Cr (VI) from aqueous solutions. Adv Powder Technol 28(1):122–130

Hasan M, Khan KA (2018) Dynamic model of Bryophyllum pinnatum leaf fueled BPL cell: a possible alternate source of electricity at the off-grid region in Bangladesh. In: Microsystem technologies micro- and nanosystems information storage and processing systems. Microsystem Technologies. Springer. https://doi.org/10.1007/s00542-018-4149-y. ISSN 0946-7076

Hasan M, Khan KA (2019) Experimental characterization and identification of cell parameters in a BPL electrochemical device. In: SN applied sciences, vol 1. Springer, p 1008. https://doi.org/10.1007/s42452-019-1045-8

Hassan L, Khan KA (2020) A study on harvesting of PKL electricity. Microsyst Technol 26(3):1031–1041. https://doi.org/10.1007/s00542-019-04625-7

Hazrat Ali M, Chakma U, Howlader D, Tawhidul Islam M, Khan KA (2019) Studies on performance parameters of a practical transformer for various utilizations, microsystem technologies. Springer. Accepted: 03 Dec 2019. https://doi.org/10.1007/s00542-019-04711-w

Khan KA (1999) Copper oxide coatings for use in a linear solar Fresnel reflecting concentrating collector. Renew Energy Int J 17(4):603–608. WREN (World Renewable Energy Network), UK, RE: 12.97/859, 1998, Publication date 1999/8/1. Pergamon

Khan KA, Hassan L, Obaydullah AKM, Azharul Islam SM, Mamun MA, Akter T, Hasan M, Shamsul Alam M, Ibrahim M, Mizanur Rahman M, Shahjahan M (2018a) Bioelectricity: a new approach to provide the electrical power from vegetative and fruits at off-grid region. Microsystem technologies. Springer. https://doi.org/10.1007/s00542-018-3808-3(0123456789().,-volV)(0123456789().,-VolV)

Khan KA, Bhuyan MS, Mamun MA, Ibrahim M, Hasan L, Wadud MA (2018b) Organic electricity from Zn/Cu-PKL electrochemical cell, In: Mandal JK et al (eds) Contemporary advances in innovative and applicable information technology. Advances in intelligent systems and computing, vol 812. © Springer Nature Singapore Pvt. Ltd., pp 75–90 (Chapter 9)

Khan KA, Hazrat Ali M, Obaydullah AKM, Wadud MA (2019a) Production of candle using solar thermal technology. In: Microsystem technologies micro- and nanosystems information storage and processing systems. Microsystem Technologies, vol 25(12). Springer. https://doi.org/10.1007/s00542-019-04390-7. ISSN 0946-7076

Khan KA, Rasel SR, Ohiduzzaman M (2019b) Homemade PKL electricity generation for use in DC fan at remote areas. In: Microsystem technologies micro- and nanosystems information storage and processing systems. Microsyst technology, vol 25(12). https://doi.org/10.1007/s00542-019-04422-2. ISSN 0946-7076

Khan KA, Mamun MA, Ibrahim M, Hasan M, Ohiduzzaman M, Obaydullah AKM, Wadud MA, Shajahan M (2019c) PKL electrochemical cell: physics and chemistry. SN Appl Sci 1:1335. https://doi.org/10.1007/s42452-019-1363-x

Klokkenburg M, Hilhorst J, Erne BH (2007) Surface analysis of magnetite nanoparticles in cyclohexane solutions of oleic acid and oleylamine. Vib Spectrosc 43:243–248

Lu W, Shen Y, Xie A, Zhang W (2010) Green synthesis and characterization of superparamagnetic Fe_3O_4 nanoparticles. J Magn Magn Mater 322:1828–1833

Nicolae CP, Davor B, Sven CV (2014) Elastic macro strain and stress determination by powder diffraction: spherical harmonics analysis starting from the Voigt model. J Appl Cryst 47:154–159

Parker FT, Foster MW, Margulies DT, Berkowitz AE (1993) Spin canting, surface magnetization, and finite-size effects in y-Fe_2O_3 particles. Phys Rev B 47:7885–7891

Payman R, Allan H (2009) A Fourier transform infrared (FTIR) and thermogravimetric analysis (TGA) study of oleate adsorbed on magnetite nano-particle surface. Appl Surf Sci 255:5891–5895

Ruhane TA, Tauhidul Islam M, Rahman MS, Bhuiyah MMH, Islam JMM, Bhuiyah TI, Khan KA, Khan MA (2017) Impact of photo electrode thickness annealing temperature on natural dye sensitized solar cell. Sustain Energy Technol Assess. https://doi.org/10.1016/j.seta.2017.01.012

Ruhane TA, Tauhidul Islam M, Rahaman MS, Bhuiyan MMH, Islam JMM, Newaz MK, Khan KA, Khan MA (2017) Photo current enhancement of natural dye sensitized solar cell by optimizing dye extraction and its loading period. Opt Int J Light Electron Opt 149:174–183

Sulistyaningsih T, Silalahi DSV, Santosa SJ, Siswanta D, Rusdiarso B (2013) Synthesis and characterization of magnetic MgAl–NO_3–HT composite via the chemical co-precipitation method. In: Proceedings of chemical, biological and environmental engineering, vol 58, pp 95–99

Impact of Asymmetric Spacer on the Performance of Dielectric Modulated TFET Biosensor

Swagata Bhattacherjee

Abstract In this paper first time, the dependence of asymmetric spacer layer on the performance of a dielectric modulated TFET biosensor is studied based on simulation technique using SILVACO ATLAS. It is observed that spacer layer has a significant role on the sensing capacity. A suitable dielectric material with suitable underlap length of the spacer layer can effectively improve the performance index of the biosensor. It is obtained that a spacer layer of dielectric constant ~10 to 15 can give best result when the underlap length is kept in the range of 5–7 nm.

Keywords Biosensor · TFET · Drain current · Transconductance efficiency · Space layer

1 Introduction

Ultrasensitive biosensors with emerging micro/nanotechnologies attract attention due to capabilities of quick detection. Electrical detection of biomolecules using Tunnel Field-Effect-Transistors (FETs) (Svintsov et al. 2012; Rawat and Paily 2015.) is very attractive due to a sharp dependence of the tunnel current on the overlapping of conduction-valence band in a gate-controlled *p–n* junction. It can alleviate the fundamental limitation in subthreshold slope (60 mV/decade) of conventional FETs due to its small thermionic leakage current and effectual variation of the barrier transparency by the gate voltage. The superior subthreshold behavior of TFETs has made this device an efficient member of biosensors. Dielectric Modulated (DM) FET-based biosensors (Kanungo et al. 2015; Kannan and Jagadesh Kumar 2013; Dwivedi and Kranti 2017, 2018; Verma et al. 2017; Wadhwa and Raj 2018) are widely used to detect charged as well neutral biomolecules by changing the effective capacitance of gate oxide with dielectric constant and charge density of biomolecules in the cavity. TFETs attain higher sensitivity when biomolecules are located at the source–channel junction. As the biomolecules are kept away from the tunneling

S. Bhattacherjee (✉)
JIS College of Engineering, Kalyani, Nadia, India
e-mail: Swagata.bhattacherjee@jiscollege.ac.in

M. Mukherjee et al. (eds.), *Advances in Medical Physics and Healthcare Engineering*, Lecture Notes in Bioengineering, https://doi.org/10.1007/978-981-33-6915-3_10

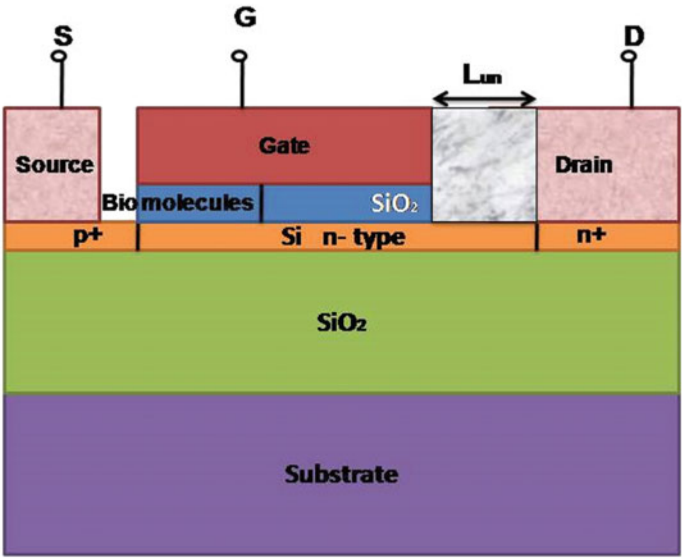

Fig. 1 Schematic diagram of dielectric modulated biosensor

junction sensitivity starts to weaken rapidly. Kanungo et al. reported that a short gate dielectric-modulated TFET biosensor showed improved sensitivity than a full gate dielectric modulated TFET (Kanungo et al. 2015). In Kannan et al., (Kannan and Jagadesh Kumar 2013), the application of impact-ionization MOS transistor as a bio-sensor is proposed where a high sensitivity which hardly varies with the charges on the biomolecule are discussed for small channel lengths (Fig. 1).

In Dwivedi and Kranti (2017) feasibility of transconductance-to-current ratio as a sensing metric for tunnel FET biosensors is evaluated where enhancement of the transconductance efficiency at lower current levels in the presence of biomolecules is analyzed. Whereas in Dwivedi and Kranti (2018) the feasibility assessment of tunneling and accumulation mode *p*-type transistor based on dielectric-modulated biosensors is presented in which the performance of devices is compared through the estimation of the change in electrical characteristics between bioreceptor and target biomolecules for a partially filled cavity. In Verma et al. (2017), a novel architecture is proposed which is basically a vertical dielectrically modulated TFET, consists of a heavily doped front gate n+-pocket and gate-to-source overlap to improve the performance of lateral biosensor. In other paper, charge-plasma based gate underlap dielectric modulated junctionless TFET is implemented for the label-free electrical recognition of biomolecules considering the dielectric modulation technique (Wadhwa and Raj 2018). Kim et al. reported on partially filled nanogaps, and proposed a parameter, ill factor, defined as the percentage of the nanogap occupied by biomolecules (Kim et al. 2009). Narang et al. provided a Poisson equation-based analytical model to account for the effect of dielectric modulation in TFETs (Narang et al. 2012). Partially filled nanogaps decrease the response of the biosensor, as the effective dielectric constant varies with position within the nanogap. Abdi and Kumar proposed the concept of deriving the sensitivity through ambipolar current in TFET (Abdi and Kumar 2015). Ahangari presented reports of a dual material gate nanowire junctionless TFET as a biosensor (Ahangari 2016). In the above-mentioned paper, the sensitivity is measured with respect to the cavity. Either dependence on the dimension of the cavity or the dielectric constant of the cavity were focused. None of the above-mentioned paper dealt with the effects of asymmetric spacer layer on the detection of the biomolecules. In this paper I am working first time on the effects of spacer layer on the detection of biomolecules, using a dielectric modulated TFET based on drain current and transonductance efficiency measurement in subthreshold region. The paper is arranged as follows. Methodology is discussed after introduction. Thereafter detailed results are analyzed followed by the conclusions at the end.

2 Methodology

The transconductance efficiency (gm/Ids*)* is a very useful performance indicator in analog circuit evaluation (Rudenko et al. 2011; Flandre et al. 2010). It can also be used as the sensing metric due to the sharp change of its value for the presence of biomolecules in the cavity. We used numerical simulation technique using ATLAS (Atlas User's Manual 2016), a 2-D device simulator to simulate an asymmetric underlap dielectric modulated TFET. The device is simulated by using a 300-nm n-type ultrathin body Si layers of 8 nm channel thicknesses with a doping concentration of 1×10^{15} cm^{-3}, 1×10^{19} cm^{-3} and 3×10^{18} cm^{-3} in formation of channel, source, and drain respectively. The front insulator consists of a 2-nm thick SiO_2 dielectric layer, whereas for bottom gate a 25 nm SiO_2 gate dielectric is used. A 100 nm $\times$ 2 nm cavity is formed along the source side. Ni is used for formation of gate while gold is used to make ohmic contacts for source and drain. We used different material with different dielectric constant and underap length (L_{un}) to form the asymmetric spacer layer at drain end. Accordingly, we have employed Fermi–Dirac statistics, concentration and field-dependent carrier mobility, velocity saturation, band gap narrowing, and band to band tunneling model for the simulation. We obtained various electrical parameters like electron concentration, surface potential, conduction and valance band energy, drain current (I_D), transconductance (g_M), etc. from the simulation. The drain currents are measured in presence (I_{Dbio}) and absence of biomolecules (I_{Dair}) and the ratio (I_{Dbio}/I_{Dair}) is taken. The transconductance and drain currents are utilized to extract the transconductance efficiency (g_M/I_D). (I_{Dbio}/I_{Dair}) and (g_M/I_D) are used to determine the sensing ability of the biomolecules.

3 Results and Discussions

The effects of asymmetric underlap on the drain current and transconductance efficiency of the biosensor for different dielectric constant of the asymmetric spacer layer are studied in the present work. Figure 2 shows the transfer characteristics of the dielectric modulated tunnel FET for two different biomolecules namely biotin (dielectric constant 2.63) and -APTES (dielectric constant 3.57) with respect to air.

From the curve it is observed that in presence of biomolecules the drain current is sharply changed with respect to the air which confirms the occurrence of biomolecules. In absence of biomolecules the cavity is filled with air which has a dielectric constant of 1 which is changed by 2.63 and 3.57 in presence of biotin and APTES respectively. Figure 3a presents the variation of the ratio of drain current in presence of biomolecules (I_{Dbio}) to the drain current in absence of biomolecules (I_{Dair}) with gate voltage for different dielectric constant whereas Fig. 3b depicts the impacts of different underlap lengths for the same. One can follow from the graphs that spacer layer has a strong impact on the drain current ratio. The ratio is maximum for Al_2O_3 when the underlap length is considered as 10 nm. The effects of asymmetric spacer layer on the transconductance efficiency are also studied which is working as the performance indicator of the device. Figure 4 depict the variation of transconductance efficiency with drain current for different dielectric materials (Fig. 4a and b) and underlap lengths (Fig. 4c and d) of the asymmetric spacer layer. The sharp change of transconductance efficiency in presence of biomolecules established the sensing ability of the tunnel FET device. It is clear that spacer layer has a strong impact on the said parameter of the device. The figure indicates that the change of tranconductance efficiency is different for different spacer layers for the presence of biomolecules in the cavity.

Figure 5a and b show the change of transconductance efficiency w.r.t. air with dielectric constant and underlap lengths of the spacer layer respectively. One can

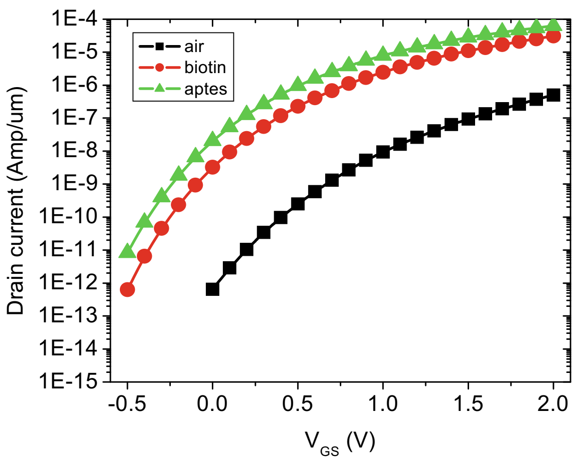

Fig. 2 Transfer characteristics for two different biomolecues with respect to air

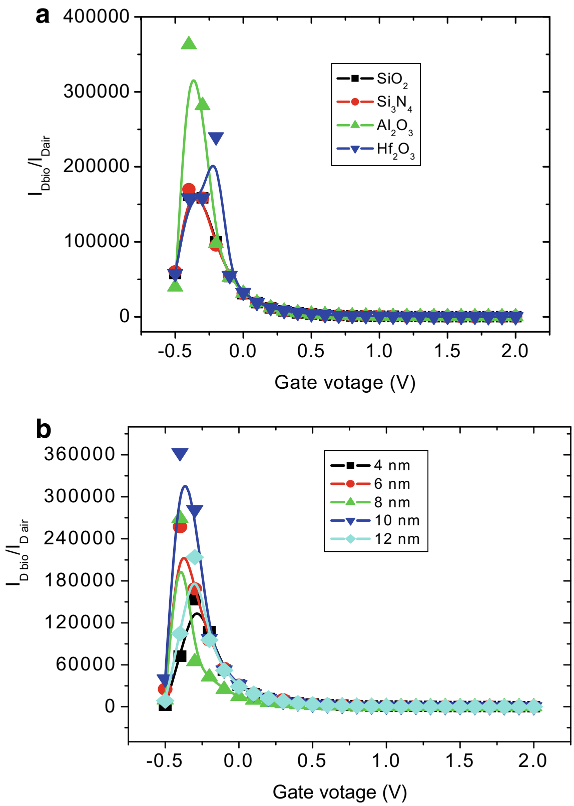

Fig. 3 **a** Ratio of I_D in presence of biomoecules to the absence of biomolecules with gate voltage for different dielectrics used for spacer layer. **b** Ratio of I_D in presence of biomoecules to the absence of biomolecules with gate voltage for different underlap (L_{un}) used for spacer layer

easily find from the Fig. 5a that transcondutance efficiency increases with dielectric constant reaches a maximum value, and the decreases with it. The curve also depicts that shift of transconductance efficiency in presence of biomolecules is maximum nearly at a dielectric constant of 10–15. Beyond that, it is decreased with increasing k value of spacer layer. On the other hand the Fig. 5b shows that the sensing parameter equally depends on L_{un}. It initially increases with L_{un}, after reaching the maximum value (~6 nm) starts to decrease. Thus from Fig. 5a and b it is clear that one can improve the sensing capacity of tunnel FET by increasing the dielectric constant of the spacer layer and expect the best performance by using a spacer layer of dielectric constant 10 keeping the underlap length ~6 nm.

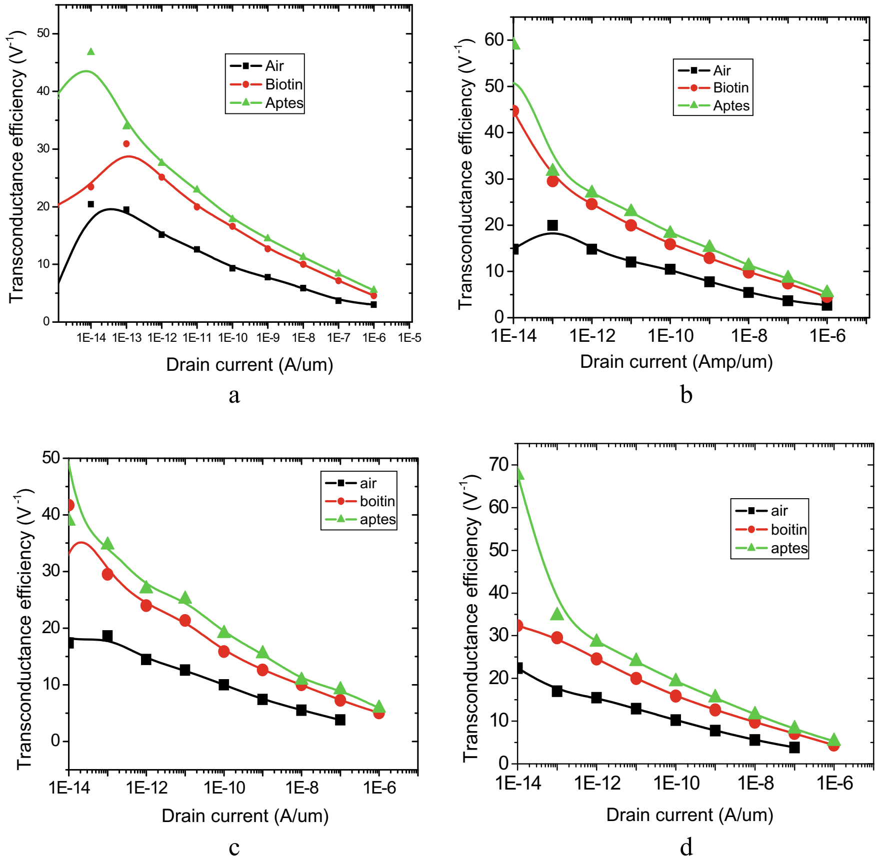

Fig. 4 Variation of transconductance efficiency with drain current for two different biomolecues with respect to air using **a** SiO_2 (L_{un} = 10 nm) **b** SiN (L_{un} = 10 nm) **c** I_{un} = 4 nm (Al_2O_3) and **d** I_{un} = 12 nm (Al_2O_3) as spacer layer

4 Conclusion

We have presented the effects of spacer layer on the performance of dielectric modulated tunnel FET-based biosensor by taking drain current and transconductance efficiency as sensing metric. Results indicate that the spacer layer plays a significant role in sensing of biomolecules. A proper selection of dielectric material and underlap can give maximum sensitivity of the device.

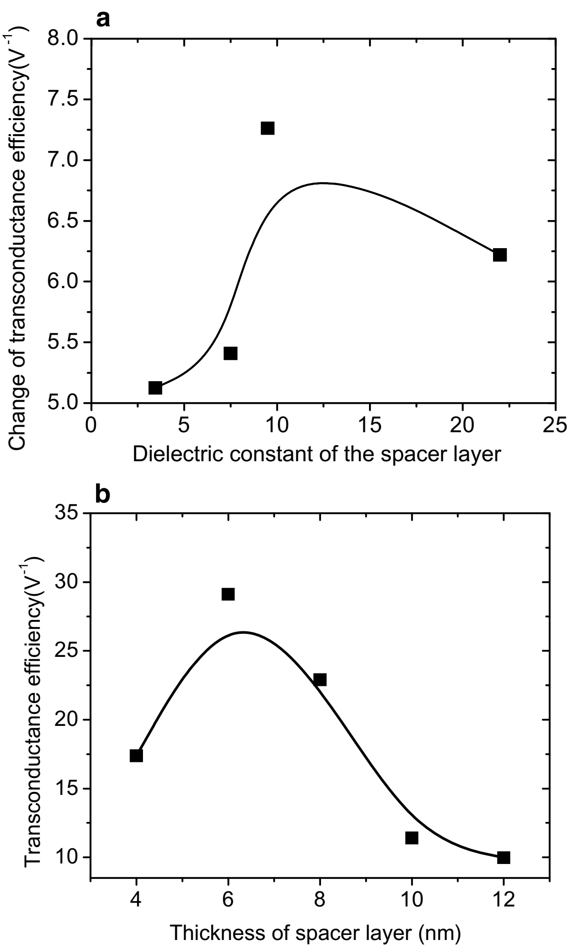

Fig. 5 **a** Shift of transconductance efficiency with dielectric constant of the spacer layer for biotin considering $L_{un} = 10$ nm **b** Change of transconductance efficiency with L_{un} of the spacer layer for biotin considering Al_2O_3 as dielectric as the material of it

References

Abdi D, Kumar MJ (2015) Dielectric modulated overlapping gate-on drain tunnel-FET as a label-free biosensor. Superlattices Microstruct 86:198–202

Ahangari Z (2016) Performance assessment of dual material gate dielectric modulated nanowire junctionless MOSFET for ultrasensitive detection of biomolecules. RSC Adv 6:89185–89191

Atlas User's Manual (2016) Device simulation software. Silvaco International Inc., Santa Clara, CA, USA

Dwivedi P, Kranti A (2017) Applicability of transconductance-to-current ratio (*gm*/*Ids*) as a sensing metric for tunnel FET biosensors. IEEE Sens J 17(4):1030–1036

Dwivedi P, Kranti A (2018) Dielectric modulated biosensor architecture: tunneling or accumulation based transistor? IEEE Sens J 18(8):3228–3235

Flandre D, Kilchytska V, Rudenko T (2010) g*m*/*Id* method for threshold voltage extraction applicable in advanced MOSFETs with nonlinear behavior above threshold. IEEE Electron Device Let 31(9):930–932

Kannan N, Jagadesh KM (2013) Dielectric-modulated impact-ionization MOS (DIMOS) transistor as a label-free biosensor. IEEE Electron Device Letts 34(12):1575–1577

Kanungo S, Chattopadhyay S, Gupta PS, Rahaman H (2015) Comparative performance analysis of the dielectrically modulated full-gate and short-gate tunnel FET-based biosensors. IEEE Trans Electron Devices 62(3):994–1001

Kim SK, Cho H, Park HJ, Kwon D, Lee JM, Chung BH (2009) Nanogap biosensors for electrical and label-free detection of biomolecular interactions. Nanotechnology 20(45):455502

Narang R, Sasidhar K V Reddy, Saxena M, Gupta RS, Gupta M (2012) A dielectric-modulated tunnel-FET-based biosensor for label-free detection: analytical modeling study and sensitivity analysis. IEEE Trans Electron Devices 59(10):2809–2817

Rawat B, Paily R (2015) Analysis of graphene tunnel field-effect transistors for analog/RF applications. IEEE Trans Electron Devices 62(8):2663–2669

Rudenko T, Kilchytska V, Arshad MKM, Raskin JP, Nazarov A, Flandre D (2011) On the MOSFET threshold voltage extraction by transconductance and transconductance-to-current ratio change methods: Part I—Effect of gate-voltage-dependent mobility. IEEE Trans Electron Devices 58(12):4172–4179

Svintsov DA, Vyurkov VV, Lukichev VF, Orlikovsky AA, Burenkov A, Oechsner R (2012) Tunnel field effect transistors with graphene channels. Int Conf Silicon 2012, St. Petersburg, 9–13 July 2012

Verma M, Tirkey S, Yadav S, Sharma D, Yadav D S. Performance assessment of a novel vertical dielectrically Modulated TFET-based biosensor. IEEE Trans Electron Devices https://doi.org/10.1109/TED.2017.2732820

Wadhwa G, Raj B. Label free detection of biomolecules using charge-plasma-based gate underlap dielectric modulated junctionless TFET. J Electron Mater. https://doi.org/10.1007/s11664-018-6343-1

Advancement and Challenges for Non-invasive Monitoring of Blood Glucose: A Review

Santu Guin and Madhurima Chattopadhyay

Abstract The aim of this study is to bring the current status as well as the future perspective of various techniques and devices for non-invasive monitoring of blood glucose. Blood glucose monitoring device is a very essential tool to assess the level of blood glucose frequently by diabetic patients as well as physicians. The most common commercialized method for blood glucose monitoring is invasive, painful, time-consuming, and expensive that requires finger pricking to draw the blood. To address this situation there is a need to develop a cost-effective noninvasive, reliable blood glucose monitoring device to improve the patient's daily life. In this context, several research articles have been studied. It has been observed that optical, thermal and electrical techniques are mainly adopted for noninvasive mode of blood glucose monitoring. Different types of spectroscopy techniques along with polarimetry and tomography are included in the optical method. Thermal emission spectroscopy and metabolic heat conformation are under thermal technique. Bioimpedance spectroscopy, electromagnetic sensing, reverse iontophoresis, millimeter, and micrometer wave sensing are included in the electrical technique. The general topology of different techniques/devices and challenges have been discussed over here.

Keywords Blood glucose monitoring · Diabetics · Non-invasive · Polarimetry · Tomography · Spectroscopy · Bioimpedance · Iontophoresis

1 Introduction

Diabetes Mellitus is a chronic, metabolic disorder that occurs when the human body becomes resistant to insulin or the pancreas is not able to make enough insulin. Currently, diabetes is the most common non-communicable disease and the World

S. Guin (✉)
Techno Main Salt Lake, Kolkata, India

M. Chattopadhyay
Heritage Institute of Technology, Kolkata, India
e-mail: madhurima.chattopadhyay@heritageit.edu

M. Mukherjee et al. (eds.), *Advances in Medical Physics and Healthcare Engineering*, Lecture Notes in Bioengineering, https://doi.org/10.1007/978-981-33-6915-3_11

Health Organization (WHO) estimated about 422 million people had diabetes globally in 2014 (World Health Organization 2020). At the end of 2019, International Diabetes Federation (IDF) estimated that 463 million adults had diabetes and this number will increase to 700 million in 2045 (International Diabetes Federation 2019). This report also shows that India is the country with second-highest number of people (20–79 years) (raphem. 77 million) living with type 2 diabetes worldwide next to China (International Diabetes Federation 2019). People with diabetes cannot properly metabolize glucose inside their body and typically pricking the fingertips by conventional glucose checking devices invasively to monitor their glucose levels (So et al. 2012). Therefore, non-invasive glucose monitoring devices overcome this painful experience by reducing the risk of infection and damage of finger tissues (So et al. 2012). Several techniques and devices for noninvasive monitoring of blood glucose have already been studied like in 1999, Khalil et al. (Khalil 1999) presented the glucose molecule and tissue properties at different wavelengths based on in-vivo and ex-vivo samples. Later in 2017, Lin et al. (2017) nicely reviewed some noninvasive devices as well as the main challenges related with glucose detection. In the same year, Chen et al. (2017) described the current scenario of the minimally invasive and noninvasive techniques for blood glucose measurement. Next year, Van Enter et al. (Van Enter and Von Hauff 2018) reviewed several properties of the glucose molecule and studied the effect on the accuracy of noninvasive techniques. Besides these, based on nanotechnology certain materials such as graphene, carbon nanotubes, etc. can also be used to develop a biosensor but they are still in early stage of research and development. A microneedle biosensor using Multiwall Carbon Nanotubes (MWCNTs) by amperometric method was developed by Jia et al. (2008). Later on, Zhigang et al. (2012) not only introduced the carbon nanotube and graphene based biosensors for glucose detection but also gave an outline of the current status with future perspective of these carbon nanomaterials. Afterwards, a carbon nanotube based transistor that is coated with pyrene-1-boronic acid molecules for glucose detection in saliva was developed by Lerner et al. (MIT 2020). Moreover, different synthetic materials like quantum dots, carbon nanotubes can be used in fluorescent technique to monitor parameters within a broad range of spectrum (Barone and Strano 2009). In this review, different techniques along with their advantages, limitations, and related devices have been considered. Various devices or companies for blood glucose sensing technology with their status as of December, 2019 are also listed here. Many of them are not commercially successful due to less sensitivity and low accuracy of the measurement (Tura et al. 2010). Some of the prototype devices are yet to be approved by the Food and Drug Administration (FDA) and the Communauté Européenne (CE).

2 Non-invasive Blood Glucose Monitoring Techniques

Based on the literature survey (So et al. 2012; Khalil 1999; Lin et al. 2017; Chen et al. 2017; Enter and Hauff 2018; Jia et al. 2008; Zhigang et al. 2012; MIT 2020;

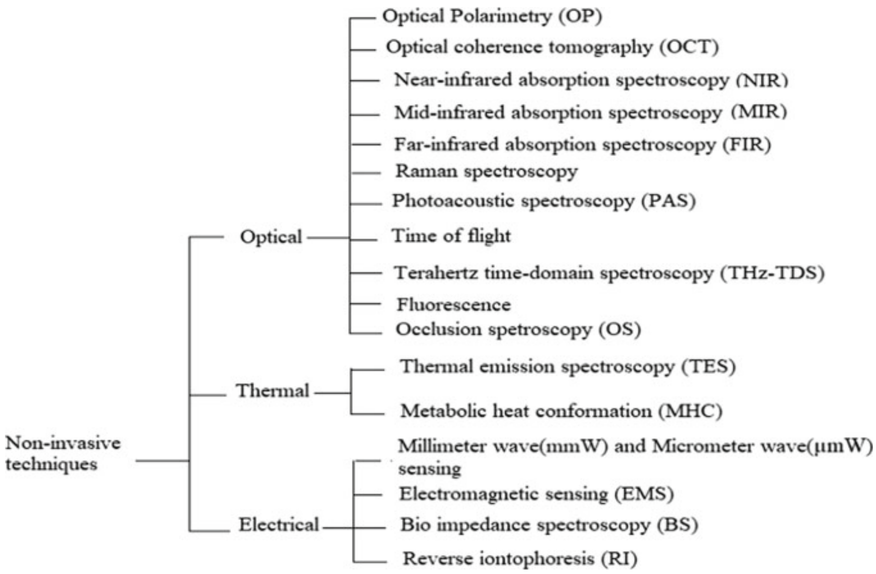

Fig. 1 Classification of non-invasive blood glucose monitoring techniques

Barone and Strano 2009; Tura et al. 2010; Malik and Coté 2010; Oliver et al. 2009; Lan et al. 2017; Coates 1998; Buchert 2004; Klonoff 1997; Cho et al. 2004; Shaker et al. 2018; Zhang et al. 2018; Potts et al. 2002a; Gourzi et al. 2005), it is found that several techniques like optical, thermal, and electrical have been used to monitor the blood glucose non-invasively as shown in Fig. 1. Basically optical technique uses the different properties of light like reflection, absorption and scattering when it passes through the biological media to interact with some molecules (Malik and Coté 2010; Oliver et al. 2009; Lan et al. 2017; Coates 1998). On the other hand, thermal techniques are based on the measurement of basal metabolic rates and heat generation by human body as it works in the far infrared region (Buchert 2004; Klonoff 1997; Cho et al. 2004). Another technique is electrical that is based on the detection of dielectric properties of glucose molecules using current, voltage, electromagnetic radiation, and ultrasound (Shaker et al. 2018; Zhang et al. 2018; Potts et al. 2002a; Gourzi et al. 2005).

2.1 Optical Polarimetry (OP)

This technique depends on the rotation of the plane of polarized light by the temperature, thickness, and concentrations of the solutes which is used to determine glucose levels in blood (Rawer et al. 2004; Gamessa 2019). This method is unaffected by pH variations but sensitive to temperature, motion and has poor system stability (Salam 2016).

2.2 Optical Coherence Tomography (OCT)

It is used to determine the glucose concentration present in blood by measuring the delay correlation between the scattered light from tissues in the sample arm and reflected light in the reference arm by employing an interferometer (Losoya et al. 2012). Hence, the refractive index increases in response to increase in glucose concentration causes a change in scattering coefficient which is used to detect the glucose concentration in blood. This technique generates high-resolution 2D image and has high in-depth scanning capability but is sensitive to motion and variations of skin temperature (Vashist 2012).

2.3 Near-Infrared (NIR) Spectroscopy

NIR spectroscopy uses a light beam in the range of 750–2500 nm wavelength which is focused on the body to measure the glucose concentration within issues (Vashist 2012). It is simple, less expensive, has high signal-to-noise ratio (SNR), high in-depth tissue penetration, and availability of low-cost materials for commercial products but due to low glucose absorption capability as well as sensitive to physiological and environmental factors, it requires multivariate analysis (Tamar et al. 2017).

2.4 Mid Infrared (MIR) Spectroscopy

MIR spectroscopy uses spectrum in the range of 2.5–10 μm (Nawaz et al. 2016). As this method is considered only reflected and scattered light as no light is transmitted through the body, the response peaks of glucose are sharp compared to NIR spectrum but have drawbacks like poor penetration and strong water absorption (Coates 1998; Tamar et al. 2017; Nawaz et al. 2016).

2.5 Far Infrared (FIR) Spectroscopy

This technique is based on light absorption in the range of 1000 μm (at 0.3 THz frequency) and 10 μm (at 30 THz frequency) due to the molecule vibration and rotation of weak bonds and heavy atom bonds (Kalaiselvi et al. 2016). The quality of this technique is less scattered compared to NIR and MIR but has disadvantages like strong absorption of water and low-level power delivered by light source (Emilia et al. 2016).

2.6 Raman Spectroscopy

Raman spectroscopy is used to estimate glucose concentration in interstitial fluids by observing the emission of scattered light (Gonzales 2019). This emission is influenced by molecular vibration, rotation, and other low-frequency transitions. Using this technique, it is easy to separate signals compared to NIR as the resulting frequency bands are narrow and peaks are distinct in nature, low cost lasers are used and less sensitive to water and temperature changes but has limitations like laser intensity and wavelength is unstable, spectral acquisition time is long enough and low signal-to-noise ratio (Coates 1998).

2.7 Photoacoustic Spectroscopy (PAS)

It measures the light absorption and releases heat energy by generating photoacoustic pressure wave which is related with glucose concentration level (Anuj et al. 2013). This technique has higher sensitivity and poor photoacoustic response towards water. Therefore, it is expensive and also sensitive to physiological and environmental factors (Tura et al. 2007).

2.8 Time of Flight (TOF) and Terahertz Time-Domain Spectroscopy (THz-TDS)

TOF is based on the absorbed radiation of short laser pulses (few picoseconds) and travel time of photons through the sample. The pulse shape can be used to detect the glucose concentration in body fluid (Alarousu et al. 2003). This technique is immune to background noise and is possible to study of a broad frequency range with a single pulse but takes long measurement time having low spatial resolution (Gonzales 2019; Alarousu et al. 2003).

THz-TDS is based on reflection and scattering of short laser pulse in the time domain (few femtoseconds) to measure the travel time by the photons and absorption of the medium (Cherkasova et al. 2016). This technique has background noise immunity but has low penetration capability due to THz radiation as well as long measurement time having low spatial resolution.

2.9 Occlusion Spectroscopy

In this technique, a red or near infrared light is passed through a human finger after applying pressure that ceases the blood flow for few seconds. At the same time, the transmitted and scattered light is detected by a detector that estimates the glucose concentration in blood (Uwadaira and Ikehata 2018). It has higher sensitivity as well as SNR but it needs compensation of signal drift (Nawaz et al. 2016).

2.10 Fluorescence

Fluorescence is based on the principle of fluorescent light emission at a particular wavelength. This technique uses a chemical compound fluorophores that keeps the track of glucose molecules in blood (Klonoff 1997). Fluorescence requires less calibration and has higher sensitivity towards glucose concentration. It is also immune to light scattering but it has short lifetime of fluorophore, biocompatibility issues and also depends on colour, pigmentation, thickness and potential toxicity to tissues (Gonzales 2019).

2.11 Thermal Emission Spectroscopy (TES)

It measures the naturally emitted infrared (IR) signals produced in the human body due to changes in the blood glucose concentration (Anuj et al. 2013; Tura et al. 2007). It has good reproducibility and does not require individual calibrations but has poor accuracy, sensitive to variation of body or tissue temperature and body movements (Buchert 2004).

2.12 Metabolic Heat Conformation (MHC)

This is involved with the measurement of physiological indices by mathematical analysis of thermal generation, hemoglobin (Hb), oxyhemoglobin (O_2Hb) and blood flow rate whose quantities are related with the glucose concentration by applying thermal, humidity, and optical sensors (Cho et al. 2004; Gonzales 2019). It is feasible and less expensive technique but suffers from strong interference of environmental conditions (Anuj et al. 2013).

2.13 Millimeter Wave (mmW) and Micrometer Wave (μmW)

As the millimeter and microwave radiation have lower energy photons and less scattering properties, it can be used to reach deeper position into the tissue with enough blood concentration (Shaker et al. 2018). It has high in-depth tissue penetration, no risk of ionization but sensitive to variations of physiological parameters like sweating, breathing, and cardiac activities and has poor selectivity (Gonzales 2019; Anuj et al. 2013; Tura et al. 2007).

2.14 Electromagnetic Sensing (EMS)

In this technique, the variations in resonant frequency shift helps to detect blood's dielectric properties which relates with blood glucose concentration (Gamessa 2019; Salam 2016). It has no risk of ionization, minimize the interference from biological components in the tissue but highly sensitive to the temperature variations (Uwadaira and Ikehata 2018).

2.15 Bioimpedance Spectroscopy (BS)

This technique involves the measurement of impedance as a function of frequency by passing a small AC current of known intensity across a tissue. The changes in RBCs membrane potential are then determined by the dielectric spectrum in the range of 100 Hz–200 MHz (Oliver et al. 2009; Vashist 2012). It is a less expensive technique and does not require statistically-derived or population-specific prediction models but requires a calibration process in which the user must take rest for one hour at least before starting the measurements and sensitive to variation of physiological parameters (Gonzales 2019).

2.16 Reverse Iontophoresis (RI)

In reverse iontophoresis (RI), the migration of Na^+ and Cl^- ions from beneath the skin towards the cathode electrode and anode electrode, respectively create an electro-osmotic flow which makes the transport of glucose molecules are extracted through the epidermis. At the cathode there is a sensor measuring the glucose concentration by oxidization of glucose oxidase (GOx) (Frontino 2013). Here electrodes are easily placed on the skin and have good correlation between glucose level in the physiological fluid and blood but users feel skin irritation, itching and it is sensitive to variations of physiological plus environmental parameters (Potts et al. 2002b).

Summary of various devices or companies for blood glucose sensing technology with their status as of December, 2019 are listed in the following Table 1.

Table 1 Summarizes a list of devices or companies for blood glucose sensing technology with their status as of December, 2019

Device	Company	Technique used	Target area	Regulatory approvals and status
BioSensors	BioSensors, Inc.	Bioimpedance spectroscopy	Skin	Appeared in 2010 but still in R&D phase (So et al. 2012)
Optical glucose monitor™ system	C8 MediSensors, Inc.	Raman spectroscopy	Skin	CE mark approved in 2011. Until, 2012 it was used as an investigational device (So et al. 2012; Gonzales 2019; Tura et al. 2007)
Hitachi non-invasive blood sugar monitoring device	Hitachi Ltd.	Metabolic heat conformation	Fingertip skin	Pending approvals from FDA and the Japan Ministry of Health (Tura et al. 2007)
Diasensor® 1000	Biocontrol Technology, Inc.	Near infrared spectroscopy	Forearm skin	CE Mark approved in 2000. Discontinued in 2002 (Frontino 2013)
GlucoWatch® G2™ Biographer	Animas Corporation (Cygnus Inc. in Redwood City, California)	Reverse iontophoresis	Wrist skin	CE mark approved in 1999. FDA approved in 2001; (Potts et al. 2002b)
Diab-spot	DiagnOptics Technologies B.V.	Skin autofluorescence	Skin	CE mark approved in December, 2011 (SCOUT DS® and Diab-spot 2012)

(continued)

Table 1 (continued)

Device	Company	Technique used	Target area	Regulatory approvals and status
Pendra®	Biovotion AG (Pendragon Medical Ltd.)	Bioimpedance spectroscopy	Wrist skin	CE mark approved in 2003. Currently not available (Wentholt et al. 2005; Chen et al. 2018; DiCesare and Lakowicz 2001)
ClearPathDS-120	Freedom Meditech Inc.	Fluorescence technique	Eye	Appeared in 2005. CE mark in December 2013 (ClearPath DS-120 2014)
G2 Mobile	ESER Digital	Metabolic heat conformation	Fingertip skin	Unknown (Tang et al. 2011)
GlucoTrack™	Integrity Applications Ltd.	Combination of ultrasonic, electromagnetic sensing, and thermal	Ear lobe skin	Appeared in 2010. CE mark approved in 2013. Up to 2018, it was available in Asia and Europe (Tamar et al. 2018)
TensorTip Combo Glucometer (CoG)	Cnoga Medical, Israel	NIR spectroscopy	Fingertip skin	Appeared in 2010. CE mark approved in 2014. FDA approval is pending (Segman 2018)
TouchTrak Pro-200	Samsung Fine Chemicals Co. Ltd	Electromagnetic sensing	Fingertip skin	Appeared in 1999. But yet to be approved (Huzooree et al. 2018)
GlucoLight Sentris-100™ Monitor	GlucoLight Corporation	Optical coherence tomography	Skin dermis	First successful clinical trial was reported in 2007 (Huzooree et al. 2018)

3 Major Challenges for Non-invasive Blood Glucose Monitoring Devices

The major challenges in the development of non-invasive blood glucose monitoring devices are sensitivity, specificity, reliability, durability, responsiveness, efficiency, portability, and authenticity (Gonzales 2019). Most of the devices are suffering from the environmental and physiological factors such as temperature, pressure, humidity, light intensity, motion, sweating, blood perfusion, skin thickness, etc. which need to be removed (Anuj et al. 2013). High SNR is required to relate with blood glucose concentration and spectral response (Tura et al. 2007). It is very important to use different algorithms and multivariate statistical calibration models such as Artificial Neural Network (ANN), partial least squares (PLS), support vector machines (SVM), etc. in order to enhance the accuracy and reliability of the sensors and to improve the readability of the data (Tura et al. 2007). If the data set is linear, principal component analysis (PCA), partial least squares (PLS) and least absolute shrinkage and selection operator (LASSO) algorithms are efficient. However, if the data is non-linear in nature logistic regression (LR) and support vector machines (SVM) are efficient (Gonzales 2019; Tura et al. 2007). Another major aim is to reduce the calibration frequency against concurrent blood glucose values, which provides a detection of glucose concentration (Uwadaira and Ikehata 2018). In order to reach high efficacy, there is a need to develop such a system that should be stable with clinically reliable sensors to measure the glucose concentration with accuracy better than 15 mg/dl (0.8 mmol/lit) in the normal environment (Uwadaira and Ikehata. 2018; Frontino 2013). Another major issue is the physiological time lag between blood and tissue glucose that decreases the accuracy of the blood glucose monitoring (Oliver et al. 2009). Mostly infrared spectroscopy is widely used, but MHC can be feasible because of inexpensive equipment used in this method and clinical results provide a good correlation coefficient of 0.91 (Vashist 2012). Therefore, multisensory data fusion technology such as combinations of bio impedance, and NIR spectroscopy or MHC and NIR spectroscopy or dielectric spectroscopy and absorption spectroscopy can be implemented for the detection and compensation of additional parameters those are responsible for non-accuracy of the sensor (Tamar et al. 2017; Nawaz et al. 2016).

4 Conclusions

This study provides the current aspects and advancement in reliable, non-invasive blood glucose monitoring systems and also discusses the potential detection techniques used by the said device. These techniques can be broadly classified into optical, thermal and electrical where it is observed that the optical techniques are more efficient among the three because they do not require reference electrode and is free from electrical hazards as well as electromagnetic interference. Again, the acceptable skin depth penetration by the optical light source and the glucose molecule which has clear optical absorption lines makes the optical technique more preferable. Also due to specific atomic bonding between carbon–oxygen-hydrogen in the glucose molecule which has definite vibration mode. This specific vibration mode enables identification of glucose molecule easily by an optical instrument.

References

Alarousu E, Hast JT, Kinnunen MT, Kirillin MY, Myllyla RA, Plucinski J, Popov AP, Priezzhev AV, Prykari T, Saarela J (2003) Noninvasive glucose sensing in scattering media using OCT, PAS, and TOF techniques. In: Proceedings of the Saratov fall meeting 2003: optical technologies biophysics and medicine V, Russia, pp 33–41

Anuj S, Md Koushik C, Shiru S, Neeraj S (2013) Blood glucose monitoring using non invasive optical method: design limitations and challenges. Int J Adv Res Electr Electron Instrum Eng (2):615–620

Barone PW, Strano MS (2009) Single walled carbon nanotubes as reporters for the optical detection of glucose. J Diabetes Sci Technol 3:242–252

Buchert JM (2004) Thermal emission spectroscopy as a tool for noninvasive blood glucose measurements. Proc SPIE 5566:100–111

Chen C, Zhao X-L, Li Z-H, Zhu Z-G, Qian S-H, Flewitt AJ (2017) Current and emerging technology for continuous glucose monitoring. Sensors 17:182

Chen L, Hwang E, Zhang J (2018) Fluorescent nanobiosensors for sensing glucose. Sensors 18:1440

Cherkasova O, Nazarov M, Shkurinov A (2016) Noninvasive blood glucose monitoring in the terahertz frequency range. Opt Quantum Electron 48:217

Cho OK, Kim YO, Mitsumaki H, Kuwa K (2004) Noninvasive measurement of glucose by metabolic heat conformation method. Clin Chem 50:1894

ClearPath DS-120® for the detection and monitoring of diabetes. NIHR Horizon Scanning Centre, University of Birmingham, September 2014

Coates J (1998) Vibrational spectroscopy: instrumentation for infrared and Raman spectroscopy. Appl Spectr Rev 33:267–425

DiCesare N, Lakowicz JR (2001) Evaluation of two synthetic glucose probes for fluorescence-lifetime-based sensing. Anal Biochem 294:154–160

Emilia WN, Magdalena K, Paulina SJ, Martin JN (2016) Electrochemical glucose sensing: is there still room for improvement? Anal Chem 88(23):11271–11282

Frontino G (2013) Future perspectives in glucose monitoring sensors. Eur Endocrinol 9(1):6–11

Gamessa TW (2019) Blood glucose monitoring techniques: recent advances, challenges and future perspectives

Villena Gonzales (2019) The progress of glucose monitoring-a review of invasive to minimally and non-invasive techniques, devices and sensors. Sensors 19(4):800

Gourzi M, Rouane A, Guelaz R, Alavi MS, McHugh MB, Nadi M, Roth P (2005) Non-invasive glycaemia blood measurements by electromagnetic sensor: study in static and dynamic blood circulation. J Med Eng Tech 29:22–26

Huzooree G, Noojehan KK, Joonas N (2018) Low-cost body area network for monitoring of diabetic patient. In: Bit A (ed) Design and development of affordable healthcare technologies, pp 135–164, last accessed 12 Dec 2019

International Diabetes Federation (2019) IDF diabetes Atlas, 9th edn. Brussels, Belgium. https://www.diabetesatlas.org, last accessed 10 Feb 2020

Jia J, Guan W, Sim M, Li Y, Li H (2008) Carbon nanotubes based glucose needle-type biosensor. Sensors 8:1712–1718

Kalaiselvi P, Anand M, Sivaguru K, Deepak S (2016) Continuous blood glucose monitoring using noninvasive technique: a review. IRJAES 1(4):142–147

Khalil OS (1999) Spectroscopic and clinical aspects of noninvasive glucose measurements. Clin Chem 45:165
Klonoff DC (1997) Noninvasive blood glucose monitoring. Diabetes Care 20:433
Lan YT, Kuang YP, Zhou LP, Wu GY, Gu PC, Wei HJ, Chen K (2017) Noninvasive monitoring of blood glucose concentration in diabetic patients with optical coherence tomography. Laser Phys Lett 14:035603
Lin T, Gal A, Mayzel Y, Horman K, Bahartan K (2017) Non-invasive glucose monitoring: a review of challenges and recent advances. Curr Trends Biomed Eng Biosci 6:1–8
Losoya Leal A, Camacho León S, Dieck Assad G, Martínez Chapa SO (2012) State of the art and new perspectives in non-invasive glucose sensors. Rev Mex Ing Biomed 33(1)
Malik BH, Coté GL (2010) Real-time, closed-loop dual-wavelength optical polarimetry for glucose monitoring. J Biomed Opt 15:017002
MIT (2020) Carbon nanotube sensor detects glucose in saliva. https://www.technologyreview.com/2013/04/30/253160/carbon-nanotube-sensor-detects-glucose-in-saliva, last accessed 10 Feb 2020
Nawaz A, Ohlckers P, Saelid S, Jacobsen M, Akram M (2016) Review: non-invasive continuous blood glucose measurement techniques. J Bioinform Diab 1:1–27
Oliver NS, Toumazou C, Cass AEG, Johnston DG (2009) Glucose sensors: a review of current and emerging technology. Diabet Med 26:197–210
Potts RO, Tamada JA, Tierney MJ (2002a) Glucose monitoring by reverse iontophoresis. Diabetes/Metab Res Rev 18:S49–S53
Potts RO, Tamada JA, Tierney MJ (2002b) Glucose monitoring by reverse iontophoresis. Diab Metab Res Rev 18 (Suppl 1):S49–S53
Rawer R, Stork W, Kreiner CF (2004) Non-invasive polarimetric measurement of glucose concentration in the anterior chamber of the eye. Graefe's Arch Clin Exp Ophthalmol 242:1017–1023
Salam (2016) The evolution of non-invasive blood glucose monitoring system for personal application. J Telecommun Electron Comput Eng (8):59–65
SCOUT DS® and Diab-spot for type 2 diabetes screening, NIHR Horizon Scanning Centre, University of Birmingham, December 2012
Segman Y (2018) Device and method for noninvasive glucose assessment. J Diab Sci Technol 12(6):1159–1168
Shaker G, Smith K, Omer AE, Liu S, Csech C, Wadhwa U, Safavi-Naeini S, Hughson R (2018) Non-invasive monitoring of glucose level changes utilizing a mm-wave radar system. Int J Mob Hum Comput Interact 10:10–29
So CF, Choi KS, Wong TK, Chung JW (2012) Recent advances in non-invasive glucose monitoring. Med Devices (Auckl) 5:45–52
Tamar L, Avner G, Yulia M, Keren H, Karnit B (2017) Non-invasive glucose monitoring: a review of challenges and recent advances. Curr Trends Biomedical Eng Biosci 6(5)
Tamar L, Yulia M, Karnit B (2018) The accuracy of a non-invasive glucose monitoring device does not depend on clinical characteristics of people with type 2 diabetes mellitus. J Drug Assess 7(1):1–7
Tang F, You Z, Wang X, Li Y, Yan Y, Fan Z (2011) Non-invasive blood glucose detector based on metabolic heat-optical method. Chinese Patent CN102293654B
Tura A, Maran S, Pacini G (2007) Non-invasive glucose monitoring: assessment of technologies and devices according to quantitative criteria. Diab Res Clin Pract 77(1):16–40
Tura A, Sbrignadello S, Cianciavicchia D, Pacini G, Ravazzani PA (2010) Low frequency electromagnetic sensor for indirect measurement of glucose concentration: in vitro experiments in different conductive solutions. Sensors 10:5346–5358
Uwadaira Y, Ikehata A (2018) Noninvasive blood glucose measurement. Nutr Ther Interv Diab Metab Syndr 489–504
Van Enter BJ, Von Hauff E (2018) Challenges and perspectives in continuous glucose monitoring. Chem Commun 54:5032–5045

Vashist SK (2012) Non-invasive glucose monitoring technology in diabetes management: a review. Anal Chim Acta 750:16–27

Wentholt IME, Hoekstra JBL, Zwart A, DeVries JH (2005) Pendra goes Dutch: lessons for the CE mark in Europe. Diabetologia 48:1055–1058

World Health Organization (2020) About diabetes. Diabetes programme. World Health Organization. https://www.who.int/health-topics/diabetes, last accessed 10 Feb 2020

Zhang R, Qu Z, Jin H, Liu S, Luo Y, Zheng Y (2018) Noninvasive glucose measurement by microwave biosensor with accuracy enhancement. In: Proceedings of the 2018 IEEE international symposium on circuits and systems (ISCAS), Florence, Italy, pp 1–4

Zhigang Z, Luis Garcia-G, Andrew JF, Huaqing X, Francis M, William IM (2012) A critical review of glucose biosensors based on carbon nanomaterials: carbon nanotubes and graphene. Sensors (12):5996–6022

Study of Non-biological Property for Identification Cancerous Skin Tissue

Somnath Chakraborty, Debjyoti Chowdhury, and Madhurima Chattopadhyay

Abstract In this paper, an array of inter-digitated (IDT) capacitive sensors has been designed for the detection of skin malignancy on the basis of change in dielectric permittivity of human skin tissue. Here, the IDT-based capacitive sensor is designed with a pair of rectangular-shaped identical electrodes and extended for an array to facilitate such identification. The identification process is based on change in dielectric permittivity of skin tissue to presence excess water contain. In order to do so, an electrical model of skin tissue is designed to which an excitation potential of 1 V is given to study the impedance profile of skin tissue. This impedance profile is seen to be different for cancerous skin with that of a normal one. Therefore, it can discriminate a normal skin from an affected one in terms of change in impedance profile. This work is executed in multi-physics-based simulation software.

Keywords Skin malignancy · Non-biological · Simulation · Electrical model

1 Introduction

Skin cancer involves abnormal growth of skin tissue which is known as skin neoplasm (Joshi and Jadon 2012), it can be broadly classified into (i) melanoma and (ii) Non-melanoma. This abnormal growth in skin tissue can invade other portions of the human body if not detected early. Skin cancer can be caused because of prolonged exposure to UV (Ultra Violate) rays or some other form of chemical agent. Exposure to UV rays is a physical agent of skin cancer (Fabbrocini et al. 2010; Malaysia 2018; Birgersson 2012). It is estimated that the incidence of non-melanoma more than 600,000 cases each year in the United States of America and is 20% greater than the melanoma. The non-melanoma category of skin cancer has two common types namely basal cell carcinoma (BCC) and squamous cell carcinoma (SCC) (Lu et al.

S. Chakraborty · D. Chowdhury (✉) · M. Chattopadhyay
Heritage Institute of Technology, Kolkata, India
e-mail: debjyoti.chowdhury@heritageit.edu

M. Chattopadhyay
e-mail: madhurima.chattopadhyay@heritageit.edu

M. Mukherjee et al. (eds.), *Advances in Medical Physics and Healthcare Engineering*, Lecture Notes in Bioengineering, https://doi.org/10.1007/978-981-33-6915-3_12

2018; Aminzadeh et al. 2014). The BCC and SCC types of skin cancer are caused due to UV exposure which damages cell DNA directly (Schoenbach et al. 2002). The uppermost layer of the human skin is divided into four layers; stratum corneum, epidermis (E–D), dermis, and subcutis. Stratum corneum (SC) is the upper-most layer of skin which consists of corneocytes cell is highly resistive in nature and has a thickness of 0.02 mm (Kasparian et al. 2009). Epidermis the immediate next layer of skin that has thickness of 0.15 mm (Baba and Burke 2008), it comprises of Keratinocyte, Melanocytes, Langerhans, and Markel cells (Martínez and Fernando 2007). Any UV radiation that falls on a skin tissue is absorbed by melanin granules in this layer which generates heat that may sometimes cause skin cancer (Kotnik et al. 2010; Joodaki and Panzer 2018). Dermis is the next layer to epidermis and has the thickness of about 0.5 up to 2 mm (Krassowska and Filev 2007) consisting of collagen (i.e. manufactured by fibroblast cells) (Sasaki et al. 2014). It also comprises of mast cells, macrophages, sweat glands (i.e. responsible for temperature regulation of skin), hair follicles, sebaceous glands, sensory, receptors and blood vessels (Chan and Ramer 2018). Below the dermis, subcutis layer is present with comprises of Lipocytes, a fat-storing cell. Also, nerve and blood vessels are sited in this layer (Salman et al. 2012). In case of skin cancer, it is observed through literature survey, that water content in the healthy skin tissue is less than that of the malignant skin tissue. Water volume fraction of stratum corneum is 0.2, epidermis and dermis are 0.65 or 0.7. In case of skin malignancy it is approximate 0.8 (Aberg et al. 2004). Due to this difference in water content malignant skin tissue exhibits a net change in relative electrical permittivity over healthy human skin tissue, therefore, the detection of skin cancer can be done on the bases of change in electrical permittivity. Therefore, this work considers only the epidermis layer and small depth of dermis layer of skin cancer detection. The human living cell membrane, is a lipid bilayer (Corovic et al. 2013) and acts as an electrochemical gateway that allows only a certain number of ions like Na^+, K^+ etc. to pass with their concentration gradient (Arena et al. 2010a). The resistive and capacitive properties of cell membrane and its surrounding are changed due to change in frequency applied through skin tissue. By tracing the relative electrical permittivity of suspected area of skin, cancerous tissue can be detected. Impedance of cancerous cell of human skin tissue changes due to change in electrical permittivity that can be measured by applying 2 mA alternating current of frequency range of 1–100 kHz. Detection of skin cancer can be broadly classified into two different techniques of (i) self-examination, by a person and (ii) skin biopsy. Skin biopsy is an invasive method and it is most popularly used for detection skin cancer, in which a sample of skin tissue from suspected area of human body is removed and sent it to a lab for testing. This process is painful takes few days to generate results (Aberg et al. 2004). On the other hand, the two other types of non-invasive method for identification and study of malignancy in skin tissue are (I) temperature (Arena et al. 2010b) and (II) impedance profile affected tissue. By studying these non-invasive methods, it can be found that the cost of the instrument involved which is a big factor in detection of skin malignancy can be greatly reduced. The change in relative permittivity in cancerous tissue of affected area of skin can be observed at a specific frequencies in the range 1–100 kHz. Therefore, impedance profile affected tissue method can be considered for detection of malignant skin tissue through capturing impedance values over a range of frequencies.

2 Electrical Model of Skin Tissue

The overall impedance value of skin can be evaluated using two electrical properties i.e. resistance (R) and capacitance (C) (Wang et al. 2014). Hence, in order to examine a complex frequency response a RC equivalent model of a skin tissue is developed where the resistance and capacitance represent the electrical nature the skin when subjected to frequency excitation. For evaluating this complex value of resistance (R) and capacitance (C) the standard Debye model is considered for calculation of the dielectric permittivity of a given skin tissue. For a certain frequency, the value of electrical permittivity can be evaluated with the following Debye equation, given by Eq. 1.

$$\varepsilon_{\mathrm{r}} = \varepsilon_{\infty} + \frac{A_{\mathrm{p}}(\varepsilon_{\mathrm{s}} - \varepsilon_{\infty})}{1 + j\omega\tau_{\mathrm{p}}} + \frac{\sigma}{j\omega\varepsilon_0} \tag{1}$$

where, ε_{r} is relative permittivity of skin, ε_{∞}, ε_{s} are the optical permittivity and static permittivity; σ is ionic conductivity; A_{p} is pole amplitude with ω as angular frequency and the value of ε_0 is 8.85 pF/m, respectively. The values for the parameters are shown in Table 1. The skin impedance model can now be then classified as (i) constant phase angle model and (ii) RC layered model (Malaysia 2018).

Each layer of skin tissue consists of one type of cell or a combination of cells. These different cell types from different layers of skin tissue act as a leaky dielectric (Lu et al. 2018). As human skin tissue is anisotropic in nature, so biological and chemical properties of different layers are not similar. Therefore, a constant phase angle model does not show accurate result for evaluation of skin tissue impedance. This work, therefore, introduces R–C models for each layer of the skin tissue that the applied frequency penetrates, shown in Fig. 1. Literature study reveals that if an alternating current is applied in a suspected area on the surface of the skin, it penetrates through it and can be picked up from another point of the same surface on the skin vicinity near the point of injection. This process of excitation of skin tissue called as electroporation, the pours in the skin tissue cells are opened with

Table 1 Optimized parameters for the Debye model (Birgersson 2012)

Sr	Tissue	ε_{∞}	ε_{s}	A_{p}	τ_{p}(ps)	σ(s/m)
1	SC	3.24	4.96	1.074	2.14	0.07
2	E–D (0.67)	5	36.55	0.946	6.07	2.60
3	E–D (0.70)	5.12	37.60	1.074	6.20	2.68
4	Tumor	5.46	56.79	0.908	6.35	2.94

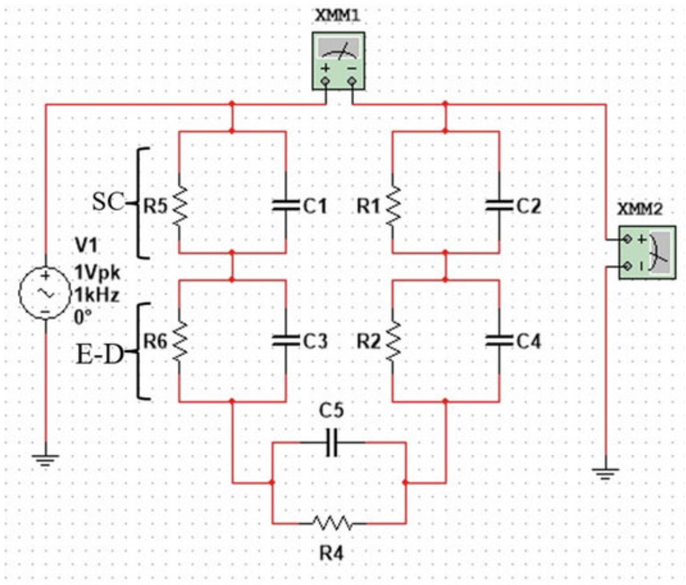

Fig. 1 Electrical circuit model of human skin tissue

a 1 V *p–p* (Lu et al. 2018) supply that causes current to flow through skin tissue. The penetration of current is proportionally depending on the gap between source electrodes (i.e., the electrode is connected with current source) and pick up electrode (i.e., the electrode where current is collected).

In this model, impedance between the electrodes and the upper surface of skin is not considered for simplicity. Therefore, an equivalent electrical circuit model of human skin tissue with different layers is designed, shown in Fig. 1.

In Fig. 1, the equivalent circuit model of skin tissue is shown; where R_1 and R_2 are the resistances of stratum corneum and combined with epidermis and dermis layers respectively. C_1 and C_2 are the capacitances of stratum corneum and combined with epidermis and dermis layers. Hence from Fig. 1, Z_1 is equivalent impedance of stratum corneum can be written as Eq. 2 and Z_2 is the combined equivalent impedance of epidermis and dermis can be written as Eq. 3.

$$Z_1 = \frac{2R_1}{1 + j\omega R_1 C_1} \tag{2}$$

$$Z_2 = \frac{3R_2}{1 + j\omega R_2 C_2} \tag{3}$$

The overall impedance of the circuit is then given by

$$Z_{\mathrm{eq}} = Z_1 + Z_2 \tag{4}$$

Table 2 Electrical parameters of skin tissue

Sr	Layers of skin	Non-cancerous		Cancerous	
		Resistance (k Ω)	Capacitance (μF)	Resistance (k Ω)	Capacitance (μF)
1	SC	56.84	0.0028	1.35	0.1176
2	E–D	19.12	0.0083	10.69	0.0094

From Eq. 4, Z_{eq} is total impedance of this equivalent circuit model. The arithmetic values of different layers of healthy skin tissue and cancerous skin tissue are shown in Table 2 (Martínez and Fernando 2007).

The arithmetic values from the Table 2, were used to obtain a frequency relation with impedance for normal skin and cancerous skin tissue, shown in Fig. 1 (Baba and Burke 2008; Martínez and Fernando 2007; Kotnik et al. 2010). This graph renders a sharp difference between malignant skin and normal skin. The impedance value of normal skin is higher than cancerous skin in a very low frequency due to difference in water content.

3 Detection System Design

3.1 Design of the Sensor

A one-dimensional array of coplanar electrodes are designed virtually in the COMSOL Multiphysics software taking width and length of each electrode as 0.04 mm * 0.04 mm and height as 0.01 mm. The gap between two consecutive electrodes is kept as 0.02 mm and the array length as 0.46 mm (Gabriel et al. 1996). These array of electrodes, the dimension of width as 0.22 mm and length as 0.46 mm, is designed to have coplanar geometry. The starting electrode is connected to 2 mA current source and the alternative electrode is grounded, this connection pattern is repeated for each electrode pair.

The dimensions of the coplanar sensor is kept constant throughout the design so that the impedance is the function of relative permittivity of skin tissue and the applied frequency. This sensor is put on a suspected area of skin for testing of malignancy of skin. Frequency dependences Debye model is used to evaluate the di-electric values of skin tissue in different frequency ranges.

The optimized parameters values which is being shown in Table 1, are put in Debye equation to find out the relative permittivity of normal skin tissue and malignant skin tissue (Stante 2009). The Figs. 2 and 3 show the sensor design and its virtually fabricated form.

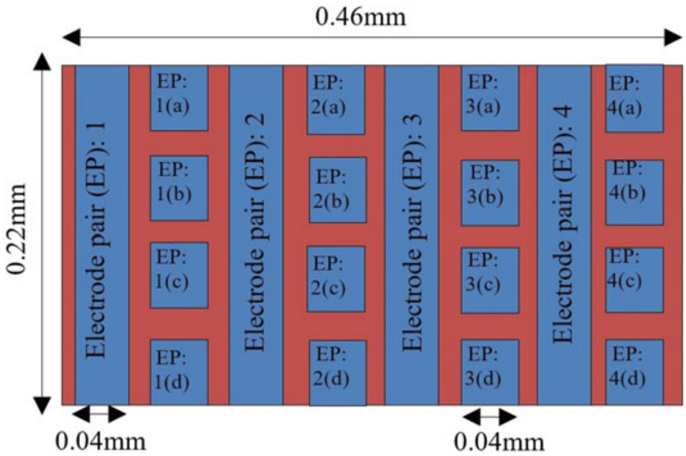

Fig. 2 Top view of the proposed sensor to study the electrical property of human skin tissue

Fig. 3 Top view of the virtually fabricated sensor

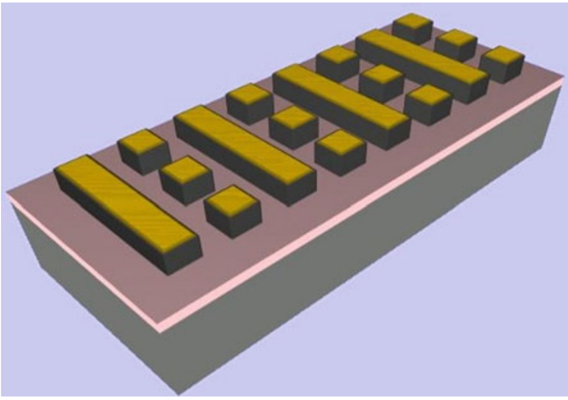

3.2 Simulation of the Sensor

A range of frequency about 1 up to 100 kHz is used to detect malignancy in skin tissue. A change in electrical permittivity of skin tissue, a non-biological parameter, can change in impedance of skin tissue that can establish a difference between normal skin from cancer skin. The human skin is a complex structure with different layers, comprising with different types of cell. For their complex structure, electrical permittivity is not same for every layers of skin. Hence, it is not possible to evaluate taking equal electrical permittivity of all the layers of skin together. So to find out relative permittivity of different layers instead of taking skin as whole, Debye equation with its optimized parameters from Table 2 are introduced. The difference water content in different layers of skin produce variation in relative electrical permittivity. In case of normal skin, with combined result of different values of di-electric constant of different layers make a gradually change in impedance with applying a frequency sweep. But in case of malignancy in skin tissue, water content in different layers of skin tissue is same. So, instead of combining effect of electrical permittivity of skin, there is an equally formed electrical permittivity caused of malignancy in skin makes gradually decreasing impedance with variation of frequencies.

4 Results and Discussion

In case of normal skin tissue layers and cancerous skin tissue, a change in electrical permittivity with the variation of applied frequency ranging from 1 to 100 kHz is found by using of Debye equation, and it is shown in Table 3. A simulation result, shown in Figs. 4 and 5, is found for cancerous skin tissue with proposed sensor using COMSOL Multiphysics software. For small change in electrical permittivity of normal skin tissue from malignant skin tissue can be isolated and detected from the graph of Figs. 4 and 5.

The change in impedance with variation of frequency reflects the alteration of di-electric values of skin tissue. Using Debye model and MATLAB software, a set of relative electrical permittivity at specific frequencies in the range of 1 to 100 kHz is found (Chattopadhyay et al. 2019; Ingole et al. 2016; Nordbotten et al. 2014).

5 Conclusion

This work based on measurement of change in electrical permittivity in skin tissue for detection of skin malignancy. The analysis of the difference of electrical permittivity of malignant skin tissue from normal skin tissue is done in COMSOL Multiphysics software and Fig. 5 is shows graphically the differences between cancerous skin tissues from normal skin tissue in terms of impedance over a range of frequencies. In the malignance of skin, water content present in the skin tissue are greater than normal skin tissue. This increase in water component changes the electrical permittivity of skin which in turn changes in impedance of skin that is identified by this proposed sensor. The Fig. 5 shows that the impedance of skin tissue is gradually decreasing with the frequency ranging from 1 to 100 kHz for non-cancerous and cancerous skin tissue. Thus, the impedance profile of an affected tissue which is a measure of change in impedance of skin as a function of electrical relative permittivity can be regarded as an alternative method of detection of skin cancer.

Table 3 Electrical parameters of skin tissue

Frequency		1 kHz	20 kHz	40 kHz	60 kHz	80 kHz	100 kHz
Sr	Skin layers	Electrical permittivity					
1	SC	1.2589E+06	6.2943E+04	3.1471E+04	2.0981E+04	1.5736E+04	1.2589E+04
2	E-D (0.65)	4.6757E+07	2.3379E+06	1.1689E+06	7.7929E+05	5.8447E+05	4.6757E+05
3	E-D (0.70)	4.8196E+07	2.4098E+06	1.2049E+06	8.0327E+05	6.0245E+05	4.8196E+05
4	Tumor	5.2872E+07	2.6436E+06	1.3218E+06	8.8120E+05	6.6090E+05	5.2872E+05

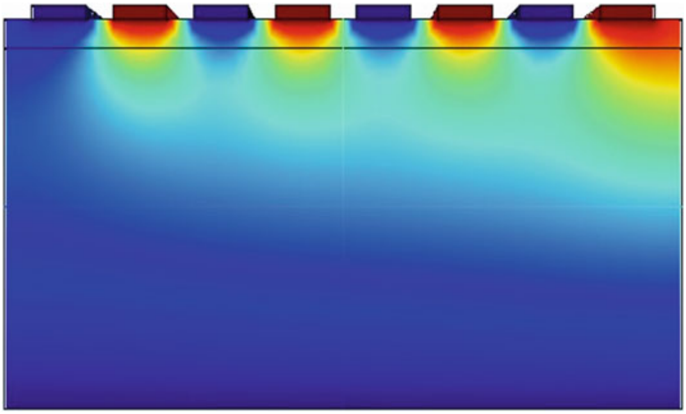

Fig. 4 Side view of simulated sensor in COMSOL multiphysics software

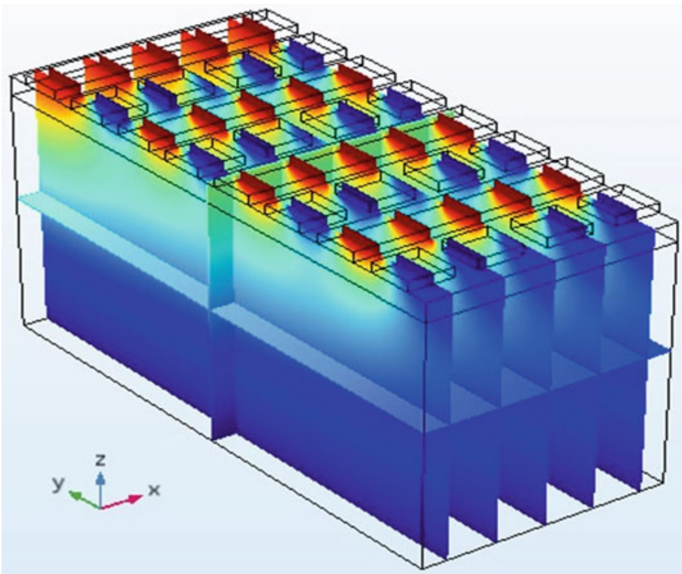

Fig. 5 The 3D view of simulated sensor in COMSOL multiphysics software

References

Aberg P et al (2004) Skin cancer identification using multifrequency electrical impedance-a potential screening tool. IEEE Trans Biomed Eng 51(12):2097–2102

Aminzadeh R, Mehrdad S, Shishegar AA (2014) Dielectric properties estimation of normal and malignant skin tissues at millimeter-wave frequencies using effective medium theory. In: 2014 22nd Iranian conference on electrical engineering (ICEE). IEEE

Arena CB et al (2010a) Theoretical considerations of tissue electroporation with high frequency bipolar pulses. IEEE Trans Biomed Eng 58(5):1474–1482
Arena CB et al (2010) Theoretical considerations of tissue electroporation with high frequency bipolar pulses. IEEE Trans Biomed Eng 58(5):1474–1482
Baba A, Burke MJ (2008) Electrical characterisation of dry electrodes for ECG recording. In: 12th WSEAS International Conference. Proceedings. Mathematics and computers in science and engineering. World Scientific and Engineering Academy and Society
Birgersson U (2012) Electrical impedance of human skin and tissue alterations: mathematical modeling and measurements. Inst för klinisk vetenskap, intervention och teknik/Dept of Clinical Science, Intervention and Technology
Chan KY, Ramer R (2018) Novel concept of detecting basal cell carcinoma in skin tissue using a continuous-wave millimeter-wave rectangular glass filled probe. Med Devices (Auckland, NZ) 11: 275; Bürgel SC et al (2015) On-chip electroporation and impedance spectroscopy of single cells. Sens Actuators B: Chemical 210:82–90
Chattopadhyay M, Chowdhury D, Sahu S (2019) Study of dielectric properties of leukocytes for the determination of malignancy by capacitive type MEMS sensor. Microsyst Technol 25(5):1613–1618
Corovic S et al (2013) Modeling of electric field distribution in tissues during electroporation. Biomed Eng Online 12(1):16
Fabbrocini G et al (2010) Epidemiology of skin cancer: role of some environmental factors. Cancers 2(4):1980–1989
Gabriel S, Lau RW, Gabriel C (1996) The dielectric properties of biological tissues: III. Parametric models for the dielectric spectrum of tissues. Phys Med Biol 41(11):2271
Ingole SP, Kakde AU, Bonde PB (2016) A review on statistics of cancer in India. J Environ Sci Toxicol Food Technol 10:107–116
Joodaki H, Panzer MB (2018) Skin mechanical properties and modeling: a review. Proc Inst Mech Eng 232(4):323–343
Joshi SK, Jadon G (2012) Introduction to neoplasm: Tumor classification a review article. Int J Adv Res Pharm Biosci 1(2):227–263
Kasparian NA, McLoone JK, Meiser B (2009) Skin cancer-related prevention and screening behaviors: a review of the literature. J Behav Med 32(5):406–428
Kotnik T, Gorazd P, Miklavcic D (2010) Induced transmembrane voltage and its correlation with electroporation-mediated molecular transport. J Membr Biol 236(1):3–13
Krassowska W, Filev PD (2007) Modeling electroporation in a single cell. Biophys J 92(2):404–417
Lu F et al (2018) Review of stratum corneum impedance measurement in non-invasive penetration application. Biosensors 8(2):31
Malaysia P (2018) A survey on skin cancer detection using skin temperature variation analysis. Int J Pure Appl Math 119(15)
Nordbotten BJ et al (2014) Estimation of skin conductance at low frequencies using measurements at higher frequencies for EDA applications. Physiol Measur 35(6):1011
Salman S, Psychoudakis D, Volakis JL (2012) Determining the relative permittivity of deep embedded biological tissues. IEEE Antennas Wirel Propag Lett 11:1694–1697
Sasaki K, Wake K, Watanabe S (2014) Measurement of the dielectric properties of the epidermis and dermis at frequencies from 0.5 to 110 GHz. Phys Med Biol 59(16):4739
Schoenbach KH et al (2002) Bioelectrics-new applications for pulsed power technology. IEEE Trans Plasma Sci 30(1):293–300
Seoane Martínez F (2007) Electrical bioimpedance cerebral monitoring. Diss. Göteborg: Chalmers tekniska högskola. Dermol-Cerne J, Miklavcic D. From cell to tissue properties—modeling skin electroporation with pore and local transport region formation. IEEE Trans Biomed Eng 65(2):458–468

Stante GC (2009) The electrical properties of human tissue for the diagnosis and treatment of melanoma skin cancer. Master's Theses and Project Reports 199

Wang Z et al (2014) Study on capacitance sensor simulation of ice thickness measurement based on ANSYS. Sens Transducers 162(1):47

Investigation of Size Evolution of Silver Nanoparticle and Its Use in Medical Field

Md. Moinul Islam, A. De, Nazmus Sakib, and Srijit Bhattacharya

Abstract Metallic nanoparticle (NP) is one the most important nanostructures used in medical purposes. However, for successful use of NPs, the size, shape, and growth kinetics should be known. In this work, we have demonstrated how silver nanoparticle (AgNP) size and growth depend on silver nitrate ($AgNO_3$) and sodium borohydride ($NaBH_4$) concentrations. The morphology of clusters is simulated by validating the plasmon spectra, generated using DDSCAT (based on discrete dipole approximation) simulation, with the experimental UV–Visible (UV–Vis) spectra. We find that at the concentration [$AgNO_3$] to [$NaBH_4$] ratio of 10:1, the nanoparticle cluster size is smallest and spherical, while for the ratio 3.3:1 this is deformed and large. For the latter, we observe quadrupole plasmon resonance. The AgNP cluster size and growth are also investigated with elapsed time and the stability of the cluster is demonstrated with entropy estimation. Thus, this work could enlighten us to select the AgNP cluster size required for medical purposes by correctly choosing the concentrations of the chemical reagents. Finally, important sectors for future studies of AgNP using γ-radiation have also been discussed, which could be useful in cancer treatment.

Keywords AgNP · DDSCAT · UV–Visible spectra · Nanomedicine · Plasmon

---

Md. M. Islam
Department of Physics, APC College, New Barrakpur, Kolkata, West Bengal 700131, India

A. De
Department of Physics, Raniganj Girls' College, Raniganj, West Bengal 713358, India

N. Sakib
Malatipur High School, North 24 Parganas, West Bengal 743445, India

S. Bhattacharya (✉)
Department of Physics, Barasat Government College, Barasat, North 24 Parganas, Kolkata, West Bengal 700124, India

M. Mukherjee et al. (eds.), *Advances in Medical Physics and Healthcare Engineering*, Lecture Notes in Bioengineering, https://doi.org/10.1007/978-981-33-6915-3_13

1 Introduction

Nanoparticles are materials having all three dimensions in the nanoscale i.e. within 1–100 nm (Kreibig and Vollmer 1995). However, the property that makes the miniscule nanoparticles (NP) so special in science and technology is the size that is much smaller than their bulk counterparts. The large surface area to volume ratio and the emergence of quantum effects owing to such minute size provide the NP altogether different optical, chemical, electrical, etc. properties over the bulk materials, which gives the former a cutting edge in different scientific fields. The nanomaterials and related science have been well-known in different fields such as Chemistry, Physics, Biology, etc. since the past age. However, only within the last decade, the nanomaterial application rate has been increased multifold. The medical science has, off late, got a new dimension piggybacked by nanomaterial applications (Riehemann et al. 2009; Whitesides 2005; Mauricio et al. 2018).

Nanomaterials and NP are used in medicine for imaging, targeted drug delivery, sensing, artificial implantation, etc. The NP can easily move freely within the human body in comparison to bigger particles. Therefore, by encapsulating therapeutic drugs, one can use NPs to deliver drugs in targeted area, especially for sustained or controlled release. As an example, the use of nanosized liposome and micelles as chemotherapy drug carrier has been known since long time. However, certain disadvantages are always associated with liposome as carrier such as aggregation and lack of stability. Moreover, there could be high production cost to reshape the liposome potentially effective for drug delivery. Recently, the advent of nanocrystals (size within 2–10 nm) or 'quantum dots' has revolutionalized biomedicine due to small size and high molar extinction coefficient (Panahi et al. 2016). Metal and oxides as NP have also several applications in the nanomedicinal field. Metals, such as gold, silver, etc., being biocompatible and having unique electronic and optical properties, may be used for ligand (e.g. protein, antibodies, etc.) conjugation. Besides, metals showing localized surface plasmon resonances (LSPR) can be applied in bioimaging for diagnostic purposes. However, toxicity to the living cells is an important issue and gold is less toxic than any other metals (Mauricio et al. 2018; Patra et al. 2010; El-Sayed et al. 2005).

The too many potential advantages of NP may have eclipsed its disadvantages, still there is dire need to study those to use the NP effectively in medicines. The major problems are aggregation or clusterization and toxicity. Table 1 highlights the size-dependent effectiveness of NP as medicinal purposes. The optimization of size (20–100 nm) is highly useful to achieve stability and less aggregation without losing much in the surface to volume ratio (Longmire et al. 2008). The major problem lies in the fact that the topic of NP stability and aggregation is still not well-understood. It is found that the issue of NP stability depends on different sectors. The selection of base fluid, reducing agent, difference between dielectric constant of nanoparticle and the base fluid, the addition of surfactants, ambient temperature, etc. all could endow NPs stability. But the concerned research studies are very rare in the existing literature (Grassian 2008; Sun and Xia 2176). Grassian (2008) in his recent paper

Table 1 Size dependence of NP in medical physics

NP size	Potential use	Disadvantages
20–100 nm	Applications within the human body. Large surface area useful for drug supply	Aggregation problem
>1 μm	Used as drug carrier for larger size	Opsonized and accumulated within the organs. High rate of aggregation
<20 nm	Good for use in cases where rapid clearance needed	Rapid clearance from blood reduces effectiveness as drug carrier

has showed the size dependent properties and surface chemistry of metallic nanoparticles in gas and liquid phase environments. Sun and Xia (2002) have demonstrated that the presence of poly vinyl pyrrolidone (PVP) in the reduction of silver nitrate with ethylene glycol determines the shape and size of silver nanoparticles (AgNP). By changing the molar ratio of PVP and $AgNO_3$ from 1.5 to 3.3, the aggregation increases. Xia et al. (2011) opined that formation of nanocrystals with specific shape could be difficult and exact knowledge of size and shape evolution of NP is still unassailable. Another work (Xiong et al. 2006) emphasizes that the production of well-defined silver nanostructures is not a trivial job. In view of these, this paper tries to explore how the shape change of NP is manifested by the LSPR. Since the prospect of nanomedicine depends entirely on the NP growth kinetics, stability, and the nature of aggregation, the lack of knowledge in this field has been a major impediment.

In the present work, therefore, we have focused on the growth kinetics of AgNP with water as base fluid. Our aim is to study the dynamics of the AgNP morphology and to understand the size correlation with stability. We have investigated the AgNP size and aggregation with the concentration of reducing agent sodium borohydride ($NaBH_4$) and metallic silver supplier $AgNO_3$. We have also used thermodynamical entropy as a probe to understand the shape and cluster size.

2 Materials and Methods

Nano silver colloid is prepared by chemical reduction, in which the $AgNO_3$ or silver nitrate solution is reduced by ice-cold reducing agent sodium borohydride ($NaBH_4$). The synthesis of the nanoparticle occurs via the following chemical reaction:

$$AgNO_3 + NaBH_4 \rightarrow Ag + 1/2H_2 + 1/2B_2H_6 + NaNO_3$$

The requirement of ice-cold temperature (T) is due to the reaction of $NaBH_4$ at higher temperature (T) producing hydrogen gas and boranes impeding the reduction of AgNP (Piñero et al. 2017; Amendola et al. 2006). In addition, to slow down the reaction rate at lower T is another aim. The $AgNO_3$ and $NaBH_4$ powders, in 99.8 and 95.8% purity, have been procured from Central Drug House, India. At first, we prepare 100 mL of 0.002 M $NaBH_4$ sample and a part of it (30 mL) is added in an Erlenmeyer flask.

The liquid is initially stirred and cooled for 20–30 min and then 3 mL of $AgNO_3$ is added dropwise into the $NaBH_4$ solution, which is stirred continuously. Emergence of AgNP can be understood when the color of the solution turns light yellow (Islam et al. 2018). We study the UV–Visible (UV–Vis) spectra of AgNP solution by (i) varying the concentration of $AgNO_3$ solution from 0.20 to 3.33 mM/cc, keeping $NaBH_4$ solution constant, (ii) varying the concentration of $NaBH_4$ ([$NaBH_4$]) from 0.03 to 0.10 mM/cc keeping [$AgNO_3$] fixed at 0.33 mM/cc, (iii) the growth kinetics with number of days elapsed after preparation.

The identification of size and shapes of NP is popularly done by using the techniques such as transmission electron microscopy (TEM), X-ray diffraction (XRD), electron energy loss spectroscopy (ELSS), etc. However, the performance of the techniques could be slow and may provide incomplete information about the particle size, shape, and agglomeration. Moreover, the cost of operation could also be high. One of the simplest measurement techniques is the experimental UV–Vis spectroscopy of NP and theoretical interpretation of the experimental plasmonic data using Discrete Dipole Approximation (DDA). This technique is cost-effective, less time-consuming as well as can emulate the NP and cluster morphology without disturbing the sample solution. This has been used rarely in the existing literature (Amendola et al. 2006; Islam et al. 2018). In this work we have used DDSCAT (Drain and Flatau 2013), a FORTRAN code based on DDA formalism.

3 Results and Discussions

The concentration of $AgNO_3$ solution ([$AgNO_3$]) is varied from 0.20 to 3.33 mM/cc, keeping the $NaBH_4$ solution constant at 0.07 mM/cc. The corresponding extinction spectra are shown in Fig. 1 and the full width at half maxima (FWHM) is depicted at the inset panel. The FWHM reduces with [$AgNO_3$] and thereafter starts to increase from a minima position. The position 2 denotes the minima, while 1 and 2 are positions with higher values of FWHM. This can be explained heuristically as follows. Position 1 has lowest number of metal particles than that of 2 and 3. The higher number of electrons than the metal particles reduces the effective potential between them, causing agglomeration and higher FWHM. At 2, the number of metal particles increases with $AgNO_3$ concentration to become comparable with the number of electrons. Therefore, at position 2 for the ratio [$AgNO_3$]:[$NaBH_4$] = 10:1, the particle size and agglomeration become smallest. At position 3, the number of metal particles increases in comparison to the existing number of electrons. These results increase in FWHM owing to non-uniformity in the amount of electrons between two metal particles. The morphology of the AgNP cluster is shown in the inset of Fig. 1. Similar dynamics of FWHM is found for another set of [$NaBH_4$] shown by red curve in the inset corroborating our heuristic argument.

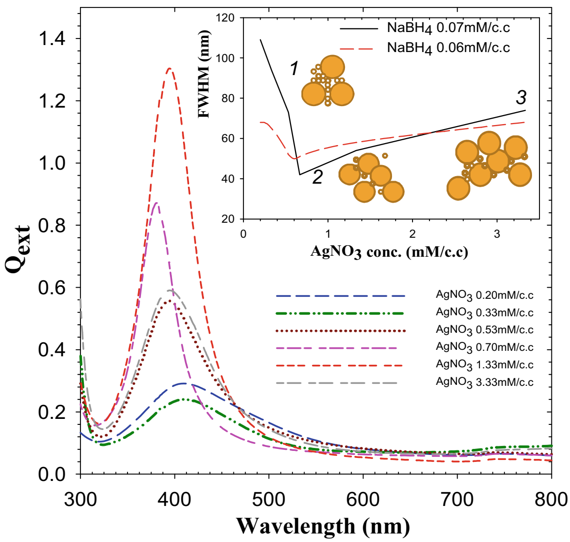

Fig. 1 (Colour online) The variation of experimental extinction spectra with the concentration of $AgNO_3$. Inset depicts FWHM as a function of $[AgNO_3]$ and possible cluster structures

In Fig. 2 the variation of extinction spectra with the concentration of $NaBH_4$ is shown, keeping $[AgNO_3]$ constant. With the increase in $[NaBH_4]$, number of electrons increases, and enhanced probability of agglomeration produces large deformed clusters. This is evident in Fig. 2, where the extinction spectra shown by blue dashed line depicts thicker FWHM along with a spike. The spike is the manifestation of quadrupole plasmon resonance owing to the deformed-shaped cluster. The corresponding ratio $[AgNO_3]$:$[NaBH_4]$ is found as 3.3:1. On the contrary, the dotted curve, for lowest $[NaBH_4]$, shows thinnest FWHM due to lower electron concentration. The corresponding cluster structures are also shown in the same figure. Interestingly, the smallest AgNP cluster is found for the ratio $[AgNO_3]$:$[NaBH_4]$ = 10:1, which is

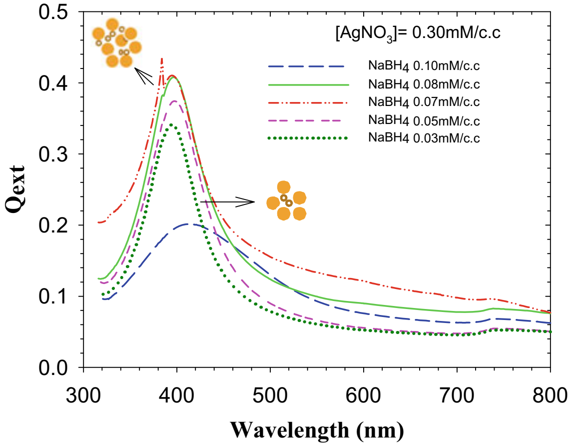

Fig. 2 (Color online) The variation of experimental extinction spectra with the concentration of $NaBH_4$. The corresponding cluster structures are also shown

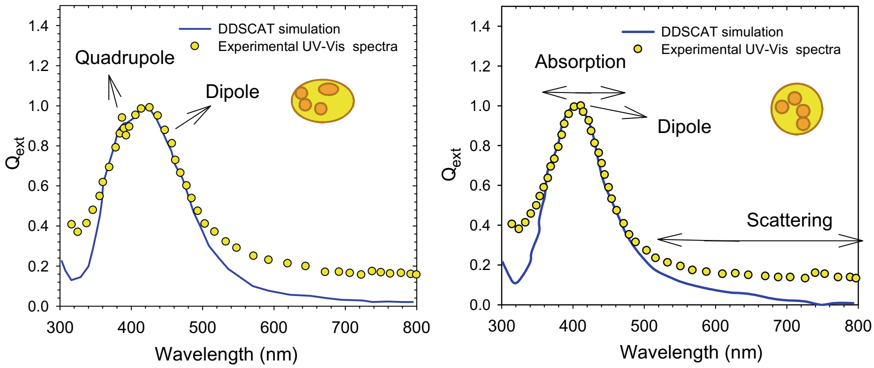

Fig. 3 (Color online) The agreement between DDSCAT simulation and experimental UV–Vis spectra. The absorption and scattering regions are also depicted. Left panel show quadrupole peak along with the dipole absorption, whereas right panel shows only dipole peak. Corresponding cluster morphology is also described

similar to the earlier case of [$AgNO_3$] variation. The cluster morphology is corroborated via DDSCAT simulation. The nice agreement between DDSCAT and experimental UV–Vis spectra in the absorption region is shown in Fig. 3 for quadrupole (left panel) as well as dipole spectra. The mismatch in the scattering region is due to the presence of different scatteres in the experimental solution, which do not affect the result. From the simulation, quadrupole mode generating cluster is found to be deformed in shape with aspect ratio 1.1:1 and size of 58 nm, while the dipole mode generating cluster is found spherical in shape with dimension of 50 nm.

To understand the stability of NP, we observe the growth dynamics of AgNP water solution in the lab with the elapsed time after preparation. For the 1st day, the manifestation of spherical morphology of AgNP can be explained by dipole UV–Vis peak with thin FWHM. In 6th Day, the solution shows quadrupole peak due to deformed cluster shape. But in the 48th day the solution shows only dipole spectra with very broad FWHM. The entropy of the AgNP water system is measured using the van't Hoff equation as per the formalism shown in van Rijjsel et al. (2011). The nanoparticle chain length is simulated using DDSCAT and corresponding absorption spectra is matched with experimental spectra. The entropy is found to increase with number of days elapsed. Actually, on day 1 of AgNP preparation, the cluster size and entropy are found smallest and the tendency to grow by aggregation is highest. Thereafter further aggregation invokes deformation and quadrupole mode of plasmon vibration is achieved with higher value of entropy. Finally, when the cluster is very large at the 48th day, the entropy is highest. Since the aggregation rate becomes almost zero at that point, entropy stabilizes and stable shape is achieved.

Thus, our work elucidates the cluster shape stability and the aggregation dynamics of AgNP in water as base fluid. The concentration ratio of $AgNO_3$ to $NaBH_4$, given by 10:1, provides us the smallest sized NP (within the diameter of 50 nm) having the highest tendency of clusterization. The smallest sized AgNP generate agglomeration which may induce Caveolae-mediated endocytosis. For the AgNPs with higher dimensions (may be understood easily from the yellow colored solution), such as AgNPs kept for 48 days, or the [$AgNO_3$] to [$NaBH_4$] ratio 3.3:1 (or less), the cluster size is achieved between 58 and 100 nm of radius. Here the utilization may be possible in macropinocytosis that involve processes instead of endocytosis (Kenzaoui et al. 2017). The deformed cluster shapes may also be used in medicinal purposes where reaction rate needs to be higher. This paper, therefore, explains how to select AgNP size based on the medicinal purposes.

Our future aim is to prepare AgNP in a greener way, which will be easier to implement in nanomedicines. Our endeavor is to generate AgNP from $AgNO_3$ solution using γ-ray radiating sources. However, we need to investigate how the rate of preparation of AgNP can be increased using small dose rate, important in human body. External radiotherapy and brachytherapy are the important processes for the exposure of human body to γ-radiation. Whether these therapies can be utilized for nanoparticle generation within the human body is a big question that needs to be answered in the near future.

Acknowledgements The authors gracefully acknowledge the financial support from Department of Science and Technology (India) to procure the UV-Visible spectrophotometer under the FIST scheme at the Department of Physics, Barasat Government College.

References

Amendola V, Polizzi S, Meneghetti M (2006) Laser ablation synthesis of gold nanoparticles in organic solvents. J Phys Chem B 110:7232

Drain BT, Flatau PJ (2013) User guide for the discrete dipole approximation code DDSCAT 7.3. arXiv:1305.6497 (26 May 2013)

El-Sayed IH, Huang X, El-Sayed MS (2005) Surface plasmon resonance scattering and absorption of anti-EGFR antibody conjugated gold nanoparticles in cancer diagnostics: applications in oral cancer. Nano Lett 5(5):829

Grassian VH (2008) When size really matters: size-dependent properties and surface chemistry of metal and metal oxide nanoparticles in gas and liquid phase environments. J Physic Chem C 112(47):18303

Islam MM, Mandal S, Bhattacharya S (2018) Investigation of the growth kinetics and multipolar plasmon resonance. Plasmonics 13:1803

Kenzaoui BH et al (2017) The agglomeration state of nanoparticles can influence the mechanism of their cellular internalisation. J Nanobiotechnol 15:48

Kreibig U, Vollmer M (1995) Optical properties of metal clusters. Springer, Berlin, p 1134

Longmire M, Choyke PL, Kobayashi H (2008) Clearance properties of nano-sized particles and molecules as imaging agents: considerations and caveats. Nanomedicine (Lond) 3(5):703

Mauricio MD et al (2018) Nanoparticles in medicine: a focus on vascular oxidative stress. Oxidative Med Cell Longevity 2018:6231482

Panahi Y et al (2016) Recent advances on liposomal nanoparticles: synthesis, characterization and biomedical applications. Artif Cells, Nanomed Biotechnol 45(4):788

Patra CR, Bhattacharya R, Mukhopadhyay D, Mukherjee P (2010) Fabrication of gold nanoparticles for targeted therapy in pancreatic cancer. Adv Drug Deliv Rev 62(3):346
Piñero S, Camero S, Blanco S (2017) Silver nanoparticles: influence of the temperature synthesis on the particles' morphology. IOP Conf Series: J Phys Conf Series 786:012020
Riehemann K et al (2009) Nanomedicine—challenge and perspectives. Angew Chem 48:872
Sun Y, Xia Y (2002) Shape-controlled synthesis of gold and silver nanoparticles. Science 298(5601):2176
van Rijjsel J et al (2011) Enthalpy and entropy of nanoparticle association from temperature-dependent cryo-TEM. Phys Chem Chemi Phys 13:12770–12774
Whitesides GM (2005) Nanoscience, nanotechnology, and chemistry. Small 1(2):172
Xia Y et al (2011) Self-assembly of self-limiting monodisperse supraparticles from polydisperse nanoparticles. Nat Nanotechnol 6:580–587
Xiong Y et al (2006) Poly(vinyl pyrrolidone): a dual functional reductant and stabilizer for the facile synthesis of noble metal nanoplates in aqueous solutions. Langmuir 22(20)8563

A Study on Light Traps for Attracting and Killing the Insects Using PKL Electricity

K. A. Khan, Rajia Sultana, Shahinul Islam, and S. M. Zian Reza

Abstract Insects can see the radiation of Ultra Violet (UV) light. Nocturnal insects emit Ultra Violet light and the light source can attract them. To keep it in mind a PKL light source has been designed and developed to kill the insects in the paddy, vegetables, flowers, and fruits field. PKL light traps have been used to reduce the damage of the paddy, flowers, vegetables, and fruits from the nocturnal moths. Some lamps are used to control the type of pests those species are attracted to yellow color. To control the flying insects in the cultivated land a new and innovative PKL electric lighting system based on LED have been designed and developed.

Keywords Nocturnal insects · Insecticide · PKL light · LED · Moths · Pest

1 Introduction

Bangladesh is a agricultural land dependent country (Coombe 1981, 1982; Costa and Robb 2002; Cowan 2009). Farmers are cultivating paddy, fruits, flowers, vegetables, etc. (Day 1941; Emura and Tazawa 2004; Khan et al. 2016a). But the insects are disturbing to cultivate crops in the field (Khan et al. 2016b, 2017; Rahman et al. 2018). That is why this work is important for the betterment of the farmers. The variation of sensitivity with the variation of wave length for UV, green, and blue color have been studied (Khan et al. 2019a, b). There are four steps of growing insects. The steps are as follows: (1) Egg (2) Larvae (3) Pupae (4) Adult. Sometimes eggs, or Sometimes larvae or, sometimes pupae or Sometimes adults are harmful for the paddy, flowers, vegetables and fruits leave from the nocturnal moths. Their sensitivity for different colors is different which is shown in the table-1. This work will help

K. A. Khan (✉)
Department of Physics, Jagannath University, Dhaka 1100, Bangladesh

R. Sultana
Primeasia University, Dhaka, Bangladesh

S. Islam · S. M. Zian Reza
Department of Physics, Uttara University, Dhaka, Bangladesh

M. Mukherjee et al. (eds.), *Advances in Medical Physics and Healthcare Engineering*, Lecture Notes in Bioengineering, https://doi.org/10.1007/978-981-33-6915-3_14

for the cultivation of lands for fruits and vegetables. Bangladesh is an agricultural-dependent country. The insects are destroying fruits and vegetables every year. This technology can help to destroy harmful insects.

2 Objective of the Study

1. To design and fabricate light traps for attracting and killing the insects using PKL electricity.
2. To Popularize the light traps for attracting and killing the insects using PKL electricity.

3 Methods and Materials

3.1 Technique of Attracting and Killing the Insects Using PKL Electricity

Figure 1 shows the technique of attracting and killing the insects using PKL electricity. A PKL electric system was set up beside the field during night time. There were two street lights for this PKL electric system. Each of the street light was 300 watts. It had been operated using PKL electricity.

It is shown (from Fig. 2) the design of a funnel type PKL light trap (Prototype). The designed light trap is low cost.

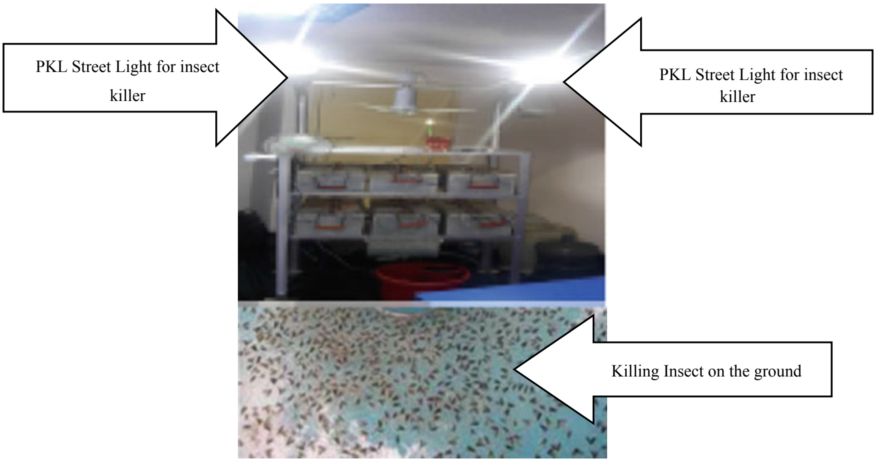

Fig. 1 Methods of attracting and killing the insects using PKL electricity

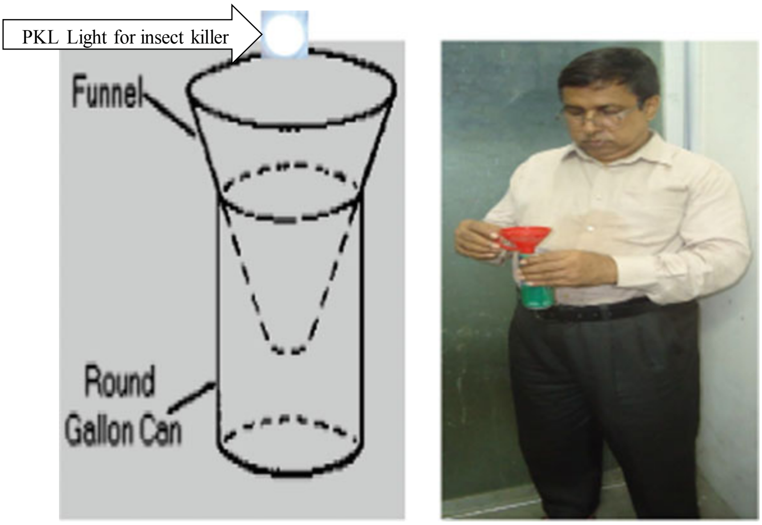

Fig. 2 Design of a funnel type PKL light trap (Prototype)

Fabrication of a Prototype PKL Light Trap for attracting and killing flying insect in the paddy, flowers and fruits field by a two small modules

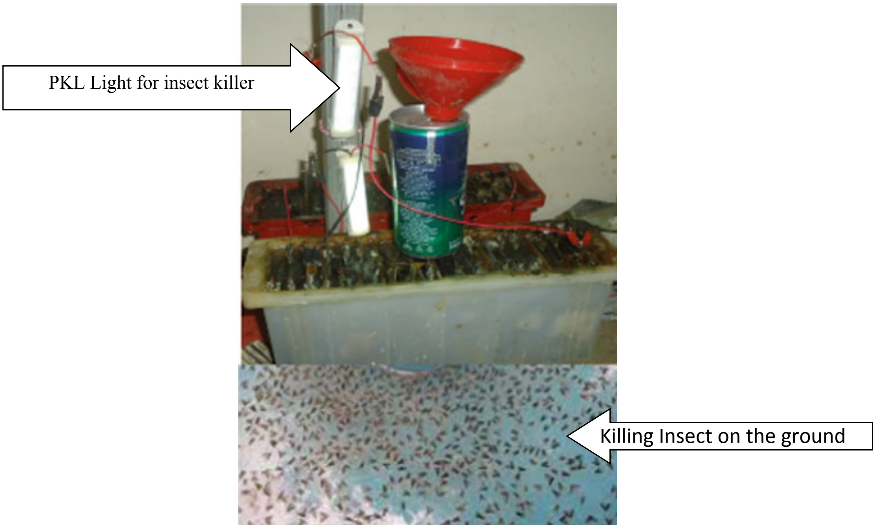

Fig. 3 Fabrication of a funnel type PKL light trap (Prototype)

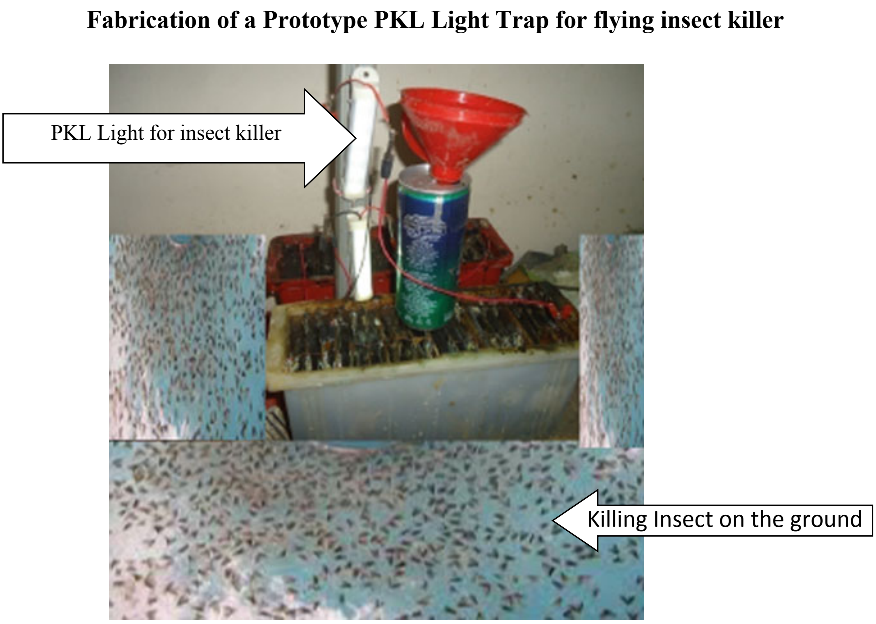

Fig. 4 Fabrication of a funnel type PKL light trap (Prototype)

It is shown (from Fig. 3) the designed and fabricated funnel type PKL light trap (Prototype). The fabricated light trap is low cost which is killing the insect on the ground (Fig. 3).

The light source was provided by PKL current (in Fig. 4) with LED Light. At the base of trap a poison bottle having potassium cyanide with a layer of plaster of parris was hanged for the killing purpose. Adult catches were recorded on daily basis. Dead insects were identified and pinned in the collection boxes. Collections of natural enemies were maintained separately from other insect pests. Effects of moth catches were evaluated on the bases of larval population of major insect pests in the treated as well as the control plot. In addition to major pests of gram and mungbean, many other species of various pests were also attracted.

Light traps (in Fig. 5) play important role in field sampling, monitoring, capturing, killing, and biodiversity studies of nocturnal insect population. Funnel-shaped light traps were used in mungbean and gram crops throughout the year. Effects of light traps were assessed by daily night collections in relation with abiotic factors based on marginal cost-benefit ratio.

Fabrication of a Prototype PKL Light Trap for attracting and killing flying insect in the paddy, flowers and fruits field

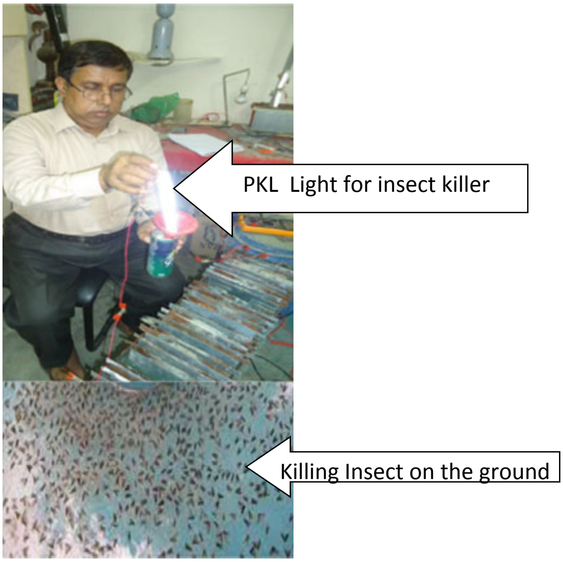

Fig. 5 Fabrication of a funnel type PKL light trap

3.2 PKL Light Sources Attracted by Insects During Night Time

It is shown (from Fig. 6) that the lights are attracted by different insects like Positive phototaxis, negative phototaxis, light adaptation, disturbance of circadian rhythm and photoperiodicity, Toxicity of UV on growth and development, Visibility control with UV-blocking film, and Dorsal light reaction.

4 Results and Discussion

It is shown (from Table 1) that the variation of Sensitivity with the variation of wave length (nm) for UV, Green, and Blue color. It is also shown (Table 1) that the variation of sensitivity for Ultra Violet decreases with the increase of wave length (nm).

The variation of sensitivity for Green decreases with the increase of wave length (nm) firstly and then increases and finally decreases. The variation of sensitivity for Blue decreases with the decrease of wave length (nm) firstly and then increases and finally decreases. It is also shown that the Sensitivity for Ultra Violet and Blue becomes 0 at the wave length (nm) of 550–600 nm.

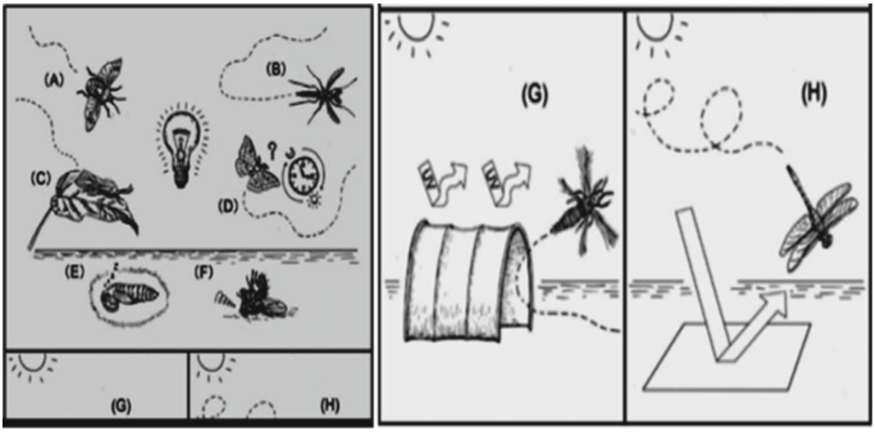

Fig. 6 Lights are attracted by insects: **a** Positive phototaxis, **b** negative phototaxis, **c** light adaptation, **d** disturbance of circadian rhythm and **e** photoperiodicity. **f** Toxicity of UV on growth and development. **g** Visibility control with UV-blocking film. **h** Dorsal light reaction

Table 1 Data for sensitivity versus wave length (nm) for UV, green, and blue color

Wave length (nm)	Sensitivity for ultraviolet	Sensitivity for green	Sensitivity for blue
300	0.28	0.12	0.08
350	1.0	0.45	0.20
400	0.10	0.21	0.75
450	0.05	0.48	0.65
500	0.02	0.75	0.07
550	0	0.80	0
600	0	0.10	0

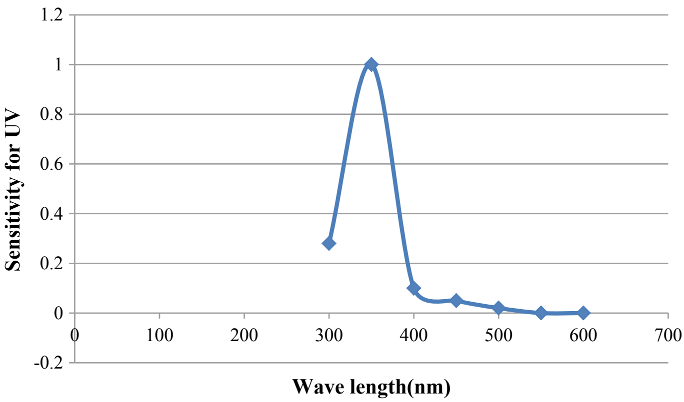

Fig. 7 Sensitivity versus wave length (nm) for UV

Figure 7 shows that sensitivity for UV increases up to 1 nm and then decreases up to 400 nm directly and finally it becomes zero. It is also shown that the maximum sensitivity is 1.00 at the wave length of 350 nm and the minimum sensitivity is 0 at the wave length of 550 and 600 nm. So that the difference between the maximum and minimum sensitivity is 1.00 and the difference between the waves lengths are (550–350) 200 nm and (500–350) 150 nm for maximum and minimum sensitivity of ultraviolet ray.

Figure 8 shows that sensitivity for green color increases and decreases from 0.10 to 0.80 nm. It is also shown that the maximum sensitivity is 0.80 at the wave length of 550 nm and the minimum sensitivity is 0.10 at the wave length of 600 nm. So that the difference between the maximum and minimum sensitivity is $0.80 - 0.10 = 0.70$ nm and the difference between the waves length is (600–550) 50 nm for maximum and minimum sensitivity of Green ray.

Figure 9 shows that sensitivity for blue color increases and decreases from 0.07 to 0.75 nm. It is also shown that the maximum sensitivity is 0.75 at the wave length of

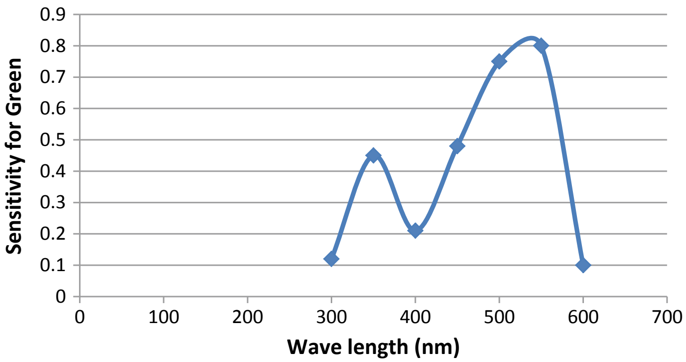

Fig. 8 Sensitivity versus wave length (nm) for green

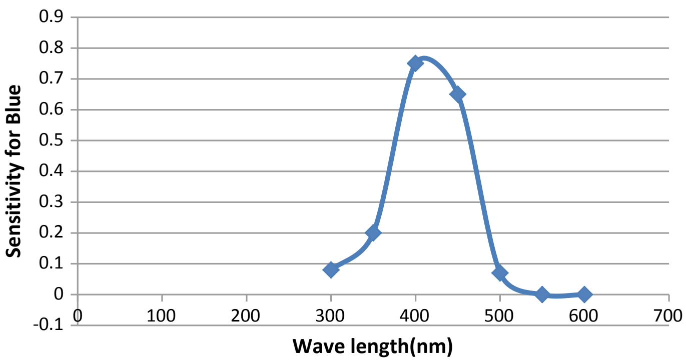

Fig. 9 Sensitivity versus wave length (nm) for blue

400 nm and the minimum sensitivity is 0 at the wave length of 550 and 600 nm. So that the difference between the maximum and minimum sensitivity is 0.75 and the difference between the wave lengths are (550–400) 150 nm and (500–400) 200 nm for maximum and minimum sensitivity of blue light.

5 Conclusions

Light traps are the best tool for the monitoring, attraction, killing, and biodiversity studies of pulses insect pest of Thal regions. This is best insect population controlling tool which can easily be manufactured at homes or small markets with idea Marginal Cost-Benefit Ratio. There are some harmful insects like black beetle, hoppers, green leap, short horn grasshoppers, and white leaf hoppers. Although there are some neutral insects. After using this PKL technology it is not needed to use insecticides in the paddy, fruits, flowers, tea garden, and vegetables field. This work will help to develop the economy of the nation. It can be used instead of fertilizer to kill the flying insects. As a result, people will get the healthy fruits, vegetables, tea, and other crops.

Acknowledgements The authors are grateful to the GARE (Grant of Advanced Research in Education) project, Ministry of Education, GoB for financing during the research work (Project/User ID: PS2019949).

References

Coombe PE (1981) Wavelength specific behaviour of the whitefly Trialeurodes vaporariorum (Homoptera: Aleyrodidae). J Comp Physiol 144:83–90

Coombe PE (1982) Visual behaviour of the greenhouse whitefly, *Trialeurodes vaporariorum*. Physiol Entomol 7:243–251

Costa HS, Robb KL (2002) Wilen CA Field trials measuring the effects of ultraviolet-absorbing greenhouse plastic films on insect populations. J Econ Entomol 95:113–120

Cowan T (2009) Gries G ultraviolet and violet light: attractive orientation cues for the Indian meal moth Plodia interpunctella. Entomol Exp Appl 131:148–158

Day MF (1941) Pigment migration in the eyes of the moth, *Ephestia kuehniella* Zeller. Biol Bull 80:275–291

Emura K, Tazawa S (2004) The development of the eco-engineering insect control technology—physical control of insect behavior using artificial lights. Eco-engineering 16:237–240 (in Japanese with English abstract)

Khan KA, Rahman A, Rahman MS, Tahsin A, Jubyer KM, Paul S (2016a) Performance analysis of electrical parameters of PKL electricity (An experimental analysis on discharge rates, capacity and discharge time, pulse performance and cycle life & deep discharge of PathorKuchi Leaf (PKL) electricity cell). In: 2016 IEEE Innovative smart grid technologies-Asia (ISGT-Asia). IEEE, 2016, pp 540–544. https://doi.org/10.1109/ISGT-Asia.2016.7796442

Khan MK,A Paul S, Rahman MS, Kundu RK, Hasan MM, Moniruzzaman M, Mamun MA (2016b) A study of performance analysis of PKL electricity generation parameters: (An experimental analysis on voltage regulation, capacity and energy efficiency of pathorkuchi leaf (PKL) electricity cell). In: 2016 IEEE 7th Power India international conference (PIICON). IEEE, 2016, pp 1–6. https://doi.org/10.1109/POWERI.2016.8077199

Khan MKA, Rahman MS, Das T, Ahmed MN, Saha KN, Paul S (2017) Investigation on parameters performance of Zn/Cu electrodes of PKL, AVL, tomato and lemon juice based electrochemical cells: a comparative study. In: 2017 3rd international conference on electrical information and communication technology (EICT). IEEE, 2017, pp 1–6. https://doi.org/10.1109/EICT.2017.8275150

Khan KA, Rahman MS, Rahman MN, Khan SA, Juel MTI, Paul S, Nirjhar MI (2019a) Electrochemical characterizations of *Bryophylum pinnatum* leaf battery. In: 2019 6th International conference on microelectronics, circuits and systems (micro) [Presented], pp 1–6

Khan MKA, Rahman A, Paul S, Rahman MS, Ahad MT, Mamun MA (2019b) An investigation of cell efficiency of pathor kuchi leaf (PKL) cell for electricity generation. In: 2019 IEEE—international symposium on advanced electrical and communication technologies. IEEE, 2019 [Presented], pp 1–6

Rahman MN, Rahman MS, Saha KN, Paul S, Khan MKA, Hazari MR (2018) Experimental investigations in pH behavior and cell potential of *Bryophyllum pinnatum* solution. In: Grand renewable energy proceedings Japan council for renewable energy. Japan Council for Renewable Energy, p 215. https://doi.org/10.24752/gre.1.0_215

Aluminum-Doped Nano-Zinc Oxide Can Act as Good Carrier for Biomedicine

Dhananjoy Roy

Abstract Proper diagnosis of the cause of trouble, dose estimation and safe reaching of medicine to the destination (DDD model) would bring effective healing result. Technology/equipments help a lot to diagnosis and identify the location of the damage. Nanoscience and nanotechnology are occupying a major part in these regards. Medicine applied orally or by injection has to pass a long route through the body parts overcoming many obstacles before reaching to destination. Nanoparticles can move faster without distortion of the passage and interact largely with infected cells as its surface-to-volume ration is larger. Zinc oxide nanoparticles (ZnO NPs), as one of the most important metal oxide nanoparticles, are popularly employed in various fields of medical science and applications due to their peculiar physical and chemical properties. Aluminum-doped zinc oxide (AZO) nanoparticles are transparent as well as conducting (TCO) material and being used as an important component in a number of electronic and imaging devices including scanner, liquid–crystal displays, OLEDs, touchscreens and photovoltaics. Both these nanomaterials have been deposited in a simple and low-cost sol–gel method.

Keywords Nano-medicine · Drug carriers · ZnO · AZO · TCO material · Sol–gel method

1 Introduction

Recently emerging nanoscience and nanotechnology may bring revolution in different field of science and engineering. Accuracy in detection of infected cells and charging of precision amount of medicine can be increased by nanoscience and nanotechnology, particularly, in the field of medical science and treatment of different type of diseases. Over the last decade, nanoscience and nanotechnology are emerging as the operating as well as controlling parts of various fields of science and technology (Sirelkhatim et al. 2015; Siddiqi et al. 2018) which are essential for

D. Roy (✉)
Department of Physics, Barasat Government. College, 10 K.N.C. Road, Barasat, West Bengal 700124, India

M. Mukherjee et al. (eds.), *Advances in Medical Physics and Healthcare Engineering*, Lecture Notes in Bioengineering, https://doi.org/10.1007/978-981-33-6915-3_15

mankind. Nanoparticles are a part of nanomaterials that are defined as a single particle of 1–100 nm in diameter. From last few years, nanoparticles have been a common material for the development of new cutting-edge applications in communications, sensing, energy storage, data storage, optics, transmission, cosmetics, biology, environmental protection and medicine due to their important optoelectronic and peculiar physiochemical properties (Smijs and Pavel 2011).

Zinc oxide (ZnO), which can exhibit a wide variety of nanostructures, possesses unique semiconducting, optical and piezoelectric properties and hence has been investigated for a wide variety of applications. Most important features of ZnO nanomaterials are low toxicity and biodegradability and can be used as an additive in a variety of materials. Therefore, ZnO-based nanomaterials have been studied for a wide variety of applications such as drug delivery, gene delivery, anticancer, antibacterial and diabetes treatment; anti-inflammation; wound healing; bio-imaging and bio-sensing of a wide array of molecules of interest (Mishra et al. 2017; Zhang and Xiong 2015).

Aluminum-doped zinc oxide (AZO) nanoparticles has all properties of ZnO in addition with increased electrical conductivity. They are an important component in a number of electronic and biomedical imaging devices including liquid–crystal displays, OLEDs, touchscreens, photovoltaics, sunscreen**,** probes for imaging retinal hypoxia, etc. (Uddin et al. 2015).

Activity and reactivity of materials vastly vary with particle shape, size and concentration of nanoparticles, bonding strength of atoms, etc., which are been rooted during the synthesis process (Narjis et al. 2020). The sol–gel process has demonstrated as the high potential to control the size, bulk and surface properties of the oxides (Baraket and Ghorbel 1998). Moreover, it has advantages due to its excellent compositional control, homogeneity on the molecular level, simplicity, low cost, performing well in atmospheric pressure without the need for expensive vacuum equipment, lower crystallization temperature, and it can be used to deposit films over a large area with a very uniform thickness (Hench and West 1990). We report here the study of dependence of size, conductivity and transparency of the synthesized nanoparticles on various depositional conditions. For AZO samples, we have doped aluminum into ZnO through a simple sol–gel technique (Znaidi 2010).

2 Experimental

2.1 Synthesis of Undoped ZnO and Al-Doped AZO Nanoparticle

We have synthesized undoped and Al-doped ZnO (AZO) nanoparticles through a simple and low-cost sol–gel method (Znaidi 2010). Undoped ZnO samples were prepared by dissolving 0.5 M of zinc acetate dihydrate $Zn(CH_3COO)_2 \cdot 2H_2O$ into 30 ml of ethanol. This solution was stirred at 80 °C for 1 h. Then the solution is allowed for crystallization by slowly annealing to room temperature. To prepare the AZO nanoparticles, different amounts of aluminum acetate $Al(OH)(CH_3COO)_2$ were dissolved in a solution of zinc acetate dihydrate and polyethylene glycol as surfactant to gain concentration at 0% (AZO 0%), 2% (AZO 2%), 3% (AZO 3%) and 4% (AZO 4%) (g/mL), respectively. This precursor solution was sintered at 80 °C for 2 h with continuous stirring by magnetic stirrer. The solution is slowly converted to gel. Then the gel was dried to powder at 60 °C following by annealing process for crystallization. By this simple method, the nanoparticles have been successfully prepared.

2.2 Characterization

The characterizations were conducted by X-ray diffraction (XRD) and UV–visible spectroscopy, and the crystallite size was calculated using the Scherrer's formula:

$$D = k\lambda/(\beta\cos\theta) \tag{1}$$

where D is the average of crystallite size, β is the full width at the half maximum of the diffraction peak, θ is the Bragg angle, λ is the wavelength of X-ray used, and k is a constant.

3 Results and Discussions

3.1 X-Ray Diffractions

Crystal structures of the prepared undoped ZnO and Al-doped AZO samples were examined by X-ray diffraction in the diffraction angle range $2\theta = 10–80°$. X-ray diffraction [Fig. 1] shows the samples are polycrystalline nano-crystal. X-ray photographs also show that peak intensity is much higher for 3% Al-doping sample than 4%. It indicates that crystal homogeneity break and more disorder phase appear for higher Al concentrations.

The crystallite size was calculated using the Scherrer's formula in Eq. (1). Calculated size of crystallites is given in Table 1. Data show that the Al doping resulted in the increase in size of crystallites.

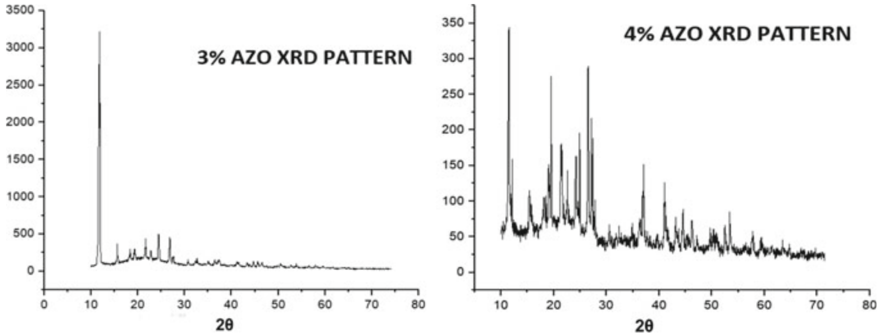

Fig. 1 XRD patterns of Al-doped ZnO at various Al concentrations

Table 1 From XRD data for 3 and 4% Al-doped ZnO

Samples	Peak position (2θ)	FWHM (full width half maxima)	Crystal size, D (nm)	Average crystal size, D_{av} (nm)
3% Al-doped AZO	11.74897	0.32112	24.86992009	26.99898166
	24.42357	0.30341	26.78952856	
	26.7863	0.27836	29.33749633	
4% Al-doped AZO	11.44373	0.28606	27.91046939	30.011019

3.2 *UV–Visible Optical Absorption*

Absorption spectra obtained in UV–visible spectroscopy show that pure ZnO has absorption peak at around 260 nm [Fig. 2a] and Al-doped samples have dual absorption peaks occurring at two positions: one at around 270 nm and other one at 300 nm [Fig. 2b and c].

This indicates that there are two types of lattices: unaffected ZnO lattice peaked at 270 nm and Al-doped AZO lattices peaked at 300 nm. Optical band gap of samples has been determined with the help of Tauc relation

$$(\alpha h\nu)^2 = A\left(h\nu - E_g\right) \tag{2}$$

where α represents absorption coefficient, A is a constant, and $h\nu$ is photon energy. Band gap value is found to be 3.6 eV for pure ZnO and 3.5 eV for AZO nanoparticles. It is also clear that band gap for these nanosamples are higher than the value of bulk ZnO.

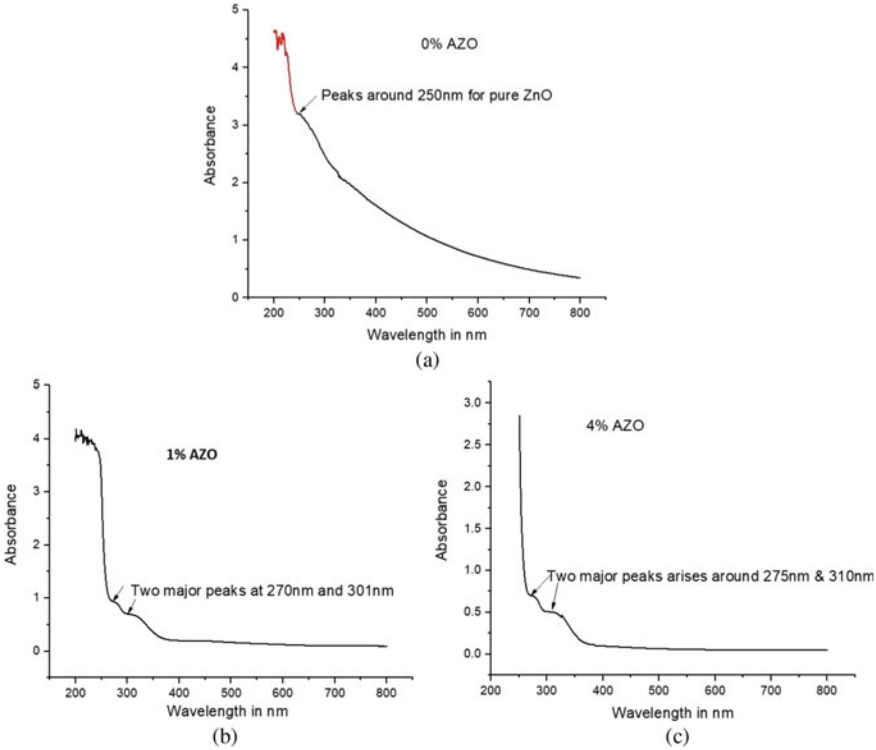

Fig. 2 UV–visible optical absorption of ZnO and AZO of different Al concentrations

3.3 Transmission or Transparency of the Materials

It is clear from the graph that undoped ZnO and Al-doped AZO samples below 4% Al concentration have transparency more than 80% and transparency reduces for higher Al concentrations [Fig. 3]. Reduction of transparencies may be due to scattering of photons by crystal defects created by doped aluminum atoms which took place in the interstitial positions or may be due to the impurity scattering present in the solution.

3.4 Study of Electrical Properties

For electrical and structural studies, DC electrical resistivity measurement has been done through a simple electrolysis method. Current–voltage characteristics of undoped and Al-doped ZnO nanoparticles with five different doping concentrations (0, 1, 3, 4, 6, 9%) are shown in Fig. 4. It is seen that the electrical current of the nanofluid increases with increasing Al dopant concentration upto 4% and then decreases for higher Al concentrations. To get a clear picture of this variation, we

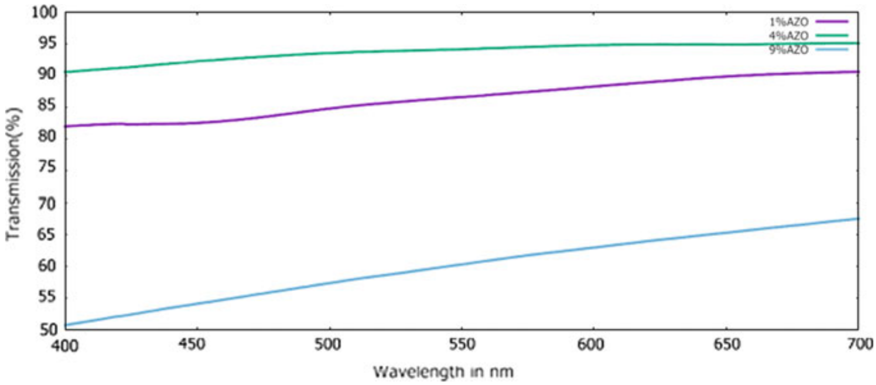

Fig. 3 Transmission of AZO for different % of Al doping

have calculated resistivity using the equation

$$\rho = R * A/L \tag{3}$$

where A is cross sectional area, L is the length of the dipped electrodes within the solution and $R = V/I$, is the resistance plotted in Fig. 5. Clearly, resistance decreases up to 4% Al concentrations and then decreases.

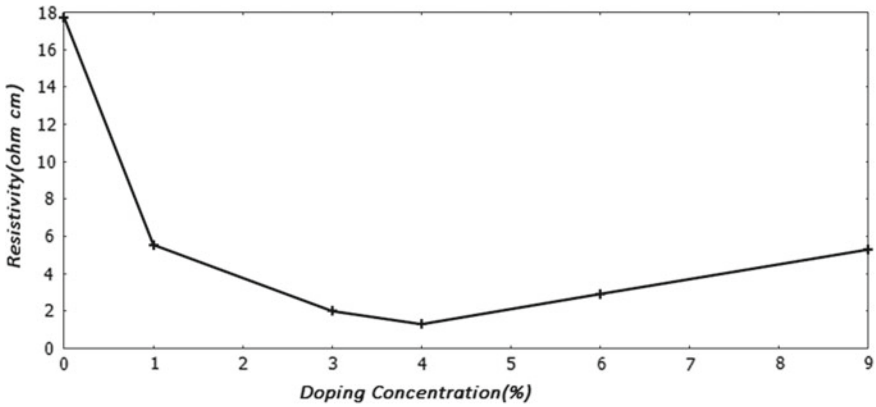

Fig. 5 Variation of resistivity of AZO samples for different Al concentrations

3.5 Discussion

All the above reported results show that Al doping into pure ZnO semiconductor crystal has a little effect on crystallinity and transmission. Possible explanation of the existence of two peaks is as follows.

- Atomic radius of Al is 125 pm which is less than Zn atom of radius ~139 pm.
- Lattice in which Zn atoms substituted by Al atoms might shrink in volume.
- Atoms of shirked lattice become closure, and there might be a change in electrons distribution.
- This new distribution might introduce shallow energy states within the band gap causing reduction in excitation energy of the valance electrons.

But all Zn ions could not be replaced by dopant Al atoms. So, obviously there are two types of lattice exist within the AZO materials: pure ZnO lattice which has a peak at around 270 nm and other one due to Zn substituted AZO lattice which has a peak at a lower energy at 310 nm. Doped Al atoms have two sites to sit within ZnO crystal: lattice site by substitution of Zn^{2+} ions and interstitial site of the crystal. Lattice site sited Al^{3+} gives one free electron and improves conductivity, but interstitial site sited Al atoms do not give free electron rather distort the crystal and introduce defects in the crystal which in turn absorb free electrons resulting decrease in conductivity.

- Initially when Al atom concentration in solution is low, Al atoms try to occupy first lattice position replacing Zn atoms through chemical reaction prioritized by their electron affinity. So, conductivity increases.
- When Al concentration is becoming high in solution, some Al atoms occupy interstitial positions. Interstitial Al creates volume defect and increases resistance of the sample.
- So for higher Al concentration, there is a competition between the effects of lattice Al and interstitial Al. Later effect dominates for higher Al concentrations.

Thus, this may be due to a competitive effect of carrier generation by substitutional Al with carrier trapping by interstitial Al. At lower concentrations, Al atoms occupy substitution position resulting increase in conductivity. But for higher concentration, more and more Al atoms occupy the interstitial positions producing defects and acting as carrier-trapping centers resulting reduction in conductivity.

4 Conclusions

Due to important optoelectronic and peculiar physiochemical properties of pure nano-ZnO can be used as drug delivery, gene delivery, anticancer, antibacterial and diabetes treatment, anti-inflammation, wound healing, bio-imaging and bio-sensing of a wide array of molecules of interest. Little toxic effect of ZnO can be used as for cancer and tumor treatments. Transparent and conducting properties of aluminum-doped AZO materials are mainly useful for imaging inside of the body system, touchscreen, etc., as well as drug carriers. AZO materials are less toxic and have no corrosive effects compared to other TCO materials available in market appealing for safer uses.

Acknowledgements The author gracefully acknowledges the financial support from the Department of Science and Technology (India) to procure the UV–Visible spectrophotometer under the FIST scheme at the Department of Physics, Barasat Government College. The author also acknowledges the Indian Association for the Cultivation of Science (IACS), Jadavpur, Kolkata, for providing XRD data.

References

Baraket L, Ghorbel A (1998) Control preparation of aluminium chromium mixed oxides by Sol-Gel process. 118:657–667

Hench LL, West JK (1990) The sol-gel process. Chem Rev 90:33–72

Mishra PK, Mishra H, Ekielski A, Talegaonkar S, Vaidya B (2017) Zinc oxide nanoparticles: a promising nanomaterial for biomedical applications. Drug Discov Today 22(12):1825–1834. View at: Publisher Site|Google Scholar

Narjis A, El Aakib H, Boukendil M, El Hasnaoui M, Nkhaili L, Aberkouks A, Outzourhit A (2020) Controlling the structural properties of pure and aluminium doped zinc oxide nanoparticles by annealing. J King Saud Univ Sci 32(1):1074–1080

Siddiqi KS, ur Rahman A, Tajuddin, Husen A (2018) Properties of zinc oxide nanoparticles and their activity against microbes. Nanoscale Res Lett 13(141)

Sirelkhatim A, Mahmud S, Seeni A, Kaus NHM, Ann LC, Bakhori SKM, Hasan H, Mohamad D (2015) Review on zinc oxide nanoparticles: antibacterial activity and toxicity mechanism. Nanomicro Lett 7(3):219–242

Smijs TG, Pavel S (2011) Titanium dioxide and zinc oxide nanoparticles in sunscreens: focus on their safety and effectiveness. Nanotechnol Sci Appl 4:95–112. View at: Publisher Site|Google Scholar

Uddin MI, Evans SM, Craft JR, Marnett LJ, Uddin MJ, Jayagopal A (2015) Applications of azo-based probes for imaging retinal hypoxia (online issues)

Zhang ZY, Xiong HM (2015) Photoluminescent ZnO nanoparticles and their biological applications. Materials 8(6):3101–3127. View at: Publisher Site|Google Scholar

Znaidi L (2010) Sol-gel-deposited ZnO thin films: a review. Mater Sci Eng B 174:18–30

Insulin Attenuated Estrogen Receptor in Neutrophil Dwindled Synthesis of Maspin in Breast Cancer

Karabi Ganguly and Swati Sikdar

Abstract ***Purpose***: The binding of either estrogen or insulin to their specific receptors on neutrophils has been reported to stimulate nitric oxide (NO) induced maspin synthesis in these cells. Experiments were carried out to determine the role of estrogen receptor interaction in the nitric oxide induced maspin synthesis in neutrophils that was preincubated with insulin. ***Methods***: Estrogen receptor positive (ER+), estrogen receptor negative (ER–) neutrophils were isolated from the blood cancer subjects. Maspin was determined by enzyme linked immunosorbent assay after in vitro translation of maspin mRNA. NO was determined by methemoglobin method. ***Results***: Immunohistochemical studies of estrogen receptor (ER) demonstrated the presence of both ERα and ERβ subtypes in the normal peripheral neutrophils and less in number in ER+ breast cancer neutrophils. In contrast, ER– breast cancer neutrophils lacked the ERα and ERβ subtypes, suggesting pathophysiological defects in the synthesis of ER (α and β) proteins in peripheral ER– neutrophils. ***Conclusion***: These results suggested that insulin dwindled maspin synthesis in normal and in breast cancer neutrophils by decreasing the estrogen receptor number in both cases.

Keywords Breast cancer · Estrogen · Estrogen receptor · Insulin · Maspin · Nitric oxide · Neutrophils

1 Introduction

Breast cancer is most frequently encountered in women and is an estrogen dependant condition (Schneider and Jackisch 1998). Estrogen plays an important role in the synthesis of an anti-breast cancer protein, maspin (Mammary Serine proteinase inhibitor, Mr. 42 kDa) which is abundantly expressed in the normal mammary epithelial cells and neutrophils, is reported to inhibit malignant breast cell invasion, angiogenesis, metastasis and promote apoptosis (Zou et al. 1994; Hojo et al. 2001; Liu et al. 1999a).

K. Ganguly (✉) · S. Sikdar
Department of Biomedical Engineering, JISCE, Kalyani, West Bengal, India
e-mail: karabi.ganguly@jiscollege.ac.in

M. Mukherjee et al. (eds.), *Advances in Medical Physics and Healthcare Engineering*, Lecture Notes in Bioengineering, https://doi.org/10.1007/978-981-33-6915-3_16

The expression of the effect of estrogen is reported to be mediated through the binding of the hormone to the nuclear receptors, and a DNA binding domain which recognizes a sequence of DNA known as hormone responsive elements (HRE) (Beato and Klug 2000).

The estrogen receptor status has prognostic significance (Maehle et al. 2009). The breast cancer tumors that had no receptors of estrogen are reported to results in worse prognostic outcome than those in cases where the receptor of this hormone was present (Rosa et al. 2008). On the basis of presence of estrogen receptor in the lesion, the breast cancer patients are classified into two groups: (1) estrogen receptor positive (ER+) and (2) estrogen receptor negative (ER−). The presence of estrogen receptor (ER+) is a better prognostic indicator for the breast cancers. In contrast, the estrogen receptor negative (ER−) tumors have been reported to have a poorer prognosis than that of the estrogen receptor positive (ER+) tumors (Rosa et al. 2008). It is seen that in patients with ER+ tumors the occurrence of metastases is 3–6 times less probable than in patients with ER− tumors. The clinical data indicated that the ER− breast cancers are less sensitive to therapy than those with ER+ tumors, and ER− patients had a shorter disease free interval than those of ER+ patients (Gelbfish et al. 1988).

Taking these reports together it could be suggested that estrogen plays important role in both the control of breast cancer and in the better prognostic outcome of the malignancy (Schneider and Jackisch 1998).

As reported earlier, estrogen and its receptors have critical role in the development and in the prognostic outcome of the human breast cancer. The role of estrogen in relation to the receptor ligand interaction in the synthesis of maspin is also having paramount importance. The interrelation between the estrogen receptors function and maspin synthesis through NO production in the control of human breast cancer is already established (Ganguly Bhattacharjee et al. 2012). The physiologic events are the consequent effects of binding of one ligand to its own receptors, which influences the binding and the effect of a second ligand to its own receptors and is known as “cross talk” between the receptors (Basrawala et al. 2006; Kahn and Sinha 1992; Freychet et al. 1971; Dutta-Roy et al. 1991; Kahn et al. 1993). We report here that estrogen and insulin were capable of stimulating maspin synthesis through the production of NO in neutrophils. The results of the investigation suggest the existence of effect of insulin on the function of estrogen in neutrophils, in the context of NO induced maspin synthesis. The possible pathological implication of the crosstalk (Ganguly Bhattacharjee et al. 2012; Kahn and Sinha 1990a; Girish et al. 2006) between the receptors of the steroid and the anti-diabetic hormone in the synthesis of the anti-breast cancer protein in human breast cancer are presented herein.

2 Materials and Methods

Ethical Clearance: The protocol used in the study was approved by the Internal Review Board, Sinha Institute of Medical Science and Technology. Appropriate permission was also obtained from the I.R.B. for the use of rabbits in the studies.

Chemicals: Recombinant Human maspin (rh Maspin) was a kind gift of Dr. Sally Twining, Dept. of Biochemistry, Medical College of Wisconsin, USA. ELISA maxisorp plates were obtained from NUNC, Denmark. Estrogen and other chemicals used were from Sigma Chemical Co.USA. ER (α and β) antibody was obtained from Thermo Fisher Scientific, NY, USA.

Preparation of Estrogen and Insulin solution: Estrogen and Insulin solution were prepared by dissolving the compounds in 0.9% NaCl, at pH 7.4.

Selection of patients with breast cancer and normal volunteers: Only female breast cancer patients between 35 and 65 years (mean 45 years, $n = 20$), participated in the study. None of them had received any therapy. Equal number of age matched normal female volunteers compared to that of the selected breast cancer subjects were asked to kindly participate in the study.

Determination of estrogen and progesterone receptor status of neutrophils from breast cancer subjects: ER statuses were determined by immunohistochemical techniques using fluorescence tagged antibodies and cells were observed and photographed. The neutrophils of the breast cancer subjects were classified as ER+ neutrophils or ER− neutrophils.

Collection of blood: The blood samples (20–25 ml) were collected by venipuncture and anticoagulated by gently mixing 1vol. of 0.13 M sodium citrate with 9 vol. of blood (Girish et al. 2006).

Immunization of the animals: Polyclonal antibodies against r-human maspin, estrogen, were raised by repeated immunization in White New Zealand rabbit (Tlaskalova-Hogenova and Stepankova 1980).

Assay of NO: Nitric oxide formation was assayed by methemoglobin method by following the protocol described before using Beckman Spectrophotometer (Model DU6) (Girish et al. 2006). The validity of the assay was confirmed by independent chemiluminescence method (Cox and Frank 1982).

Preparation of neutrophil suspension and the incubation of the isolated neutrophils with estrogen and insulin: Neutrophils isolated from the citrated blood samples suspended in HBBS buffer at pH 7.4 (6 × 109 cells/L) were incubated for 2.5 h at 23 °C with 200 μU of porcine insulin to reach equilibrium then were again incubated with different concentrations of estrogen and another set of neutrophils incubated with different concentrations of only estrogen for 4 h at 37 °C under sterile conditions (Klock and Bainton 1976).

In vitro ***translation of maspin–mRNA***: In vitro translation of maspin–mRNA: Nucleic acids containing maspin mRNAs were isolated by Trizol methods from the neutrophils isolated from blood samples from breast cancer patients and from the normal volunteers (Cook et al. 2000). The nucleic acid preparation was incubated with ribosomal preparation, mixture of all amino acids (0.1 μmol each/ml) and 2 mM ATP as described (Zimmerman et al. 1979). After 6 h of incubation under sterile condition, the reaction mixture at 0 °C was centrifuged at 10,000 g for 10 min. The supernatant was used for the determination of maspin by ELISA as described below.

Enzyme linked immunosorbant assay (ELISA) for Maspin: Maspin was quantitated by ELISA using polyclonal antibody developed against rh Maspin (Girish et al. 2006). ELISA was performed by the method as described before (Engvall et al. 1972).

Scatchard plot analysis of the equilibrium binding of estrogen to its receptor in neutrophils: The neutrophils with the bound estrogen were separated from the unbound hormones by filtration over GF/C filter (Kahn and Sinha 1990b). The concentrations of estrogen in the sample were determined by ELISA. The dissociation constant (Kd) and the receptor numbers (n) were determined from Scatchard plots (Scatchard 1949).

Statistical analyses: The results obtained are presented as mean ± SD. The significance of the results was determined by Students' t-test, and $p < 0.005$ was considered to be significant.

3 Results

Determination of estrogen receptor subtype (α and β) in normal, ER+, ER– in peripheral neutrophils in blood: Immunohistochemical studies of the statuses of estrogen receptor in ER+ neutrophils and in the normal peripheral neutrophils demonstrated the presence of both α and β subtype of estrogen receptors. In contrast, the ER– neutrophils from the breast cancer patients showed the absence of both α and β subtype ER, suggesting pathophysiological defects in the synthesis of estrogen receptors proteins (α and β) in the peripheral neutrophils (Fig. 1).

Scatchard plot of the equilibrium binding of estrogen to intact normal neutrophils: Scatchard plot of the equilibrium binding of estrogen to normal neutrophils demonstrated typical homogeneous estrogen receptor population (Line A in Fig. 2). The analysis of the binding characteristics showed there were $4.179 \pm 1.02 \times 107$ estrogen receptor binding sites/cell, with dissociation constant (Kd) 0.926 nM.

Detail of the equilibrium binding of estrogen to neutrophils was carried out as described in Materials and Methods. The estrogen was quantitated by ELISA using polyclonal antibody raised in rabbits as described in the Materials and Methods.

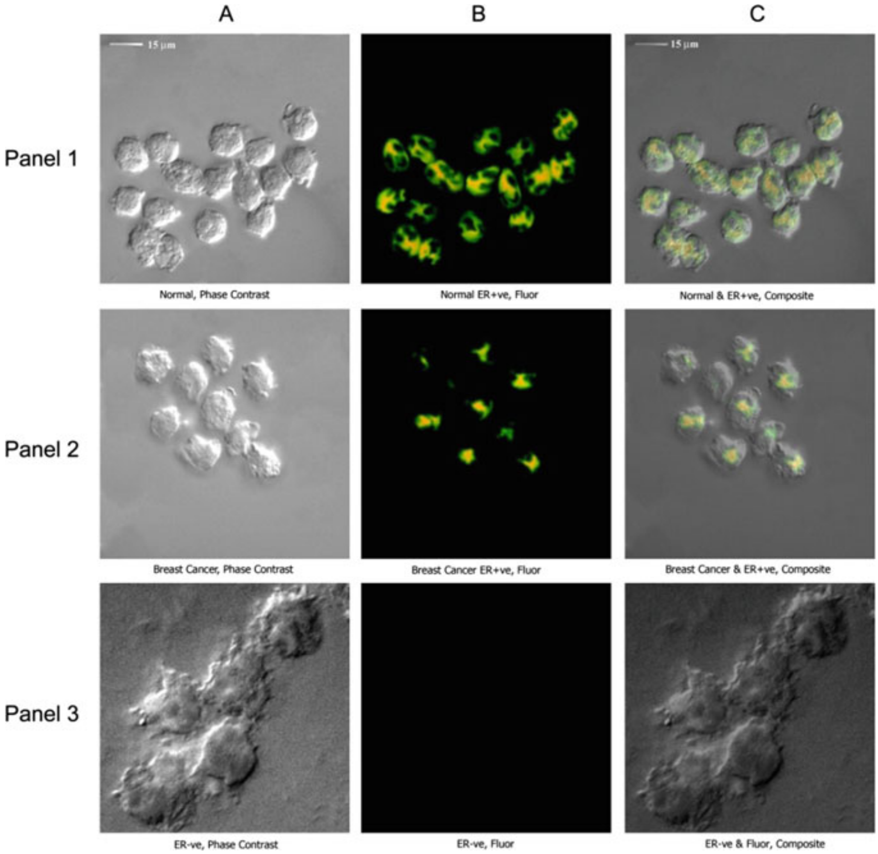

Fig. 1 Immunohistochemistry of estrogen receptors in neutrophils from normal and breast cancer patients: The panel 1 (A, B, C), panel 2 (A, B, C), panel 3 (A, B, C) represent normal (ER+) neutrophils, Breast Cancer (ER+) neutrophils and Breast Cancer (ER–) neutrophils, respectively. The figure presented is the typical representative of 6 more experiments using neutrophils from 6 different subjects from each group. The immunohistochemistry for estrogen receptor was determined as described in the Materials and Methods

In the experiment, the neutrophils were treated with 200 μunits of insulin for 2.5 h at 23 °C before these cells were used for the study of binding of estrogen without removing insulin from the cell suspension.

Effect of pre-incubation of neutrophils with insulin on the binding of estrogen to its receptors on these cells: Scatchard plot of the equilibrium binding of estrogen to the neutrophils pre-incubated with insulin was constructed (Line B in Fig. 2) and compared with that constructed using neutrophils that were not pre-incubated with insulin (Line A in Fig. 2). It was found that as a result of incubation of neutrophils with insulin the binding affinity for estrogen to its receptors in neutrophils remained essentially unchanged which demonstrated Kd = 1.072 nM compared to Kd of the

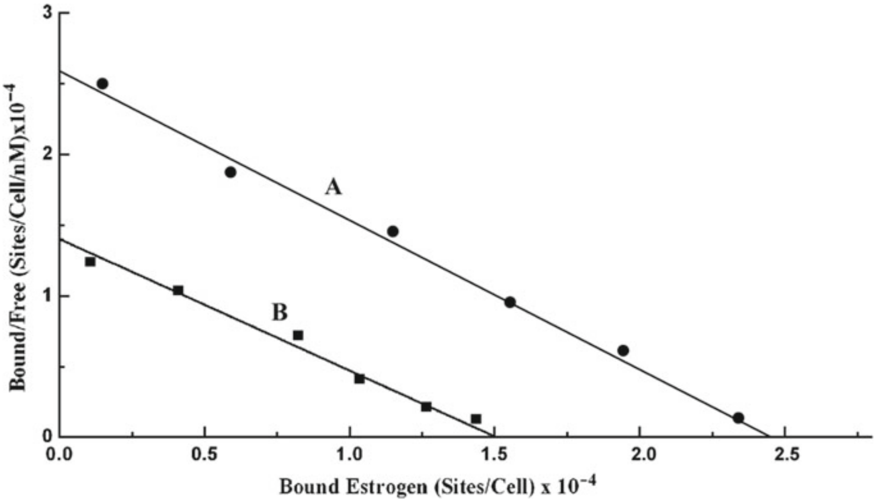

Fig. 2 Scatchard plot of estrogen binding to normal neutrophils pre-incubated with or without insulin: **a** Scatchard plot of equilibrium estrogen binding to normal neutrophils. **b** Scatchard plot of equilibrium estrogen binding to the normal neutrophils pre-incubated with insulin

binding of estrogen is 0.926 nM in the neutrophils that were not pretreated with insulin. The estrogen receptors which were 4.179 × 107/cell in the untreated cells was found to be decreased to 2.586 × 107/cell ($p < 0.005$, $n = 6$) after the same cell were treated with 200 μU of insulin.

The effect of estrogen on the synthesis of NO and maspin in normal ER+ and ER– neutrophils pre-incubated with insulin: It was found that the pre-incubation of normal ER+ neutrophils with insulin resulted in the significant impairment of the synthesis of both NO and maspin in these cells when compared to the control (Table 1). The treatment of normal ER– neutrophils which failed to produce either NO or maspin when treated with estrogen also failed to produce these agents when these cells were pretreated with insulin.

Table 1 The effect of estrogen on the synthesis of NO and maspin in normal ER+ and normal ER– neutrophils pre-incubated with insulin

Addition	Maspin (nM/6 × 10^9 cells)		NO (μM/ 6 × 10^9 cells)	
	ER+	ER–	ER+	ER–
Estrogen (0.6 nM) cells not pre-incubated with insulin	2.383 ± 0.014*	0	1.829 ± 0.072***	0
Estrogen (0.6 nM) + Insulin (200 μU) cells pre-incubated with insulin	1.454 ± 0.004*	0	0.889 ± 0.003***	0

($P < 0.005$, $n = 10$), ***($P < 0.005$, $n = 10$)

Table 2 The effect of estrogen on the synthesis of NO and maspin in breast cancer ER+ and Breast Cancer ER– neutrophils pre-incubated with insulin

Addition	Maspin (nM/6 × 10^9 cells)		NO (μM/ 6 × 10^9 cells)	
	ER+	ER–	ER+	ER–
Estrogen (0.6 nM) cells not pre-incubated with insulin	1.422 ± 0.029**	0	0.887 ± 0.003****	0
Estrogen (0.6 nM) + Insulin (200 μU) cells pre-incubated with insulin	0.790 ± 0.004**	0	0.470 ± 0.003****	0

($P < 0.005$, $n = 10$) ****($P < 0.001$, $n = 10$)

The effect of estrogen on the synthesis of NO and maspin in Breast Cancer ER+ and ER– neutrophils pre-incubated with insulin: It was found that the pre-incubation of breast cancer ER+ neutrophils with insulin resulted in the significant furthermore impairment of the synthesis of both NO and maspin in these cells when compared to the control (Table 2). The treatment of breast cancer ER– neutrophils which failed to produce either NO or maspin when treated with estrogen also failed to produce these agents when these cells were pretreated with insulin.

4 Discussions

Hormones bind to their specific receptors on the cell surface to accomplish their specific physiological effects in the target cells. Ligand (hormone)-receptor binding results in the expression of the hormone effects. The negative cooperativity or positive cooperativity between the hormone receptors may significantly either down-regulate or up-regulate respectively the activity of unrelated hormones in the system (De Meyts et al. 1978). Insulin, a hypoglycemic hormone has its specific functions, in this case influenced the activity of estrogen which is known to induce the synthesis of maspin, an anti-breast cancer protein through the NO synthesis in normal as well as from the breast cancer neutrophils (Ganguly Bhattacharjee et al. 2012). ER- reported to produce worse prognostic outcome of the disease when compared to that in ER+ breast cancer neutrophils (Kiba et al. 2008).

It has been reported that ER+ neutrophils from the breast cancer patients produced less amount of NO induced maspin synthesis compared to normal control (Ganguly Bhattacharjee et al. 2012). The pre-incubation of ER+ neutrophils with insulin resulted in the attenuation of estrogen receptor number in the intact neutrophils and declined NO induced maspin production by estrogen.

Our results implied that the systemic presence of insulin might adversely affect the systemic production of the anti-breast cancer protein due to the insulin induced heterologous downregulation of the steroid receptor numbers in the neutrophils that not only resulted in the declined estrogen induced maspin synthesis, but also inhibited NO synthesis induced by the steroid in these cells.

It may be speculated that in Type 2 diabetes mellitus which causes hyperinsulinemia due to systemic insulin resistance might actually lead to worse prognostic outcome in breast cancer. On the other hand in Type 1 diabetes where insulin synthesis is completely impaired might be beneficial in breast cancer in terms of maspin synthesis (Hojo et al. 2001; Liu et al. 1999b; Berg et al. 1987; Jazieh et al. 2004).

References

Basrawala Z, Alimirah F, Xin H, Mohideen N, Campbell SC, Flanigan RC, Choubey D (2006) Androgen receptor levels are increased by interferons in human prostate stromal and epithelial cells. Oncogene 25(19):2812–2817

Beato M, Klug J (2000) Steroid hormone receptors: an update. Hum Reprod Update 6(3):225–236

Cook L, Ross AM, Knight GB, Agnello V (2000) Use of whole blood specimens for routine clinical quantitation of hepatitis C virus RNA does not increase assay sensitivity. J Clin Microbiol 38:4326–4331

Cox RD, Frank CW (1982) Determination of nitrate and nitrite in blood and urine by Chemiluminiscence. J Anal Toxicol 6:148–152

De Meyts P, Van Obberghen E, Roth J (1978) Mapping of the residues responsible for the negative cooperativity of the receptor-binding region of insulin. Nature 273(5663):504–509

Dutta-Roy AK, Kahn NN, Sinha AK (1991) Interaction of receptors for prostaglandin E1/prostacyclin and insulin in human erythrocytes and platelets. Life Sci 49(16):1129–1139

Engvall E, Perlmann P (1972) Enzyme-linked immunosorbant assay, ELISA. 3. Quantitation of specific antibodies by enzyme-labeled anti-immunoglobulin in antigen-coated tubes. J Immunol 109:129–135

Freychet P, Roth J, Neville DM Jr (1971) Insulin receptors in the liver: specific binding of (125 I)insulin to the plasma membrane and its relation to insulin bioactivity. Proc Natl Acad Sci USA 68(8):1833–1837

Ganguly Bhattacharjee K, Bhattacharyya M, Halder UC, Jana P, Sinha AK (2012) The role of neutrophil estrogen receptor status on maspin synthesis via nitric oxide production in human breast cancer. J Breast Cancer 15(2):181–188

Gelbfish GA, Davidson AL, Kopel S, Schreibman B, Gelbfish JS, Degenshein GA et al (1988) Relationship of estrogen and progesterone receptors to prognosis in breast cancer. Ann Surg 207(1):75–79

Girish GV, Bhattacharya G, Sinha AK (2006) The role of insulin dependent NO synthesis in the impaired production of maspin in human breast cancer. J Cancer Res Clin Oncol 132:389–398

Hojo T, Akiyama Y, Nagasaki K (2001) Association of maspin expression with the malignancy grade and tumor vascularization in breast cancer tissues. Cancer Lett 171:103–110

Jazieh AR, Kyasa MJ, Hutchins L (2004) Phase I clinical trial of tamoxifen and interferon alpha in the treatment of solid tumors. J Appl Res 4(3):464–469

Kahn NN, Sinha AK (1990) Stimulation of prostaglandin E 1 binding to human blood platelet membrane by insulin and the activation of adenylate cyclase. J Biol Chem 265:4976–4981

Kahn NN, Sinha AK (1992) Down regulation of alpha 2 adrenergic receptor numbers in platelets by insulin. Biochim Biophys Acta 1134(3):292–296

Kahn NN, Bauman WA, Hatcher VB, Sinha AK (1993) Inhibition of platelet aggregation and the stimulation of prostacyclin synthesis by insulin in humans. Am J Physiol 265(6 Pt 2):H2160–H2167

Kiba T, Inamoto T, Nishimura T et al (2008) The reversal of recurrence hazard rate between ER positive and negative breast cancer patients with axillary lymph node dissection (pathological stage I–III) 3 years after surgery. BMC Cancer 8:323

Klock JC, Bainton DF (1976) Degranulation and abnormal bactericidal function of granulocytes procured by reversible adhesion to nylon wool. Blood 48:149–161

Liu T, Pemberton PA, Robertson AD (1999a) Three-state unfolding and self-association of maspin, a tumor-suppressing serpin. J Biol Chem 274:29628–29632

Maehle BO, Collett K, Tretli S, Akslen LA, Grotmol T (2009) Estrogen receptor beta an independent prognostic marker in estrogen receptor alpha and progesterone receptor-positive breast cancer? APMIS 117(9):644–650

Rosa FE, Caldeira JR, Felipes J, Bertonha FB, Quevedo FC, Domingues MA et al (2008) Evaluation of estrogen receptor alpha and beta and progesterone receptor expression and correlation with clinicopathologic factors and proliferative marker Ki-67 in breast cancers. Hum Pathol 39(5):720–730

Scatchard G (1949) The attractions of proteins for small molecules and ions. Ann Y Acad Sci 51:660–672

Schneider HP, Jackisch C (1998) Potential benefits of estrogens and progestogens on breast cancer. Int J Fertil Womens Med 43:278–285

Tlaskalova-Hogenova H, Stepankova R (1980) Development of antibody formation in germ-free and conventionally reared rabbits: the role of intestinal lymphoid tissue in antibody formation to *E. coli* antigens. Folia Biol (Praha) 26:81–93

Van den Berg HW, Leahey WJ, Lynch M, Clarke R, Nelson J (1987) Recombinant human interferon alpha increases oestrogen receptor expression in human breast cancer cells (ZR-75-1) and sensitizes them to the anti-proliferative effects of tamoxifen. Br J Cancer 55(3):255–257

Zimmerman R, Paluch U, Sprinzl M, Neupert W (1979) Cell-free synthesis of the mitochondrial ADP/ATP carrier protein of *Neurospora crassa*. Eur J Biochem 99:247–252

Zou Z, Anisowicz A, Hendrix MJ, Thor A, Neveu M, Sheng S, Rafidi K, Seftor E, Sager R (1994) Maspin, a serpin with tumor-suppressing activity in human mammary epithelial cells. Science 263:526–529

Design of Novel Glucose Sensor with In-built Memory Functionality for Real-Time Health Condition Monitoring

Purbasha Ray, Swarnav Mukhopadhyay, and Arpan Deyasi

Abstract A novel glucometer circuit is proposed in this manuscript with an in-built memory chip so that data of a patient can be continuously monitored for the level of glucose present in h(is/er) blood for the last 6 months. The potentiometric Si-based glucose sensor has the added advantage in terms of fabrication point-of-view owing to existing matured microelectronics technology, making it a low-cost device. With 66.3% of sensitivity and 726% higher ON current than the CNT-based glucose sensor as per available published data, the present system may exhibit better acceptability with matured fabrication techniques. Anyone can calculate the percentage changes with the reference level of glucose level, and therefore, we are able to find out the changes with respect to the previous data values. With an easy quantitative analysis, this prototype can easily be accessed by most of the people around the world irrespective of financial limitations.

Keywords Sensitivity · Glucometer · ON current · Continuous tracking · Memory element · Si-technology

1 Introduction

Nowadays, biosensors are the most demanding application we need for our society as daily usage, so the need of manufacturing efficient sensor devices also draws a lot of attention. In recent data, it is said that by 2030, the global population of diabetic patients will reach up to 500 million (Wang 2008). As a result, millions of people are required to test their glucose concentration on blood, and thus, glucose becomes the most tested analyzer in biosensors. Such a high demanded device thus covering 85% of the entire biosensor market (Wang 2008).

P. Ray (✉) · S. Mukhopadhyay
Department of Electronics and Telecommunication Engineering, Jadavpur University, Kolkata 700032, India

A. Deyasi
Department of Electronics and Communication Engineering, RCC Institute of Information Technology, Kolkata 700015, India

M. Mukherjee et al. (eds.), *Advances in Medical Physics and Healthcare Engineering*, Lecture Notes in Bioengineering, https://doi.org/10.1007/978-981-33-6915-3_17

Many researchers recently focused on CNT-based sensors which is not a matured technology as many of our researchers are working still to understand its property (Pitroda et al. 2016). It is quite expensive to fabricate and also not robust. CNT-based sensors are not as compatible with circuits and are not as reliable as Si-based FET biosensor. Now as using CuO nanowire-based extended-gate field-effect transistor (FET) the sensitivity of the sensor can effectively calculate the glucose concentration within 1–12 mM range (Mishra et al. 2020). Whereas theoretically Si-based FET biosensor can go through a more dynamic range, i.e., from 2 to 50 mM glucose concentration which covers the normal diabetic range to a moderate range up to the hyper diabetic range.

Glucometer is a small, low-cost, portable electronic device used to measure the concentration level of glucose in blood. A small test strip is in general attached (Feldman 2003) with this portable device in order to determine the glucose level in the blood of the sample. A few literatures are available where several types of controllers are proposed (Latha et al. 2012; Renesas V850 2011; Gupta and Aggarwal 2013) for efficient and quick data analysis in order to produce low-cost devices. Generally, diabetes is a long-term disease, so its value has to be recorded or observed over months to know its growth, but in previous meters (Latha et al. 2012; Renesas V850 2011) are focused on that certain value when it is taken; and therefore it becomes virtually impossible to get the previous values from the meter as there was no memory element present. Also it is impossible to know the food effect which changes the glucose concentration on blood through the previous glucometer.

In this paper, it has been introduced a potentiometric Si-based FET biosensor. Since Silicon technology is a mature one, more robust and reliable than any other material, so it can be easily considered for fabrication of a new prototype. It can be manufactured and designed in IC technology. Si-based MOSFET sensors are cost-effective too. Amperometric sensors, which are widely used in the market, are very much sensitive to environmental changes and foreign particles, whereas using potentiometric sensors, the sensitivity due to environmental changes is very much less compared to amperometric sensors. Here, Glucose oxide-based enzyme is used to monitor the glucose level in blood, because of its ability to find the glucose analyte accurately. We have performed analytical modeling of the current with respect to glucose concentration for Si-based FET biosensor. So, Si-based FET biosensors have high selectivity, high drain current, accurate response and it is economically cheap.

The following sections include the structural analysis, working principle of the glucose sensor, results and their following discussions. Finally, the paper is concluded with all the advantages of using the Si-based BIO-FET sensor for our society.

2 Structure and Working Principle

As shown in Fig. 1, silicon P-type substrate along with N+ Drain and source region is considered for the design. GO_x is coated above the drain and source electrode as well

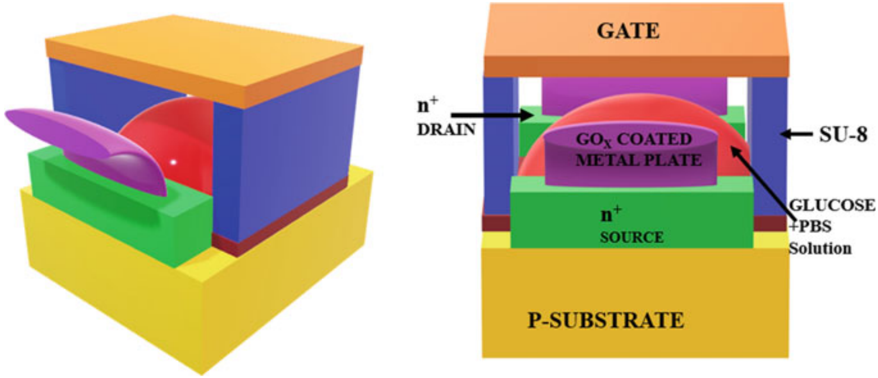

Fig. 1 Basic device structure for the prototype design

as inside the SU-8 walls as the glucose can react in the presence of GO_x with oxygen (O_2) and form gluconic acid ($C_6H_{12}O_7$) and H_2O_2. SiO_2 insulating layer is etched by reactive ion etching to form the cavity. Now the gate electrode is deposited above the SU-8 layer. SU-8 is grown above the SiO_2 layer, which will act as a receptor as well as an insulating layer to protect the substrate from the glucose and PBS solution.

The device length is 20 μm and the width of the device is 50 μm as shown in Fig. 2. The thickness of Cavity, SiO_2 and P-substrate is the following 500 nm, 2 nm and 50 μm, respectively. As the SiO_2 insulating layer is present between substrate and PBS-glucose solution it will act as a capacitor.

As shown in Fig. 3, SiO_2 grown on Si-substrate, it would be in the form of silicon aldehyde where OH group will be present by default at the surface, and thus, it will act as a receptor. When oxide grows over silicon substrate, it has the dangling bonds with oxygen which due to entropy automatically creates a bond with H2-present in

Fig. 2 Dimension of the MOSFET

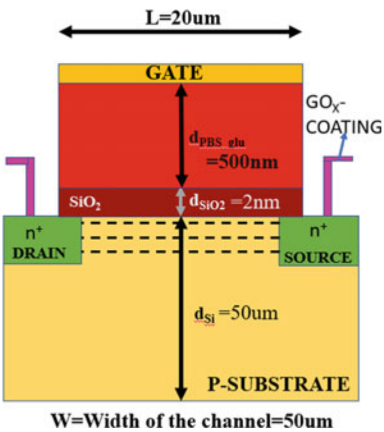

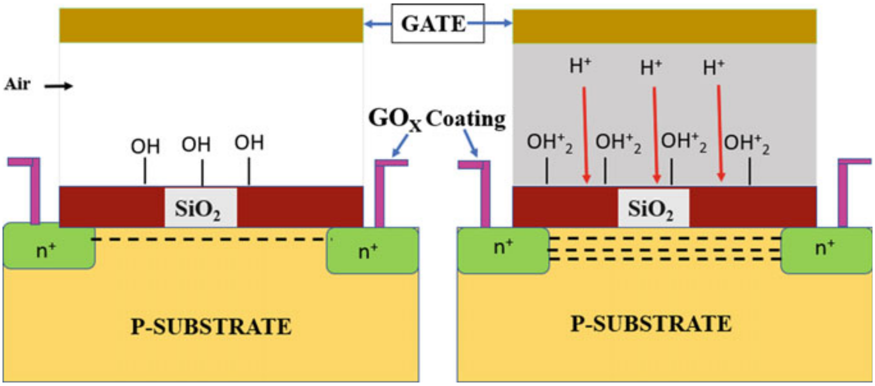

Fig. 3 Ionic movement inside the device

the moisture. So, in the presence of Air, applied gate bias will invert the channel thus producing the drain current.

By applying the PBS solution, due to protonation and deprotonation, charges will be developed above the insulating layer, which will increase the surface potential for which the drain current will eventually increase.

$$\mathbf{SiOH{+}H^+ \leftrightarrow SiOH_2^+}$$

In the presence of O_2 and GO_x, the glucose solution will create gluconic acid ($C_6H_{12}0_7$) and H_2O_2. H_2O_2 will be ionized and form H^+ and OH^- ions.

$$\mathbf{C_6H_{12}O_6 + O_2 \xrightarrow[GO_x]{} C_6H_{12}O_7 + H_2O_2}$$

Now the H^+ will be directed toward the insulating layer, due to the presence of positive gate bias, hence the charges above the insulating layer will increase, and this will attract a greater number of electrons into the channel and thus increasing the drain current further. Therefore, there will be a net increase in drain current in presence of glucose molecules. OH^- ions will be attracted toward gate electrodes.

3 Analytical Model

According to Si-based FET biosensor, some modeling approaches applied (Rahmani et al. 2013) to the device. Varying the drain voltage (V_d) from 0 to 0.7 V. So, when there is no solution only the air is present in the cavity, then the total capacitance C_{t_AIR} represented below:

$$C_{t\_\mathrm{AIR}} = \frac{C_1 \, . \, C_2 \, . \, C_{\mathrm{AIR}} \, .}{C_1 \, . \, C_2 + C_2 \, . \, C_{\mathrm{AIR}} + C_1 \, . \, C_{\mathrm{AIR}}} \tag{1}$$

where C_1 is the capacitance of substrate region (F/A), C_2 is the capacitance of oxide region (F/A), CAIR is Capacitance of AIR region (F/A)

$$C_{\mathrm{AIR}} = \frac{\xi_{\mathrm{air}}}{d_{\mathrm{cavity}}}; \, C_1 = \frac{\xi_{\mathrm{Si}}}{d_{\mathrm{Si}}}; \, C_2 = \frac{\xi_{\mathrm{SiO_2}}}{d_{\mathrm{SiO_2}}}$$

Here, the thickness of d_{cavity} and $d_{\mathrm{PBS\_gluare}}$ same. Now when the PBS-glu will be present in the cavity then capacitance will be

$$C_t = \frac{C_1 C_2 C_3}{C_1 C_2 + C_2 C_3 + C_1 C_3} \tag{2}$$

where C_3 is the capacitance of PBS and glucose region, given by

$$C_3 = \frac{\xi_{\mathrm{glu}}}{d_{\mathrm{PBS\_glu}}}$$

Now the current when there is no solution present in the cavity, drain current is the function of gate voltage (V_{g}) and drain voltage (V_{d}). Thus, the drain current is (Pourasl et al. 2014)

$$I_{D-\mathrm{AIR}} = \phi_{\mathrm{AIR}} \cdot \frac{2 \, . \, V_{\mathrm{gt}} V_{\mathrm{d}} - V_{\mathrm{d}}^2}{1 + (V_{\mathrm{d}}/V_{\mathrm{c}})} \tag{3}$$

where

$$\phi_{\mathrm{AIR}} = (\mu \, . \, C_{t\_\mathrm{AIR}})/(2 \, . \, L)$$

$$V_{\mathrm{c}} = (V_{\mathrm{sat}}/\mu) \, . \, L$$

'L' indicates effective length of the channel, μ denotes mobility of the carrier, and other parameters have usual meaning.

To analysis, the glucose concentration effect on current, first apply the PBS solution to observe the change in current. Hence, analysis of the I–V curve (Pourasl et al. 2014)

$$I_{D-\mathrm{PBS}} = \phi \, . \, \frac{2 \, . \, (V_{\mathrm{gs}} + V_{\mathrm{pbs}} - V_{\mathrm{t}}) V_{\mathrm{d}} - V_{\mathrm{d}}^2}{1 + (V_{\mathrm{d}}/V_{\mathrm{c}})} \tag{4}$$

where

$$\phi = (\mu \, . \, C_t)/(2 \, . \, L)$$

Now by applying the glucose to the solution in the presence of GO_x and O_2, it will form Gluconic acid and H_2O_2. The corresponding drain current is (Feldman 2003)

$$I_{\mathrm{D-glu}} = \phi \,.\, \frac{2\,.\,(V_{\mathrm{gs}} + V_{\mathrm{pbs}} + V_{\mathrm{glu}} - V_{\mathrm{t}})V_{\mathrm{d}} - V_{\mathrm{d}}^2}{1 + (V_{\mathrm{d}}/V_{\mathrm{c}})} \tag{5}$$

where V_{glu} is the voltage due to glucose concentration. Based on an iteration method demonstrated in []. The concentration control parameter as a function of glucose concentration expressed in a piecewise exponential model as

$$V_{\mathrm{glu\_Fg}} = 1.42 - e^{(-0.1.F_{\mathrm{b}})};\ F_{\mathrm{b}} > 0\,\mathrm{mM} \tag{6}$$

4 Result and Discussion

Based on the equations, we have simulated the behavior of the device and compared it with data of existing costly devices. From Fig. 4 the drain voltage is varying from 0.1 to 0.7 V. When the gate voltage is applied, the surface potential increases, which in turn, enhances the current. But applying the PBS solution, the surface potential increases due to protonation and deprotonation, and thus, surface charge on the SiO_2 layer increases somewhat, due to that more band bending in the channel region so the drain current increases, in presence of PBS solution which is shown in the plot.

From Fig. 5, we can conclude that as the glucose concentration increases, the corresponding drain current eventually increases up to a certain limit, then it saturates.

Fig. 4 Variation of drain current with and without PBS

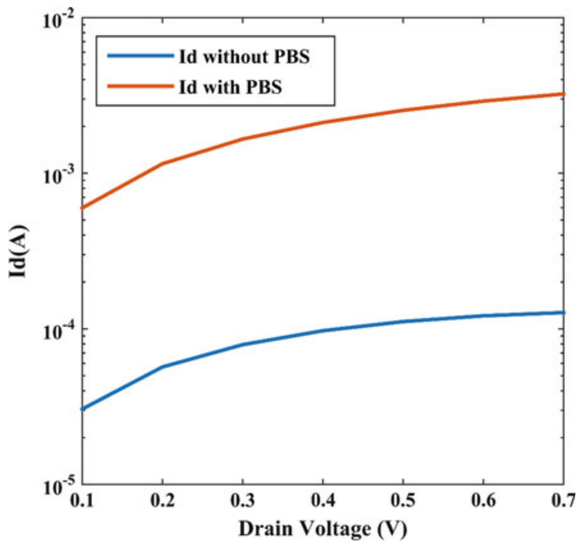

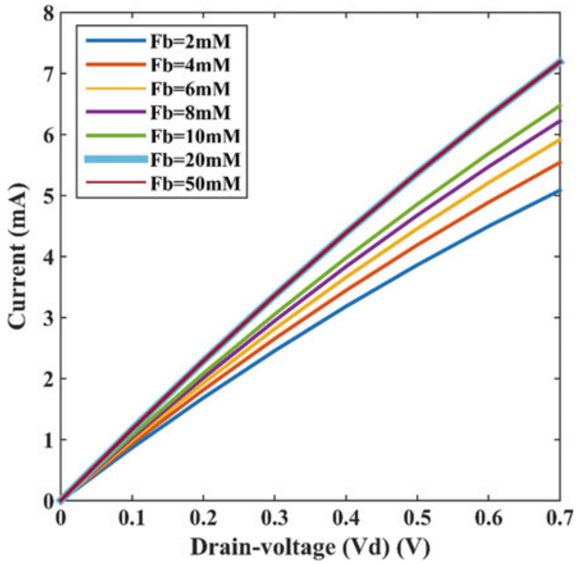

Fig. 5 Variation of drain current for different glucose concentration (Fb)

As concentration of glucose is varied from 2 to 20 mM, the consecutive changes in drain current can be observed very accurately. Above 20 mM concentration, the drain current saturates. Because after reaching a threshold of concentration value, electrons in the channel reach a degeneracy limit.

As shown from Fig. 6, it is quite evident that the sensitivity of Si-based FET BIOsensor is higher than CNT-based sensor. The glucose concentration is varied from 2 to 50 mM and the corresponding sensitivity is calculated accordingly. The sensitivity increases exponentially as the concentration increases. The relative permittivity of Silicon is 11.8 where the relative permittivity of CNT is 3.3 (Pourasl et al. 2014). As the permittivity of Si is more so the net band bending in presence of same potential will be much higher than CNT. Thus, the change in drain current will also be more in Si-based glucose sensors. Thus, the enhancement of sensitivity is around 66.3% compared to CNT-based (Pourasl et al. 2014).

5 Circuit Modeling

In the circuit analysis (Fig. 7), the input current range varies from 5.265 to 7.154 mA, and the input current directly goes to the differential amplifier, which increases the gain, here the gain almost increases up to 10 times. Then the analog output value from the differential amplifier directly goes to Arduino-Uno analog input (here A0). Now the Arduino-Uno is used as an analog-to-digital converter from where we get

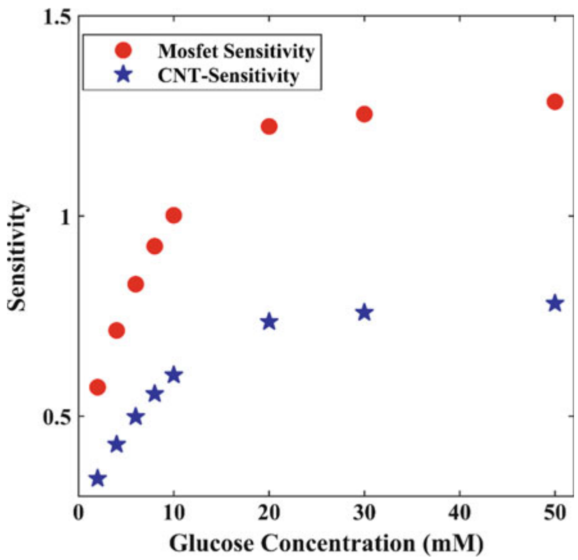

Fig. 6 Comparative analysis of sensitivity with published result

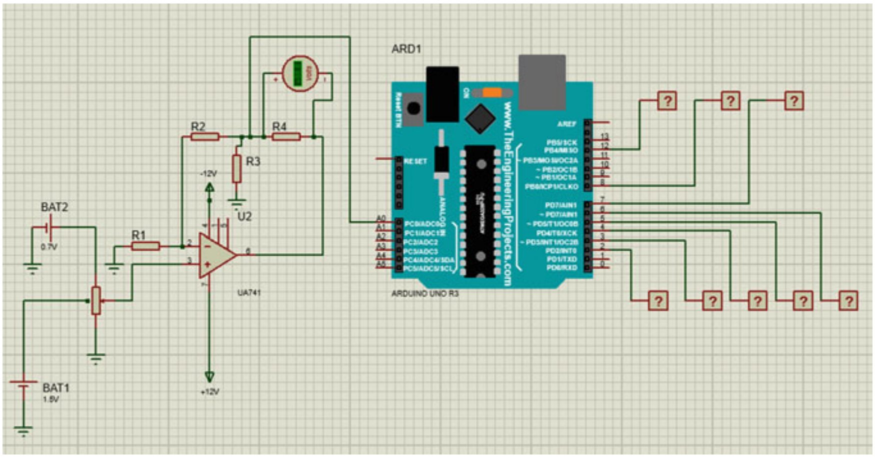

Fig. 7 Circuit layout of the prototype

the digital output as shown in the table. By analyzing the digital output value, the glucose concentration on blood can easily be found.

Corresponding output is represented in Table 1. Percentage change is given in Table 2.

Table 1 Variation of glucose concentration with current

Current (mA)	Digital output								Glucose (mg/dl)
	D7	D6	D5	D4	D3	D2	D1	D0	
5.265	0	0	0	0	0	0	0	0	50
5.39	0	0	0	1	0	0	0	0	60
5.509	0	0	1	0	0	0	0	1	70
5.621	0	0	1	1	0	0	0	0	80
5.727	0	0	1	1	0	0	0	0	90
5.827	**0**	1	0	0	1	1	0	0	100
5.922	0	1	0	1	1	0	0	1	110
6.012	0	1	1	0	0	1	0	1	120
6.097	0	1	1	1	0	0	0	0	130
6.178	0	1	1	1	1	0	1	1	140
6.254	1	0	0	0	0	1	1	0	150
6.326	1	0	0	0	1	1	1	1	160
6.395	1	0	0	1	1	0	0	1	170
6.459	1	0	1	0	0	0	0	1	180
6.521	1	0	1	0	1	0	1	0	190
6.578	1	0	1	1	0	0	1	0	200
6.633	1	0	1	1	1	0	0	1	210
6.685	1	1	0	0	0	0	0	0	220
6.734	1	1	0	0	0	1	1	0	230
6.781	1	1	0	0	1	1	0	1	240
6.825	1	1	0	1	0	0	1	1	250
6.866	1	1	0	1	1	0	0	1	260
6.906	1	1	0	1	1	1	1	0	270
6.943	1	1	1	0	0	0	1	1	280
6.979	1	1	1	0	1	0	0	0	290
7.012	1	1	1	0	1	1	0	1	300
7.044	1	1	1	1	0	0	0	1	310
7.074	1	1	1	1	0	1	0	1	320
7.102	1	1	1	1	1	0	0	1	330
7.129	1	1	1	1	1	1	0	0	340
7.154	1	1	1	1	1	1	1	1	350

Table 2 Computation of percentage change w.r.t. normal dataset

Sl. No	Test name	Normal range (Ref) (mg/dL)	Value (mg/dL)	Percentage change with Ref	Percentage change w.r.t. previous value
1	Glucose Fasting	70–100	105	5% (Increased)	0
	Glucose PP	75–140	125	10.71 (Decreased)	0
2	Glucose Fasting	70–100	113	13% (Increased)	7% (Increased)
	Glucose PP	75–140	168	20.71% (Increased)	30.71% (Increased)
3	Glucose Fasting	70–100	96	4% (Decreased)	3% (Decreased)
	Glucose PP	75–140	130	7% (Decreased)	23.71% (Decreased)
4	Glucose Fasting	70–100	95	5% (Decreased)	2% (Decreased)
	Glucose PP	75–140	130	7% (Decreased)	0
5	Glucose Fasting	70–100	116	16% (Increased)	14% (Increased)
	Glucose PP	75–140	160	14.28% (Increased)	23.07% (Increased)

6 Conclusion

Results obtained from the prototype clearly indicate that the proposed device has improved sensitivity compared to the existing published data, and therefore can be considered as a suitable candidate for glucose level tracking. As the design considers conventional Si-based MOSFET compared to the costly CNT, so the cost of the device may be acceptable for most of the people. The device is extremely suitable for diabetic patients as it may be purchased within financial limits by a large section of the people.

References

Feldman B (2003) Electrochemical blood glucose test strips for people with diabetes. Diab Technol Ther

Gupta M, Aggarwal H (2013) Design and implementation of PSoC based cap sense for medical touch system saliva vs blood glucose meter. Int J Adv Res Comput Sci Softw Eng 3(5)

Latha NA, Murthy BR, Sunitha U (2012) Design and development of a microcontroller based system for the measurement of blood glucose. Int J Eng Res Appl 2(5):1440–1444

Mishra AK, Jarwal DK, Mukherjee B, Kumar A, Ratan S, Jit S (2020) CuO Nanowire-based extended-gate field-effect-transistor (FET) for pH sensing and enzyme-free/receptor-free glucose sensing applications. IEEE Sens J 20(9):5039–5047
Pitroda J, Jethwa B, Dave SK (2016) A critical review on carbon nanotubes. Int J Constr Res Civil Eng 2(5):36–42
Pourasl AH, Ahmadi MT, Rahmani M, Chin HC, Lim CS, Ismail R, Tan MLP (2014) Analytical modelling of glucose biosensors based on carbon nanotubes. Nanoscale Res Lett 9:33
Rahmani M, Ahmadi M, Karimi H, Kiani M, Akbari E, Ismail R (2013) Analytical modeling of monolayer graphene-based NO_2 sensor. Sens Lett 11:270–275
Renesas V850 MCU Improves BGM design, Renesas Electronics Application Note (2011)
Wang J (2008) Electrochemical glucose biosensors. Chem Rev 108(2):814–825

Strained Engineered-Induced Mobility P^+IN^+ Photodiode—A Novel Opto-sensor for Biomedical Application

Arnima Das, Abhijit Kundu, Arpita Santra, Maitreyi R. Kanjilal, and Moumita Mukherjee

Abstract Nowadays, electrical switching circuits depend on PIN diode extensively. Non-invasive biomedical circuits are greatly influenced by the sensitivity of biosensors. The optical sensors are the key components in those circuits. The potential of PIN devices such as opto-sensors is studied in this paper. Si technology is the most mature one in modern industry. Therefore, the opto-sensitivity and photo-responsivity of the devices are studied by developing a quantum modified drift diffusion model. In this paper, the characteristics of PIN diode are studied which is made of silicon with a very small amount of carbon doping within it, and this strained material shows immense promise to the field of MMW and THz science and technology, and more precisely in biomedical domain for its modified band structure and electron transport characteristics, due to incorporation of artificial strain within this. Authors have studied the prospect of carbon doping selectively in Si PIN devices so as to increase the sensitivity of its application.

Keywords Strained band gap · Photo-responsivity · Mm-wave propagation

1 Introduction

Nowadays, electrical switching circuits depend on PIN diode extensively. Non-invasive biomedical circuits are greatly influenced by the sensitivity of biosensors. The optical sensors are the key components in those circuits. The potential of PIN devices such as opto-sensors is studied in this paper. Si technology is the most mature one in modern industry. Therefore, the opto-sensitivity and photo-responsivity of the devices are studied by developing a quantum modified drift diffusion model. In this

A. Das (✉) · A. Santra · M. R. Kanjilal
Narula Institute of Technology, Agarpara, Kolkata, India
e-mail: arnima.das@nit.ac.in

A. Kundu
Chaibasa Engineering College, Chaibasa, Jharkhand, India

M. Mukherjee
Adamas University, Kolkata, India

M. Mukherjee et al. (eds.), *Advances in Medical Physics and Healthcare Engineering*, Lecture Notes in Bioengineering, https://doi.org/10.1007/978-981-33-6915-3_18

paper, the characteristics of PIN diode are studied which is made of silicon with a very small amount of carbon doping within it, and this strained material shows immense promise to the field of MMW and THz science and technology, and more precisely in biomedical domain for its modified band structure and electron transport characteristics, due to incorporation of artificial strain within this. Authors have studied the prospect of carbon doping selectively in Si PIN devices so as to increase the sensitivity of its application. Microwave switches are widely used in different communication and detection systems. But the conventional classical drift diffusion (CLDD) model has certain limitations like inter-sub-band tunneling, hot carrier effect, quantum size effect, realistic field and temperature-dependent carrier density effect which degrade the overall performance of PIN diode (Chen 1993). To overcome this, efforts have been made to design PIN diode model using strained band gap.

2 Theory

The band gap engineering relies on the developments in the crystal growth (Perelman et al. 2001). As the band structure determines several important electronic and optical characteristics, so band gap engineering is one of the most powerful techniques for designing new semiconductor materials and devices. When two different materials are used to form the junction of the diode, then there may be a mismatch between both the lattices (Rahmani et al. 2016). And the lattices try to make them fit anyhow, which create strain at or near the interface of two different materials. The strain between two layers of material is simply a force acting in plane which is compensated by the attractive/repulsive forces between the atoms in the lattice. Li and Zang (2017) represent the electric field of the intrinsic region of the PIN diode and numerically expressed as

$$E(x,t) = \frac{-\partial V(x,t)}{\partial x} \tag{1}$$

The instantaneous voltage, at intrinsic region, is determined from the electric field profile

$$V_i(t) = \int_{x=0}^{x=W} E(x,t) \tag{2}$$

So, the hole and electron current density can be expressed as

$$J_p(x,t) = -q\mu_p\left[C_p(x,t)\frac{\partial}{\partial x}V(x,t) + \left(\frac{K_B T_j}{q}\right)\frac{\mathrm{d}}{\mathrm{d}x}C_p(x,t)\right] \tag{3}$$

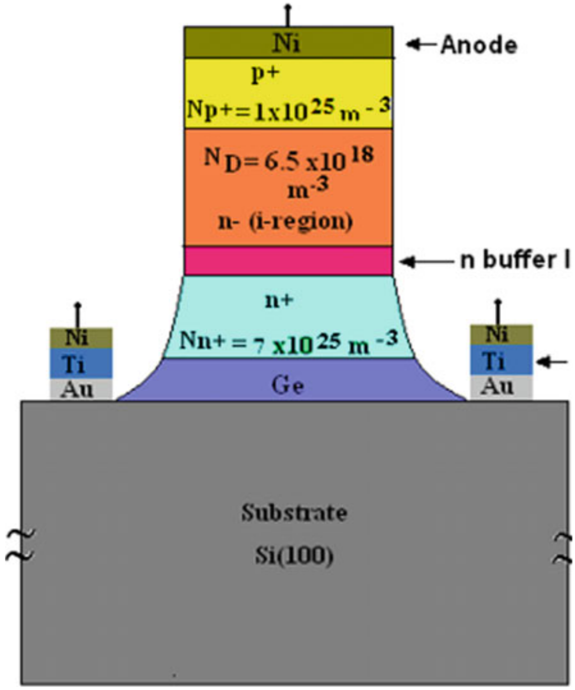

Fig. 1 Structure of PIN diode

$$J_n(x,t) = -q\mu_n\left[C_n(x,t)\frac{\partial}{\partial x}V(x,t) + \left(\frac{K_B T_j}{q}\right)\frac{\mathrm{d}}{\mathrm{d}x}C_n(x,t)\right] \tag{4}$$

From the above equations, the total current density due to holes and electrons can be given by Fig. 1.

The doping profile of designed $P^{+}IN^{+}$ diode is shown in Fig. 2.

The strain, ε, in the layer due to the lattice mismatch can be expressed in terms of the lattice constants of the layer and the substrate and is given by (Sahbudin 2004):

$$\varepsilon = a_{\text{substrate}} - \frac{a_{\text{layer}}}{a_{\text{substrate}}} \tag{5}$$

$a_{\text{substrate}}$ is the lattice constant of the substrate, and a_{layer} is the lattice constant of the layer.

Strain induces a shift in the energy levels than that of the unstrained conduction and valence bands. Here, in this paper, we have investigated the band structure of strained SiC (Khan and Copper 2000), where the heterojunction is made by silicon with 10% of carbon doping in it. We have extracted band parameters and analyzed electron transport phenomena which shows much higher performance than the unstrained SiC (Kundu et al. 2021; Atabaev and Juraev 2018) in terms of critical electric field distribution at breakdown, I–V characteristics, series resistance, power dissipation and

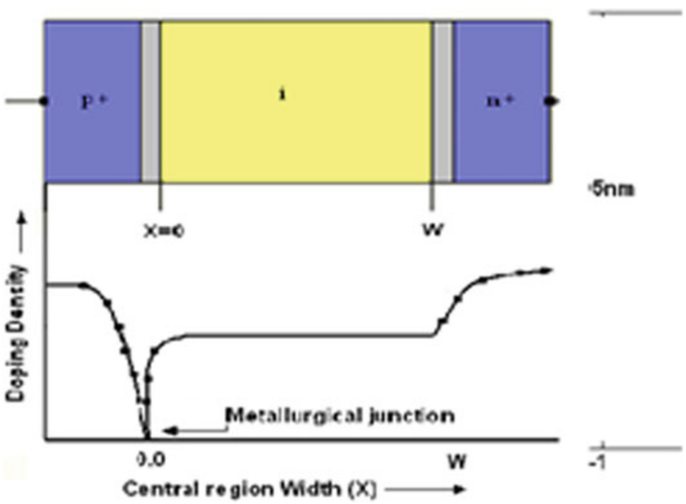

Fig. 2 Doping profile of designed P⁺IN⁺ diode

reverse recovery current, photo-responsivity and quantum efficiency. The proposed PIN model works in THz frequency region and may be used for medical imaging purposes.

3 Result

In recent year, the dynamics of carriers induced by electric field in the semiconductor superlattices is the much-interested area of research. The photoelectrical characteristics of the designed PIN photodiode are obtained by solving Poisson's equation and continuity equation (Figs. 3, 4, 5, 6 and 7; Table 1).

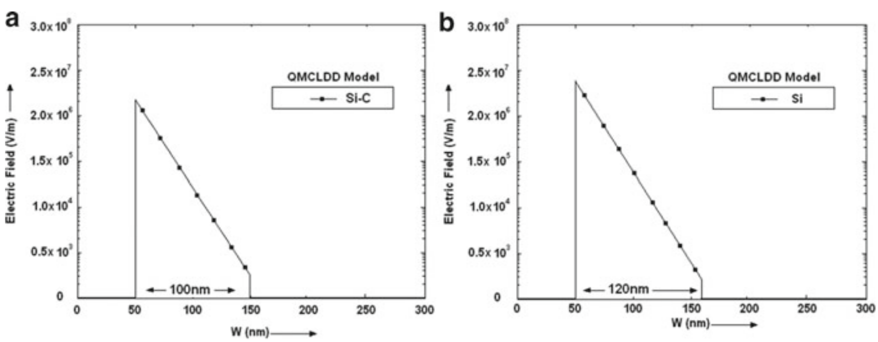

Fig. 3 Response of electric field with wavelength for **a** strained Si and **b** unstrained Si

Fig. 4 V–I characteristics for unstrained Si and strained Si

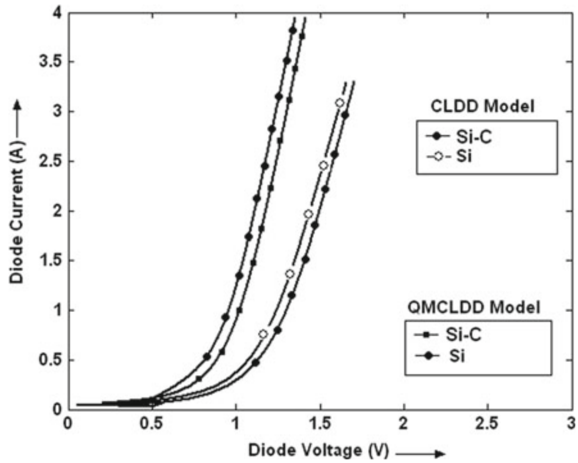

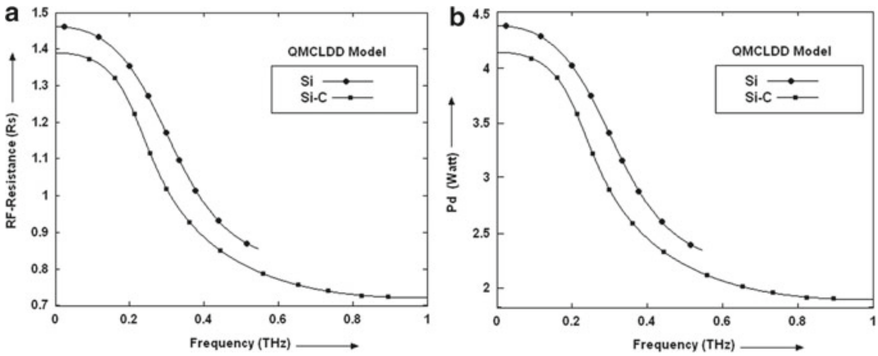

Fig. 5 Response of **a** RF resistance with frequency, **b** dissipated power with frequency for strained Si and unstrained Si

4 Conclusion

The concept of band gap engineering in enhancing the photo-current response of strained PIN devices is studied thoroughly in the report. It is observed that compared to unstrained silicon, strained (carbon doped) silicon is more efficient in THz frequency region. The future and larger study will fix immense application in case of medical instruments and electronics industry.

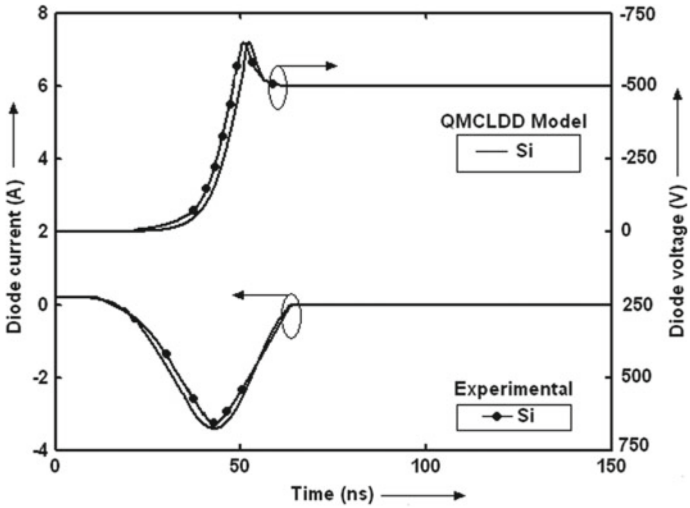

Fig. 6 Response of diode current and voltage with time

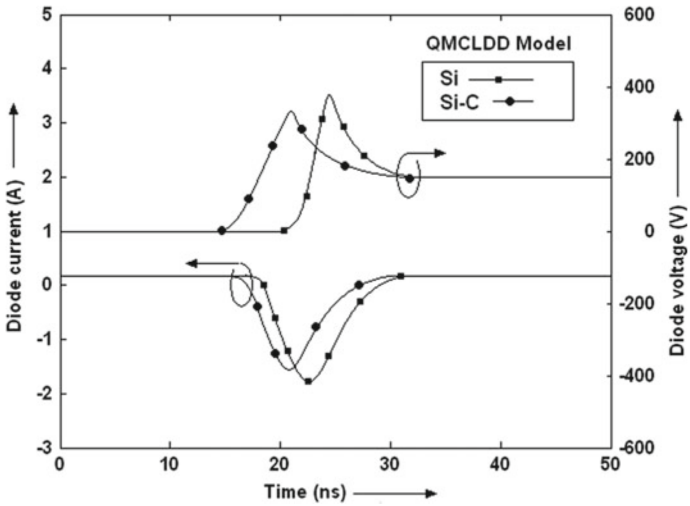

Fig. 7 Response of diode current and voltage with time compared with strained Si

Table 1 Design specifications for strained Si and unstrained Si

Device under test (DUT)	Design frequency (f_d) (THz)	i region /low-doped (n^-) region width (W) (nm)	Doping concentration of i region (n^-) (10^{18}) (m^{-3})	Doping concentration of heavily doped n region (Nn^{++}) (10^{25}) (m^{-3})	Doping concentration of heavily doped p region (Np^{++}) (10^{25}) (m^{-3})
Si	0.35	120	4.0	6.0	4.0
Si–C	0.75	100	6.5	7.0	5.0

References

Atabaev IG, Juraev KN (2018) Research of pin based on 4H-SiC fabricated by low-temperature diffusion of boron. Adv Mater Sci Eng 2018:1–10. https://doi.org/10.1155/2018/8797031

Chen WK (1993) Electronic Archive: new semiconductor materials, characteristics and properties (Online). In: Linear networks and systems (Book style). Wadsworth, Belmont, CA, pp 123–135. https://www.ioffe.ru/SVA/NSM/Semicond/Si/SiC. Accessed Feb 2018

John Bosco Balaguru R, Jeyaprakash BG, School of Electrical & Electronics Engineering SASTRA University, Quantum Wells, Quantum Wires, Quantum Dots, Quantum Limit of Conductance, Quantum Capacitance & Quantum HALL Effect, NPTEL—Electrical & Electronics Engineering—Semiconductor Nanodevices, Joint Initiative of IITs and IISc—Funded by MHRD

Khan IA, Copper JA (2000) Measurement of high-field electron transport in silicon carbide. IEEE Trans Electron Devices 47:269–273. https://doi.org/10.1063/1.4807162

Kundu A, Adhikari S, Das A, Kanjilal MR, Mukherjee M (2021) Design and characterization of asymetrical super-lattice Si/4H-SiC pin photo diode array: a potential opto-sensor for future applications in bio-medical domain. Microsyst Technol. https://doi.org/10.1007/s00542-018-4119-4

Li L, Zang Y (2017) Photoelectric properties of Si doping superlattice structure on 6H-SiC (001). MDPI Mater 583:1–6

Perelman Y, Ginosar R (2001) App Phys Lett 82:3973. https://doi.org/10.1063/1.1579553; A low-light-level sensor for medical diagnostic applications. IEEE J Solid State Circuits 36:1553–1558

Rahmani F, Golshani M, Sarbishei M (2016) Deriving relativistic Bohmian quantum potential using variational method and conformal transformations. PRAMANA C Indian Acad Sci J Phys 86(4):747–761

Sahbudin S (2004) Development of silicon planar photodiode. In: The 4th annual seminar of national science fellowship, pp 466–471

Vasilesk D, Drift-diffusion model: introduction

Fusion-Based Multimodal Brain Tumor Detection Using Convolution Neural Network

Soumyabroto Banerjee, Sneha Roy, and Arpita Das

Abstract Early detection and proper treatment of brain tumor are essential to prevent permanent damage of brain even patient death. Present study proposes an automatic, effective approach to detect brain lesions in early stage including fusion of multimodal images to enrich the information content. As the convolution neural network (CNN) extracts the required features, fused images improve the quality of the feature bank which in turn enhances the classification accuracy. Present work also develops the modified architecture of CNN that contains only few parameters compared to the standard CNN model (VGG-16) available in Google Colab. Hence, the computation time is low, and this architecture is trainable on a local PC with standard RAM. Experimental results show the assessment of classification accuracy in terms of well-known receiver operating characteristic method, and the outcomes produce satisfactory results.

Keywords MRI · SPECT-Tc · Multimodal fusion · CNN architecture

1 Introduction

Brain tumor classification is one of the most important and difficult tasks in many medical-image applications because it usually involves a huge amount of data. Artifacts due to patient's motion, limited acquisition time, and soft tissue boundaries are usually not well defined. There are large class of tumor types which have variety of shapes and sizes. They may appear indifferent sizes and types with different image intensities. Some of them may also affect the surrounding structures that change the image intensities around the tumor. Before the treatment of chemotherapy, radiotherapy, or brain surgeries, there is a need for medical practitioners to confirm the boundaries and regions of the brain tumor and determine where exactly it is located and the exact affected area. Brain tumor classification acts as a pre-requisite stage

S. Banerjee (✉) · S. Roy · A. Das
Department of Radio Physic and Electronics, University of Calcutta, Kolkata, India

A. Das
e-mail: adrpe@caluniv.ac.in

M. Mukherjee et al. (eds.), *Advances in Medical Physics and Healthcare Engineering*, Lecture Notes in Bioengineering, https://doi.org/10.1007/978-981-33-6915-3_19

for doctors to identify the tumor before performing surgeries to identify the exact location of the tumor. A computer-aided diagnosis (CAD) system is designed to aid the radiologist in the diagnosis of such tumors.

However, a single imaging procedure alone cannot provide all the necessary information for medical diagnosis (Goyal and Wahla 2015). For example, in magnetic resonance imaging (MRI), T1weighted scans, MRT1 imaging technique produces the detailed anatomical structure while, T2-weighted scans, MRT2 prominently highlights the differences between the normal and pathological structure of tissues. Hence, the anatomical features like shrinking of gray matter, enlargement of ventricles, etc., are visualized from MRI (Bhattacharya et al. 2012; Chang et al. 2002). On the other hand, positron emitted computed tomography (PET) and single photon emission computed tomography (SPECT) provide functional information like blood flow, food activity, and metabolism of affected organs. The goal of image fusion is to integrate complementary information from each images merged together to form a superior quality resultant image than any of the input images (Bhattacharya et al. 2012; Mukherjee and Das 2020; Horn et al. 2009). Hence, we have designed a simple CNN model which is trainable in general computer using the fused MRI and SPECT images. Proposed CNN model can extract the significant features of MRI and SPECT and classify the tumors more accurately than the single modality images. The schematic of the proposed work is described in Fig. 1.

The rest of the article is arranged as follows. Proposed methodology is described in Sect. 2. Section 3 gives the experimental results, and a comparative study between the proposed architecture and the standard VGG-16 architecture. Finally, a conclusion is drawn in Sect. 4.

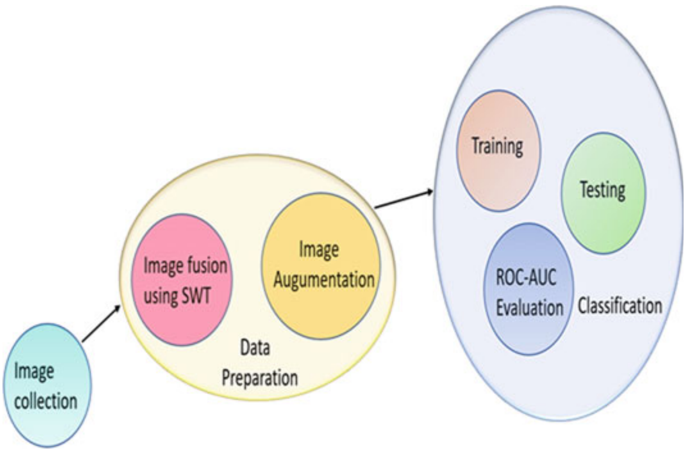

Fig. 1 Entire algorithmic overview

2 Methodology

2.1 Image Collection

The images were collected from the given website (https://www.med.harvard.edu/aanlib/home). Two types of images were mainly collected—**magnetic resonance imaging (MRI)** and **single photon emission computed tomography (SPECT) images**. The images were collected by changing the time axis and taking different slices along the axial plane and time axis.

2.2 Data Preparation

The final dataset was prepared using the following two steps:

1. **Image fusion using Shift Invariant Wavelet Transform (SWT)**: The images were fused using SWT in order to extract multimodal features. It is a type of **Discrete Wavelet Transform** which omits both down sampling in the forward and up sampling in the inverse transforms (Sari-Sarraf and Brzakovic 1997). Primary advantages of SWT are it (a) produces less artifacts, (b) can better preserve the information of source images.

Process: Each channel of the two RGB images (MR-T2 and SPECT-TC) to be fused were first decomposed into *approximate matrix* and *details matrix* using SWT-based decomposition as shown in Fig. 2. The *approximation matrices* of both the images (MR-T2 and SPECT-TC) were *linearly blended* for each channel (RGB). The *details matrices* of each channel (RGB) were combined using *principal component analysis (PCA)* approach (Mishra et al. 2017) to integrate the information of three channels (RGB). Finally, inverse SWT was performed to produce the fused image containing information of all modality source images (MR-T2 and SPECT-TC). Figure 3 describes that PCA-based blending contains better clarity than the simple average blending.

2. **Image Augmentation**: Then, the number of collected images was not enough for efficient training of the CNN architecture. So, the number of images was increased with the help of image augmentation. Image data augmentation is a technique that can be used to artificially expand the size of a training dataset by creating modified versions of images in the dataset. Apart from creating more number of samples, it also helps in preventing over fitting. Some of the image augmentation techniques used for enhancing our dataset are mentioned as:

    (a) ***Flipping***: An image flip means reversing the rows or columns of pixels in the case of a vertical or horizontal flip, respectively.
    (b) ***Cropping***: Cropping can be used as a processing step for image data with mixed height and width dimensions of each image.

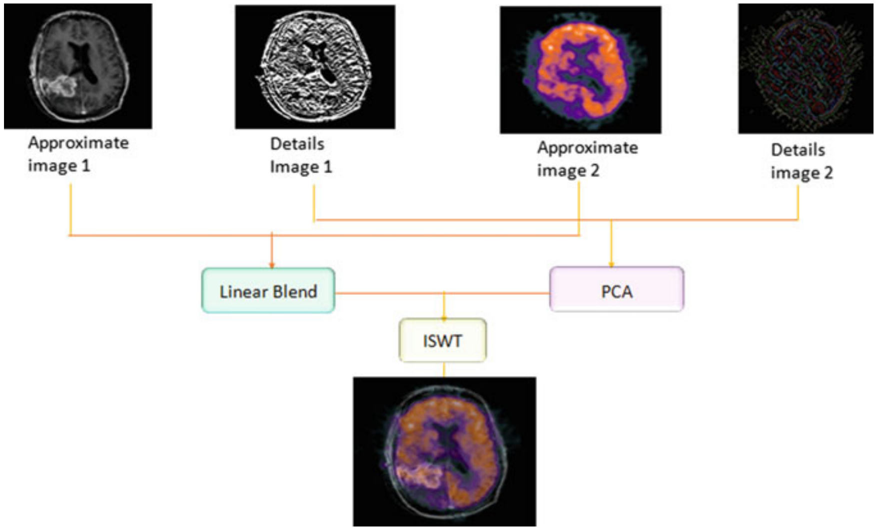

Fig. 2 Process flow of input images

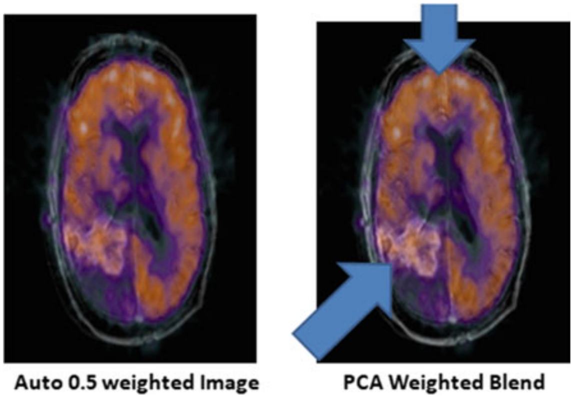

Fig. 3 (left) Auto-generated same weighted (0.5) blend; (right) PCA weighted blend using proposed algorithm

(c) ***Rotation***: Rotation augmentations are done by rotating the image right or left on an axis between 1° and 359°. After the final dataset was prepared, it was divided into **training, testing**, and **validation dataset—(80%–15%–5%, respectively)**.

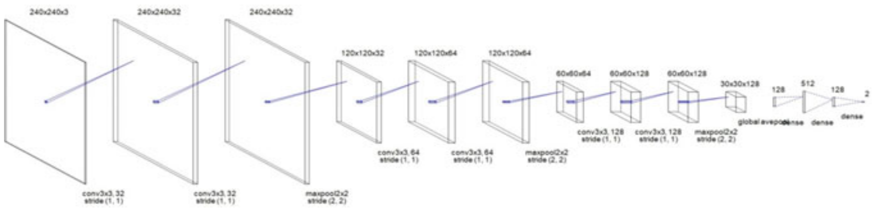

Fig. 4 Proposed architecture

2.3 *Classifier Building*

We build our CNN model which is trainable on a local PC having negligible GPU-CUDA support. We have built the proposed model as shown in Fig. 4 by keeping the reference VGG16 architecture as baseline model. The architecture of the proposed model is as follows:

- We use three CNN blocks of two CNN layers each.
- Each CNN block is followed by a MaxPool layer.
- Each MaxPool layer has a **Dropout of 0.2**.
- The CNN is translated into linear features using a global average pooling 2D layer to average out the intensities along channels.
- The CNN features are mapped into a dense network of two layers.
- We use a softmax to output the probabilities of two classes as follows:

  1: Presence of Tumor
  0: Absence of Tumor

2.4 *Training and Testing of the Proposed Model*

2.4.1 Model Summarization

The model is written and compiled entirely using Tensor flow 2.2.0 and is compatible with versions >2.0+. Epochs trained over: **500**.

Optimizer: The model uses **Adam** optimizer (Kingma and Ba 2014). It uses a decay hyperparameter to optimize the learning rate, $\beta_1 = 0.9$ and $\beta_2 = 0.99$. It computes the first and second order moments in order to estimate the decay rate of the steps. We use the Adam to back-propagate the gradients as well and optimize our loss. The main advantages of using **Adam** optimizer over other stochastic optimizers are listed as:

(a) **Adaptive Gradient Algorithm** (AdaGrad) maintains per-parameter learning rate that improves performance on problems with sparse gradients (e.g., natural language and computer vision problems).

(b) **Root Mean Square Propagation** (RMSProp) also maintains per-parameter learning rates that are adapted based on the average of recent magnitudes of the gradients for the weight (e.g., how quickly it is changing). This means the algorithm does well on online and non-stationary problems (e.g., noisy). It basically computes the learning rate not only based on the first moment—mean, but also based on the second moment—gradient. It uses an exponential moving average of gradients and also squared gradients over the loss plane to reach a much more global minima.

(c) **Loss Function**: Categorical cross entropy (Ho and Wookey 2020) is used to compute the log loss.

$$\mathrm{CE} = -\sum_{i=1}^{n} Yi \log(\widehat{Y}i)$$

where $n = 2$, $\widehat{Y}$ is the predicted label, and Y is the actual ground truth label.

2.4.2 Training Reports

The accuracy and loss of training process are shown in Figs. 5 and 6.

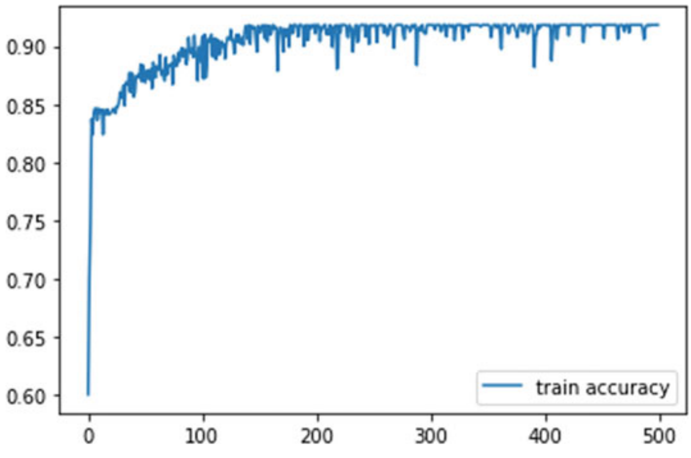

Fig. 5 Accuracy plot of the training process

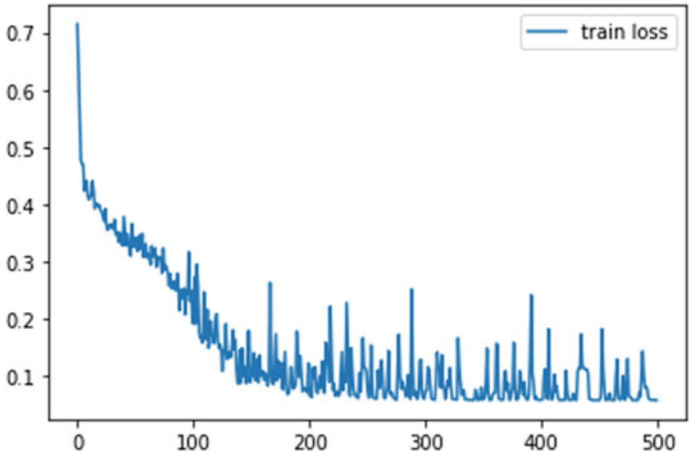

Fig. 6 Loss plot of the training process

Table 1 Comparison between the proposed architecture and the standard VGG-16

S. No.	Proposed architecture	VGG-16 (baseline architecture)
1	No. of trainable parameters: 418,978	No. of trainable parameters:138,000,000
2	No of layers: 9	No. of layers: 16
3	Training time: 5–9 h on CPU[a]	Training time: 1 day on CPU[a]
4	Requirement fit: Fits to our problem	Requirement fit: Over fits to our problem

[a]CPU in consideration is an Intel Core i3-6th Generation processor

2.5 Comparison of the Proposed Architecture

A comparison has been described in Table 1 between the proposed architecture and the standard VGG-16 architecture. Figure 7 also shows that the proposed model consists of less number of parameters compared to VGG-16 architecture.

3 Results

3.1 Firing Patterns at the Different Layers of the Proposed Architecture

The main idea of using our CNN model is that we try to increase the number of channels in the later layers and to reduce the individual image dimensions as it progress through the network with less computation burden. As we do not intend to reduce the image dimensions in the progressing convolutional layers, we use padded

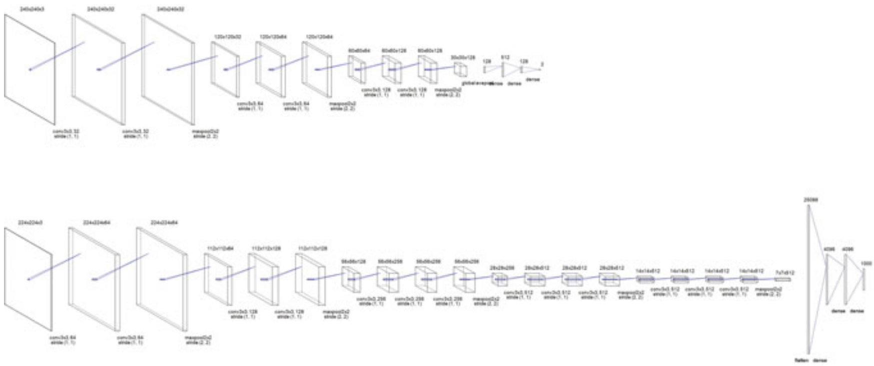

Fig. 7 (top) Proposed architecture (with much lesser parameters than VGG-16 architecture); (bottom) Standard VGG-16 architecture

CNN blocks followed MaxPool block where the entire image dimension is reduced but expanded on the channels. We use *Relu Function* as shown in Eq. (1) which an activation function is used to map continuous values in positive range (Asadi and Jiang 2020).

$$\text{Relu Function:} \quad f(x) = \max(0, x) \tag{1}$$

The firing pattern of each layer of the proposed architecture has been shown in detail in Fig. 8. The heat maps of the firings are clearly represented with alternating blue and yellow indicators.

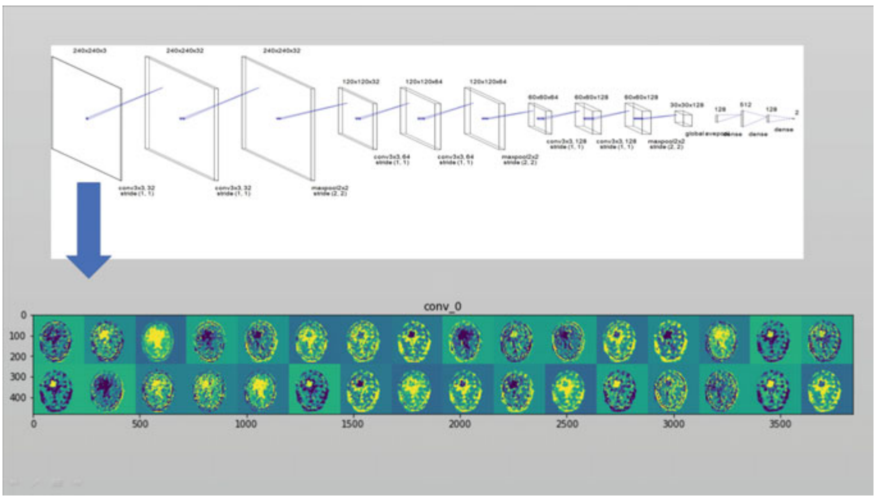

Fig. 8 Firing pattern of the first convolution layer of the first CNN block

The first layer of the CNN learns the basic visual level details. The overall structure of the image remains the same. The later layers use a fully connected dense network which is used to translate the 3D image channel structure into a linear structure. The dense network is used to feed into a *Softmax Layer* (Asadi and Hui 2020) as shown in Eq. (2) for probabilistic output of the classes: (Goyal and Wahla 2015).

$$\text{Softmax Layer:} \quad f(x)_i = \frac{e^{xi}}{\sum_{j=1}^{K} e^{xj}} \tag{2}$$

The layers learn more and more complex features as we move deeper into the layers but as the layer increases, problem of vanishing gradients start to set in. Here, the initial layers may learn the various edge features and recognize those edges. All the convolutional layers use a 3×3 filter with stride = 1 and padding = same.

The following layers preserve/detect more sophisticated features and edges. These layers can understand features with more 'inner' meaning. Figure 9 describes the heat map firings of the second convolution layer of the second CNN block which learns more sophisticated features than the absolute initial layers but less sophisticated features than the third CNN Block (Hochreiter 1998). The dimensions of image are reduced, but the number of images is increased significantly.

As shown in Fig. 10, we use dropout (Srivastava et al. 2014) layer of 20% dropout after each CNN block to prevent over fitting of the images. These dropout layers are only used in training and do not contribute to model inference. The purpose of the dropout layer is to randomly drop 20% of the connections defined during a forward/backward pass through the network. Not only the nodes, but also the edges are dropped during the pass. Dropout is essential because of the inter-neuron co-dependency which exists during the training. It curbs the importance of the individual

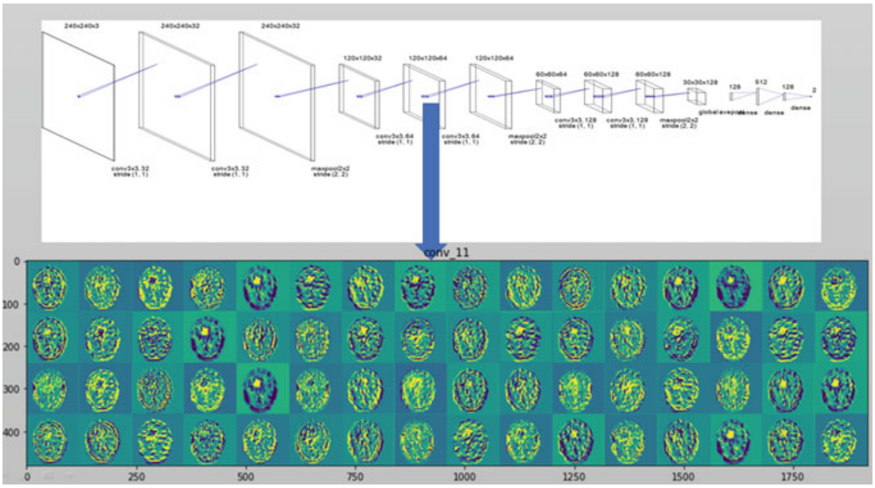

Fig. 9 Firing pattern of the second convolution layer of the second CNN block

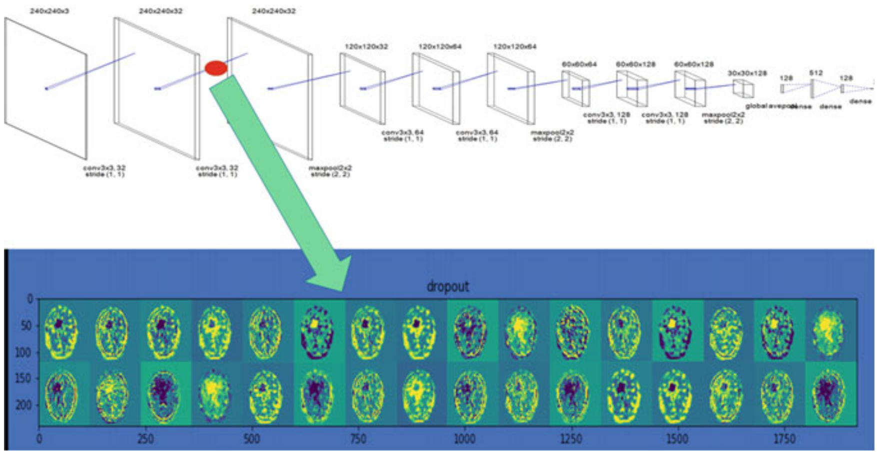

Fig. 10 Firing pattern of the dropout layer (0.2 dropout)

neurons and prevents over fitting. Dropout also forces the neurons to learn more robust features. It has been observed that dropout requires almost the double number of epochs to converge.

3.2 ROC Comparison

A comparative study of ROC of the proposed architecture using fused images, single modality MRI, SPECT images, and ROC of VGG-16 architecture is shown in Fig. 11. Table 2 also describes the values of the outcomes.

In the proposed architecture, as the fused images contain information of both modalities, number of significant features extracted from them is of better quality

Fig. 11 ROC analysis of the proposed architecture

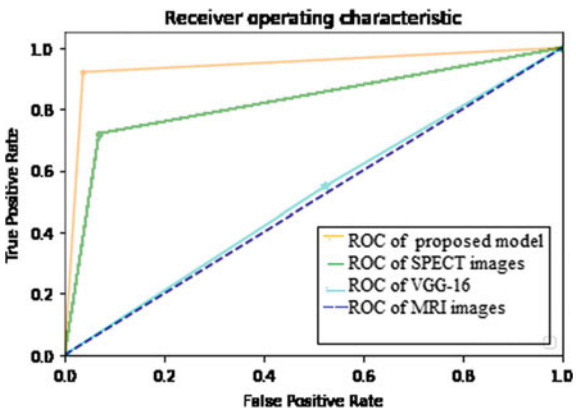

Table 2 Values of the outcomes

ROC analysis	TPR	FPR
Proposed architecture with fused image	0.980	0.040
Proposed architecture with MRI	0.500	0.502
Proposed architecture with SPECT	0.720	0.096
VGG-16 architecture with fused image	0.570	0.580

compared to the single modality. Hence, the classification accuracy of the fused images is superior to individual MR-T2 and SPECT-TC images.

4 Conclusion

As the proposed architecture of CNN has much lesser parameters (418,978) than the VGG-16 architecture (16,946,242), this model performs better as compared to the standard VGG-16. The main advantage of this model is that it is trainable on a local PC with standard RAM (about 8 GB) without any supporting GPUs (such as Google Colab) which are required in the VGG-16 architecture.

The areas of future work are:

(1) Improving the existing dataset of images structure into 3D model view of the brain without sampling through the layers.
(2) Developing U-Net like structures that can help build segmentation network to segment out critical locations.
(3) Fine tune the parameters and hyperparameters even further to reduce training and inference time.
(4) Extend the network as a generic network for various bio medical applications—liver, lung, prostate, etc.

References

Asadi B, Jiang H (2020) On approximation capabilities of ReLU activation and Softmax output layer in neural networks. arXiv:2002.04060

Bhattacharya M, Das A, Chandana M (2012) GA based multiresolution fusion of segmented brain images using PD, T1 and T2 weighted MR modalities. Neural Comput Appl 21(6):1433–1447

Chang DJ, Zubal IG, Gottschalk C, Necochea A, Stokking R, Studholme C, Corsi M, Slawski J, Spencer SS, Blumenfeld H (2002) Comparison of statistical parametric mapping and SPECT difference imaging in patients with temporal lobe epilepsy. Epilepsia 43(1):68–74

Goyal S, Wahla R (2015) A review on image fusion. IJIRCCE 3(8):7582–7588

Ho Y, Wookey S (2020) The real-world-weight cross-entropy loss function: modeling the costs of mislabeling. IEEE Access 8:4806–4813

Hochreiter S (1998) The vanishing gradient problem during learning recurrent neural nets and problem solutions. Int J Unc Fuzz Knowl Based Syst 6:107–116. https://doi.org/10.1142/S0218488598000094

Horn JF, Habert MO, Kas A, Malek Z, Maksud P, Lacomblez L, Giron A, Fertil B (2009). Differential automatic diagnosis between Alzheimer's disease and frontotemporal dementiabased on perfusion SPECT images. Artif Intell Med 47(2):147–158

Johnson KA, Becker JA, The Whole Brain Atlas. Available online at: https://www.med.harvard.edu/aanlib/home

Kingma D, Ba J (2014) Adam: a method for stochastic optimization. In: International conference on learning representations

Mishra S, Sarkar U, Taraphder S, Datta S, Swain D, Saikhom R, Panda S, Laishram M (2017) Principal component analysis. Int J Livestock Res. https://doi.org/10.5455/ijlr.20170415115235

Mukherjee S, Das A (2020) Vague set theory based segmented image fusion technique for analysis of anatomical and functional images. Expert Syst Appl 159:113592

Sari-Sarraf H, Brzakovic D (1997) A shift-invariant discrete wavelet transform. IEEE Trans Signal Process 45(10):2621–2630

Srivastava N, Hinton G, Krizhevsky A, Sutskever I, Salakhutdinov R (2014) Dropout: a simple way to prevent neural networks from overfitting. J Mach Learn Res 15:1929–1958

Performance Analysis of Multiplexer Using Adiabatic Logic and Gate Diffusion Technique

D. N. Mukherjee, S. Biswas, S. Panda, and B. Maji

Abstract In the present scenario, power consumption is a vital issue in low power circuit design. The adiabatic logic and the conventional CMOS logic styles are widely used in low power VLSI design. The power saving is more effective in adiabatic circuit compared to conventional CMOS logic. In compared to gate diffusion technique, an adiabatic logic required more number of transistors, and more power is needed. The objective of this paper is to design and implement of 4:1 multiplexer using different adiabatic logic styles and gate diffusion technique and compares them in terms of the power dissipation and transistor count. The simulation has been done by using the EDA Tanner tools.

Keywords Adiabatic logic · ECRL · PFAL · 2N-2N2P · Adiabatic array logic · PCRL · GDI · Power dissipation · Transistor count

1 Introduction

In portable devices, the power dissipation can be decrease by different design techniques. The adiabatic logic technique is one of the ideal techniques to achieve these demands. In adiabatic logic style, the power dissipation can be reduced by the recycling the energy from the load capacitance and back to the supply (Yemiscioglu and Lee 2012). In the recent years, several adiabatic or energy recovery logic architectures have been proposed (Yemiscioglu and Lee 2012; Konwar et al. 2014; Yasoda and Kaleem Basha 2013; Padmaja and SatyaPrakash 2012; Tomita et al. 2010; Morgenshtein et al. 2002). So, the total energy of this system remains constant. In adiabatic

D. N. Mukherjee (✉) · S. Biswas
Bankura Unnayani Institute of Engineering, Bankura, India

S. Panda
Department of Electronics & Communication Engineering, Narula Institute of Technology, Kolkata, India

B. Maji
Department of Electronics & Communication Engineering, National Institute of Technology, Durgapur, India

M. Mukherjee et al. (eds.), *Advances in Medical Physics and Healthcare Engineering*, Lecture Notes in Bioengineering, https://doi.org/10.1007/978-981-33-6915-3_20

logic, the outputs are valid in a particular phase of power supply. The gate diffusion input technique (GDI) is used to minimize the complexity of logic circuit design. In this paper, the multiplexer has designed using different adiabatic logic styles and compares them with GDI technique. Section 2 describes the general introduction of multiplexer. Section 3 describes the design of 4:1 multiplexer with different logic styles. Section 4 shows the simulation results. Finally make conclusion which is demonstrated at Sect. 5.

2 4:1 Multiplexer

The 4:1 multiplexer is one type of combinational logic circuit which has four inputs and one output. At a time, only one input is transmitted to the output, which is controlled by the combination of select lines (Konwar et al. 2014). The graphical symbol of 4:1 multiplexer is shown in Fig. 1. Let us assume that the four inputs A_0, A_1, A_2, and A_3 are individually transmitted to the output (Y) by controlling the select lines S_0 and S_1. The truth table of 4:1 multiplexer is shown in Table 1. The final output of 4:1 multiplexer is expressed by Eq. 1.

$$Y = \overline{S_0 S_1} A_0 + \overline{S_0} S_1 A_1 + S_0 \overline{S_1} A_2 + S_0 S_1 A_3 \tag{1}$$

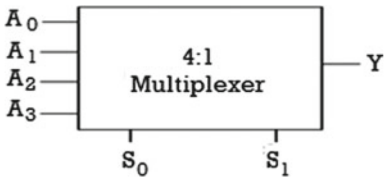

Fig. 1 Block diagram of 4:1 multiplexer

Table 1 Truth table of 4:1 multiplexer

Select line		Output
S0	S1	Y
0	0	A_0
0	1	A_1
1	0	A_2
1	1	A_3

3 Design of 4:1 Multiplexer Using Different Logic Styles

Adiabatic logic is a low power VLSI circuit which is much different from the static CMOS circuits. The advantage of static CMOS circuit over the adiabatic circuit is that it has full output voltage swing. Whereas the drawback of the static CMOS is that the power dissipation takes place during each switching operation from 0 to 1 and from 1 to 0. The adiabatic circuit is an adiabatic CMOS in nature. The main characteristic of adiabatic logic system is that there is no energy transformation from the system to environment and vice versa. The adiabatic circuit has ability to recycling the energy by giving the stored energy from the circuit to the supply. For this reason, the adiabatic logic circuit is also known as reversible logic circuit. Adiabatic logic can be divided into two types: one is the reversible logic, and another is the energy or charge recovery logic. The energy or charge recovery logic is again divided into two types depending upon the amount of recovery of charges: one is the full energy or charge recovery logic, and another is the partial or quasi energy recovery logic. The classification of adiabatic logic is shown in Fig. 2.

3.1 *ECRL-Based Multiplexer Design*

Efficient charge recovery logic (ECRL) is an example of partially adiabatic logic family. This logic style was proposed by Moon and Jeong. The ECRL logic is shown Fig. 3. ECRL logic consists of two cross-coupled PMOS transistors M1 and M2 and two functional blocks of NMOS transistors (Yasoda and Kaleem Basha 2013). To recover and reuse the supply energy, an AC power supply is used. The cross-coupled PMOS transistors are used for full output voltage swing both in pre-charge and recover phase. Two complementary outputs produce a constant load capacitance

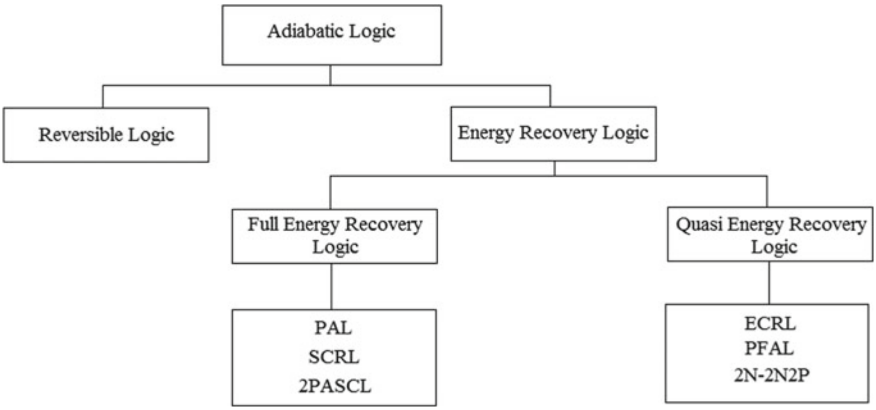

Fig. 2 Classification of adiabatic logic

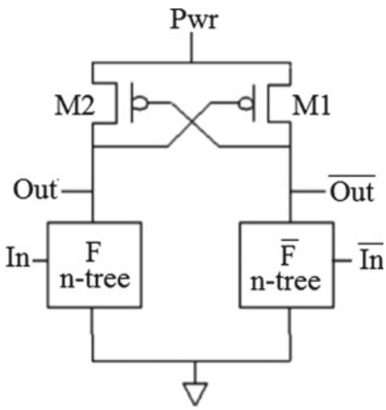

Fig. 3 Diagram of ECRL logic

through the power clock generator. The total circuit operation is performed by four phase intervals. According to the fixed input signal, the outputs are evaluated in the first phase, which is called evaluation phase. In the second phase, outputs are kept fixed, which is called hold phase. In the recovery phase, the charge is recovered efficiently which is delivered by the supply. In the last phase, the valid inputs are being prepared in the previous phase, which is called wait phase.

3.2 PFAL Logic-Based Multiplexer Design

Positive feedback adiabatic logic (PFAL) is a dual rail network (Padmaja and SatyaPrakash 2012), which can partially recover energy. The PFAL logic is shown in Fig. 4. To avoid the logic-level degradation on two complemented outputs, a latch is constructed by two PMOS transistors and two NMOS transistors. The logic function realization is prepared by the two NMOS functional blocks. These NMOS blocks are connected in parallel with the PMOS transistors of the latch. The advantage of PFAL logic over ECRL logic is that at the time of charging of capacitor, the equivalent resistance is smaller due to the parallel connection of NMOS functional blocks

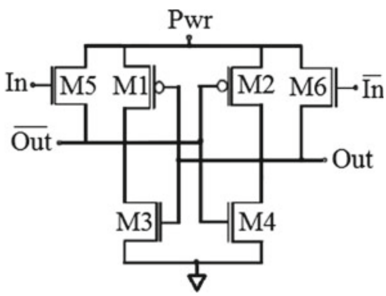

Fig. 4 Diagram of PFAL logic

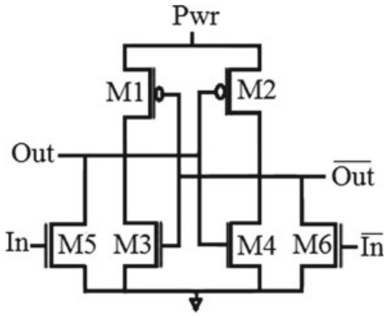

Fig. 5 Diagram of 2N-2N2P logic

with the PMOS transistors of the latch. When the input ‘In’ is high, the transistors M5, M4, and M1 are in on state then the complement of the output will follow the changes of the power supply, and the output will be connected to the ground. When the power clock reaches to V_{dd}, the output will be zero and the complement of the output will be V_{dd}. The recovery of energy is done by the transistor M1 when the power clock changes from V_{dd} to 0.

3.3 2N-2N2P Logic-Based Multiplexer Design

2N-2N2P logic (Konwar et al. 2014) is similar to PFAL logic, where a latch is constructed by two PMOS transistors and two NMOS transistors. Two NMOS blocks are used to realize the logic functions. These NMOS blocks are connected in parallel with the NMOS transistors of the latch. The total circuit operation is done by the four phase clocking interval. The 2N-2N2P logic is shown in Fig. 5.

3.4 Adiabatic Array Logic-Based Multiplexer Design

The adiabatic array logic (AAL) is an array of transmission gates, where AND operation is done by AND plane of transmission gates and OR operation is done by wired-OR plane (Tomita et al. 2010). An AC power supply is used to operate adiabatic array logic. The 2:1 multiplexer using adiabatic array logic is shown in Fig. 6.

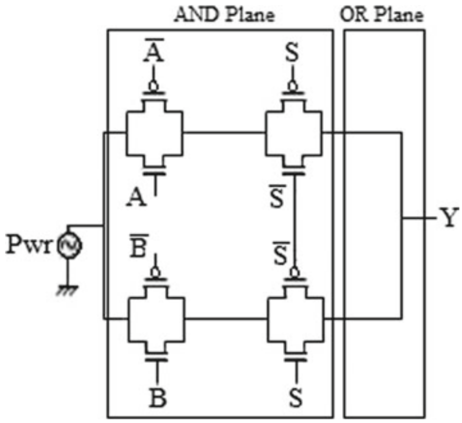

Fig. 6 2:1 multiplexer using adiabatic array logic

3.5 Proposed Charge Recovery Logic-Based Multiplexer Design

In the proposed charge recovery logic (PCRL), the load capacitor is charging and discharging through the same path, so the complexity of the circuit is reduced. The proposed charge recovery logic is shown in Fig. 7 where the source terminal of both the M1 transistor and the P2 transistor are connected with the power clock. Consider that the load capacitor is at first uncharged. When the input terminal is connected with the high logic level, then M1 transistor is in ON state and the gate terminal of both PMOS transistors is connected with power clock. Output voltage is still logic zero regardless of whether there are any adjustments in the clock signal. So, capacitor does not store any charge. When the input signal is at low logic level, then M1 transistor is OFF and both PMOS transistors are in ON state. So, in this condition, the output will follow the changes of the power supply.

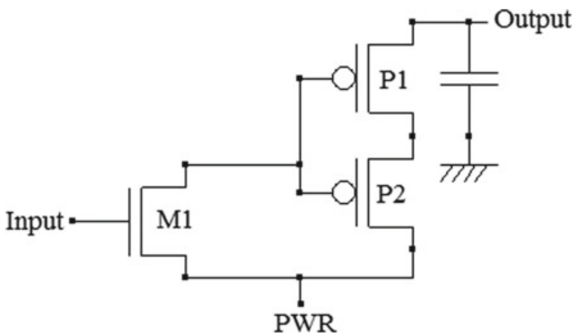

Fig. 7 Proposed charge recovery logic

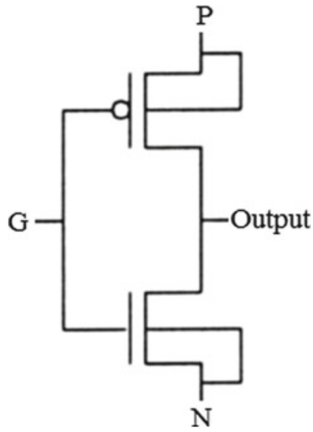

Fig. 8 Diagram of single GDI cell

3.6 GDI Technique-Based Multiplexer Design

Gate diffusion input (GDI) technique is efficient to design any complex logic functions using two transistors-based circuit arrangement (Morgenshtein et al. 2002). This design technique requires less number of transistors. A single GDI cell consists by one PMOS transistor and one NMOS transistor which is shown in Fig. 8. The GDI technique has three input terminals gate, drain, and source. The drain terminals of two transistors are shorted to get the output of a logic function. The gate terminals are shorted and connected to input. The sources of two transistors are connected with inputs. The GDI technique can perform different Boolean function by changing the input configuration.

4 Simulation Results

In this research work, the 4:1 multiplexer has designed by different adiabatic logic styles and compared with GDI technique in terms of power consumption and transistor count. The results are simulated by EDA Tanner tools in 180 nm technology at 1.5 V supply voltage. The schematic of 4:1 multiplexer using ECRL, PFAL, 2 N-2N2P, AAL, PCRL, and GDI techniques is shown in Figs. 9, 10, 11, 12, 13, and 14, respectively. Table 2 shows the performance analysis of multiplexer using different logic styles. After the simulation, it has been observed that the power consumption is less in PCRL logic than the other adiabatic techniques. It is also observed that the less number of transistors is required in GDI technique to design a multiplexer.

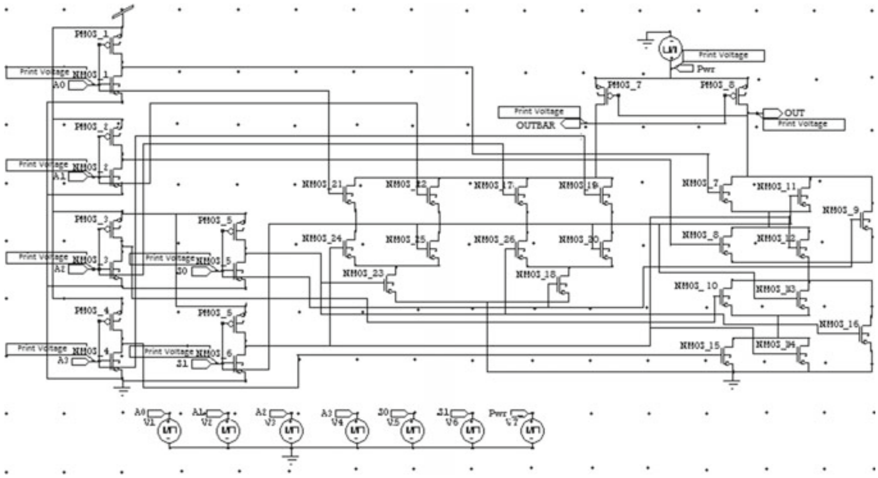

Fig. 9 Schematic of 4:1 multiplexer using ECRL logic

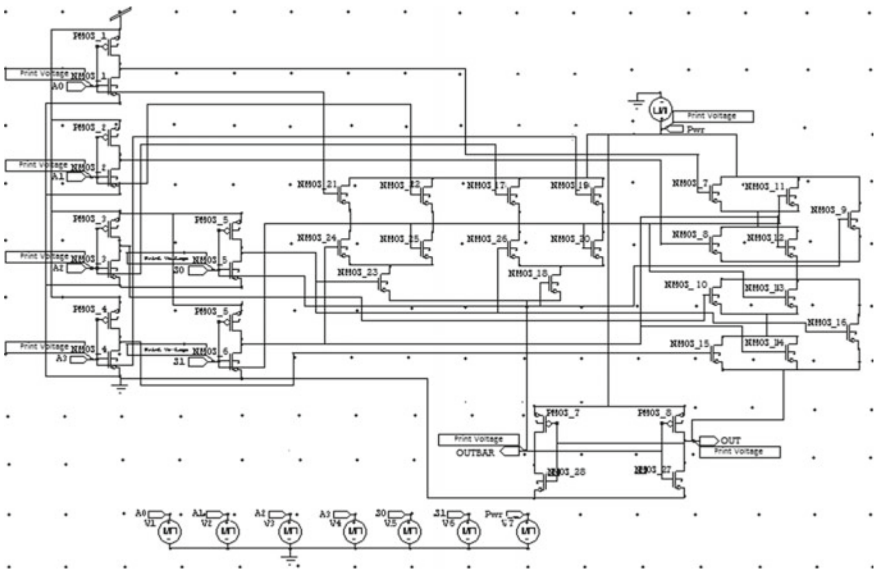

Fig. 10 Schematic of 4:1 multiplexer using PFAL logic

5 Conclusion

After the simulation and comparison of 4:1 multiplexer using different logic styles, the final conclusion is that the PCRL logic is more superior to other adiabatic logic

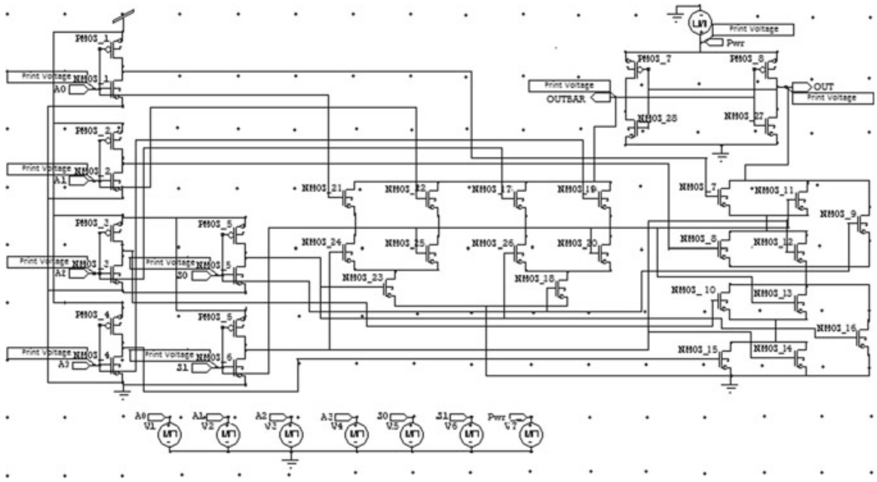

Fig. 11 Schematic of 4:1 multiplexer using 2 N-2N2P logic

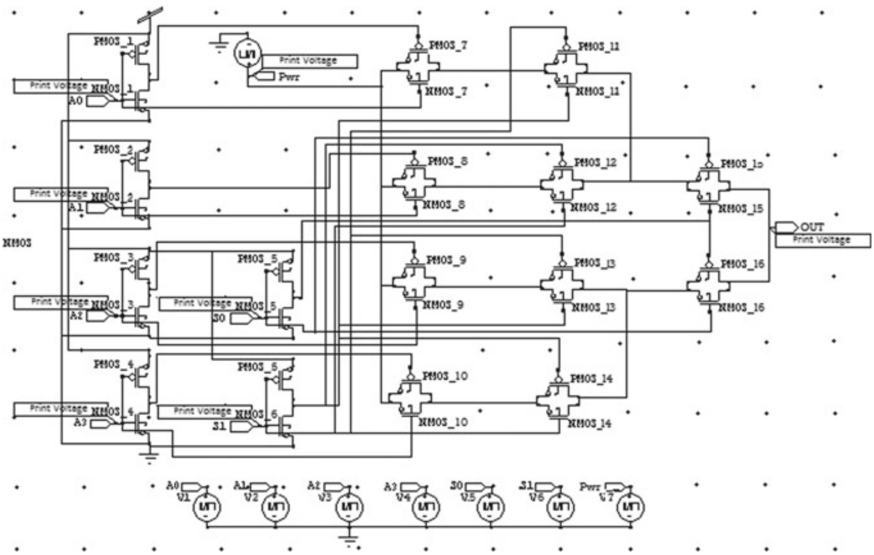

Fig. 12 Schematic of 4:1 multiplexer using AAL logic

technique in terms of power consumption and transistor count. The power consumption in GDI logic has almost 60.74% less than PCRL logic. It is also found that the transistor count in GDI logic is almost 75% less than PCRL logic. So, GDI logic is more superior to adiabatic logic in terms of designing of smaller circuit area with less power consumption.

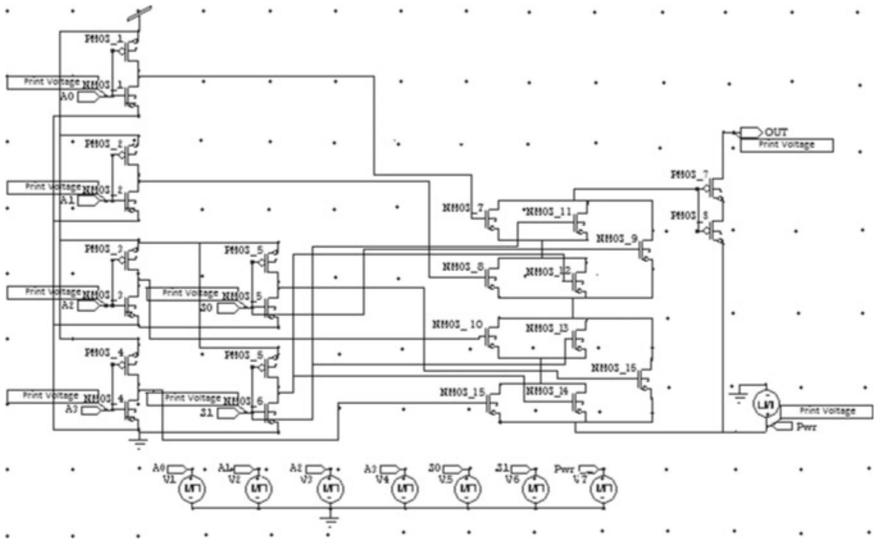

Fig. 13 Schematic of 4:1 multiplexer using PCRL logic

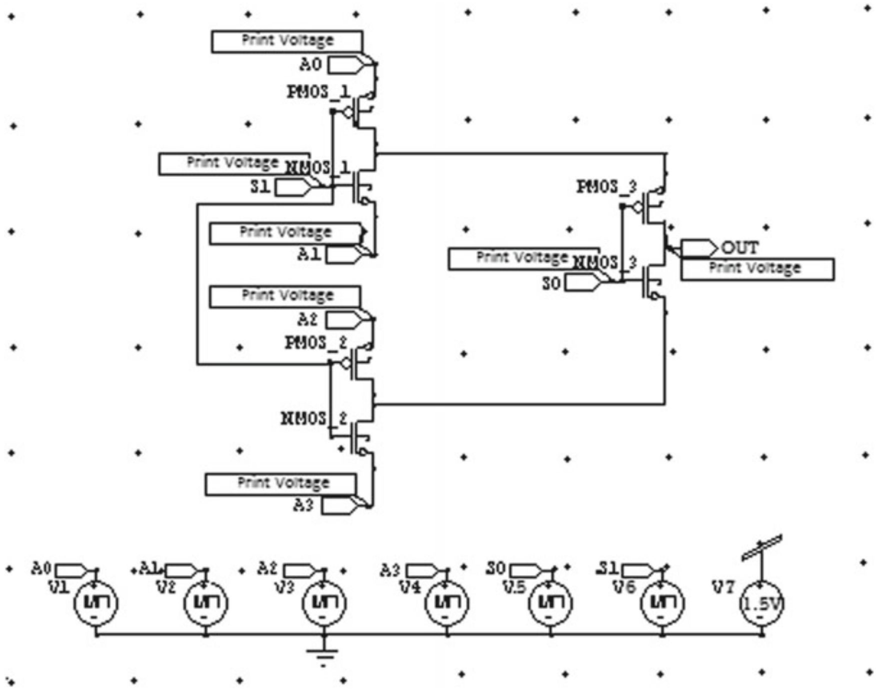

Fig. 14 Schematic of 4:1 multiplexer using GDI technique

Table 2 Performance comparison of multiplexer

Circuit logic	Power consumption	Transistor count
ECRL	23.16	34
PFAL	22.77	36
2 N-2N2P	25.94	36
AAL	22.05	32
PCRL	21.32	24
GDI	8.37	6

References

Konwar S, Singha TB, Roy S, Vanlalchaka RH (2014) Adiabatic logic based low power multiplexer and demultiplexer. In: International conference on computer communication and informatics. IEEE, Coimbatore, India, pp 1–5

Morgenshtein A, Fish A, Wagner IA (2002) Gate-diffusion input (GDI)—a technique for low power design of digital circuits: analysis and characterization. In: International symposium on circuits and systems. IEEE, Phoenix-Scottsdale, AZ, USA, pp 477–480

Padmaja M, SatyaPrakash VNV (2012) Design of a multiplexer in multiple logic styles for Low Power VLSI. Int J Comput Trends Technol 3(3):467–471

Tomita Y, Takahashi Y, Sekine T (2010) Adiabatic array logic. In: International conference on signals and electronic systems. IEEE, Gliwice, Poland, pp 269–272

Yasoda B, Kaleem Basha S (2013) Performance analysis of energy efficient and charge recovery adiabatic techniques for low power design. IOSR J Eng 3(6):14–21

Yemiscioglu G, Lee P (2012) 16-bit clocked adiabatic logic (CAL) logarithmic signal processor. In: 55th international Midwest symposium on circuits and systems. IEEE, Boise, ID, USA, pp 113–116

Power Efficient Magnitude Comparator Using Adiabatic Logic and Gate Diffusion Technique

S. Biswas, D. N. Mukherjee, S. Panda, and B. Maji

Abstract In the advanced technology, designing of low power, high speed portable devices is a challenging issue. Power dissipation can be minimized by using adiabatic logic style. In compared to gate diffusion input technique, an adiabatic logic required more number of transistors, and more power is needed. This paper demonstrates the design and implementation of 2-bit magnitude comparator using different adiabatic logic styles and comparing with the gate diffusion input technique in terms of power consumption and transistor count. The simulation has been done by using the DSCH and Microwind software.

Keywords Adiabatic logic · ECRL · PFAL · 2N-2N2P · GDI technique · Power dissipation · Transistor count

1 Introduction

The power dissipation can be reduced by different logic technique and technologies. Adiabatic logic technique is one of the ideal techniques which can achieve these demands. In the recent years, several adiabatic or energy recovery logic architectures have been proposed (Anuar et al. 2010; Bakshi and Sharma 2013; Teichmann 2012; Sathe et al. 2007; Kumar and Sharma 2013; Zang et al. 2014). In adiabatic logic style, AC power supply is used to perform the total operation of the circuit. In adiabatic logic style, the power dissipation can be reduced by recycling the energy from the load capacitance and back to the supply. So, the total energy of this system remains constant. In adiabatic logic, the outputs are valid in a particular phase of

S. Biswas (✉) · D. N. Mukherjee
Bankura Unnayani Institute of Engineering, Bankura, India

S. Panda
Department of Electronics & Communication Engineering, Narula Institute of Technology, Kolkata, India

B. Maji
Department of Electronics & Communication Engineering, National Institute of Technology, Durgapur, India

M. Mukherjee et al. (eds.), *Advances in Medical Physics and Healthcare Engineering*, Lecture Notes in Bioengineering, https://doi.org/10.1007/978-981-33-6915-3_21

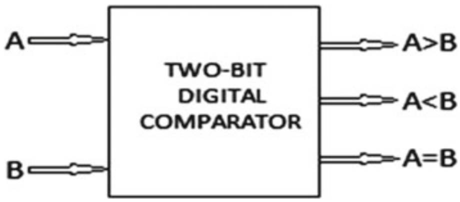

Fig. 1 Block diagram of 2-bit magnitude comparator

power supply. Gate diffusion technique (GDI) is used to minimize the complexity of logic circuit design. Magnitude comparator can be used in digital signal processing, central processing unit, microcontroller, etc. In this research work, a 2-bit magnitude comparator has designed using different adiabatic logic styles and compares them with GDI technique. Section 2 presents the general introduction of magnitude comparator. Section 3 describes the design of 2-bit comparator with different logic styles. Section 4 shows the comparative study of different techniques. Section 5 demonstrates the final conclusion.

2 2-Bit Magnitude Comparator

Magnitude comparator is a combinational logic circuit, where two digital signals are compared in terms of their relative magnitudes. After the comparison of two signals, magnitude comparator decides whether two signals are equal or not that will express by Eqs. (1), (2), and (3). The block diagram of 2-bit magnitude comparator is shown in Fig. 1.

$$A > B = A0\bar{B}0 + (A0 \odot B0)A1\bar{B}1 \tag{1}$$

$$A < B = \bar{A}0B0 + (A0 \odot B0)\bar{A}1B1 \tag{2}$$

$$A = B = (A0 \odot B0)(A1 \odot B1) \tag{3}$$

3 Design of 2-Bit Magnitude Comparator Using Different Logic Styles

3.1 2-Bit Magnitude Comparator Using ECRL Logic

Efficient charge recovery logic (ECRL) is an example of partially adiabatic logic family. This logic style was proposed by Moon and Jeong. The ECRL logic is shown

Fig. 3. ECRL logic consists of two cross-coupled PMOS transistors M1 and M2 and two functional blocks of NMOS transistors (Teichmann 2012). To recover and reuse the supply energy, an AC power supply is used. The cross-coupled PMOS transistors are used for full output voltage swing both in pre-charge and recover phase. Two complementary outputs produce a constant load capacitance through the power clock generator. The total circuit operation is performed by four phase intervals. According to the fixed input signal, the outputs are evaluated in the first phase, which is called evaluation phase. In the second phase, outputs are kept fixed, which is called hold phase. In the recovery phase, the charge is recovered; efficient charge recovery logic (ECRL) is an example of partially adiabatic logic family. ECRL is not able to pick up the power clock which performs like quasi adiabatic logic style (Bakshi and Sharma 2013).The schematic of ECRL-based 2-bit comparator is shown in Fig. 2. ECRL logic-based 2-bit comparator is designed two cross-coupled PMOS transistors and two functional blocks of NMOS transistors. To perform the total operation of the circuit, an AC power supply is used. Two complementary outputs produce a constant load capacitance through the power clock generator. The total circuit operation is performed by four phase intervals of power supply.

3.2 2-Bit Magnitude Comparator Using PFAL Logic

Positive feedback adiabatic logic (PFAL) can partially recover energy. In this logic technique, a latch is designed by two PMOS transistors and two NMOS transistors (Bakshi and Sharma 2013). The logic function realization is prepared by the two NMOS functional blocks. These NMOS blocks are connected in parallel with the PMOS transistors of the latch. The schematic of 2-bit magnitude comparator using PFAL logic is shown in Fig. 3.

3.3 2-Bit Magnitude Comparator Using 2N-2N2P Logic

In this logic technique, a latch is designed by two PMOS transistors and two NMOS transistors. Here the logic function realization can be done by two NMOS blocks. These NMOS blocks are connected in parallel with the NMOS transistors of the latch. The schematic of 2-bit comparator using 2N-2N2P logic is shown in Fig. 4.

3.4 GDI Technique-Based Multiplexer Design

Gate diffusion input technique is more efficient to design any circuit using less number of transistors. A single GDI cell consists by one PMOS transistor and one NMOS transistor. The gate terminal of two transistors is shorted and connected with

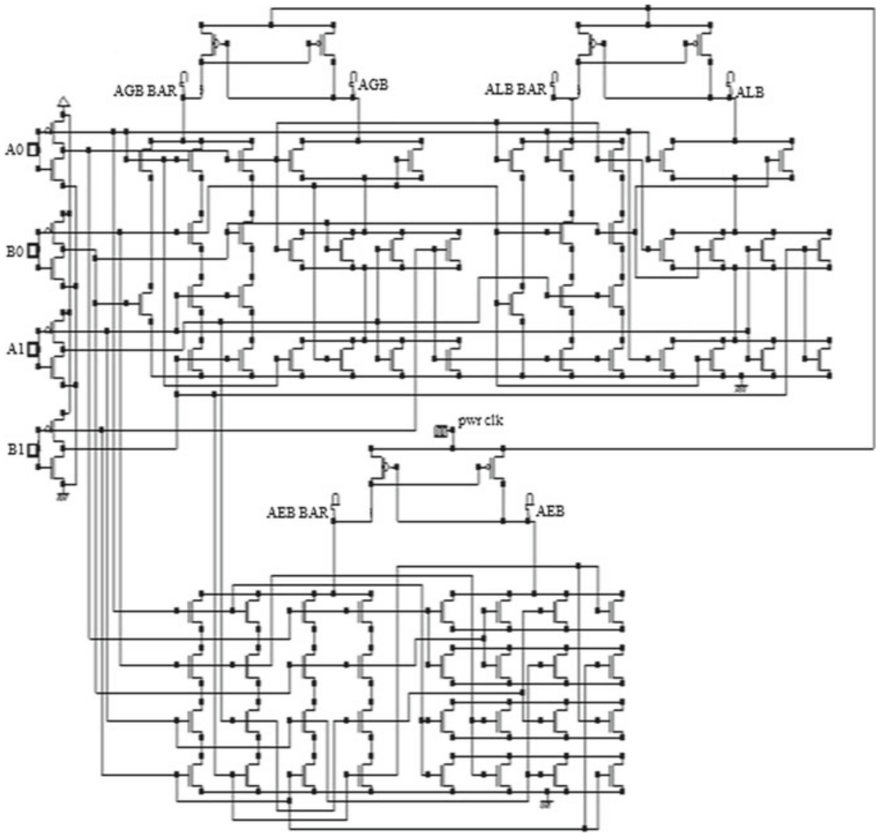

Fig. 2 Schematic of 2-bit comparator using ECRL logic

input signal. The drain terminals of two transistors are shorted to get the output of a logic function. The sources of two transistors may connect with inputs. The schematic of GDI-based 2-bit comparator is shown in Fig. 5.

4 Comparison of GDI and Adiabatic Logic Styles

The GDI and adiabatic logic styles are compared in terms of power consumption and transistor count. Table 1 shows the performance analysis of 2-bit comparator using different logic styles. After the simulation of 2-bit digital comparator using different logic styles, it is observed that the power dissipation is comparatively less in PFAL logic than other logic styles. The simulation result shows that the less number of transistors is required in GDI technique than other adiabatic logic styles.

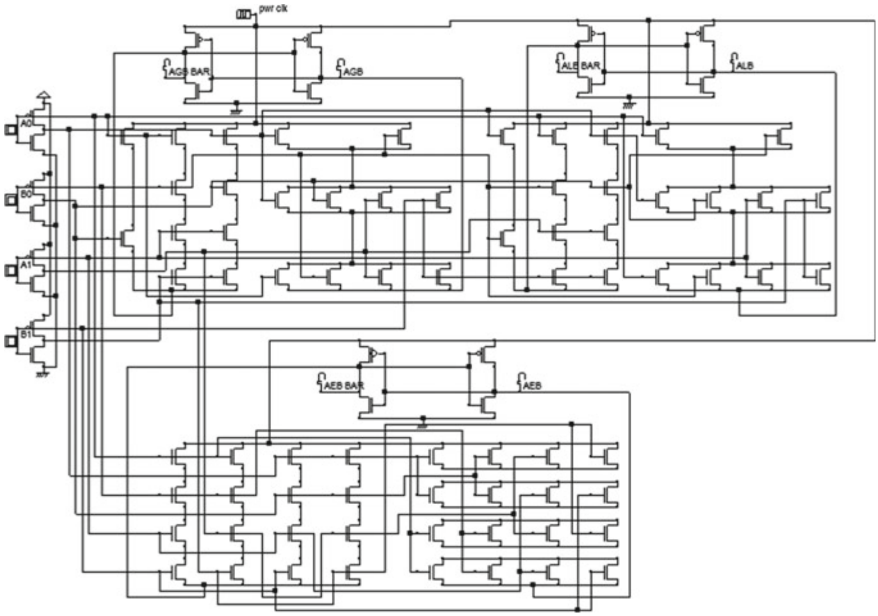

Fig. 3 Schematic of 2-bit comparator using PFAL logic

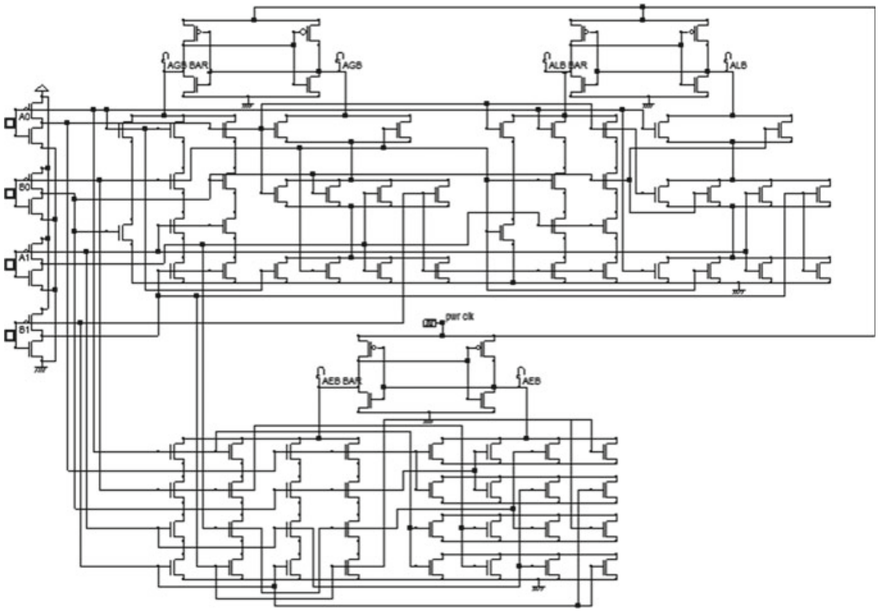

Fig. 4 Schematic of 2-bit comparator using 2N-2N2P logic

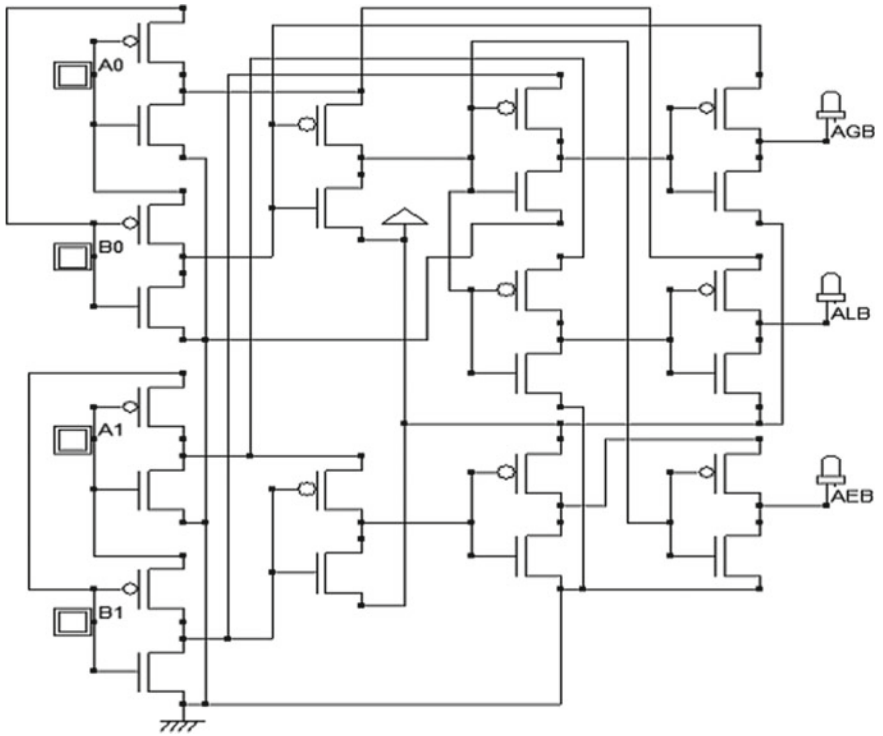

Fig. 5 Schematic of 2-bit comparator using GDI logic

Table 1 Performance comparison of comparator

Circuit logic	Power consumption	Transistor count
ECRL	6.11	86
PFAL	5.23	92
2N-2N2P	6.67	92
GDI	4.03	24

5 Conclusion

The various logic techniques are proposed to improve the performance of 2-bit magnitude comparator. After simulation of all kind of logic circuits, it is concluded that the power can be reduced in the gate diffusion technique. It has been found that the transistor count in GDI logic is almost 72% less than PFAL logic. So, the GDI technique is better than adiabatic logic styles.

References

Anuar N, Takahashi Y, Sekine T (2010) Two phase clocked adiabatic static CMOS logic and its logic family. J Semicond Technol Sci 10(1)

Bakshi AK, Sharma M (2013) Design of basic gates using ECRL and PFAL. In: International conference on advances in computing, communication and informatics. IEEE

Kumar A, Sharma M (2013) Design and analysis of MUX using Adiabatic Techniques ECRL and PFAL. In: International conference on advances in computing, communication and informatics. IEEE

Sathe VS, Chueh J-Y, Papaefthymiou MC (2007) Energy-efficient GHz-class charge-recovery logic. IEEE J Solid-State Circ 42(1)

Teichmann P (2012) Adiabatic logic, future trend and system level perspective, vol XVII. Springer, 166 p

Zang F, Hu J, Cheng W (2014) Power-gating scheme and modeling of near-threshold adiabatic flip-flops. Telkomnika Indonesian J Electr Eng 12(1):89–97

Slope Transit Time Based Cuffless Portable Systolic Blood Pressure Estimation

A. Chatterjee, S. Pal, and M. Mitra

Abstract This paper outlines a method of cuffless noninvasive continuous Systolic Blood Pressure (SBP) measurement based on PPG signal. Circuit for PPG signal acquisition has been presented and techniques for noise removal have been discussed. Feature as Slope Transit Time has been selected from PPG, followed by Support Vector Machine (SVM) regression method to estimate SBP. Experimental results performed on a standard SBP yielded errors which falls within the permissible range. The methodology shown in the paper can be used as home-based cuffless BP monitoring

Keywords Arduino Uno · PPG signal · Slope transit time · Systolic blood pressure

1 Introduction

Blood pressure (BP) measurement is essential for assessing critical health conditions specifically for subjects identified with high/low blood pressure, elderly, or those who are having cardiovascular problems. The existing commercial method of BP measurement is cuff-based which doesn't provide continuous beat-beat BP measurement; moreover it can't be used for long term as it causes discomfort to the subject due to continuous cuff inflation and deflation. This problem intensifies more when the said subject remains in sleeping condition.

Studies have been published on cuffless method of BP measurement but most of them concentrated on Pulse Transit Time (PTT) based BP measurement which requires extraction of PPG and ECG signal in tandem (Cattivelli and Garudadri 2009). Geddes et al. showed a relationship between Pulse Wave Velocity and BP (Geddes et al. 1981).

Moens Kortweg equation expressed PWV in terms of artery dimension, blood density, and artery wall elasticity to compute Pulse Transit Time from which Blood

A. Chatterjee (✉) · S. Pal · M. Mitra
Department of Applied Physics, University of Calcutta, Kolkata 700009, India

M. Mitra
e-mail: mmaphy@caluniv.ac.in

M. Mukherjee et al. (eds.), *Advances in Medical Physics and Healthcare Engineering*, Lecture Notes in Bioengineering, https://doi.org/10.1007/978-981-33-6915-3_22

Pressure was estimated (Mack et al. 2009). The Moens-Kortweg equation is written below.

$$\mathrm{PWV} = \frac{L}{\mathrm{PTT}} = \frac{\sqrt{hE_0 \exp^{\xi P}}}{\rho R} \tag{1}$$

where PWV is the Pulse Wave Velocity, L is the length of the vessel, PTT is the Pulse Transit Time, h is the thickness of the vessel. R is the vessel's radius, ρ is the blood density, E_0 is the zero pressure modulus, ξ is a constant that depends on a specific vessel, and P is the blood pressure.

Time difference between J peak of ballistocardiography waveform and systolic peak of PPG was used to correlate with systolic and diastolic BP (Mack et al. 2009). Few researchers calculated VTT collecting PPG signal in conjunction with heart sound waveform and subsequently used that for BP estimation (Foo et al. 2006). An accurate recognition algorithm of the feature points based on wavelet analysis and time-domain characteristics of the pulse wave was designed in a study that also used Markov Model and performed non-invasive blood pressure estimation (Liu et al. 2017). PPG-based BP estimation using Kalman filtering and neural network was proposed by researchers (Kurylyak et al. 2013). A support vector machine-based BP prediction was also proposed (Liang et al. 2016).

A BP estimation method based on the physical model of wrist skin tissues and pulse wave velocity (PWV) was proposed by few researchers (Lazazzera et al. 2019). A study was published aiming to establish systolic BP and diastolic BP estimation models based on machine learning on pulse transit time and characteristics of pulse waveform (Kachuee et al. 2016). A paper was published where gradient boosting decision tree (GBDT) was applied while predicting blood pressure rates based on the human physiological data collected by the EIMO device (Zhang et al. 2019).

This paper paves a way of cuffless SBP estimation based only on PPG signal extraction without the need for ECG signal collection and also overcomes shortfalls associated with PTT-based BP prediction.

2 Methodology

2.1 Data Collection and Acquisition

An experiment was conducted on 25 subjects with mean age ± standard deviation of 40.16 ± 14.27 years and varied physical condition in a biomedical signal processing lab.PPG signal was collected from their fingertip in supine position at 250 Hz sampling rate for a duration of 3 min.HRM 2511E PPG sensor was used for signal extraction. The sensor was embedded in a cap which was attached to the subject's fingertip for data collection. The extracted signal was filtered and amplified through a signal conditioning block. The signal condition block is shown in Fig. 1

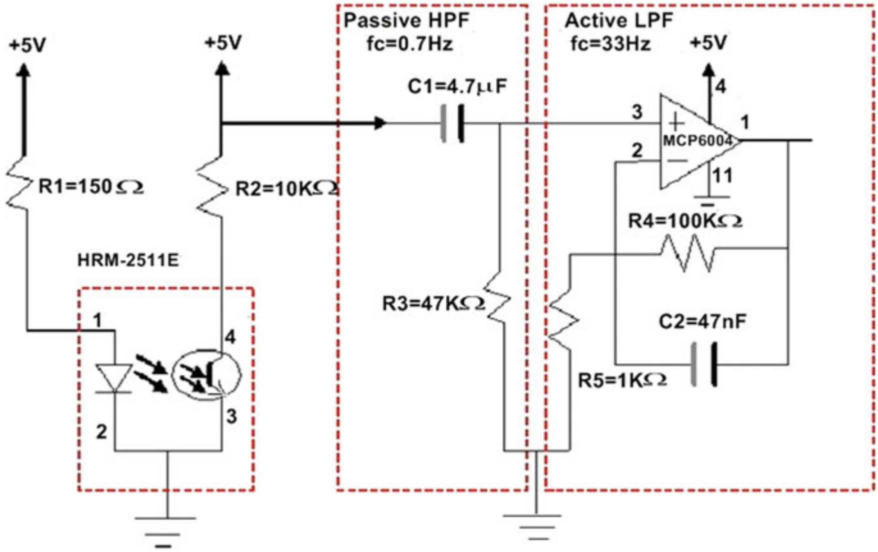

Fig. 1 PPG signal acquisition block

was comprised of a high pass filter having cut off frequency 0.7 Hz, a low pass filter having cut off frequency 33 Hz and a MCP6004 OPAmp by which filtered signal was amplified. The obtained signal was interfaced with computer via Arduino Uno Interfacing device as shown in Fig. 2; which was further brought to the MATLAB for signal depiction, feature extraction, and data analysis.

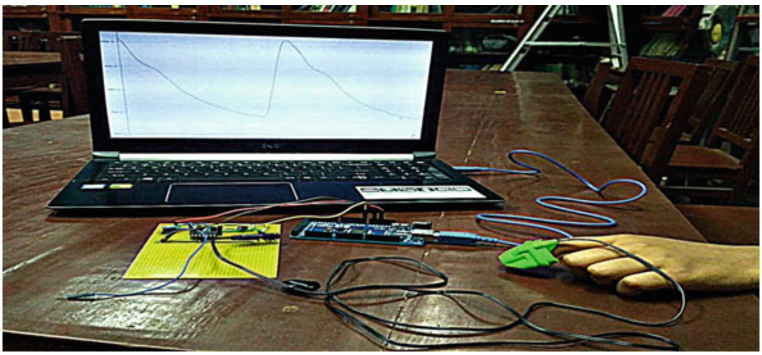

Fig. 2 Signal acquisition from a subject and plotting at Arduino IDE

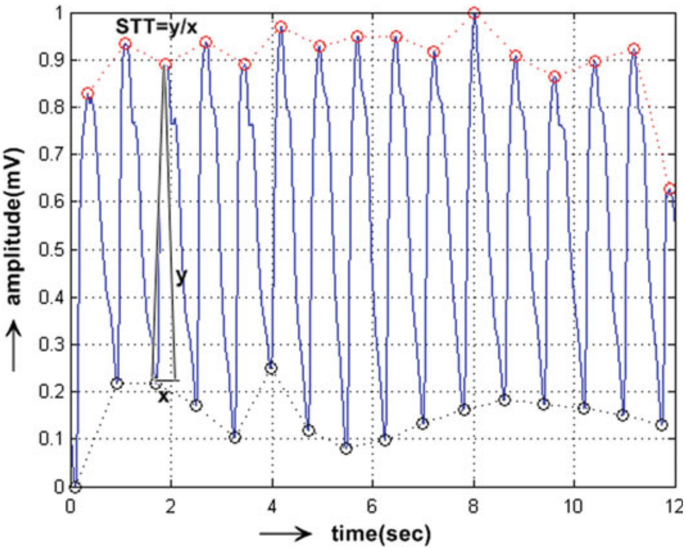

Fig. 3 Depiction of extracted PPG signal on MATLAB

2.2 Data Preprocessing

The extracted signal was subjected to power line interference which was removed by 5 point moving average filter as the power line frequency is 50 Hz and the sampling frequency of the acquired PPG signal was 250 Hz. Baseline wandering noise was also added to the extracted signal which was eliminated by a 208 point median filter as the frequency of the baseline noise lie in the range of 0.8–1.2 Hz in case of PPG signal and the sampling frequency of the acquired PPG signal was 250 Hz.

3 Feature Extraction

The time gap between the foot of one PPG pulse and the peak of consecutive PPG pulse has been evaluated to obtain slope transit time (STT) and. The obtained STT later correlated with SBP by applying different Regression techniques (Fig. 3).

4 Results and Discussions

This study has proposed Systolic Blood Pressure Estimation method based on Slope Transit Time computation of PPG signal. The time gap between foot of one PPG pulse and peak of consecutive PPG pulse has been calculated to determine STT.

The obtained data of STT was split into 70:30 for training and testing. 70% of the data was used to train three different regression algorithms (Quadratic SVM, Linear Regression, Binary Tree) which were selected in this study and after that the trained model was applied 30% of the test dataset to predict SBP estimation. Four different types of error metrics (R^2, Percentage of Error, Mean Absolute Error, Mean Absolute Error, Mean Absolute Percentage Error, Root Mean Square Error) were used to evaluate the performance of the selected machine learning models. It has been observed that Quadratic SVM yields best result in estimating SBP amongst other models (Table 1).

The Bland–Altman plot shown in Fig. 4 is well-known method for assessing the agreement between two methods of clinical measurement. The horizontal spread of the above-shown plot displays the agreement of actual BP which was measured by sphygmomanometer with the estimated BP using our method. It is also evident from

Table 1 Performance of the model in estimating SBP

Regression method	R^2	Percentage error	Mean absolute error	Mean absolute percentage error	Root mean square error
Quadratic SVM	0.92	3.0682	0.1815	0.1334	1.0103
Linear Regression	0.88	4.2430	0.2571	0.1844	1.3569
Binary Tree	0.77	4.9111	0.2949	0.2135	1.714

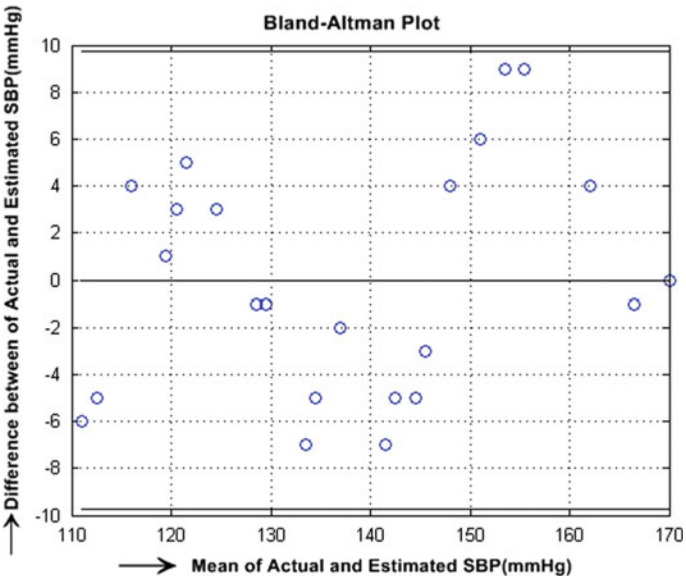

Fig. 4 Bland–Altman Plot of actual and estimated SBP

this plot that the error between actual and estimated SBP lies between ± 9 mmHg which falls within the maximum ambit (± 10 mmHg) of allowable range.

5 Conclusion

This paper illustrates a method of PPG-based cuffless continuous SBP estimation. Slope Transit Time has been selected as a feature of PPG signal which have been utilized to correlate with SBP. A compact portable system has been designed to extract PPG signal from fingertip and thereafter the feature selected from that PPG waveform has been employed to estimate SBP. However, the algorithm is tested on few numbers of subjects; so our future challenge is to run this same algorithm on an extended database to validate the efficacy of this model to simulate SBP more accurately than the other standard models available in literature.

References

Cattivelli FS, Garudadri H (2009) Noninvasive cuffless estimation of blood pressure from pulse arrival time and heart rate with adaptive calibration. In: IEEE 6th international workshop on wearable and implantable body sensor networks, pp 114–119, USA

Foo JYA, Lim CS, Wang P (2006) Evaluation of blood pressure changes using vascular transit time. Physiol Meas 27(8):685–694

Geddes LA, Voelz M, James S, Reiner D (1981) Pulse arrival time as a method of obtaining systolic and diastolic blood pressure indirectly. Med Biol Eng Comput 19(5):671–672

Kachuee M, Kiani MM, Mohhamadzade H, Shabany M (2016) Cuffless blood pressure estimation algorithms for continuous health care monitoring. IEEE Trans Biomed Eng 64(4):859–869

Kurylyak Y, Barbe K, Lamonaca F, Grimaldi D, Moer DV (2013) Photoplethysmogram-based blood pressure evaluation using Kalman filtering and neural networks. In: IEEE international symposium on medical measurements and applications (MeMeA)

Lazazzera R, Belhaj Y, Carrault G (2019) A non-invasive continuous blood pressure estimation approach based on machine learning. Sensors 19(11):2557

Liang B, Duan K, Xie Q, Atef M, Qian Z, Wang G, Lian Y (2016) Live demonstration: a support vector machine based hardware platform for blood pressure prediction. In: IEEE biomedical circuits and systems conference (BioCAS), Sanghai, China

Liu X, Ji Z, Tang Y (2017) Recognition of pulse wave feature points and non-invasive blood pressure measurement. J Signal Process Syst 87(2)

Mack DC, Patrie JT, Suratt PM, Felder RA, Alwan M (2009) Development and preliminary validation of heart rate and breathing rate detection using a passive, ballistocardiography-based sleep monitoring system. IEEE Trans Inf Technol Biomed 13(1):111–120

Zhang B, Ren J, Wang B, Cheng Y, Wei Z (2019) Health data driven on continuous blood pressure prediction based on gradient boosting decision tree algorithm. IEEE Access: Pract Innov Open Solutions 7:423–433

Colon Cancer Detection Using Watershed Transformation Technique

Priyanka Ghose and Madhuchanda Mitra

Abstract Colon cancer is regarded as one of the most common type of cancer worldwide. Effective analysis of the colonoscopy images becomes helpful for the diagnosis process. This paper describes automatic detection of colon cancer from the colonoscopy images. Hence, the detection mechanism has been implemented with the application of image segmentation technique for a better understanding of the colonoscopy images. Object oriented texture analysis along with watershed transformation, which is used as the segmentation technique, has been used in this work. Watershed has been selected as it gives an advantage to distinguish region of interests which are close to each other. Otsu's method is also considered at the thresholding step. Image processing technique is applied as the pre-processing step which helps the final segmentation result by enhancing the input image quality. The proposed technique successfully detects the region of cancer cells from arbitrary colonoscopy images which are available in open source. The areas which are extracted by this process are then set to the minimum position within the same topological surface.

Keywords Colon cancer · Colonoscopy image · Image thresholding · Image segmentation · Watershed method

1 Introduction

Cancer is uncontrolled proliferation of the tissues present in an organ, and colon is one of the major components of large intestine, which is the final part of our digestive tract. Colon cancer is a type of cancer that begins in the large intestine (colon). There are many reasons of colon cancer likes—inflammatory intestinal conditions, chain smoking, obesity, increasing age such as age above 50 years, diabetes, alcohol, family

P. Ghose (✉)
Department of Information Technology, GCETT, Serampore, India

M. Mitra
Department of Applied Physics, Faculty Council for Post-Graduate Studies in Engineering and Technology, Calcutta University, Kolkata, India
e-mail: mmaphy@caluniv.ac.in

M. Mukherjee et al. (eds.), *Advances in Medical Physics and Healthcare Engineering*, Lecture Notes in Bioengineering, https://doi.org/10.1007/978-981-33-6915-3_23

history of colon cancer, low intake of fruits, and heavy intake of red meat and fats. Colonoscopy is a high-quality imaging technique which produces the structure of human organ in more defined manner.

The primary objective of the colonoscopy procedures is to check the status of the colon of the patient, with the aim to find possible lesions and cancer polyps on it. Several image processing techniques have been used by many researchers. Image segmentation is another important mechanism which is also used in computer vision application for polyp detection. There are multiple challenges in polyp detection in colonoscopy images—non uniform appearances, partial or lateral views of the polyps in the images, blurred images, uniform texture, etc. So generically, detection of different types of polyps from various colonoscopy images is a practical challenging problem of image analytics.

As part of our work, we started with polyp detection by applying few methods—shape descriptors, texture and colour descriptors, pseudo colour image processing and K-means clustering. We tried to use few standard shapes-based method—ellipse fitting, means of curvature for object classification, object recognition and object identification tasks. As our input images came from a high definition interleaved video source, correction of the specular highlights is very much needed. As the result, the detection was not very accurate for arbitrary polyp shapes by applying the shape-based method. We also applied pseudo colour image processing—a technique that maps each of the grey levels of a black and white image into an assigned colour. This coloured image, when displayed, can make the identification of certain features easier for the observer. It has been applied by using picture colour normalization and image intensity normalization for polyp detection, but that also gave poor result in terms of arbitrary polyp detection. After that we tried searching of polyp through 3D ROI image with 3D templates using convolution-based filtering. But here also we did not get satisfactory outcome (Fig. 1).

Then, image segmentation using K-means clustering method was considered as next approach. Hence, number of clusters was predefined for individual image. But polyp detection was also unsuccessful (Fig. 2). Finally, we have detected the region of cancer cells from colonoscopy images using image segmentation technique–Marker- controlled watershed transformation, prior to apply necessary image processing steps. Rest of this paper is organized as follows: Section 2 describes

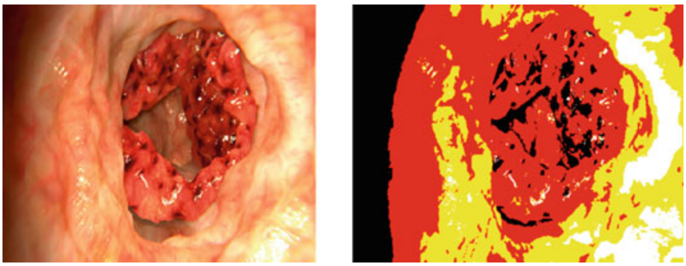

Fig. 1 Input image (left) and its corresponding output (right) for pseudo colour processing

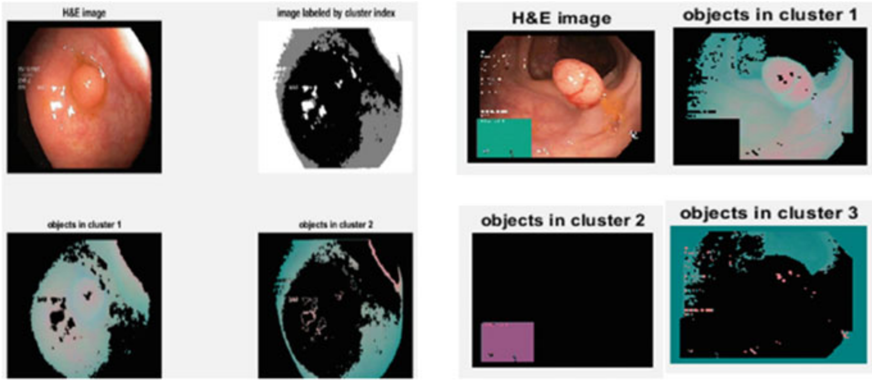

Fig. 2 Input image and its clustering outputs for two clusters (left) and input image and its clustering outputs for three clusters (right)

related work; Section 3 presents the proposed methodology, and Section 4 brings our result and conclusion and the scope for future work.

2 Related Work

Rebecca Siegel et al. have described various statistical data on colon cancer (Siegel et al. 2017). They have presented various case studies for different groups of patients, geographies, etc., with statistical inferences. It becomes very useful to know the overall perspectives of colon cancer.

Bernal and others aim for automatic polyp detection by using a model of polyp appearance in the context of the analysis of colonoscopy videos (Bernal et al. 2012). Their method consists of three stages: region segmentation, region description and region classification. They introduced a formula to represent the image based on an assumption with different factors on optics—ambient intensity, ambient reflection constant, attenuation factor, etc. Tarik and others have proposed a method to automatically detect the polyp's region based on a Gaussian mixture model, Esperance maximization algorithm, Hough transform, and region growing (Tarik et al. 2016). They have used Hough transform feature extraction technique in image analysis for cycloid detection along with a fixed threshold value for region growing which is initialized with the cycloid centres. Refika and Bulent introduced a new approach for polyp localization in colonoscopy images (Doğan and Yilmaz 2018). They used vascularization density feature on the tissue surface for the localization of the polyp site on colonoscopy images. Tumour vascularization is closely related to tumour growths.

CNN or convolutional neural network is a well-defined deep learning technique under computer vision paradigm. Many new problems are solved using CNN, which

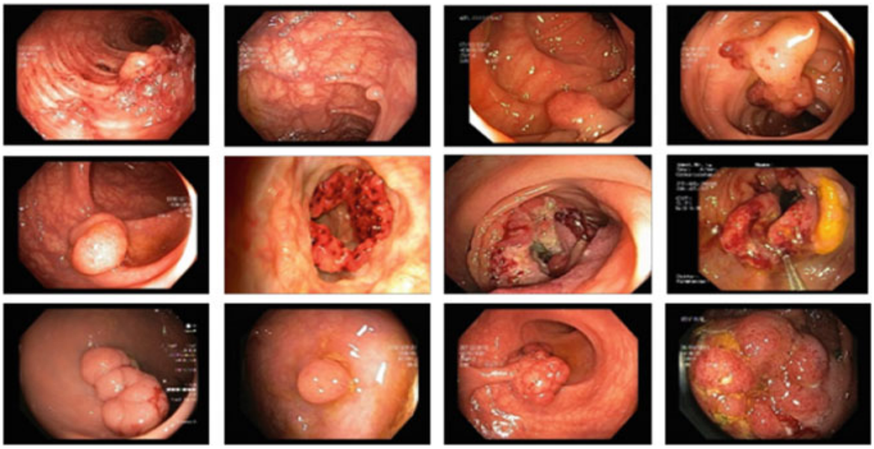

Fig. 3 Sample colonoscopy images with various types of polyps are present (https://www.shutterstock.com/video/clip-5591762-intestine-cancer-virtual-colonoscopy)

is considered as the basis of different computer vision applications (object detection, image segmentation, etc.). Mojtaba Akbari et al. used fully convolutional network (FCN) for polyp segmentation from colonoscopy images (Akbari et al. 2018). Computer-aided detection is another approach for polyp detection. Nima et al. used this technique (Tajbakhsh et al. 2016) by applying hybrid context-shape approach. They used edge detection and edge classification techniques as fulfilment of the same. Atreyee and Aditya have worked to detect liver cancer purely based on image processing techniques (Dutta and Dubey 2019). They obeyed image pre-processing, de-noising, and segmentation of MRI image.

3 Proposed Workflow

3.1 Data Collection

We have started our experiment with commonly available open-source images. These images consist of different types of polyps with various shapes and arbitrary locations. Few sample colonoscopy images are shared in Fig. 3.

3.2 Pre-processing

With the aim of improving the image quality by enhancing some of its features, this is a very standard process adhered in almost every image processing related work. Our pre-processing step starts with scaling or resizing of the input images to consider a fixed size. Next step of pre-processing was grayscale conversion of the resized image. Our next step was to apply a suitable thresholding technique, and to do so, we considered Otsu's method for automatic image thresholding. The basis of Otsu's method is greyscale image, what we already prepared.

Otsu's theory assumes that the image contains two level of pixel which are foreground pixel and background pixel (bi-modal histogram) and calculates the optimum threshold by separating them into two classes. We considered Otsu's theory described in the paper (https://www.shutterstock.com/video/clip-5591762-intestine-cancer-virtual-colonoscopy) as follows. Assuming an image is represented in L grey levels [0, 1, …, $L-1$]. The number of pixels at level i is denoted by n_i, and the total number of pixels is denoted by $n_1 + n_2 + \cdots + n_L$. The probability of grey level i is denoted by as follows:

$$p_i = \frac{n_i}{N}, \quad p_i \geq 0, \quad \sum_{0}^{L-1} p_i \tag{1}$$

In the bi-level thresholding method, the pixels of image are divided into two classes C_1 with grey levels [0, 1, …., t] and C_2 with grey levels [$t+1$, …., $L-1$] by the threshold t. The grey level probability distributions for the two classes are given as:

$$w_i = P_r(C_1) = \sum_{i=0}^{t} p_i \text{ and } w_2 = P_r(C_2) = \sum_{i=t+1}^{L-1} p_i \tag{2}$$

The means of the two classes C_1 and C_2 are as follows:

$$u_1 = \frac{\sum_{i=0}^{t} i p_i}{w_1} \text{ and } u_2 = \frac{\sum_{i=t+1}^{tL-1} i p_i}{w_2} \tag{3}$$

The total mean of grey levels is denoted by u_T is as follows:

$$u_T = w_1 u_1 + w_2 u_2 \tag{4}$$

Then, the class variances are described below:

$$\sigma_1^2 = \frac{\sum_{i=0}^{t} (1-u_1)^2 p_i}{w_1}, \quad \sigma_2^2 = \frac{\sum_{i=t+1}^{L-1} (1-u_2)^2 p_i}{w_2} \tag{5}$$

Finally, the within-class variance (σ_W^2) becomes:

$$\sigma_w^2 = \sum_{k=1}^{N} w_k \sigma_k^2 \tag{6}$$

Between-class variance (σ_B^2) becomes:

$$\sigma_B^2 = w_1(u_1 - u_T)^2 + w_2(u_2 - u_T)^2 \tag{7}$$

The total variance of grey levels becomes:

$$\sigma_T^2 = \sigma_W^2 + \sigma_B^2 \tag{8}$$

Otsu method chooses the optimal threshold t by maximizing the between-class variance, which is equivalent to minimize the within-class variance, since the total variance (the sum of the within-class variance and the between-class variance) is constant for different partitions. Final objective function obtained by Otsu method is mentioned below:

$$\begin{aligned} t &= \arg\left\{\max_{0\le t\le L-1}\left\{\sigma_B^2(t)\right\}\right\} \\ &= \arg\left\{\min_{0\le t\le L-1}\left\{\sigma_W^2(t)\right\}\right\} \end{aligned} \tag{9}$$

3.3 *Image Segmentation*

Image segmentation is the process of partitioning an image into multiple segments. This may include visualization, estimation of volume of the interest object, detecting abnormalities like tumours, polyps, etc. We used marker-controlled watershed segmentation process to identify the area of cancer cells present in the colon in the input colonoscopy image.

The concept of watersheds is well known in topography, and it is a morphological-based method of image segmentation. The gradient magnitude of an image is considered as a topographic surface for the watershed transformation. The complete division of the image through watershed transformation relies mostly on a good estimation of image gradients. The result of the watershed transform is degraded by the background noise and produces the over segmentation. Also, under segmentation is produced by low contrast edges generate small magnitude gradients, causing distinct regions to be erroneously merged (Bernal et al. 2012). Different approaches may be employed to use the watershed principle for segmentation. Local minima of the gradient of the image may be chosen as markers; in this case, an over segmentation is produced, and a second step involves region merging. Marker-controlled watershed transformation makes use of specific marker positions which have been either explicitly defined by the user or determined automatically with morphological operators or other ways. It is comprised of the following steps: compute a segmentation function; compute foreground markers—these are connected blobs of pixels within each of the

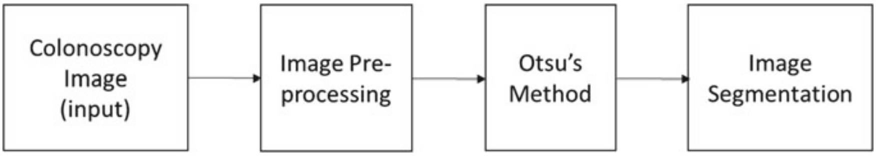

Fig. 4 Basic block diagram

objects; compute background markers: these are pixels that are not part of any object; modify the segmentation function, so that it only has minima at the foreground and background marker locations; compute the watershed transforms of the modified segmentation function.

The locations, which are extracted by this process, are then set to the minimum position within the same topological surface. Separating objects of an image is one of the difficult methods which watershed segmentation simplifies. Image segmentation use watershed transform to locate the foreground and background object location. Image feature extraction is one of the most important technique of image processing. This stage enhances the segmented area of the image by superposing it on the original colour image. It also uses different techniques and algorithm to isolate and detect various shapes and portions of the image. Our overall flow becomes as in Fig. 4.

4 Results and Conclusion

4.1 Experimental Results

This section illustrates the result obtained in different stages of our work. For the below colonoscopy image (Fig. 5a), there is a big polyp region with irregular shape—some portions are thin and some are fat. There is also colour mismatch in the polyp region with respect to the non-polyp region. Again, in the polyp region also, combinations of red and black spots are present. Then, Otsu's transformation is done to obtain the following thresholded result (Fig. 5b). After Otsu's transformation,

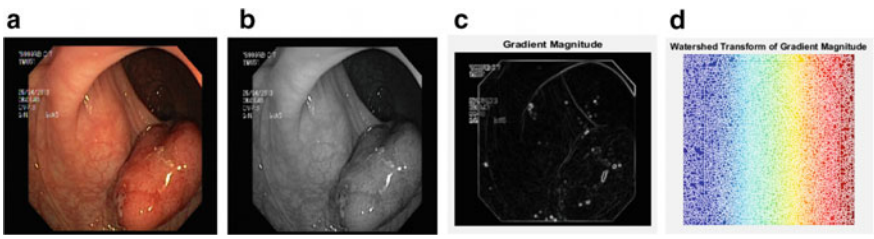

Fig. 5 **a** Input colonoscopy image. **b** Output image by Otsu's transformation. **c** Output of gradient magnitude. **d** Watershed transform of gradient magnitude

gradient magnitude was taken as a segmentation function to obtain the following result (Fig. 5c). Gradient magnitude is a deterministic approach which is basically used in edge detection. The image is segmented by using watershed transform to get the following result (Fig. 5d). In the next step, opening and closing by reconstruction are done on gradient magnitude output. It is a combination customized erosion and dilation techniques of image processing. By applying these dark spots, bold marks have been removed (Fig. 6a–d). Morphological techniques—"opening by reconstruction" and "closing by reconstruction" have been used as a cleaning procedure, i.e. to enhance the image quality. To compute the foreground markers, regional maxima is done (Fig. 6e).

Then, regional maxima is superimposed on the original image to create the basis of the detection. For our case, it is to create the basis or interpretation of the polyp region detection. This is shown in Fig. 7a, b.

As a visualization technique, markers with object boundaries are directly superimposed on the original image (Fig. 8a). Coloured watershed label matrix is another supporting intermediate step to get the final result (Fig. 8b). For the colour image, colour labels are being superimposed transparently on the original result. This is the final step to produce the desired segmented region as shown in Fig. 8c.

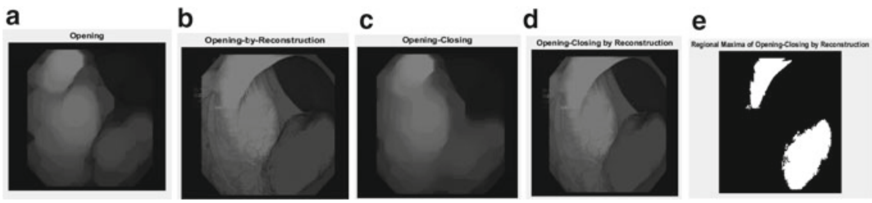

Fig. 6 **a** Opening algorithm. **b** Opening by reconstruction. **c** Opening-closing algorithm. **6** Opening-closing by reconstruction. **e** Regional maxima of opening-closing by reconstruction

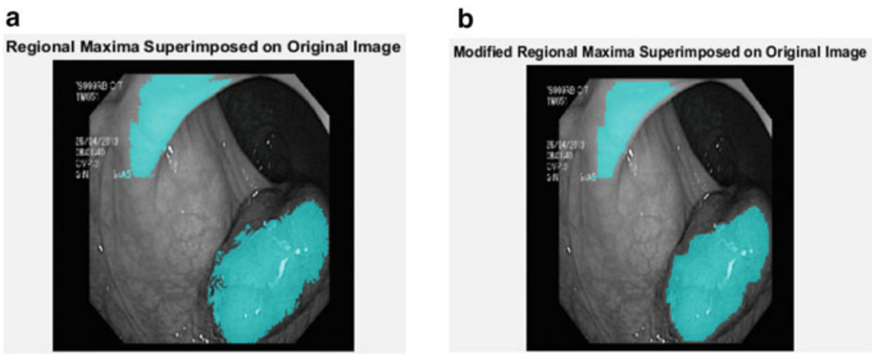

Fig. 7 **a** Regional maxima superimposed on original Image. **b** Modified regional maxima superimposed on original image

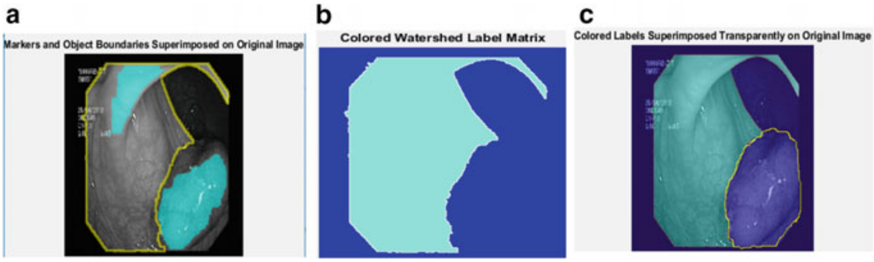

Fig. 8 **a** Markers and object boundaries superimposed on original image. **b** Colored watershed label matrix on original image, **c** Coloured labels superimposed transparently on original image

Finally, in the result, polyp regions have been detected successfully from arbitrary input images. Hence, two results are shared in Fig. 9a, b.

4.2 Conclusion and Future Scope

Different colonoscopy images are acquired from the open source in Internet (https://www.shutterstock.com/video/clip-5591762-intestine-cancer-virtual-colonoscopy). Basic Otsu's pre-processing technique is used. For segmentation technique, marker-controlled watershed segmentation is used, and it is observed that for all the images, segmentation is performed accurately. In this paper, we proposed segmentation method to detect the area of cancer affected cells (polyp region). Hence, the accuracy factor is around 88–93%. There are some non-polyp regions are also getting covered for few sample colonoscopies images (Fig. 10). The accuracy factor has been calculated by checking the average pixel count of the detected polyp region, with respect to the entire image.

Our future aim is to create a practical and automatic solution for the healthcare industry. So, we have targeted to detect individual polyps from the region of a cancer affected cells of the colon with high accuracy, i.e. removing the void or non-polyp region. There is also a significant scope to use AI techniques—powered by deep learning-based semantic segmentation to detect the polyp region.

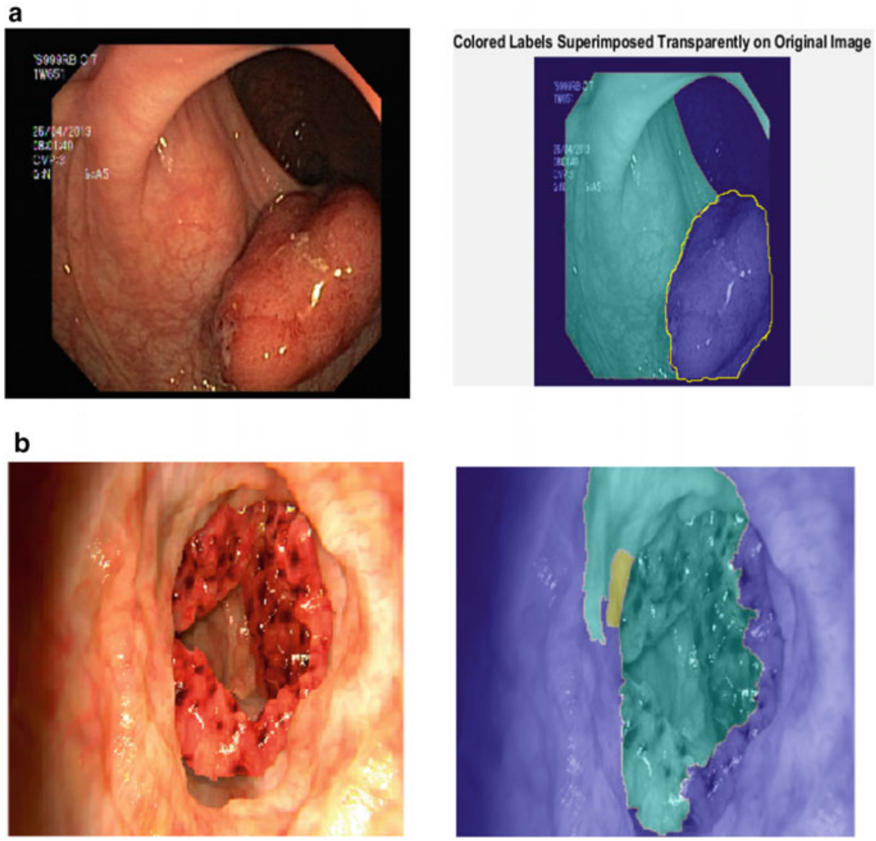

Fig. 9 **a** Input image—1 (left), result (right)—segmented polyp region. **b** Input image—2 (left), result (right)—segmented polyp region

Fig. 10 Void area shown in the polyp detected region from Fig. 9b

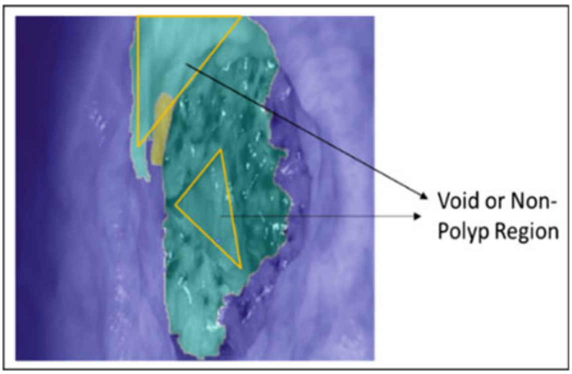

References

Akbari M, Mohrekesh M, Nasr-Esfahani E, Reza Soroushmehr SM, Karimi N, Samavi S, Najarian K (2018) Polyp segmentation in colonoscopy images using fully convolutional network. IEEE, pp 69–73

Bernal J, Sánchez J, Vilariño F (2012) Towards automatic polyp detection with a polyp appearance model. Pattern Recogn 45(9):3166–3182

Doğan RS, Yilmaz B (2018) Polyp localization in colonoscopy images using vessel density. IEEE

Dutta A, Dubey A (2019) Deon of liver cancer using image processing techniques. In: International conference on communication and signal processing, pp 0315–0318, April 4–6

https://www.shutterstock.com/video/clip-5591762-intestine-cancer-virtual-colonoscopy

Siegel RL, Miller KD, Fedewa SA, Ahnen DJ, Meester RGS, Barzi A, Jemal A (2017) Colorectal cancer statistics. CA. Cancer J. Clin. 67(3):177–193

Tajbakhsh N, Gurudu SR, Liang J (2016) Automated polyp detection in colonoscopy videos using shape and context information, vol 35, no 2. IEEE, pp 630–644

Tarik G, Khalid A, Jamal K, Benajah DA (2016) Polyps's region of interest detection in colonoscopy images by using clustering segmentation and region growing. IEEE, pp 455–459

Fabrication and In Vitro Testing of Bio-synthetic Patch for Burn Wounds

Vaibhavi Sonetha, Madhura Deshmukh, Dhwani Teli, Prashali Vichare, Dharak Dave, Hinal Shah, Raj Shah, Shreya shetty, Sejal Gothi, Vineeta Khanapuri, and Kartikee Dhokar

Abstract *Objective* Traditional gauze dressings, occlusive, and transparent film dressings for treating burns cause discomfort to patients either due to sepsis formation or by undesirable skin adherence. This study focuses on fabricating and evaluating a biocompatible patch for the treatment of burn wounds which can promote re-epithelization, reduce healing time, prevent scarring and eschar formation, avoid septicemia, and reduce patient's discomfort. *Methods* The proposed patch is bi-layered. The top layer made of polydimethylsiloxane acts as the mechanical support and the bottom layer is a drug matrix with antibacterial drug silver (I) sulfadiazine incorporated in it. *Results* The fabricated patch is evaluated for various parameters related to wound healing such as the release of the drug, swelling index, bio-adhesion, and ability to kill pathogens. *Conclusion* The evaluated parameters depicted that the patch was quite efficient for treatment and its design has an advantage over the current treatments available. *Significance* The unique design of the patch and ease of application can make it popular for use among patients.

Keywords Burns · Patch · Re-epithelization · Antibacterial · Wound healing · Silver (I) sulfadiazine

1 Introduction

Burns are tissue damage resulting from overexposure to heat, solar radiation, and chemical/electrical contact. They are painful and complex to handle and treat. They are mainly categorized into three: first degree, second degree, and third-degree burns. First degree burns are epidermal burns and resolve in 3–5 days without scarring. Second degree and third-degree burns involve the epidermis and a portion of the dermis. It takes about 3–6 weeks for the wound to heal. Current treatments like gauze dressings and occlusive dressings often lead to scarring and discomfort to the patients. Few treatments like biobrane provide re-epithelization, but lack antibacterial

V. Sonetha (✉) · M. Deshmukh · D. Teli · P. Vichare · D. Dave · H. Shah · R. Shah · S. shetty · S. Gothi · V. Khanapuri · K. Dhokar
Department of Biomedical Engineering, Dwarkadas J Sanghvi College of Engineering, Mumbai, Maharashtra, India

M. Mukherjee et al. (eds.), *Advances in Medical Physics and Healthcare Engineering*, Lecture Notes in Bioengineering, https://doi.org/10.1007/978-981-33-6915-3_24

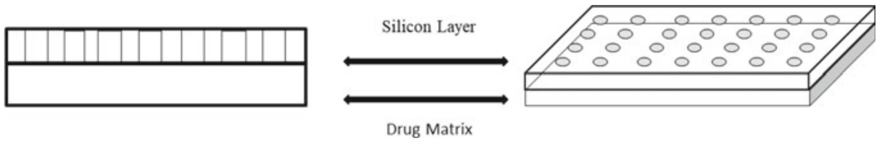

Fig. 1 Schematic of burn wound healing patch

property which may lead to sepsis formation (Bairagi et al. 2019). Other treatments like Acticoat have antibacterial drugs but lack re-epithelization property often leading to scarring at the wound site (Aziz et al. 2012). Hence, there is a need for an efficient burn wound healing solution which reduces healing time, patient discomfort, and prevents sepsis formation.

2 Design

The design consists of a bi-layered patch in which the top layer acts as a mechanical support and the bottom layer is a drug matrix with antibacterial drugs incorporated in it. The top layer is made up of silicone elastomer (polydimethylsiloxane). The drug matrix consists of chitosan and gelatin which have effective re-epithelization properties. The drug used in this patch is Silver (I) Sulfadiazine (SSD), which is a topical formulation consisting of silver nanoparticles and is proven to be effective in healing burn wounds Munteanu et al. (2016). Figure 1 shows the schematic of burn wound healing patch.

3 Method

Silver (I) Sulfadiazine (SSD) of 98% purity was purchased from Malti Enterprises (Mumbai, India) (Lazovic et al. 2005). Chitosan was purchased from Otto Chemie Pvt. Ltd. (Mumbai, India) (Cheung et al. 2015). The pH range is 7 to 9. Gelatine 240 Bloom was purchased from Rajesh chemicals (Lazovic et al. 2005). Butylated Hydroxyanisole (BHA) from Omkar Chemicals Pvt. Ltd. (Mumbai, India). The optimum formulation found out is SSD 1% w/w; chitosan 1% w/w; gelatin 10% w/w; BHA 0.02% w/w; and PEG 400 2% v/v. The drug matrix of the patch is formulated in 2% glacial acetic acid. The silicon top layer is fabricated using the casting technique.

The negative aluminium mould is fabricated using CNC micromachining of dimensions 80 mm in length, 40 mm wide, and 1 mm depth as shown in Fig. 2. The mould has cylindrical rods of 2 mm height and 1 mm diameter at the offset of 12.7 mm from respective centres to provide ventilation.

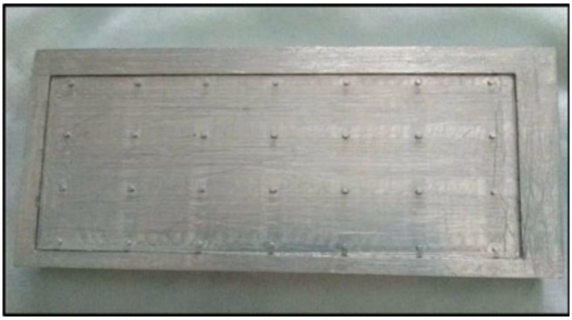

Fig. 2 Aluminium mould for silicon layer

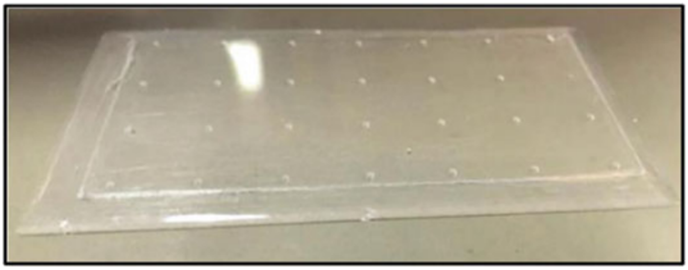

Fig. 3 Silicon top layer

The silicon top layer is cast moulded by pouring a mixture of silicone elastomer and its curing agent in 10:1 proportion and heating at 150 °C for 20 min. The PDMS layer is then peeled off from the mould as shown in Fig. 3.

The drug matrix consists of chitosan, gelatine, SSD, and antioxidant BHA and plasticizer PEG 400. It is formulated in 2% glacial acetic acid. The solution is poured in an aluminium mould of dimensions 80 mm length, 40 mm width, and 2 mm depth. The mould is then placed in an oven at 45 °C for 1 h. The patch is peeled from the mould after drying, which forms the bottom layer.

The silicon top layer is hydrophobic and hence the drug matrix does not adhere to it. The silicon top layer is placed in the plasma asher at 70 W for 10 min to make it hydrophilic. The drug matrix will then adhere to the hydrophilic surface of the silicon top layer as shown in Fig. 4.

4 Testing and Result

4.1 In Vitro Drug Release Study

The drug release study is performed by using Franz diffusion apparatus in phosphate buffer solution (PBS) of pH 7.4. A definite area of the patch is placed in the donor

Fig. 4 Bio-synthetic patch for burn wound

compartment of the Franz diffusion cell. A 1 ml sample is withdrawn at periodic intervals and absorbance is obtained at 250 nm by UV–VIS spectrometry. The same procedure is performed on the placebo set as a blank.

4.2 Swelling Index Study

The drug matrix layer should show good swelling and water holding capacity. This is measured by the swelling index (SI) of the formulation. It is defined as the percentage of fluid absorbed by the patch at equilibrium. The pre-weighed sample of the patch is soaked in a PBS solution (pH 7.4) at room temperature. Soaked samples were removed after 24 h and excess liquid is removed after bloating. The sample is then weighed (Wojcik and Gawriuczenkow 2017). Swelling index of the patch is calculated using the following formula (1).

$$\%\ \text{Swelling Index (SI)} = [(W2 - W1)/W1] \times 100 \tag{1}$$

$W1$ and $W2$ are the weights of the patch before and after swelling, respectively.

4.3 Minimum Inhibitory Concentration Study

The antimicrobial effect of the formulation was checked by the agar diffusion technique. Silver sulfadiazine is an antibacterial agent and possesses activity against a wide range of gram-positive and gram-negative bacteria. It also shows activity against fungi strains. Therefore, the formulation is checked for its antibacterial activity against bacteria such as Escherichia coli and Staphylococcus aureus. The result of the formulation is compared to the placebo formulation and marketed cream (Chikezie 2017). The setup for this study is shown in Fig. 5.

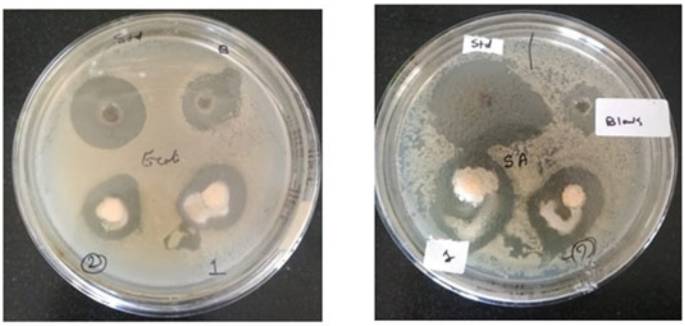

Fig. 5 Experimental setup of MIC study

4.4 Bio-adhesion Study

It is a measure of force needed to overcome the adhesive bond between the patch and biological tissue. This is carried out by in-house pulley system and weight required to detach the sponge from pig ear skin was recorded. The bio-adhesive strength was calculated by the formula given below:

$$\text{Bio-adhesive strength} = \text{weight required (g)}/\text{Area}\left(\text{cm}^2\right) \quad (2)$$

5 Results and Discussion

Figure 6 shows the in vitro drug release study of the patch. A sustained drug release is observed for three hours. The release of SSD in PBS is found to be 8.4%, 22.3%, 28.16%, and 33.5% in 30 min, 1 h, 2 h, and 3 h, respectively.

The swelling index of the patch is found to be 1624.05% in 24 h. $W1$ is 13.62 g and $W2$ is 0.79 g. This indicates that moisture retaining capacity of the patch is high and will prevent fluid exudation and eschar formation.

The patch formulation showed a better antimicrobial effect than marketed 1% silver (I) sulfadiazine creams. Placebo formulation also provides an antimicrobial activity to some extent.

The bio-adhesion study result is 48 mg/cm^2. This will provide sufficient adhesivity of the patch to the wound site.

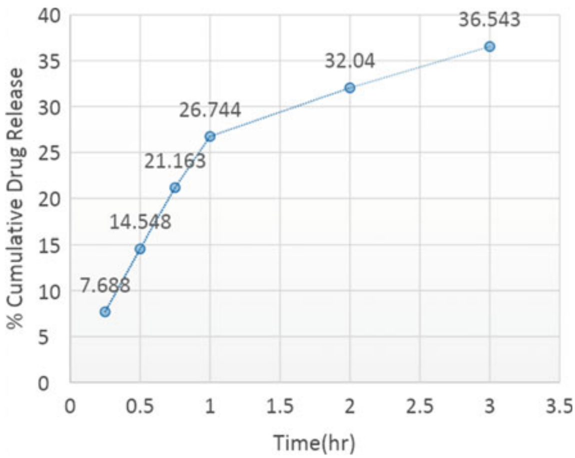

Fig. 6 Graph of % CDR of SSD from patch versus time in PBS (pH 7.4)

6 Conclusion

The traditional and current treatments for treating burn wounds are not idealistic as they cause discomfort to the patient as well as take a very long healing time with the risk of eschar and sepsis formation. A bi-layered burn wound healing patch is designed that aims at reducing the complications of treating burn wounds while keeping the patient's comfort in mind. It provides ventilation, re-epithelialization and prevents sepsis, scar, and eschar formation. The patch consists of a silicon top layer and a drug matrix as the bottom layer. The top layer is perforated, insoluble, and hydrophobic which provides stability and strength to the drug matrix beneath it. The drug matrix layer consists of chitosan, gelatine, and SSD. Chitosan helps in haemostasis and tissue regeneration, gelatine regulates repair of extracellular matrix and avoids fluid loss, SSD being an antimicrobial agent prevents sepsis formation (Fong and Wood 2006). The materials used in the patch are degradable and biocompatible. The patch can be used for a deep second degree and third-degree burn wounds. The patch needs to be further tested for drug kinetics, moisture loss, folding endurance, blood compatibility, biodegradability, mechanical strength, and wound healing in animals.

Acknowledgements We are thankful to Dr. Vaibhavi A. Sonetha for guiding us throughout the research. We gratefully acknowledge the help of Dr. Bhanuben Nanavati College of Pharmacy, Mumbai. We are also thankful to the Indian Institute of Technology, Bombay, for providing us with equipment required throughout. We are grateful to the University of Mumbai for funding this project.

References

Aziz Z, Abu S, Chong N (2012) A systematic review of silver-containing dressings and topical silver agents (used with dressings) for burn wounds. Burns 38:307–318

Bairagi A, Griffin B, Tyack Z, Vagenas D, McPhail S, Kimble R (2019) Comparative effectiveness of Biobrane®, RECELL® Autologous skin Cell suspension and Silver dressings in partial thickness paediatric burns: BRACS randomised trial protocol. Burns & Trauma 7

Cheung R, Ng T, Wong J, Chan W (2015) Chitosan: an update on potential biomedical and pharmaceutical applications. Marine Drugs 13:5156–5186

Chikezie I (2017) Determination of minimum inhibitory concentration (MIC) and minimum bactericidal concentration (MBC) using a novel dilution tube method. Afr J Microbiol Res 11:977–980

Fong J, Wood F (2006) Nanocrystalline silver dressings in wound management: a review. Int J Nanomed 1:441–449

Lazovic G, Colic M, Grubor M, Jovanovic M (2005) The application of collagen sheet in open wound healing. Ann Burns Fire Disasters 18(3):151–156

Munteanu A, Florescu I, Nitescu C (2016) A modern method of treatment: the role of silver dressings in promoting healing and preventing pathological scarring in patients with burn wounds. J Med Life 9(3):306–315

Wojcik E, Gawriuczenkow I (2017) Determination of swell index and swelling pressure from suction tests—a case study of Neogene clays from Warsaw (Poland). Geological Quarterly

On Some Studies of Micro-strip Patch Antenna for Bio-Medical Applications

Arpita Santra, Arnima Das, Abhijit Kundu, Maitreyi R. Kanjilal, and Moumita Mukherjee

Abstract In recent researches on bio-medical sciences, stress has been given on the detection procedures where the systems need compact and suitable configuration to be flexible. In this research, idea importance has been extended on the designing of a suitable substrate integrated waveguide (SIW) micro-strip patch antenna suitable in the Ka band. The Ka band has been taken because many of the bio-medical accelerators require this band flexibility. Ansoft HFSS software has been used for the simulation study. Our prime objective is to validate the proposed antenna for the bio-medical application.

Keywords Bio-medical · Micro-strip · Substrate integrated waveguide

1 Introduction

1.1 Bio-medical Accelerators

Ion sources support wide applications of ion beams by providing a stable supply of ions to accelerators. Medical applications of ion accelerators are classified into two categories: treatment and diagnosis. Radiation has unique characteristics of penetration and biological effects. Since radiation was discovered a century ago, tons

A. Santra (✉) · A. Das · M. R. Kanjilal
Narula Institute of Technology, 81, Nilgunj Road, Agarpara, Kolkata, West Bengal 700109, India
e-mail: arpita.santra@nit.ac.in

A. Das
e-mail: arnima.das@nit.ac.in

M. R. Kanjilal
e-mail: maitreyi.kanjilal@nit.ac.in

A. Kundu
Chaibasa Engineering College, Chaibasa, Jharkhand, India

M. Mukherjee
Adamas University, Kolkata, West Bengal 700126, India

M. Mukherjee et al. (eds.), *Advances in Medical Physics and Healthcare Engineering*, Lecture Notes in Bioengineering, https://doi.org/10.1007/978-981-33-6915-3_25

of effort have gone into applying these characteristics to treat deep-seated tumors. Technological advancements of radiotherapy focused only on the issues of the way to deliver a sufficient dose to a tumor and the way to decrease damage to normal organs surrounding the tumor to the as low as possible level. The dose concentration depends on the type of radiation. Charged-particle radiotherapy is a crucial treatment method; in it, the accelerated ionic beam itself is getting used for patient treatment. The great localized physical dose distribution given by charged particles was known since the 1940s, and it had been long expected to be utilized for radiotherapy. However, demonstration of the treatment took much time because accelerator performance was not sufficient until the 1950s. Today, two distinctly different radiotherapy methods are being applied: protons or heavy ions (mostly carbon ions). The essential difference between these two methods is that the biological effectiveness on tumors. The relative biological effectiveness (RBE) of proton beam is almost one; it is almost same as RBE of x rays. On the opposite hand, the RBE of a heavy-ion beam is increased to 2–4 round the culmination of the particles. This advantage comes from the high linear energy transfer of heavy ions. Another example of the heavy-ion beam treatment method is boron neutron capture therapy (BNCT). BNCT also gives an honest localized dose distribution through a singular process. A patient receives the injection of a drug that contains boron atoms in its formula. The drug features a special characteristic that it concentrates during a tumor. When the patient is irradiated with neutrons from outside, the boron atom captures a neutron and decays to alpha and Li particles. Since these particles have a brief range, they provide an outsized dose only near the concentration point of the drug. Neutrons are presently produced by reactors, but it is expected that reactors are often replaced with proton accelerators. The production of radiopharmaceuticals is additionally a crucial role for medical accelerators, and it is an extended history. In vivo diagnostic methods like single photon emission computerized tomography (SPECT) or positron emission tomography (PET) have rapidly spread worldwide. On the opposite hand, in vitro diagnostic approaches using ^{125}I or ^{59}Fe have gradually declined. Combinations of devices are important. As for ion sources, requirements for medical applications are beam intensity, stability (both short and long term), reproducibility, simplicity of operation, convenience of maintenance, reliability, and safety. It is a substantial issue the way to obtain the above performance at an inexpensive cost within the case of a treatment facility; the irradiation cannot be aborted or retried which makes reliability and safety the foremost important requirements.

Here, we have considered the design of micro-strip patch antenna to be utilized for radiation therapy.

1.2 Design of the Antenna

In current status of medical science, the requirements for compact and flexible detection instruments are increasing day to day. Ka band is usually referred to the frequencies between 26 and 40 GHz whose wavelengths range from 1.11 to 7.5 mm.

Fig. 1 Common SIW structure

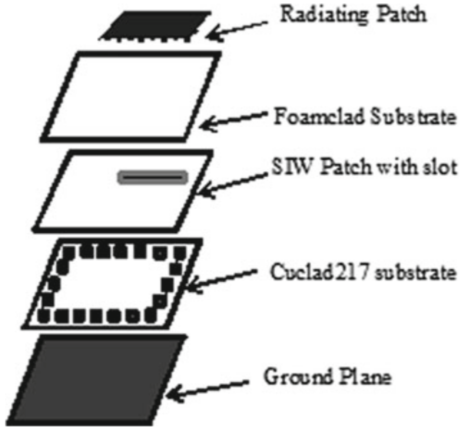

The modeling and characterization of the planar rectangular waveguide are now possible by a newly promising technology called substrate integrated waveguide technique (SIW), developed by Wu (2001).

The substrate integrated waveguide (SIW) offers several advantages over the classic all-metal waveguide, such as a low profile, a lightweight, a planar structure, and ease of integration with other planar circuits on the same substrate. The SIW structure gives a platform to substrate integrated circuits (SICs), as it is compatible to integrate all microwave and millimeter wave active and passive components on the same substrate, such as the oscillators, amplifiers, filters, couplers, antennas, etc.

The SIW technology also gives conformability in the system design. The commonly used SIW structure has been shown in Fig. 1. In this structure, the ground plane is associated with one substrate, and on the top of this layer, a layer of slot along with another substrate layer is attached, and the patch is attached on the top of all these layers giving a final SIW structure.

1.3 Characterization of the Antenna

The SIW is composed of densely arranged metallic posts that realize the bilateral edge walls (Che et al. 2008) as shown in Fig. 1. The basic parameters of the SIW are the distance between the two parallel metallic vias, i.e., the width of the waveguide 'a', diameter of metallic vias 'd' distance between two consecutive vias 's'. The width 'w' of the SIW can be determined by formula (Cassivi et al. 2002) in Eq. 1.

$$w = a - \left\{\left(d^2\right)/(0.95s)\right\} \tag{1}$$

The high Q property of SIW cavities can be improved with the use of frequency selective surfaces (FSS) on its cavity. The SIW-FSS (Deslandes and Wu 2006) leads to the advantages of low insertion loss; hence, high Q-factor (Che et al. 2008) will be due to the closed cavity nature, as in the conventional FSS.

2 Results

The plot of S_{11} shows that the simulated antenna can be utilized in the Ka band as it shows in Fig. 2 suitable frequency response near 30 GHz. Also the radiation pattern has been shown in Fig. 3.

In Fig. 3, the radiation pattern of the simulated antenna is showing a characteristics which is near to the doughnut shape; so, we can use this antenna with 90° tilt for the radiation therapy in this frequency range of 30 GHz.

In Fig. 4, the directivity is shown, and it is relevant to the application in terms of bio-medical accelerators, so we can rely on this antenna and may use this for radiation therapy.

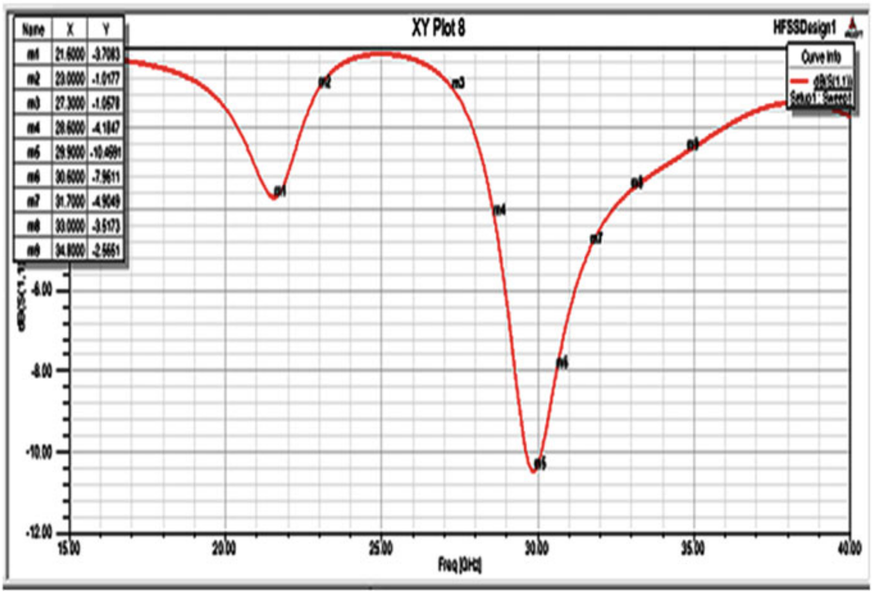

Fig. 2 Frequency versus S_{11} plot of the simulated antenna

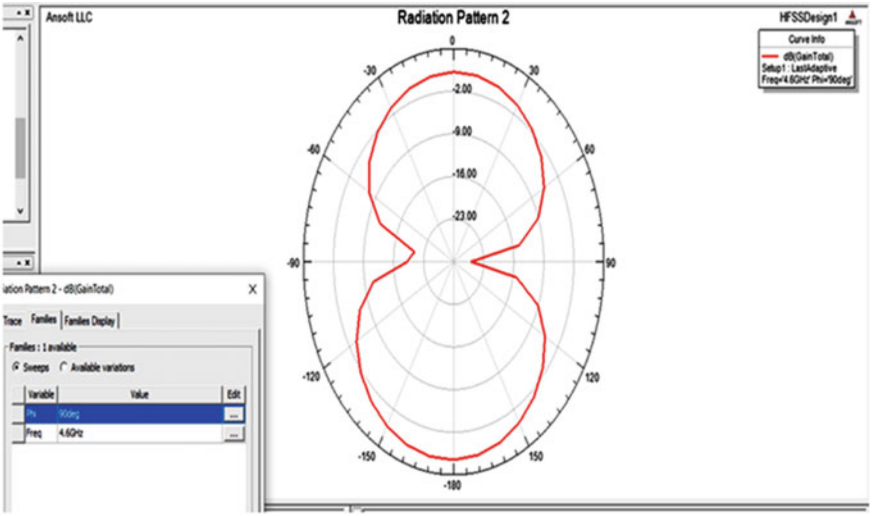

Fig. 3 Radiation pattern at 90° of the simulated antenna

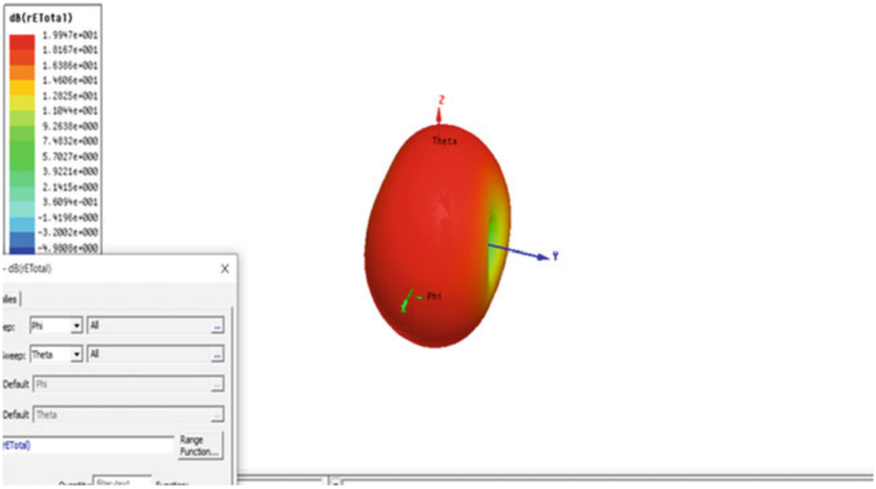

Fig. 4 Directivity of the simulated antenna

3 Conclusion

The proposed antenna can radiate along the length of the guided structure uniformly and continuously which will be a suitable characteristics leading to bio-medical applications. It has been observed that SIW-based antennas in the modern wireless system open new era for the development of highly compact and integrated systems.

Our proposed antenna is validated with all required characteristics, and the antenna is suitable for application in bio-medical accelerators.

References

Cassivi Y, Perregrini L, Arcioni P, Bressan M, Wu K, Conciauro G (2002) Dispersion characteristics of substrate integrated rectangular waveguide. IEEE Microw Compon Lett 12(9):333–335

Che W, Deng K, Wang D, Chow YL (2008) Analytical equivalence between substrate-integrated waveguide and rectangular waveguide. IET Microwaves Antennas Propag 2(1):35–41

Deslandes D, Wu K (2006) Accurate modeling, wave mechanisms, and design considerations of a substrate integrated waveguide. IEEE Trans Microwave Theory Tech 54(6):2516–2526

Wu K (2001) Integration and interconnect techniques of planar and nonplanar structures for microwave and millimeter-wave circuits-current status and future trend. In: Microwave conference (APMC' 01), pp 411–416

Pre-transfusion Blood Testing Device

Antara Dandekar, Samiksha Save, Siddhi Bhandarkar, Milparnika Desai, Jinang Shah, Priyank Lapsia, Malay Bhagat, Rutuja Zinjal, Preeta Shah, Nomi Shital, Sasha Hakhu, Shreya Nair, Manali Salvi, and Mrunal Rane

Abstract Our device is meant to test compatibility between two similar blood groups (Schmidt et al. in Physiologie des Menschen: mit Pathophysiologie. Springer, Heidelberg, 2011). Clumping reaction may occur even with blood transfusion between the same blood groups. Due to unaccounted antibodies on the RBCs, the patient may develop certain reactions which if untreated could be fatal. Therefore, there is a need for a method or device that can perform this testing on two blood groups to be tested, check the degree of compatibility and produce immediate results. The device will be a point-of-care testing (POCT) device which would be able to replace the available time-consuming and expensive methods that are used to determine blood compatibility (https://www.sastra.edu/plasma/blood.pdf). Our project aims at addressing a problem not only prevalent in our country but also globally. The main aim is to make the device available in every government hospital in rural as well as urban areas.

Keywords Clumping · Antibodies · POCT · Blood compatibility

1 Introduction

Blood is one of the most important components in the human body carrying out the functions of immunity (Schmidt et al. 2011). If a person loses a large quantity of blood, this quantity of blood must be immediately regained (https://www.sastra.edu/plasma/blood.pdf). The required amount of blood has to be drawn out from a donor and given to the recipient. This life-saving process is called transfusion (https://www.unipune.ac.in/other_academics_and_serive_units). Before the blood is transfused into the patients, it needs to go through a series of tests. These tests determine the compatibility of the donor's blood. The patient's blood needs to be compatible (matched) with the donor's blood because, incompatibility results in a series of post-transfusion reactions like acute hemolytic reaction, delayed hemolytic reaction, febrile, allergic urticarial, allergic anaphylaxis, etc. in the patient's body which many

A. Dandekar · S. Save · S. Bhandarkar · M. Desai · J. Shah · P. Lapsia · M. Bhagat · R. Zinjal · P. Shah · N. Shital · S. Hakhu · S. Nair · M. Salvi (✉) · M. Rane
Biomedical Department, DJSCE, Vile-Parle (W), Mumbai 400056, India

M. Mukherjee et al. (eds.), *Advances in Medical Physics and Healthcare Engineering*, Lecture Notes in Bioengineering, https://doi.org/10.1007/978-981-33-6915-3_26

a time proves to be fatal. The technique used to determine the compatibility of blood is called blood cross-match. There are around 34 various blood grouping systems and 300 variants used all over the world. Though the most commonly used blood grouping systems are the ABO and Rhesus systems.

Apart from these blood groups, there exist many other blood grouping systems which are based on various other antigens (https://www.ncbi.nlm.nih.gov/pmc/articles/PMC4260296/). The antigens like Anti-K, which is most commonly used after antigen Rh; Duffy, which is found in plasma; Kidd, which are proteins found in the kidneys also affect blood compatibility. These are the antigens that come into the picture when we consider blood transfusion in two similar blood groups. Antibodies can affect the blood compatibility in two similar blood groups, as new antibodies are continuously being formed in the body, and also atypical antibodies, which are formed in the body after a previous transfusion. These factors affect blood compatibility in two similar blood groups, leading to hemolytic reactions, rashes, bacterial contamination and in adverse cases, even death.

Every year our nation requires about 4 core units of blood, out of which only a meager 40 lakhs units of blood are available. More than 38,000 blood donations are needed every day. A total of 30 million blood components are transfused each year (https://www.ncbi.nlm.nih.gov/pmc/articles/PMC4260296/). The aim of the project is to develop a rapid test method for testing the compatibility of a patient's blood and the donor's blood. Our innovation includes a strip cassette and a point-of-care testing (POCT) device, i.e., a reader which uses the biosensor strip for the measurement of the degree of compatibility. This new technology is one of its kinds, which would be able to replace the available time-consuming and expensive methods. We aimed at making the prototype of the strip. The strip will be the actual site of reaction. The reader is a user-friendly standalone device which is compact and sturdy in design with the ability to display accurate results in just a few minutes. We try to assess a problem not only prevalent in our country but also globally, widening the reach of innovation from domestic markets to international markets. Our aim is to make the device available in every government hospital in rural as well as urban areas. The technique used to determine the compatibility of blood is called blood cross-match (https://www.ncbi.nlm.nih.gov/books/NBK2267/https://en.wikipedia.org/wiki/Blood_type).

1.1 Tube Method

It is based on the principle of immuno–haematology. Agglutination is the clumping of particles, occurring when donor red blood cells and recipient's serum mixed together and indicates that the donor and recipient blood types are incompatible. This happens due to antigen-antibody reactions. In this method, sample suspension is prepared by mixing saline, recipient's serum and the donor's blood. Then, the mixture is allowed to incubate at 37 °C for 45 min. Then an agglutination catalyst known as Coombs sera is added. The clumping reaction between antigen-antibody occurs if the blood groups are incompatible (Fig. 1) (Swarup et al. 2008; https://en.wikipedia.org/wiki/coombs_test).

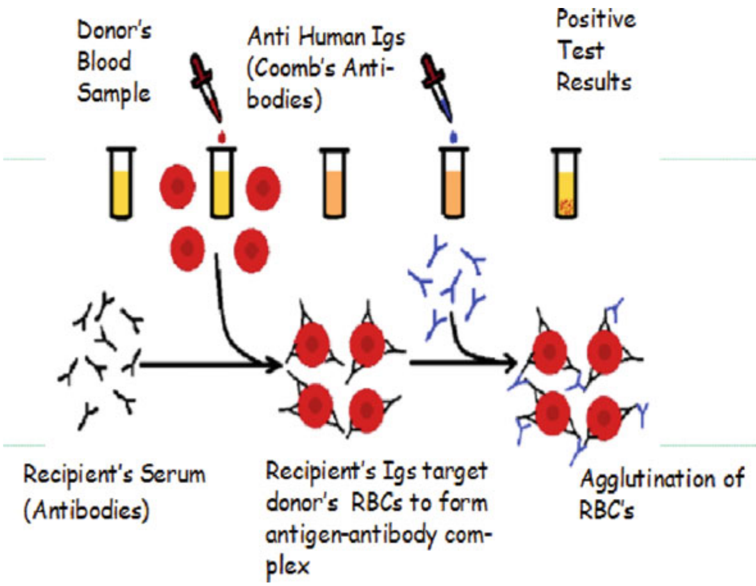

Fig. 1 Indirect Coomb's test (https://europepmc.org/backend/ptpmcrender.fcgi?accid=PMC2065689&blobtype=pdf)

Fig. 2 Gel-based method with DAT (Direct AHG test) card (https://rb.gy/wbiklr)

1.2 Gel-Based Method

The gel-based method facilitates the detection of immunoglobulin or complement bound to RBCs by using the DAT card. This method is shown to guarantee greater safety in blood transfusion with shorter incubation time, approximately 15 min. This is however comparatively very expensive. The competence of trained technologist is required to validate the results of the automated system in the gel-based method which is an added requirement for the procedure (https://europepmc.org/backend/ptpmcrender.fcgi?accid=PMC2065689&blobtype=pdf).

2 Materials and Methods

Existing methods to test blood compatibility are tube method and gel method (Swarup et al. 2008).

In our method, the sample suspension consisting of the mixture of donor and recipient's blood is poured onto the strip. The strip is designed in such a way that the clots and plasma will be separated. The isolated clumps will be brought to the reader patch of the strip where the RBG sensor module will transmit white light and detect the RGB content of the light reflected. The microcontroller controls the RGB sensor and the LCD screen where the degree of compatibility will be displayed. Since the values of the sensor change with change in the degree of compatibility, a fixed distance was kept between the strip and the sensor. The reader is a portable device working on a 5 V battery. The strip can be replaced and inserted smoothly and the output is shown on a LCD display. Along with this, the output can also be shown on a monitor via Bluetooth connectivity (future prospect).

(a) *Product Design, Strip prototype:* The strip consists of 3 layers as shown in Fig. 3. The membranes under consideration were Nitro Cellulose (NC) membrane of 0.45- µm pore size and steel membrane with 5-µm pore size. The size of RBCs is in the range 6–8 µm. Initially, the sample mixture is prepared by mixing the 10 µL donor's blood and 25 µL recipient's blood

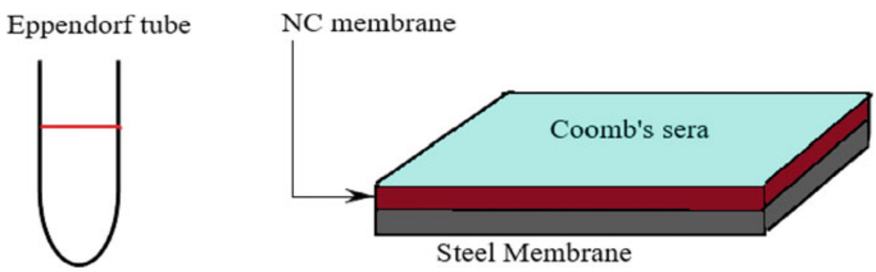

Fig. 3 Strip design

along with 1 mL saline is made by mixing them in the Eppendorf tube. The sample is then placed on the testing strip consisting of a base of 5-µm pore size steel membrane, over which a middle layer of NC membrane is placed. The membrane performs an important function of filtering out the serum (unreacted antibodies) as this may result in erroneous results. The strip has a final coating of Coomb's serum, which acts as a catalyst. If there are any unreacted antibodies, they may hinder the reaction between Coomb's serum and the RBCs which may produce false results. Properties of NC membrane filter include higher strength and flexibility with narrow pore size distribution and also increased temperature stability. The steel membrane provides necessary mechanical strength for the durability of the strip.

(b) *Reader*: The reader is constructed for measuring and displaying the degree of compatibility. The R, G, B (Red, Green, Blue) intensity of the resulting clump on the strip is measured. We have used RGB color sensor module TCS34725 (https://cdn-shop.adafruit.com/datasheets/TCS34725.pdf) which outputs a degree of compatibility (+1 up to + 4) proportional to the red color intensity of RBCs on a 16 * 2 LCD display. Arduino Nano is used as the microcontroller and is best suited because of its small size. It takes the input from the

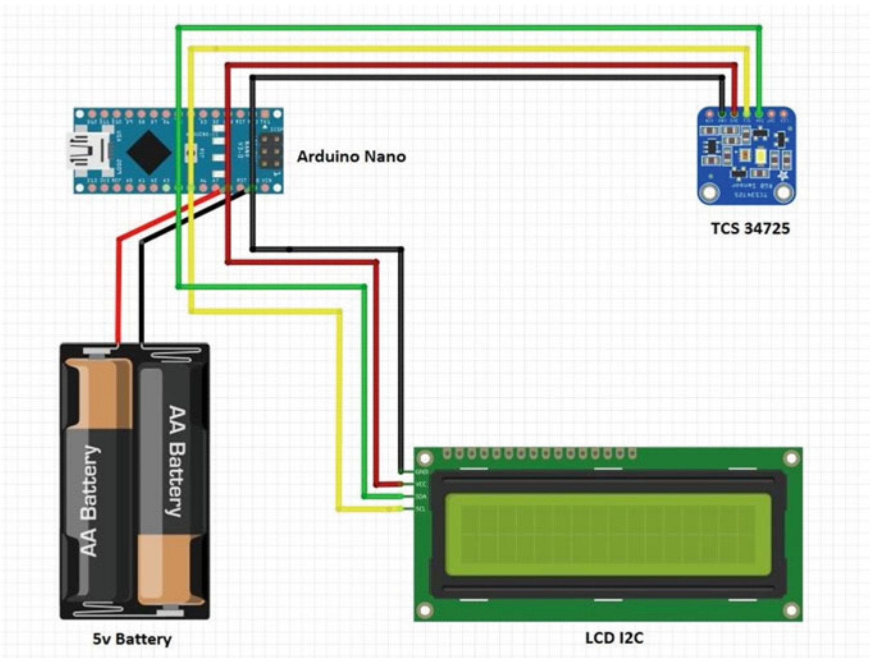

Fig. 4 Circuit diagram of the reader [prepared using fritzing software tool]

TCS34725 color sensor module, calibrates the degree of compatibility of the blood groups based on the clump formation's red color intensity and displays the result on the LCD. The choice of interface and measurement technique depends on the desired resolution and data acquisition rate.

3 Results

During the course of testing, it was found that the distance between the sensor and the strip affects the intensity of red color of the clot. Two different distances between the strip and the sensor were taken—1 and 2 cm. A total of 16 samples were tested both with the traditional tube method and the considered strip reader prototype for comparison. All the samples under consideration were Rh positive samples. Different readings of non-gel-based samples were taken on NC membrane: our method, as well as a glass Petri dish: traditional method. All the readings were taken at a fixed distance of 1 cm since the values were observed to be varying at varying distances. The readings indicate that there is a considerable amount of difference in the R-values of samples in Petri dish, and on NC membrane but the graph of both the methods follows the same line of graph. Thus, it can be concluded that the new strip and reader prototype method is comparable to the traditional tube method in terms of accuracy. A larger database with a greater number of blood group cross matches would help to determine the degree of compatibility and help in reader calibration.

4 Conclusion

We conclude that we have successfully built a prototype for the reader part of a rapid test for detecting the blood compatibility of patients and donors' blood. The reader design is complete and its housing is compact, portable and easy to use. The R, G, B (Red, Green, Blue) values (in OD) of the sensor change with the change in the intensity of light reflected by the blood. However, the change in the *R*-value is more substantial in comparison with the others, because of the color of the red blood cells.

Also, a database is to be built in order to make calibration of readings easier as display of degree of compatibility will be direct, instead of display of RGB values on the reader. A serial communication system and memory can be added to store the data on the hospital database as well. Design of an automated liquid handling system would enable batch testing of samples. The automated system could also help in avoiding even a slight chance of manual error in cases like sample preparation, sample dispensing, etc. We are trying to convert our research project into a commercial product. The highlight of this project is affordability. We use simple resources available in the market. For the strip, as NC membrane absorbs all clots, a membrane other than NC membrane which acts as a semi-permeable membrane that retains only the blood clots and filters out everything else can also be considered. Alginate gel

Table 1 Graph plotted with the blood groups on horizontal axis and its corresponding *R*-values plotted on the vertical axis. It shows a good amount of similarity in the line of graph in the R-values of the samples in petri dish—which is shown in red-colored line—and *R*-values of samples on NC membrane—which is shown in blue-colored line

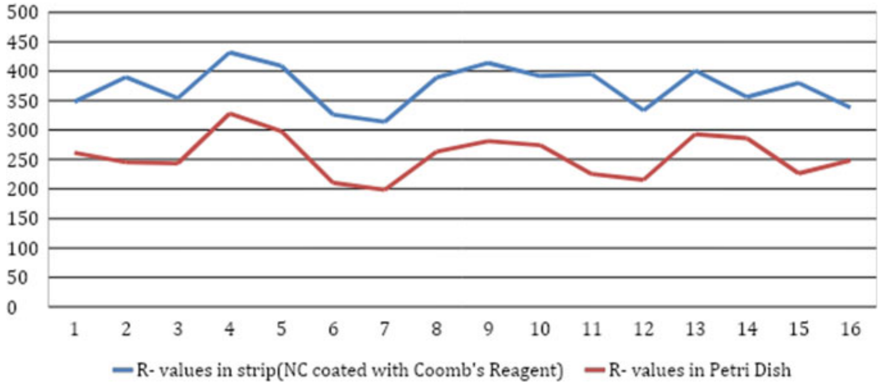

for making Coomb's gel, instead of the currently used method of gelatin is another possibility. This will guarantee that the gel stays intact even at room temperature. Coomb's gel testing with a 10um Steel membrane as well as NC membrane of pore size greater than 10 μm is to be done. The aim is to fabricate a cost-effective and efficient point-of-care testing device for checking blood compatibility within same blood groups prior to transfusion to ensure accuracy in readings and complete safety in blood transfusion-related procedures. We aim at making our device available to every hospital in the country.

References

Schmidt R, Lang F, Heckmann M (2011) Physiologie des Menschen: mit Pathophysiologie. Springer, Heidelberg. https://www.ncbi.nlm.nih.gov/books/NBK279392/

Swarup D, Dhot PS, Kotwal J, Verma AK (2008) A comparative study of blood cross matching using conventional tube and gel method. MJAFI 64(2)

Modeling of DC Motor-Based Dexterous Arm System Performance Study and Optimization Techniques

Swati Barui, Moumita Ghosh, and Biswarup Neogi

Abstract System development of arms control modeling with DC motor is the matter of interest. The researches and developments are going on the field that the gripper must be able to carry out a task effectively only when it is allotted with proper methods of grasping. The implementation of such includes various interrelated matters like design approach, rigidity, strength, position, motion and grasp control. So, the control model is very much required to propose measures for optimizing the control parameters without any interfacing with the machinist. The performance analysis of a dexterous arm model using optimization technique is the focused area of the present work. This approach would proceed toward the constancy to grasp by the application of a controlled force of the gripping. The parametric analysis is not limited to traditional tuning; advanced optimization techniques are adopted. The experimental perspective moves toward the development of artificial gripper to achieve consistency in given task by reducing the complexity.

Keywords Dexterous arm · DC motor · Tuning approach · Upper extremity · Optimization techniques

1 Introduction

Artificial arm is the most vital functional part of any automated robotic system. This portion is able to perform different gripping tasks such as adaptation, exploration, and pretension (Neogi 2011). To work with the artificial arm various elements are integrated and the information is relayed through. With the provision of control theory and optimization technique developmental approach toward the desired effect on the output of the system will be satisfied (Barui et al. 2016). The control and feedback constitute a compromise solution between the simplest clinical prosthetic hand and the more sophisticated dexterous robotic recommended in the paper of Scherillo

S. Barui (✉)
Electronics and Communication Engineering, Narula Institute of Technology, Kolkata, India

M. Ghosh · B. Neogi
Electronics and Communication Engineering, JIS College of Engineering, Kalyani, India

M. Mukherjee et al. (eds.), *Advances in Medical Physics and Healthcare Engineering*, Lecture Notes in Bioengineering, https://doi.org/10.1007/978-981-33-6915-3_27

et al. (2003). Any artificial parts like hand, finger can be moved using DC geared motors (Aung 2007). Advancements in skill to integrate attributes reflect the dexterity expansion. Dexterity comes in appliance of motor skills of the arm. DC motor can generate constant torque irrespective of the speed. Torque is the spinning force that fabricates rotation on a shaft. With16 degree of freedom, Robotics hand MA-1 was designed and built by R. Suarez, of which the control system consisted of 16 position control loops, independently controlling each of the 16 DC motors in the paper of Meng et al. (2006). In this present framework, an approach is taken to design a DC motor controlled artificial arm module. A virtual arrangement is developed to examine different aspects of control theory. The system is also reasonable as it is incorporated with a set of real masses. Mathematical representation through an experiment is attempted for proposed open-loop control model. This will introduce the proper transfer functional model of the proposed design through comparative study of the tuning results. Advanced tuning methods like Genetic Algorithm (GA), Particle Swarm Optimization (PSO) are used to recognize the optimal result toward the development of robotic arm. This method would ensue toward the intention of identifying the contour of the objects with real-time position for the development of the appropriate gripper. The tuning process eliminates instability smoothly within stipulated time and can accept some deviation in the process.

2 Control Technology of DC Motor Controlled Artificial Arm

An approach to model the armature controlled DC geared motor mathematically is shown here. The transfer function of the angular shift of motor in the shaft and the armature input voltage is derived hereunder. The circuit diagram of the motor used for dexterous hand is shown in Fig. 1.

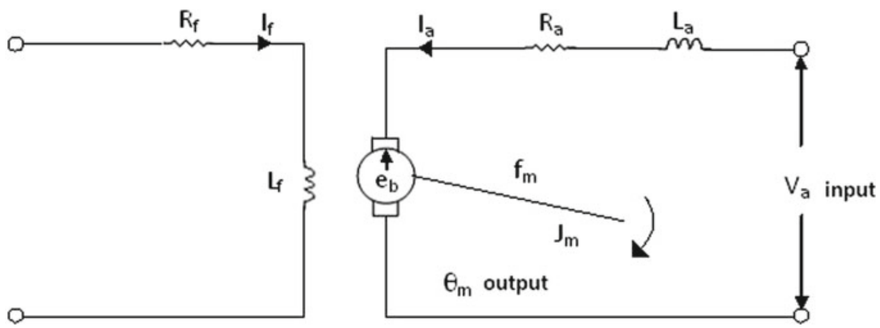

Fig. 1 Circuit diagram of the motor used for hand prosthesis

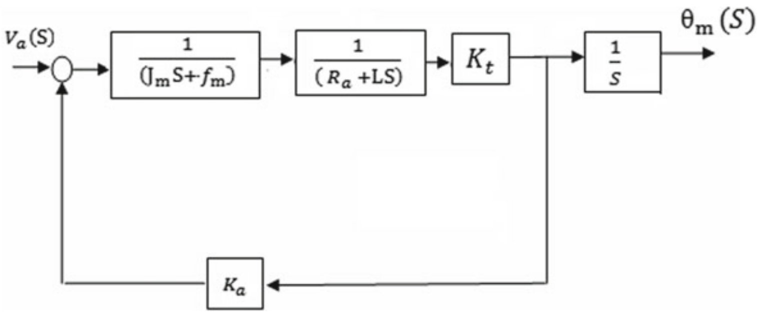

Fig. 2 Block representation of the system

The input voltage V_a is applied to the armature which has a resistance of R_a and inductance of L_a. The field current if supplied to the field winding is kept constant and thus the armature input voltage controls the motor shaft output in Fig. 2.

At motor shaft, the moment of inertia is J_m and the viscous friction coefficient is f_m. The angular shift in the motor shaft is θ_m. Now, using Kirchhoff's law and Newton's law the following relation is formed (Aung 2007).

$$\frac{\theta_m(S)}{V_a(S)} = \frac{K_t}{\{S(J_m S + f_m)(R_a + LS)\} + K_a K_t} \tag{1}$$

Now, the motor torque (T_m) is found by

$$T_m = \alpha_m J_m + \omega_m f_m \tag{1a}$$

where ω_m and α_m are the corresponding angular velocity and angular acceleration. So, the system open-loop transfer function is

$$G_o(S) = \frac{K_t}{\{S(J_m S + b_m)(R_a + LS)\}} \tag{2}$$

2.1 Experimental Methods and Design Approach

The DC motor can be represented by a second-order continuous linear transfer function, where each pole represents the mechanical and electrical characteristics of the system. The motor torque constant (K_t) that relates the motor torque (T_m), delivered by the motor to the current level is estimated from the Eq. (1a) which has a linear slope between these variables (Verma et al. 2013; Aung 2007), obtained experimentally. The motor torque (T_m) is found by using a string, a pulley of known radius (0.5 cm) and weight of known mass while measuring the current. The back EMF constant

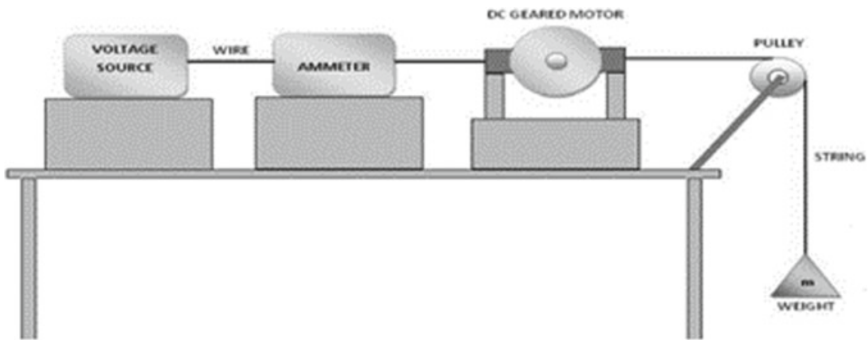

Fig. 3 Experimental setup

is K_b which is considered equal to torque constant (K_t). Armature resistance (R_a = 13 Ω) is measured directly by opening the conduction coil circuit using a digital multimeter. Armature inductance (L_a) is usually negligible and was assumed as a low value (0.1H). The experimental setup is shown in Fig. 3.

The motor moment of inertia (J_m) and the viscous friction coefficient (f_m) are obtained from the linear DC motor equations. The angular acceleration and the angular velocity of the motor are measured by using a tachometer and motor current is measured by using an ammeter (Aung 2007; Nikhil and Deivanathan 2018). The experimental values are tabulated in Table 1.

Substitution of the experimental values in the motor torque equations reduces to the equations which are given in Table 2.

Comparing the equations of Table 2 different values of Jm and fm are calculated those are given in Table 3.

Applying the values of Table 3 in Eq. (2) different open-loop transfer functions are generated for each set. Among these transfer functions, four transfer functions (one from each set) are taken into consideration based on their open-loop responses. Those are given in Table 4.

Table 1 Measured parameter of motor arm control system

Mass (m) [g]	Current (Ia) [mA]	RPM	Time (t) [s]	Angular velocity (ω_m) [rad/s]	Angular acceleration (α_m) [rad/s^2]	Torque (T_m) [N-m]
50	0.6	155	4.91	16.22	3.3041	2.4525×10^{-3}
100	0.8	151.67	4.99	15.87	3.1813	4.905×10^{-3}
150	0.9	146.33	5.013	15.31	3.054	7.3575×10^{-3}
200	0.99	145	5.021	15.17	3.021	9.81×10^{-3}

Table 2 Torque equations for different weight

Set No.	Weight of the pulley	Torque equation
1	50	$0.002453 = 3.3041\, J_m + 16.22\, f_m$
2	100	$0.004905 = 3.1813\, J_m + 15.87\, f_m$
3	150	$0.0073557 = 3.054\, J_m + 15.31\, f_m$
4	200	$0.00981 = 3.021\, J_m + 15.17\, f_m$

Table 3 Different values of J_m and f_m for different set

Set number	Moment of inertia of the DC geared motor (J_m) [N-m s^2/rad]	Viscous friction of the DC geared motor (f_m) [N-m s/rad]	Set number	Moment of Inertia of the DC geared motor (J_m) [N-m-s/rad]	Viscous friction of the DC geared motor (f_m) [N-m s/rad]
SET 1	0.06×10^{-4}	1.5×10^{-4}	SET 2	0.4526×10^{-4}	3×10^{-4}
	1.040×10^{-4}	1.3×10^{-4}		1.450×10^{-4}	2.8×10^{-4}
	2.51×10^{-4}	1×10^{-4}		2.9469×10^{-4}	2.5×10^{-4}
	3.495×10^{-4}	0.8×10^{-4}		3.94×10^{-4}	2.3×10^{-4}
	3.986×10^{-4}	0.7×10^{-4}		5.4411×10^{-4}	2×10^{-4}
	4.968×10^{-4}	0.5×10^{-4}		10.42×10^{-4}	1×10^{-4}
SET 3	0.528 X 10^{-4}	4.7×10^{-4}	SET 4	0.8371×10^{-4}	6.3×10^{-4}
	1.53×10^{-4}	4.5×10^{-4}		2.343×10^{-4}	6×10^{-4}
	2.533×10^{-4}	$4. \times 10^{-4}$		4.854×10^{-4}	5.5×10^{-4}
	4.03×10^{-4}	4×10^{-4}		7.365×10^{-4}	5×10^{-4}
	6.543×10^{-4}	3.5×10^{-4}		9.875×10^{-4}	4.5×10^{-4}
	9.050×10^{-4}	3×10^{-4}		12.38×10^{-4}	4×10^{-4}

Table 4 Selected transfer functions

S. No.	Open-loop transfer function
G_{01} (s)	$\frac{4.0875\times10^5}{0.06s^3+9.3s^2+195s}$
G_{02} (s)	$\frac{6.13125\times10^5}{0.453s^3+61.84s^2+390s}$
G_{03} (s)	$\frac{8.175\times10^5}{0.528s^3+73.34s^2+611s}$
G_{04} (s)	$\frac{9.909\times10^5}{0.837s^3+115.12s^2+819s}$

Table 5 Tuning results after tuning with genetic algorithm

S. No.	Open-loop transfer function	Turning results using GA technique
G_{01}	$\frac{4.0875\times10^5}{0.06s^3+9.3s^2+195s}$	$K_p = 0.0435$ $T_i = 0.250775$ $T_d = 0.0790$
G_{02}	$\frac{6.13125\times10^5}{0.453s^3+61.84s^2+390s}$	$K_p = 0.34225$ $T_i = 0.9970$ $T_d = 0.03075$
G_{03}	$\frac{8.175\times10^5}{0.528s^3+73.34s^2+611s}$	$K_p = 0.39228$ $T_i = 0.99285$ $T_d = 0.03502$
G_{04}	$\frac{9.909\times10^5}{0.837s^3+115.12s^2+819s}$	$K_p = 0.3678$ $T_i = 0.6452$ $T_d = 0.1249$

3 Advanced Tuning Techniques Approach

The Tuning is based on a continuous domain analysis that can show inconsistent performance when applied with discrete controller. So advanced tuning methods like Genetic algorithm (GA) and Particle swarm optimization (PSO) are attempted for betterment of result through a comparative analysis.

3.1 Simulation with Genetic Algorithm (GA)

Genetic algorithm (GA) is a technique based on natural selection and natural genetics mechanism. This method is used to get optimized result for a system through iteration. Here, every iteration gives a set of solutions called population instead of single result. Then each solution directs to a desired one through ranking (Banerjee et al. 2014; Nikhil and Deivanathan 2018). Tuning results with response characteristics, and their corresponding closed-loop responses are given in Table 5 and Figs. 4 and 5.

It is clear from the responses that after GA tuning, the systems give less overshoot and take lesser time to achieve stability.

3.2 Simulation with Particle Swarm Optimization (PSO)

Particle swarm optimization (PSO) is an optimization technique based on population and uses the algorithm of bird flocking. At first, a group of random solutions are chosen, and then optima are searched by updating populations (Salem 2014; Neogi

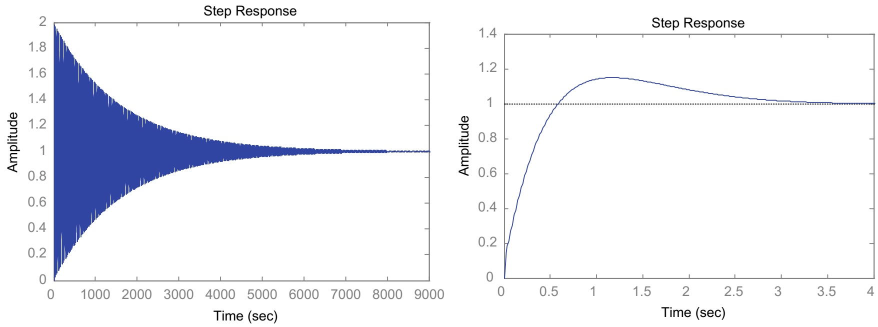

Fig. 4 Closed-loop response of G_{01} and G_{02} after tuning using genetic algorithm technique

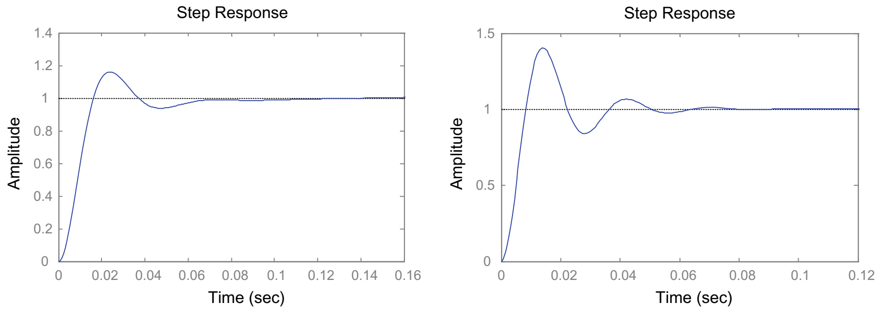

Fig. 5 Closed-loop response of G_{03} and G_{04} after tuning using genetic algorithm technique

et al. 2019). Tuning results with response characteristics, and their corresponding closed-loop responses are given in Table 6 and Figs. 6 and 7.

Table 6 Tuning results after tuning with genetic algorithm particle swarm optimization

S. No.	Open-loop transfer function	Turning results using PSO technique
G_{01}	$\frac{4.0875\times10^5}{0.06s^3+9.3s^2+195s}$	$K_p = 0.0328$, $T_i = 0.1312$, $T_d = 0.0610$
G_{02}	$\frac{6.13125\times10^5}{0.453s^3+61.84s^2+390s}$	$K_p = 0.34214$, $T_i = 0.7083$, $T_d = 0.9862$
G_{03}	$\frac{8.175\times10^5}{0.528s^3+73.34s^2+611s}$	$K_p = 0.35226$, $T_i = 0.08527$, $T_d = 0.99279$
G_{04}	$\frac{9.909\times10^5}{0.837s^3+115.12s^2+819s}$	$K_p = 0.3782$, $T_i = 0.10932$, $T_d = 0.1191$

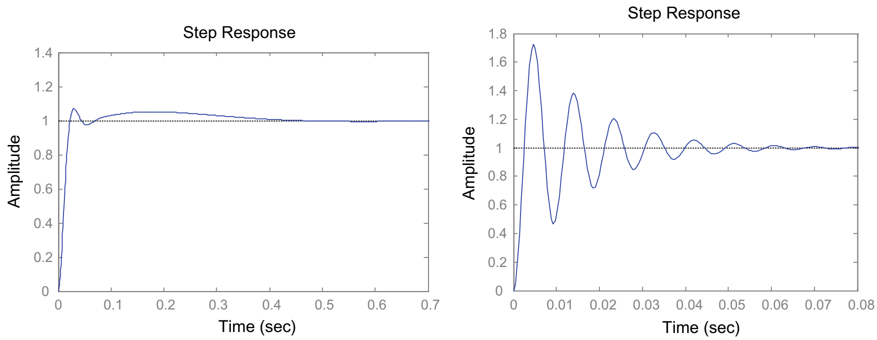

Fig. 6 Closed-loop response of G_{01} and G_{02} after tuning using PSO technique

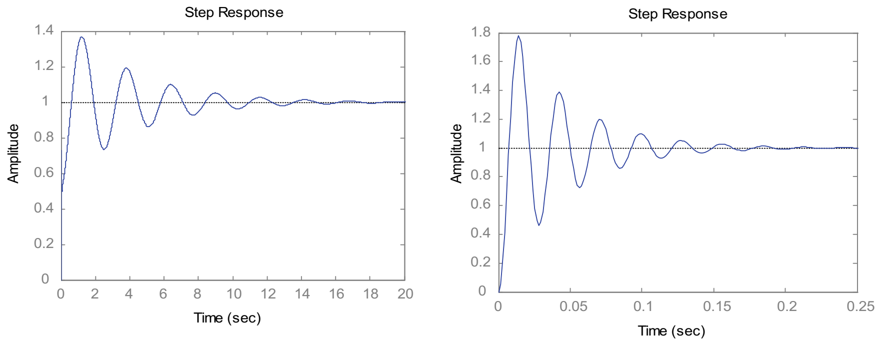

Fig. 7 Closed-loop response of G_{03} and G_{04} after tuning using PSO technique

3.3 Comparative Study for Perfect Tuning

The comparative analysis of the control parameters (overshoot and settling time) is shown in Table 7. The obtained results show that the tuning of systems by PSO has more convergence rate and higher performance. It is apparent that set 2 transfer function with PSO technique is showing best response among others in terms of system parameters.

4 Conclusions

This development involves response analysis with the comparative study of control parameter performances by applying optimization techniques to achieve proper tuned model of the DC motor-based artificial arm system. The experimental approach constructs the preliminary sets of transfer functions. The introduction of the genetic

Table 7 Comparative study of system parameters with different tuning techniques

S. No.	Open-loop transfer function	Using genetic algorithm technique		using particle swarm optimization technique	
		Maximum overshoot	Settling time (s)	Maximum overshoot	Settling time (s)
G_{01}	$\frac{4.0875\times10^5}{0.06s^3+9.3s^2+195s}$	1.98	6140	1.07	0.341
G_{02}	$\frac{6.13125\times10^5}{0.453s^3+61.84s^2+390s}$	1.15	2.88	1.73	0.0569
G_{03}	$\frac{8.175\times10^5}{0.528s^3+73.34s^2+611s}$	1.16	0.0633	1.37	11.9
G_{04}	$\frac{9.909\times10^5}{0.837s^3+115.12s^2+819s}$	1.4	0.0587	1.78	0.159

algorithm and particle swarm optimization techniques gives better parametric values than the conventional approach. The set 2 transfer function tuned with PSO might be opted for further analysis. In future, the nonlinearity effect would also be imposed for this particular system.

References

Aung WP (2007) Analysis on modeling and simulink of DC motor and its driving system used for wheeled mobile robot. World Acad Sci Eng Technol 32:299–360

Banerjee S, Sinha D, Bhatia S, Kumari P, Das Z, Bandyopadhyay S, Neogi B (2014) Optimal design approach towards standard electromyography (EMG) controlled hand prosthesis system. In: IEEE international conference on control, instrumentation, energy and communication (CIEC), Jan–Feb 2014. https://doi.org/10.1109/CIEC.2014.6959063

Barui S, Manna D, Neogi B (2016) System tuning and stability analysis in discrete domain for a standard dexterous arm model. Int J Adv Res Electr Electron Instrum Eng 5(4):2887–2892. ISSN (Print): 2320-3765. ISSN (Online): 2278-8875

Meng Q, Wang H, Li P (2006) Dexterous under water robot hand: HEU Hand II. In: International conference on mechatronics and automation, Luoyang, China, 25–28 June 2006

Neogi B (2011) On design and analysis of prosthetic control introducing simulation method. Ph.D. thesis, Jadavpur University, Kolkata, pp 183–190

Neogi B, Barui S, Das S, Paul S, Ghosh J, Ghosh S (2019) Tuning and transfer functional modelling of a prosthetic arm. J Comput Methods Sci Eng 19:243–256. https://doi.org/10.3233/JCM-180880

Nikhil SS, Deivanathan R (2018) Modelling and analysis of DC motor actuator for an electric gripper. J Eng Sci Technol 13(4):862–874. ISSN: 1823-4690

Salem FA (2014) Modeling, simulation and control issues for a robot ARM; education and research. I.J. Intell Syst Appl

Scherillo P, Siciliano B, Zollo L (2003) Parallel force/position control of a novel biomechatronich and prosthesis. In: International conference on advanced intelligent mechatronics (AIM 2003), pp 920–925

Verma S, Chatterjee A, Pal Singh H, Kumar A, Garg K, Chattopadhyay K (2013) A design approach for myoelectric arm with hand and wrist motions using single actuator. Int J Adv Manuf Technol 67:5–8. ISSN 0268-3768

Room Temperature Detection of Formaldehyde with Economical and Ecofriendly Graphene Quantum Dot Ink Treated Paper-Based Sensor

Shreyasi Das, Poulomi Chakrabarty, Tamal Dey, Sumita Santra, Soumen Das, and Samit K. Ray

Abstract Renewed interest for volatile organic compound (VOC) sensors using nanomaterials are increasing due to several limitations of existing commercially available sensors for healthcare, food quality, and environmental applications. A disposable, flexible, and room temperature, paper-based formaldehyde sensor has been developed using graphene quantum dot ink as the sensing material. The PEDOT:PSS conductive ink acts as an electrode on the porous paper substrate with graphene quantum dot ink as sensing material making the device novel, low cost, and potential candidate for large area roll to roll solution process-able formaldehyde sensors fabrication. The sensitivity is measured for a concentration varying from 7 to 20 ppm exposure of formaldehyde at ambient temperature at dry air condition. The sensor device shows a sensitivity of 0.26% at 15 ppm HCHO. The p-type GQDs reveal a resistance increment of the sensing film in presence of reducing gas HCHO, which is explained using charge transfer dynamics between sensing film and HCHO molecules. The finding may lead to new opportunities in flexible formaldehyde sensors operating at room temperature for healthcare applications.

Keywords Paper-based sensors · Formaldehyde sensor · Graphene quantum dots

S. Das · P. Chakrabarty · T. Dey
School of Nano Science and Technology, Indian Institute of Technology, Kharagpur, India

S. Santra · S. K. Ray (✉)
Department of Physics, Indian Institute of Technology, Kharagpur, India
e-mail: physkr@phy.iitkgp.ac.in

S. Das
School of Medical Science and Technology, Indian Institute of Technology, Kharagpur, India

S. K. Ray
S. N. Bose National Centre for Basic Sciences, Kolkata, India

M. Mukherjee et al. (eds.), *Advances in Medical Physics and Healthcare Engineering*, Lecture Notes in Bioengineering, https://doi.org/10.1007/978-981-33-6915-3_28

1 Introduction

Monitoring of volatile organic compounds (VOC) such as formaldehyde (HCHO) is crucial as HCHO has detrimental effects on human health, including irritation and dryness of the skin, nose, throat, and olfactory organs (Srivastava et al. 2000). It is a common mucous-membrane irritant that engenders conjunctivitis and lacrimation (Liu et al. 2018). This colorless, flammable chemical is one of the most common carbonyl compounds that can be found naturally in various raw foods like meat, fish, milk, or dairy products and packaged food by way of preservatives (Zhang et al. (2014)). Exposure to HCHO can cause eye irritation at 0.3–0.9 ppm concentration in industrial workers and might develop conjunctivitis and lacrimation for exposure in the range of 4–20 ppm. In 2006, the International Agency for Research on Cancer (IARC) of the WHO and in 2011 the National Toxicology Program of the US Department of health and human services categorized HCHO as a human carcinogen (Guzman et al. 2018). During the last decades, highly sensitive yet low-cost, HCHO sensors with broad detection range and fast response had drawn considerable attention to the scientific community. Traditional chemiresistive HCHO sensors were fabricated using semiconductor oxides sensing film with high sensitivity and detection range (Afzal et al. 2012). Recently Khampho et al. have been invented an HCHO sensor with AgO_x doped SnO_2 sensing film for good response at high temperature (350 °C) (Khamfoo et al. 2020). However, these sensors work at high operating temperatures (200–600 °C), leading to high power consumption, flammability risk, and requirement of rigid, costly substrates like quartz or glass (Liu 2014; Yamazoe 2005). For obvious reasons, detecting HCHO at room temperature with low power consumption and an absence of flammability risk on flexible and environment-friendly sensing platforms needs further investigation.

Nowadays, room temperature HCHO sensors using various nanomaterials are investigated due to large surface to volume ratio, and edge functionalization properties (Cheng et al. 2010; Robinson et al. 2008; Huang 2012). The discovery of graphene opens up plenty of research opportunities with different new nanomaterials in fundamental and application domains, including flexible electronics, biodegradable sensors, non-toxic biomedical drug delivery, etc. Graphene quantum dots (GQD) (Shen et al. 2012), a derivative of graphene, is the newest member of the graphene family with three-dimensional confinement of carbon domains, possessing excellent properties like low toxicity, size-dependent electronic properties, and excellent biocompatibility (Ponomarenko 2008). The existence of functional groups at the edges of GQDs helps test gas molecules to interact, leading to potential candidates for sensing applications (Shen et al. 2012; Dey et al. 2018). A recent study has shown that the composition of Ag-doped perovskite-type oxide $LaFeO_3$ sensing film with GQD reduces the operating temperature from 90 to 55 °C and provides greater selectivity in VOC sensing by functionalizing GQDs with different dopants (Zhang et al. 2018). Another report demonstrated the room temperature isopropanol sensor with GQD-TiO_2 heterojunction sensing film and showed a response value of 13.8 at 50 ppm (Shao et al. 2016). However, the Silicon substrate with gold finger electrodes makes the device fabrication process difficult, time-consuming, expensive and demands industrial machinery support. Furthermore, GQDs embedded in a conjugated polymer matrix has been used for room temperature VOC sensors on industrially fabricated SiO_2/Silicon substrate (Gavgani 2015). However, inexpensive, eco-friendly paper-based sensors might solve the problems related to the cost and hazardous industrially processed silicon-based sensors and offer great potential for flexible e-skin sensors (Wang 2009). Since the extraction of environmentally benign cellulose paper from wood pulp, different cellulose derivatives have found tremendous applications in various low-cost, flexible sensors. However, a challenging key point in the paper-based sensor device fabrication is the porous nature of the paper substrate that hinders the making of a continuous, smooth film of nanomaterials on it. Thus, various electrode design techniques on cellulose papers have been developed to block the papers' porous structures, including inkjet printing, drawing with pencils or ball pens filled with conductive ink, etc. (Seekaew et al. 2014; Wu et al. 2014). Earlier, some groups have reported commercially available conducting polymer poly3,4-ethylenedioxy thiophene: polystyrenesulphonate (PEDOT:PSS) based solution process-able electrodes for optoelectronic applications such as solar cell (Tang et al. 2015; Lee 2017), LED (Kim et al. 2013), and photodetectors (Liu et al. 2015; Aga et al. 2014) due to their high electrical conductivity, aqueous solution process-ability, superior environmental stability and biocompatibility, superior film-forming properties, and fine-tuning of their physicochemical properties (Kim et al. 2011). PEDOT:PSS film possesses a unique structure of entangled conductive PEDOT domains with an insulating PSS matrix that can be used to tailor its electronic properties (Dehsari et al. 2014; Kim et al. 2011), which makes it a promising candidate as electrodes in paper sensors.

In this work, we have fabricated a novel disposable, biocompatible, all solution-processed, room temperature, paper-based HCHO sensor using conducting ink of PEDOT:PSS as an electrode and GQDs-based colloidal ink as the sensing material. Graphene Quantum Dots are synthesized from graphite powder using modified Hummers' method followed by amiditive cutting in conc. HNO_3/H_2SO_4 solution and subsequent reduction by hydrothermal reaction (Dey et al. 2020). Further, a continuous film of desirable conductance is achieved as electrodes on the porous paper substrate by successive spin-coating of PEDOT:PSS. Our experiment reveals that GQD ink on PEDOT:PSS electrodes shows the response from 7 ppm exposure of HCHO under dry air conditions even at room temperature. The study shows that the GQD ink on conductive PEDOT:PSS electrode on the paper substrate can be effectively utilized to overcome the limitation of expensive industrial-made HCHO sensors.

2 Experimental Section

2.1 Graphene Quantum Dot Synthesis

Synthesis of graphene quantum dots in bottom-up technique from graphite flakes is followed by three different steps: a) Preparation of graphene oxide using modified hammer's method; b) Acid cutting of GO to form graphene oxide quantum dots; c) Hydrothermal reduction to form GQDs.

Chemical oxidation of Graphite flakes: Graphene oxide is synthesized by a modified hammer's method as reported earlier. Shortly, 750 mg of graphite powder and 750 mg of $NaNO_3$ were added with 37.5 mg of H_2SO_4 and stirred constantly on an ice bath till the temperature reaches 0 °C. Next, at this very low temperature, 4.5 g $KMnO_4$ was added to the mixture dropwise under stirring to avoid an explosion. After that, the mixture was transferred to a 40˚C water bath and allowed to stir for 1 h. Then 60 ml water was added to the mixture and stirred for 30 min at 95 °C operation temperature. After that the mixture was removed from the heater and150 ml water is added to dilute the mixture. Finally, 4.5 ml H_2O_2 was added for the quenching of the reaction. Leave the mixture for about 5 h to settle down and then filter the mixture using 4.5 μm pore-sized Whatman filter paper. Then wash the sample with DI water by centrifuging it at 20,000 rpm 4–5 times until the solution reached pH 7. Finally, 250 ml of DI water is added to make a graphene oxide solution.

Acid cutting of graphene oxide sheets: To reduce the size of graphene oxide sheets, as-synthesized GO sheets were treated with H_2SO_4 and HNO_3 mixture (1:3 ratio) and the whole solution was ultra-sonicated for 24 h. Finally, the mixture was washed up to pH 7 by centrifuging 5–6 times. The resultant solution is graphene oxide quantum dots (GOQDs).

Hydrothermal reduction of graphene oxide quantum dots: GQDs were synthesized by the hydrothermal method using GOQDs as precursor material. 10 ml of uniformly dispersed GOQD solution was transferred into a Teflon lined autoclave (100 ml) and heated at 200 °C for 12 h. After removing from the hydrothermal chamber, GQDs were transferred into DMF to make a uniformly dispersed solution.

2.2 Sensor Device Fabrication

Sensor devices were fabricated on flexible disposable Whatman cellulose chromatography papers as substrate. To fabricate electrodes on cellulose paper substrate, PEDOT:PSS was drop casted at a separation distance of 1 mm. The sensing layer was prepared by bridging the gap between the two electrodes by GQD ink from DMF solvent. The remnant DMF solvent was completely removed keeping in a vacuum chamber. Further, multiple sequential drop-casting steps were performed to acquire resistance of the order of KΩ at a separation distance of 3 mm.

2.3 Sensing Unit

The gas sensing unit (GSU) used in our experiment is a custom-made setup consists of mass flow controllers (MFCs), gas mixers, gas cylinders, an airtight chamber, a data acquisition (DAQ) system, and a computer as shown in Fig. 1b. The sample chamber is made up of stainless steel maintaining great isolation between the inner and outer environments. Air and H_2 gas flow rates were controlled through MFCs from Alicat. Steel pipes were connected with the different parts of the sensors system. By varying the different flow rates of air and hydrogen, the different concentrations of H_2 were achieved. In the gas mixer, two gases were mixed properly before coming into the test chamber. HCHO vapor is created by flowing dry air inside a container containing HCHO solution. Inside the test chambers, there were four probes, capable of measuring two devices simultaneously. The outputs of the sensors were connected in Agilent 349,721 LXI DAQ unit fitted with 34901A 20 channel multiplexer switches and a digital ohmmeter. BenchLink Data Logger Pro software was used for sensor response data acquisition. In this study, the change of sensor resistance due to different concentrations of formaldehyde was measured using DAQ system at room temperature. The outlet gas test chamber was connected through a bubbler up to the outside of the room so that the gases can be thrown out from the room.

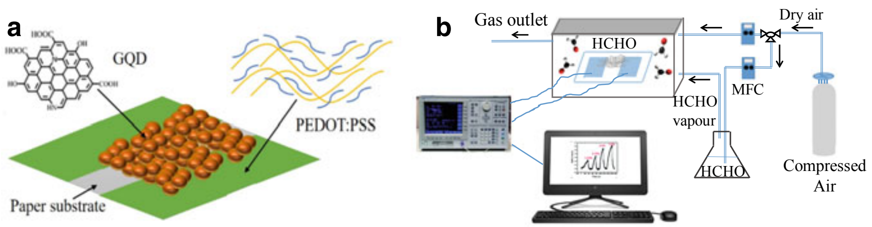

Fig. 1 **a** Schematic of the paper-based sensing device with PEDOT:PSS electrodes and GQD ink sensing material. **b** Schematic representation of the gas sensing setup

3 Result and Discussion

3.1 Sample Characterization

The structural characterization of as-synthesized GQDs was performed using high-resolution transmission electron microscopy (HRTEM) [JEOL, JEM-2100F]. Atomic force microscopy (AFM) [Agilent Technology, 5500 AFM] was used to predict the height of the GQDs in tapping mode for further knowledge about the structure of synthesized GQDs. Further, Raman spectroscopy was performed with a 514 nm wavelength Argon laser and a spectrometer [JobinYvon Horiba T64000] for confirmation of molecular bonding present in the material. For optical characterization of the material, ultraviolet–visible (UV–Vis) absorption spectroscopy with a fiber probe-based Avaspec-3648 spectrometer combined with broadband Deuterium and Halogen excitation sources, is performed on GQDs in the solution phase. For steady-state Photoluminescence studies, the GQD sample was analyzed in solution using a He-Cd Laser of excitation wavelength of 325 nm and a monochromator [TRIAX-320] equipped with a photomultiplier detector [Hamamatsu R928].

The TEM image of as-prepared GQDs from graphite powder indicates monodispersed GQDs with an average diameter of 4 nm, distributed on the TEM grid as depicted in Fig. 2a. The AFM image with the corresponding height profile in the inset (Fig. 2b) provides a height measurement of an average of ~4 nm. AFM image of Fig. 2b shows a uniform distribution of GQD nanoparticles over a large area.

Figure 2c shows Raman spectra of as-synthesized GQDs under 514 nm laser excitation. Two distinct Raman peaks are observed at ~1342 cm^{-1} and ~1590 cm^{-1} representing the D and G band, respectively, which are the characteristic peaks of graphene-based materials. The 'crystalline' G band is attributed to the primary in-plane vibrational mode at Γ point of the Brillouine zone. Moreover, the disordered 'D' band arises due to the existence of defects and functional groups in chemical synthesized GQDs and represents the breathing mode of clustering hexagonal aromatic rings. The characteristic 2D.

The 2D Raman peak of graphene at ~2700 cm^{-1} is reduced for GQDs due to three-dimensional confinement of carbon domains. Figure 2d represents a typical UV absorption spectrum (blue curve) and photoluminescence emission spectrum (red curve) of as-synthesized GQDs in an aqueous solution. An intense absorption peak is observed at ~295 nm, which contributes to the π–π^* transition in the molecular orbital of sp^2 hybridized carbon domains from the hexagonal core of GQDs. The photoluminescence spectrum of GQDs (the red curve) depicts two peaks at ~440 nm and ~520 nm. The intense peak at 440 nm is due to the electronic transition from sp^2 hybridized confined carbon core states, and the relatively weaker one is due to the emission from radiative shallow trap states arises due to the presence of surface functional groups.

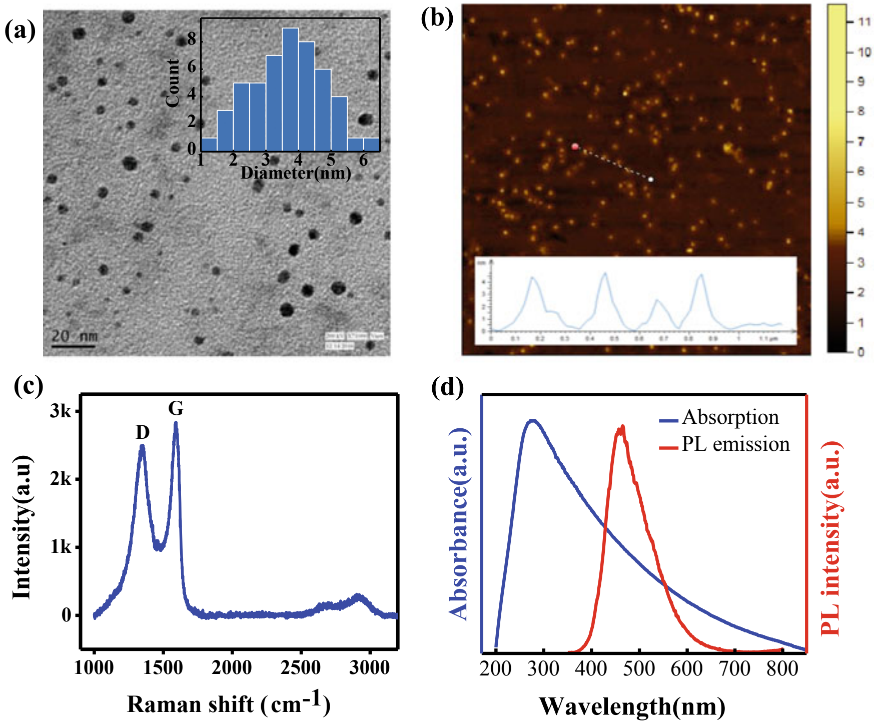

Fig. 2 **a** TEM image of GQDs showing particles dispersed uniformly over the area. **b** AFM image of mono-dispersed GQDs with average height 4 nm showing in height profile along the line drawn in the image. **c** Raman spectrum of as synthesised GQDs showing distinct G and D bands. **d** Optical absorption spectra and photoluminescence spectra of GQDs

3.2 Gas Sensing Performance Evaluation

The working principle of the chemiresistive sensor is hinged on the resistance change due to the interaction between the gas molecules and the surface of the sensing material. The fabricated device is mounted inside a custom-made gas sensing unit and exposed to dry air for about 1 h to get a stable baseline. After achieving a stable baseline, the sensing device is exposed to different concentrations of HCHO for a constant time of 10 min, followed by restricting the HCHO flow and allowing dry air inside the chamber for another 10 min for recovery of the sensing film. After achieving a stable baseline under dry air exposure, upon test gas molecules exposure, the resistance of the devices increases or decreases due to interaction between the gas molecules and the sensing layer. Again, in the absence of test gas at dry air condition, the resistance of the devices recoils to its initial position, which results in dynamic sensor response. The response of the device is calculated using the equation (Liu et al. 2015)

$$\%\text{Response} = \frac{R_{\text{Test gas}} - R_{\text{Baseline}}}{R_{\text{Baseline}}} \times 100\% \tag{1}$$

where R_{Testgas} is the resistance of the sensing film at respective ppm exposure of test gas and R_{Baseline} is the resistance of the same in dry air condition.

The fabricated device is mounted on the sensing chamber and exposed to different ppm of formaldehyde concentrations starting from 7 ppm. Under HCHO exposure the sensing film resistance starts to increase and gets saturated, but after stopping the HCHO flow the resistance starts to decrease. The response of the device at four concentrations of HCHO is depicted in Fig. 3. The sensor response is calculated from experimental data using Eq. 1 and shown in Table 1. The device shows 0.15%

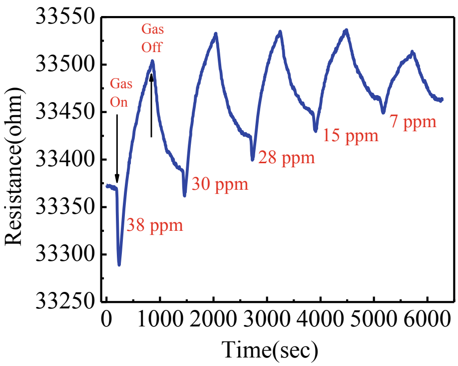

Fig. 3 Sensor response upon with different concentration of HCHO exposure

Table 1 Calculated responsivity of the device for different ppm of HCHO gas exposure

Gas concentration (ppm)	Initial resistance (ohm)	Final resistance (ohm)	% Percent responsivity
38 ppm	33,359 $\pm$0.05	33,504 $\pm$0.05	0.44
30 ppm	33,388 $\pm$0.05	33,533 $\pm$0.05	0.42
28 ppm	33,425 $\pm$0.05	33,533 $\pm$0.05	0.33
15 ppm	33,450 $\pm$0.05	33,534 $\pm$0.05	0.26
7 ppm	33,466 $\pm$0.05	33,512 $\pm$0.05	0.15

response on a minimum of 7 ppm under HCHO exposure. The chemical synthesis route incorporated oxygen-containing defect sites on GQD carbon domains, which withdraws electrons from the material, making it a p-type semiconducting material with majority carrier holes. HCHO is a reducing gas with electron donating character. Adsorption of HCHO molecules on the surface of GQD leads to electron transfer into the material from HCHO molecules and a decrease in hole concentration in the intrinsically p-type GQD layer occurs. The decrement of majority carrier concentration results in the lower conductivity of the material which leads to an increase of resistance of the sensing film.

In the case of the recovery process, after restricting the HCHO flow, dry air is started to flow into the chamber which accelerates the desorption process of HCHO molecules from GQD surface. This desorption process disrupts the electron transfer into GQD film, leading to the recovery of the film resistance. Additionally, an anomalous behavior has been observed in the sensor response for every concentration of gas flow. However, the initial decrease in resistance can be attributed to experimental error due to very low ppm of HCHO flow inside the chamber which starts to increase after a few seconds.

The performance of our device is comparable with available literature as shown in Table 2.

4 Conclusion

Graphene quantum dots are synthesised successfully from graphite powder using a top-down method followed by characterization with optical spectroscopic techniques. For device fabrication, we have chosen low-cost disposable cellulose paper substrate and solution-processed PEDOT:PSS conducting ink as electrodes. Graphene quantum dot ink has been drop cast between the PEDOT:PSS electrodes as the sensing material for formaldehyde sensing. The novel fabricated devices are completely solution-processed, low cost, and biocompatible. Formaldehyde sensing has been performed using the devices at the lowest concentration of 7 ppm with responsivity 0.15%. The fabricated low-cost novel disposable sensors may lead to new opportunities in the room temperature flexible formaldehyde sensors for healthcare applications with very simple fabrication techniques.

Table 2 Comparison of recent HCHO sensing devices on the basis of fabrication cost, environment-friendly and device response

Sensing material	Substrate	Electrodes	Gas concentration	Performance	Operating temp.	References
Mesoporous $ZnSnO_3$ NP	Ceramic tube with a Cr-Ni coil for heating	Au	50 ppm	Response (Rg/Ra) = 32	210 °C	Wang et al. (2019)
SnO/SnO_2 nanocomposite	Al_2O_3 tube with Pt heating wire	Au	50 ppm	Response 80	120 °C	Li et al. (2019)
SnO_2/AgO_X	Al_2O_3 substrate	Au	2000 ppm	Response 495	350 °C	Khamfoo et al. (2020)
Au/SnO_2 chip	Alumina substrate	Al_2O_3 (Comb like)	20 ppm	Response 1.01	Room temp	Chung et al. (2014)
rGO/MoS_2 hybrid film	PEN flexible substrate	Ti/Au IDE	10 ppm	2.4% response	Room temp	Li (2017)
GQD/TiO_2	SiO_2/Si	Au IDE	50 ppm	Response 13.8	Room temp	Shao et al. (2016)
GQD	Cellulose paper	PEDOT:PSS Film	15 ppm	0.26% response	Room temp	Our work

References

Afzal A, Cioffi N, Sabbatini L, Torsi L (2012) NOx sensors based on semiconducting metal oxide nanostructures: progress and perspectives. Sens Actuators, B Chem 171–172(2012):25–42

Aga RS, Lombardi JP, Bartsch CM, Heckman EM (2014) Performance of a printed photodetector on a paper substrate. IEEE Photonics Technol Lett 26(3):305–308

Cheng Z, Li Q, Li Z, Zhou Q, Fang Y (2010) Suspended graphene sensors with improved signal and reduced noise. Nano Lett 10(5):1864–1868

Chung FC, Wu RJ, Cheng FC (2014) Fabrication of a Au@SnO_2 core-shell structure for gaseous formaldehyde sensing at room temperature. Sens Actuators B Chem 190:1–7

Dehsari HS, Shalamzari EK, Gavgani JN, Taromi FA, Ghanbary S (2014) Efficient preparation of ultralarge graphene oxide using a PEDOT:PSS/GO composite layer as hole transport layer in polymer-based optoelectronic devices. RSC Adv 4(98):55067–55076

Dey T, Mukherjee S, Ghorai A, Das S, Ray SK (2018) Surface state selective tunable emission of graphene quantum dots exhibiting novel thermal quenching characteristics. Carbon NY 140:394–403

Dey T, Mukherjee S, Ghorai A, Das S, Ray SK (2020) Effects of size and localized states in charge carrier dynamics and performance of solution-processed graphene quantum dots/silicon heterojunction near-UV photodetectors. J Phys Chem C 124(22):12161–12167

Gavgani JN (2015) A room temperature volatile organic compound sensor with enhanced performance, fast response and recovery based on N-doped graphene quantum dots and poly(3,4-ethylenedioxythiophene)-poly(styrenesulfonate) nanocomposite. RSC Adv 5(71):57559–57567

Gogurla N, Sinha AK, Santra S, Manna S, Ray SK (2014) Multifunctional Au-ZnO plasmonic nanostructures for enhanced UV photodetector and room temperature NO sensing devices. Sci Rep 4

Guzman JMCC, Tayo LL, Liu CC, Wang YN, Fu LM (2018) Rapid microfluidic paper-based platform for low concentration formaldehyde detection. Sens Actuators B Chem 255:3623–3629

Huang X (2012) Reduced graphene oxide-polyaniline hybrid: preparation, characterization and its applications for ammonia gas sensing. J. Mater Chem 22(42):22488–22495

Khamfoo K, Inyawilert K, Wisitsoraat A, Tuantranont A, Phanichphant S, Liewhiran C (2020) Formaldehyde sensor based on FSP-made AgOx-doped SnO2 nanoparticulate sensing films. Sens Actuators B Chem 309

Kim YH, Sachse C, MacHala ML, May C, Müller-Meskamp L, Leo K (2011) Highly conductive PEDOT:PSS electrode with optimized solvent and thermal post-treatment for ITO-free organic solar cells. Adv Funct Mater 21(6):1076–1081

Kim YH, Lee J, Hofmann S, Gather MC, Müller-Meskamp L, Leo K (2013) Achieving high efficiency and improved stability in ITO-free transparent organic light-emitting diodes with conductive polymer electrodes. Adv Funct Mater 23(30):3763–3769

Lee CP (2017) A paper-based electrode using a graphene dot/PEDOT:PSS composite for flexible solar cells. Nano Energy 36:260–267

Li X (2017) Flexible room-temperature formaldehyde sensors based on rGO film and rGo/MoS_2 hybrid film. Nanotechnology 28(32)

Li N, Fan Y, Shi Y, Xiang Q, Wang X, Xu J (2019) A low temperature formaldehyde gas sensor based on hierarchical SnO/SnO_2 nano-flowers assembled from ultrathin nanosheets: synthesis, sensing performance and mechanism. Sens Actuators B Chem 294:106–115

Liu H (2014) Physically flexible, rapid-response gas sensor based on colloidal quantum dot solids. Adv Mater 26(17):2718–2724

Liu Z, Parvez K, Li R, Dong R, Feng X, Müllen K (2015) Transparent conductive electrodes from graphene/PEDOT:PSS hybrid inks for ultrathin organic photodetectors. Adv Mater 27(4):669–675

Liu CC, Wang YN, Fu LM, Huang YH (2018) Microfluidic paper-based chip platform for formaldehyde concentration detection. Chem Eng J 332:695–701

Ponomarenko LA (2008) Chaotic dirac billiard in graphene quantum dots. Science 320(5874):356–358

Robinson JT, Perkins FK, Snow ES, Wei Z, Sheehan PE (2008) Reduced graphene oxide molecular sensors. Nano Lett 8(10):3137–3140

Rong Q (2018) Design of ultrasensitive Ag-$LaFeO_3$ methanol gas sensor based on quasi molecular imprinting technology. Sci Rep 8(1):1–12

Seekaew Y, Lokavee S, Phokharatkul D, Wisitsoraat A, Kerdcharoen T, Wongchoosuk C (2014) Low-cost and flexible printed graphene-PEDOT:PSS gas sensor for ammonia detection. Org Electron 15(11):2971–2981

Shao S, Wang W, Zhou K, Jiang F, Wu H, Koehn R (2017) GQDs-TiO_2 heterojunction based thin films for volatile organic compounds sensor with excellent performance at room temperature. Mater Lett 186:193–197

Shen J, Zhu Y, Yang X, Li C (2012) Graphene quantum dots: emergent nanolights for bioimaging, sensors, catalysis and photovoltaic devices. Chem Commun 48(31):3686–3699

Srivastava PK, Pandit GG, Sharma S, Rao AM (2000) Volatile organic compounds in indoor environments in Mumbai, India. Sci Total Environ 255:161–168

Tang Z, Elfwing A, Melianas A, Bergqvist J, Bao Q, Inganäs O (2015) Fully-solution-processed organic solar cells with a highly efficient paper-based light trapping element. J Mater Chem A 3(48):24289–24296

Wang L (2009) Simple, rapid, sensitive, and versatile SWNT-paper sensor for environmental toxin detection competitive with ELISA. Nano Lett 9(12):4147–4152

Wang B, Yu J, Li X, Yin J, Chen M (2019) Synthesis and high formaldehyde sensing properties of quasi two-dimensional mesoporous $ZnSnO_3$ nanomaterials. RSC Adv 9(26):14809–14816

Wu X, Li F, Wu W, Guo T (2014) Flexible organic light emitting diodes based on double-layered graphene/PEDOT:PSS conductive film formed by spray-coating. Vacuum 101:53–56

Yamazoe N (2005) Toward innovations of gas sensor technology. Sens Actuators B Chem 108(1–2) (SPEC. ISS., 2–14, 2005)

Zhang YM, Lin YT, Chen JL, Zhang J, Zhu ZQ, Liu QJ (2014) A high sensitivity gas sensor for formaldehyde based on silver doped lanthanum ferrite. Sens Actuators, B Chem 190:171–176

Zhang Y, Zhao J, Sun H, Zhu Z, Zhang J, Liu Q (2018) B, N, S, Cl doped graphene quantum dots and their effects on gas-sensing properties of Ag-$LaFeO_3$. Sens Actuators B Chem 266:364–374

Mn–Zn–Ferrite PVDF Composite Material as Electromagnetic Pollution Reducer

Soumyaditya Sutradhar and Madhumita Mukhopadhyay

Abstract This work has investigated the electromagnetic interference shielding effectiveness (EMI-SE) of Mn–Zn–ferrite–Poly(vinylidene fluoride) (MZF-PVDF) composites in the microwave/GHz frequency range. The modulation of EMI-SE of MZF-PVDF composite structures was observed due to the variation of MZF nanofillers weight percentage inside the matrix of PVDF. The polycrystalline phase of MZF-PVDF composite structures was identified by X-ray diffraction (XRD) analysis. The presence of polar β-phase of PVDF matrix in the MZF-PVDF composite structures was observed and estimated by the FTIR analysis. The variation of magnetization as a function of applied magnetic field shows a maximum magnetization of 15.8 emu/g of MZF-PVDF composite materials, whereas the variation of dielectric permittivity due to the formation of MZF-PVDF interfaces inside PVDF matrix was observed in the frequency dependent dielectric response study. The high value of SE of nearly −32 dB at a matching frequency of 11.5 and 14 GHz has been observed for MZF-PVDF composites and this high SE of MZF-PVDF composites makes them most efficient candidate for the fabrication of lightweight, flexible, laminated electromagnetic pollution reducer (EPR).

Keywords PVDF · Dielectric polarization · EMI shielding effectiveness

1 Introduction

The growing use of smartphones and other electronic gadgets enhances various hazardous effects all-around of our society. The excessive use of the smartphones and electronic gadgets in the radio frequency (RF) region (100 kHz–10 GHz) or microwave (MW) region (8–18 GHz) is the most essential cause for the growing

S. Sutradhar (✉)
Department of Physics, Amity Institute of Applied Sciences (AIAS), Amity University Kolkata, Kolkata, West Bengal 700135, India

M. Mukhopadhyay
Department of Chemistry, Amity Institute of Applied Sciences (AIAS), Amity University Kolkata, Kolkata 700135, WB, India

M. Mukherjee et al. (eds.), *Advances in Medical Physics and Healthcare Engineering*, Lecture Notes in Bioengineering, https://doi.org/10.1007/978-981-33-6915-3_29

hazardous effects of electromagnetic radiation on human, animal, and plant life. The pollution caused by electromagnetic radiation is immensely responsible to create some serious problems such as it affects various parts of our brain, it creates cataracts in our eyes, it causes problem to pregnancy as well as it destroys the nutrients value of food products and generates carcinogenic compounds in certain food. This electromagnetic pollution can also affect plants by producing the aberration in chromosomes; destruction of DNA structure, reduction of growth of plants, reduction of seed germination as well as it also kills plant seeds (Hao et al. 2015; Robinette et al. 1980). In recent time, the research work on polymer-based composite materials takes the highest attention of the research community due to their multifunctional behavior in different technological applications (Sharma et al. 2014; Zhang et al. 1998). In this direction, the combination of magnetic nanofillers such as Ni–Zn–Cu–ferrite, Mn–Zn–Cu–ferrite, various forms of hexaferrite nanoparticles and polar phase of PVDF can be used to develop the most potential composite system applicable to combat against the harmful effects of electromagnetic pollution by generating high value of EMI-SE (Chakraborty et al. 2020; Saha et al. 2019; Sutradhar et al. 2019). PVDF is well known for its polymorphism and this PVDF is available with its five different crystalline phases called α-, β-, γ-, δ- and ε-phase (Saha et al. 2018). Among these five different crystalline phases, α-, β- and γ-phases/polymorphs are the most common types available therein. Here, α-phase is the non-polar phase, whereas β- and γ- are the polar phases, and these phases are the most interesting for different technological applications as they are responsible for the generation of piezoelectric, pyroelectric and ferroelectric responses in PVDF-based composite structures (Salimi and Yousefi 2003). Here, in the present work, we have selected soft-magnetic materials, i.e., Mn–Zn–ferrite (MZF) nanoparticles and PVDF as the potential components for the fabrication of MZF-PVDF composite materials and the EMI-SE of these MZF-PVDF composite structures in the microwave/GHz region of frequency [X-band (8–12 GHz) and K_u-band (12–18 GHz)] has been investigated along with the structural, morphological, chemical, magnetic and dielectric studies.

2 Synthesis of Materials

The MZF nanoparticles with desired composition of $Mn_{0.5}Zn_{0.5}Fe_2O_3$ were synthesized by sol–gel method. The sol–gel derived as-prepared MZF solid powder was annealed at 600 °C for 3 h in hot air furnace in order to get the required crystallographic phase and crystallite size of MZF nanofiller system. MZF-PVDF composite materials were prepared by solution casting method and different weight percentage of MZF nanofillers (10 and 20 wt%) were incorporated into the thick transparent gel of PVDF. The homogeneous mixture of MZF nanofillers and the PVDF gel was casted on a clean and warm glass plates, and the glass plates were placed inside the hot air oven to evaporate off the solvent (DMF) at 110 °C. After few hours of heating inside the hot air oven, the heterojunction laminated composites of MZF-PVDF were collected from the oven. The detailed specifications of synthesis and characterization techniques have been provided in the previous publications (Chakraborty et al. 2020; Saha et al. 2019; Sutradhar et al. 2019).

3 Results and Discussion

3.1 XRD Analyses

XRD patterns of PVDF and MZF-PVDF composite structures have been displayed in Fig. 1(I). All the peaks in the XRD pattern given in Fig. 1(I) are matched very well with that of the desired phases of MZF nanoparticles (JCPDS file no. 10–0325) (Fig. 1(I)a) and PVDF matrix (JCPDS file no. 38–1638) (Fig. 1(I)b). It is interesting to mention here that no extra peak due to any other secondary phases has been found in any of the XRD patterns. Figure 1(I) also shows that the XRD pattern of composite materials matched very well with that of the desired phase of MZF and PVDF. Different peaks of the XRD patterns also confirm the presence of α-, β-, and γ-phase crystallizations of PVDF in the composite materials (Guo et al. 2010). The average crystallite diameter of MZF nanoparticles has been estimated from the broadening of 100% intense peak (311) given in Fig. 1(I)a by using the Scherrer equation

$$\langle D\rangle_{(311)} = \frac{0.9\lambda}{\beta_{\frac{1}{2}}\cos\theta} \tag{1}$$

Here, D is the average nanocrystalline diameter, λ is the wavelength of the incident X-ray beam, θ is the corresponding Braggs angle, and $\beta_{\frac{1}{2}}$ is the full width at

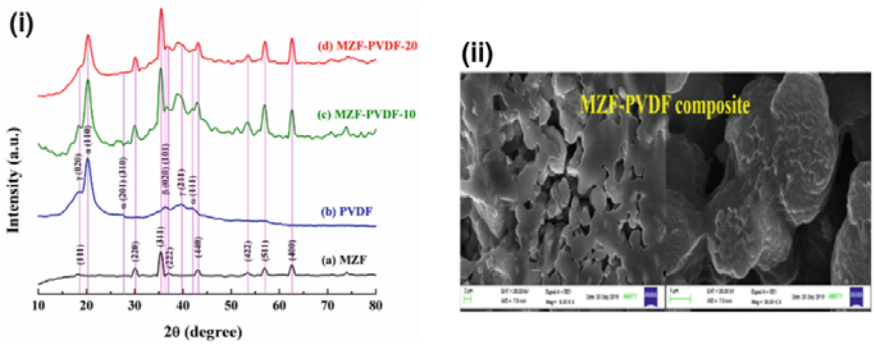

Fig. 1 (I) XRD image of the **a** MZF, **b** PVDF, **c** MZF-PVDF-10, and **d** MZF-PVDF-20 and (II) FESEM image of MZF-PVDF-10

half maximum (FWHM) of the (311) peak. The average nanocrystallite diameter of MZF nanoparticles has been estimated from Fig. 1a and it is nearly ~18.6 nm and the corresponding lattice parameter is 0.849 nm. The variation of peak intensity in Fig. 1(I)c, d has been observed due to the variation of β-phase crystallization in the MZF-PVDF composite structures. Also, it is important to mention here that the variation of β-phase crystallization in the MZF-PVDF composite structures has been found due to the successful incorporation of the MZF nanofillers in the matrix of PVDF. The incorporation of MZF nanofillers in the matrix of PVDF leads to the formation of interaction between the MZF nanofillers and the PVDF matrix at the interfaces inside these MZF-PVDF composite structures.

3.2 Morphological Analysis

Figure 1(II) reveals the morphology of MZF-PVDF composite structure. It is clear from the given figure that the micrograph of MZF-PVDF is spherulite in nature. This spherulite structure over the surface of the MZF-PVDF composite materials confirms the presence of β-phase crystallization of the PVDF matrix in all the composite structures (Saha et al. 2018). Also, from the given micrograph, it is clear that MZF nanofillers are present inside the matrix of PVDF, and the incorporation of MZF nanofillers inside the matrix of PVDF is responsible for the enhancement of the polar β-phase crystallization of the PVDF matrix. This phenomenon also confirms the presence of interfaces between the MZF nanofillers and PVDF matrix in all the MZF-PVDF composite structures.

3.3 Chemical Analysis

Figure 2(I) shows the Fourier transform infrared (FTIR) absorption spectra of PVDF and MZF-PVDF composite structures (MZF-PVDF-10 and MZF-PVDF-20). The FTIR spectrum of PVDF shows characteristic peaks at 495 cm^{-1} (CF_2 waging), 540 cm^{-1} (CF_2 bending), 620 cm^{-1} (CF_2 bending), 770 cm^{-1} (CF_2 skeletal bending), 817 cm^{-1}, and 982 cm^{-1} (CH_2 rocking) assigned to the IR bands of non-polar α phase of PVDF, and three peaks at 524 cm^{-1} (CF_2 stretching), 847 cm^{-1} (CH_2 rocking, CF_2 stretching, and skeletal C–C stretching,) and 898 cm^{-1} (CH_2 and CF_2 groups generated from the CH_2 rocking and CF_2 stretching) conforming the presence of polar β-phase of PVDF (Prabhakaran and Hemalatha 2016). Figure 2(I) also shows the intensity variation of the characteristic absorption bands corresponding to non-polar α-phase and polar β-phase of PVDF in all the MZF-PVDF composite structures. In the present study, the relative intensity of the characteristic absorption bands corresponding to polar β-phase of PVDF has been enhanced with respect to the non-polar α-phase for MZF-PVDF composite structures (MZF-PVDF-10 and MZF-PVDF-20). Hence, the FTIR results indicate the sustainability of β-phase of PVDF

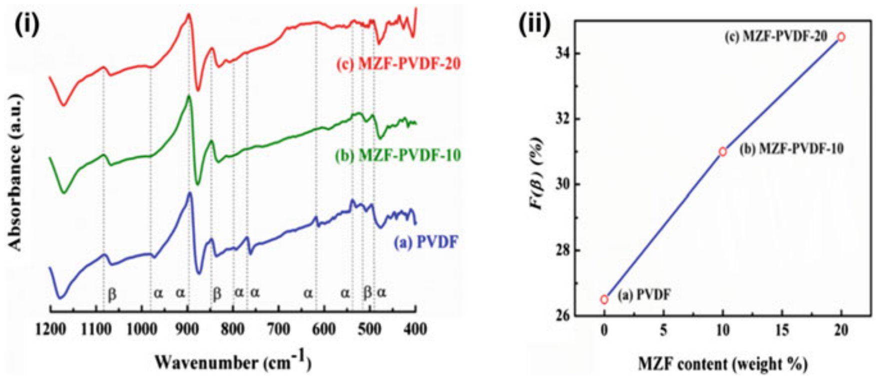

Fig. 2 (I) FTIR spectra of **a** PVDF, **b** MZF-PVDF-10, and **c** MZF-PVDF-20 and (II) variation of β-phase fraction as a function of MZF content in **a** PVDF, **b** MZF-PVDF-10, and **c** MZF-PVDF-20

even in presence of MZF nanofillers as well as the transformation of non-polar α-phase to polar β-phase of PVDF due to the incorporation of the MZF nanofillers inside the PVDF matrix. The β-phase fraction ($F(\beta)$) has been estimated in the present study for PVDF and ($F(\beta)$) of ~26.4% has been observed for PVDF. ($F(\beta)$) has also been estimated for MZF-PVDF composite structures and it varies from 26.4% for PVDF to 31% for MZF-PVDF-10 and 34.5% for MZF-PVDF-20. The calculation of β-phase fraction ($F(\beta)$) has been done from the FTIR spectra using Lambert–Beer law as given in Eq. 2 (Gregorio and Cestari 1994).

$$F(\beta) = \frac{A_\beta}{\left(\frac{K_\beta}{K_\alpha}\right)A_\alpha + A_\beta} \tag{2}$$

Here, A_α and A_β are the absorbance at 770 cm^{-1} and 847 cm^{-1}, respectively, and K_α (6.1 × 10^4 cm^2 mol^{-1}) and K_β (7.7 × 10^4 cm^2 mol^{-1}) are the absorption coefficients at their respective wavenumbers. Figure 2(II) shows the variation of β-phase fraction ($F(\beta)$) with the incorporation of MZF nanofillers in the PVDF matrix. From Fig. 2(II), it is clear that with the variation of loading fraction of MZF nanofillers, the β-phase fraction ($F(\beta)$) varies and the maximum value of β-phase fraction ($F(\beta)$) (nearly ~34.5%) has been achieved for MZF-PVDF-20. The interaction between the MZF nanofillers and the polymer matrix leads to this enhancement of β-phase fraction. When the filler content is low, the effective interfacial area between the PVDF and the MZF nanofillers is less and with the increment of the homogeneously dispersed MZF nanofillers inside the PVDF matrix the interfacial area increases. Hence, the number of aligned chains having 'all-trans' (TTTT) conformation has been enhanced and leads to the successful increment of the fraction of β-phase for the MZF-PVDF composite structures.

3.4 Static Magnetic Study

Static hysteresis loops of MZF-PVDF-10 and MZF-PVDF-20 have been recorded at room temperature (300 K), and the maximum applied magnetic field was ~50,000 Oe. The systematic developments of the magnetization with the increasing loading percentage of the MZF nanofillers in the matrix of PVDF have also been observed in Fig. 3. Figure 3a, b represents the magnetic hysteresis loops of MZF-PVDF-10 and MZF-PVDF-20, respectively, at RT. It is clear from the hysteresis loops of MZF-PVDF-10 and MZF-PVDF-20 that the magnetization curves are more or less saturated at around ~50,000 Oe, which indicates the soft-magnetic nature of the composite materials. Close inspection of these hysteresis loops revealed that the value of magnetization increases very slowly even when the applied field is 50,000 Oe. This happens mainly due to the presence of a small fraction of superparamagnetic (SPM) particles in the composite structures at RT. The maximum magnetization (M_{max}) of MZF-PVDF-10 and MZF-PVDF-20 has been extracted from the different loops recorded at 300 K and the value of M_{max} of 8.7 emu/g and 15.8 emu/g, respectively, corresponding to MZF-PVDF-10 and MZF-PVDF-20 have been observed for the present study. From the values of M_{max} of MZF-PVDF-10 and MZF-PVDF-20, it is quite clear that the overall magnetic response increases with the increasing loading percentage of MZF nanofillers inside the matrix of PVDF, which is normally happened in case of nanocrystalline ferrite materials. The high values of M_{max} of MZF-PVDF-10 and MZF-PVDF-20 even in presence of the PVDF matrix make them most suitable for different applications in the domain of magnetic and magneto-electric effect. The differences observed in the coercive field for MZF-PVDF-10 and MZF-PVDF-20 suggest that all the nanofillers are successfully encapsulated inside

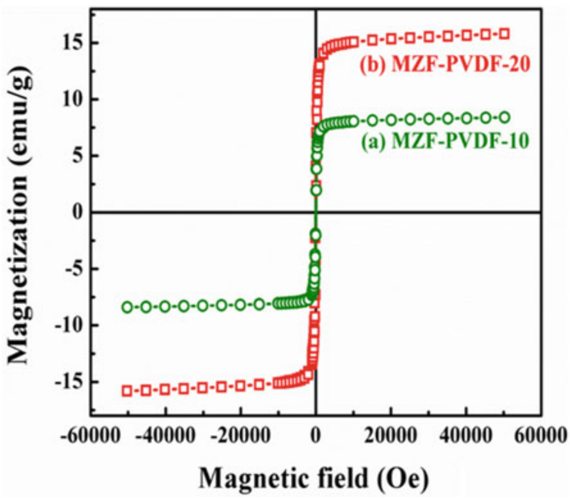

Fig. 3 Hysteresis loops of **a** MZF-PVDF-10 and **b** MZF-PVDF-20 composite materials at RT

the matrix of PVDF due to which dipolar and/or exchange interaction comes into play among the magnetic nanofillers. Thus, the dipolar and/or exchange interaction is strongly modulated by the presence of PVDF matrix. Also, from the magnetic measurement, it is clear that the MZF-PVDF composite materials are quite able to modify the structure as well as the orientation of the PVDF matrix when the material is subjected to the external magnetic field and this property of the material is mostly helpful for the consideration of these composite materials as the potential candidate for microwave absorption.

3.5 Dielectric Study

The variations of real part of dielectric constant (ε') and dielectric loss tangent (tanδ) as a function of frequency at room temperature of PVDF and MZF-PVDF composite structures (MZF-PVDF-10 and MZF-PVDF-20) have been measured and the observed graphs are shown in Fig. 4(I) and (II), respectively. Frequency dependent ε′ is an important study to understand the usefulness of these MZF-PVDF composite structures as a potential candidate for EMI-SE. A high-quality EMI-SE requires responses due to magnetization, electric polarization as well as the effective coupling between them. In this section, we have discussed the modulation of the dielectric response of MZF-PVDF composite structures due to the incorporation of MZF nanofillers inside the matrix of PVDF. Dielectric response of MZF-PVDF composite structures is characterized by complex permittivity of the material which is represented by (Debnath et al. 2018)

$$\varepsilon = \varepsilon' - j\varepsilon'' \tag{3}$$

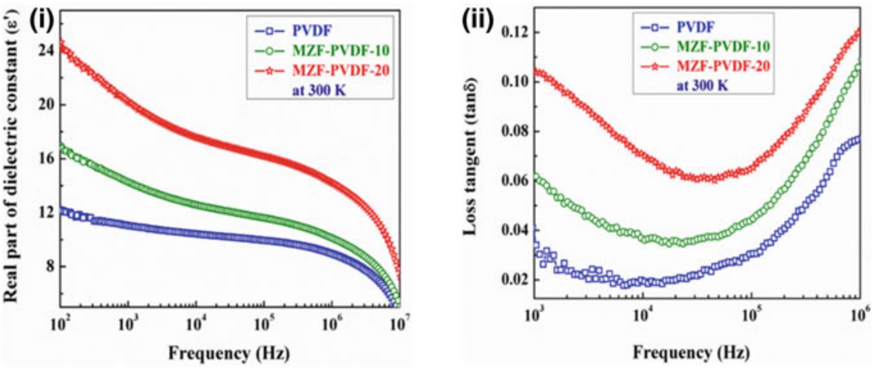

Fig. 4 Variation of (I) ε' with frequency and (II) tanδ with frequency of PVDF, MZF-PVDF-10, and MZF-PVDF-20

Here, in Eq. (3), the symbols have their usual meanings. The value of ε' has been estimated to understand the behavior of electrostatic energy storing ability of MZF-PVDF composite structures in presence of externally applied alternating electric field. ε' of PVDF and MZF-PVDF composite structures has been calculated by using the formula (Ansari et al. 2012)

$$\varepsilon' = \frac{Cd}{\varepsilon_0 A} \tag{4}$$

where C is the capacitance of the sample, d and A are thickness and area, respectively, of PVDF and MZF-PVDF composite structures, and ε_0 is the free space permittivity. It is quite clear from Fig. 4(I) that the value of ε' of PVDF and MZF-PVDF composite structures has increased gradually from bare PVDF to MZF-PVDF-10 and then from MZF-PVDF-10 to MZF-PVDF-20. The maximum value of ε' has been observed for MZF-PVDF-20. The variation of ε' as a function of frequency can be explained most conveniently with the help of two major phenomena. The first one is the variation of intrinsic β-phase crystallization of the host PVDF structure due to the incorporation of the MZF nanofillers in the matrix of PVDF. The second one is the Maxwell–Wagner–Sillars interfacial polarization effect which appears due to the heterogeneous medium consisting of two different phases of MZF nanofillers and the PVDF matrix (Wagner 1913; Maxwell 1929). The presence of two different component materials inside the structure of MZF-PVDF composite generate dissimilar permittivity and conductivity and this effect causes accumulation of the carrier charges at the interfaces of MZF-PVDF composite structures. In the present study, the number of effective interfaces between MZF nanofillers and the PVDF matrix increases with the increasing amount of MZF nanofillers inside the matrix of PVDF and the maximum polarization effect has been observed with 20 wt% of MZF nanofillers in the matrix of PVDF (MZF-PVDF-20). From the given Fig. 4(II), it is quite clear that the dielectric loss tangent (tan δ) decreases with the increase in frequency at RT (300 K). This type of variation of dielectric loss tangent (tan δ) appears due to the presence of space charge polarization inside the composite structures. It has been observed in Fig. 4(II) that the dielectric loss tangent (tan δ) increase with the increasing loading percentage of MZF nanofillers inside the PVDF matrix. This type of behavior appears partially by the higher tan δ of the MZF nanofillers relative to those of the β-phase of PVDF and partially by the structural mismatch of the MZF nanofillers with the PVDF matrix due to the incorporation of the MZF nanofillers in the matrix of PVDF. The structural mismatch is likely to induce localized space charges as well as Maxwell–Wagner–Sillars interfacial polarization as explained above, thereby producing an additional input to tan δ. As compared to PVDF, the MZF-PVDF composite structures show relatively stronger frequency dependence within the lower frequency range. The polarization in ferrites such as MZF system originates from the electronic exchange between coexisting Fe^{2+} and Fe^{3+} ions in the B-site or octahedral site of the spinel phase which cannot follow the frequency of the externally applied electrical field beyond a certain critical value and gradually decreases with increasing frequency. As a result, tan δ of PVDF and MZF-PVDF decreases with the increasing frequency. However, from Fig. 4(II), it can be inferred that once the frequency is over 100 kHz, the relaxation mechanism associated with the β-phase of PVDF dominates the overall dielectric behavior. In this study, tan δ of MZF-PVDF in the higher-frequency range (above 100 kHz) follows the same trend to that of PVDF system. It shows that this particular observation of these MZF-PVDF composite structures is not from Maxwell–Wagner–Sillars interfacial polarization in the higher-frequency range but rather from the intrinsic dielectric properties of the MZF and PVDF systems.

3.6 Shielding Effectiveness Study

Figure 5a, b shows the variation of the shielding effectiveness (SE) within the frequency range of 8–18 GHz frequency for the MZF-PVDF composite materials. It is quite clear from Fig. 5a, b that SE in the microwave range of frequency has been enhanced due to the presence of magnetic MZF nanofillers inside the matrix of PVDF. The value of SE of MZF-PVDF composite materials in the microwave range of frequency has been estimated. Interestingly, the maximum value of SE of nearly ~ -31.9 dB at a matching frequency of 11.5 GHz has been observed in case of 20 wt% of MZF nanofillers loaded PVDF composite material (MZF-PVDF-20) and nearly ~−31.8 dB at a matching frequency of 14 GHz has been observed in case of 10 weight % of MZF nanofillers loaded PVDF composite material (MZF-PVDF-10). Here, in the present composite materials, the structure of PVDF has been modified due to its interaction with MZF nanofillers, and the PVDF has been transformed into a polar dielectric polymer. Due to the presence of both magnetic dipolar contributions of MZF nanofillers and electric dipolar contributions of MZF nanoparticles and the electroactive β- and γ-phase of PVDF, SE has been enhanced. Thus, the presence of MZF nanofillers in the matrix of PVDF improves SE of the composite materials. These low-cost MZF-PVDF composite materials with good flexibility, small thickness, lightweight can be potentially used for the reduction of electromagnetic pollution. MZF nanoparticles and polar PVDF interact with the microwave radiations and act as the active center for microwave absorption process and lead to the capacity of SE property. Now, in case of bare PVDF, the presence of dielectric loss contributes to the energy loss of EM wave, whereas in case of magnetic MZF nanofillers, the presence of magnetic loss due to eddy current loss is more significant than the dielectric loss. Thus, both magnetic loss and dielectric loss are out of balance in case of individual components such as magnetic MZF nanofillers and the polar PVDF matrix, which induces poor EMI-SE. However, in the MZF-PVDF composite structures, EMI-SE is enhanced because of the well matching of the magnetic loss and dielectric loss originated from magnetic MZF nanofillers and PVDF matrix present in the same composite structures. So, the formation of a heterojunction composite structure of MZF-PVDF and the effective interaction of these composite structures with the EM radiation in the GHz frequency range make them useful for the fabrication of EM pollution reducer.

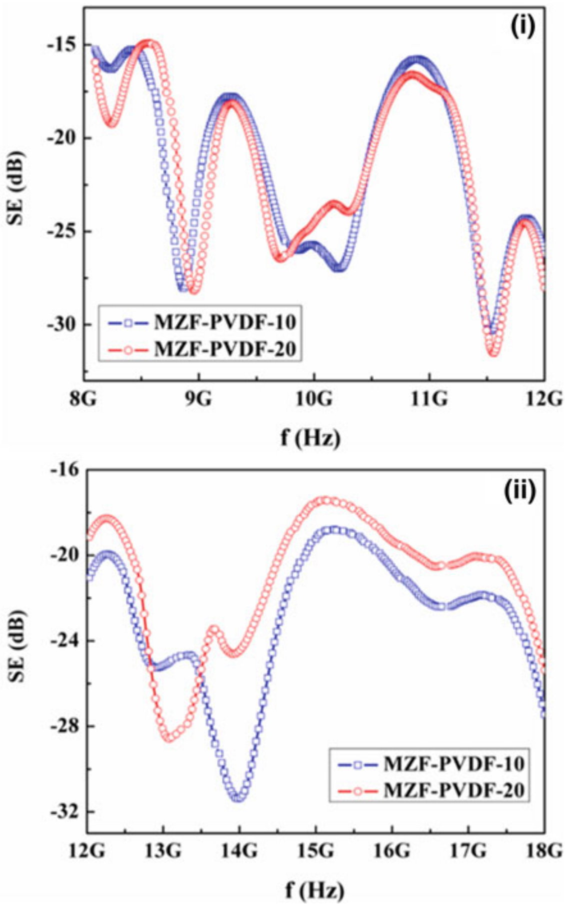

Fig. 5 SE of MZF-PVDF composite materials within **a** X-band (8–12 GHz) and **b** K_u-band (12–18 GHz)

4 Conclusion

In the present report, we have successfully synthesized MZF-PVDF composite materials using a very simple solution casting method. The presence of large area of interfaces between MZF nanofillers and PVDF matrix plays the most significant role during wave-matter interaction and the composite materials provide large EMI-SE of the composite materials. The large magnetizations of 8.7 and 15.8 emu/g corresponding to MZF-PVDF-10 and MZF-PVDF-20 composite materials and significantly large dielectric polarization have been observed in the composite materials. The effective interaction of EM waves with magnetic and dielectric dipoles present inside the MZF-PVDF composite structures play the most significant role for the enhancement of SE of MZF-PVDF composite materials. A maximum of nearly −

32 dB of SE at a matching frequency of 11.5 and 14 GHz corresponding to MZF-PVDF-10 and MZF-PVDF-20 composite materials has been observed in this report. This high SE of MZF-PVDF composite materials is very useful for the designing of an efficient electromagnetic pollution reducer.

Acknowledgements The authors would like to acknowledge Amity University Kolkata for providing necessary support for this research work.

References

Ansari SA, Nisar A, Fatma B, Khan W, Chaman M, Azam A, Naqvi AH (2012) Temperature dependent anomalous dielectric relaxation in Co doped ZnO nanoparticles. Mater Res Bull 47:4161–4168

Chakraborty T, Debnath T, Bhowmick S, Bandyopadhyay A, Karmakar A, Das S, Sinha Mahapatra A, Sutradhar S (2020) Enhancement of EMI shielding effectiveness of flexible Co_2U-type hexaferrite ($Ba_4Co_2Fe_{36}O_{60}$)-poly(vinylidene fluoride) heterostructure composite materials: an improved radar absorbing material to combat against electromagnetic pollution. J Appl Phys 128:095301–095314

Debnath T, Saha P, Patra N, Das S, Sutradhar S (2018) Hydrothermal process assists undoped and Cr-doped semiconducting ZnO nanorods: frontier of dielectric property. J Appl Phys 123:194101–194114

Gregorio R, Cestari M (1994) Effect of crystallization temperature on the crystalline phase content and morphology of poly(vinylidene fluoride). J Polym Sci B Polym Phys 32:859–870

Guo Y, Liu Y, Wang J, Withers RL, Chen H, Jin L, Smith P (2010) Giant magnetodielectric effect in 0−3 $Ni_{0.5}Zn_{0.5}Fe_2O_4$-poly(vinylidene-fluoride) nanocomposite films. J Phys Chem C 114:13861–13866

Hao YH, Zhao L, Peng RY (2015) Effects of microwave radiation on brain energy metabolism and related mechanisms. Mil Med Res. 2:4–11

Maxwell JC (1929) Electricity and magnetism, vol I. Oxford University Press, Oxford

Prabhakaran T, Hemalatha J (2016) Magnetoelectric investigations 1178 on poly (vinylidenefluoride)/$NiFe_2O_4$ flexible films fabricated through solution casting method. RSC Adv 6:86880−86888

Robinette CD, Silverman C, Jablon S (1980) Effects upon health of occupational exposure to microwave radiation (radar). Am J Epidemiol 112:39–53

Saha P, Das S, Sutradhar S (2018) Influence of Ni-Zn-Cu-ferrite on electroactive β-phase in poly(vinylidene fluoride)- Ni-Zn-Cu-ferrite nanocomposite film: unique metamaterial for enhanced microwave absorption. J Appl Phys 124:045303–045312

Saha P, Debnath T, Das S, Chatterjee S, Sutradhar S (2019) β-Phase improved Mn-Zn-Cu-ferrite-PVDF nanocomposite film: a metamaterial for enhanced microwave absorption. Mater Sci Eng B 245:17–29

Salimi S, Yousefi AA (2003) FTIR studies of β-phase crystal formation in stretched PVDF films. Polym Test 22:699–704

Sharma M, Singh MP, Srivastava C, Madras G, Bose S (2014) Poly(vinylidene fluoride)-based flexible and lightweight materials for attenuating microwave radiations. ACS Appl Mater Interface 6:21151–21160

Sutradhar S, Saha S, Javed S (2019) shielding effectiveness study of barium hexaferrite-incorporated, β-phase-improved poly(vinylidene fluoride) composite film: a metamaterial useful for the reduction of electromagnetic pollution . ACS Appl Mater Interfaces 11(26):23701–23713
Wagner KW (1913) The distribution of relaxation times in typical dielectrics. Ann Phys 40:817–819
Zhang QM, Bharti V, Zhao X (1998) Giant electrostriction and relaxor ferroelectric behaviour in electron-irradiated poly(vinylidene fluoride-trifluoroethylene) copolymer. Science 280:2101–2104

A New Approach of Using Microscopic Image Aided Computer Programming for Evaluation of Porosity and Aerosity: Case Studies Using Polymeric Films and Functional Matrices

Abhra Giri, Subir K. Patla, Madhumita Mukhopadhyay, Jayanta Mukhopadhyay, Monalisa Mukherjee, Ruma Ray, and Sujata Tarafdar

Abstract Porous polymer films of Poly-[Ethylene oxide] (PEO) are synthesized by solution casting technique using gamma irradiated: (a) PEO powder (S-series) and (b) PEO—methanol solution (L-series). Pore phase is though a defect, but form instantaneously during preparation. Optimization of the pore content, its size and distribution enable tailoring of associated properties for multifaceted applications of functional materials. The experimental pore-size distribution of the PEO films is studied using BET (Brunauer–Emmet–Teller) adsorption technique and reported as function of irradiation dose, irradiation state (S- and L-series) and polymer concentration (2 and 4 wt%). A newer computer program [$PROG_{IMAGE\text{-}POR}$] is reported for determination of porosity, its size and distribution of perturbed PEO films using SEM images and correlated with that obtained from BET technique. The novelty of $PROG_{IMAGE\text{-}POR}$ lies in the exposure of newer or undetected pore regime in which experimental pore regime exists as a part. This method could be analyzed for mapping of porosity and average pore size. $PROG_{IMAGE\text{-}POR}$ bears the novelty of using image from either 2D or 3D imaging system and could be applied for intricate composite/layered system.

A. Giri · S. K. Patla · R. Ray
Department of Physics, Gurudas College, Kolkata 700054, West Bengal, India

S. K. Patla · S. Tarafdar
Department of Physics, Condensed Matter Physics Research Centre, Jadavpur University, Kolkata 700032, West Bengal, India

M. Mukhopadhyay (✉)
Department of Chemistry, Amity Institute of Applied Sciences (AIAS), Amity University, Kolkata 700135, West Bengal, India

J. Mukhopadhyay
Energy Materials & Devices Division, CSIR-Central Glass and Ceramic Research Institute, Kolkata 700032, India

Academy of Scientific and Innovative Research (AcSIR), Gaziabad 201002, India

M. Mukherjee
Amity Institute of Biotechnology, Amity Institute of Click Chemistry Research and Studies, Amity University Uttar Pradesh, Sector-125, Noida 201303, Uttar Pradesh, India

M. Mukherjee et al. (eds.), *Advances in Medical Physics and Healthcare Engineering*, Lecture Notes in Bioengineering, https://doi.org/10.1007/978-981-33-6915-3_30

Uniqueness of $PROG_{IMAGE\text{-}POR}$ lies in the exposure of newer pore regime in which experimental pores exist as a part. Theoretical analysis based on aerosity (2D-pores) and porosity (3D-pore) gives an estimate of the tortuous path of void space.

Keywords Porosity · Morphology · Pore-size distribution · Computer program · Gray-scale pixel · Gamma irradiation

1 Introduction

Pores (or voids) are formed in polymer films irrespective of any preparation technique like gel casting, emulsion freeze drying, acylation, solution casting, etc. (Laera et al. 2016; Yu et al. 2011). Easily soluble and fusible polymers are well used in the aforementioned techniques. However, certain conjugated polymer, e.g., polythiopene, etc. being insoluble and infusible do not fit into such procedures. Conducting porous material is well studied due to their important applications in the field of electrolytic capacitors, battery separators and electrode materials (Fusalba et al. 1999; Ren and Pickup 2001; Brown et al. 2018). Furthermore, porous polymer films having micro- and sub-micrometer pores have multiple applications in water purification, separation, scaffolds for tissue engineering, low dielectric constant materials for microelectronic devices, band gap materials, solid supports for sensors and catalysts, etc. (Lima et al. 2012; Lin et al. 1997; Hubbell and Langer 1995; Hedrick et al. 1998; Deutsch et al. 2000; Jiang et al. 1999; Park and Xia 1998). The basic challenge lies in the optimization of pore-size and porosity distribution based on the purpose of application. Preparation of two or three-dimensional ordered porous structure is reported by Jiang et al. and Cassagneau et al. using templating method wherein self-assembled colloidal microspheres are utilized (Cassagneau and Caruso 2002; Jiang and McFarland 2004).

In lieu of this above discussion, pore phase has recently emerged as an important subject to be well studied and optimized for multifaceted applications. Study of pore phase bears significance in identification of individual grain interfaces through the indirect outcome of the processes at micro-scale also termed as pore scale by Wildenschild et al. (2013). Identification and investigation of such pore scale are found to primarily govern the large-scale phenomena in industrially viable materials, e.g., polymer, ceramic, etc. Emphasis on the study of pore phase helps in understanding the material properties, neglecting the outcomes at very high and smaller scales. Study of porosity in terms of quantification and distribution involved multiple well-studied tools, viz. adsorption technique (BET technique, nitrogen adsorption) (Stephan and Teeters 2003; Ricco et al. 1989), intrusion procedures as mercury porosimetry (Calvo et al. 1995; Mukhopadhyay et al. 2012), X-ray tomography, etc. (Pyun et al. 2007). X-ray tomography has numerous advantages of generating 3-D information and for opaque porous media, about process and variables of importance to substrate flow and transport phenomena (Myers et al. 2011; Culligan et al. 2004). In addition, tomographic imaging enables quantification of pore scale (Wildenschild and

Sheppard 2013). In case of fluid flow and transport processes, techniques such as focused ion beam-scanning microscopy (FIB-SEM) and TEM tomography are in development stage wherein representation of elementary volume is not well suited presently (Wildenschild and Sheppard 2013). The major disadvantages associated with X-ray tomographic imaging include artifacts produced by sample rotation and metal mountings, costly instrumentation, long measurement time for single sample, destructive nature for soft matter and large data files. In fact, real-time imaging is not possible from tomographic technique; however, coded aperture imaging using a multi-slit code combined with CCD detectors provides real-time imaging.

In line with the aforementioned findings, morphological studies based on electron beam source can be indirectly used to study the pore phase. Some case studies on the applicability of such microscopic tool in conjunction with a developed simple computer program are discussed in this chapter. A novel computer program termed as PROGIMAGE-POR is developed and coupled with microscopic images for the determination of porosity, its size and distribution and is correlated with the experimental outcomes. The case studies are primarily reported using porous Poly(ethylene oxide), PEO films perturbed using high energy gamma dose (1–30 kGy, in powder and methanol solution state). Experimental porosity and pore-size distribution (PSD) of such polymer sample are studied using BET (Brunauer–Emmet–Teller) adsorption technique. Compared to numerous techniques employed for porosity and PSD viz. mercury porosimetry, Rutherford backscattering spectroscopy and small-angle neutron scattering (SANS) (Mogilnikov et al. 1999; Dourdain et al. 2005; Yim et al. 2003), etc., BET method is can be employed due to its simple and reliable measurement procedure (Gregg and Sing 1982).

The prime intention of the present amalgamation among the computer program with the morphological study is not to compare the resultant porosity obtained from experimental BET and PROGIMAGE-POR. However, the novelty of PROGIMAGE-POR lies in the exposure of newer or undetected pore regime. Experimental results on porosity and pore distribution have been standardized by several set of investigations fulfilling the criterion of reproducibility. For any technique or comparative approach, statistical analyses of error are the intrinsic arena involved therein. The subsequent subsections of the chapter will focus on such error analyses with respect to the case studies using standard deviation. Application of such novel approach using combined computer program and morphological image analyses is undertaken primarily on the dual phasic PEO films perturbed differently by gamma radiation as stated above. In addition, effectiveness of the program is reported in terms of its application for intricate composites.

2 Methodology

Self-standing polymer films (~200 μm) of Poly (ethylene oxide) (B.D.H., England, Mol Wt. 10^5) were prepared using gamma irradiated powder and methanol solution of PEO. Samples in the form of PEO powder (termed as S-series) and methanol

Table 1 Sample identification of experimental Poly(ethylene oxide) films

Sample irradiated	Concentration of PEO (g mL^{-1})	Sample ID					
		Dose (kGy)					
		1	5	10	15	20	30
Powder irradiation	0.02	2S-1	2S-5	2S-10	2S-15	2S-20	2S-30
	0.04	4S-1	4S-5	4S-10	4S-15	4S-20	4S-30
Solution irradiation	0.02	2L-1	2L-5	2L-10	2L-15	2L-20	2L-30
	0.04	4L-1	4L-5	4L-10	4L-15	4L-20	4L-30

Porosity and pore-size distribution of PEO films obtained from γ-irradiated powder and methanol solution: Study using adsorption technique

solution (L-series) were irradiated using Co_{60} source with dose rate of 6.4 kGy h^{-1} in air. Gamma doses were varied in the range of 1–30 kGy followed by preserving the irradiated samples in airtight vacuum desiccator in order to protect from moisture and other external agents. The detail of film preparation by solution casting method using methanol as solvent is already described elsewhere (Mukhopadhyay et al. 2016) and sample identifications are given in Table 1, wherein the concentration of PEO was maintained at 0.02 and 0.04 g mL^{-1}, respectively.

For experimental determination of porosity and pore-size distribution (PSD), PEO films prepared from unirradiated; irradiated powder and methanol solution were subjected to BET analyzer [Quantachrome Instruments]. The microstructural images of the experimental polymer samples were characterized using scanning electron microscopy (SEM) [FEIC-QUO-35357-0614 with Bruker Quantax 100]. These SEM images were employed as an input source file for PROGIMAGE-POR. The experiments were repeated on different part of single film to judge the standardization of film preparation. In the present context, the presented results are averaged from such multiple outcomes for all irradiation doses. In order to study the effectiveness and repeatability of the present program, standard deviation of the average porosity is calculated for backscattered SEM images. Backscattered mode being the only parameter, dependent on atomic number of elements, standard deviation of average porosity is least and establishes the proposed program to be universally accepted for monophasic system.

3 Fundamentals of the Program (PROG$_{\text{IMAGE-POR}}$)

This section of chapter enlightens the readers about the basics of the program developed and applied for the polymer system. The primary intention is to analyze porosity and a new concept of **aerosity** applicable for 2D context. The basic flow chart for determination of porosity by PROG$_{\text{IMAGE-POR}}$ is shown in Fig. 1. SEM images of experimental PEO samples are converted to *8bit type* image using ImageJ software and saved as *text image* with.*txt* file extension.

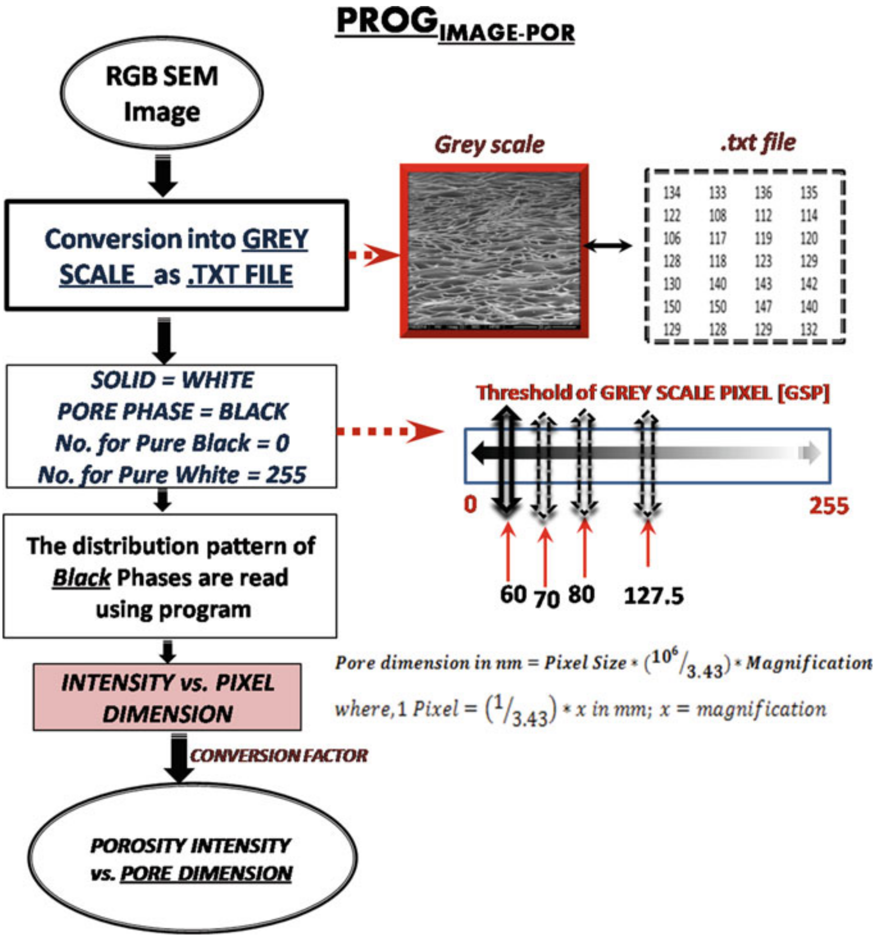

Fig. 1 Schematic flow chart for the developed program [$\mathrm{PROG}_{\mathrm{IMAGE\text{-}POR}}$]

Each of these text images contains integer numbers ranging from 0 to 255 as a 2D array with dimension *width * height* of the SEM image. Integer numbers come from the pixel value of the corresponding *8bit* SEM image. Here 0 corresponds to perfect black color and 255 corresponds to perfect white color. Other numbers in between 0 and 255 give the variation in gray scale. We have termed these numbers as gray-scale pixel (GSP). We have set GSP to a particular threshold value GSP_{th} to signify solid ($GSP > GSP_{th}$) or void ($GSP < GSP_{th}$) phase.

FORTRAN program was developed to find out the porosity value of the images setting GSP value where text images are the input files. In our $\mathrm{PROG}_{\mathrm{IMAGE\text{-}POR}}$ GSP, values are varied in the range of 50–127.5 (Fig. 1). The outcome of $\mathrm{PROG}_{\mathrm{IMAGE\text{-}POR}}$ is obtained in the form of "*Pore-size distribution [Porosity Intensity vs. Pixel dimension]*" and "*Average porosity [Av. Porosity vs. dose]*". The pixel dimension as obtained from program is converted to pore dimension using Eqs. 1 and 2. Equation 2 is calculated from IMAGEJ software.

$$\text{Pore dimension in nm} = \text{Pixel Size} * \left({10^6}/{3.43}\right) * \text{Magnification} \tag{1}$$

$$\text{where, } 1 \text{ Pixel} = \left({1}/{3.43}\right) * x \text{ in mm; } x = \text{magnification} \tag{2}$$

The SEM images being two dimensional pose a problem in the selection of depth of the pore phases as it lacks the third dimension. We can get better result by stacking sequentially image of each layer of the polymer sample if possible.

In actual practice, however, the shape of the pore remains an important aspect which remains inconspicuous or neglected. However, during pore formation either in situ or as an influence of high energy perturbation (in the present case), the path and configuration of the pore influence the void thereby affecting the associated material parameters. In the following chapters, aerosity is computed for such polymer-based systems considering cylindrical, spherical and tortuous cylindrical type of pores.

4 Discussions

4.1 CASE STUDY-1: Perturbed Poly(-Ethylene Oxide)

The applicability of the program as discussed is applied to study the pore-size distribution of poly-[ethylene oxide] (PEO) subjected to gamma irradiation in the dose range 1 to 30 kGy. Furthermore, the mentioned polymer system is irradiated both in powder and liquid state in two concentrations as mentioned in Table 1. The table also lists the nomenclature of sample along with the irradiation history.

The distribution of pore phase in perturbed pristine PEO system is found to depend on the physical state subjected to gamma irradiation. The present section illustrates the influence of gamma irradiation on porosity and pore-size distribution of PEO films studied using BET technique.

The average dimension of pores lies within 100–500 nm for PEO films prepared using irradiated powder (2/4-S-series) and/or methanol solution (2/4-L-series) as observed from Figs. 2 and 3. In addition to the mentioned pore-dimension regime, smaller pores of <100 nm exists for unirradiated PEO matrix which disappear upon subsequent irradiation. The extent of multimodal pore distribution is high for 2S- and 4S-series at lower irradiation doses which subsequently becomes unimodal with much smaller pores with increment in dose. Similar trend is observed for 2L- and 4L-series (Fig. 3). Increase in irradiation dose generates excited radicals which stabilize through mobilization of polymer chains thereby forming larger spherulites. Growth in the size of spherulites minimizes pore phase (low % porosity) and shifts pore dimension to lower regime (from right to left in Figs. 2 and 3) with increase in irradiation.

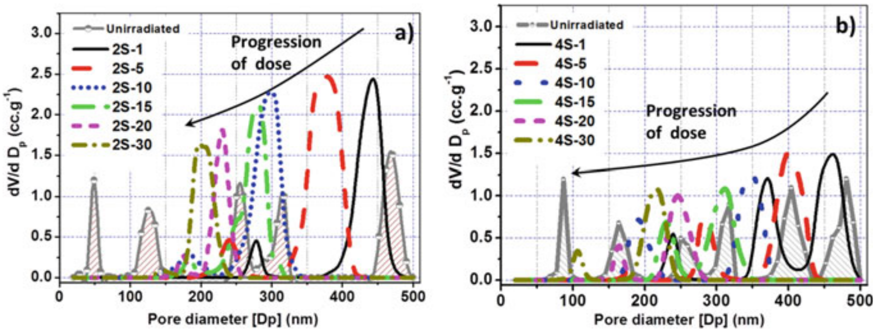

Fig. 2 Pore-size distribution determined from BET technique for: **a** 2S- and **b** 4S-series as a function of irradiation dose

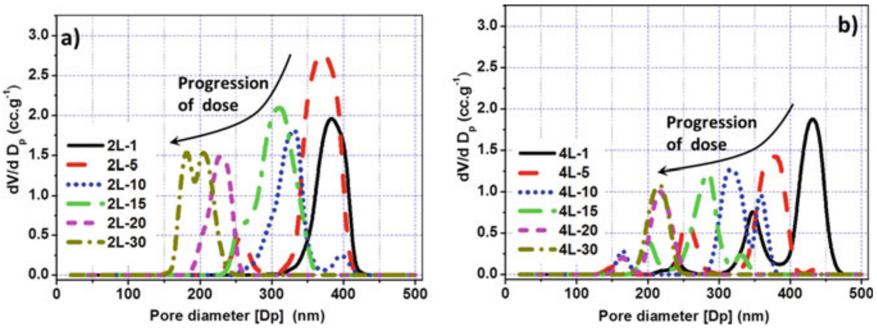

Fig. 3 Pore-size distribution determined from BET technique for: **a** 2L- and **b** 4L-series as a function of irradiation dose

In the present context, air assisted irradiation of either PEO powder or methanol solution promotes scission as already established in our earlier communication (Mukhopadhyay et al. 2016).

However, most of the gamma radiation is absorbed by the solvent during solution irradiation which generates –CH_2OH radical that acts as a cross-linking agent owing their higher mobility. Consequently, % porosity is lower for both 2/4L-series compared to 2/4S-series (Fig. 4).

Irrespective of powder or solution state irradiation, predominant contribution of scission increases % porosity sharply till 5 kGy in all the samples. However, with further increase in dose, matrix densification results due to the formation of innumerable scission fragments in S-series. 2/4L-series possess much lower porosity compared to S-series with sharp declining trend after 5 kGy. Compared to powder irradiation, high energy perturbation of PEO solution enables a pattern in pore distribution having lesser modality (uniform distribution). As expected, 4L-series having higher concentration is found to be denser (low porosity) with sharp reduction in porosity after irradiated with dose 5 kGy. The significant outcome as observed from

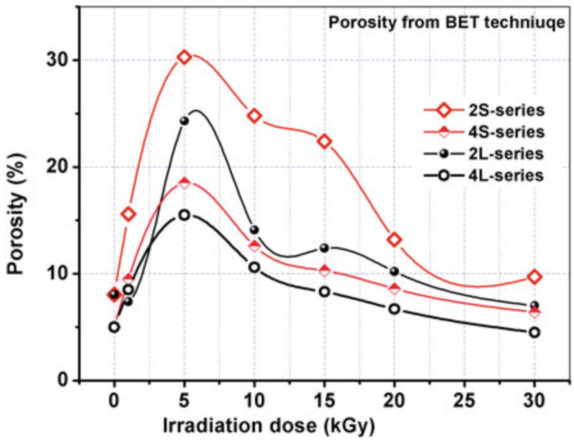

Fig. 4 Average porosity (in %) as a function of irradiation dose for 2/4S- and 2/4L- series obtained from BET technique

Figs. 2, 3 and 4 is that selective regime of % porosity with unique pore-size distribution is obtained with a specific irradiation dose and state of the polymer. This helps in selection of experimental polymer system for explicit application.

Implementation of PROG$_{\text{IMAGE-POR}}$ in Pristine Perturbed PEO

Experimental tools are though specific; possess certain limitations in estimation of porosity of soft polymer films. The instrumentation for BET technique is based on the inert gas adsorption through the pores of PEO film followed by fitting to certain standard isotherm. The outcome in the form of pore-size distribution is therefore indirectly dependent on the type of isotherm which closely matches with the experimental results. Conceptually, such experimental techniques might either rule out or encompass certain non-existent pore sizes within the sample. The present section intends to implement a computer program [PROG$_{\text{IMAGE-POR}}$] based on two-dimensional scanning electron microscopy (SEM) images of PEO films synthesized with irradiated power and/or methanol solution. The program is executed on five selective magnifications from 100× to 10,000× for each experimental polymer films. Based on the gray-scale image of SEM, ImageJ software converts it into.*txt* format. After that, the program considers variable regime of gray-scale pixel (GSP) ranging from 60 to 127.5 with 0 for pure black and 255 for pure white. Pores are considered to be *black* and matter (polymer) to be *white*. In such variable GSP, the program is used to study the distribution of *BLACK* (pore phase) within the SEM.*txt* files. As magnification of scanning electron microscopy enhances from 100× to 10,000×, newer facts/information regarding the image [bulk or pore] are revealed and prior evidences are wiped off. Optimum threshold of GSP is considered to be 70 upon comparison with the % porosity studied from BET technique as shown in Fig. 5. The average porosity obtained from GSP 60 is too low, whereas higher limit of GSP 80 and 127.5 shows much higher porosity with erratic distribution which is irrelevant with the magnitude and distribution of the PEO film porosity. The importance of PROG$_{\text{IMAGE-POR}}$ is in unrevealing the pore dimensions as a function of SEM

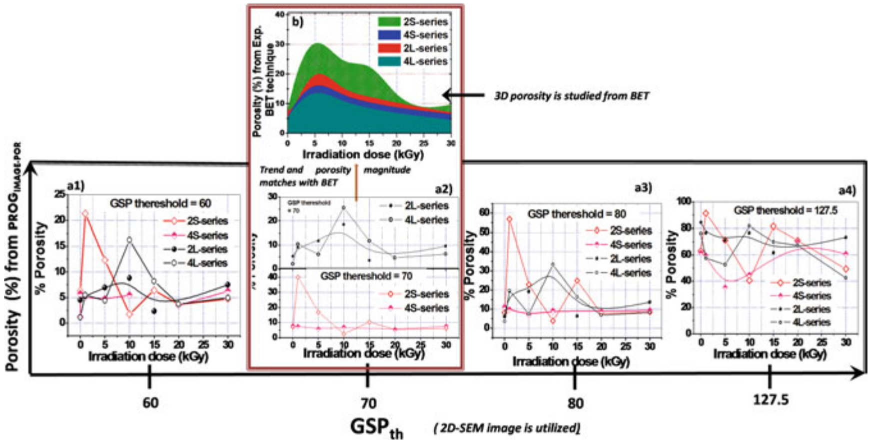

Fig. 5 Average porosity (in %) as a function of irradiation dose for 2/4S- and 2/4L- series obtained from PROG$_{IMAGE\text{-}POR}$ for gray-scale threshold (GSP$_{th}$): **a1** 60, **a2** 70, **a3** 80 and **a4** 127.5. Close matching of **a2** GSP$_{th}$ 70 is shown with **b** average porosity of 2/4S- and 2/4L-series as determined by BET

magnification for the irradiated samples rather than comparing the magnitude and distribution of pores with that obtained from BET. One of the major shortcomings of PROG$_{IMAGE\text{-}POR}$ is in the: (a) consideration of 2D images for porosity calculation and (b) using gray-scale image having pixel value within 0–255 rather than binary image. However, the prime intention of the authors is to discuss the initial simplest approach of PROG$_{IMAGE\text{-}POR}$ which is capable of understanding the influence of gamma dose on the pore phase of PEO matrix using any specific image obtained by any technique as revealed in Fig. 6. The useful imaging modes as shown in Fig. 6 enable easy determination of sample porosity, but possess certain limitations which restrict the

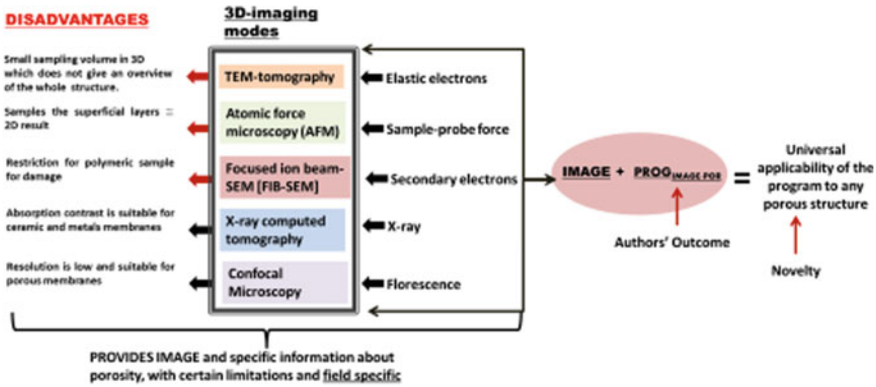

Fig. 6 Schematic representation for list of 3D-imaging modes with applicability of the program PROG$_{IMAGE\text{-}POR}$

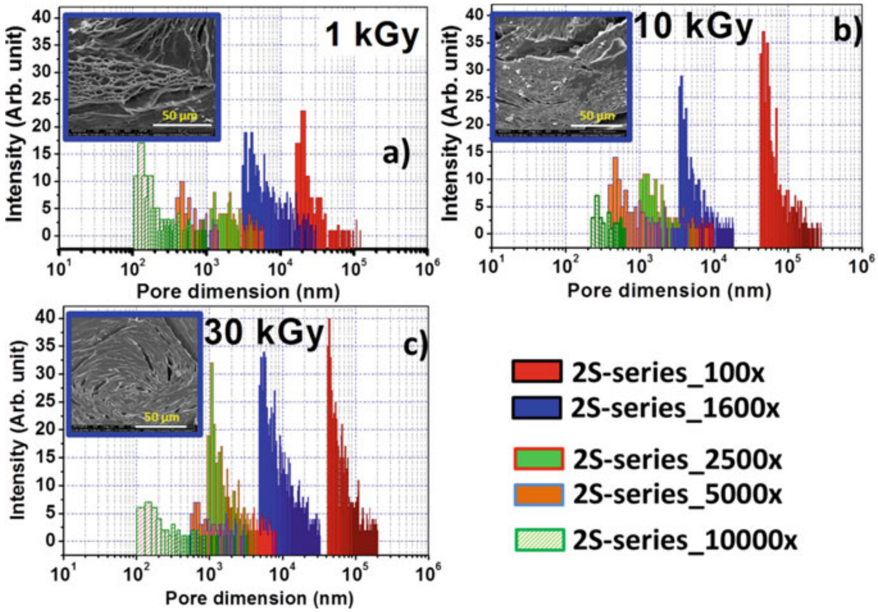

Fig. 7 Pore-size distribution obtained from $PROG_{IMAGE\text{-}POR}$ as a function of SEM magnification for 2S-series irradiated at: **a** 1 kGy, **b** 10 kGy and **c** 30 kGy. *The inset figures correspond to the SEM micrographs of the concern irradiation dose at 2500× magnification*

general applicability. The reported program possesses the flexibility in considering image obtained of any one of the 3D tools described in Fig. 6 containing specialized sample information. Hence, all these special evidences obtained from selective 3D technique could be generalized using $PROG_{IMAGE\text{-}POR}$ for effective determination of porosity or any other feature of the sample.

Figures 7, 8, 9 and 10 describe the pore-size distribution obtained from $PROG_{IMAGE\text{-}POR}$ using SEM images for 2/4-S- and 2/4-L-series for 1, 10 and 30 kGy in five magnification regimes from 100× to 10,000×, respectively. The representative SEM images for the particular dose are also given in the inset at only one magnification.

The given SEM images are only representative of the polymer sample at a particular irradiation dose. During programming, multiple images from identical magnification are given as input in order to enhance the accuracy. As expected, irrespective of sample type, it could be visualized that the size distributions obtained from $PROG_{IMAGE\text{-}POR}$ (Figs. 7, 8, 9 and 10) are not exactly similar with the experimental distribution pattern (Figs. 2 and 3). With increase in magnification for a particular dose, smaller pores (10^2–10^3 nm) are revealed.

It could be noted that experimental BET techniques show pore size within 100–500 nm, i.e., ~10^2 nm. However, this experimental regime of pore dimension exists only at higher magnification as calculated from $PROG_{IMAGE\text{-}POR}$. At still lower magnification from 100× to 5000×, larger pores within 10^3–10^5 nm (0.1 mm) are found to

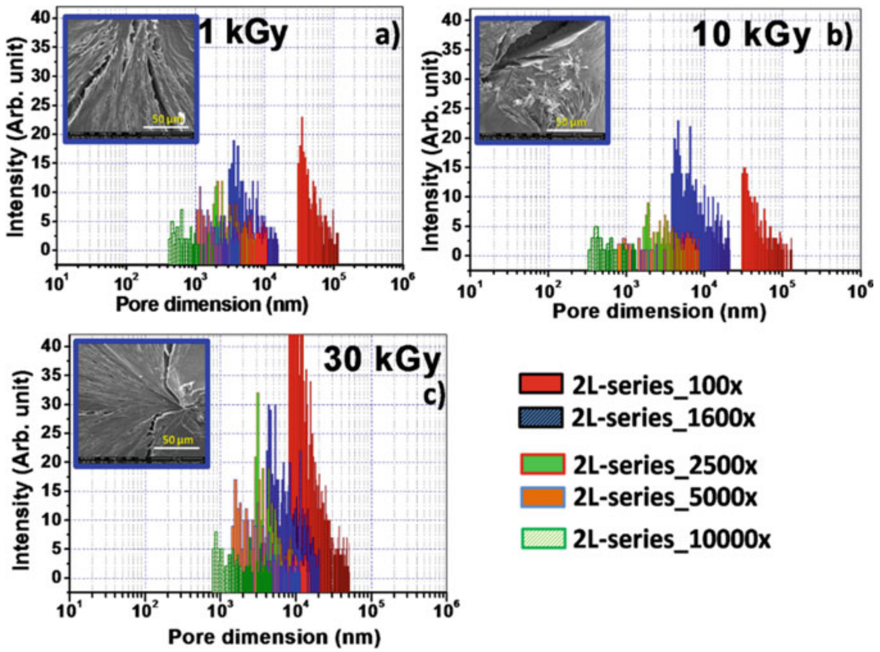

Fig. 8 Pore-size distribution obtained from $PROG_{IMAGE\text{-}POR}$ as a function of SEM magnification for 2L-series irradiated at: **a** 1 kGy, **b** 10 kGy and **c** 30 kGy. *The inset figures correspond to the SEM micrographs of the concern irradiation dose at 2500× magnification*

exist. It could be noted that the intensity of the larger pores (~10^4 to 10^5 nm) is higher for 30 kGy dose irrespective of sample type compared to the lower irradiation doses. This is in agreement with the predominance of scission at higher gamma irradiation dose. This is in agreement with the predominance of scission at higher gamma dose exposed in air atmosphere. The comparison of pore distribution at 5000× for 2/4-S- and 2/4-L-series is shown in Fig. 11 as a function of gamma dose of 1 kGy (Fig. 11a), 10 kGy (Fig. 11b) and 30 kGy (Fig. 11c), respectively.

This graph elucidates the influence of gamma dose on the nature of pore distribution of all samples at intermediate magnification of 5000x. It is observed that 50,000× magnification unveils pore in the dimension of ~10^3 nm irrespective of sample type. Lower dose of 1 kGy generates uniform distribution of pore with intermediate intensity.

Dose exposed in air atmosphere. The comparison of pore distribution at 5000× for 2/4-S and 2/4-L-series is shown in Fig. 11 as a function of gamma dose of 1 kGy (Fig. 11a), 10 kGy (Fig. 11b) and 30 kGy (Fig. 11c), respectively.

Population (i.e., intensity) of pores is found to increase with dose increment to 10 kGy especially for 2/4S-series. Erratic distributions are obtained with highest dose of 30 kGy which generates smaller pore (less than 10^2 nm) for 2S-series and larger pores (greater than 10^3 nm) for 2L-series. It has already stated previously that

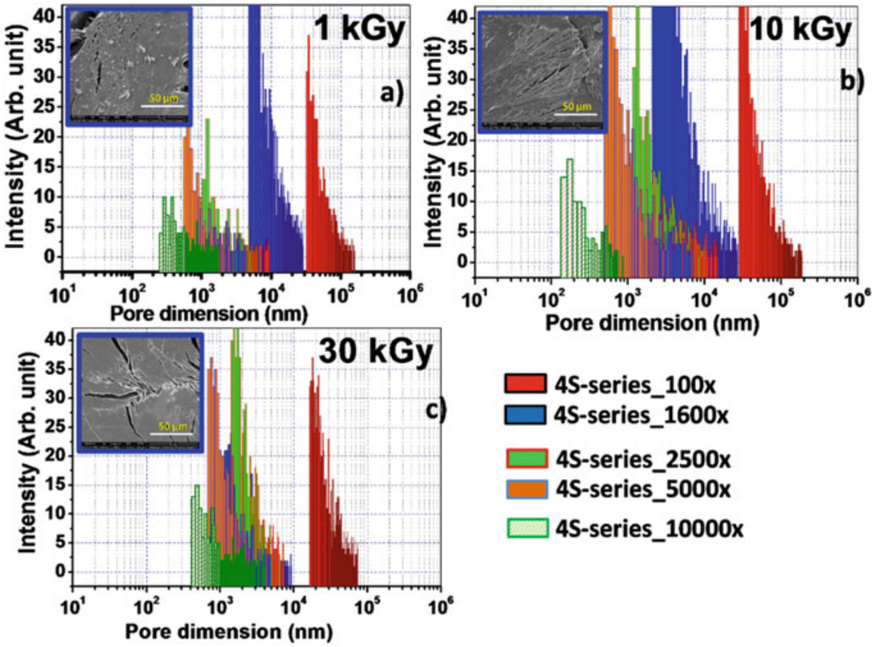

Fig. 9 Pore-size distribution obtained from $\text{PROG}_{\text{IMAGE-POR}}$ as a function of SEM magnification for 4S-series irradiated at: **a** 1 kGy, **b** 10 kGy and **c** 30 kGy. *The inset figures correspond to the SEM micrographs of the concern irradiation dose at 2500× magnification*

aim of the present program based on the image of sample is to unveil the newer pore dimension existing within the sample and not to compare the magnitude of porosity trends with the experimental findings. Such discernment among experimental BET technique and the results obtained from $\text{PROG}_{\text{IMAGE-POR}}$ is shown in Fig. 12c1–c4 . Figure 12a and b shows average porosity (%) obtained from experimental BET study and that from $\text{PROG}_{\text{IMAGE-POR}}$ considering optimum GSP of 70. The practical applicability of such program is further established using backscattered SEM images for PEO system.

Feasibility of $\text{PROG}_{\text{IMAGE-POR}}$ for any monophasic system.

Detailed discussion on the application of $\text{PROG}_{\text{IMAGE-POR}}$ for irradiated PEO system (in solid and liquid phase) in Figs. 5, 6, 7, 8, 9, 10, 11 and 12 enables the study of porosity and pore-size distribution in the regimes which are not revealed through BET technique. However, reliability and repeatability are an issue for such SEM-based methods which imbibe variation in contrast, brightness, user variability and instrument dependence. Owing to such fact, the SEM micrographs were captured for the experimental samples using two modes:

(a) Secondary mode (SE) represented by $e = 0$
(b) Backscattered mode (BSE) represented by $e = 1$.

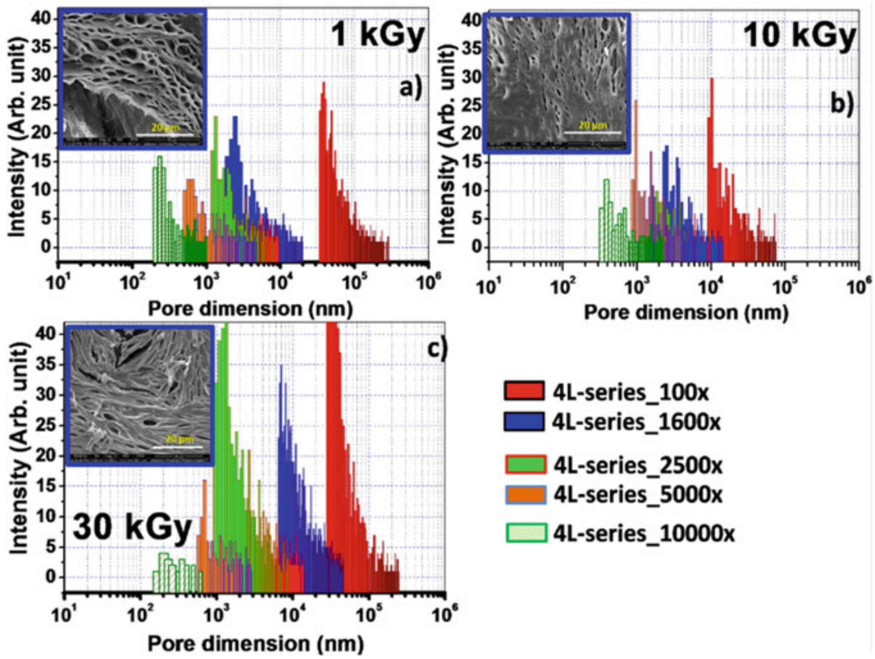

Fig. 10 Pore-size distribution obtained from PROG$_{\text{IMAGE-POR}}$ as a function of SEM magnification for 4L-series irradiated at: **a** 1 kGy, **b** 10 kGy and **c** 30 kGy. *The inset figures correspond to the SEM micrographs of the concern irradiation dose at 5000× magnification*

where e is the fitting parameter.

BSE images are limited to a gray-scale range because they only record one variable, average Z (atomic number, signature of element variation).

Therefore, "brighter" BSE intensity correlates with greater average Z in the sample, and "dark" areas have lower average Z. BSE images are very helpful for obtaining high-resolution compositional maps of a sample and for quickly distinguishing different phases. In SE modes, electron beams are scattered from the surface of sample. However, during BSE mode, the scattering of electron beam results from the volume element of the sample and thereby consists of information about the three-dimensional morphology as a function of atomic number. Consequently, in light of such background, at a fixed contrast, brightness of the BSC modes has been altered as per Table 2. Average porosity and the corresponding standard deviation are determined using variable gray-scale threshold (GSP_{th}) ranging from 60 to 120 and are shown in Table 3. The respective SEM images based on the mentioned three conditions of BSE mode are shown in Table 2 along with the variation of P_{av} [including Sd] with GSP is shown in Fig. 13. In comparison with the results of BSE mode, the results using the program are also shown for secondary mode of imaging ($e = 0$). The details of parameters for SE mode and variation of average porosity as a function of GSP are shown in Table 4, and the micrographs are shown in Fig. 14.

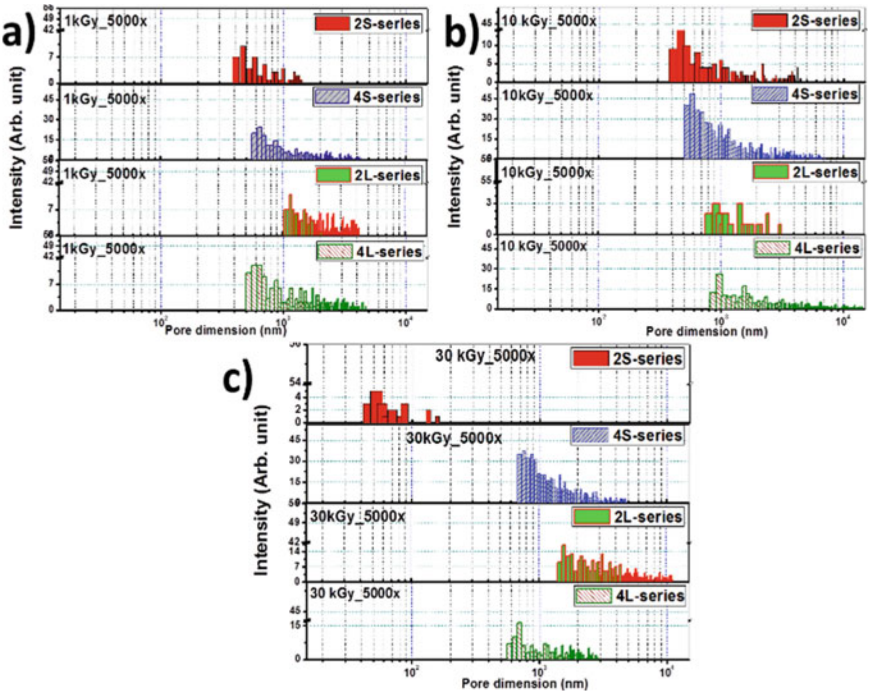

Fig. 11 Pore-size distribution obtained from $\mathrm{PROG}_{\text{IMAGE-POR}}$ for 2/4S- and 2/4L-series at 5000 × magnification irradiated at: **a** 1 kGy, **b** 10 kGy and **c** 30 kGy

It is to be noted that, the magnitude of average porosity varies within a narrow range with a reducing error (Sd) with GSP_{th} increment for BSE mode. The magnitude of average porosity is satisfactory for GSP_{th} below 90 for BSE. However, the present program is found to be more relevant upon incorporation of backscattered mode in SEM imaging as seen from the mentioned results.

Therefore, the reliability of the porosity and pore-size distribution as determined from the computer program [$\mathrm{PROG}_{\text{IMAGE-POR}}$] is established and can be well applied for monophasic systems. In case of multiphase, parameters need to be re-verified and tested accordingly.

4.2 CASE STUDY-2: Importance of $\mathrm{PROG}_{\text{IMAGE-POR}}$ for Intricate Matrices

The aforementioned section elucidates application of $\mathrm{PROG}_{\text{IMAGE-POR}}$ on porosity and its distribution for PEO films prepared with gamma irradiated powder and methanol solution. Being a film with uniform morphology throughout, the study of porosity and its distribution using any technique is fairly simple. However, in

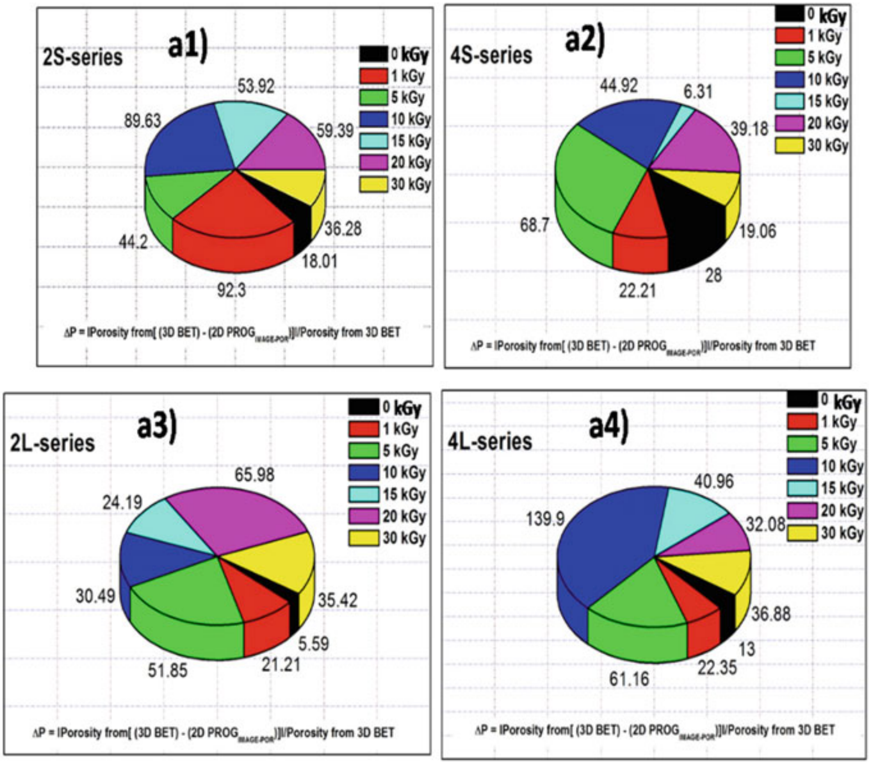

Fig. 12 a1–a4 Analysis of variation in average porosity among experimental BET and PROG$_{IMAGE-POR}$ as a function of irradiation dose for: **c1** 2S-, **c2** 4S-, **c3** 2L- and **c4** 4L- series

Table 2 Details of parameters for various SEM imaging modes

	Contrast	Brightness
BSE mode [$e = 1$]	60	50
	60	60
	60	75
	55	60
SE mode	65	65
[$e = 0$]	70	75

experimental material science, complex structures do exit whose study in terms of porosity is difficult. An account of such matrices is shown in Fig. 15.

Variety of thin films may be formed on different substrates, which show intricate layered structures. In this context, it is noteworthy to mention graphene-molybdenum disulfide-based films which are widely used in electrochemistry (Kumar et al. 2015). In these structures specially Fig. 15b and c, morphology and porosity of individual layer are different and in combination form a functional material. Study of porosity

Table 3 Average porosity as a function of GSP for BSE mode [$e = 1$]

GSP threshold	Average porosity [P_{av}]	Standard deviation (Sd)
60	0.374	0.096
70	0.382	0.085
80	0.392	0.074
90	0.403	0.062
100	0.414	0.048
110	0.427	0.033
120	0.441	0.017

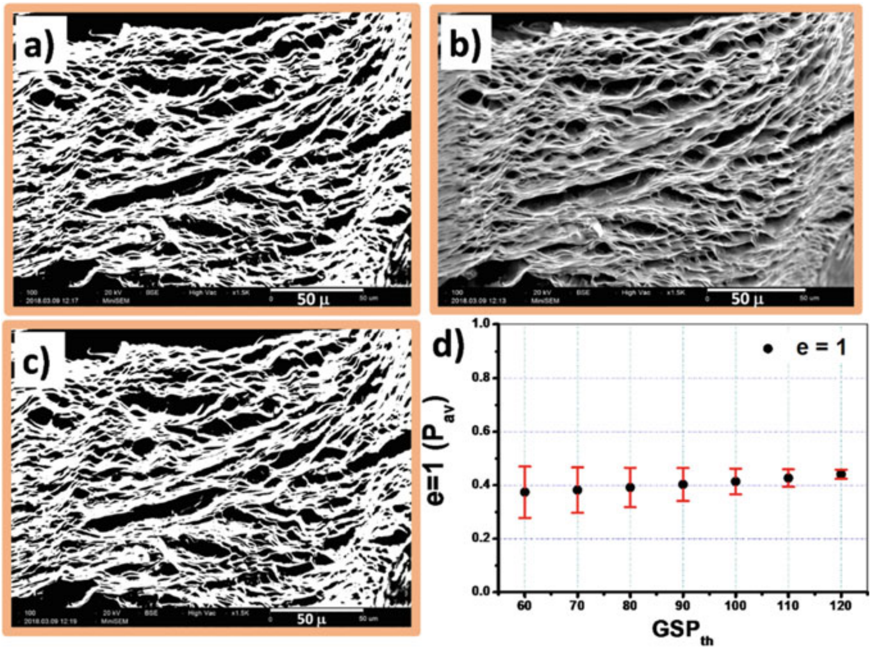

Fig. 13 SEM images of 4S-series at 15 kGy in BSE mode for 1500 × magnification using: **a** C = 60; B = 50, **b** C = 60; B = 60, **c** C = 60; B = 75 and **d** variation of average porosity (with Sd) as a function of GSP. C = Contrast, B = Brightness and Sd = Standard deviation

for such material is stringent since experimental tools give an average porosity of the monolith. In other way, each layer has to be differently prepared and tested, for study the porosity in detail. In such situation, the present $\mathrm{PROG}_{\mathrm{IMAGE\text{-}POR}}$ is expected to be functional with different inputs of images from variable imaging tools in different orientations.

Table 4 Average porosity as a function of GSP for SE mode [$e = 0$]

GSP threshold	Average porosity [P_{av}]	Standard deviation (Sd)
60	0.325	0.043
70	0.368	0.075
80	0.412	0.154
90	0.452	0.232
100	0.488	0.298
110	0.517	0.348
120	0.514	0.389

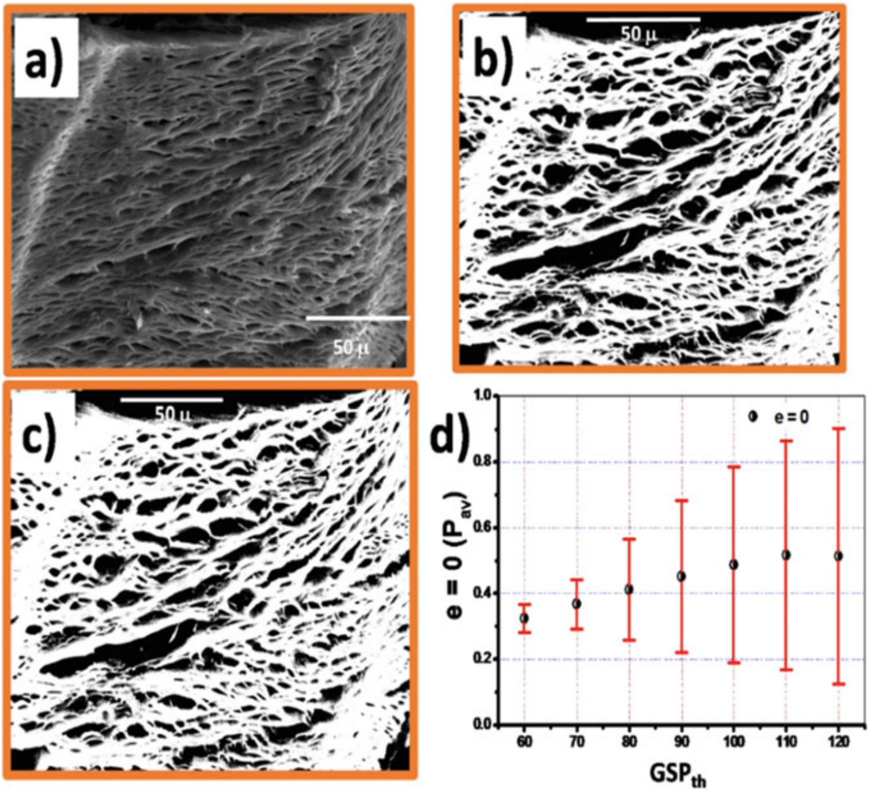

Fig. 14 SEM images of 4S-series at 15 kGy in SE mode for 1500 × magnification using: **a** C = 55; B = 60, **b** C = 60; B = 65, **c** C = 70; B = 75 and **d** variation of average porosity (with Sd) as a function of GSP. C = Contrast, B = Brightness and Sd = standard deviation

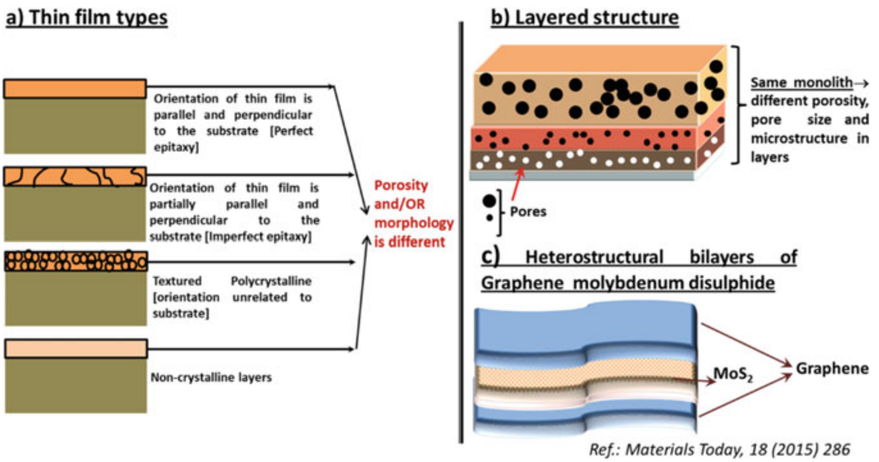

Fig. 15 Schematic of some complex matrices viz. **a** thin film categories, **b** layered structure and **c** Heterostructural bilayers onto which PROG$_{\text{IMAGE-POR}}$ could be proved functional

4.3 Correlation Among Porosity and Aerosity for Understanding the Configuration of Pores

The arrangement of void space in three-dimensional matrix is termed as porosity, whereas the same is known as aerosity when considered for two-dimensional context. In the present section, the authors intend to highlight the path and configuration of pores formed as an influence of gamma irradiation within PEO matrix. The representative considerations of symmetry are shown in Fig. 16.

Case 1*: The pores are considered to be cylindrical type with curved surface perpendicular to XY plane. [Fig. 16a].*

Let $r =$ radius of each circular pore in XY plane, $h =$ height of the film, $a =$ length of the film, $b =$ breadth of the film, $n =$ number of pores in XY plane, $\varphi =$ aerosity, $\Phi =$ porosity.

$$\therefore \varphi = \frac{n\pi r^2}{ab} \text{ and } \Phi = \frac{n\pi r^2 h}{abh} = \varphi \tag{3}$$

Case 2*: The pores are considered to be of spherical type. [Fig. 16b].*

Let $r =$ radius of each spherical pore, $d =$ distance between centers of consecutive spheres along the plane perpendicular to XY, $h =$ height of the film, $a =$ length of the film, $b =$ breadth of the film, $n =$ number of pores in XY plane, $m =$ number of pore layers parallel to XY plane, $\varphi =$ aerosity, $\Phi =$ porosity.

$$\therefore \varphi = \frac{n\pi r^2}{ab} \text{ and } \Phi = \frac{mn\frac{4}{3}\pi r^3}{abh} \therefore \frac{\Phi}{\varphi} = \frac{m\frac{4}{3}r}{h} \tag{4}$$

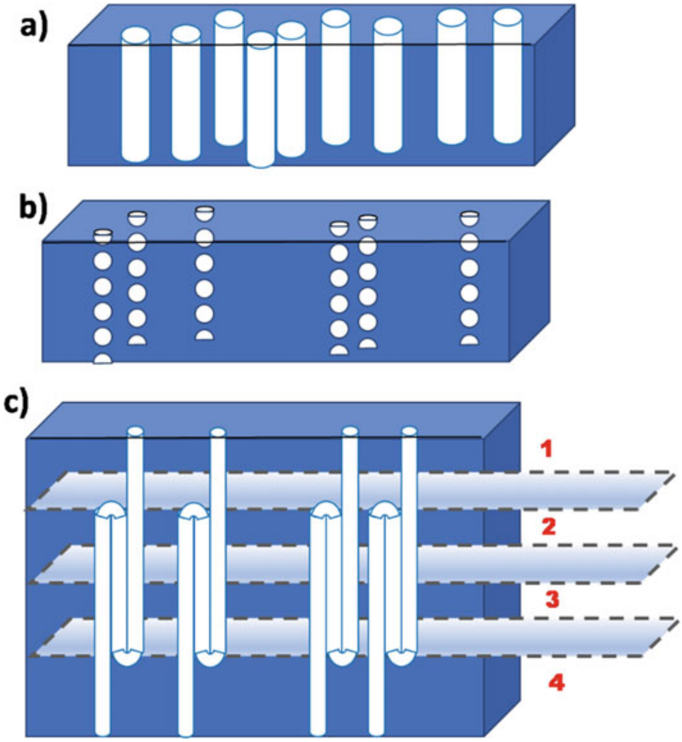

Fig. 16 Schematic diagram of various simple pore type distributions; **a** cylindrical, **b** spherical and **c** tortuous cylindrical

Now it can be shown that $h = \text{md}$ with $d \geq 2r$. Again let $f = \frac{d}{2r} \geq 1$

$$\therefore \frac{\Phi}{\varphi} = \frac{4}{3}\frac{r}{d} = \frac{4}{3f} \therefore \Phi = \frac{4}{3f}\varphi$$

If we consider connected spherical pore along the plane perpendicular to XY, then $d = 2r$, i.e., $f = 1$.

$$\therefore \Phi = \frac{4}{3}\varphi \tag{5}$$

Case 3*: The pores are considered to be tortuous cylindrical type with curved surface perpendicular to XY plane. [Fig. 16c].*

Let r = radius of each circular pore in XY plane, h = height of the film, a = length of the film, b = breadth of the film, n = number of pores in XY plane, k = number of equal divisions of height, φ = aerosity, Φ = porosity.

Table 5 Correlation table among porosity and aerosity of irradiated PEO films

S. No.	Irradiation dose, kGy	Porosity from BET, P_v	Porosity from SEM, P_a	$\varsigma = Pv/Pa$	Mean ς	Mean k
1	0	8.05	5.26	1.530418251	1.4	3
2	1	7.4	8.97	0.824972129		
3	5	24.3	11.7	2.076923077		
4	10	14.1	18.4	0.766304348		
5	15	12.4	15.4	0.805194805		
6	20	10.2	3.47	2.939481268		
7	30	7	9.48	0.738396624		

$$\begin{aligned} \therefore \varphi = \frac{n\pi r^2}{ab} \text{ and } \Phi &= \frac{n\pi r^2 \frac{h}{k} + 2n\pi r^2\left(1 - \frac{2h}{k}\right) + n\pi r^2 \frac{h}{k}}{abh} \\ &= 2\left(1 - \frac{1}{k}\right)\frac{n\pi r^2 h}{abh} = 2\left(1 - \frac{1}{k}\right)\varphi \end{aligned} \tag{6}$$

If $k = 4$ (four parts are shown in red in the above figure), then:

$$\Phi = 2\left(1 - \frac{1}{4}\right)\varphi = 1.5\varphi \tag{7}$$

Table 5 shows the correlation among 3d and 2d void space and the magnitude of "k" for the present polymer system 2L-series. The factor correlating porosity and aerosity is termed as ς such that:

$$\zeta = \frac{\Phi}{\varphi} \tag{8}$$

Again, $\varsigma = 2\left(1 - \frac{1}{k}\right)$.

The average magnitude of "k" for the present PEO system 2L-series is determined to be 3 which gives an estimate of the tortuous path of the void space within the matrix.

5 Concluding Remarks

A new, simple and novel computer program termed as $\mathrm{PROG}_{\mathrm{IMAGE\text{-}POR}}$ is reported for study of porosity and its distribution of Poly (ethylene oxide) (PEO) films prepared with gamma irradiated [1–30 kGy] powder (2/4S-series) and methanol solution (2/4L-series). The algorithm uses any sort of sample image as the input source file. The morphology could be obtained from any 2D-or 3D imaging software, e.g., SEM, TEM, tomographic image, etc. In the present case SEM micrographs of perturbed polymer films are used as the source file. It is found that the experimental data related to porous structure of PEO films obtained from BET (100–500 nm) measurements appears to be a part of the entire range of pore spectrum (~10^2 to 10^5 nm) obtained from 2D SEM image-based program, $PROG_{IMAGE\text{-}POR}$. The study on porosity of the polymer films is thus studied as a function of gamma irradiation dose, irradiation state, concentration of polymer and magnification of imaging tool (SEM) from $PROG_{IMAGE\text{-}POR}$. Feasibility of the present computer program is further established using standard deviations simulated from backscattered SEM (BSE) images for monophasic PEO system. BSE images being dependent on the atomic number of elements provide relevant information about the image. Standard deviation in average porosity is obtained for BSE images which confirm the applicability of program for monophasic system. Attempt has been made to correlate aerosity and porosity of the polymer films so as to understand the configuration of pores. Theoretical analysis based on aerosity (2D pores) and porosity (3D pore) of the present system gives an estimate of the tortuous path of the void space by considering the pores to be tortuous cylindrical type with curved surface perpendicular to *XY* plane. The applicability of this simple program is studied in case of certain intricate microstructures of thin films, layered structure, etc. wherein the usual techniques are restricted.

Acknowledgements The Corresponding author MM acknowledges Amity University, Kolkata, for infrastructural support. SKP is thankful to Inter-University Accelerator Centre (IUAC), Delhi, for providing Junior Research fellowship. Dr. Paramita Bhattacharyya and Miss. Suchisrawa Ghosh of Department of Food Technology, Jadavpur University, Kolkata, are acknowledged for extending their support in using the gamma irradiation chamber. The Authors also acknowledge FIST-2, DST Government of India, at the Physics Department, Jadavpur University, for providing the facility of SEM microscope. JM acknowledges Director, CSIR- CGCRI for kind permission to present the work. Dr. Monalisa Mukherjee acknowledges AIBN, AICCRS, Amity University, Noida, for necessary support.

Conflicts of Interest There are no conflicts to declare.

References

Brown JR, Seo Y, Hall LM (2018) Ion correlation effects in salt-doped block copolymers. Phys Rev Lett 120:127801

Calvo JI, Hernandez A, Pradanos P, Martibnez L, Bowen WR (1995) Pore size distributions in microporous membranes II. Bulk characterization of track-etched filters by air porometry and mercury porosimetry. J Colloid Interface Sci 176:467–478

Cassagneau T, Caruso F (2002) Semiconducting polymer inverse opals prepared by electropolymerization. Adv Mater 14:34–38

Culligan KA, Wildenschild D, Christensen BSB, Gray WG, Rivers Mark L, Tompson AFB (2004) Interfacial area measurements for unsaturated flow through a porous membrane. Water Resour Res 40:1–12

Deutsch M, Vlasov YA, Norris DJ (2000) Conjugated polymer photonic crystals. Adv Mater 12:1176–1180

Dourdain S, Bardeau JF, Colas M, Smarsly B, Mehdi A, Ocko BM, Gibauda A (2005) Determination by X-ray reflectivity and small angle x-ray scattering of the porous properties of mesoporous silica thin films. Appl Phys Lett 86:113108–113111

Fusalba F, Mehdi NE, Breau L, Belanger DL (1999) Physicochemical and electrochemical characterization of polycyclopenta [2,1-b;3,4-b‘] dithiophen-4-one as an active electrode for electrochemical supercapacitors. Chem Mater 11:2743–2753

Gregg SJ, Sing SW (1982) Adsorption, surface area and porosity, 2nd edn. Academic Press, New York

Hedrick JL, Miller RD, Hawker CJ, Carter K, Volksen RW, Yoon DY, Trollsas M (1998) Templating nanoporosity in thin-film dielectric insulators. Adv Mater 10:1049–1053

Hubbell JA, Langer R (1995) Tissue engineering. Chem Eng News 73:42–54

Jiang P, McFarland MJ (2004) Large-scale fabrication of wafer-size colloidal crystals, macroporous polymers and nanocomposites by spin-coating. J Am Chem Soc 126:13778–13786

Jiang P, Hwang KS, Mittleman DM, Bertone JF, Colvin VL (1999) Template-directed preparation of macroporous polymers with oriented and crystalline arrays of voids. J Am Chem Soc 121:11630–11637

Kumar NA, Dar MA, Gul R, Baek JB (2015) Graphene and molybdenum disulfide hybrids: synthesis and applications. Mater Today 18:286–329

Laera AM, Mirenghi L, Schioppa M, Nobile C, Capodieci L, Scalone AG, Benedetto FD, Tapfer L (2016) Fabrication of 3D carbon nanotube networks. Mater Res Exp 3(1–8):085007

Lima E, Raphael E, Sentanin F, Rodrigues LC, Ferreira RAS, Carlos LD, Silva MM, Pawlicka A (2012) Photoluminescent polymer electrolyte based on agar and containing europium picrate for electrochemical devices. Membrane filtration with complex branching pore morphology. Mater Sci Eng B 177:488

Lin VSY, Motesharei K, Dancil KPS, Sailor MJ, Ghadiri MR (1997) A porous silicon-based optical interferometric biosensor. Science 278:840–843

Mogilnikov KP, Polovinkin VG, Dultsev FN, Baklanov MR (1999) Calculation of pore size distribution in the ellipsometric porosimetry: method and reliability. MRS Proc 565:81–86

Mukhopadhyay M, Mukhopadhyay J, Das Sharma A, Basum RN (2012) Engineered anode structure for enhanced electrochemical performance of anode-supported planar solid oxide fuel cell. Int J Hydrogen Energy 7:2524–2534

Mukhopadhyay M, Saha M, Ray R, Tarafdar S (2016) A study on the effect of gamma irradiation on Poly [-Ethylene Oxide]: structural modification and variation in the kinetics of isoconversional phenomena. Indian J Phys 90:1133–1147

Myers GR, Kingston AM, Varslot TK, Turner ML, Sheppard AP (2011) Dynamic tomography with a priori information. Appl Opt 50:3685–3690

Park SH, Xia YN (1998) Fabrication of three dimensional macroporous membranes with assemblies of microspheres as templates. Chem Mater 10:1745–1747

Pyun A, Bell JR, Won KH, Weon BM, Seol SK, Ho JJ, Macosko CW (2007) Synchrotron X-ray microtomography for 3D imaging of polymer blends. Macromolecules 40:2029–2035

Ren X, Pickup PG (2001) Simulation and analysis of the impedance behaviour of electroactive layers with non-uniform conductivity and capacitance profiles. Electrochim Acta 46:4177–4183

Ricco AJ, Frye GC, Martin SJ (1989) Determination of BET surface areas of porous thin films using surface acoustic wave devices. Langmuir 5:273–276

Stephan AM, Teeters D (2003) Characterization of PVdF-HFP polymer membranes prepared by phase inversion techniques I. Morphology and charge–discharge studies. Electrochim Acta 48:2143–2148

Wildenschild D, Sheppard AP (2013) X-ray imaging and analysis techniques for quantifying pore-scale structure and processes in subsurface porous medium systems. Adv Water Resour 51:217–246

Yim JH, Lyu YY, Jeong HD, Song SA, Hwang IS, Lee JH, Mah SK, Chang S, Park JG, Hu YF, Sun JN, Gidley D (2003) The preparation and characterization of small mesopores in siloxane-based materials that use cyclodextrins as templates. Adv Funct Mater 13:382–386

Yu QZ, Dai ZW, Lan P (2011) Fabrication of high conductivity dual multi-porous poly (l-lactic acid)/polypyrrole composite micro/nanofiber film. Mater Sci Eng B 176:913–920

In-Silico Studies of Alzheimer's Disease Affected Brain Using a Novel Terahertz Thermography Technique

Swarnava Biswas, Debajit Sen, and Moumita Mukherjee

Abstract Alzheimer's disease (AD) is a dynamic disorder that causes brain cells to become extremely thin or weak and dies. Alzheimer's disease is the most widely recognized reason for dementia, a persistent decrease in thinking, behavioural and social aptitudes that disturbs an individual's capacity to work autonomously. This paper for the first time reports a new scheme of diagnosis of AD by studying the corresponding Terahertz (THz) thermographs. A solid-state source of THz radiation (IMPATT oscillator), capable of working at room temperature, is proposed in this paper and the THz non-linear characteristic of the device and system are studied through an in-house developed quantum modified classical drift diffusion simulator. A COMSOL-based THz-thermograph model is further developed and a comparative analysis of normal brain tissues and AD affected brain tissues thermographs are reported. To the best of authors' knowledge, this is the first report on studying of the prospects of an exotic type non-invasive Terahertz $\langle$ p+−n−n+$\rangle$ radiation source for use in T-Ray thermography studies of AD detection with Terahertz radiation exposure.

Keywords Avalanche transit time device · Alzheimer's disease · Large-signal impedance and admittance study · Noise-study · Non-linear quantum drift diffusion simulator · Room temperature characteristics · Terahertz source and radiation system · T-Ray thermograph study

S. Biswas
The Neotia University, Sarisha, West Bengal 743368, India

D. Sen
ELMAX Systems and Solutions, Kolkata, West Bengal 700045, India

M. Mukherjee (✉)
Adamas University, Kolkata, West Bengal 700126, India
e-mail: moumita.mukherjee@adamasuniversity.ac.in

M. Mukherjee et al. (eds.), *Advances in Medical Physics and Healthcare Engineering*, Lecture Notes in Bioengineering, https://doi.org/10.1007/978-981-33-6915-3_31

1 Introduction

There is an expanding interest for building up a better comprehension of brain problems. Photonics offers a scope to consider cerebrum tissue and analyses brain maladies, for example, brain tumours and Alzheimer's disease (AD). AD is generally a progressive neurogenerative disorder (Shi et al. 2016) which mainly causes dementia, with miss of cognitive functions, thinking skills and memories. More effective treatments can be achieved by early detection of AD. In recent days AD can be diagnosed by Cerebrospinal fluid (CSF) analysis, MRI imaging of brain, neuro-psychological testing, blood testing and some other methods. Sometimes these traditional methods are very costly (Nestor et al. 2004) and time taking process and the main problem is their accuracy may depend upon the disease complexity (Porter et al. 2000). Generally, the brain undergoes several pathological changes due to AD, such as progressive shrinkage of the brain, enlargement of lateral ventricle and shriveling of the hippocampus (Reitz and Mayeux 2014). Progressive accumulation of beta amyloid plaques and tau tangles inside the brain are the major changes in the brain that occurs with AD (Harrington 2012). Among all methods and techniques developed, till date, for early diagnosis of AD, the most promising technique is non-invasive medical imaging technique. Terahertz ray is not energetic enough to dissociate the chemical bonds or ionize molecules or atoms, so it can be said that T- ray imaging has no harmful effect to living organisms, unlike cancer causing high-energy photons such as X- rays and UV rays (Fan et al. 2014; Cheon et al. 2016; Mahato et al. 2018). Since this is comparatively safe for humans, T-Ray imaging technique has created new avenue for detecting various diseases. To investigate soft tissues, T-Ray imaging can be used as an essential tool because of strong water absorptions in the terahertz region and its non-ionizing and low-scattering properties in tissues. THz imaging systems are expected to detect the early stage of AD before it is visible or sensitive to any other identification means. As a matter of fact, refractive index and absorption coefficient of the AD affected brain tissue are higher in comparison with the normal brain tissue due to higher water content and structural changes that occur in AD. Thus T-Ray imaging is profoundly sensitive to water content on account of the latter attenuation and in this way water assimilation is obvious in estimating soft tissues, which clarifies the difference seen among normal and AD affected tissues.

2 Materials and Methods

The details of modelling of the terahertz source device are summarized elsewhere (Kundu and Mukherjee 2019; Xuan and Roetzel 1997). The software COMSOL Multiphysics® is used for the thermograph model. After satisfying appropriate boundary conditions, Maxwell's equations are solved here. Specific absorption rate (SAR) is calculated here with the help of computation. This is followed by the solving of Bio-heat (Pennington (2017)) equations to generate the temperature thermograph of the brain model that includes both healthy and AD affected tissues. The T-Ray radiation will incident of the organ under test. The in-silico bio-model of human brain has been developed and identification is carried out with axisymmetric transverse magnetic formulation. This is followed by the simplification of Maxwell's equations (Dhillon et al. 2017) to a wave equation in H_φ:

$$\nabla \times \left[\left(\varepsilon_r - \frac{j\sigma_\varepsilon}{\omega\varepsilon_0} \right)^{-1} \nabla \times H_\varphi \right] - \mu_r k_0^2 H_\varphi = 0 \tag{1}$$

where $\sigma_\varepsilon =$ electrical conductivity. Once the magnetic field H_φ is solved from Eq. (1), the electric field E is simulated. Let $N =$ unit normal vector for a surface.

$$N \times E \tag{2}$$

The first-order boundary condition (Xie et al. 2008) is used at outer boundaries of tissues.

$$N \times \sqrt{\varepsilon} E - \sqrt{\mu} H_\varphi = -2\sqrt{\mu} H_{\varphi 0} \tag{3}$$

The details of the mathematical model for the generation of terahertz are described elsewhere (Adhikari et al. 2020a, b; Mukherjee 2019). Dielectric, thermal as well as blood perfusion properties of Healthy and AD affected tissues are complex functions of EM-waves, oscillation frequency and tissue. The corresponding properties are summarized in Table 1. Experimentally available and verified data have been used for the study (Zhu et al. 2013).

After going through distinctive accessible techniques, it is chosen to perform picture processing on the said pictures. The picture would be gone through colour threshold filter for the lowest and the highest extremities of the colour range that could be changed over to white and grey scale, separately. It gave some measure of varieties to the picture however the presence of the red gradient within the yellow and black regions may cause classification problems. The colour in the picture comes because of pixels which are nothing but colour arrays of red, blue, and green. The colour threshold filter simply converts the arrays having the highest and the lowest values to black and white, respectively. Therefore, the image will again be sent through two other filters to inverse the colours and remove gradient within regions. After the first filter, to get more perspective out of the picture threshold inversion was done and the complete colour matrix was inversed. Finally, the binary filter was applied to remove

Table 1 Experimental parameters for COMSOL model

Parameters	Normal brain tissue	AD affected tissue
Relative permittivity (ε)	7.38	5
Electrical conductivity [[σ, Unit $= \left(\frac{\text{Siemens}}{\text{meter}}\right)$]]	48.2	100

all gradient colours by setting the colour values as constant. For example, even after applying the inversion filter, the green region had difference in colour gradient which was removed and set as constant green.

The image after applying filter has its region of interest superimposed on the original image to provide a better reference. As it can be seen that the processed image provides four distinct regions of interest which are much better compared to the original image. After plotting both the sets of images corresponding to the time of exposure of the radiation and considering the distance of the arc of outermost region, it can be seen quite clearly that the malignant region is much larger and hence correctly distinguishable. It can be observed that not only the black region, if we compare the normal and the AD affected pictures at the same time frame, the temperature variation regions, all the bands are increased in size of the AD affected picture from the normal one which is a distinctive feature to extract AD affected information.

In the end, it can be concluded that after applying image processing the provided set of images have enough variations that can be fed into classifier machine. The proposed AI model is being studied to a wide and large set of images of both categories containing variations of the variables such as time of exposure and frequency. A threshold of normalcy to malignancy can be established. The limitation of the proposed model is that the findings are purely based on provided images having a set of properties like image quality, image depth, image size, etc. and may or may not change with the change of any of the properties. Therefore, it would be better if the image processing layer can be removed and it could be directly applied to certain algorithms to the output numbers (if any) from the terahertz imaging system.

3 Results and Discussions

The authors have developed an equivalent brain model using COMSOL Multiphysics® software combined with the newly developed QCNLDD model. The brain model is considered as a cylindrical cone of 120 mm × 50 mm dimension.

The phantom model consists of brain tissues of white matter and grey matter. The skin thickness has not been considered in the analysis. Again, another brain phantom is designed with the parameters of AD affected brain tissues both in grey and white matter, respectively. The phantom model is subjected to a series of external radiation of 0.1 THz frequency.

The output relevant thermographs are studied and reported here in the paper for comparison. At the beginning of the analysis, several grid resolutions are tested and compared for greater accuracy. The default grids and the refined grids for 0.1 THz DUTs are shown in Fig. 1. Figures 2 and 3 show the terahertz thermographs of normal brain tissues versus AD affected brain tissues under similar exposure conditions. It is observed that as a result of incident radiation at 0.1 THz frequency, T-Ray power absorption does not reflect any significant temperature gradient within the normal brain model. On the other side, for the AD affected case, the thermographs

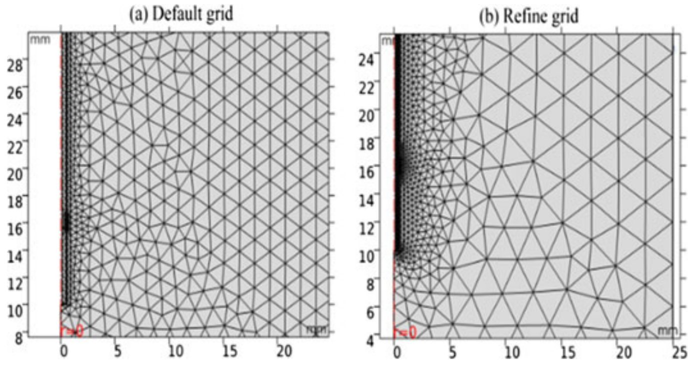

Fig. 1 Grid design for DUT under T-Ray exposure

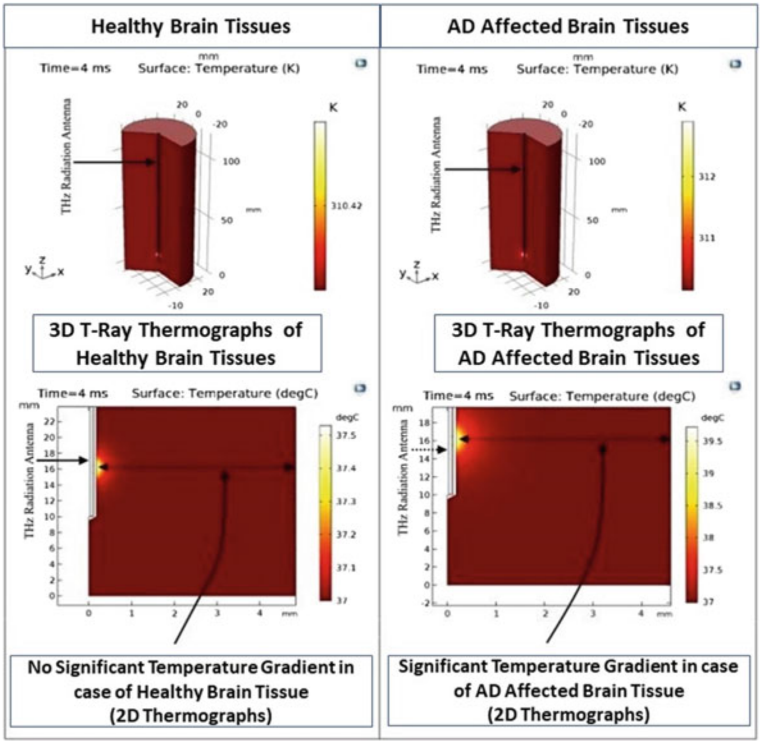

Fig. 2 Terahertz thermographs of AD affected versus healthy brain tissues

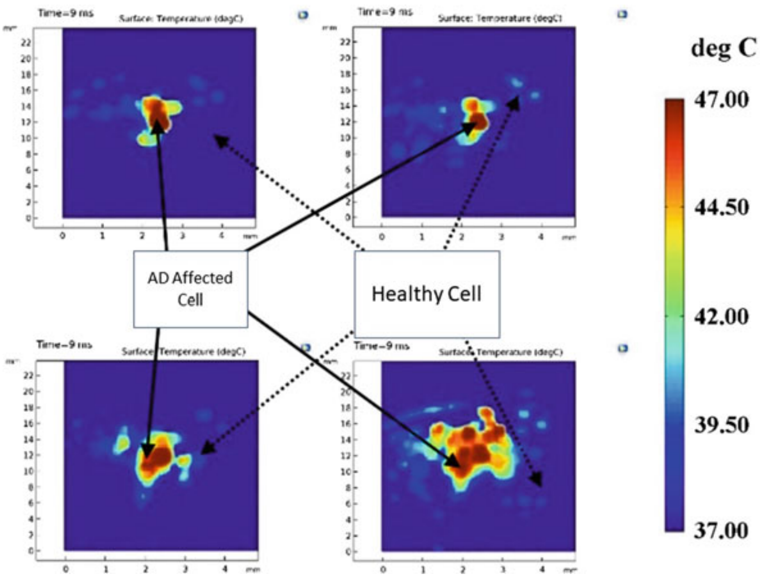

Fig. 3 Terahertz planar thermographs of AD affected versus healthy brain tissues

reflect a noticeable temperature gradient (approximately a rise in temperature from 37 to 43 °C), as a result of water contents in damaged cell. The comparative study has revealed that the T-Ray's non-ionizing thermal imaging is an efficient technique in AD screening and may be employed as a complimentary technique of existing CT scan or MRI imaging. The thermal stability of the device is ensured by introducing diamond heat sink and pulse mode operation of the device. Diamond, having high thermal conductivity, is good for heat spreading, and, in this way, the junction temperature of the device is kept near the ambient temperature.

The temperature increase is due to the change in relative permittivity and conductivity in AD affected brain tissues. The cell damage is greatest in proximity to the T-Ray emitter and decreased gradually with distance. The published literature has not yet reported regarding the detection of AD affected brain tissues accurately with non-ionizing T-Ray techniques. Here is the novelty of the study in designing/developing a cost-effective, compact and room temperature non-ionizing thermography technique and corresponding in-silico detection of AD. To the best of authors' knowledge, this is the first-ever report on T-Ray thermography study in AD and corresponding comparison with the normal healthy brain tissues. Also, in comparison with many imaging modalities, done earlier, THz has the highest accuracy in early detection of AD as observed in the present study (Table 1).

4 Conclusions

For the first time prospects of Terahertz radiation is studied for detecting early stage AD in brain cell. The study has been done in-silico by developing a generalized thermograph model. The validity of the study is well established and the accuracy limit is as good as ~90%. The optimization study in terms of incident radiation frequency range and time of exposure is done and the study reveals that 0.1 THz would be the optimum incident radiation with 2–5 s of exposure for generating distinctive images. To the best of authors' knowledge, this is the first report on prospects of Terahertz thermograph study to detect AD affected brain tissues. The study will be useful for future diagnostic modality development and further extended in vitro and in vivo studies.

References

Adhikari S, Bhatia D, Mukherjee M (2020b) Super-lattice GaN/AlxGa1-xN nanoscale MITATT oscillator as terahertz radiation source: novel application in breast cancer imaging. Sens Int 1:100014

Adhikari S, Jayanthu S, Mukherjee M (2020) Design and analysis of novel room temperature T-Ray source for biomedical imaging: application in full body prosthetics. In: Computer vision and machine intelligence in medical image analysis. Springer, Singapore, pp 137–148

Cheon H, Yang HJ, Lee SH, Kim Y, Son JH (2016) Terahertz molecular resonance of cancer DNA. Sci Rep

Dhillon SS, Vitiello MS, Linfield EH, Davies AG, Hoffmann MC, Booske J, Castro-Camus E (2017) The 2017 terahertz science and technology roadmap. J Phys D Appl Phys 50(4):043001

Fan S, He Y, Ung BS, Pickwell-MacPherson E (2014) The growth of biomedical terahertz research. J Phys D Appl Phys 47(37):374009

Harrington CR (2012) The molecular pathology of Alzheimer's disease. Neuroimaging Clinics 22(1):11–22

Kundu A, Mukherjee M (2019) Physics based non-linear large-signal analysis of multiple-graphene layer exotic pin (p++–n−−n–n++) devices and ultra-fast SPST/SPDT/SPMT switches on Si/3C-SiC (100) substrates for application in THz-communication. Microsyst Technol 1–22

Mahato K, Kumar A, Maurya PK, Chandra P (2018) Shifting paradigm of cancer diagnoses in clinically relevant samples based on miniaturized electrochemical nanobiosensors and microfluidic devices. Biosens Bioelectron 100:411–428

Mukherjee M (2019) Prospects of avalanche transit time terahertz radiation source in biomedical imaging: application feasibility in health engineering. In: Biomedical engineering and its applications in healthcare. Springer, Singapore, pp 549–569

Nestor PJ, Scheltens P, Hodges JR (2004) Advances in the early detection of Alzheimer's disease. Nat Med 10(7):S34–S41

Pennington JS (2017) Optimization of miniaturized resonant microwave cavities for use in Q-thrusters

Porter RJ, Lunn BS, Walker LL, Gray JM, Ballard CG, O'Brien JT (2000) Cognitive deficit induced by acute tryptophan depletion in patients with Alzheimer's disease. Am J Psychiatry 157(4):638–640

Reitz C, Mayeux R (2014) Alzheimer disease: epidemiology, diagnostic criteria, risk factors and biomarkers. Biochem Pharmacol 88(4):640–651

Shi L, Shumyatsky P, Rodríguez-Contreras A, Alfano RR (2016) Terahertz spectroscopy of brain tissue from a mouse model of Alzheimer's disease. J Biomed Opt 21(1):015014
Xie Y, Guo B, Li J, Ku G, Wang LV (2008) Adaptive and robust methods of reconstruction (ARMOR) for thermoacoustic tomography. IEEE Trans Biomed Eng 55(12):2741–2752
Xuan Y, Roetzel W (1997) Bioheat equation of the human thermal system. Chem Eng Technol Ind Chem Plant Equip Process Eng Biotechnol 20(4):268–276
Zhu Y, Chandra P, Shim YB (2013) Ultrasensitive and selective electrochemical diagnosis of breast cancer based on a hydrazine–Au nanoparticle–aptamer bioconjugate. Anal Chem 85(2):1058–1064

Identification of Shape Using Circularity Approach for Medical Image Analysis

Soumen Santra, Dipankar Majumdar, and Surajit Mandal

Abstract Cancer is one of the most serious health problems where patient's condition deteriorates day by day rapidly. In medical diagnosis, cancer cell should be detected by using such an image processing technique which gives quick result. For doing this, we introduce an approach where images can be divided into several geometrical shapes for proper analysis. By using this process, the operation is much easier as we can get better information about the cancer-affected cells. The image contains basic geometric shapes. The geometric shapes of the cell can be recognized by measuring circularity of the cell objects present in the image. It also gives the number of basic objects in image as results. Here, circularity is used as an invariant shape descriptor.

Keywords Shape descriptor · Invariant shape descriptor · Carcinogenic cell · Cell shape · Circularity

S. Santra (✉)
Department of MCA, Techno International New Town, Kolkata, West Bengal 700156, India

D. Majumdar
Department of IT, RCC Institute of Information Technology, Kolkata, West Bengal 700015, India

S. Mandal
Department of ECE, B.P. Poddar Institute of Management & Technology, Kolkata, West Bengal 700016, India

M. Mukherjee et al. (eds.), *Advances in Medical Physics and Healthcare Engineering*, Lecture Notes in Bioengineering, https://doi.org/10.1007/978-981-33-6915-3_32

1 Introduction

In medical image processing, an image may consist of a large number of cells, and the nature of which cannot be predicted through naked eyes. Medical practitioners bring the idea and take decision after seeing the X-ray or CT scan or PET scan images. Various image processing techniques can be exploited to extract the features of the cells which, in turn, help us to understand their nature. To analyze the shape of the cells, we work upon the region of interest (ROI). Once an image is obtained and digitized in the form of a matrix, then each portion of it is defined. The digitized forms of images are considered as raw images. Various image processing techniques are applied on the raw images to determine their different features. Pre- and post-image processing techniques are often used along with the principal technique to extract better information from the images. However, care must be taken in selecting these pre- and post-processing techniques because inappropriate methods and high computation techniques may also lead to loss of information in the final image preventing medical practitioners from proper diagnosis of the patients. The computational methodology of an image, in addition to the principal technique, involves many steps such as assessment, acquisition, rasterization, quality enhancement, noise reduction, binarization, segmentation, extraction of hidden features, matching, transformation, alignment, and 3D reconstruction. Simple processing techniques are always desirable as they have less computation time and less complexity. A medical image is usually a high-quality image. To improve the quality of the image further and for better image analysis, following pre-processing techniques may be adopted: noise reduction, proper geometric identification, smoothening of edges, resolution enhancement, and illumination correction or homogenization. The computational methods of image processing and analysis may find applications in multiple domains such as in surveillance, biomechanics, and bio-engineering and material sciences.

At the earlier stage of life, humans recognize objects through different types of geometrical shapes and structures and separate them from each other by their nature followed by shapes (Olson 2011; Gonzalez et al. 2016). So, it is important to know about the features of different types of geometrical structures by which an analyzer can differentiate one from another. The nature of cell images can also be classified based on its shape and size (Zhang and Guojun 2004).

An edge determines the boundary of continuity which separates ROI from its background region (Zhang and Guojun 2004; Dougherty and Cheng 1995; Xiaolong et al. 2017; Wang et al. 2012; Liu et al. 2011). The edges form different shapes and signify a meaningful sense toward the recognition of objects. In Fig. 1, we introduce various basic geometrical shapes. Based on these shapes, we can get an idea about the images through the structuring elements whether those are circles or any type of polygons such as triangle, rectangle, and pentagon. These basic objects also combine with each other and form hybrid shapes. These figures are contaminated or mixed in some ratios and in some inline or outline clustered design and form different shapes. If we convert any hybrid shape into a circular path and calculate the corresponding

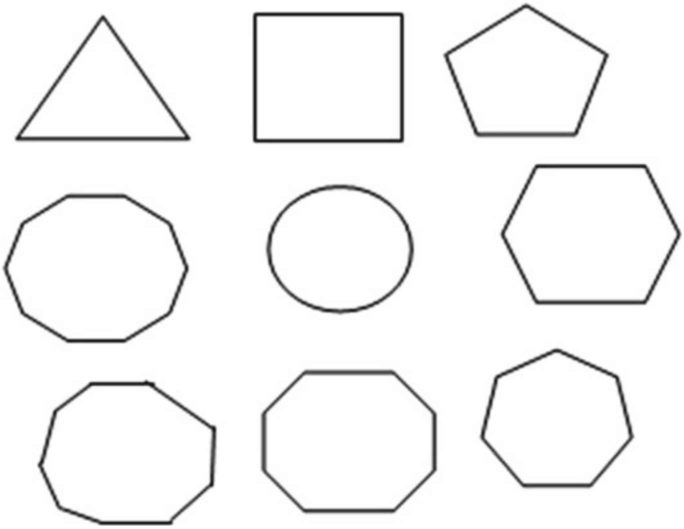

Fig. 1 Basic geometric shapes

circularity, then its value is expected to remain constant even if it undergoes any type of deformations or heterogeneous transformations like rotation, translation, shearing, etc., and its proportionate ratio should remain the same as before. Clustered or shape identifications are also possible using putative point matching feature, but they do not always work for all types of rotations, translations, and deformations through inline or outline operations (Maragos 1989). But circularity methodology which we discuss here overcomes all types of homogeneous transformations completely as an invariant shape descriptor feature element. Any type of image analysis for medical diagnosis depends on computer vision and pattern analysis (Santra and Mandal 2020; Santra et al. 2019a, b) and is very much important for the rapid and proper treatment of patient of cell-related disease. These fields are always changing day by day and time to time where one technique overrides another technique to resolve the drawbacks of previous one.

Olson (2011) proposed circularity values of various shapes of object. The application of multi-texture pattern to identify the shape of an object in local region was introduced by Gonzalez et al. (2016). Zhang and Guojun (2004) reported a brief explanation of shape descriptor tool based on 2-D and 3-D perspective view. Dougherty and Cheng (1995) proposed the idea of texture pattern based on granular approach on images whether noisy effects are there. Xiaolong et al. (2017) illustrated how edge detection approach helps in component analysis of morphological techniques and find out the shape boundary or interior plane through shape classification approach based on space domain approaches. Wang et al. (2012) used height function as a robust shape descriptor feature for shape matching. Liu et al. (2011) introduced shape retrieval technique from image using shape matching procedure for micro-structure image objects. Maragos (1989) explained the reconstruction of pattern spectrum and introduced it into shape classification concept through opening and closing filter for multi-lateral and multi-pattern images. We are introducing new Shape descriptor tool here which basically works on Circularity feature. It finds shape of various objects as an invariant way and also traces hybrid shape which is missing in previous works. In Sect. 2, we discuss the circularity shape descriptor. In Sect. 3, various images are analyzed using the circularity shape descriptor, and the results are also discussed.

2 Image Analysis Parameter: Circularity

Shape is one of the significant image analysis parameters based on dimension. It plays an important role where proper object recognition of tiny particles is not possible through naked eyes. Perimeter, area, centroid, diameter, bay or hole, chord length, moment, longitude, latitude, surface waviness, aspect ratio, thickness, etc., are components by which we define the shape of an object in the field of medical image analysis (Santra and Mandal 2020; Santra et al. 2018; 2019a, 2019b;). Beyond these parameters, circularity is one of the versatile and influential features of cell shape by which we can recognize the object. Circularity is defined as a closed path around the surface of an object. It represents a path which starts from a point and ends at the same point after traversing each point on the surface of the object and converts any shape of an object into a closed path. The features are hidden parameters of an image which are normally not visible, but if we extract it, then we acquire knowledge data about the image. The model diagram which extracts hidden features like circularity from an image through digital methodology is shown in Fig. 2.

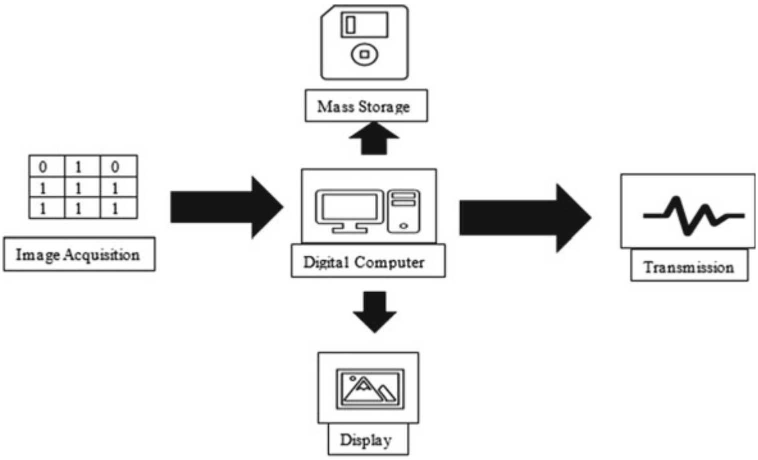

Fig. 2 Model diagram for feature extraction of image

A digitized image is stored in the form of a table (2-D matrix). Circularity is obtained based on blob measurement where blob represents clustered form of pixels or shape of an object within an image. It finds the group of pixels and avoids that pixel which is in the isolated form. It traverses along the boundary or perimeter of the continuous clustered form of pixels. Here, these clustered pixels give the idea of the shape of the object or cell present in the medical image. Circularity indicates the presence of shape or collection of shapes which gives the idea of nature of the cells.

3 Results

After executing the invariant shape descriptor tool, we represent the output in Tables 1, 2, 3, and 4 for the alphabets character (A-K), basic geometric shapes, Kimia-99 (https://github.com/mmssouza/kimia99), and carcinogenic cell, respectively.

In Maragos (1989), we have shown circularity of A-E character set and identified the shape, but Table 1 represents the same of A-K.

In Table 2, we have shown the presence of hybrid shapes (Olson 2011) in different polygons with their corresponding circularity values. Whereas Table 3 represents circularity values of Kimia-99 (https://github.com/mmssouza/kimia99) dataset.

Here, the presence of multi-variate objects within the image can easily be detected by this tool as we can see in Table 1 that the fifth image of letter 'B' contains both triangle and circle.

From Tables 1, 2, 3, and 4, we can easily understand the efficiency of this tool which works upon various objects and identifies the shape or combination of more than one shapes. It also indicates which shape tends to convert into which shape in future. It can easily find out the various shape structures which present in carcinogenic cell. The malign cell system changes gradually from one shape to another shape exponentially with time. This shape changing pattern can easily be traced by this invariant shape descriptor tool.

4 Conclusion

The invariant shape descriptor tool recognizes the shape of a cell or an object in an image where the shape of the object changes with time as in the case of a cancer cell due to its abnormal and rapid growth. We have also shown the number of various shapes present in a single object. In future, we will show that the number of objects in cancer-affected cells is much higher than that of the normal cells which will clearly indicate the rapid growth of cancer-affected cells. It will help the medical practitioners to diagnose the disease more accurately.

Table 1 Circularity values for A-K characters

Triangle 1.817	Rectangle 1.284 Triangle 1.988	Rectangle 1.736 Triangle 1.778	Rectangle 1.379 Triangle 2.968	Rectangle 1.398 Triangle 1.566	Rectangle 1.363 Triangle 2.364
Rectangle 1.513 1.259 1.26	Triangle 1.678 1.602 Circle 1.193	Triangle 1.583 1.598 2.176	Rectangle 1.47 Triangle 1.902 1.625	Triangle 1.755 1.585 Circle 1.075	Rectangle 1.436 1.342 Triangle 1.681
Rectangle 1.413	Rectangle 1.416	Rectangle 1.516	Rectangle 1.383	Rectangle 1.435	Rectangle 1.512
Rectangle 1.506 1.293	Rectangle 1.453 1.411	Rectangle 1.418 Triangle 3.385	Rectangle 1.381 Triangle 1.672	Rectangle 1.21,1.36 Triangle 1.87,1.72	Rectangle 1.428 Triangle 2.914
Rectangle 1.342 Rectangle 1.312	Rectangle 1.417 Rectangle 1.344	Rectangle 1.389 Rectangle 1.292	Rectangle 1.405 Rectangle 1.325	Rectangle 1.361 Rectangle 1.326	Rectangle 1.312 Rectangle 1.35
Rectangle 1.419	Rectangle 1.391	Rectangle 1.299	Rectangle 1.3	Rectangle 1.244	Rectangle 1.263
Rectangle 1.267	Rectangle 1.268	Rectangle 1.276	Rectangle 1.275	Rectangle 1.312	Rectangle 1.273
Rectangle 1.258	Rectangle 1.278	Rectangle 1.249	Rectangle 1.25	Rectangle 1.249	Rectangle 1.292
Rectangle 1.253	Rectangle 1.249	Rectangle 1.27	Rectangle 1.28	Rectangle 1.251	Rectangle 1.248
Rectangle 1.259	Rectangle 1.258	Rectangle 1.267	Rectangle 1.284	Rectangle 1.267	Rectangle 1.328

Table 2 Circularity values for basic geometric shapes

Triangle 1.685	Triangle 1.635	Triangle 1.748 Rectangle 1.315	Triangle 1.665 Rectangle 1.313	Rectangle 1.508 Circle 0.986	Triangle 6.086 Circle 1.083
Heptagon 1.399,1.14	Heptagon 1.374,1.13	Heptagon 1.706 Decagon 1.063	Decagon 1.442 1.446	Heptagon 1.575 Decagon 1.837	Heptagon 1.575 Decagon 1.837
Heptagon 1.671,1.793	Heptagon 1.82,1.567	Heptagon 2.461 Pentagon 1.033	Heptagon 2.484 Pentagon 1.34	Heptagon 1.55,2.656	Heptagon 2.673 Decagon 1.165

Table 3 Circularity values with shapes for Kimia-99 dataset

Rectangle 1.402	Rectangle 1.397	Triangle 1.720	Heptagon 1.67	Heptagon 1.657	Triangle 1.720	Rectangle 1.480
Triangle 1.774	Triangle 1.813	Heptagon 1.631	Decagon 1.580	Decagon 1.739	Hexagon 1.684	Pentagon 1.454
Rectangle 1.391	Octagon 1.572	Octagon 1.569	Heptagon 1.520	Triangle 1.688	Triangle 1.831	Rectangle 1.469
Heptagon 1.783	Octagon 1.975	Triangle 1.764	Triangle 1.824	Hexagon 1.631	Triangle 1.977	Rectangle 1.450
Decagon 1.252	Decagon 1.233	Decagon 1.264	Decagon 1.276	Decagon 1.329	Decagon 1.265	Pentagon 1.433

Table 4 Circularity values with shapes for carcinogenic cell structure

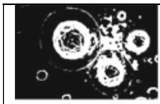	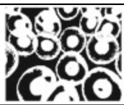			
Heptagon 1.815,1.817, 1.834,2.114, 2.242,2.455, 2.374,2.659, 2.883,3.701, 3.647,3.875, 3.964,4.707, 4.666,4.512, 4.558,6.855, 12.562,15.714, 17.146, Decagon 1.175	Heptagon 37.826 Decagon 1.016 Hexagon 0.949,0.991 Pentagon 0.929	Heptagon 37.007, 44.054, 10.732, 6.548	Decagon 1.353 Heptagon 9.691 ,1.740, 33.160 ,2.362	Heptagon 19.258,3.339, 4.021,7.517, 2.596,6.248 Decagon 1.131

References

Dougherty ER, Cheng Y (1995) Morphological pattern spectrum classification of noisy shapes: exterior granulometries. Pattern Recogn 28(1):81–98

Gonzalez E, Bianconi F, Fernandez A (2016) An investigation on the use of local multi-resolution pattern for image classification. Elsevier Information Science, Amsterdam

Liu G-H, Li Z-Y, Zhang L, Xu Y (2011) Image retrieval based on micro-structure descriptor. Pattern Recogn 44:2123–2133

Liu X, Deng Z, Yang Y (2019) Recent progress in semantic image segmentation. Artif Intell Rev 52:1089–1106

Maragos P (1989) Pattern spectrum and multiscale shape representation. IEEE Trans Pattern Anal Mach Intell II(7)

Olson E (2011) Particle shape factors and their use in image analysis—part 1: theory. Particle Technol Lab 15(3)

Santra S, Mandal S (2020) A new approach towards invariant shape descriptor tools for shape classification through morphological analysis of image. In: 2nd international conference on computational advancement in communication circuit and system (ICCACCS-2018). Springer lecture note entitled "Computational advancement in communication circuits and systems

Santra S, Mukherjee P, Sardar P, Mandal S, Deyasi A (2018) Object detection in clustered scene using point feature matching for non-repeating texture pattern. In: Conference on control, signal processing and energy system (CSPES 2018). Lecture note of electrical engineering. Springer, Berlin

Santra S, Mandal S, Das K, Bhattacharjee J, Roy A (2019a) A modified canny edge detection approach to early detection of cancer cell. In: IEEE 3rd international conference on electronics, materials engineering & nanotechnology (IEMENTech)

Santra S, Mandal S, Das K, Bhattacharjee J, Deyasi A (2019b) A comparative study of Z-transform and fourier transform applied on medical images for detection of cancer segments. In: IEEE 3rd international conference on electronics, materials engineering & nanotechnology (IEMENTech)

Wang J, Bai X, You X, Liu W, Latecki LJ (2012) Shape matching and classification using height functions. Pattern Recogn 33:134–143

Yu X, Lin X, Dai Y, Zhu K (2017) Image edge detection based tool condition monitoring with morphological component analysis. Elsevier, Amsterdam

Zhang D, Lu G (2004) Review of shape representation and description techniques. Pattern Recogn 37(2004):1–19, https://doi.org/10.1016/j.patcog.2003.07.008

Matrix of Skin Color Satisfaction, Body-Image Cognitive Distortions and Self-esteem of the Young Adults

Abbasuddin Mallick, Maitrayee Paul, Nazia Ahmed, Shreyasi Biswas, Sanchita Ghosh, and Neloy Kumar Chakroborty

Abstract Body-image cognitive distortions and self-esteem are two socially important parameters which are reported to be associated with the skin color satisfaction in the young people. However, much of the research till date has been conducted on the populations of color in the color-stratified Western societies and on women, with contradictory results. To better understand the depths of associations between these parameters, we investigated whether greater skin color satisfaction is connected to lower body-image cognitive distortions and higher self-esteem among the young Indian men and women. Data were collected from 145 participants (male 73 and female 72), between ages 18 and 26 years. Results showed a general preference for lighter skin color among the participants with men, in our sample, expressed significant negative and positive associations of skin color satisfaction respectively with body-image cognitive distortions and self-esteem. However, skin color satisfaction is not a good predictor of self-esteem in our study, unlike the parameter body-image cognitive distortions. The findings are discussed in lights of self-perception and mental health of the young adult Indian men and women in a multi-colored society

A. Mallick
Rice Education, Belghoria, Kolkata, India

M. Paul
School of Life Science and Biotechnology, Department of Biotechnology, Adamas University, Barasat, West Bengal, India

N. Ahmed
Department of Microbiology, Fergusson College, Pune, India

S. Biswas
Webster University, Bangkok, Thailand

S. Ghosh
West Bengal State University, Barasat, West Bengal, India
e-mail: sanchitaghosh@wbsu.ac.in

N. K. Chakroborty (✉)
Thapar School of Liberal Arts and Sciences, Thapar Institute of Engineering and Technology, P.O. Box 32, Bhadson Road, Patiala 147004, Punjab, India
e-mail: neloy.chakroborty@thapar.edu

M. Mukherjee et al. (eds.), *Advances in Medical Physics and Healthcare Engineering*, Lecture Notes in Bioengineering, https://doi.org/10.1007/978-981-33-6915-3_33

that has internalized the norms of somatic beauty, established by the culture and media.

Keywords Body-image cognitive distortions · Skin color satisfaction · Self-esteem · Mental health · Indian population

1 Introduction

Self-esteem and body-image cognitive disturbance have been widely acknowledged as two of the most salient factors that play significant roles on the sociocultural development of young people. The complex construct of self-esteem is predicted by self-worth, racial, ethnic, cultural and national identities of individuals (Mecca et al. 1989; Canabal, 1996; Crocker et al. 1994; Crocker 1999; Phinney et al. 1997). Similarly, body-image cognitive disturbance is associated with the developments of gender and personal identities, body mass index and mental perceptions of media images (Usmiani and Daniluk 1997; Bell et al. 2007, Kamps and Berman 2011, Latiff et al. 2018; Shaw et al. 2004). Substantial amount of research work, investigating the roots of self-esteem and cognitive distress toward the perceived blemishes in one's physical appearance, have reported associations of these two social and mental health determinants with the measures of skin color preference and satisfaction. This is particularly visible in the women of African American diaspora as reports found that this group is strongly influenced by the societal norms of beauty and attractiveness, which are dictated by white skin and Caucasoid features, such that their self-worth, self-esteem and body satisfaction depend on their skin color and skin color satisfaction (Bond and Cash 1992; Falconer and Nevile 2000; Coard et al. 2001; Thompson and Keith 2001; Hill 2002, Bryant and Baker 2003; Gullickson 2005; Watt 2006; Grabe and Hyde 2006; López 2008; Telzer and Vazquez Garcia 2009; Mucherah and Frazier 2013).

However, disagreements in the results of these studies together with particular focus on the females lead to the relationships between skin color, self-esteem and body-image dissatisfaction inconclusive as well as preclude possible gender effects. In addition, the abovementioned and other studies, exploring the relationships of skin color with the health determinants, are largely limited to the African, Hispanic and Asian diasporas living in America and Canada (Sahay and Piran 1997; Sweet et al. 2007; Telzer et al. 2009; Kiang and Takeuchi 2009; Bhagwat 2012), which inevitably leads to a dearth of quantitative research among the Asian societies, like India. To expand our knowledge on the possible roles of skin color satisfaction in mediating the association between self-esteem and cognitive biases toward body image in a society where the cultural trends have institutionalized skin color-based prejudice and established social hierarchy, correlating success in life with lighter skin color (Gosai 2010; Baker 2010; Ayyar and Khandare 2013), we conducted our study on an Indian population, including both genders, and addressed the following research questions:

1. Is higher skin color satisfaction associated with lower dissatisfaction with one's own body and higher self-esteem?
2. Do male and female have differences in perceptions of skin color satisfaction, body-image cognitive distortions and self-esteem?
3. Is skin color satisfaction a strong predictor of self-esteem?

Implications of the findings are discussed considering the concept of 'selfness' as well as psychological well-being of individuals as self-esteem and body-image dissatisfaction are also strong predictors of mental health status in the young and aged groups (Harter 1993; Davison and McCabe 2005; Cash et al. 2004; Hrabosky et al. 2009).

2 Method

2.1 Research Setting

A comparative study was conducted in Adamas University, Barasat (District: North 24-parganas, State: West Bengal), between the months of January and April of 2018 and 2019. Participants (both male and female) were all students of the university with an age range of 18–26 years and speaking Bengali as their mother language. There were 73 male and 72 female students who belonged to either 'Upper High' (0.68%) or 'High' (86.20%) or 'Upper middle' (12.41%) or 'Lower Middle' (0.68%) socioeconomic status (SES).

2.2 Interview Protocol

The interviews were conducted in the classrooms of the School of Life Science and Biotechnology during the daytime between 10.00 am and 5.00 pm. During the interview, respondents were requested to fill out a combined questionnaire containing identity and demographic questions (such as name, family name, gender, age, religion, caste, mother language and educational attainment) and questions to measure socioeconomic status or SES (monthly household income and expenditure), as well as items from the instruments measuring skin color satisfaction (SCS), assessment of body-image cognitive distortions (ABCD) and self-esteem (SE). Responses were recorded, and scores were calculated for these parameters.

2.3 Tools Used

Socioeconomic status (SES) was estimated using the six-variable scale developed by Dudeja and colleagues (Dudeja et al. 2015) in which subjects were asked to respond to questions on their locality of residence, educational attainment, occupation of their parents, family possessions and monthly per capita income.

The skin color questionnaire (SCQ) administered in our survey follows the modifications of the original SCQ scale, developed by Bond and Cash (Bond and Cash 1992) for African-Americans, by Falconer and Neville (2000). The first three items of this modified skin color satisfaction scale (SCSS) are identical with the SCQ scale developed by Bond and Cash (1992), assessing the skin color satisfaction, self-perceived skin color (lighter–darker) and perceived ideal skin color (light–dark). These three SCQ items were further modified in our survey to make them compatible for the Bengali-speaking population. The three items are as follows. (a) 'How satisfied are you with the shade (lightness or darkness) of your own skin color?' Responses are ranging from 1 (extremely dissatisfied) to 9 (extremely satisfied). (b) 'Compared to most Bengali people, I believe my skin color is….' Alternative responses range from 1 (extremely light) to 9 (extremely dark); high scores indicate subject's perception that his/her own skin color is darker or lighter than other Bengalis. (c) 'If I could change my skin color, I would make it lighter or darker.' Again in a nine-point scale, the responses range from 1 (much lighter) to 9 (much darker); high or low scores are indicating desires to have a different skin color. Four additional items which were originally introduced by Falconer and Neville (Falconer and Neville 2000) over the three-item SCQ scale to measure skin color satisfaction more stably were modified to make them compatible for our race.

The uni-dimensional, 18-item form-A of the assessment of body-image cognitive distortions (ABCD), developed by Thomas Cash and colleagues (Cash et al. 1996; Jakatdar et al. 2006; Rudiger et al. 2007), was used in our survey. Statistical analysis showed that the ABCD was predictable from several body-image evaluations. Each question presents a hypothetical situation and a mental conversation that some people might have in that situation, and we wanted to know how characteristic the thought patterns of the subject would be in different situations. There are no correct or incorrect answers, and the scale evaluates participant's responses by five alternative answers from 'not at all like me', to 'slightly like me', to 'moderately like me', to 'mostly like me', until 'exactly like me' for situations such as 'Imagine that you're flipping through a magazine that has pictures of very attractive models of your gender. Would you compare your looks to theirs and think that you don't look very good?', 'When you think about the aspects of your appearance with which you're dissatisfied, do you think that most people also dislike those aspects of your looks?'.

Rosenberg's self-esteem scale is a continuous ten-item scale which was used to assess the self-ascribed global self-esteem of the subjects (Rosenberg 1965) by scoring the positive and negative feelings of the subjects. Some of the items are 'On the whole, I am satisfied with myself', 'I am able to do things as well as most other people', 'I feel that I'm a person of worth, at least on an equal plane with others' and 'All in all, I am inclined to feel that I am a failure'.

The subscales and scales used in our survey have the range of values from 1 to 72 with higher values representing higher socioeconomic status, higher satisfaction with one's own skin color, higher dissatisfaction with one's own body image and higher self-esteem. Independent samples t-Test for equality of means, Pearson's linear correlation and hierarchical multiple regression analysis were performed on the data to test the hypotheses. Gender, SCS and ABCD were used as independent variables and SE as a dependent variable in the analyses.

3 Results

3.1 Preference for Skin Color in the Participants

We first investigated whether the genders differ in their preference for skin color. For this, we scored the responses for the two items of the skin color satisfaction scale—'I wish the shade of my skin was darker' and 'I wish my skin was lighter'. Analysis of the first item showed that 28.7% male and 51.3% female participants strongly disagreed with this statement. Overall, a total of 76.7% male and 88.8% female expressed disagreement to the same statement, and only 9.6% of the total participants showed preference to the darker skin tone. Results of the independent samples *t*-Test showed more number of females disagreed than their male counterpart (t = -2.39, $df = 143$, $p = 0.018$). Analysis of the second item shows that only 12.3% male and 15.2% female participants strongly agreed with the statement whereas 19.3% of the total participants disagreed. However, a general preference for lighter skin tone is manifested as 67.5% of the total participants showed agreement with the statement. The independent samples *t*-Test, however in this case, showed no significant difference between the responses of the two genders ($t = 0.89$, $df = 143$, $p = 0.27$).

3.2 Difference in Scores for the Self-Perception Parameters Between the Genders

Independent samples *t*-Test was applied on the assessed parameters related to self-perception, i.e., skin color satisfaction (SCS), assessment of body-image cognitive distortions (ABCD) and self-esteem (SE). No significant difference in scores was found between the male and female participants for skin color satisfaction (t = 0.007, $df = 143$, $p = 0.9$) and assessment of body-image cognitive distortions ($t = -0.54$, $df = 143$, $p = 0.58$). However, males scored significantly higher than their female counterpart for the parameter 'Self-esteem or SE' (mean score for male:

28.71, mean score for female: 27.29, t-test for equality of means: $t = -2.03$, $df = 143$, $p = 0.04$), but due to nearly equal standard deviations for SE in the two groups, with nearly identical sample size, (male: $N = 73$, SD = 4.33, female: $N = 72$, SD = 4.08), we did not consider that the mean scores of SE are significantly different between the genders and thus pooled the data for further analyses.

3.3 Correlation Analyses

Person's linear correlation analysis was conducted on the pooled data for the parameters to understand the natures of association between them, viz. socioeconomic status (SES), SCS, ABCD and SE. In the pooled data, we found a significant positive relationship between SES and SCS (see Table 1). This effect, however, was found only for the male but not for the female participants (male: $r = 0.37$, $p = 0.001$; female: $r = -0.006$, $p = 0.96$) when we analyzed the data separately for the two groups. In fact, the females demonstrated a weak negative association. We next investigated the relationship between SCS and ABCD in the pooled data and found a significant negative relationship ($r = -0.22$, $p = 0.006$) (see Table 1 and Fig. 1). Like before, the significant association was only present in the males but not in the females (male: $r = -0.32$, $p = 0.005$; female: $r = -0.1$, $p = 0.4$). SCS also showed a significant positive association with SE in the pooled sample ($r = 0.17$, $p = 0.03$) (see Table 1 and Fig. 2), but when the data for the groups were separately analyzed, only males but not the females showed the effect (male: $r = 0.23$, $p = 0.04$; female: $r = 0.1$, $p = 0.36$). In the pooled analysis, SE also showed a significant negative association with ABCD ($r = -0.31$, $p < 0.001$) (see Table 1 and Fig. 3), and unlike before, this time, both male and female participants showed significant negative associations between SE and ABCD (male: $r = -0.39$, $p = 0.001$; female: $r = -0.24$, $p = 0.03$).

Table 1 Pearson's correlation matrix for socioeconomic status and self-perception variables

	SES	SCS	ABCD	Se
SES		$r = 0.23$ $\boldsymbol{p = 0.05}$	$r = 0.05$ $p = 0.49$	$r = 0.03$ $p = 0.64$
SCS	$r = 0.23$ $\boldsymbol{p = 0.05}$		$r = -0.22$ $\boldsymbol{p = 0.006}$	$r = 0.17$ $\boldsymbol{p = 0.03}$
ABCD	$r = 0.05$ $p = 0.49$	$r = -0.22$ $\boldsymbol{p = 0.006}$		$r = -0.31$ $\boldsymbol{p < 0.001}$
SE	$r = 0.03$ $p = 0.64$	$r = 0.17$ $p = 0.03$	$r = -0.31$ $\boldsymbol{p < 0.001}$	

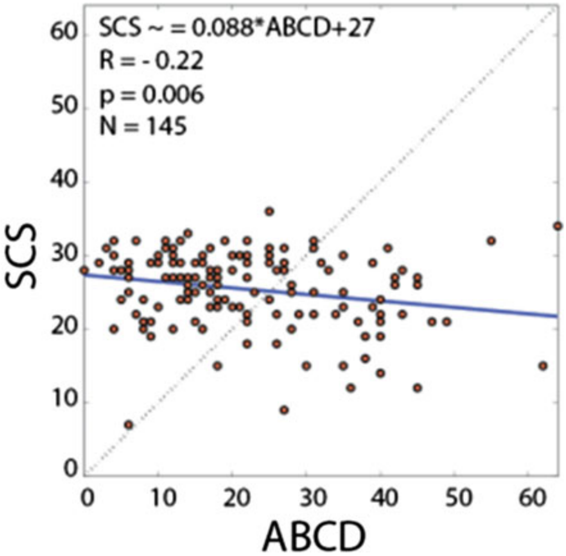

Fig. 1 Linear regression plot between SCS and ABCD with regression equation, coefficient and p-value for the pooled population ($N = 145$)

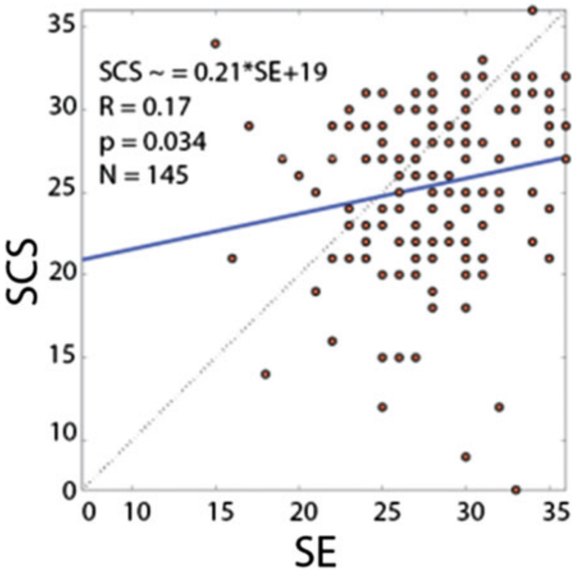

Fig. 2 Linear regression plot between SCS and SE with regression equation, coefficient and *p*-value for the pooled population

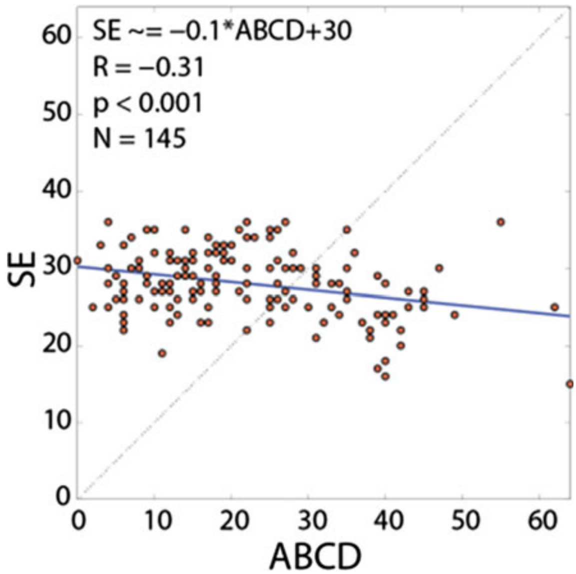

Fig. 3 Linear regression plot between SE and ABCD with regression equation, coefficient and p-value for the pooled population

3.4 Hierarchical Multiple Regression Analysis

The correlation analysis revealed that skin color satisfaction is negatively associated with body-image cognitive distortions and positively associated with self-esteem. This means that the more satisfied a person is with his/her skin color, the less dissatisfied he/she is with the body image and higher is his/her self-esteem. We performed a hierarchical multiple regression analysis to find out whether SCS is a predictor of SE in our sample, i.e., whether SCS explains a significant portion of the variance of SE. In Model 1, ABCD, as an independent variable, predicted SE as 9.6% of the variance of SE was explained by ABCD with a statistically significant change in the F-value: $R^2 = 0.096$, F-change = 15.21, $p_{\text{F-Change}} < 0.001$. Model 2, which included SCS as the second predictor variable, showed a jump in R^2 from 0.096 to 0.108 but the change in F-value was not significant, F-change = 1.90, $p_{\text{F-Change}} = 0.17$. The ANOVA table although showed significant p values for both Model 1 and Model 2, as Model 2 includes ABCD as one of the predictor variables; however, standardized β coefficient was only significant for ABCD ($\beta = -0.28, p = 0.001$) and not for SCS ($\beta = 0.11, p = 0.17$). We thus conclude that SCS is a weak predictor of SE in our sample as it only explains 1.2% of variance of SE beyond what has been explained by ABCD.

4 Discussion

The famous work of Thompson and Keith (2001) has demonstrated the close link between the stereotypes of attractiveness and skin color preferences in the African-American women, which eventually affects their overall self-esteem. The preference for lighter skin tone is not limited to African-Americans, but it is a worldwide trend as the Japanese, Chinese, Indonesians and different South Asian-Canadian communities reported a common high preference for lighter skin tone (Saito 1996; Sahay and Piran 1997). The results of our comparative study also showed a clear preference for lighter skin color among the Indian men and women such that, if given the option, they would like to have lighter skin color. This supports the previous findings on the notion of feminity and white beauty in the Indian societies (Ayyar and Khandare 2013). However, unlike the previous finding in the African-American women (Mucherah and Frazier 2013), the results of the present study revealed that skin tone satisfaction is not a strong predictor of body dissatisfaction and self-esteem in the young Indian women. On the contrary, men in our sample have satisfied the hypothesis that relates higher skin color satisfaction with lower dissatisfaction with the body and higher self-esteem. Men's preference for lighter skin tone as well as the differences between the genders is indicating that in the twenty-first century, the self-perception and body image are more affected by skin tone in the young Indian men than the women. This probably is a consequence of the establishment of a hegemonic masculinity that is dominated by fair-skinned beauty prototype and has earned enormous popularity in neoliberal India (Kareithi 2014). We also had participants who favored darker skin tone which we speculate due to the prevailing idea of the current generation which does not consider lighter skin tone as an asset in life that governs educational attainment and overall success (Gullickson 2005). The results on the associations between SCS, ABCD and SE though require careful interpretation along with requirement of further studies on larger sample, to dissect out the intertwine nature of these constructs, addressing questions that can illustrate the full-scale effect of skin color satisfaction on the well-being of individuals and emphasize on the contributions of several parameters, such as life's satisfaction, subjective happiness, educational attainment, professional success and altruistic behavior to the self-esteem of individuals.

5 Conclusion

The study has disclosed preference for lighter skin color in the young Indian men and women. The results also relate higher skin color satisfaction with lower body-image dissatisfaction and higher self-esteem prevalently for the men than for the women.

Acknowledgements This work was supported by the School of Life Science and Biotechnology, Adamas University, Barasat, West Bengal, India.

References

Ayyar V, Khandare, L (2013) Mapping color and caste discrimination in Indian society. In The Melanin Millennium. Springer, Dordrecht. 71–95
Bell BT, Lawton R, Dittmar H (2007) The impact of thin models in music videos on adolescent girls' body dissatisfaction. Body image 4:137–145
Bhagwat R (2012) The relationship of skin tone to physical and mental health outcomes in South Asian Americans. Rutgers University-Graduate School-New Brunswick
Bond S, Cash TF (1992) Black beauty: skin color and body images among African American College women. J Appl Soc Psychol 22:874–888
Bryant Jr A, Baker SB (2003) The feasibility of constructing profiles of native Americans from the people of color racial identity attitude scale: A brief report. Meas Eval Couns Dev 36:2–8
Canabal I (1996) Latino group identities, collective and personal self-esteem. ProQuest Information & Learning
Cash TF, Phillips KA, Santos MT, Hrabosky JI (2004) Measuring negative body image: validation of the Body Image Disturbance Questionnaire in a nonclinical population. Body image 1:363–372
Coard SI, Breland AM, Raskin P (2001) Perceptions of and Preferences for Skin Color, Black Racial Identity, and Self-Esteem Among African Americans. J Appl Soc Psychol 31:2256–2274
Crocker J (1999) Social stigma and self-esteem: Situational construction of self-worth. J exp soc psychol 35:89–107
Crocker J, Luhtanen R, Blaine B, Broadnax S (1994) Collective self-esteem and psychological well-being among White, Black, and Asian college students. In: Pers Soc Psychol Bull 20:503–513
Davison TE, McCabe MP (2005) Relationships between men's and women's body image and their psychological, social, and sexual functioning. Sex roles 52:463–475
Dudeja P, Bahuguna P, Singh A, Bhatnagar N (2015) Refining a socio-economic status scale for use in community-based health research in India. J Postgrad Med 61:p. 77
Falconer JW, Neville HA (2000) African American college women's body image: An examination of body mass, African self-consciousness, and skin color satisfaction. Psychol Women Q 24:236–243
Gosai A (2010) India's myth of fair-skinned beauty. The Guardian
Grabe S, Hyde JS (2006) Ethnicity and body dissatisfaction among women in the United States: A meta-analysis. Psychol Bull 132, 622–640
Gullickson A (2005) The significance of color declines: A re-analysis of skin tone differentials in post-Civil Rights America. Soc Forces 84:156–180
Harter S (1993) Causes and consequences of low self-esteem in children and adolescents. Self-Esteem, Ed: Springer 1993:87–116
Hill ME (2002) Skin color and the perception of attractiveness among African Americans: Does gender make a difference? Social Psychology Quarterly 65:77–91
Hrabosky JI, Cash TF, Veale D, Neziroglu F, Soll EA, Garner DM et al (2009) Multidimensional body image comparisons among patients with eating disorders, body dysmorphic disorder, and clinical controls: a multisite study. Body Image 6:155–163
Jakatdar TA, Cash TF, Engle EK (2006) Body-image thought processes: The development and initial validation of the Assessment of Body-Image Cognitive Distortions. Body Image 3:325–333
Kamps CL, Berman SL (2011) Body image and identity formation: The role of identity distress. Revista Latinoamericana De Psicología 43:267–277
Kareithi PJ (2014) Hegemonic masculinity in media. Media and gender: a scholarly agenda for the Global Alliance on Media and Gender 30
Kiang L, Takeuchi DT (2009) Phenotypic bias and ethnic identity in Filipino Americans. Social Science Quarterly 90:428–445
Latiff AA, Muhamad J, Rahman RA (2018) Body image dissatisfaction and its determinants among young primary-school adolescents. Journal of Taibah University Medical Sciences 13:34–41

López I (2008) But you don't look Puerto Rican: The moderating effect of ethnic identity on the relation between skin color and self-esteem among Puerto Rican women. Cultural Diversity and Ethnic Minority Psychology 14:102

Mecca A, Smelser NJ, Vasconcellos J (1989) The social importance of self-esteem. Univ of California Press, Calfornia

Mucherah W, Frazier AD (2013) How deep is skin-deep? The relationship between skin color satisfaction, estimation of body image, and self-esteem among women of African descent. J Appl Soc Psychol 43:1177–1184

Phinney JS, Cantu CL, Kurtz DA (1997) Ethnic and American identity as predictors of self-esteem among African American, Latino, and White adolescents. J Youth Adolesc 26:165–185

Rosenberg M (1965) Rosenberg self-esteem scale (RSE). Acceptance and Commitment Therapy. Measures Package 61:18

Sahay S, Piran N (1997) Skin-color preferences and body satisfaction among South Asian-Canadian and European-Canadian female university students. The Journal of Social Psychology 137:161–171

Saito MA (1996) Comparative study of color preferences in Japan, China and Indonesia, with emphasis on the preference for white. Percept Mot Skills 83(1):115–128

Sweet E, McDade TW, Kiefe CI, Liu K (2007) Relationships between skin color, income, and blood pressure among African Americans in the CARDIA Study. Am J Public Health 97:2253–2259

Telzer EH, Vazquez Garcia HA (2009) Skin color and self-perceptions of immigrant and US-born Latinas: The moderating role of racial socialization and ethnic identity. Hispanic Journal of Behavioral Sciences 31:357–374

Thompson MS, Keith VM (2001) The blacker the berry: Gender, skin tone, self-esteem, and self-efficacy. Gender & Society 15:336–357

Usmiani S, Daniluk J (1997) Mothers and their adolescent daughters: Relationship between self-esteem, gender role identity, body image. J Youth Adolesc 26:45–62

Watt SK (2006) Racial identity attitudes, womanist identity attitudes, and self-esteem in African American college women attending historically Black single-sex and coeducational institutions. Journal of College Student Development 47:319–334

Review the Performance of Different Digital Modulation Techniques with Suitable Error Control Codes in Telehealth Services

Bishal Das, Nisarga Chand, and Angsuman Sarkar

Abstract Being the primary medium of communication in the present world, the usage and development of wireless digital communication are increasing day by day. Due to low cost, high-speed secure data transmission, and less noise than analog transmission, digital modulation techniques are widely used in many industrial and healthcare sectors. However, for long-distance transmission, selection of inappropriate modulation techniques, by choosing the right coding technique, often leads to more cost, less signal strength, and even more obscurity. Even sometimes for the usage of high-rated modulation techniques for small-distance results significant issues and unnecessary energy wastage in wireless sensor networks. This paper discusses the selection of right and reliable modulation techniques (e.g., BPSK, BASK, BFSK) using the desired coding techniques such as convolution code or Reed-Solomon code based on the significant distance and security by showing the comparison of each aspect of transmission using MATLAB simulation. Now, for transmission of a signal, the major part depends on the inside and outside noise that affects the signal strength. So, this paper also aims to the transmission with right combinations of both coding and modulation techniques as well as transmit them under AWGN channel and Rayleigh channel that can able to make an atmosphere of real-life noise. The all-over idea proposed in this paper includes four ways to clarify the result that covers the comparison of SNR and BER ratio of each modulation techniques, transmission under AWGN and Rayleigh channel, transmission using convolution and RS code for signal strength, and finally putting all together to find the best way of transmission. Synthetic data is used to simulate this experimental work.

Keywords Bit error rate · Signal to noise ratio · AWGN channel · Rayleigh channel · Reed-Solomon coding · Convolution coding technique

B. Das · N. Chand (✉)
Adamas University, Kolkata, India

A. Sarkar
Kalyani Government Engineering College, Kalyani, Nadia, India
e-mail: angsumansarkar@ieee.org

M. Mukherjee et al. (eds.), *Advances in Medical Physics and Healthcare Engineering*, Lecture Notes in Bioengineering, https://doi.org/10.1007/978-981-33-6915-3_34

1 Introduction

Throughout the human evolution, communication technology holds a vital role. Whether it was a caveman of early Stone Age or today's evolved human being or animals or trees, each and every living thing leads their life with communicating each other. In early time,after World War 1, humanity realized that the analogous one-to-one communication is very much time consuming as well as the security is low. From that point, the enhancement of communication technologies was making headlines. In 1980s, the emergence of digital communication based on digital technologies promoted the faster way of the communication system and its standardization development as well as reliability (Zhang et al. 2010). Digital modulation uses the discrete representation of signals which includes modifying amplitude, phase, and frequency. But on the other hand, with time, heavy noise issue, whether natural or manmade, has disrupted the signal transmission as well as the quality. As well as the use of high-rated modulation, data transmission for a small distance in industrial sector often leads to unnecessary energy loss. Not only in industrial sectors but also in healthcare areas modern communication is heavily used in recent years. For example, telehealth is the hot potato in recent years (El-Miedany 2017). Patients can able to have a one-to-one communication with their preferable doctor on Web where doctors can give the right suggestion to their patients. Also, nowadays pagers can share information on a patient's status to let them know test results are in or inform them of an emergency. Even in few cases, such process communications are used to transfer patient's details when the responsibility for a role is handed off from one medical professional to another. So, eventually as the personal details of the patient transferring through Web from one place to another, security as well as the transmission speed matters the most. So, it became very important to transmit the signal with the proper selection of modulation techniques as well as the proper coding technique for secured desired range transmission with a considerably low amount of noise in wireless sensor networks (WSN) which is responsible for monitoring the signal strength lifetime and helps travel to the desired distance depending on the physical condition of the outer environment (Fadhil and AlSabbagh 2012). For the better improvement of signal having low noise effect, Reed-Solomon code (RS) and convolution code play a big role to regenerate an amount of the distorted signal. This could be measured and showed through the signal to noise ratio (SNR) versus bit error rate (BER) graph (Dawood et al. 2014; Awon et al. 2012). So, depending on some criteria such as portability, reliability, transmission speed and security, this paper will analyze the performance on various modulation techniques under some noise channels using both coding and non-coding technique on MATLAB simulation module to compare and show the best possible way of transmission. In addition, two frequently used basic channels such as AWGN and Rayleigh have been used (Awon et al. 2012; Wali and Fayadh 2017).

2 Channel Models and Parameters

In this section, the working as well as the mathematical principle for noted channels as AWGN and Rayleigh fading channel and the parameters for graph calculation BER and SNR has been described as follows (Salih and Suliman 2011):

2.1 AWGN Channel

Additive white Gaussian noise or AWGN is a basic noise model used in information theory to virtually mimic the effect of many random processes that occur in nature. The main reason for naming additive because of adding significant amount of noise to send signals that cannot be multiplied, Gaussian because of the noise in this channel is normally random and white due to its equality of power in every frequency. In mathematical form, the signal capacity of AWGN can be expressed as Eq. (1)

$$C = \frac{1}{2}\log\left(1 + \frac{P}{N}\right) \tag{1}$$

where

P maximum channel power.

2.2 Rayleigh Channel

It is basically a statistical model having a propagation environment especially used in radio channels or wireless medium when no dominant propagation along the line of sight exists between the path of transmitter and receiver. The intensity probability of Rayleigh channel can be mathematically expressed as Eq. (2)

$$F_R(r) = \frac{r}{\sigma^2}\exp\left(-\frac{r^2}{2\sigma^2}\right) \quad \text{for } r \geq 0 \tag{2}$$

where

σ^2 difference of random variable.
r envelop amplitude of Rx signal.

2.3 BER

Bit error rate or BER is the number of error bits that have been corrupted by noise, divided by the total number of transferred bits. It is simply the average number received error bits divided by received total bits. If one error bit out of every million is received, the mathematical notation for BER is expressed as (3)

$$\text{BER} = \frac{1\ \text{error bit}}{10^6\ \text{bits}} = 10^{-6} \tag{3}$$

2.4 SNR

Signal to noise ratio or SNR is the ratio of the signal power to noise power expressed in decibels (dB). If the ratio is higher than 1:1 that means, there is more signal as compared to noise. For better calculation in signal study, SNR expressed as (4)

$$\text{SNR} = \frac{P_{\text{signal}}}{P_{\text{Noise}}} \tag{4}$$

where

P refers to average power of signal and noise, respectively.

3 Transmission and Simulation

In this section, the overall signal transmission and the MATLAB simulation will be discussed thoroughly with flowchart as follows.

3.1 Signal Transmission

The transmitting and receiving of a desired signal (such as BPSK, BFSK, QPSK) can be described as per the simulation flowchart shown in Fig. 1. This structure corresponds the selection of a signal that can be easily generated; depending on the distance, it may cover and send under both AWGN and Rayleigh fading channel to find and conclude which signal is less affected with noise while signal transmission at the time of receiving. And for better security and less noise effect, different channel coding part is used such as RS and convolution coding. Again, the signal transmits from the transmitter with coding and non-coding system under both AWGN and Rayleigh fading channel to compare the overall result in SNR versus BER plotting. At the time of receiving the signal, the coding technique will also detect and reconstruct the noise effected bits to enhance the signal power so that efficiency of the coding technique could be measured (Sheik Dawood and Athisha 2013; Balakrishnan et al. 2007).

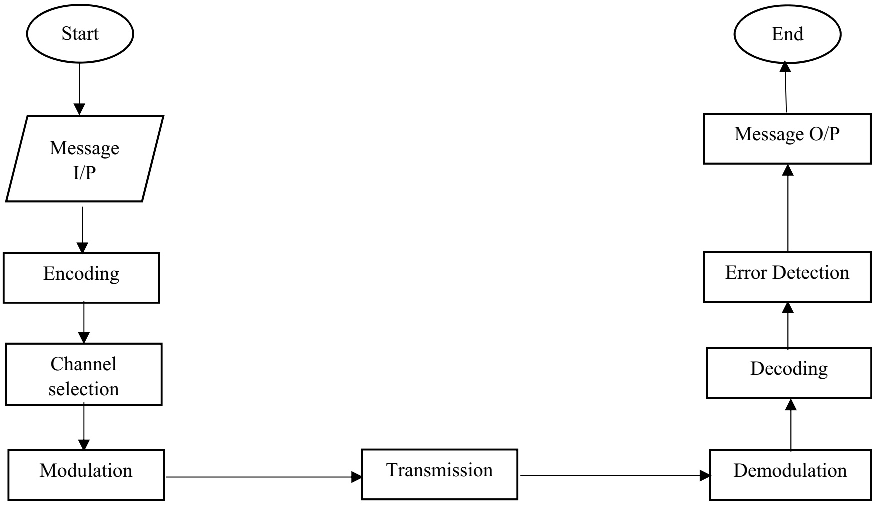

Fig. 1 Block diagram of the signal transmission under noise channels on MATLAB

3.2 Simulation Flowchart

See Fig. 1.

4 Performance Study of Various Modulated Signals Under Channels

In this section, the comparison of different modulated signals under both AWGN and Rayleigh fading channel will be discussed to show how the message signals get effected and distorted in transmission. The below graphical figures are for analyzing the whole scenario and will be measured in terms of SNR as 'X-axis' and BER as 'Y-axis.'

4.1 Analysis of Different Signals Under AWGN Channel

Various types of energy-efficient modulation scheme for WSNs are chosen and transmitted under AWGN channel by the aid of SNR versus BER plot using MATLAB simulation. The following Fig. 2 shows how the signal curve is changing when SNR is increasing. Performance under AWGN channel for each of the modulation techniques is clearly visible on Table 1, with respect to the calculation of SNR and BER parameters.

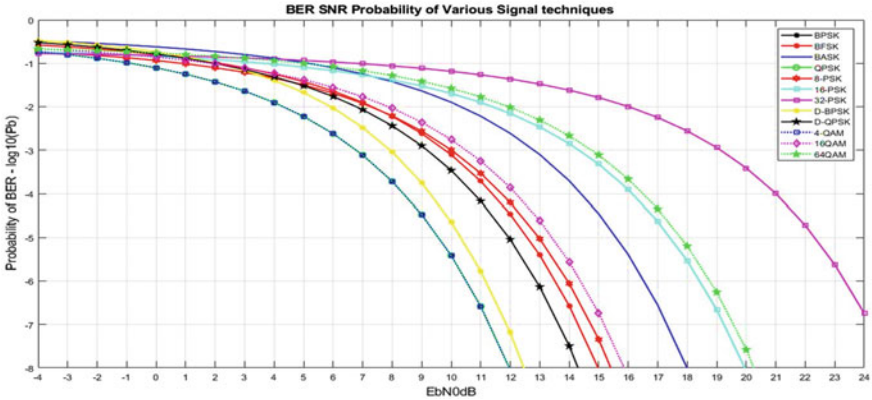

Fig. 2 SNR versus BER comparison of different modulated signals under AWGN channel

Table 1 SNR versus BER calculation table of different modulated signals under AWGN channel

SNR versus BER						
Modulation techniques	At minimum range of SNR		At mid-range of SNR		At optimum range of SNR	
	SNR (dB)	BER	SNR (dB)	BER	SNR (dB)	BER
BPSK	4	0.0102	8	0.000158	12	0.00000001
BFSK	4	0.10	8	0.00630	12	0.0000316
BASK	4	0.158	8	0.0398	12	0.002511
QPSK	4	0.0102	8	0.000158	12	0.00000001
8-PSK	4	0.0398	8	0.00630	12	0.0000794
16-PSK	4	0.10	8	0.05011	12	0.00794
32-PSK	4	0.1	8	0.1	12	0.0316
D-BPSK	4	0.0316	8	0.0010	12	0.0000000631
D-QPSK	4	0.0316	8	0.00316	12	0.000010
4-QAM	4	0.0102	8	0.000158	12	0.00000003
16-QAM	4	0.10	8	0.01	12	0.0001258
64-QAM	4	0.1584	8	0.0630	12	0.01

So, as it is clear from Table 1, BPSK and QPSK have the lowest BER among all the signal modulations. So, for further calculation studies under Rayleigh fading channel, we will use BPSK and QPSK as the primary technique.

4.2 Analysis and Comparison of BPSK Signal Under Rayleigh Fading Channel

The following Fig. 3 shows the change of BER performance with the increasing SNR under Rayleigh fading channel. To compare and obtain the best data result between Rayleigh and AWGN channel, both of the signals have been plotted together including the comparison table as shown in Table 2.

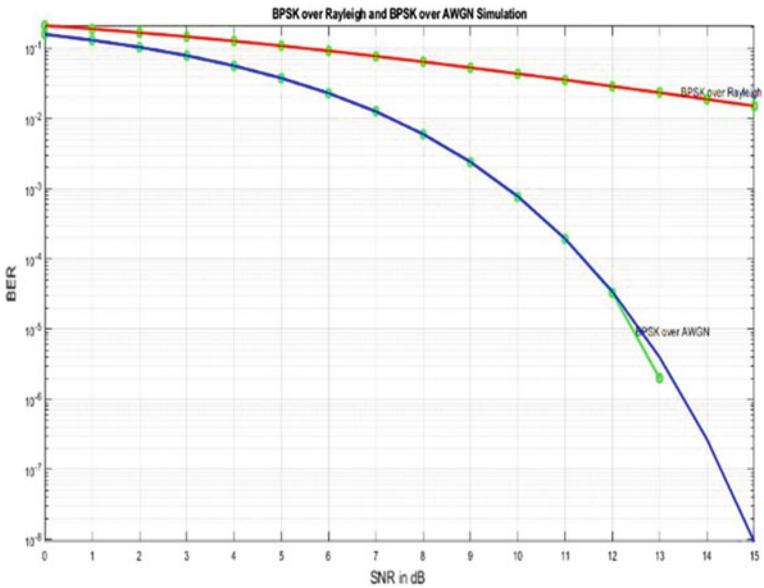

Fig. 3 SNR versus BER comparison of BPSK under Rayleigh and AWGN channel

Table 2 SNR versus BER calculation table of BPSK under Rayleigh and AWGN channel

SNR versus BER						
Channel	At minimum range of SNR		At mid-range of SNR		At optimum range of SNR	
	SNR (dB)	BER	SNR (dB)	BER	SNR (dB)	BER
AWGN	4	0.0398	8	0.00398	13	0.00000125
Rayleigh	4	0.1995	8	0.0398	13	0.0125

4.3 Analysis and Comparison of QPSK Signal Under Rayleigh Fading Channel

With the similar fashion like BPSK, in this section, Fig. 4 and Table 3 show the BER and SNR comparison on their performance under both Rayleigh and AWGN channel and comparison table depending on the calculation, respectively.

Now, as we can see BPSK under AWGN channel has the lower BER than Rayleigh fading as well as compared to QPSK under both AWGN and Rayleigh. So, for general purpose, we will use BPSK as the primary technique for our next step.

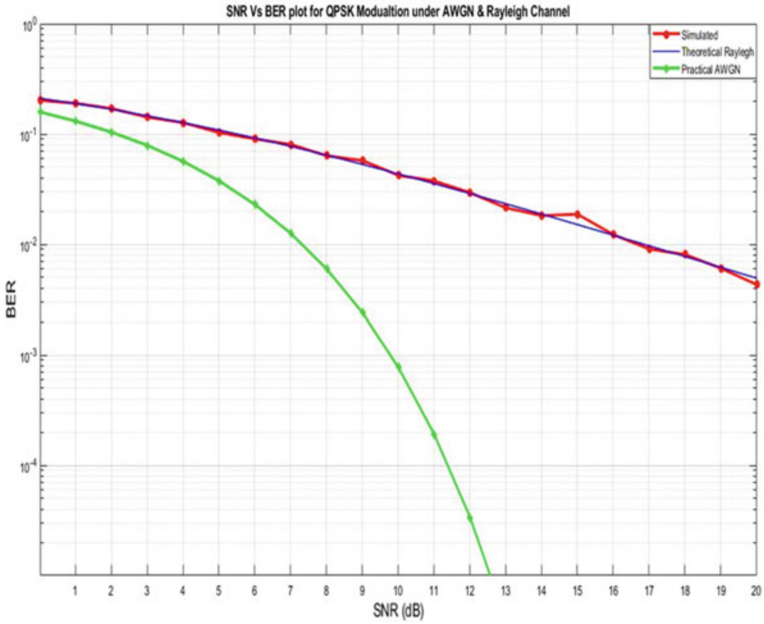

Fig. 4 SNR versus BER comparison of QPSK under Rayleigh and AWGN channel

Table 3 SNR versus BER calculation table of QPSK under Rayleigh and AWGN channel

SNR versus BER						
Channel	At minimum range of SNR		At mid-range of SNR		At optimum range of SNR	
	SNR (dB)	BER	SNR (dB)	BER	SNR (dB)	BER
AWGN	4	0.0398	8	0.00398	12	0.00001584
Rayleigh	4	0.1258	8	0.0398	12	0.0158

4.4 Analysis of BPSK Transmission Under AWGN Channel with RS Coding

In this section, we will transmit the BPSK signal under AWGN channel. But apart from the previous curve, this time we will code the BPSK signal with Reed-Solomon code before the transmission as shown in Fig. 5. For better visualization, both coded BPSK and non-coded BPSK signal have been transmitted, and the BER has been calculated in terms of increasing SNR as shown in Table 4.

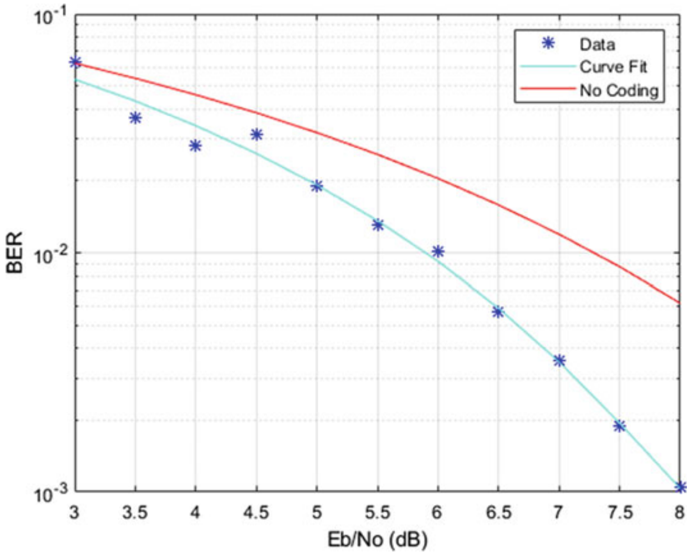

Fig. 5 SNR versus BER comparison of BPSK using RS code under AWGN channel

Table 4 SNR versus BER calculation table of BPSK using RS code under AWGN channel

SNR versus BER						
Signal	At minimum range of SNR		At mid-range of SNR		At optimum range of SNR	
	SNR (dB)	BER	SNR (dB)	BER	SNR (dB)	BER
BPSK	4	0.0239	5.5	0.014	8	0.0039
BPSK + RS	4	0.0158	5.5	0.010	8	0.001

4.5 Analysis of BPSK Transmission Under AWGN Channel with Convolution Coding

Using the same methodology as 4.4 column, in this section, we will transmit the BPSK signal under AWGN channel using convolution coding technique as shown in Fig. 6. Like the previous one, to show the comparison between coding and non-coding technique, we will transmit both and measure the BER as shown in Table 5.

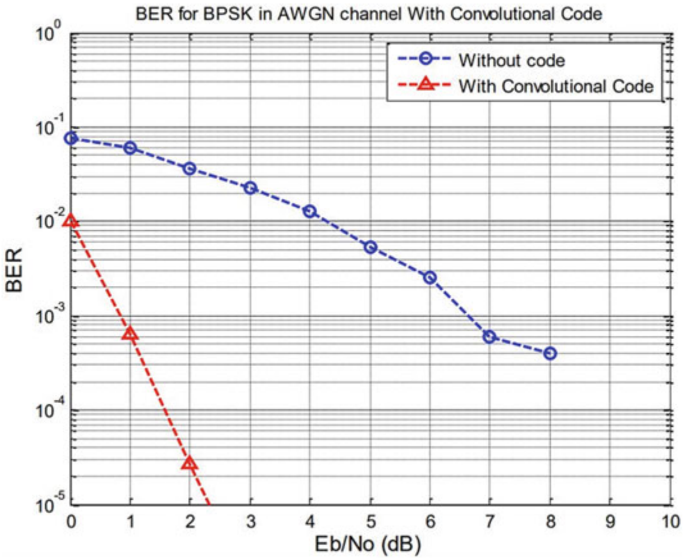

Fig. 6 SNR versus BER comparison of BPSK using convolution code under AWGN channel

Table 5 SNR versus BER calculation table of BPSK using convolution code under AWGN channel

SNR versus BER						
Signal	At minimum range of SNR		At mid-range of SNR		At optimum range of SNR	
	SNR (dB)	BER	SNR (dB)	BER	SNR (dB)	BER
BPSK	0	0.0501	1	0.0316	2	0.0177
BPSK + Conv	0	0.01	1	0.000316	2	0.0000158

Table 6 SNR versus BER calculation table of BPSK with RS and convolution code under AWGN channel

Coding technique	At minimum range of SNR		At optimum range of SNR	
	SNR (dB)	BER	SNR (dB)	BER
BPSK + Reed-Solomon	4	0.0158	8	0.0010
BPSK + Convolution	0	0.0100	2	0.0000158

5 Final Simulation Result

So, we have almost compared each of the modulation signals under AWGN channel and found the best technique to compare the BER under both AWGN and Rayleigh fading channel. Finally, we transmit the BPSK signal with RS and convolution code under AWGN channel and measure the BER and SNR as shown in Figs. 5 and 6, respectively. So, on the final stage of our paper, we will now compare the SNR versus BER table of BPSK using both RS and convolution code as shown in Table 6.

In Table 6, we can see that the BPSK signal with Reed-Solomon coding has BER of 0.0158 when the SNR is 4 dB and 0.0010 in 8 dB. But in case of BPSK with convolution coding technique, the BER is 0.0000158 in just 2 dB, and from Fig. 6, we can assume that the signal noise getting almost null before even SNR reaching 3 dB.

6 Conclusion

So, from the above analysis, we can conclude that the digital transmission system generally has better performance under AWGN channel. Among all the transmission techniques, BPSK modulation system has the better performance in terms of covering long distance with measurably less noise effect as compared to others. For the second performance, we can say that QPSK can also be used for a significant long-distance transmission. Similarly, BASK can be used for lower distance. In terms of better security and faster transmission, BPSK with convolution coding can be used as it has the lowest noise effect compared to all transmission system including BPSK with Reed-Solomon coding technique. So, from the above result, we can use the right modulation techniques, depending on the path distance so that the unnecessary energy loss could resist as well as depending on the security of patient's personal information in the healthcare sectors, so that the authenticity and privacy can be kept as high in an emergency situation. Last but not the least, it is better to say that with rapidly changing world, where Internet grabs the market irrespective of IT sectors or healthcare sectors, the digital communication system is getting promising day by day as well as making itself a supergiant in terms of reliability, connectivity, and more time-efficient technology.

References

Awon NT, Ashraful Islam M, Mizanur Rahman M, Touhidul Islam AZM (2012) Effect of AWGN & fading (Raleigh & Rician) channels on BER performance of a WiMAX communication system. (IJCSIS) Int J Comput Sci Inf Secur 10(8):11–17

Balakrishnan G, Yang M, Jiang Y, Kim Y (2007) Performance analysis of error control codes for wireless sensor networks. In: Proceedings of international conference on information technology (ITNG'07), pp 876–879

Dawood M, Jenifer C, Sikkandhar RA, Athisha G (2014) Performance analysis of Gaussian minimum shift keying (GMSK) with error control codes in wireless sensor networks

El-Miedany Y (2017) Telehealth and telemedicine: how the digital era is changing standard health care. Smart Homecare Technol TeleHealth 4:43–51. https://doi.org/10.2147/SHTT.S116009

Fadhil AM, AlSabbagh HM (2012) Performance analysis for bit-error-rate of DS-CDMA sensor network systems with source coding. TELKOMNIKA Indonesian J Electr Eng

Salih SHO, Suliman MMA (2011) Implementation of adaptive modulation and coding technique. Int J Sci Eng Res 2(5)

Sheik Dawood M, Athisha G (2013) Performance analysis of modulation and coding to maximize the lifetime of wireless sensor network. Int Rev Comput Softw (IRECOS) 8(10)

Wali MK, Fayadh RA, Al_taee DY (2017) Performance of AWGN and fading channels on wire. Int J Wirel Commun Networking Technol 6(3)

Zhang Q, Xing X et al (2010) Transmission performance simulation analysis of BF-SK signals in Gaussian and Rayleigh channel. J Shanxi Normal Univ

Bioengineering of Plant System with CRISPR Technology: A Review Perspective

Swarnav Bhakta, Shreya Banerjee, Mayank Srivastava, and Divya Srivastava

Abstract Plants are the source of food, fresh oxygen, useful metabolites, and they can be said as source of life on our planet. These green autotrophic creatures are subjected to a number of challenges throughout their life cycle from sowing the seed to post-harvesting of the yield. These challenges may be due to some biotic factors like pathogens, insects and other living body which compete with plants and kill them or may be any abiotic factor-like environmental condition including drought, soil salinity, humidity and many more like climate change. To solve this problem and provide a better life to the plants, bioengineering is really helpful. With the help of different tools of bioengineering, the plant variety can be improved, and it can equally fight against all type of stress conditions not only this but also the productivity can also be improved as good nutritional food is the need of today. Although, till today, a number of genome editing tools have been introduced, but all have some limitations. To overcome all the problems, a very powerful tool "CRISPR technology" came into the light. CRISPR stands for clustered regularly interspaced short palindromic repeats, and it was first discovered in prokaryotic cells to protect them from viral infection by developing an adaptive immune system. This concept was used to develop a new genetic engineering tool named as CRISPR technology, and this advancement has proved itself as a revolutionizing event for the scientific world. CRISPR technology generates targeted DNA breaks in living cells with the tendency to introduce a number of positive variations in DNA during the process of cellular DNA repair, and this tendency makes CRISPR more efficient than the other genetic engineering tools for plant system. This chapter summarizes all conceptual information about CRISPR technology, recent advancement in this technique and also

S. Bhakta · D. Srivastava (✉)
Department of Biotechnology, School of Life Science and Biotechnology, Adamas University, Kolkata 700126, India
e-mail: divya.srivastava@adamasuniversity.ac.in

S. Banerjee
Department of Microbiology, School of Life Science and Biotechnology, Adamas University, Kolkata 700126, India

M. Srivastava
Department of Mechanical and Automation Engineering, Amity University Ranchi, Ranchi, Jharkhand 834001, India

M. Mukherjee et al. (eds.), *Advances in Medical Physics and Healthcare Engineering*, Lecture Notes in Bioengineering, https://doi.org/10.1007/978-981-33-6915-3_35

discusses why CRISPR technology is now considered as the best possible technology to improve crop varieties.

Keywords Cas9 · Cas12 · CRISPR · Gene-editing tool

1 Introduction

CRISPR stands for Clustered Regularly Interspaced Short Palindromic Repeats which was first discovered in prokaryotes as a part of their adaptive immune system. After understanding the mode of action of CRISPR, scientists could successfully edit the genome of a mammalian cells and introduced this gene-editing tool as CRISPR technology (Jinek et al. 2012). In recent years, CRIRP technology has been implemented to improve the genome of plants as well to improve the crop yield, productivity, health and stability during climate change. This chapter reviews sevaral successful studies on CRISPR-Cas9 and CRISPR-Cas12 as genome editing tools for plant system and it also explains improvement in crop yield and quality, regulation in gene expression and epigenome editing followed by future aspects of CRISPR technology.

1.1 CRISPR-Cas9 as a Genome Editing Tool for Plants

CRISPR–Cas9 is a class 2, type II CRISPR system of genome editing that has been adapted for genome manipulation in the broad range of organisms with the capability of targeting more than one gene at a time, including both coding and non-coding along with open reading frame and untranslated regions. Cas9 protein comprises of six domains, Rec I, Rec II, RuvC, HNH, Bridge Helix and Protospacer Adjacent Motif (PAM) interacting domain. When Cas9 protein finds the potential target sequence of PAM having 5′-NGG-3′ sequence, immediately upstream of PAM cleavage will occur, and the DNA target will start melting due to the catalytic domain of the Cas9 protein. Single-guide RNA assembles Cas9 for cleaving genome after recognizing and binding to sequence of interest followed by a PAM. This emerging technique has been efficiently used for large-scale production of biotechnology products, treatment of deadly disease and also to modify a broad range of plant species, including Arabidopsis (Li et al. 2018), wheat (Okada et al. 2019), soybean (Li et al. 2015), maize (Lee et al. 2019), rice (Macovei et al. 2018) and many more (Table 1).

Table 1 Applications of CRISPR technology in different crops

Crops	Target genes	Gene functions	Applications	Refs.
Rice	ALS	ALS encodes acetolactate synthase, which is involved in the biosynthesis of the branched amino acid	To increase resistance against herbicide	Sun et al. (2016)
Wheat	TaMLO homologs	It involves in inhibiting resistance pathway to powdery mildew	To increase resistance against powdery mildew in wheat	Wang et al. (2014)
Soybean	GmPPD1 and GmPPD2	It involves in the transcriptional regulation of cell division in Arabidopsis	Inheritable site directed mutagenesis	Kanazashi et al. (2018)
Maize	ZmAgo18a and ZmAgo18b (Argonaute 18) and Dihydroflavonol 4-reductase or anthocyaninless	It involves in the biosynthesis of 24-nt phasiRNA in anthers	For mutagenesis frequency and heritability	Char et al. (2017)
Tomato	SlIAA9	SlIAA9 is a key gene controlling parthenocarpy	To generate parthenocarpic tomato plants	Ueta et al. (2017)

1.2 CRISPR-Cas12 as a Genome Editing Tool for Plants

Cas12b, also known as C2c1, is a class 2V-B endonuclease. It recognizes target sequences with a distal 5′-T-rich PAM sequence and generates staggered double-strand breaks with 7-nt 5′-overhangs by using both CRISPR-RNA and trans-activating CRISPR-RNA (tracrRNA) for target recognition, which can be engineered as a single-guide RNA. Initially, it was observed that Cas12b needs an optimum temperature around 48–50 °C; hence, it was not considered as suitable genome editing tool for plant or animal system but later by exploring diverse Cas12b orthologues, researches could find that it exhibits efficient editing activity at a broader range of temperatures. Further, Cas12b orthologs were screened from multiple organisms and engineered to increase efficiency at lower temperatures for broader range of applications (Strecker et al. 2019).

1.3 Improvement in Crop Yield and Quality

CRISPR genome editing tool has been successfully implemented in different crop varieties at different aspects such as sulfonylurea herbicide resistance is increased in rice by using CRISPR Cas9 system, which induces point mutation due to knock in within rice acetolactate synthase (ALS) gene by agrobacterium mediated transformation (Sun et al. 2016). In the first acquisition stage of this process, the target DNA gets inserted into host CRISPR sequence after identifying the invading DNA and a spacer sequence to generate immunological memory as that can be seen in acquired immunity. Then, protein Cas9 gets expressed in expression stage, and the CRISPR sequence is transcribed into a precursor RNA transcript followed by hybridization of non-coding tarns-activating CRISPR-RNA and pre-CRISPR-RNA, which leads to maturation of RNA with the help of Cas9 protein. In the final stage of interference, Cas9 protein recognizes the desired DNA target after getting signal from mature RNA which leads to the cleavage and degradation of the foreign invading DNA.

1.4 Regulation in Gene Expression and Epigenome Editing

The powerful and versatile CRISPR-Cas is not limited just to facilitate genome editing but also it plays a vital role in the regulation of gene expression by interacting with the regulatory regions like promoter, enhancers and transcription factors. The emergence of CRISPR interfering (CRISPRi) system in the living organisms led to the discovery of novel gene regulatory elements, and scientists could understand their functions in wide range expression level of target genes. (Rodríguez-Leal et al. 2017; Zhang et al. 2018). CRISPR-CAS system can be more promising and helpful for gene knockdown in bacterial cells as it overcomes the problems associated with RNAi such as cell death through disruption of the genomic DNA (Cho et al. 2018). With the advancement in this existing technique CRISPR-Cas9, a new technique came into the light that is CRISPR–dCas9 (“dead” Cas9). Gene knockdown by CRISPR–dCas9 (“dead” Cas9) was achieved through guide RNA-directed binding of dCas9 to regulatory region followed by blocking RNA polymerase elongation to the downstream gene (Qi et al. 2013). In plant cells, implication of certain synthetic transcriptional repressor like SRDX by fusion with C-terminus of dCas9 can improve the efficiency of the repression. Thus, SRDX-dCas9, which acts as an endogenous transcription factors, can repress the endogenous target gene transcription (Lowder et al. 2015; Piatek et al. 2015). Besides the repression, dead Cas-activators are also used for activation of target sites at the same time through CRISPR activation technology, which helps to regulate complex pathways (Deaner et al. 2017). An overview of the regulation in gene expression is represented in a schematic view in Fig. 1.

Apart from the genome editing, CRISPR system can also regulate the expression through epigenetic modification. In this context, dCas9 fusion proteins, which acts as a sequence-specific epigenome converter, can regulate the expression level by

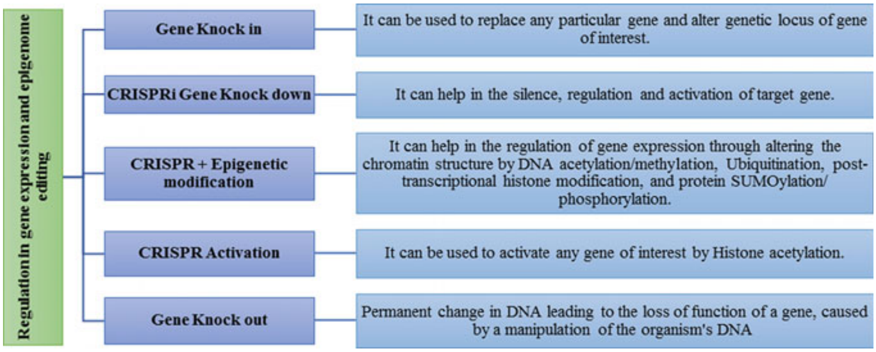

Fig. 1 Overview of the regulation in gene expression and epigenome editing

modifying the epigenetic status. dCas9 with epigenetic regulatory factors can regulate the chromatin structure and gene expression patterns involved of plant development through many epigenetic modifications such as methylation facilitated by methyltransferases, acetylation by acetylase and many more like phosphorylation, SUMOylation and ubiquitination, (Yamamuro et al. 2016; Shrestha et al. 2018). One of the most recent application of this epigenome editing through DNA methylation was achieved in arabidopsis (Gallego-Bartolomé et al. 2018). Previously, in plant biotechnology, traditional breeding techniques helped to increase the crop yield very efficiently, but it could not fulfill the demand of nutritional food with increasing population. Implication in plant breeding for the improvement of crop through CRISPR technology is the most promising area of research nowadays (Haque et al. 2018). Not only in agriculture but also this technology has gained importance in industrial as well as medical researches as also it provides a promising platform to convert the plants into bio-factory to synthesis recombinant proteins, edible vaccines and various improve secondary metabolites on a large scale.

2 Future Perspectives

Plants exhibit many medicinal values for diseases of broad range like less lethal to fatal diseases without imparting any harmful or side effects for the consumers. CRISPR Cas9 technology can be a promising tool to upregulate the genes that are responsible for expressing metabolites like apigenin, luteolin and many more such metabolites particularly in *Ocimum* species (tulsi) plant to produce these metabolites in more quantity to improve the medicinal value of plants and metabolites. On the other hand, in the field of agriculture, the farmers are facing a huge challenge for preserving raw fruits and vegetables for a longer period of time due its less shelf life. So, to overcome this challenge, the genes responsible for ripening can be downregulated to slow down the process of ripening; then, the shelf life of these fruits and vegetables can be increased, and they can be preserved for a longer time without the investment of much maintenance cost for them which will definitely benefit the agricultural industries in the long run. Apart from this, many genes, which play a crucial role in stress (drought, salinity, etc.) tolerance and disease resistance to plants, can be upregulated through CRISPR technology. Apart from all the discussed importance, many areas related to plant science, like identification of target sites with optimized and inducible regulation and the discovery of novel regulators of plant genome, remain obscure. This lacuna can show a new path toward a new discovery for future.

References

Char SN, Neelakandan AK, Nahampun H et al (2017) An agrobacterium-delivered CRISPR/Cas9 system for high-frequency targeted mutagenesis in maize. Plant Biotechnol J 15(2):257–268

Cho S, Shin J, Cho BK (2018) Applications of CRISPR/Cas system to bacterial metabolic engineering. Int J Mol Sci 19(4):1089

Deaner M, Mejia J, Alper HS (2017) Enabling graded and large-scale multiplex of desired genes using a dual-mode dCas9 activator in Saccharomyces cerevisiae. ACS Synth Biol 6:1931–1943

Gallego-Bartolomé J, Gardiner J, Liu W et al (2018) Targeted DNA demethylation of the Arabidopsis genome using the human TET1 catalytic domain. Proc Natl Acad Sci U S A 115(9):E2125–E2134

Haque E, Taniguchi H, Hassan MM, Bhowmik P, Karim MR, Śmiech M, Zhao K, Rahman M, Islam T (2018) Application of CRISPR/Cas9 genome editing technology for the improvement of crops cultivated in tropical climates: recent progress, prospects, and challenges. Front Plant Sci 9:617

Jinek M, Chylinski K, Fonfara I, Hauer M, Doudna JA, Charpentier E (2012) A programmable dual-RNA-guided DNA endonuclease in adaptive bacterial immunity. Science 337:816–821

Kanazashi Y, Hirose A, Takahashi I et al (2018) Simultaneous site-directed mutagenesis of duplicated loci in soybean using a single guide RNA. Plant Cell Rep 37(3):553–563

Lee K, Zhang Y, Kleinstiver BP, Guo JA, Aryee MJ, Miller J, Malzahn A, Zarecor S, Lawrence-Dill CJ, Joung JK, Qi Y, Wang K (2019) Activities and specificities of CRISPR/Cas9 and Cas12a nucleases for targeted mutagenesis in maize. Plant Biotechnol J 17(2):362–372

Li Z, Liu ZB, Xing A, Moon BP, Koellhoffer JP, Huang L, Ward RT, Clifton E, Falco SC, Cigan AM (2015) Cas9-guide RNA directed genome editing in soybean. Plant Physiol 169(2):960–970

Li C, Chen C, Chen H, Wang S, Chen X, Cui Y (2018) Verification of DNA motifs in Arabidopsis using CRISPR/Cas9-mediated mutagenesis. Plant Biotechnol J 16(8):1446–1451

Lowder LG, Zhang D, Baltes NJ, Paul JW 3rd, Tang X, Zheng X, Voytas DF, Hsieh TF, Zhang Y, Qi Y (2015) A CRISPR/Cas9 toolbox for multiplexed plant genome editing and transcriptional regulation. Plant Physiol 169(2):971–985

Macovei A, Sevilla NR, Cantos C, Jonson GB, Slamet-Loedin I, Čermák T, Voytas DF, Choi IR, Chadha-Mohanty P (2018) Novel alleles of rice eIF4G generated by CRISPR/Cas9-targeted mutagenesis confer resistance to Rice tungro spherical virus. Plant Biotechnol J 16(11):1918–1927

Okada A, Arndell T, Borisjuk N et al (2019) CRISPR/Cas9-mediated knockout of Ms1 enables the rapid generation of male-sterile hexaploid wheat lines for use in hybrid seed production. Plant Biotechnol J 17(10):1905–1913

Piatek A, Ali Z, Baazim H et al (2015) RNA-guided transcriptional regulation in planta via synthetic dCas9-based transcription factors. Plant Biotechnol J 13(4):578–589

Qi LS, Larson MH, Gilbert LA et al (2013) Repurposing CRISPR as an RNA-guided platform for sequence-specific control of gene expression. Cell 152(5):1173–1183

Rodríguez-Leal D, Lemmon ZH, Man J, Bartlett ME, Lippman ZB (2017) Engineering quantitative trait variation for crop improvement by genome editing. Cell 171:470–480

Shrestha A, Khan A, Dey N (2018) cis-trans engineering: advances and perspectives on customized transcriptional regulation in plants. Mol Plant 11(7):886–898
Strecker J, Jones S, Koopal B et al (2019) Engineering of CRISPR-Cas12b for human genome editing. Nat Commun 10:212
Sun Y, Zhang X, Wu C et al (2016) Engineering herbicide-resistant rice plants through CRISPR/Cas9-mediated homologous recombination of acetolactate synthase. Mol Plant 9(4):628–631
Ueta R, Abe C, Watanabe T et al (2017) Rapid breeding of parthenocarpic tomato plants using CRISPR/Cas9. Sci Rep 7:507
Wang Y, Cheng X, Shan Q et al (2014) Simultaneous editing of three homoeoalleles in hexaploid bread wheat confers heritable resistance to powdery mildew. Nat Biotechnol 32(9):947–951
Yamamuro C, Zhu JK, Yang Z (2016) Epigenetic modifications and plant hormone action. Mol Plant 9(1):57–70
Zhang H, Si X, Ji X et al (2018) Genome editing of upstream open reading frames enables translational control in plants. Nat Biotechnol 36:894–898

Effects of Food Production and Consumption on Environment and Climate

Soumili Sen, Manoj Kumar Singh, and Arpita Das

Abstract Our body needs food for nutritional support, energy, growth, and repair. A good balance diet of fresh food makes us healthy. People from different cultural and economic background consume different types of foods. The production, processing, distribution, and consumption of different types of food directly influence human health and our environment. We mainly depend on agriculture for food production. Due to high population, global food demand increases day by day and more food production is required to make up the food demand. For rapid production to make up the huge food demand, farmers use more pesticides and fertilizers that directly impact on our environment. Agriculture is one of the main important sources of greenhouse gas emissions. Excess use of fertilizers, pesticides, and herbicides in agricultural land wash away by rainwater into water bodies and create hazards to aquatic life. The different types of fertilizer and pesticides also cause the acidification of soils and accumulations of heavy metals on soil that affects the soil microbial biodiversity. Food production and consumption cause various types of environmental effects such as air, water, soil pollution and impacts on our health, aquatic flora and fauna, and soil microorganisms.

Keywords Food demand · Agriculture · Pesticides · Fertilizers · Greenhouse gas emission

1 Introduction

Food is important for us to make healthy. It provides nutritional support and energy for our growth and maintaining all the functions in our body. Both animal and vegetable foods contain water, carbohydrate, proteins, fats, vitamins, and minerals (Gerbens-Leenes and Nonhebel 2002). Food is not solely necessary for our survival; however, additionally food is a vital criterion for cultural identity (Carlsson-Kanyama and Linden 2001). Food consumption differs between social classes within societies as

S. Sen · M. K. Singh · A. Das (✉)
Department of Biotechnology, School of Life Science and Biotechnology, Adamas University, Barasat, West Bengal 700126, India

M. Mukherjee et al. (eds.), *Advances in Medical Physics and Healthcare Engineering*, Lecture Notes in Bioengineering, https://doi.org/10.1007/978-981-33-6915-3_36

well as between nations (Carlsson-Kanyama and Linden 2001). Sometimes some places are famous for their special food products. Every day, vast quantities of different types of food are produced, processed, distributed, and consumed, and these activities directly influence human health and our environment (Duchin 2005). Due to the production and consumption of food products, environmental pollutants are released and cause harm to humans and the environment (Kramer 2000). For the food production, we directly depend on agriculture. The use of nutrients and pesticides in agriculture may lead to emissions of minerals and various toxic compounds to air, water, and soil (Kramer 2000). Food production effects carbon and nitrogen cycle in ecosystems (Xia et al. 2016). Worldwide, agricultural activity, particularly livestock production account for about a fifth of total greenhouse gas emissions and contribute to global climate change (McMichael et al. 2007). About 18% of the global greenhouse gas emissions are caused by livestock production, and the main contributors are methane (CH_4) from enteric fermentation, nitrous oxide (N_2O) from manure and fertilizer, and carbon dioxide (CO_2) from land-use change and agricultural energy use (Stehfest et al. 2009). One-quarter of global greenhouse gas (GHG) emissions is caused by land clearing, crop production, and fertilization (Tilman et al. 2011). A shift from the production and consumption of livestock products of ruminant origin (beef, lamb, mutton, milk) to those of monogastric origin (pork, chicken, eggs) has been believed as a measure to minimize greenhouse gas emissions (Friel et al. 2009). Green house gas was the major contributor of global warming. The production, transport, processing, and marketing of foods affect not only anthropogenic-based emissions but also biological, physical, and chemical interactions (Gonzalez et al. 2011). Fertilizer can harm marine, freshwater, and terrestrial ecosystems (Tilman et al. 2011). Nitrogen and phosphorus levels in marine, freshwater, and terrestrial ecosystems have increased due to the uses of fertilizers (Conley et al. 2009). Eutrophication refers to an excessive richness of nutrients, usually in the form of phosphorus or nitrogen compounds, into a water body in sufficient quantities to increase primary production (Todd et al. 2010). *Saccharomyces cerevisiae* which is used in winemaking, baking, brewing industries have the capability of bioremediation of heavy metals (Massoud et al. 2019). Lead (Pb), cadmium (Cd), zinc (Zn), mercury (Hg), nickel (Ni), arsenic (As), chromium(Cr), gold (Au), platinum (Pt), and uranium (U) are removed by S. cerevisiae (Massoud et al. 2019). Fertilizer increases the acidity of soil that prevents the growth of plant (Barak et al. 1997). Inorganic fertilizer causes metal accumulation in soil and increases the concentration of heavy metals in soil (Atafar et al. 2010). For the application of pesticides to the soil, several soil microbial enzymes are hampered or affected. Soil microbial biomass is affected by the use of chemical fertilizers and pesticides (Kalia and Gosal 2011) (Table 1).

2 Food Demand and Agriculture

The current world population is 7.7 billion. The world population grew from 2.5 billion in 1950 to 6.1 billion within the year 2000 (Carvalho 2006). By the year 2050,

Table 1 Different types of pesticides cause various environmental effects (Valavanidis and Vlachogianni 2011)

Type of pesticide	Environmental effects
Nitrophenols, chlorophenols, creosote, petroleum oils	Environmental pollution, toxicity to water organisms
Polychlorinated organics (DDT, dieldrin, aldrin, lindane, heptachlor, endin) chlorinated cyclodienes	Persistent, bioaccumulation, ecological effects
Organophosphates (parathion, malathion, mevinphos), carbamates (aldicarb, carbaryl, baygon)	Lower persistence, some environmental problems
Synthetic pyrethroids, avermectins, biological pesticides	Lack of selectivity, resistance
Genetically engineered organisms less toxic and persistent, Biopesticides, natural predators, pheromones	Microbiological ecology, monopoly of products, amenable environmental problems
Integrated pest management, natural predators, organic agriculture	Less dangerous to ecosystems and wildlife

the world population is calculated to reach 9.1 billion (Carvalho 2006). Population size and density determine the food demand and monetary income (Veldkamp and Fresco 1996). Due to high population, global food demand increases day by day and more food production is necessary to make up the food demand. We directly depend on agriculture for food production. Recently, the land available to produce the food is shrinking because of urbanization and use of agricultural land for other purposes (Hobbs 2007). The food price is also a big fact. For poorest people, it is difficult to purchase higher prices food products for their healthy diet (Godfray et al. 2010). For more rapid food production in lower prices on the inadequate agricultural land, more different types of chemical fertilizer as well as pesticides are used. Agro-chemical-based intensive agriculture has contributed substantially to the emission of the very powerful greenhouse gases CH_4 and N_2O, and the entry of pollutants (excessive nitrogen and phosphorus, pesticide and heavy metals) into water bodies and soils (Smil 1997). Different types of pesticides are used in agriculture to protect crops from insect pests, weeds, and fungal diseases, and different types of fertilizers are used to increase fertility of soil or land. Improper and incorrect use of pesticides and fertilizers leads to tremendous environmental issues (Khan et al. 2010). The followings factors result in the improper and incorrect use of pesticides and fertilizers: (1) Farmers have little knowledge about their application, (2) Use them at improper time and field conditions, (3) Lack of awareness about IPM, (4) Government pesticide oriented policies, (5) Improper storage and manhandling of pesticides and fertilizers, (6) Disposal of obsolete pesticides and fertilizers, (7) Banned pesticides still in use (Khan et al. 2010) (Fig. 1).

For the next 30 years, more fertilizer will be used to obtain more agricultural products (Savci 2012). The use of nitrogen fertilizer (both mineral and organic)

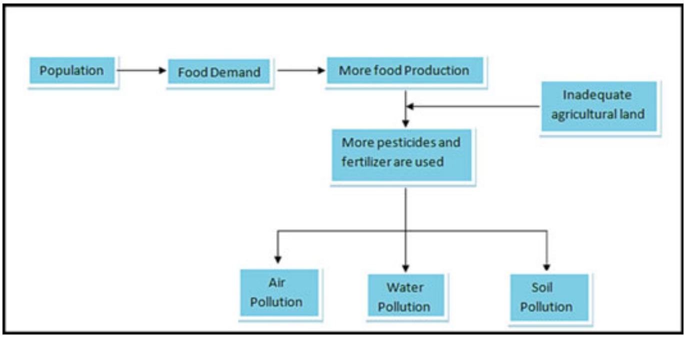

Fig. 1 Overview scenario how food production causes different types of pollution in agricultural aspects

has been increasing globally in most of the regions in recent decades (Lu and Tian 2013). Globally, 4.6 million tons of chemical pesticides are sprayed per year into the environment (Zhang et al. 2011). About 500 pesticides are used for mass application of which organochlorined pesticides, some herbicides and the pesticides containing mercury, arsenic, and lead are highly poisonous to the environment (Zhang et al. 2011).The heavy metal content in fertilizers is generally as follows: phosphoric fertilizer > compound fertilizer > potash fertilizer > nitrogen fertilizer (Boyd 2010).

3 Effects on Air

The impact of global air pollution on climate and the environment is a new focus in atmospheric science (Akimoto 2003). Agriculture was the major source of green house emissions globally (Vetter et al. 2017). Agricultural production is currently accounting for 18% of total GHG emissions in India (Vetter et al. 2017). Agricultural activities increase the emissions of CO_2, CH_4 and N_2O from the terrestrial biosphere into the atmosphere, because of the manipulations of the C and N cycles and environmental conditions necessary to produce food in sufficient quantity and quality (Oenema et al. 2001). Fresh vegetables, cereals, and legumes contribute to the lowest GHG emissions and meats and fruits transported by air contribute the highest total GHG emissions, whereas eggs, certain fish, and frozen vegetables are found in the midrange (Carlsson-Kanyama and González 2009). The air pollution percentage of Bangladesh in the year 2001 from the food industry is 38.7% (Alam 2009) (Table 2).

It was calculated that globally 2.7 Tg of nitrogen (N) are lost annually due to food waste at food consumption (i.e., 9% of global food consumption), and the virtual nitrogen (nitrogen delivered to the environment) linked to the global food waste is 6.3 TgN/yr (Grizzetti et al. 2013) (Figs. 2 and 3).

Table 2 Summary of GHG emissions in India from the agriculture sector in thousand tons (I.N.C.C.A. 2010)

Name of green house gases	CH_4	N_20	$C0_2$ eq
Total emissions	13,767.80	146.07	334,405.50
Enteric fermentation	10,099.80	–	212,095.80
Manure management	115.00	0.07	2436.70
Rice cultivation	3327.00	–	69,867.00
Soils	–	140.00	43,400.00
Crop residue	226.00	6.00	6606.00

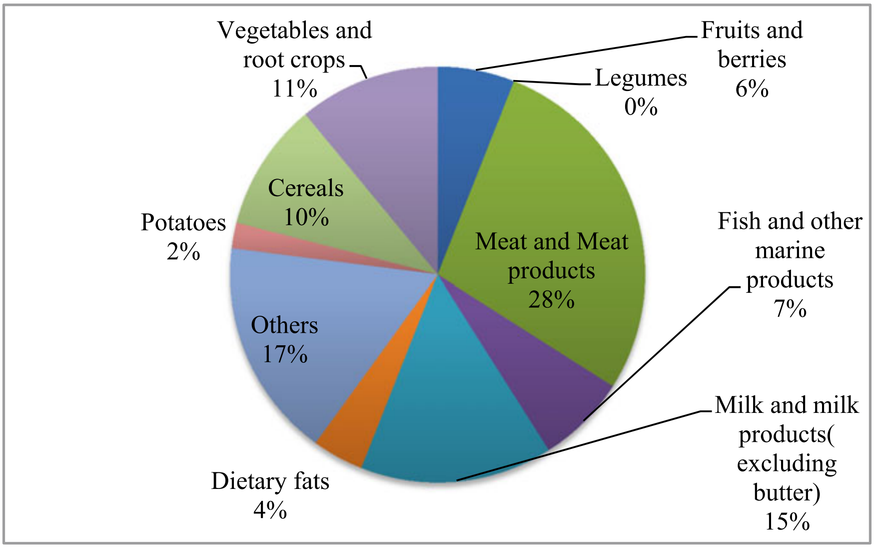

Fig. 2 Total CO_2 emission due to different types of food consumption in Sweden (Wallén et al. 2004)

4 Effects on Water

Water is the essential compounds for living organisms. Two-third parts of a living organism consists of water, and 90% of cell contains water (Matta et al. 2014). Biochemical reactions those occur in living organisms require an aqueous medium (Matta et al. 2014). But today water pollution is major problem to our environment. Agriculture sector and food industry contribute to cause water pollution. Agricultural activities including application of fertilizers and pesticides are the potential non-point sources of groundwater pollution (Pye and Patrick 1983). Excess fertilizer, herbicides, and pesticides are washed by rain into water bodies and cause serious hazard to aquatic life (Owa 2013). The fertilizers that are commonly used in agriculture are mainly nitrogen- and phosphorus-based. Nitrogen-rich fertilizer compounds cause the deficiency of dissolved oxygen in rivers, lakes, and coastal

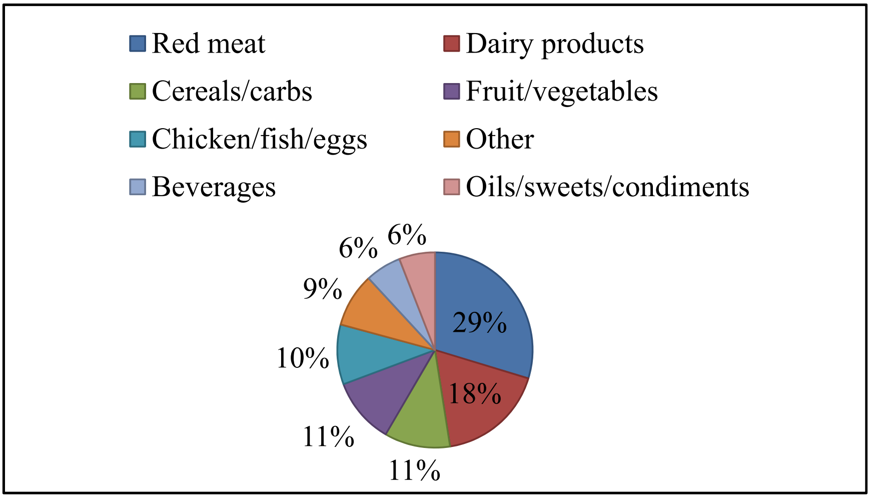

Fig. 3 GHG emission from different types of foods for an average US household (Engelhaupt 2008)

zones which have devastating effects on aquatic fauna (Chaudhry and Malik 2017), and dissolved oxygen is essential for respiration of fish and other aquatic organisms (Gorde and Jadhav 2013). Application of large amounts of nitrogen fertilizers contributes to excessive nitrate accumulation in soils and leaching into groundwater bodies (Akhavan et al. 2010). The groundwater associated with extensive agricultural ecosystems consists of sufficiently high concentrations of nitrite and nitrates or of pesticides and their residues and become unhealthy for human consumption (Tilman 1999). Some pesticides such as DDT (most commonly used pesticide for insect control) are seriously dangerous once it enter into water bodies as a result of its concentration rises along the food chain (Owa 2013). Excess fertilization and manure production cause the accumulation of phosphorus in soil, some of which is transported to aquatic ecosystems (Carpenter et al. 1998). Phosphorus-rich soils are washed into lakes, where some of the phosphorus dissolves and stimulates growth of phytoplankton and aquatic plants (Carpenter 2005). Eutrophication occurs when lakes and rivers are enriched with N, P, K, and other nutrients from eroded or leached fertilizers, algae and other micro- and macro-plants frequently explode in growth (Pimentel 1996). Excessive enrichment of nutrients causes an intensification of all biological activity and typically leads to vast changes in the composition and structure of aquatic food webs (Smith et al. 2006). Eutrophication may promote the proliferation and expansion of cyanobacterial harmful algal blooms (O'neil et al. 2012). Some algal blooms are harmful because they produce some toxic chemicals that cause illness or moralities to humans and aquatic organisms (Villacorte et al. 2015). Some harmful algal blooms which do not produce toxic compounds produce the algal biomass and algal organic matter (AOM) that can accumulate in high concentrations near or below the water surface (Villacorte et al. 2015).The water pollution percentage of Bangladesh in the year 2001 from the fertilizers/pesticides industries is 6.6% (Alam 2009). The water pollution percentage of Bangladesh in the year 2001 from the food industry is 12.1% (Alam 2009).

5 Effects on Soil

Soil is the basic, fundamental, and important part of our environment. Excess soil acidification due to the excess use of fertilizers, particularly nitrogen fertilizer, is a major factor in worldwide soil deterioration (Wallace 1994). As soil microorganism (mainly bacteria) convert ammonium-containing fertilizer (NH_4–N) to nitrate-N (NO_3–N) and in this oxidation process H+ is utilized, so the soil is acidified (Anderson et al. 2013). Besides nitrogen (mainly ammonium) fertilizer, sulfur, aluminum, and iron sulfate fertilizer act as a major soil acidifying agents (Haynes and Swift 1986). Soil is the habitat of soil microorganisms and maintains the biodiversity, assemblage, and activity of soil microflora and soil fauna (Emmerling et al. 2002). Soil microorganisms play an important role in nature and are critical to ecosystem function and the well-being of plants, animals, and humans (Francis 1982). Conservation agriculture, organic farming, and conventional agriculture causes a long-term effects on major soil organisms such as microbes, nematofauna, and macrofauna (Henneron et al. 2015). The uses of fertilizers and pesticides for agriculture have contributed to the accumulation of heavy metals in soils (Alloway and Jackson 1991). Some heavy metals are present in phosphorus fertilizers or other chemical fertilizers (Huang and Jin 2008). The exposure of heavy metals affects the microbial growth and survival. Heavy metals such as copper (Cu), cadmium (Cd), and zinc (Zn) affect biological processes in ecosystems (Hiroki 1992). Heavy metals affect soil microbial processes and decrease the number and activity of soil microorganisms, and thus, heavy metals exhibit toxicity toward soil biota (Jiwan and Ajah 2011) (Fig. 4).

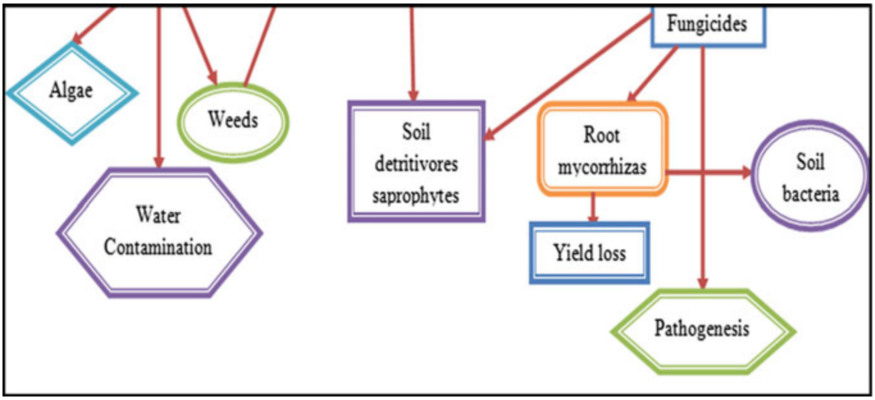

Fig. 4 Schematic diagram of impacts of pesticides (Davydov et al. 2018)

6 Conclusion

Food production and consumption impact considerably on environment and climate. Food production contributes to climate change, eutrophication, soil acidification in fact it effects on the aquatic flora and fauna and soil microorganism. To control the hazards, we should take some necessary steps: (1) Increase farmer's level of knowledge about the proper and use of pesticides and fertilizer. (2) The hazardous pesticides and fertilizer should be banned. (3) Increase the use of bio-fertilizers and pesticides. (4) New farming technology should be used to minimizing the use of pesticides and fertilizer. (5) Decrease the consumption of high GHG emission food products.

Acknowledgements We duly acknowledge Honorable Chancellor, Adamas University, Kolkata, India, for providing us the infrastructure and facilities. This research work is financially supported by Seed fund for university sponsored research project, under Adamas University, India.

References

Akhavan S, Abedi-Koupai J, Mousavi SF, Afyuni M, Eslamian SS, Abbaspour KC (2010) Application of SWAT model to investigate nitrate leaching in Hamadan-Bahar Watershed, Iran. Agric Ecosyst Environ 139(4):675–688

Akimoto H (2003) Global air quality and pollution. Science 302(5651):1716–1719

Alam GJ (2009) Environmental pollution of Bangladesh—it's effect and control. Pulp Paper 51(13.17)

Alloway BJ, Jackson AP (1991) The behaviour of heavy metals in sewage sludge-amended soils. Sci Total Environ 100:151–176

Anderson NP, Hart JM, Sullivan DM, Hulting AG, Horneck DA, Christensen NW (2013) Soil acidity in Oregon: understanding and using concepts for crop production. OSU Extension Service, OSU Extension Catalog. EM9061, 22. https://catalog.extension.oregonstate.edu/sites/catalog/files/project/pdf/em9061.pdf

Atafar Z, Mesdaghinia A, Nouri J, Homaee M, Yunesian M, Ahmadimoghaddam M, Mahvi AH (2010) Effect of fertilizer application on soil heavy metal concentration. Environ Monit Assess 160(1–4):83–85

Barak P, Jobe BO, Krueger AR, Peterson LA, Laird DA (1997) Effects of long-term soil acidification due to nitrogen fertilizer inputs in Wisconsin. Plant Soil 197(1):61–69

Boyd RS (2010) Heavy metal pollutants and chemical ecology: exploring new frontiers. J Chem Ecol 36:46–58

Carlsson-Kanyama A, González AD (2009) Potential contributions of food consumption patterns to climate change. Am J Clin Nutr 89:1704S–1709S

Carlsson-Kanyama A, Linden AL (2001) Trends in food production and consumption: Swedish experiences from environmental and cultural impacts. Int J Sustain Dev 4:392–406

Carpenter SR (2005) Eutrophication of aquatic ecosystems: bistability and soil phosphorus. Proc Natl Acad Sci U S A 102:0002–0005

Carpenter SR, Caraco NF, Correll DL, Howarth RW, Sharpley AN, Smith VH (1998) Nonpoint pollution of surface waters with phosphorus and nitrogen. Ecol Appl 8(3):559–568

Carvalho FP (2006) Agriculture, pesticides, food security and food safety. Environ Sci Policy 9(7–8):685–692

Chaudhry FN, Malik MF (2017) Factors affecting water pollution: a review. J Ecosyst Ecography 7(225):2–5

Conley DJ, Paerl HW, Howarth RW, Boesch DF, Seitzinger SP, Havens KE, Lancelot C, Likens GE (2009) Controlling eutrophication: nitrogen and phosphorus. Science 323(5917):1014–1015

Davydov R, Sokolov M, Hogland W, Glinushkin A, Markaryan A (2018) The application of pesticides and mineral fertilizers in agriculture. In: MATEC web of conferences, vol 245, p 11003. EDP Sciences

Duchin F (2005) Sustainable consumption of food: a framework for analyzing scenarios about changes in diets. J Ind Ecol 9(1–2):99–114

Emmerling C, Schloter M, Hartmann A, Kandeler E (2002) Functional diversity of soil organisms—a review of recent research activities in Germany. J Plant Nutr Soil Sci 165(4):408–420

Engelhaupt E (2008) Do food miles matter? Environ Sci Technol 42:3482–3482

Francis AJ (1982) Effects of acidic precipitation and acidity on soil microbial processes. Water Air Soil Pollut 18(1–3):375–394

Friel S, Dangour AD, Garnett T, Lock K, Chalabi Z, Roberts I, Butler A, Butler CD, Waage J, McMichael AJ, Haines A (2009) Public health benefits of strategies to reduce greenhouse-gas emissions: food and agriculture. Lancet 374(9706):2016–2025

Gerbens-Leenes PW, Nonhebel S (2002) Consumption patterns and their effects on land required for food. Ecol Econ 42(1–2):185–199

Godfray HCJ, Beddington JR, Crute IR, Haddad L, Lawrence D, Muir JF, Pretty J, Robinson S, Thomas SM, Toulmin C (2010) Food security: the challenge of feeding 9 billion people. Science 327(5967):812–818

Gonzalez JA, Konishi Y, Bruno M, Valoy M, Prado, FE (2011) Interrelationships among seed yield, total protein and amino acid composition of ten quinoa (Chenopodium quinoa) cultivars from two different agroecological regions. J Sci Food Agric. 92(6):1222–1229

Gorde SP, Jadhav MV (2013) Assessment of water quality parameters: a review. J Eng Res Appl 3:2029–2035

Grizzetti B, Pretato U, Lassaletta L, Billen G, Garnier J (2013) The contribution of food waste to global and European nitrogen pollution. Environ Sci Policy 33:186–195

Haynes RJ, Swift RS (1986) Effects of soil acidification and subsequent leaching on levels of extractable nutrients in a soil. Plant Soil 95(3):327–336

Henneron L, Bernard L, Hedde M, Pelosi C, Villenave C, Chenu C, Bertrand M, Girardin C, Blanchart E (2015) Fourteen years of evidence for positive effects of conservation agriculture and organic farming on soil life. Agron Sustain Dev 35(1):169–181

Hiroki M (1992) Effects of heavy metal contamination on soil microbial population. Soil Sci Plant Nutr 38(1):141–147

Hobbs PR (2007) Conservation agriculture: what is it and why is it important for future sustainable food production? J Agric Sci 145:127–132

Huang SW, Jin JY (2008) Status of heavy metals in agricultural soils as affected by different patterns of land use. Environ Monit Assess 139(1–3):317–322

I.N.C.C.A. (2010) India: greenhouse gas emissions 2007

Jiwan S, Ajay SK (2011) Effects of Heavy Metals on Soil, Plants, Human Health and Aquatic Life. Int j res chem environ 1(2):(15–21)

Kalia A, Gosal SK (2011) Effect of pesticide application on soil microorganisms. Arch Agron Soil Sci 57(6):569–596

Khan MJ, Zia MS, Qasim M (2010) Use of pesticides and their role in environmental pollution. World Acad Sci Eng Technol 72:122–128

Kramer KJ (2000) Food matters: on reducing energy use and greenhouse gas emission from household food consumption. Ph.d. Thesis. Center for Energy and Environmental Studies of the University of Groningen (IVEM RUG), The Netherlands, retrieved from: www.foodmatters.tmfweb.nl

Lu C, Tian H (2013) Net greenhouse gas balance in response to nitrogen enrichment: perspectives from a coupled biogeochemical model. Glob Change Biol 19(2):571–588

Massoud R, Hadiani MR, Hamzehlou P, Khosravi-Darani K (2019) Bioremediation of heavy metals in food industry: application of Saccharomyces cerevisiae. Electron J Biotechnol 37:56–60
Matta G, Kumar R, Kumar A, Kumar A (2014) Effect of industrial effluent on ground water quality with special reference to DO, BOD and COD. J Sustain Environ Res 3(2):183–186
McMichael AJ, Powles JW, Butler CD, Uauy R (2007) Food, livestock production, energy, climate change, and health. Lancet 370(9594):1253–1263
Oenema O, Velthof G, Kuikman P (2001) Technical and policy aspects of strategies to decrease greenhouse gas emissions from agriculture. Nutr Cycl Agroecosyst 60(1–3):301–315
O'neil JM, Davis TW, Burford MA, Gobler CJ (2012) The rise of harmful cyanobacteria blooms: the potential roles of eutrophication and climate change. Harmful Algae14:313–334
Owa FD (2013) Water pollution: sources, effects, control and management. Mediterr J Soc Sci 4(8):65–69
Pimentel D (1996) Green revolution agriculture and chemical hazards. Sci Total Environ 188:S86–S98
Pye VI, Patrick R (1983) Ground water contamination in the United States. Science 221(4612):713–718
Savci S (2012) An agricultural pollutant: chemical fertilizer. Int J Environ Sci Dev 3(1):73–77
Smil V (1997) China's environment and security: simple myths and complex realities. SAIS Rev 17(1):107–126
Smith VH, Joye SB, Howarth RW (2006) Eutrophication of freshwater and marine ecosystems. Limnol Oceanogr 51(1part2):351–355
Stehfest E, Bouwman L, Van Vuuren DP, Den Elzen MG, Eickhout B, Kabat P (2009) Climate benefits of changing diet. Clim Change 95(1–2):83–102
Tilman D (1999) Global environmental impacts of agricultural expansion: the need for sustainable and efficient practices. Proc Natl Acad Sci 96(11):5995–6000
Tilman D, Balzer C, Hill J, Befort BL (2011) Global food demand and the sustainable intensification of agriculture. Proc Natl Acad Sci U S A 108:20260–20264
Todd PA, Ong X, Chou LM (2010) Impacts of pollution on marine life in Southeast Asia. Biodivers Conserv 19(4):1063–1082
Valavanidis A, Vlachogianni T (2011) Agricultural pesticides: ecotoxicological studies and environmental risk assessment. Sci Adv Environ Toxicol Ecotoxicol Issues. https://chem-tox-ecotox.org/wp
Veldkamp A, Fresco LO (1996) CLUE: a conceptual model to study the conversion of land use and its effects. Ecol Model 85(2–3):253–270
Vetter SH, Sapkota TB, Hillier J, Stirling CM, Macdiarmid JI, Aleksandrowicz L, Green R, Joy EJ, Dangour AD, Smith P (2017) Greenhouse gas emissions from agricultural food production to supply Indian diets: implications for climate change mitigation. Agr Ecosyst Environ 237:234–241
Villacorte LO, Tabatabai SAA, Dhakal N, Amy G, Schippers JC, Kennedy MD (2015) Algal blooms: an emerging threat to seawater reverse osmosis desalination. Desalin Water Treat 55(10):2601–2611
Wallace A (1994) Soil acidification from use of too much fertilizer. Commun Soil Sci Plant Anal 25(1–2):87–92
Wallén A, Brandt N, Wennersten R (2004) Does the Swedish consumer's choice of food influence greenhouse gas emissions? Environ Sci Policy 7(6):525–535
Xia L, Ti C, Li B, Xia Y, Yan X (2016) Greenhouse gas emissions and reactive nitrogen releases during the life-cycles of staple food production in China and their mitigation potential. Sci Total Environ 556:116–125
Zhang W, Jiang F, Ou J (2011) Global pesticide consumption and pollution: with China as a focus. Proc Int Acad Ecol Environ Sci 1(2):125–130

Hiding IoT Communication Using DCT Difference Modulation (DCTDM)

Pabak Indu and Souvik Bhattacharyya

Abstract In the past few decades, the involvement of the Internet and technologies has become an integral part of our life. From morning till evening, we come across many automated devices which are connected via the Internet some of these devices share various information over the network. While making our life easy, these IoT devices also attract many malicious actors who exploit different vulnerabilities of the IoT devices. As IoT devices operate with limited power and computational resources. These devices lack a strong cryptographic protocol and compromising various data and opening many doors for malicious activities. One such device is IoT-based CCTV cameras, and these devices are made to keep us safe, but the very same devices are used to exploit various network flaws and harm our system and steal our data. There had been multiple incidents where the recordings or images captured by these devices are stolen or tampered for malicious reasons. To overcome this problem, authors have proposed a DCTDM-based arithmetic randomization method in this paper. This method conceals the images or recordings captured by the IoT-based CCTV cameras in a set of predefined images or videos and transmitted across the network for further processing or storing. This method not only protects the data but also protects the very existence of the data.

Keywords IOT · Steganography · DCTDM

1 Introduction

In the past few years, IoT devices have become an integral part of our day-to-day life. On a normal day, a human being comes across many IoT devices to perform various tasks, starting from some basic to life-saving activities. One such device is a CCTV camera connected over the network, used to maintain our security and

P. Indu (✉)
Department of CSE, Adamas University, Kolkata, West Bengal 700126, India

S. Bhattacharyya
Department of CSE, University Institute of Technology, The University of Burdwan, Bardhaman, West Bengal 713104, India

M. Mukherjee et al. (eds.), *Advances in Medical Physics and Healthcare Engineering*, Lecture Notes in Bioengineering, https://doi.org/10.1007/978-981-33-6915-3_37

wellbeing. But unfortunately, what happens if these very devices, used to keep us safe, get compromised. Following are examples of such reported incidents.

"Robbers use CCTV footage to plan break-ins" (Kanth and Mathew 2018)—Many CCTV cameras are installed in different areas to maintain the law and order. But a group of malicious actors had gained access to these CCTV networks and traced the pattern for the local authorities, patrolling the area. Based on this identification, they had planned for a break-in.

"Somebody's Watching: Hackers Breach Ring Home Security Cameras" (Vigdor 2019)—In this busy life schedule, where both parents are working and they do not have any trusted person back at their home to look after their kids and use such kind of security devices. These devices not only have a visual device but an interactive audio device installed in it. These devices help parents to interact with the kids while they are not present physically. In Dec 2019, the incident got reported where a malicious actor had hacked into these devices and was interacting with the child camouflaging himself as Santa clause and giving her instruction to perform various things. But soon, the parents had discovered the incident and reported to local authorities.

Such incidents have inspired the authors to conduct the research work and find a suitable solution to secure the CCTV footages from malicious actors, where many researchers are working on various encryption-based protocols to secure the recorded or captured media. In this paper, authors have proposed a solution based on steganographic protocol as it not only secures the data but also hides the very existence of the data. The paper is organized in such a way that Sect. 2 depicts some existing solutions by various researchers to address the security of the footage recorded or captured by CCTV cameras, where Sects. 3 and 4 give us insight into the proposed method, describe the experimental results, and compare the proposed method with some existing methods. Section 5 draws the conclusion.

2 Some Existing Solutions

In the study conducted by Seralathan et al. (2018), separate ID and passwords are associated whenever a camera is installed and the recording goes directly to the remote server and stored under the security protocol of the service providing company. But there had been multiple incidents where the attacker uses a Nmap, Snoop, or Wireshark tools to detect and intervene the transmission of the media.

Valente et al. (2019) had shown different traffic and security analysis methods such as Swann surveillance devices, Telnet attacks, and many traffic analysis methods used by different malicious actors to identify the video or image sent over the network by the devices.

Figure 1 shows the working principle for the method proposed by Ullah et al. (2017) where they had used signcryption to secure the footage of the CCTV cameras.

Signcryption is a resource-efficient technique that implements signature and encryption in a single step and achieves a lower computational and communicational

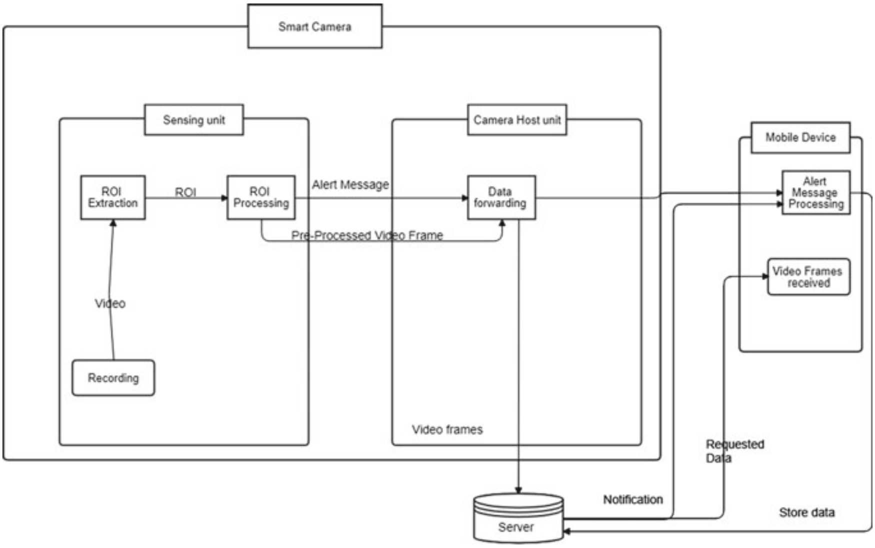

Fig. 1 Smart cameras with onboard signcryption for securing IoT applications (in courtesy Ullah et al. 2017)

cost than the traditional approach. In this paper, the authors had used an EC-based signcryption directly on the sensing unit of the camera.

U. Albalawi et al. in their research paper (Albalawi et al. 2016) had proposed a steganography-based image hiding technique, which works on the nonmoving image captured by a camera and then transmits the hidden image to the cloud storage as shown in Fig. 2.

Dorothy et al. (2017) had proposed security protocol for a very commonly used device for both industry and home users, where the device is installed with a camera to identify the visitor as described in Fig. 3. The device captures the image of the visitor then sends it to the cloud storage. In the cloud storage, the image gets encrypted, and using some mobile devices, the users can access the cloud storage and gain access to the image.

3 Proposed Method

3.1 Embedding Protocol

In this protocol, the authors have proposed a DCT-based steganographic protocol to embedded the image or the video frames captured by the CCTV devices. The devices are accompanied by a small-scale computing facility with minimum power and computational requirement.

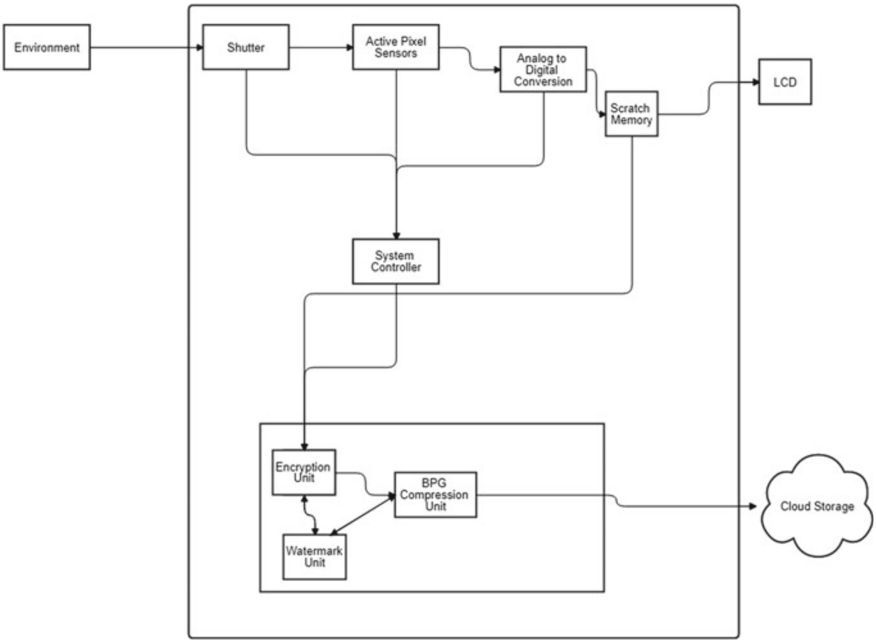

Fig. 2 SBPG working principle (in courtesy Albalawi et al. 2016)

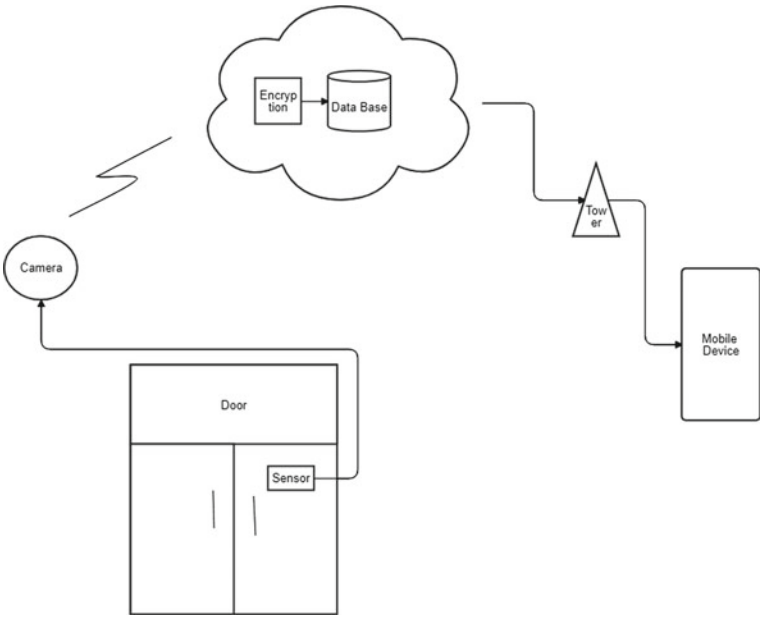

Fig. 3 IoT-based home security through digital image processing algorithms (in courtesy Dorothy et al. 2017)

Algorithm

Step 1: Select a preloaded cover image randomly.
Step 2: Divide the image in a 3 × 3 block.
Step 3: Capture the image using CCTV or separate it into multiple video frames.
Step 4: Divide the CCTV image or video frame into 3 × 3 block.
Step 5: Apply DCT on both cover image and the CCTV image.
Step 6: Combine the center pixel of cover image with the individual pixel of the CCTV image.
Step 7: Apply inverse DCT on the resultant matrix and regenerate the image.

Figure 4 describes the embedding and extraction principle for the proposed method.

3.2 Extraction Protocol

Algorithm

Step 1: Divide the stego image in a 3 × 3 block.
Step 2: Apply DCT on each block of image.
Step 3: Make an approximation based on the neighboring pixel values.
Step 4: Extract the additional value after normalizing by approximation.
Step 5: Reconstruct the image matrix.
Step 6: Apply inverse DCT on the resultant matrix and regenerate the image.

4 Experimental Results

To establish the results of the proposed method, the authors have performed a series of tests such as mean square error, peak signal-to-noise ratio, entropy, and RS analysis.

4.1 Mean Square Error (MSE)

It describes the average squared intensity between cover and stego image (Al-Najjar and Soong 2012). Equation 1 shows the mathematical representation of MSE, where NM is the size of the cover image and $e(m, n)$ is the stego image. Figure 5 describes the variation of MSE and PSNR based on different embedding capacity for the proposed method.

$$\mathrm{MSE} = \frac{1}{NM} \sum_{m=0}^{M-1} \sum_{n=0}^{N-1} e(m, n)^2 \tag{1}$$

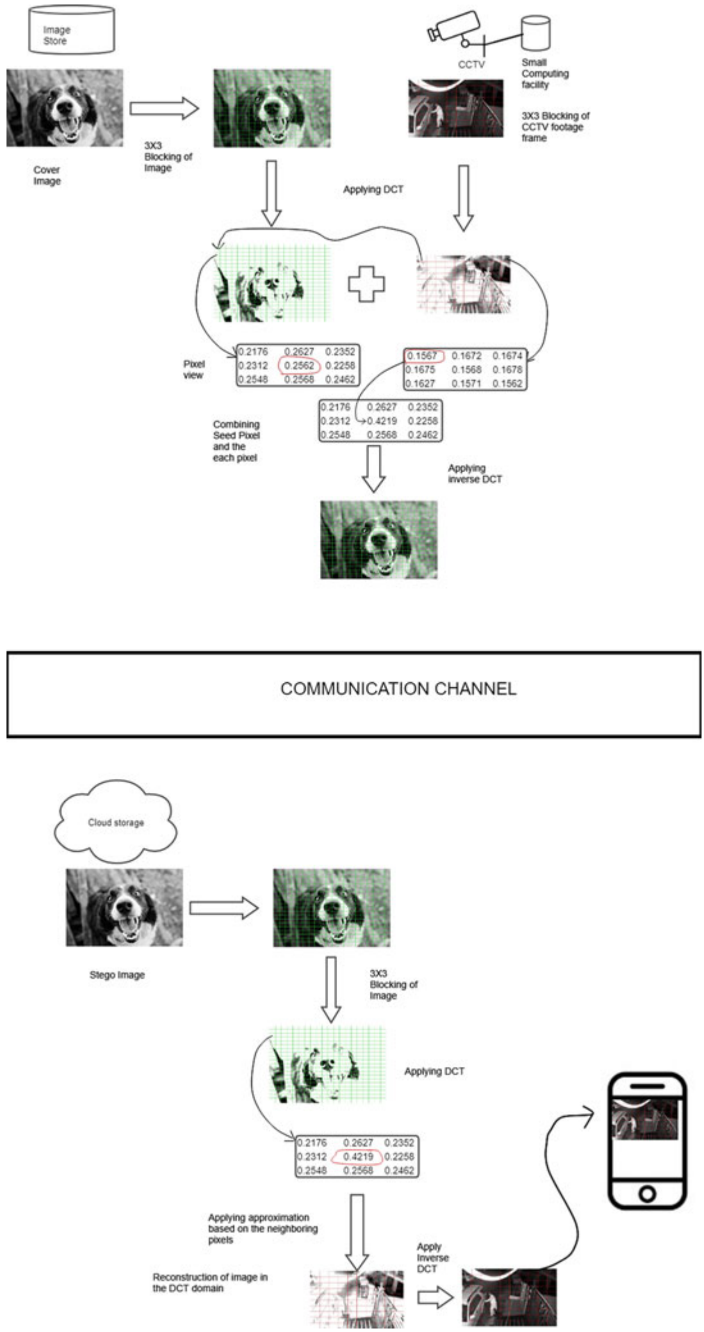

Fig. 4 Hiding IoT communication using DCT difference modulation (DCTDM)

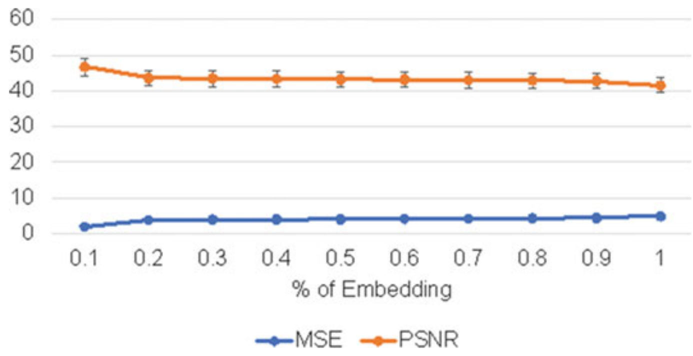

Fig. 5 Performance metrics (MSE and PSNR)

4.2 Peak Signal-to-Noise Ratio (PSNR)

It depicts the quality of the image based on the signal-to-noise ratio, which is based on the pixel difference between cover and stego image (Jean-Bernard Martens 1998). It estimates the quality of the stego image in comparison with cover image. Equation 2 shows the mathematical representation of PSNR, where S is the maximum possible of the image.

$$\mathrm{PSNR} = 10\log_{10}\frac{S^2}{\mathrm{MSE}} \tag{2}$$

4.3 Entropy

Entropy (Shannon 1948) is used to estimate the degree of uncertainty associated with the random variables. Equation 3 describes entropy calculation, where S represents the entropy, T is the thermodynamic temperature of a closed system divided into an incremental reversible heat represented by dQ. Figure 6 represents the entropy distribution on the proposed method.

$$\Delta S = \int \frac{\mathrm{d}Q}{T} \tag{3}$$

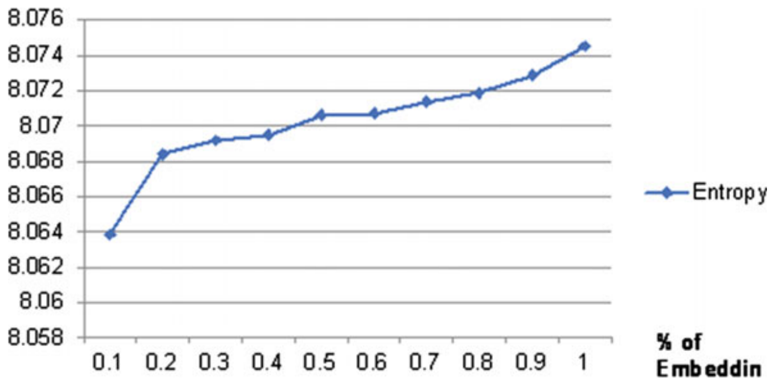

Fig. 6 Entropy distribution

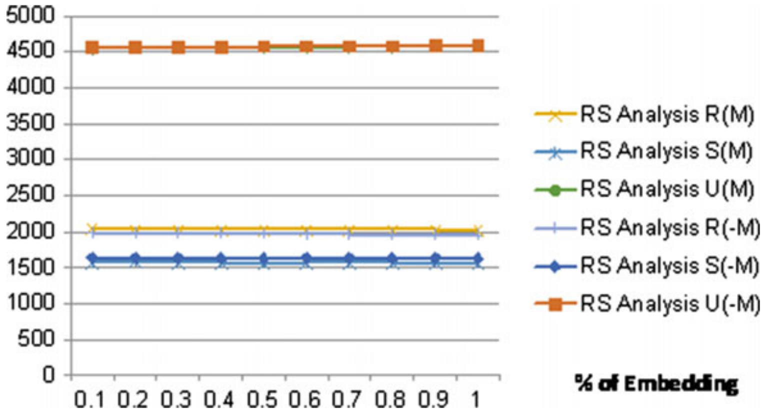

Fig. 7 RS analysis performance for the proposed method

4.4 Analysis on Stego Images

RS analysis is one of the modern-day analysis techniques to identify the LSB changes between images, which will eventually reveal the performance of the proposed method under different scale of attack as shown in Fig. 7.

4.5 Comparison Between the Proposed Method and Existing Approaches

Table 1 shows the comparison between the existing solutions and the proposed methods.

Table 1 Comparison between the proposed method and existing approaches

	Smart cameras with onboard signcryption for securing IoT applications (Ullah et al. 2017)	SBPG (Albalawi et al. 2016)	IoT-based home security through digital image processing algorithms (Dorothy et al. 2017)	Proposed method
Application area	Applicable on both still image and video	Applicable on only still image	Applicable only on still image	Applicable on both still image and video
Use of method	Cryptography	Steganography	Cryptography	Steganography
Performance testing	No	Limited testing	No	Extensive testing of different types of attacks and performance measures
Communication between server and device	Not secure	Not secure	Not secure	Secure as implementation is done at the device end

5 Conclusion

Though IoT has become an integral part of our day-to-day life. The main concern of securing IoT devices comes with low power and low computing facility availability with the devices. In most of the case, the devices face computational challenges and had to communicate over the network to its remote server for minimum computations. Under these circumstances, proposing a suitable and robust security method is challenging. In this presentation, the authors had tried to explore a new dimension for IoT security by combining discrete cosine transform (DCT) with some replacement techniques for a secure communication.

References

Albalawi U, Mohanty SP, Kougianos E (2016) Sbpg: a secure better portable graphics compression architecture for high speed trusted image communication in the IoT. In: 2016 17th international conference on thermal, mechanical and multi-physics simulation and experiments in microelectronics and microsystems (EuroSimE). IEEE

Al-Najjar YAY, Soong DC (2012) Comparison of image quality assessment: PSNR, HVS, SSIM, UIQI. Int J Sci Eng Res 3(8). ISSN 2229-5518

Dorothy AB, Britto S, Kumar R, Jerlin Sharmila J (2017) IoT based home security through digital image processing algorithms. In: 2017 world congress on computing and communication technologies (WCCCT). IEEE

Jean-Bernard Martens LM (1998) Image dissimilarity. Signal Process 70(3):155–176

Kanth A, Mathew A (2018) Robbers use CCTV footage to plan break-ins. The New Indian Express. Published dated 17.09.2018. https://www.newindianexpress.com/specials/2018/sep/17/robbers-use-cctv-footage-to-plan-break-ins-1872895.html. Access date 24.09.2020

Seralathan Y, Oh TT, Jadhav S, Myers J, Jeong JP, Kim YH, Kim JN (2018) IoT security vulnerability: a case study of a web camera. In: 2018 20th international conference on advanced communication technology (ICACT). IEEE, pp 172–177

Shannon CE (1948) A mathematical theory of communication. Bell Syst Tech J 27:379–423

Ullah S, Rinner B, Marcenaro L (2017) Smart cameras with onboard signcryption for securing IoT applications. In: 2017 global internet of things summit (GIoTS). IEEE

Valente J, Koneru K, Cardenas A (2019) Privacy and security in internet-connected cameras. In: 2019 IEEE international congress on internet of things (ICIOT). IEEE, pp 173–180

Vigdor N (2019) Somebody's watching: hackers breach ring home security cameras. The New York Times dated 15.12.2019. https://www.nytimes.com/2019/12/15/us/Hacked-ring-home-security-cameras.html. Access date 24.09.2020

Arterial Blood pH Monitoring Using a Fingertip Device to Predict Cardiovascular as Well as Respiratory Diseases

Ashita Dandekar, Mansi Vaze, Shruti Dodani, and Mrunal Rane

Abstract If the blood pH levels are not maintained and the body's acid–base balance remains disturbed for a long time, it may lead to severe acidosis/alkalosis. These conditions may develop into resistance to the action of insulin and infused catecholamines, alteration in oxygen binding to haemoglobin, decreased cardiac output, causing major diseases like heart failure and cancer. So to address this issue, it becomes important to measure pH levels at an early stage. Currently, pH measurement being invasive in nature involves risk of infections, whereas the non-invasive approach offers safety and cost-effectiveness. Hence, we propose a fingertip device prototype similar to a pulse oximeter but which measures the pH levels. For this measurement of pH, the 'Henderson–Hasselbalch' equation is used. It requires the concentration of bicarbonate ions and the amount of partial pressure of CO_2 for the estimation of buffer pH. The device works on the principle of infrared absorption of CO_2 and reflectance properties. Firstly, it calculates the CO_2 levels, thereby deriving the bicarbonate levels and then substituting it in the above equation to get the blood pH value. The device, thus, displays the pH values, followed by early recommendations. As we are already measuring the CO_2 levels, incorporation of a heart rate sensor additionally will predict cardiovascular as well as respiratory diseases. Further, an alert is sent to the user so that he/she can consult a medical practitioner.

Keywords Beer–Lambert's law · Photoplethysmography · Henderson–Hasselbalch equation · Transcutaneous pCO_2

1 Introduction

1.1 Need for Non-invasive Blood pH Measurement

The current technique which is largely used for the measurement of arterial blood pH is invasive in nature. It is carried out by a blood gas analyser. The process of removing arterial blood is more painful than the normal venepuncture which is carried out for

A. Dandekar (✉) · M. Vaze · S. Dodani · M. Rane
Dwarkadas J. Sanghvi College of Engineering, Mumbai 400056, India

M. Mukherjee et al. (eds.), *Advances in Medical Physics and Healthcare Engineering*, Lecture Notes in Bioengineering, https://doi.org/10.1007/978-981-33-6915-3_38

normal blood tests. The success of this procedure greatly depends on the skill of the health worker. Any deviation from the proper safety technique can cause injury to the patient. If repeated punctures are attempted at the same site, the risk of complications increases. Also, the blood sample needs to be analysed within 10 min of collection for accurate results. Thus, continuous pH monitoring using this method is impossible. Therefore, it is required to develop a device that can measure the arterial blood pH non-invasively.

1.2 Importance of Blood pH Measurement

It is important to know your blood pH levels as any drastic variations in them may cause malfunctioning of regular body processes. It primarily affects the kidneys and the lungs.

The kidneys are responsible for excreting acids in urine, producing and regulating bicarbonates, thereby maintaining the blood pH levels. The lungs are responsible for regulating blood pH through the process of exhaling carbon dioxide. When these get affected, all other processes linked to it start to fall back.

When blood pH levels are not maintained in its normal range of 7.35–7.45, it may either lead to acidosis (pH < 7.35) or alkalosis (pH > 7.45) (Brinkman and Sharma 2020). Both the conditions can go unnoticed at the beginning due to lack of non-invasive pH measurement. This will then lead to many acid–base disorders. Such as increased or decreased HCO_3^- ion concentration followed by renal failure or, reduced or increased CO_2 elimination leads to respiratory disorders and finally heart failure.

1.3 Effects of Imbalance in Blood pH

Few major effects that can occur are as follows:

Resistance to the action of insulin and infused catecholamines; low blood pH is a sign that the action of insulin is not being carried out properly. Without the presence of insulin, many of the body's cells cannot take glucose from the blood, and therefore, the body uses other sources of energy. This can be an indication that the person has diabetes. Catecholamines are hormones made by adrenal glands. Adrenal glands send catecholamines into the blood when the person is physically or emotionally stressed. When a person is stressed, it can lead to some breathing problems and thus affect the lungs, thereby leading to variations in pH.

When a person's pH level goes low, there is an alteration in oxygen binding to haemoglobin. It can lead to accumulation of CO_2 inside our blood and when this happens the affinity between oxygen and haemoglobin is hampered. Thus, the oxyhaemoglobin complexes are not formed, which means that person would be facing cardiovascular or respiratory diseases. This will eventually lead to decreased cardiac output and ultimately may lead to heart failure as well (Frangiosa et al. 2006).

1.4 Acid–Base Balance—Anatomy and Physiology

The acid–base balance is maintained in the body using its buffering systems. These systems help blood to maintain the narrow pH range. A buffer is a chemical system that resists change in pH. By exhaling CO_2, the respiratory tract raises the pH value. The renal system also regulates blood pH by excreting hydrogen ions or conserving bicarbonate ions. This process takes days to show its effect. Proteins that are made up of amino acids can act as buffers by binding to hydrogen and hydroxyl ions with its positively charged amino groups. The pulmonary capillaries reverse this process and reformation of CO_2 takes place. This CO_2 gets diffused in the air sacs. The diffused CO_2 is released into the atmosphere. Respiratory system plays an important role in maintaining blood pH. CO_2 in the blood readily reacts with water to form carbonic acid. The levels of CO_2 and carbonic acid are in equilibrium. The increase in rate and depth of respiration allows more exhalation of CO_2. This adjusts the pH and helps it to reach the normal value. The chemical reactions occur in the pulmonary capillaries of the lungs. Minor adjustments in the breathing are enough to regulate pH. For example, while exercising, there is excess of CO_2 produced in the body. This increases respiration rate in order to balance the increased CO_2 production. This helps to prevent the body from developing acidosis. CO_2 is used in chemoreceptors as a signal. The peripheral blood sensors signal the brain so that it can provide immediate alterations to the respiratory rate. The renal regulation of acid–base balance consists of the metabolic part of the buffering system. The sodium ions are reabsorbed from the filtrate in exchange of H^+ ions by an antiport mechanism in the apical membranes of the cell lining of the renal tubule. The cells produce bicarbonate ions. When CO_2 is available, the carbonic acid formation takes place (OpenStax 2016). The bicarbonate ion passes into the peritubular capillaries and returns to the blood. The hydrogen ion is secreted into the filtrate, where either it can be a part of the new water molecule or get removed by the urine.

2 Methods and Measurements

2.1 Calculation of pH

There is a famous equation called the Henderson–Hasselbalch equation. In chemistry and biochemistry, this equation estimates pH of a buffer solution. Hence, it can be used to calculate the blood pH. Given the concentration of bicarbonate ion and partial pressure of carbon dioxide, we can find the value of blood pH.

$$pH = pK_a + \log_{10}\frac{[A^-]}{[HA]} \tag{1}$$

pH	acidity of buffer solution
pK_a	negative logarithm of K_a
K_a	acid dissociation constant
$[A^-]$	concentration of an acid
[HA]	concentration of conjugate base.

In case of blood, the buffer solution is the bicarbonate buffering system. pK is derived from dissociation constant of the part of acid in the buffering system. The buffering capacity is optimal when pH = pK. For the bicarbonate buffering system in blood, this value of pK is 6.1.

2.2 *Calculation of pH Under Normal Conditions*

pK is 6.1 under normal conditions.

$$[H_2CO_3] = k_{HCO_2} \times pCO_2 \tag{2}$$

where $[H_2CO_3]$ is the concentration of carbonic acid, k_{HCO_2} is the blood carbonic acid solubility and pCO_2 is the partial pressure of carbon dioxide. k_{HCO_2} is a constant value of 0.03 (mmol/L)/mmHg. Hence, for the denominator part of the H–H equation, the dissolved CO_2 concentration ($pCO_2 \times 0.03$) can be used instead of $H2CO_3$ (Messina and Patrick 2020).

The normal value of $HCO_3{}^-$ is 24 mEq/L, $PaCO_2$ is 40 mm Hg, and base-to-acid ratio is 20:1 (Marano et al. 2015). We know that normal blood pH is approximately 7.4. By putting the values in the H–H equation, the base-to-acid ratio comes out to be 20:1 and pH to be 7.4 after calculation. This verifies the correctness of the equation.

$$pH = pK + \log_{10}\left[\frac{HCO_3^-}{pCO_2} \times 0.03\right] \tag{3}$$

$$pH = 6.1 + \log_{10}\left[\frac{HCO_3^-}{pCO_2} \times 0.03\right]$$

$$pH = 7.4$$

2.3 Measurement of Arterial pCO_2

For the Henderson–Hasselbalch Equation, it is required to measure the partial pressure of CO_2 and bicarbonate ion concentration. A non-invasive method is preferable as it avoids pricking and ensures continuous pH measurements. Dr. Severinghaus was the first to describe measurement of pCO_2 via human skin. It is based on the phenomenon that CO_2 gas diffuses very easily through human skin and tissue. Dr. Severinghaus used a pCO_2 electrode. The tissue used for measurement was stabilized with temperature (Severinghaus 1960). The pCO_2 values were measured above 130 mm Hg on slightly blanched skin. The research was able to prove that the relationship between skin surface pCO_2 and arterial blood pCO_2 ($PaCO_2$) is linear and in the range from 20 to 74 mm Hg. Later, developments included heating of electrodes which led to increased supply of arterial blood to the capillaries of the skin. The value obtained correlates with the $PaCO_2$. The temperature elevated sensor gives a high value of transcutaneous partial pressure of CO_2 ($tcpCO_2$) (Severinghaus and Bradley 1958). A correction is made in the $tcpCO_2$ value as close to the $PaCO_2$ value as possible.

Nowadays, CO_2 is measured by finding the pH of an electrolyte layer. This layer is separated from the skin surface. The measurement includes transcutaneous electrochemical sensors. A change in the pH and the logarithm of pCO_2 change are related to each other mathematically. The potential difference between a pH glass electrode and an Ag/AgCl reference electrode determines the pH (Eberhard 1980).

2.4 Measurement of Bicarbonate Ion Concentration in Blood

First we measure the total blood CO_2 in the blood. The percentage of bicarbonate ions out of the total blood CO_2 is approximately 68% CO_2, being a major greenhouse gas absorbs infrared light effectively. An infrared light of 15 μm can be chosen, since at this wavelength, the absorption by CO_2 molecule is maximum.

Beer–Lambert's Law can be used to determine the CO_2 concentration.

$$A = \log_{10}\left[\frac{I_0}{I_1}\right] = \varepsilon l c \tag{4}$$

where

I_0 is the incident light intensity.
I_1 is the transmitted light intensity.
A is the absorbance.
ε is the molar attenuation coefficient or absorptivity of the attenuating element.
l is the path length of light.
c is the concentration of the attenuating element.

The design of this module can include: an infrared LED placed above the finger and photodetectors placed below the finger. These photodetectors will measure the transmitted light intensity. This logarithmic ratio of original intensity and transmitted intensity will be proportional to the concentration of CO_2 in the blood, keeping other parameters in the mathematical equation of Beer–Lambert's law as constant. This module developed for estimation of bicarbonate concentration can then be tested and well-calibrated by taking various sample readings. The design of this module will also take into account the interference of ambient light, thereby reducing error in the readings. Hence, the LED-detector arrangement will be enclosed in an opaque shield. Also, the amount of infrared absorption by other molecules present in blood can lead to errors which can be corrected.

3 Principle

This involves the principle of Beer–Lambert's law, photoplethysmography (PPG) in optical heart-rate sensors, and change in pH to determine pCO_2.

1. Beer–Lambert's Law: Beer–Lambert's law states that loss of light intensity is directly proportional to the properties of material through which light passes. In other words, there is a linear relationship between the concentration and the absorbance of the solution, which enables the concentration of a solution to be calculated by measuring its absorbance. This law will be useful in estimating bicarbonate ion concentration.
2. Photoplethysmography: It is an optical technique
3. pCO_2 electrodes: The change in pH relates to that measures volumetric variations in the $tcpCO_2$ and heating of the skin ensures that microvascular tissue bed (Webster 2010). It requires human skin $tcpCO_2$ is close to the $PaCO_2$ value. Contact and measures heart rate non-invasively.

4 Device Prototype Block Diagram

See Fig. 1 and Table 1.

5 Additional Verification Using Formulae

See Table 2.

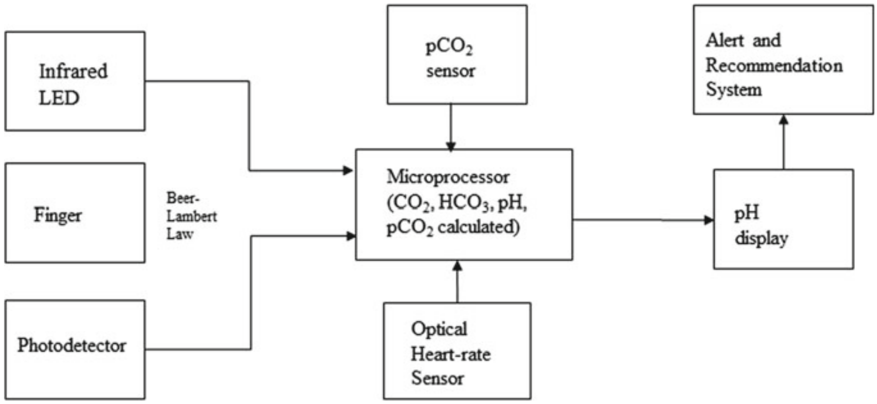

Fig. 1 Block diagram

6 Working

1. Infrared (IR) light of 15 μm is incident on the fingertip. This incident IR light intensity (I_0) value is fed to the microprocessor. Part of which gets absorbed by the arterial blood and remaining gets transmitted.
2. This transmitted light is detected by the photodetector. That is the intensity of transmitted light (I_1) is detected and then this value is fed to the microprocessor.
3. The microprocessor calculates the absorbance value as per Beer–Lambert's law, by substituting the values of I_0 and I_1 in this equation:

$$A = \log_{10}\left[\frac{I_0}{I_1}\right]$$

4. We know that the absorbance value is directly proportional to the concentration of the unknown, i.e. the concentration of CO_2.
5. Hence, the concentration of CO_2 will be calculated by substituting the value of absorbance in this equation:

$$c = \frac{A}{\varepsilon l} \tag{5}$$

6. Where ε and l (average diameter of the arterial capillaries) will be constant values.
7. The bicarbonate ion concentration will be calculated by the following equation:

$$[HCO_3^-] = 0.68 * [CO_2] \tag{6}$$

Table 1 Condition, possible diseases and compensation predicted out of measured readings of pCO_2, HCO_3^-, pH

pCO_2(mm-Hg)	HCO_3^- (mmol/L)	pH	Condition	Possible disease	Disturbance	Compensation
35–45	2	7.35–7.45	Normal	None	None	None
Less than 40	Less than 24	Less than 7.35	Metabolic acidosis	– Renal diseases – Diabetic ketoacidosis – Lactic acidosis – Venoconstriction – Decreased cardiac output – Changes in mental state	1 mEq/L decrease in HCO_3^-	1.3 mm Hg decrease in pCO_2
47 and above	24 and above	7.49 and above	Metabolic alkalosis	– Antacid ingestion – Gastric suction – Bartter's syndrome – Renal artery stenosis – Renin secreting tumour	1 mEq/L increase in HCO_3^-	0.7 mm Hg decrease in pCO_2
–	–	7.27	Acute respiratory acidosis	– Acute respiratory oedema – Respiratory muscle paralysis	1 mm Hg increase in pCO_2	0.1 mEq/L increase in HCO_3^-
55 and above	Less than 22	7.32	Chronic respiratory acidosis	– Chronic obstructive pulmonary disease – Emphysema – Chronic bronchitis – Bronchial asthma	1 mm Hg increase in pCO_2	0.4 mEq/L increase in HCO_3^-
–	–	7.53	Acute respiratory alkalosis	– Hypoxia – Hyperventilation	1 mm Hg decrease in pCO_2	0.2 mEq/L decrease in HCO_3^-

(continued)

Table 1 (continued)

pCO_2(mm-Hg)	HCO_3^- (mmol/L)	pH	Condition	Possible disease	Disturbance	Compensation
–	–	7.48	Chronic respiratory alkalosis	– Asthma exacerbation – Meningitis	1 mm Hg decrease in pCO_2	0.4 mEq/L decrease in HCO_3^-

https://www.slideserve.com/ranit/laboratorium-interpretation-of-acid-base-electrolites-disorders. https://doctorlib.info/physiology/physiology-2/67.html. https://www.amboss.com/us/knowledge/Acid-base_disorders

Table 2 Changes in pCO_2 and pH depending on primary conditions

Primary disorder	Expected changes
Metabolic acidosis	$pCO_2 = 1.5 \times HCO_3^- + (8 \pm 2)$
Metabolic alkalosis	$PCO_2 = 0.7 \times HCO_3^- + (21 \pm 2)$
Acute respiratory acidosis	Change in pH = $0.008 \times (pCO_2 - 40)$
Chronic respiratory acidosis	Change in pH = $0.003 \times pCO_2 - 40)$
Acute respiratory alkalosis	Change in pH = $0.008 \times (40 - pCO_2)$
Acute respiratory alkalosis	Change in pH = $0.017 \times (40 - pCO_2)$

https://uichildrens.org/health-library/acid-base-disorders

8. At the same time, the sensor values taken from the transcutaneous pCO_2 electrode and from the optical heart rate sensor are fed to the microprocessor (Mindt et al. 1982).
9. Now the microprocessor computes the arterial blood pH by substituting the values of $[HCO_3^-]$, pCO_2, pK (which is a constant of value 6.1)
10. The value of pH hence obtained is displayed on the screen of the device.
11. If the displayed pH is not in the normal range, an alert is given on the screen stating the condition of the patient, whether it is Acidosis or Alkalosis. Thereby giving quick dietary recommendations.
12. But if the pH of a person is continuously in abnormal range for more than 15–20 days, an alert is given by predicting any probable disease the person may face and accordingly doctor's consultation is recommended.

7 Application of the Device Prototype

1. Our device prototype is capable of predicting cardiovascular as well as respiratory diseases.
2. It can be used in research, for finding the relationship between acidity and migraine attacks in case of migraine related patients, because continuous pH readings can be recorded without hampering the patient's comfort.
3. Also, it can be used for continuous monitoring of blood pH level for the patients suffering from hyperacidity without the need of pricking.
4. pH can be considered and measured as a fitness parameter along with heart rate.

8 Future Scope

1. This device can also be modified in such a way that it can include other parameters such as blood glucose, blood viscosity and blood flow velocity.
2. The pH imbalance and the diseases related to it is a topic still under research. There are diseases which are directly an effect of pH imbalance, while others that are indirectly related to pH.
3. It can be modified to enable sending patient data to the family doctor immediately in case of heart and hyperacidity patients.
4. The device can also be developed to measure skin pH. The low pH of the wounded skin indicates healing while higher pH indicates chronic wounds.
5. Migraine, headaches and reflux are an effect of pH imbalance. This can be researched upon with continuous testing through the device.

9 Conclusion

pH is an important blood parameter which needs to be taken into account for prediction of certain diseases. If the human body is not capable of making immediate changes using the buffering systems, it leads to malfunction of lungs and kidneys. This may eventually lead to heart failure. Hence, early detection of abnormal pH values using our proposed device will save a person's life. The device will be equipped with a battery power source for easy portability. Also, the device uses a non-invasive method of measurement that makes it easy to handle. It is a self-care device that can be used by individuals of all age groups. The voltage output from the photodetector and the readings of pCO_2 electrode will be used to calculate pH. A net result will be displayed by the alphanumeric display. This result will include pH value, heart rate and lifestyle recommendation in case of mild pH imbalance conditions. In extreme pH conditions, the device will also have an alert system that will warn the patient about serious consequences related to health and whether it is required to consult a medical practitioner.

References

Brinkman JE, Sharma S (2020) Respiratory alkalosis [Updated 2020 July 26]. In: StatPearls [Internet]. StatPearls Publishing, Treasure Island (FL). Available from: https://www.ncbi.nlm.nih.gov/books/NBK482117/

Eberhard P, Schäfer R (1980) A sensor for noninvasive monitoring of carbon dioxide. Br J Clin Equip 5:224–226

Frangiosa A, De Santo LS, Anastasio P, De Santo NFG (2006) Acid-base balance in heart failure. J Nephrol 19(Suppl 9):S115–20. PMID: 16736434

Marano M, D'Amato A, Marano S (2015) A very simple formula to compute pCO_2 in hemodialysis patients. Int Urol Nephrol 47(4):691–694. https://doi.org/10.1007/s11255-015-0913-4. Epub 2015 Jan 23. PMID: 25613433

Messina Z, Patrick H (2020) Partial pressure of carbon dioxide (PCO_2) [Updated 2020 Aug 16]. In: StatPearls [Internet]. StatPearls Publishing, Treasure Island (FL). Available from: https://www.ncbi.nlm.nih.gov/books/NBK551648/

Mindt W, Eberhard P, Schäfer R (1982) Monitoring of PCO_2 by skin surface sensors. Biotelemetry Patient Monit 9:28–35

OpenStax, anatomy & physiology. OpenStax CNX. 26 Feb 2016. https://cnx.org/contents/14fb4ad7-39a1-4eee-ab6e-3ef2482e3e22@8.24.

Severinghaus JW (1960) Methods of measurement of blood and gas carbon dioxide during anaesthesia. Anesthesiology 21:717–726

Severinghaus JW, Bradley AF Jr (1958) Electrodes for blood PO_2 and PCO_2 determination. J Appl Physiol 13:515–520

Webster JG (ed) (2010) Medical instrumentation: application and design, 4th edn. Wiley, Hoboken, NJ

Comparative Study on Predictive Mathematical Models for Risk Assessment of nCOVID-19 Pandemic in India

Swarnava Biswas, Anoop Kumar Prasad, Debajit Sen, Dinesh Bhatia, and Moumita Mukherjee

Abstract The entire world faced locked down scenario due to the outbreak of nCOVID-19 corona virus outbreak. The fast and relentless spread nCOVID-19 has basically segmented the populace only into three subclasses, namely susceptible, infected, and recovered compartments. Adapting the classical SIR-type epidemic modeling framework, the direct person-to-person contact transmission is taken as the direct route of transmission of nCOVID-19 pandemic. In this research, the authors have developed two models of the nation-wide trends of the outburst of the nCOVID-19 infection using an SIR model and also an ARIMA model. They have studied the quantile plots, regression residual plots and R pair plots of the dataset by simple supervised machine learning algorithms. This study compares both models and higher correlation of the developed models with reality which suggests the extent of accuracy of these models. The study also suggested some possible way-out to get rid of this situation by providing a trade-off between 'flattening of the curve' as well as less economic turbulence. The projections are intended to provide an action plan for the socioeconomic counter measures to alleviate COVID-19 in India.

Keywords COVID-19 · Corona virus · Pandemic · India · SEIR modeling · Epidemic model · ARIMA model

S. Biswas (✉)
The Neotia University, Sarisha, West Bengal 743368, India

A. K. Prasad
Royal School of Engineering and Technology, Guwahati, Assam 781035, India

D. Sen
ELMAX Systems and Solutions, Kolkata, West Bengal 700045, India

D. Bhatia
North-Eastern Hill University, Shillong, Meghalaya 793022, India

M. Mukherjee
Adamas University, Kolkata, West Bengal 700126, India
e-mail: moumita.mukherjee@adamasuniversity.ac.in

M. Mukherjee et al. (eds.), *Advances in Medical Physics and Healthcare Engineering*, Lecture Notes in Bioengineering, https://doi.org/10.1007/978-981-33-6915-3_39

1 Introduction

The quantity of nCOVID-19 cases keeps on raising at a shocking rate around the world. This virus is the seventh of corona virus that tainted people; the initial four caused gentle indications and were recognized during the 1960s, yet the fifth furthermore as SARS-COV, and the 6th as MERS-CoV that showed up in 2003 and 2012 separately, created serious symptoms (Cascella et al. 2020). In December 2019, the seventh infection which was named SARS-CoV-2 (recently known as 2019-nCoV) rose in Wuhan (Adhikari et al. 2020), China, and was named as COVID-19 sickness in February 2020 by the World Health Organization (WHO), by which the disease was later proclaimed as a pandemic in March 2020 (Lai et al. 2020). The corona virus disease can be asymptomatic as well, or cause mild, moderate, or severe symptoms (Novel 2020). The latter one causes acute respiratory distress syndrome (ARDS), and subsequently, the patient will require mechanical ventilation, and some others may get admitted to the ICU (Adhikari et al. 2020). Regardless of a large number of preventive and control gauges that have been executed in numerous nations, this novel corona virus is being exceptionally infectious and has been rapidly surging overall (Monllor et al. 2020). As of April 20, 2020, the absolute number of tainted individuals is over 2.5 million in more than 212 nations, of which about 30% and 40% are in the USA (https://www.cdc.gov/coronavirus/2019-ncov/cases-updates/cases-in-us.html) and Europe (https://www.ecdc.europa.eu/en/geographical-distribution-2019-ncov-cases), separately, and these numbers are significantly expanding, which keep on antagonistically impact in individuals' lives, medical care offices, and nations' economies. Hence, it is clear that determining the future surge of this pandemic using the accessible information is of high significance so as to comprehend the current circumstance, assess the seriousness of the pandemic, and help the governments put well-tailored strategies and productive decisions to combat the disease and limit new infections in the upcoming days. As of now, some researches have proposed distinctive mathematical and machine learning-based forecasting models to appraise the spread of the malady and decide its effect (Shinde et al. 2020), internationally (Petropoulos and Makridakis 2020) and for explicit nations, for example, the USA (Liu and Guo 2020), China (Al-Qaness et al. 2020), Italy (Perone 2020), Spain (Monllor et al. 2020), France (Fanelli and Piazza 2020), India (Gupta and Pal 2020), Japan (Sugishita et al. 2020), among others.

In this work, we utilized the SIR model and ARIMA model to gauge the number of new COVID-19 daily cases in India in the following month. The ARIMA model has been recently to foresee the elements of COVID-19 malady in the most influenced 15 nations (Kumar et al. 2020; Ete et al. 2020) and indicated a reasonable prediction that are practically indistinguishable from the current circumstance in those nations. Another investigation that used this model mainly focused on Italy and Spain and the prediction results showed an acceptable accuracy for the daily number of affected cases in these two countries (Monllor et al. 2020). It is highly essential to forecast the upcoming pandemic situation of India where the people are belonging from a large diversified background. In this way, it is imperative to estimate the future pattern of the pandemic, and appropriately, present a lot of valuable proposals for the specialists with respect to how to diminish the spread of the ailment and actualize 'new normal' measures to combat this situation in our country.

2 Materials and Methods

2.1 SIR Model

The main objective of this paper is to forecast the effect of the COVID-19 pandemic in Indian scenario by appropriate machine learning techniques. The SIR model is generally used for forecasting the nature of pandemic and its van estimate that it might wreak on humanity. This mathematical model explains the logic behind the estimation of the outbreak of any epidemic. This can act as a preliminary model to keep a check on the infrastructure requirements. We have used a basic version of the model to predict the number of affected individuals a little ahead of time.

The following equations were framed to have an initial level understanding of the epidemic effect on the society.

$$\mathrm{d}S(t)/\mathrm{d}t = -aS(t)I(t) \tag{1}$$

$$\mathrm{d}I(t)/\mathrm{d}t = aS(t)I(t) - bI(t) \tag{2}$$

$$\mathrm{d}R(t)/\mathrm{d}t = bI(t) \tag{3}$$

$$x = a/b \tag{4}$$

where S, I, and R represent the number of susceptible, infected, and recovered individuals of India, respectively. The variables 'a' and 'b' denote the infection rate and recovery rate, respectively. Here 'x' is known as the reproducibility rate. It can be said that, if the value of $x < 1$, then it can be concluded that the pandemic is under control.

The above model begins with the following assumptions:

Initially, the entire population of India is taken as susceptible and it is further assumed that the susceptible and infected portion of the population equally mixes with each other. The first equation further states that the rate at which the susceptible portion enters the infected portion. The constant of proportionality governing the same is 'a', which is calculated by the compound annual growth rate (CAGR).

Similarly, the second equation explains the rate at which some portion of the infected set leaves the same to come under the recovered category. The constant of proportionality governing the same is 'b', which is also calculated by the CAGR.

The third equation explains the recovery rate of the affected population. This ideally starts with '0' and reaches the entire population.

The last and probably the most important factor in the equation is the reproducibility rate, which is the rate at which a single individual can affect others. The pandemic is supposed to get flattened once this factor comes below '1'.

2.2 ARIMA Model

In this paper, the authors have applied a widely utilized and popular statistical method for time series forecasting of COVID-19 cases in India, that is the ARIMA model. ARIMA model is an acronym that stands for auto-regressive integrated moving average model, and it belongs to a class of model which can be used for capturing a suite of different standard temporal structures in time-series data.

The key aspects of the model are:

AR: Autoregression. This model can be used for the dependent relationship between an observation and some number of lagged observations.

I: Integrated. This model deals with the differencing of the raw observations from an observation at the previous time step which are used to make the time series stationary.

MA: Moving Average. This model that is used to measure the dependency between an observation and a residual error from a moving average model applied to lagged observations.

The authors have specified these components in the model as a parameter.

A standard notation which is used of ARIMA (p, d, q) where the parameters can be substituted with integer values to quickly indicate the specific ARIMA model to be used.

The parameters of the ARIMA model are defined as follows:

p: The number of lag observations that are included in the model, known as the lag order.

d: This is known as the degree of differencing which can be defined as the number of times that the raw observations are differenced.

q: It represents the order of moving average, i.e., the size of the moving average window.

The ARIMA forecasting equation for a stationary time series is regression-type and a linear equation and here the predictors are consisted of lags of the dependent variable and/or lags of the forecast errors (https://people.duke.edu/~rnau/411arim.htm).

Predicted value of $v = a$ constant and/or a weighted sum of the recent values of V and/or a weighted sum of recent values of the errors.

The forecasting equation is given as follows. Here

'v' denotes the dth difference of 'V',

$$\text{If } d = 0, vt = Vt \tag{5}$$

$$\text{If } d = 1, vt = Vt - Vt - 1 \tag{6}$$

$$\begin{aligned}\text{If } d = 2, vt &= (Vt - Vt - 1) - (Vt - 1 - Vt - 2) \\ &= Vt{-}2Vt - 1 + Vt - 2\end{aligned} \tag{7}$$

So, it can be said as in terms of v, the general forecasting equation is:

$$v_t^* = \mu + \phi_1 v_{t-1} + \cdots + \phi_p v_{t-p} - \theta_1 e_{t-1} - \cdots - \theta_q e_{t-q} \tag{8}$$

Here, θ represents the moving average parameter.

A sign of a pattern or structure can be used for suggesting the capacity of the model to capture more information, and then the model can be used for making better predictions. The authors here found some patterns and structures and then explored the residual errors from that. The non-randomness of the errors can be a seen from these patterns. However, the expectation of the authors is that the residual errors to be random, because that means that the model is capable to capture all of the structure, and it can be said that the only error left is the random fluctuations in the time series that cannot be modeled.

The authors in this paper have developed a forecast model to forecast what will be the values of COVID-19 affected individuals in the next time step with the help of the data, in reference to inputs received in the previous time step. This type of persistence forecast model (PFM) is also known as 'naive forecast' models.

After the dataset (https://www.mohfw.gov.in/; https://covidindiaupdates.in/) is loaded in R studio, a supervised machine learning problem is formulated. We have created a lagged version of the dataset where the input variable is taken as the prior time step ($t - 1$) and the output variable is taken as the next time step ($t + 1$). Then the authors have split the dataset into training and test sets. A total 70% of the data is kept for training, and the remaining 30% is used for the test set. Once split, the authors have separated the train and test sets into their input and output components. The persistence model is applied by predicting the output value (O) as a function of the input value (x). Regression residual errors (RRE) are generally defined as the forecast errors on any time series regression problem. The residual errors are then calculated as the difference between the expected outcome and the prediction. The authors have calculated the residual error by the following mathematical equation:

$$E(x) = O{-}F \tag{9}$$

where $E(x)$ is the residual error, O denotes the expected outcomes as a function of the input value (x), and F represents the forecasted value.

Generally, the potential of the forecasting skills of the models can be explained as a summary of these residual errors. Instead of the authors in this paper have collected these individual residual errors across all the forecasts and given a better understand of the forecast model by using those residual errors. The array of residual errors can be wrapped in a Pandas data frame and plotted directly.

Further, they have plotted a quantile plot for the comparison of two distributions with respect to their similarity. To check the normality of the distribution of residual errors, they can be checked quickly by using such *Q*–*Q* plots. This has been done by ordering and comparing the values with an idealized Gaussian distribution.

3 Results and Discussions

The pandemic trend as calculated from the SIR model as shown in Fig. 1. In Fig. 2, the linear and logarithmic models of confirmed, recovered, deaths, and active cases are plotted against time. The authors have worked on backdated data to give an idea of the spread of affected individuals per million over days. In our dataset (https://www.mohfw.gov.in/; https://covidindiaupdates.in/), the first confirmed case in India was reported in January, and the last date considered is August 31, 2020. The first two plots describe the number of people infected against the number of days in linear scale and semi-log scale respectively. A semi-log or semi-logarithmic graph, generally used for data with exponential relationships, or where one variable covers a large range of values, has one axis on a logarithmic scale, the other on a linear scale. It is evident from the third figure, from day 80 (starting January 28, 2020) the infected cases took an exponential growth and gradually increased. After 70 days, there was increase in the recovered cases a well. The fourth figure explained the logarithmic version of SIR model which shows that parameters have been well-fitted.

In case of ARIMA models (Fig. 3a), the authors have plotted the number of total infected COVID-19 cases with time and in Fig. 3b. the total left cases are plotted

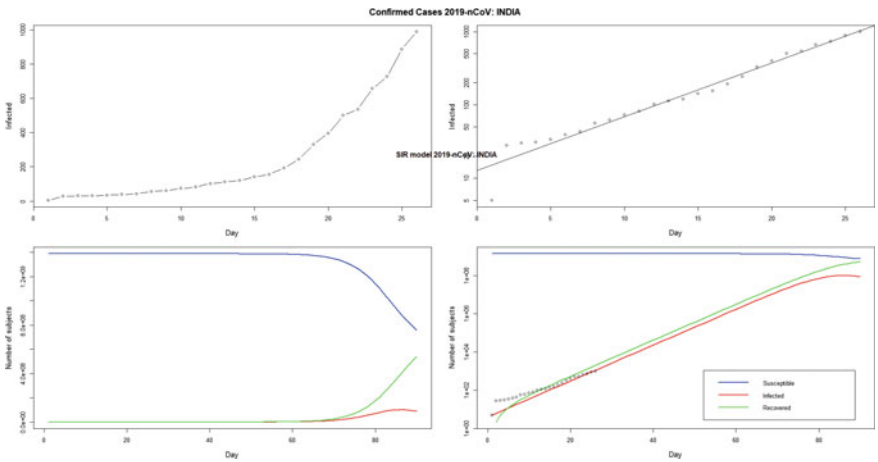

Fig. 1 SIR model of COVID-19 cases in India

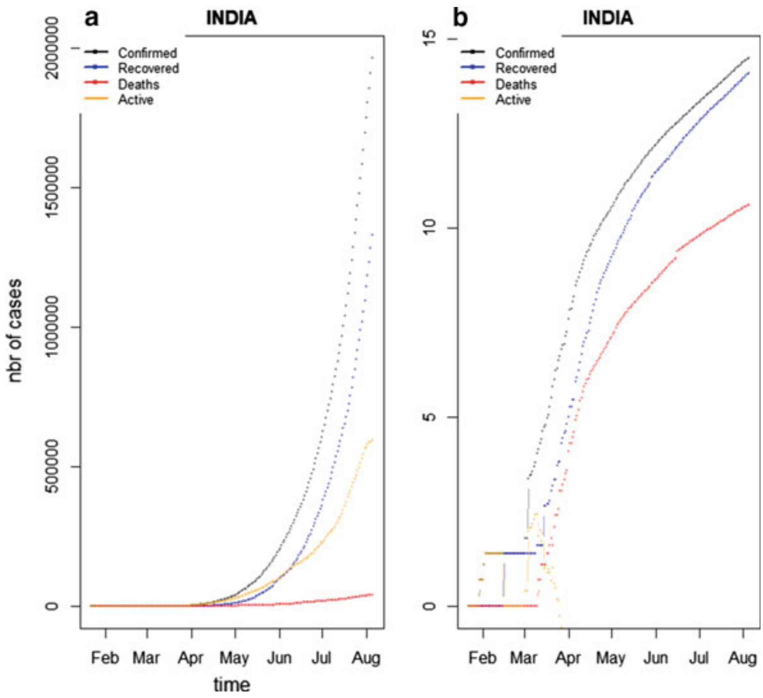

Fig. 2 **a** Linear model and **b** logarithmic model of number of confirmed, recovered, deaths, and active cases against time

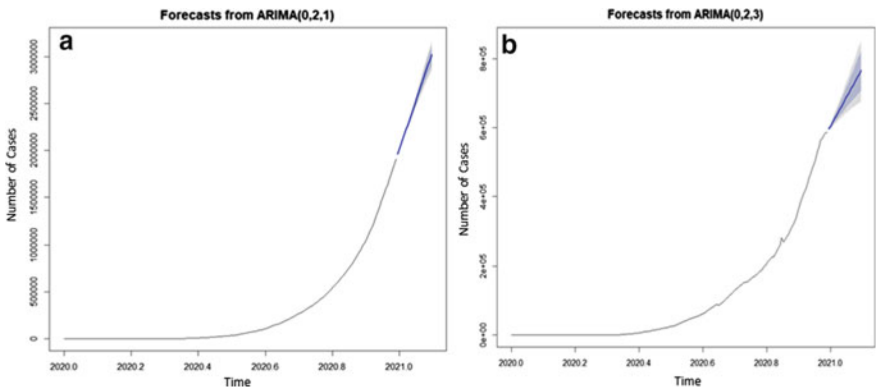

Fig. 3 **a** Forecasting ARIMA model using only confirmed cases. **b** Forecasting ARIMA model of using only total left (= Confirm Cases – Death − Recovered)

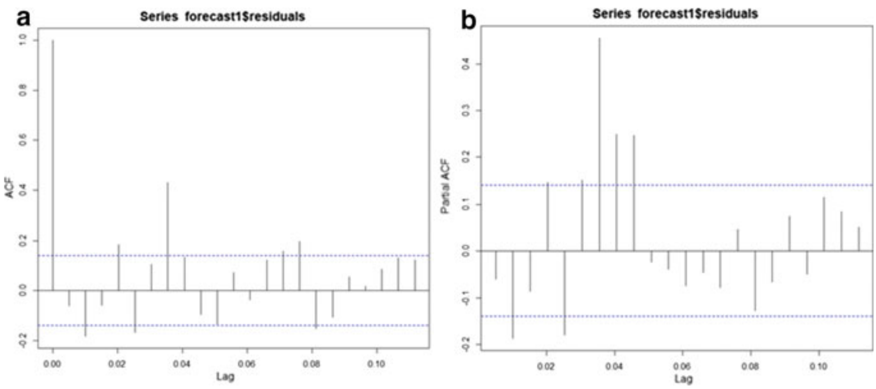

Fig. 4 **a** Coefficients of correlation between a time series and lags of itself. **b** Partial coefficients of correlation between a time series and lags of itself

against time. Total left case is the difference of confirmed cases from the summation of death and recovered cases. It can be said that, it is highly uncertain about a disease which is communal in its nature to predict with its out growing rate. It is quite possible to follow time series prediction for knowing the forecast nature of the ongoing pandemic. This ARIMA model is showing a close correlation with the SIR model.

In this paper, the auto-correlation function (ACF) is defined as a function to provide the values of auto-correlation of COVID-19 cases in India with its lagged values. We plot these values against the lags. In Fig. 4a, this ACF plots describes how well the present number of confirmed cases is related with its past values. It is merely a bar chart of the coefficients of correlation between a time series of confirmed COVID-19 cases in India and lags of itself. Partial auto-correlation function (PACF) is defined as the correlation of the residuals. Figure 4b describes a plot of the partial correlation coefficients between the series of confirmed COVID-19 cases and lags of itself. The authors have found the optimum features of the AR process using the PACF plot, as it is used to remove the variations explained by earlier lags, so we get only the relevant features.

Figure 5 describes the plot of regression residual forecast errors over a time as a line plot. The plot is random around the value of 0 and not showing any trend or cyclic structure. Regression residuals can be used for regression models with ARIMA errors and are calculated as the original data minus the effect of regression variables. In this paper, the authors have calculated the summary statistics on the residual errors for forecasting of COVID-19 cases in India. We are primarily interested in the mean value of the residual errors, and from the figure, it is evident that a value which is quite near to zero can suggest that there is no bias in the forecast model, whereas positive and negative values suggest a positive or negative bias in the forecasts made. It is quite necessary to check about a bias in the forecasts as it has to be directly corrected in forecasts prior to their use or evaluation.

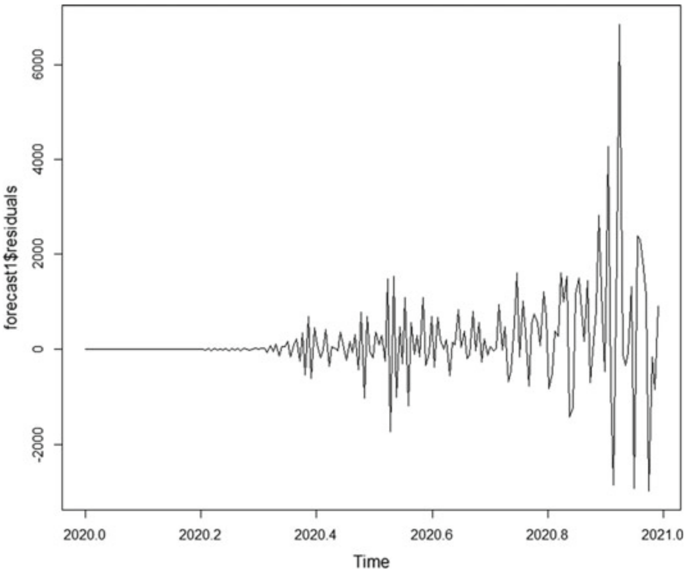

Fig. 5 Forecast residuals plot against time

A *Q*–*Q* plot or quantile plot is employed to check the plausibility of the assumption and if violated, it shows what data points contribute to the violation. The authors have drawn a scatter plot where a comparison between the two distributions is shown as a diagonal line from the bottom left to the top-right of the plot. In Fig. 6, we can see a rough straight-line behavior which can prove that both sets of quantiles came from the same distribution. So, it can be said that the forecast model is accurate and obvious departures from this expectation can be estimated.

The summaries of the results of various model fitting functions can be derived by using a generic summary function. The function generally invokes particular methods which depend on the class of the first argument. The calculated accuracy of our forecast model is 93.331%.

The R pair plot function generally returns a plot matrix and it consists of scatterplots for each variable combination of a data frame. Here the diagonal shows the names of the four numeric variables of our example data. The other cells of the plot matrix show a scatterplot (i.e., correlation plot) of each variable combination of our data frame.

In Fig. 7, the first graphic in the first row illustrates the correlation between confirmed and death cases; the second graph in the first row illustrates the correlation between confirmed and recovered cases; the last graph in the first row illustrates the correlation between confirmed and total left cases. The left figure in the second row illustrates the correlation between confirmed and x death cases once more and so on.

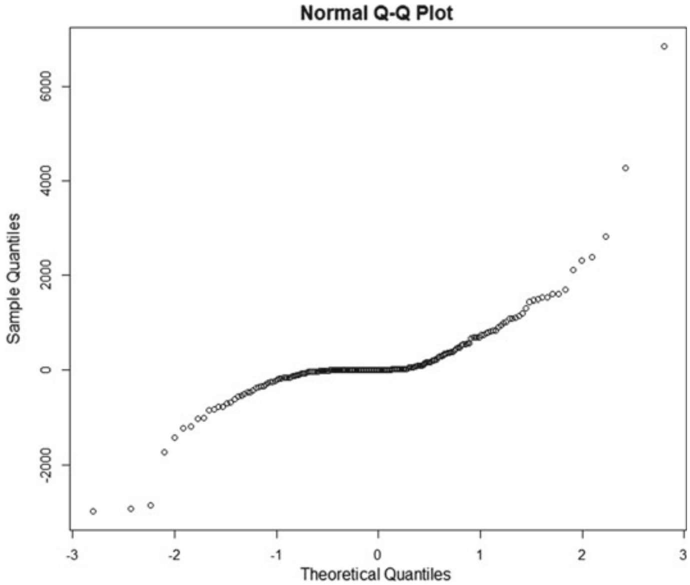

Fig. 6 Plot of theoretical quantiles against sample quantiles (Q–Q plot)

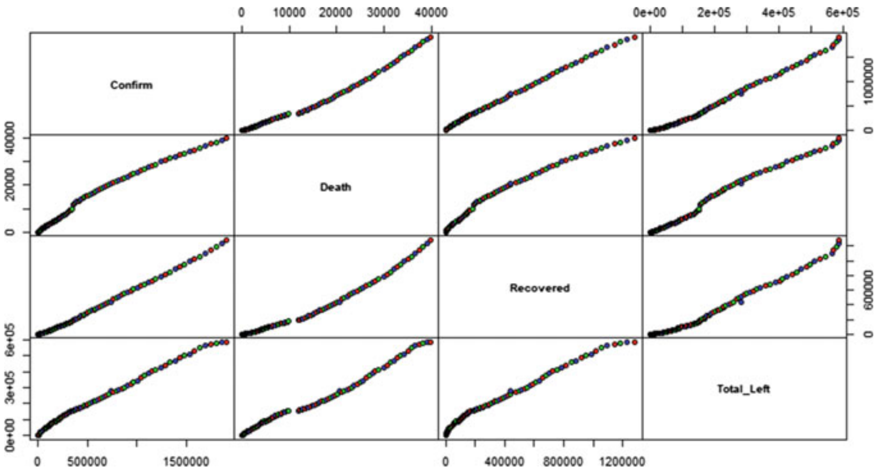

Fig. 7 R pair plot between confirm, death, recovered, and total _left cases

4 Conclusions

In this paper, SIR model and ARIMA model are explicitly used to a suite of standard structures in time-series data of COVID-19 cases in India, and it provides a simple yet powerful method for making skillful time series forecasts. Here the authors have developed a machine learning model by avoiding the multicollinear features, and the authors have also constructed a linear regression model in this paper and then included the specified number and type of terms. To remove trend and seasonal structures that negatively affect the regression model of COVID-19 cases in India, we have prepared the data by an appreciable degree of differentiating to make the model stationary. Here adopting an ARIMA model for a time series of COVID-19 cases in India confirms the assumptions of the model in the raw observations and in the residual errors of forecasts from the model. In addition to this, the authors have found the optimum features of the AR and MA process using the PACF and ACF plots, respectively.

According to the observations from both the models, we find that in between 100 and 200 days, the number of affected individuals would be varying in order of 1 million per 10 million in case of India. To counter such precedented spike, the requirement of the necessary infrastructure with all possible testing facilities for successful COVID detection remains. Since the reverse transcription polymerase chain reaction (RT-PCR) incurs a cost factor, and time factor hence the objective of more tests to identify and isolate the affected individuals may be defeated, particularly in an Indian scenario. Almost all diagnostic centers are mostly equipped with medical instruments such as SPO_2 monitoring machine, thermal gun, laboratory for complete blood count (CBC) test and radiography imaging instruments like X-ray or CT scan in some specialized centers. So, any artificial intelligence-based image processing techniques which mainly deals with radiographic images employing X-ray and CT scans can be a complementary tool to detect and isolate the COVID-19 patients of India. Our suggestion is to deploy some AI-based aids to all diagnostic centers inclusive of the ones that have the infrastructure to conduct tests with RT-PCR which would address the critical requirements of this severe problem by accelerating the process of identification and isolation of the affected individuals. This proposed AI-based model will not replace the existing acceptable test form, but it will be particularly beneficial to the less privileged centers to conduct the mass testing and if required sent the suspicious ones for an RT-PCR-based test procedure. This in turn would help save time and costs incurred in screening of the population. Our research group is presently working to develop AI enabled multi-hypothesis-based techniques for initial detection of COVID-19 infections in India which if successfully tested would be beneficial for testing huge numbers of patients.

References

Adhikari SP, Meng S, Wu YJ, Mao YP, Ye RX, Wang QZ, Sun C, Sylvia S, Rozelle S, Raat H, Zhou H (2020) Epidemiology, causes, clinical manifestation and diagnosis, prevention and control of coronavirus disease (COVID-19) during the early outbreak period: a scoping review. Infect Dis Poverty 9(1):1–12

Al-Qaness MA, Ewees AA, Fan H, Abd El Aziz M (2020) Optimization method for forecasting confirmed cases of COVID-19 in China. J Clin Med 9(3):674

Cascella M, Rajnik M, Cuomo A, Dulebohn SC, Di Napoli R (2020) Features, evaluation and treatment coronavirus (COVID-19). In: Statpearls [internet]. StatPearls Publishing
Ete T, Fanai V, Bamon A, Khan SA, Kumar U, Kumar A, Mishra A (2020) Disease, drugs, and dilemma: a review of cardiovascular implications of novel COVID-19. Clin Infect Immun 25–30
Fanelli D, Piazza F (2020) Analysis and forecast of COVID-19 spreading in China, Italy and France. Chaos Solitons Fractals 134:109761
Gupta R, Pal SK (2020) Trend analysis and forecasting of COVID-19 outbreak in India. medRxiv
https://covidindiaupdates.in/. Accessed 15 Oct 2020
https://people.duke.edu/~rnau/411arim.htm. Accessed 15 Oct 2020
https://www.cdc.gov/coronavirus/2019-ncov/cases-updates/cases-in-us.html. Accessed 15 Oct 2020
https://www.ecdc.europa.eu/en/geographical-distribution-2019-ncov-cases. Accessed 15 Oct 2020
https://www.mohfw.gov.in/. Accessed 15 Oct 2020
Kumar P, Kalita H, Patairiya S, Sharma YD, Nanda C, Rani M, Rahmani J, Bhagavathula AS (2020) Forecasting the dynamics of COVID-19 pandemic in top 15 countries in April 2020: ARIMA model with machine learning approach. medRxiv
Lai CC, Shih TP, Ko WC, Tang HJ Hsueh PR (2020) Severe acute respiratory syndrome coronavirus 2 (SARS-CoV-2) and corona virus disease-2019 (COVID-19): the epidemic and the challenges. Int J Antimicrob Agents 105924
Liu Z, Guo W (2020) Government responses matter: predicting covid-19 cases in US under an empirical Bayesian time series framework. medRxiv
Shinde GR, Kalamkar AB, Mahalle PN, Dey N, Chaki J, Hassanien AE (2020) Forecasting models for coronavirus disease (COVID-19): a survey of the state-of-the-art. SN Comput Sci 1(4):1–5
Monllor P, Su Z, Gabrieli L, Montoro A, Taltavull de La Paz MDLP (2020, 29 March) COVID-19 infection process in Italy and Spain: are the data talking?. Available at SSRN: https://ssrn.com/abstract=3566150. https://doi.org/10.2139/ssrn.3566150
Novel, Coronavirus Pneumonia Emergency Response Epidemiology (2020) The epidemiological characteristics of an outbreak of 2019 novel coronavirus diseases (COVID-19) in China. ZhonghuaLiuxingbingxue Zazhi 41(2):145
Perone G (2020) An ARIMA model to forecast the spread of COVID-2019 epidemic in Italy. arXiv preprint arXiv:2004.00382
Petropoulos F, Makridakis S (2020) Forecasting the novel coronavirus COVID-19. PLoS ONE 15(3):e0231236
Sugishita Y, Kurita J, Sugawara T, Ohkusa Y (2020) Forecast of the COVID-19 outbreak, collapse of medical facilities, and lockdown effects in Tokyo, Japan. medRxiv

A Review on Isolation of Keratin Protein from Non-conventional Resources and Its Application in Daily Diet to Enhance Hair Quality

Priyanka Jana, Rudra P. Saha, and Arpita Das

Abstract Rather than dumping the big quantity of keratinous waste, in particular birds' feathers, demands greater fee-added application. To hold up body systems, protein is an important nutrient and also a critical factor for beauty merchandise. Chicken feathers contains excessive amount of keratin protein and also the right protein source. The hair, skin and nails (tissues) are made up through epithelial cells. Keratins are best protein called for imparting strength and resilience to cells that shape the hair, skin and nails. Those proteins also are allowed tissues to withstand damage from friction, minor trauma, which includes scratching and rubbing. It will be a great help for the society and industry if we can plan to insert these portions in our daily diet. Even though all of us recognize human's frame digest soluble keratin protein by using trypsin and pepsin (secretion of the leader cellular, pepsin, the proteolytic enzyme of the belly is normally chargeable for much less than 20% of the protein digestion which happens within the gastrointestinal tract). Ingesting this keratin protein complement someone can get all blessings of keratin protein. The existing paintings report the effects of experiments aimed at making ready water-soluble keratin. In this record, we are going to speak about techniques to prepare water-soluble keratin protein from non-conventional sours. In this, chicken feather is used, and we can speak about the techniques of extraction of soluble keratin protein from feathers.

Keywords Keratin protein · Non-conventional protein sources · Food supplement · Chicken feathers

1 Introduction

Whole world is facing various problems due to air pollution like sinus problems, allergies, scalp irritation and also hair loss. This can also happen in indoor. Volatile organic compounds (VOCs) are release in air by several households which people

P. Jana · R. P. Saha · A. Das (✉)
Department of Biotechnology, School of Life Science and Biotechnology, Adamas University, Barasat, West Bengal 700126, India
e-mail: arpita.das@adamasuniversity.ac.in

M. Mukherjee et al. (eds.), *Advances in Medical Physics and Healthcare Engineering*, Lecture Notes in Bioengineering, https://doi.org/10.1007/978-981-33-6915-3_40

use regularly. In this generation, almost everybody spends their most time in closed buildings which are controlled by artificial air environments. Cooling and heating systems are also released VOCs (Langer et al. 2008). VOCs are major pollutants in indoor air, and these pollutants are deposited on the scalp, hair which is causing the scalp irritation and also hair loss (Wang et al. 2007).The skin and hair are first barrier which exposed to the pollution. The large and small suspended airborne particles along with gaseous, smoke pollution deposit on scalp and also hair, which is the cause of the scalp irritation and damage hair. At mining and also construction region, activity is showing the particle matter (PM) in high concentration. The dust of mercury, lead, zinc and other heavy metals can affect the people who living beside the mining areas and also damaged their hair (Huang et al. 2012; Qu et al. 2012). Electromagnetic radiation which was created by cell phones can also be a reason of hair loss. A review paper shows a study, which is showing that a single-strand DNA breakage in root of human hair cells when it exposed to a radiation of mobile phones (Çam and Seyhan 2012). Hair loss can happen after changing the residence and also the workplace and a long travelling distance, exposure to dusty wind and strong sunlight or excess heat or cold, smoke, smog, construction and mining areas and also fertilizer and cement factories and oil rigs, petroleum transport. A research study shows that swimming pool water which is chlorinated can also be the reason of hair loss (Rajput 2015).

Although there is no escape from pollution, there are things which people can do to prevent damage their hair. They have to have keratin protein in their daily diet. Keratin protein helps to nourish hair which is also good for skin (Basita et al. 2018). This protein helps hair to prevent breakage, heat damage, frizz and also important for maintaining strong and healthy hair. Sources of keratin are deriving from surprisingly wide range of foods. It is because many vitamins, minerals and nutrients found in foods either fortify the keratin already present in the body or encourage its production and regulation. The sources of keratin actually reside in entire subgroups of foods. The following foods provide great sources of keratin: red meat, egg, salmon, almonds, nuts, blueberries, oysters, etc.

The global population which is growing too fast is changing the socio-demographics, which will increase the pressure on the world's expedients to provide different kinds of food. The huge order for protein which is animal-based is anticipated unfavourable on environment, which also generates emissions of greenhouse gas and requires area of land and water. So, crisis people need supplementary food, and the source should be non-conventional.

Chicken feathers contented huge amount of keratin protein and it is also a non-conventional source. While feathers are often considered as a by-product of poultry production (often a waste by-product). Chicken feather is bio-resource which content 750 g protein per kg crude and poultry factories produce a huge number of feathers, and also this large number of feathers burning is not economically effective. Disposal of feathers is also not environment friendly. Chicken feathers consist of approximately 90% keratin. The worldwide annual feather amount is about 8×105 tonnes (Grazziotin et al. 2006).

Depending on secondary structure, keratin proteins are divided into alpha-keratins and beta-keratins. Alpha-keratins are found in the hair, the skin and the wool of mammals. These are primarily fibrous and helical in structure. Beta-keratins occur in animal like reptiles and also in bird. The amino acid composition of keratin is varying, and it is depended on the tissue (Gupta et al. 2012). In a research, it was shown that keratin protein can be soluble, although we know that it is an insoluble protein. And this soluble keratin protein would extract from chicken feather (Sinkiewicz et al. 2017). In a explore, we institute the progression to all set a water-soluble and not poisonous protein consequent from keratin from sources of keratin such as brute hair, fur, feather, wool, hooves, horns, claws, shells, nails and keratinous materials such as meals organized from them. This water-soluble keratin protein is processed by hydrolysis (Kadri et al. 1976). So, a supplementary food product of keratin protein can be used as a good source of keratin.

2 Non-conventional Source

Keratin-based trash resources like wool and barren feathers of chicken are motivating investigations for people benefits. The fowl activity generates millions kg of discarded feathers of chicken apiece annum, which makes the down copious keratin source, which is discarded of by landfilling or ignition, and the contemporary disposal techniques through landfilling or ignition are not accordingly environmentally pleasant. Feathers and wool are the on the whole copious sources of keratin worldwide look for to their utilisation in the cloth and foodstuff industry, correspondingly (Li and Wang 2013; McGovern 2000). Wool is used in clothing industry, and the outcome is a load null of un-spinnable passing fleece rubbish. Wool is 95% keratin, of which 60 wt% is sappy keratin, and 26% is durable keratin . These feathers consist 90% of beta-keratin (Stiborova et al. 2016). The fowl manufacturing produces a colossal null sum of chicken fluff as uncultivated during meat making (Tesfaye et al. 2017).

Chicken down as the non-conventional stool pigeon of keratin compassion in humanity agricultural stated, in 2013, that 58 billion chickens are slaughtered apiece year. If we think 2 kg slaughter-heaviness of a chicken with 5–7% of fluff for each chicken, a least possible of 5.8 billion kg of feathers of chicken are fashioned apiece day as a by-product (Swetlana and Jain 2010). USA and India produce approximately 1.044 billion kg and 140 million kg chicken feathers, as become emaciated stuff for each year, correspondingly (Khardenavis et al. 2009). Two to three tonnes of chicken fluff bottle be fashioned by a slaughterhouse which processes 50,000 chickens apiece day (Gupta et al. 2012). According to Tesfaye, South Africa produces 258 million kg of feathers of chicken as a by-product as producing meat (Tesfaye et al. 2017). Insignificant amounts of these fluffs are second-hand as advantageous products, for low-value applications like innate nosh which expense about 13 rand and nourishment, and the other momentous portion is measured as a garbage note (Veerabadran et al. 2012). Feathers of chicken have about 90% keratin protein (Swetlana and Jain 2010). Keratin is extremely valued protein, and the cost of keratin from a human being section sells for Rs-2840 for each gram. Hence, keratin can be able to extract from feathers of chicken which is converted into basic and worthwhile foodstuffs, and moreover, tin enhances beyond consequence and revenue to the capon industry. Biomedical applications are among the applications of keratin (Rouse and Dyke 2010; Kakkar et al. 2014).

3 Keratin Extraction Techniques

Keratin extraction is ended by contravention convincing disulphide bonds those crosslink keratin molecules. Depending on extraction technique, keratin chains may furthermore be shortened during the process (Ayutthaya et al. 2015). This segment describes extraction techniques of keratin from assorted sources. Keratin extraction methods may produce keratin proteins with uncommon substantial properties like viscosity, molecular load and other which anon have emotional impact properties of the decisive goods that will be created from keratin. The separate methodologies of keratin extraction technologies for waste chicken feathers are as follows:

3.1 Chemical Procedure of Keratin Extraction

It uses chemical substances to extract keratin from keratinous fibres. The mainly commonly used chemicals are sinking agents, oxidizing agents, ionic liquids, and (Sinkiewicz et al. 2017) hydrolysis extraction methodology requires an outsized sum of alkaline element compounds which includes sodium hydroxide (Rouse and Dyke 2010). Cysteine is actual finely turned to alkalis, and subsequently, the sum of cysteine decreases added hurriedly than lessening method. But the hydrolyzed keratin remnants unspoiled during the deal with. (McGovern 2000; Tsuda and Nomura 2014) (Fig. 1).

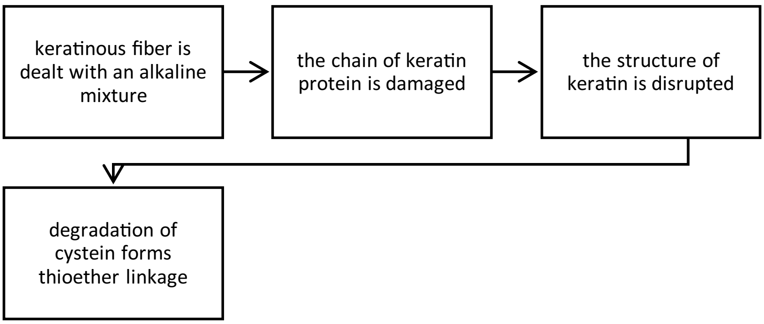

Fig. 1 Chemical procedure of keratin extraction (Rouse and Dyke 2010)

The dropping agents are—chemicals which is containing thiol (thioglycolic acid and also thioglycolate salts) and sulphite-o-lysis agents (like sodium sulphite and sodium bisulphite and sodium meta-bisulphite) and also 2-mercaptobisulphite (Aluigi et al. 2008). To enhance the extractability of keratin, plummeting agents are regularly used with denaturing agents and surfactants (Shavandi et al. 2017).

3.2 Keratin Extraction Using Sodium Meta-Bisulphite

Ayutthaya investigated keratin extraction from feathers of chicken by means of concentrations of the sodium meta-bisulphite (Ayutthaya et al. 2015). According to the German centralized stream Management Act, sodium meta-bisulphite poses to some extent risk in duty be neutralized before discharging, like treating using sodium hypochlorite solution (Khumalo et al. 2019).

3.3 Keratin Extraction Using Sodium Bisulphite

In a research investigation, one gram of pre-treated feathers of chicken was deep in 25 ml of aqueous suspension of 0.5 M sodium bisulphite, 8 M urea and 0.08 M SDS. Sodium bisulphite is non-combustible but it is harmful if swallowed, liberates noxious gases once it reacts with acids, endangers aquatic life; so, its disposal duty be illegal by stirring into sodium hypochlorite (Khumalo et al. 2019).

3.4 Extraction of Keratin Using Thioglycolic Acid

The other keratin extraction method is employed by thioglycolic acid. Pre-Gupta investigation, the comparison yield of keratin was 8.8% (Kakkar et al. 2014). Thioglycolic acid is noxious, and it causes severe skin burn and also eye damage and also inhalation. This substance should be stored in 2–8 °C for the reason that of its combustibility. Although Hatakeyama extend by 75% of yield by using the mixture of thioglycolic acid and sodium hydrated oxide for wheedle out keratin from sheep wool, this method is modifying for keratin extraction from chicken feathers, despite the fact that permitted to dissolving time of 16 h for a clarification pH consequence of 13 (Hatakeyama et al. 2009).

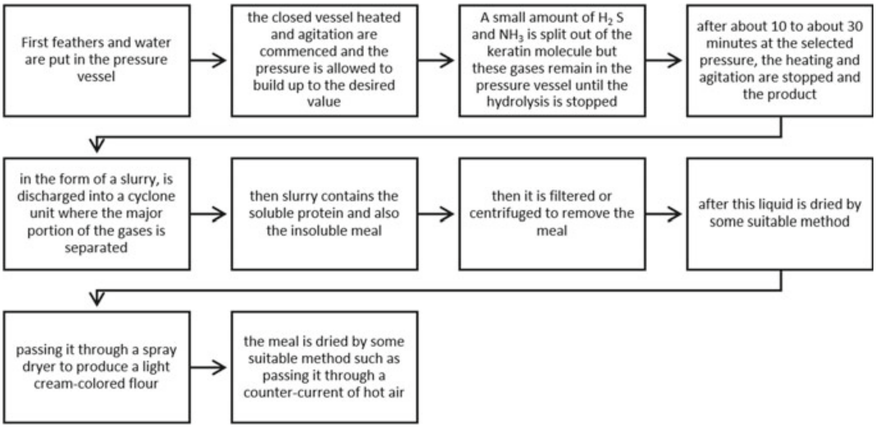

Fig. 2 Procedure of extraction of water-soluble and edible keratin protein from chicken feather (Kadri et al. 1976)

3.5 *Extraction of Keratin by Using Imidazole Ionic Liquids*

According to Ji investigation, the description showed that maximum yield of 75.1% by means of [Bmim] Cl ionic liquid under extraction time of hour at 90 °C (Ji et al. 2014). Imidazole ionic liquids are toxic. They set off skin irritation, acute discernment irritation and respiratory irritation (Khumalo et al. 2019). The liquid may be perilous if a big shot consumed expected to its moderate toxicity point (Hodge and Sterner 1949).

4 Digestibility of Isolated Pool and Limitation

In a research, we found the method to prepare a water-soluble and edible protein derived from keratin from sources of keratin like hair, fur, feather, wool, hooves, horns, claws, shells, nails and keratinous resources such as meals organized from them. Past solutions of proteins are prepared from such sources that the protein has usually been so degraded or contaminated that it has been unsatisfactory for use as a food and for many other uses (Kadri et al. 1976) (Fig. 2).

5 Application of the Isolated Protein as Food Supplement

The water-soluble keratinaceous protein prepared by the S. H. Kadri's method of this research is useful as a foodstuff either by itself or an additive in other foodstuffs including cereal and soybean flour, meats, animal feed, candy, soft and fruit drinks. The nutritive value of foods for human consumption is enhanced by the addition to of the soluble protein which contains all of the essential amino acids like tyrosine, histidine, aspartic acid, methionine, valine, threonine, proline, cysteine, glycine, isoleucine, serine, glutamic acid, arginine, leucine, phenylalanine, lysine, tryptophan and alanine. The foodstuff provided by this report is especially useful as it is essentially free of water-insoluble protein which contained in keratinous meals and is substantially completely digestible by the pepsin within the alimentary canal of humans and animals (Kadri et al. 1976). Keratins though find applications in food, pharmaceutical, cosmetic and fertilizer industry, considerable amount of these products is wasted repeatedly. Acid, alkali or enzymes hydrolyze keratin and hydrolysates have number of applications (Gousterova et al. 2005; Grazziotin et al. 2006). Cosmetics based on keratin preparations have been reported for the treatment of human hair and skin (Kim et al. 1990). Isolation of keratins from above-stated methods yields a digestible raw protein product with potentially significant nutritional value. The naturally high levels of the amino acid cysteine in keratin suggest potential for dietary enhancement of the biological thiols' taurine and glutathione, which have diverse and important roles in health including potent antioxidant activity. Furthermore, keratins are a source of mixed amino acids which may have broad application as a protein supplement (Stipanuk et al. 2006; Silva et al. 2010). Stuart Houltham et al. has reviled in his study that daily consumption of keratin at doses above one gram and up to a significant proportion of daily protein requirement shows that the keratin supplements consumed up to 40 g per day for 5 days did not cause adverse gastrointestinal or other acute onset illness and is therefore safe for general consumption (Houltham et al. 2014).

6 Application of Keratin Protein in Market

In Indian market, there are many keratin supplements for hair that are available in many ways like hair oil, shampoo, conditioner and also protein powder, gums. After extracting keratin protein from non-conventional source, we get two kinds of keratin proteins. Some extraction method gives us edible keratin protein, and some gives us not soluble keratin protein. Those not soluble keratin proteins are used in hair product and hair treatment industry, and those edible keratin proteins are used in food industry (like protein powder and gums). Non-soluble keratin protein which we get from extraction and people cannot eat is useful which we can use in cosmetic industry for caring people's hair. Near there are a number of brands of the keratin mane treatment, entirely with about a parallel elemental substance structure. Hair cleansing, shape the modulation of hair is one of the physical highlights simpler to adjust. Haircare engineering has full-grown gift matter to devote radiance and adjustment a few mane attributes. Beard purifying substance was remembered for this plot in flimsy of the truth that, initially, they are broadly utilized and they weight mostly the highlights of beard makeup plane (perfection, sparkle, combability and hydrophobicity), and furthermore, they are as well utilized in the carrying out of locks mould blend adjustments to get back moustache properties (pI, hydrophobicity other than the string exterior highlights).

7 Conclusion

Normally, human cannot digest keratin protein. So, in this modern world, with unhealthy food hobbies, people need supplementary keratin food products to control their hair fall as we all know keratin is good for hair. There are many methods by which keratin protein can be extracted from non-conventional source but maximum method's output is toxic, and also human cannot process it. In hydrolysis method, the extracted keratin protein is water-soluble, and human can easily digest this protein by their enzymes such as pepsin. This method's outcome product is cream coloured powder. So, we can use this in any kind of food product such as flour, candy, gum, soft drink and also in cultured meats. People can easily have keratin protein by consuming this food product in daily basis and also avoid their hair problems. Keratin has compact structural and robust mechanical properties which attract life science researchers for the proper understanding of physical, chemical and biological properties of keratin. Research on keratin is directed towards the advancement of numerous biomaterials having keratin for practice in application of biomedical field. For example, in recent days, hair damage (caused by UV radiation from sunlight, pollution, and nutrient-deficient food supplements) can be repaired by synthetic treatment of keratin. Additionally, keratinous materials have diverse hierarchal structures and functions that can be useful for development or architecture of new structure for the human benefit. In this modern generation, the amount of stress and technology is increasing at a very high pace. In this current scenario, food habits are getting affected the most, this in turn results in loss of proper nutrition. Due to lack of nutrition, necessary proteins are not available to the body such as keratin which is necessary for hair, skin, nails, etc. As lack of keratin occurs, it needs to be replenished in the body for that we need supplements of keratin. In this study, we have shown how to extract keratin from chicken feathers.

Acknowledgements We duly acknowledge Honourable Chancellor, Adamas University, Kolkata, India for providing us the infrastructure and facilities. This research work is financially supported by Seed fund for university sponsored research project (Ref No. AU/REG/2019-20/12/008), under Adamas University, India.

References

Aluigi A, Vineis C, Varesano A (2008) Structure and properties of keratin/peo blend nanofibres. Eur Polymer J 44(8):2465–2475

Ayutthaya SIN, Tanpichai S, Wootthikanokkhan J (2015) Keratin extracted from chicken feather waste: extraction, preparation, and structural characterization of the keratin and keratin/biopolymer films and electros puns. J Polym Environ 23(4):506–516

Basita A, Asghara F, Sadafb S, Waheed AM (2018) Health improvement of human hair reshaping using recombinant keratin K31. Biotechnol Rep (Amst) 20:00279–00288

Çam ST, Seyhan N (2012) Single-strand DNA breaks in human hair root cells exposed to mobile phone radiation. Int J Radiat Oncol Biol Phys 88(5):420–424

Gousterova A, Braikova D, Goshev I, Christov P, Tishinov K, Vasileva-Tonkova E (2005) Degradation of keratin and collagen containing wastes by newly isolated thermo-actinomycetes or by alkaline hydrolysis. Lett Appl Microbiol 40(5):335–340

Grazziotin A, Pimentel FA, De Jong EV, Brandelli A (2006) Nutritional improvement of feather protein by treatment with microbial keratinase. Anim Feed Sci Technol 126(1):135–144

Gupta A, Kamarudin NB, Kee CYG (2012) Extraction of keratin protein from chicken feather. J Chem Chem Eng 6(8):732–737

Hatakeyama R, Tomita Y, Takigami S (2009) Preparation of water-soluble wool keratin and its application for human hair. Trans Mater Res Soc Jpn 34(3):399–402

Hodge HC, Sterner JH (1949) Tabulation of toxicity classes. Am Ind Hygiene Assoc Quart 10(4):93–96

Houltham S, Starck C, Stannard S (2014) Two week keratin-based protein supplementation is comparable in gastrointestinal handling to a milk-based equivalent. J Hum Nutr Food Sci 2(4):1047–1054

Huang M, Wang W, Leung H, Chan CY, Liu WK (2012) Mercury levels in road dust and household TSP/PM2.5 related to concentrations in hair in Guangzhou, China. Ecotoxicol Environ Saf 81:27–35

Ji Y, Chen J, Lv J, Li Z, Xing L, Ding S (2014) Extraction of keratin with ionic liquids from poultry feather. Sep Purifi Tech 132:577–583

Kadri SH, Hanover P, Allen WM, Ky L, Pikel Ill OL (1976) Method for the preparation of water-soluble keratinaceous protein using saturated steam and water 75. United States Patent

Kakkar P, Madhan B, Shanmugam G (2014) Extraction and characterization of keratin from bovine hoof: A potential material for biomedical applications. Springer Plus 3:596

Khardenavis AA, Kapley A, Purohit HJ (2009) Processing of poultry feathers by alkaline keratin hydrolysing enzyme from Serratia sp. Hpc 1383. Waste Manag 29(4):1409–1415

Khumalo M, Tesfaye T, Sithole B (2019) Possible beneficiation of waste chicken feathers via conversion into biomedical applications. Int J Chem Sci 17(1):304–314

Kim WM, Kendahl W, Sherman L (1990) Protein additives for hair treatment composition. U.S. Patent 4,906,460

Langer S, Modanova J, Arrhenius K, Ljungstrom E, Ekberg L (2008) Ultrafine particles produced by ozone/limonene reactions in indoor air underlow/closed ventilation conditions. Atmos Environ 42:4149–4159

Li R, Wang D (2013) Preparation of regenerated wool keratin films from wool keratin-ionic liquid solutions. J Appl Polym Sci 127(4):2648–2653

McGovern V (2000) Recycling poultry feathers: more bang for the cluck. Environ Health Perspect 108(8):A366–A369

Qu CS, Ma ZW, Yang J, Liu Y, Bi J (2012) Human exposure pathways of heavy metals in a lead-zinc mining area, Jiangsu Province, China. PLoS ONE 7(11):e46793

Rajput R (2015) Understanding hair loss due to air pollution and the approach to management. Hair Transplant 5(1):1–7

Rouse JG, Dyke ME (2010) A review of keratin-based biomaterials for biomedical applications. Materials (basel) 3(2):999–1014

Shavandi A, Silva TH, Bekhit AA (2017) Keratin: dissolution, extraction and biomedical application. Biomater Sci 5(9):1699–1735

Silva LA, Silveira PC, Ronsani MM, Souza PS, Scheffer D, Vieira LC, Benetti M, De Souza CT, Pinho RA (2010) Taurine supplementation decreases oxidative stress in skeletal muscle after eccentric exercise. Cell Biochem Funct 29(1):43–49

Sinkiewicz I, Sliwinska A, Staroszczyk H (2017) Alternative methods of preparation of soluble keratin from chicken feathers. Waste Biomass Valorization 8(4):1043–1048

Stiborova H, Branska B, Vesela T (2016) Transformation of raw feather waste into digestible peptides and amino acids. J Chem Technol Biotechnol 91(6):1629–1637

Stipanuk MH, Dominy JE Jr, Lee JI, Coloso RM (2006) Mammalian cysteine metabolism: new insights into regulation of cysteine metabolism. J Nutr 136(6):1652S–1659S

Swetlana N, Jain P (2010) Feather degradation by strains of bacillus isolated from decomposing feathers. Braz J Microbiol 41(1):196–200

Tesfaye T, Sithole B, Ramjugernath D (2017) Valorisation of chicken feathers: Recycling and recovery routes. In: Proceedings, Sardinia. Clean Technol Environ Policy 19:2363–2378

Tsuda Y, Nomura Y (2014) Properties of alkaline-hydrolyzed waterfowl feather keratin. Anim Sci J 85(2):180–185

Veerabadran V, Balasundari SN, Devi DM (2012) Optimization and production of proteinaceous chicken feather fertilizer by proteolytic activity of bacillus sp. Mptk6. Indian J Innovations Dev 1(3):193–198

Wang S, Ang HM, Tade MO (2007) Volatile organic compounds in indoor environment and photocatalytic oxidation: state of the art. Environ Int 33(5):694–705

Miniaturized Flexible Monopole Antenna for Wearable Biomedical Applications

Susamay Samanta, Sagnik Chakrabarti, Aniket Jana, P. Soni Reddy, and Kaushik Mandal

Abstract A miniaturized monopole antenna is presented in this paper for wearable biomedical applications. The proposed monopole antenna consists of a modified diamond shape patch with coplanar waveguide (CPW) feed designed on a low cost, easily available, and flexible acrylic sheet of thickness 0.3 mm. Four rectangular slits are loaded into a conventional diamond shape patch to lower the frequency of resonance and achieve the desired structural compactness. The operating frequency of the proposed antenna is 2.4 GHz of the industrial, scientific, and medical (ISM) band. The operational bandwidth of the antenna is 135 MHz (2.37–2.505 GHz) covering the entire ISM band (2.4–2.5 GHz). The proposed antenna has a low profile and is compact in size with an overall dimension of $0.16\lambda_0 \times 0.248\lambda_0 \times 0.0024\lambda_0$ (20 mm × 31 mm × 0.3 mm). A peak gain of 1.84 dBi with an omnidirectional radiation pattern and radiation efficiency of 96% is achieved at 2.4 GHz. The performance of the proposed antenna is also analyzed for conformal free space and on-body loading scenarios. The stable performance of the proposed antenna in the different conformal on-body scenarios studied establishes its candidature for wearable biomedical applications.

Keywords Biomedical antenna · Conformal antenna · Flexible antenna · On-body antenna · Wearable antenna

1 Introduction

Telemedicine or remote monitoring of patients has evolved as an important tool to effectively screen the patients during the recent global pandemic situation involving highly contagious diseases like COVID-19. The telemedicine applications allow the

S. Samanta (✉) · S. Chakrabarti · A. Jana
Adamas University, Kolkata, West Bengal 700126, India

P. S. Reddy
University of Kalyani, Nadia, West Bengal 741235, India

K. Mandal
University of Calcutta, Kolkata, West Bengal 700009, India

M. Mukherjee et al. (eds.), *Advances in Medical Physics and Healthcare Engineering*, Lecture Notes in Bioengineering, https://doi.org/10.1007/978-981-33-6915-3_41

healthcare providers to monitor elderly patients or patients with highly contagious diseases without any chance of infection transmission. An essential requirement of these applications is that the sensor and antenna components needed to perform the monitoring should be incorporated on the patients' clothes or body (Basir and Yoo 2019; Liu et al. 2019) such that the sensor data can be easily transmitted/received remotely (Gao et al. 2018).

The 2.4 GHz industrial, scientific, and medical (ISM) band has been extensively used in these applications. Flexibility, compactness, and omnidirectional radiation pattern are the key requirements of wearable antennas. Along with these, the specific absorption rate (SAR) levels of the antenna should comply with the IEEE/IEC 62704-1 standard. Flexible antennas using different types of substrates have been explored in the literature for designing antennas for wearable applications like inkjet-printed paper-based antennas (Mansour et al. 2015), textile antennas (Alemaryeen and Noghanian 2019), and polydimethylsiloxane-based antennas (Simorangkir et al. 2018). Although these antennas provide good flexibility for conformal applications, they suffer from low-radiation efficiency or have overall large dimension.

In this paper, a compact modified diamond-shaped antenna based on a low cost, thin, flexible acrylic sheet substrate loaded with four rectangular slits is presented for wearable biomedical applications. The antenna is excited with a CPW feed network. The proposed antenna is analyzed for different bending scenarios. The antenna design and simulation have been done using CST Studio Suite®.

2 Antenna Design and Geometry

2.1 Antenna Design for Non-conformal and Conformal Applications

The detailed geometries of the proposed monopole antenna for both conformal and non-conformal applications are given in Fig. 1. The antenna is designed on a flexible acrylic sheet substrate having $\varepsilon_r = 1.7$, tan$\delta = 0.02$, and thickness (h) = 0.3 mm. The proposed antenna is derived from a conventional diamond shape patch having side length of 13.4 mm. Four rectangular slits each of length 12 mm and width 0.5 mm are loaded strategically into the conventional diamond shape patch to make the antenna design compact. The spacing between the four slits is kept at $D_1 = 2.5$ mm, $D_2 = 1.5$ mm, and $D_3 = 3.4$ mm for non-conformal applications. A coplanar waveguide (CPW) feed is used to excite the patch. The proposed antenna consists of partial ground plane to achieve an omnidirectional radiation pattern. The proposed antenna operates in the industrial, scientific, and medical (ISM) band with resonating frequency of 2.4 GHz and an overall dimension of $0.16\lambda_0 \times 0.248\lambda_0 \times 0.0024\lambda_0$ (20 mm × 31 mm × 0.3 mm), where λ_0 is the free-space wavelength corresponding to 2.4 GHz.

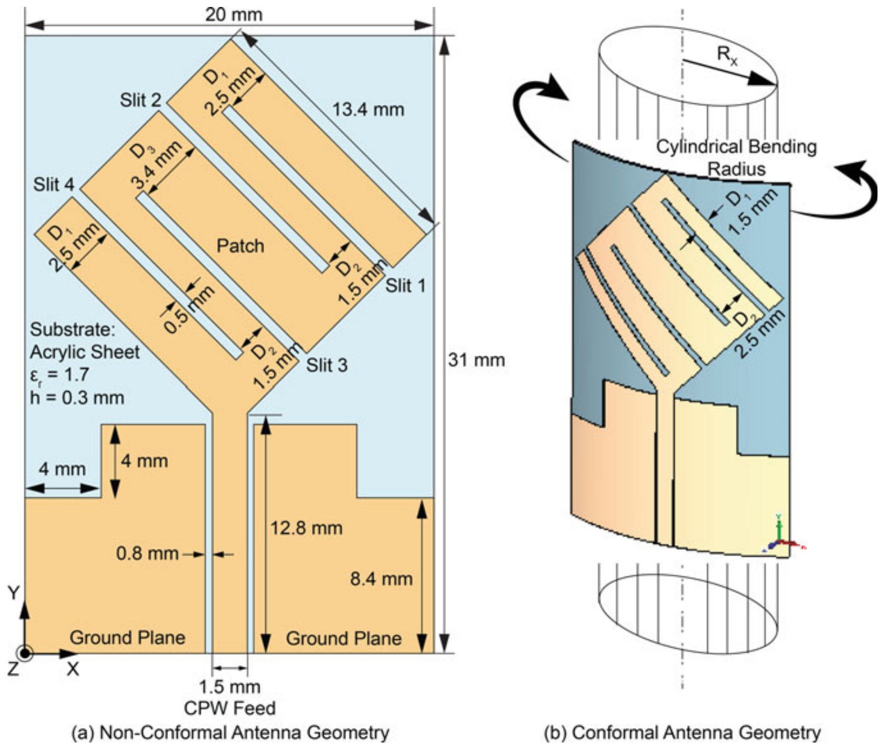

Fig. 1 Detailed geometry of the proposed antenna. **a** Non-conformal structure, **b** conformal structure with cylindrical bending

For conformal applications, all dimensions of the proposed antenna are kept same except the spacing between the slits, i.e., D_1 and D_2. The values of D_1 and D_2 are optimized to keep the resonating frequency of the antenna within the ISM band during bending for conformal applications. The modified values of spacing between the slits are $D_1 = 1.5$ mm and $D_2 = 2.5$ mm. The proposed antenna is cylindrically bent along the X-axis with a bending radius R_X.

2.2 Antenna Design Evolution

The detailed development of the proposed antenna design is shown in Fig. 2. The corresponding S_{11} versus frequency characteristics of each design step are also depicted in Fig. 2a. The design begins with a conventional diamond shape patch (Ant. 1) with a rectangular partial ground plane resonating at 3.48 GHz. Two rectangular slits are loaded on either side of the conventional patch (Ant. 2) at a distance of 7.4 mm apart as shown in Fig. 2a. The modified patch resonates at 3.1 GHz. Next,

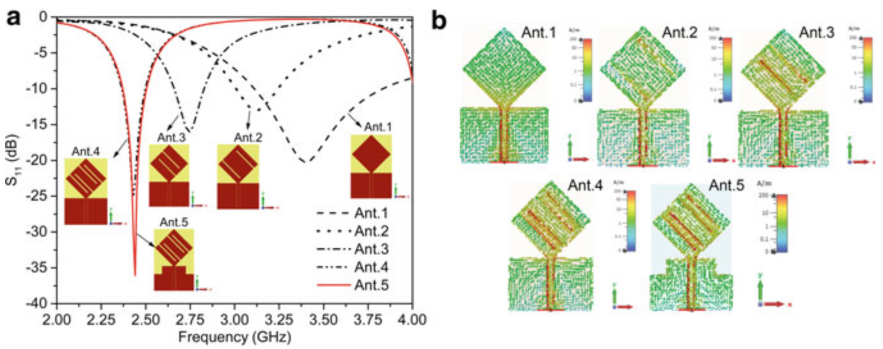

Fig. 2 **a** Detailed antenna design evolution of the proposed antenna along with the simulated S_{11} versus frequency characteristics and **b** simulated vector current distribution on the radiating patch and ground plane surfaces corresponding to each design steps

a pair of slits placed in a position complimentary to that used in Ant. 2 is explored with the distance between the two slits reduced to 3.5 mm (Ant. 3). The resonating frequency of the modified patch shifts to 2.75 GHz. Next, the slits position used in Ant. 2 and Ant. 3 are combined such that the final patch design consists of four rectangular slits (Ant. 4). The final patch resonates at 2.37 GHz. In order to tune the resonating frequency to 2.4 GHz, the rectangular partial ground plane is finally modified using two square corner slits of 4 mm × 4 mm dimension.

The current distributions on the radiating patch and the ground plane surfaces corresponding to each design step are shown in Fig. 2b. It is clear from the figure that with the introduction of slits, the current vectors on the surface of the conventional patch get perturbed. Subsequently, the path length of the surface current vectors gets increased which leads to the shift in the resonating frequency toward the lower end, and thus, compactness in the antenna design is achieved.

3 Results and Discussion

3.1 Antenna Radiation Characteristics (Non-conformal Structure)

The simulated 2D far-field radiation characteristics of the proposed non-conformal antenna structure in both the E-plane and H-plane are shown in Fig. 3. The proposed antenna has an omnidirectional radiation pattern with a characteristic dumbbell-shaped radiation pattern in the E-plane and a circular-shaped radiation pattern in the H-plane. The proposed antenna provides a peak gain of 1.84 dBi with a radiation efficiency of 96% at 2.4 GHz.

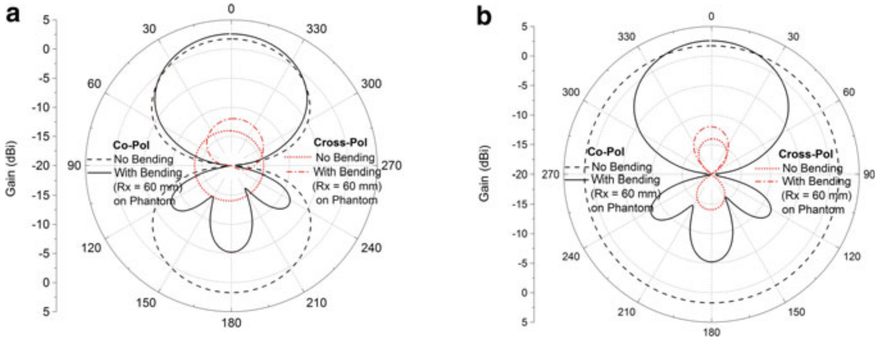

Fig. 3 Simulated 2D far-field radiation characteristics of the proposed antenna structure in both the **a** E-plane and **b** H-plane for non-conformal (no bending) and conformal (with bending R_X = 60 mm on the phantom model) scenarios

3.2 *Wearable Application Analysis of the Proposed Antenna (Conformal Structure)*

Conformability Analysis. The proposed antenna design is tested for conformability by bending the antenna cylindrically along the X-axis with bending radius R_X = 20 mm, 40 mm, 60 mm, and 80 mm. The corresponding S_{11} versus frequency characteristics for all bending scenario is depicted in Fig. 4. The proposed conformal antenna structure when subjected to different bending scenarios gives stable performance with a peak gain of 1.84 dBi at 2.4 GHz.

On-body Performance Analysis. The proposed conformal antenna structure with $R_X = 60$ mm is loaded on a phantom model shown in Fig. 4b for on-body performance analysis. The phantom model is designed with different concentric layers of skin, fat, muscle, and bone having radius 55 mm, 52 mm, 45 mm, and 30 mm, respectively, to

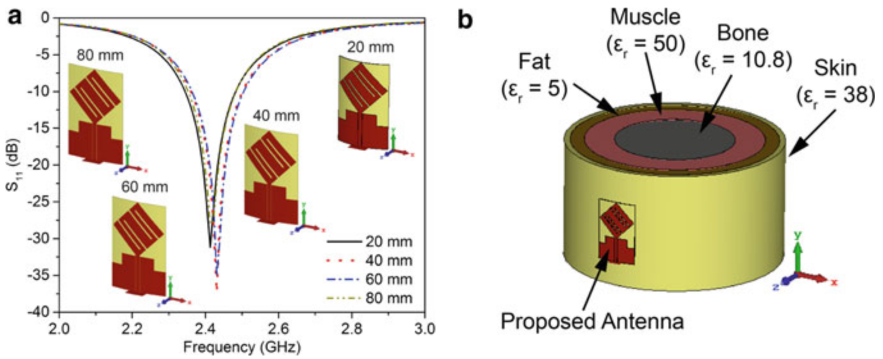

Fig. 4 **a** Simulated S_{11} versus frequency characteristics for all bending scenario and **b** phantom model with the proposed antenna (R_X = 60 mm) for on-body and SAR analysis

Table 1 Performance comparison of the proposed antenna with other wearable antenna designs

Reference antenna	Size (mm^3)	Gain (dBi)	Radiation efficiency (%)	Material used
Raad et al. (2016)	$31 \times 34 \times 0.0508$	1.68	91.6	Polyimide based
Yan and Vandenbosch (2016)	$100 \times 100 \times 3$	2	45	Flexible high-permittivity substrate
Chen and Ku (2015)	$38 \times 38 \times 3$	2.2	60	FR4
Ullah et al. (2018)	$40 \times 35 \times 0.6$	1	50	Flexible photo paper
Proposed antenna	$20 \times 31 \times 0.3$	1.81	96	Flexible acrylic sheet

imitate a human body section. The radiation characteristics of the proposed antenna with $R_X = 60$ mm in both the radiation planes is shown in Fig. 3. The proposed antenna radiates a gain of 2.74 dBi in the broadside direction.

3.3 Performance Comparison of the Proposed Antenna with Other Wearable Antenna Designs

The performance comparison of the proposed antenna with other wearable antenna designs operating in 2.4 GHz ISM band is presented in Table 1. Compared to other antenna designs, the proposed antenna is compact in size and operates with comparable gain offering better radiation efficiency.

4 Conclusion

A low cost, compact, flexible acrylic sheet-based planar monopole antenna has been analyzed in this paper for wearable biomedical applications in different bending scenarios. The on-body integration of the proposed antenna shows stable performance with a good gain of 2.74 dBi in the broadside direction. The relatively small size of the antenna (20 mm × 31 mm) and 0.3 mm thickness makes it highly suitable for wearable biomedical applications.

References

Alemaryeen A, Noghanian S (2019) On-body low-profile textile antenna with artificial magnetic conductor. IEEE Trans Antennas Propag 67(6):3649–3656

Basir A, Yoo H (2019) A stable impedance-matched ultrawideband antenna system mitigating detuning effects for multiple biotelemetric applications. IEEE Trans Antennas Propag 67(5):3416–3421

Chen Y, Ku TA (2015) Low-profile wearable antenna using a miniature high impedance surface for smart watch applications. IEEE Antennas Wirel Propag Lett 15:1144–1147

Gao G-P, Hu B, Wang S-F, Yang C (2018) Wearable circular ring slot antenna with EBG structure for wireless body area network. IEEE Antennas Wireless Propag Lett 17(3):434–437

Liu LW, Kandwal A, Cheng Q, Shi H, Tobore I, Nie Z (2019) Non-invasive blood glucose monitoring using a curved Goubau line. Electronics 8(6):662

Mansour AM, Shehata N, Hamza BM, Rizk MRM (2015) Efficient design of flexible and low cost paper-based inkjet-printed antenna. Int J Antennas Propag 845042

Raad HK, Al-Rizzo HM, Abbosh AI, Hammoodi AI (2016) A compact dual band polyimide based antenna for wearable and flexible telemedicine devices. Progress Electromagnet Res C 63:153–161

Simorangkir RBVB, Kiourti A, Esselle KP (2018) UWB wearable antenna with a full ground plane based on PDMS-embedded conductive fabric. IEEE Antennas Wireless Propag Lett 17(3):493–496

Ullah MA, Islam MT, Touhidul A, Ashraf FB (2018) Paper-based flexible antenna for wearable telemedicine applications at 2.4 GHz ISM band. Sensors 18:4214. https://doi.org/10.3390/s18124214

Yan S, Vandenbosch GAE (2016) Radiation pattern reconfigurable wearable antenna based on metamaterial structure. IEEE Antennas Wirel Propag Lett 15:1715–1718

A Novel Encryption Technique to Protect Patient Health Information Electronically Using Playfair Cipher 15 by 14 Matrix

Nisarga Chand, Subhajit Bhattacharyya, and Angsuman Sarkar

Abstract Healthcare data such as patient name, DOB, address, phone number, fax number, E-mail address, etc., need to be kept private to protect patient privacy. It has been found that unauthorized person always try to get this information. With the help of proper encryption technique, we can protect the information. Play fair cipher is a very much well-known encryption technique for text messages. It is an example of a digraph substitution cipher. In this technique, pair of alphabets (digraphs) was encrypted instead of a single alphabet. That is why, it becomes so strong and not easy to break by conventional method. Play fair is fairly fast to apply and calls for no unique tools. It converts a plain text to cipher text message mathematically with the help of a secret key. Likewise, while restoring the original message from encrypted message, the same secret key has been used. However, the traditional play fair cipher supports only 25 uppercase alphabets. Here, in our work, we use 210 characters instead of 25 characters earlier, which make the cipher text stronger. These 210 characters include all the alphanumeric characters as well as 148 special characters supported by MATLAB. Here, we carried out cryptanalysis and found that the cipher is a strong one also it is thus almost impossible to be broken by any cryptanalytic attack. Finally, we have represented the final result with the help of MATLAB with two iteration steps.

Keywords Play fair cipher · Encryption · Iteration steps · Special characters · Cryptanalysis

N. Chand (✉)
Adamas University, Kolkata, India

S. Bhattacharyya
Mallabhum Institute of Technology, Bishnupur, Bankura, India

A. Sarkar
Kalyani Government Engineering College, Kalyani, Nadia, India
e-mail: angsumansarkar@ieee.org

M. Mukherjee et al. (eds.), *Advances in Medical Physics and Healthcare Engineering*, Lecture Notes in Bioengineering, https://doi.org/10.1007/978-981-33-6915-3_42

1 Introduction

In the year 2000 surprisingly, it has been found that many patients got free samples of medication recommendations for the disease they were just diagnosed a few months ago. The case amazed the patients that how the pharmaceutical companied came to know about their disease. A high level and prolonged investigation were initiated which proved that a physician, a pharmaceutical company, and a well-known pharmacy chain were involved in this case of the breach of confidentiality.

So, the government needed to come forward and create guidelines to protect patient privacy. Then, Health Insurance Portability and Accountability Act (HIPPA) comes into picture in the year 1996 (Cohen and Mello 2018). According to HIPPA, any information that can recognize a patient is regarded protected health information (PHI). Anything related to health, treatment or billing that could identify a patient is PHI. This includes (a) Name, (b) DOB, (c) Address, (d) Phone number, Fax number, (e) e-mail address etc.

Healthcare data generally means protected health information (PHI) which must be kept confidential, so that no unauthorized person can access it (Kayaalp 2018). The most common method to guard information is the technique of encryption and decryption. In encryption sender, conceal the message with a secret key following some sort of rules. These rules and the secret key are only known to the person who is supposed to receive the message. With the proper set of rules, the secret key receiver restores the original message that is referred to as symmetric encryption (Stallings 2006). The encryption method to protect the health information must be very strong, so that if somehow this information goes into wrong hand, it cannot be decoded very easily. The traditional encryption structure be made up of original message which needs to be encrypted, a set of rules called encryption algorithm, confidential key, cipher text, again a set of rules called decryption algorithm. We require a sturdy encryption algorithm with a view to encrypt the original message content into cipher text (Kahate 2007). The one who encrypt and transmit the message and the one who collect and decrypt the message have to acquire the confidential key, so that any third party cannot access it. Amidst each and every prevailing encryption algorithm, play fair cipher dominates.

The basic building block of play fair cipher algorithm is a 5 by 5 matrix and a secret keyword (Kahate 2007). Each element of this 5 by 5 matrix is filled by secret key first and then with alphabets which are not present in the keyword sequentially. Twenty-five English uppercase alphabets are only allowed in this algorithm, that is why we have enhanced the previous matrix size from 5×5 to 15×14, so that we can incorporate sixty-two alphanumeric as well as one forty-eight special characters in it.

Table 1 5 × 5 traditional play fair cipher matrix with keyword AMPHE

A	M	P	H	E
B	C	D	F	G
I/J	K	L	N	O
Q	R	S	T	U
V	W	X	Y	Z

2 Traditional Play Fair Cipher

Conventional play fair cipher uses a 5 × 5 matrix, and each element of this matrix is filled up by twenty-five distinct English alphabets (Khan 2015a). First the confidential keyword is placed without any repetition of letters while traversing row wise sequentially. Remaining elements of the matrix is being filled up by rest of the letters in alphabetical order. Here, we choose confidential keyword as "AMPHE," and the resultant conventional matrix is shown in Table 1.

Play fair cipher algorithm always consider I & J as one letter. It is visible that the policies of encryption practice a couple of plaintext characters. If there are even numbers of characters in the original message, then the algorithm works fine. But if somehow the original message consists of odd number of characters, then an extra letter X is appended after the termination of original message (Khan 2015b). In addition, if same letter found in any pair, then an extra letter X is inserted between them, and again new pair of letters are reconstructed.

The protocols are mentioned below:

(i) Original digraphs which is appeared in the same row are changed by the immediate right contents, also the first content of the row circularly attached with the last content. As an example, UV is converted to VW during the encryption process.
(ii) Original digraphs which is appeared in the same column are changed by the below contents in the matrix, also the top content of the column circularly attached with the last content. As an example, HF is converted to FP during the encryption process.
(iii) Most of the cases, if the digraphs are not mentioned in the same row or column, then choose other two intersecting points as a content of the rectangular shape. So that, SU is converted to LX, and CA becomes BM (Bhattacharyya et al. 2014).

3 Modified 15 × 14 Play Fair Cipher Algorithm

This revised play fair cipher algorithm uses a 15 by 14 matrix, 210 characters instead of 25 earlier, and a keyword. Out of 210 characters, 148 are special characters which are supported by MATLAB. The elements of the matrix are filled up by characters

Table 2 15 × 14 play fair cipher matrix with keyword Eagle$*&™

E	a	g	l	e	$	*	&	™	!	"	#	%	(	)
+	,	-	.	/	0	1	2	3	4	5	6	7	8	9
:	;	<	=	>	?	@	A	B	C	D	F	G	H	I
J	K	L	M	N	O	P	Q	R	S	T	U	V	W	X
Y	Z	\	_	`	b	c	d	f	h	i	j	k	m	n
o	p	q	r	s	t	u	v	w	x	y	z	{	|	}
~	¡	¢	£	¤	¥	¦	§	©	ª	«	¬	-	®	¯
°	±	²	³	´	µ	¶	·	¸	¹	º	»	¼	½	¾
¿	À	Á	Ã	Ã	Ä	Å	Æ	Ç	È	É	Ê	Ë	Ì	Í
Î	Ï	Ð	Ñ	Ò	Ó	Ô	Õ	Ö	×	Ø	Ù	Ú	Û	Ü
Ý	Þ	ß	à	á	â	ã	ä	å	æ	ç	è	é	ê	ë
ì	í	î	ï	ð	ñ	ò	ó	ô	õ	ö	÷	ø	ù	ú
û	ü	ý	þ	ÿ	Œ	œ	Š	š	Ÿ	Ž	ž	ƒ	ˆ	˜
–	—	‘	’	‚	“	”	„	†	‡	•	‰	‹	›	€

of keyword first from left hand side to right hand side and from upper to lower, and the remaining elements of the matrix are filled up by rest characters.

3.1 Assumption

In this algorithm implementation, two keywords are taken. First one is Eagle$*&™, and the second one is Blue@158™. With the assist of those two keywords, two new 15 by 14 matrices have been formed which are depicted in Tables 2 and 3.

3.2 Algorithm

- At first, user enter the message which needs to be encrypted.
- In the second stage, any space between the words of the entered message is removed.
- In the third stage, symbol "X" is inserted in the middle of two characters which are same.
- In the fourth stage, the output of the second stage is encrypted with the help of the keyword "Eagle$*&™".
- The output of the fourth stage is again encrypted with the help of the keyword "Blue@158™" in the fifth stage.
- For same row pair character if any one of the characters situated at last column, then during encryption, it becomes foremost column character. And for same

Table 3 15 × 14 play fair cipher matrix with keyword Blue@158™

<table>
<tr><td>B</td><td>l</td><td>u</td><td>e</td><td>@</td><td>1</td><td>5</td><td>8</td><td>™</td><td>!</td><td>"</td><td>#</td><td>$</td><td>%</td><td>&</td></tr>
<tr><td>(</td><td>)</td><td>*</td><td>÷</td><td>,</td><td>-</td><td>.</td><td>/</td><td>0</td><td>2</td><td>3</td><td>4</td><td>6</td><td>7</td><td>9</td></tr>
<tr><td>:</td><td>;</td><td><</td><td>=</td><td>></td><td>?</td><td>A</td><td>C</td><td>D</td><td>E</td><td>F</td><td>G</td><td>H</td><td>I</td><td>J</td></tr>
<tr><td>K</td><td>L</td><td>M</td><td>N</td><td>O</td><td>P</td><td>Q</td><td>R</td><td>S</td><td>T</td><td>U</td><td>V</td><td>W</td><td>X</td><td>Y</td></tr>
<tr><td>Z</td><td>\</td><td>_</td><td>`</td><td>a</td><td>b</td><td>c</td><td>d</td><td>f</td><td>g</td><td>h</td><td>i</td><td>j</td><td>k</td><td>m</td></tr>
<tr><td>n</td><td>o</td><td>p</td><td>q</td><td>r</td><td>s</td><td>t</td><td>v</td><td>w</td><td>x</td><td>y</td><td>z</td><td>{</td><td>|</td><td>}</td></tr>
<tr><td>~</td><td>¡</td><td>¢</td><td>£</td><td>¤</td><td>¥</td><td>¦</td><td>§</td><td>©</td><td>ª</td><td>«</td><td>¬</td><td>-</td><td>®</td><td>¯</td></tr>
<tr><td>°</td><td>±</td><td>²</td><td>³</td><td>´</td><td>µ</td><td>¶</td><td>·</td><td>¸</td><td>¹</td><td>º</td><td>»</td><td>¼</td><td>½</td><td>¾</td></tr>
<tr><td>¿</td><td>À</td><td>Á</td><td>Ã</td><td>Ã</td><td>Ä</td><td>Å</td><td>Æ</td><td>Ç</td><td>È</td><td>É</td><td>Ê</td><td>Ë</td><td>Ì</td><td>Í</td></tr>
<tr><td>Î</td><td>Ï</td><td>Ð</td><td>Ñ</td><td>Ò</td><td>Ó</td><td>Ô</td><td>Õ</td><td>Ö</td><td>×</td><td>Ø</td><td>Ù</td><td>Ú</td><td>Û</td><td>Ü</td></tr>
<tr><td>Ý</td><td>Þ</td><td>ß</td><td>à</td><td>á</td><td>â</td><td>ã</td><td>ä</td><td>å</td><td>æ</td><td>ç</td><td>è</td><td>é</td><td>ê</td><td>ë</td></tr>
<tr><td>ì</td><td>í</td><td>î</td><td>ï</td><td>ð</td><td>ñ</td><td>ò</td><td>ó</td><td>ô</td><td>õ</td><td>ö</td><td>÷</td><td>ø</td><td>ù</td><td>ú</td></tr>
<tr><td>û</td><td>ü</td><td>ý</td><td>þ</td><td>ÿ</td><td>Œ</td><td>œ</td><td>Š</td><td>š</td><td>Ÿ</td><td>Ž</td><td>ž</td><td>ƒ</td><td>ˆ</td><td>˜</td></tr>
<tr><td>–</td><td>—</td><td>‘</td><td>’</td><td>‚</td><td>“</td><td>”</td><td>„</td><td>†</td><td>‡</td><td>•</td><td>‰</td><td>‹</td><td>›</td><td>€</td></tr>
</table>

column pair character if any one of the characters situated at first column, then during encryption, it becomes rearmost row character. This is a very vital rule for encryption.

- Next, in the sixth stage, we decrypt the output of fifth stage with Keyword "Blue@158™" and then again decrypt the output of fourth stage with the keyword "Eagle$*&™".
- The above-mentioned vital rule for encryption is also applied in case of decryption process.
- From the last stage, we get the original message back which is the output of step number two.

3.3 Simulation Flowchart

See Fig. 1.

3.4 Matrix Formation with Keyword

See Tables 2 and 3.

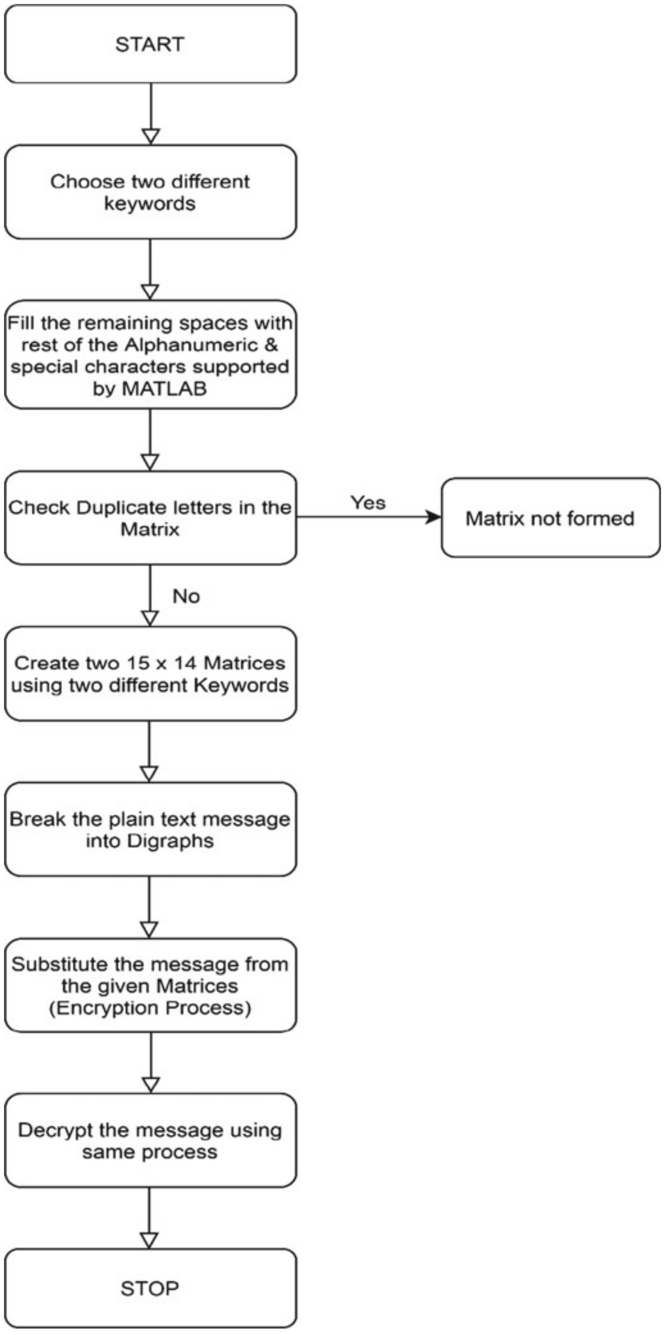

Fig. 1 Flowchart of encryption & decryption process using 15 × 14 play fair cipher matrix

4 Cryptanalysis of Modified Cipher

Encryption is used to protect the information from attackers who are always tried to decrypt the original message from encrypted text. Different forms of cryptanalytic attacks are discussed below.

- As the matrix size is 15 × 14, we can choose the secret key in 210! (Factorial 210) different ways. So, it can be easily concluded that it is immune to brute force attack.
- If frequency analysis cipher text attack is used to decrypt the message, then also number of combinations to be searches would be 210 * 210 = 44,100.
- But if somehow attacker knows the encrypted message and original message behind this encrypted message, then he can easily get the key and decrypt all the message encrypted using this key.

5 Advantages of 15 × 14 Play Fair Cipher Algorithm

The primary downside of conventional play fair cipher is that original message can be constructed using only 25 English uppercase alphabets. One cannot include lowercase English alphabets, special characters, and decimal numbers in it. To triumph over the disadvantages, we put into effect a changed cipher which employs a 15 × 14 matrix to be able to incorporate nearly all of the printable characters supported through MATLAB. So, any secret message can be encrypted with the help of this methodology.

6 Experimental Result

To implement the modified play fair cipher 15 by 14 matrix, we have used MATLAB. In Fig. 2, we have presented the result that we have obtain in MATLAB. From the figure, one can easily identify original text message, two strong encrypted message and finally decrypted message which is same as original message.

7 Conclusion

The main objective of this paper was to secure healthcare data of patient which is at risk now a days according to survey conducted by different agencies. For this purpose, a new strong encryption technique has been demonstrated here. In our work, we have used the original play fair cipher concept and enriched it by adding more features into it. Also, the limitations of earlier play fair cipher matrices like 5 × 5, 6

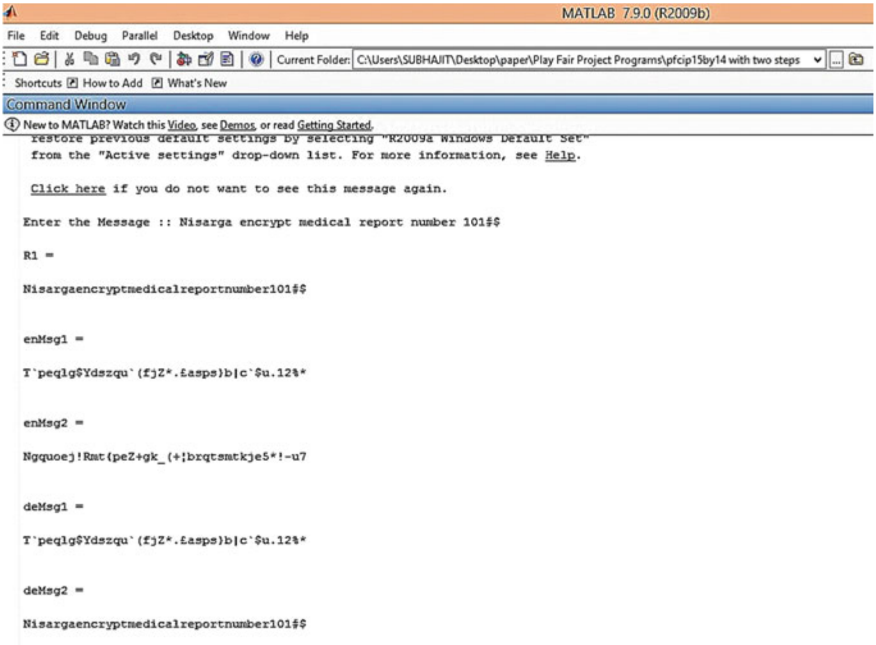

Fig. 2 Output of 15 × 14 play fair cipher algorithm

× 6 and 10 × 9 have been eliminated in this work. Here, we have enriched the basic play fair cipher by adding two additional features. First one is enhanced matrix size which is of size 15 × 14. As the matrix size is increased, we can easily incorporate more characters into our matrix. So, the second additional feature is incorporation of almost all characters supported by MATLAB into our new enhanced matrix. So naturally, it has been found that our encrypted message looks very strong than earlier one. For further enhancement of our work, two key can be used one for encryption of message and other for decryption of message. Also, modern encryption method such as steganography can be included to enrich the security of information. So, at last, we can conclude that this work can help the people in coming future so secure their medical privacy.

References

Bhattacharyya S, Chand N, Chakraborty S (2014) A modified encryption technique using playfair cipher 10 by 9 matrix with six iteration steps. Int J Adv Res Comput Eng Technol 3:307–312

Cohen IG, Mello MM (2018) HIPAA and protecting health information in the 21st century. JAMA 320(3):231–232. https://doi.org/10.1001/jama.2018.5630

Kahate A (2007) Cryptography and network security, 2nd edn. Tata McGraw-Hill Publishing Company Limited, New Delhi

Kayaalp M (2018) Patient privacy in the era of big data. Balkan Med J. 35(1):8–17. https://doi.org/10.4274/balkanmedj.2017.0966

Khan SA (2015a) Design and analysis of playfair ciphers with different matrix sizes. Int J Comput Netw Technol 3:117–122

Khan SA (2015b) Design and analysis of playfair ciphers with different matrix sizes. Int J Comput Netw Technol 3(3):117–122

Stallings (2006) Cryptography and network security: principles and practice, 4th edn. Prentice Hall

Study on Resource Monitoring of E-Healthcare System

Riya Sil, Naren Debnath, and Abhishek Roy

Abstract The recent outbreak of global pandemic of coronavirus (COVID-19) has shown us a wide scope of improvement in electronic healthcare management. It is very much visible since the patients have to avail medical facilities thereby maintaining the rules of social distancing and isolation to break the chain of virus transmission within the society. To achieve this objective, advanced information and communication, technology-based video conferencing tools may be widely used to deliver medical consultancy to the patients in this pandemic situation. Since this entire electronic communication is dependent on the internet, which is itself an open digital space, this electronic communication between the patients and the medical practitioners are highly susceptible to infringement attempt of the adversary. Even the hardware component used by the patients during this electronic healthcare transaction like the camera, speaker, etc. of the end-devices may remain under the control of adversary even after the completion of the electronic transaction. As a result, the adversary may record any personal moment or personal file system of the user without its knowledge. To de-escalate and arrest the access of adversary over the resources of user, it is pertinent to study the risk factors and their security protocols in similar cases to manage the vulnerabilities and to propose the enhanced security model to ensure the integrity of the electronic healthcare transaction. In this paper, authors have studied those existing security protocols to propose a secured audio and video conferencing system through wired and wireless network with control and command of all the resources with the actual user only. The objective of this study is to maintain a logfile in a secure manner to note down the access and release of resources during the audio and video conference.

Keywords Resource monitoring · Log maintenance · Security protocol

---

R. Sil (✉) · N. Debnath · A. Roy
Adamas University, Kolkata, West Bengal, India

M. Mukherjee et al. (eds.), *Advances in Medical Physics and Healthcare Engineering*, Lecture Notes in Bioengineering, https://doi.org/10.1007/978-981-33-6915-3_43

1 Introduction

The recent outbreak of coronavirus (COVID-19) infection has led to enormous number of problems in our daily life. In a country like India, where Information Technology is one of the biggest hubs (Khomiakova 2007), everything is getting digitized to avoid the spread of infection through contamination. It is getting reflected most in the field of communication where humans are making it a regular practice to communicate through online medium to follow the rules of social distancing and isolation to break the chain of virus transmission within the society. Healthcare is one such sector where nowadays most of the work is done online (Alam et al. 2018) to avoid contamination with the deadly coronavirus. The security services (Pirbhulal et al. 2019) have advanced in the e-healthcare system (Hamza et al. 2020) or electronic healthcare system.

The usage of online healthcare has helped in providing online medical facilities to peoples that includes patients, doctors, and others. The entire communication take place over the internet, that is, itself an open digital space. Therefore, the details that have been shared over the internet have suddenly become more critical for any service sector and is highly vulnerable to transgression attempt of the adversary (Vora et al. 2018). For example, if there is an important company call, one has a high chance that the data might get stolen. Similarly, in healthcare sector, if a patient is talking to his doctor, with a highly sensitive healthcare issue, there is a high chance of the information to fall into the hands of a cybercriminal who might be waiting to steal the identity of the person to commit fraud or identity theft (Kagan et al. 2020).

The authors have organized the remainder of the paper as follows. Section 2 explains about the risk factors of online video conference, i.e., hardware and software risks. Section 3 discusses on literature survey on recent vulnerabilities/attacks. Section 4 mentions the literature survey on recent security protocols. Section 5 finally concludes the discussion of the paper and also explores the knowledge gained and future scope of this research work.

2 Risk Factors of Online Video Conference

For the past few months since the outbreak of coronavirus in the society, videoconferencing and teleconferencing (Celio et al. 2017) have been leading the society by helping people to communicate with each other. Use of tools for online communication has suddenly increased ever since the lockdown period had started to control the spread of the virus (Ko et al. 2004). Unfortunately, the rush to work from home and the immense pressure of office had introduced a huge amount of data leakage risks and has led to many security hazards (Rousmaniere et al. 2014). Specially in case of video conferencing that can lead to vulnerable confidentiality and security fissures. Some of the video conferencing tools like Microsoft Teams, Zoom, WebEx Meetings, Google Hangout, and many more makes daily communication easier. Meeting people like colleagues, doctors, or friends are just a click away (Tsai et al. 2010). But this process of transmission can make a pathway for the access of data or information by the cybercriminals thus one should know the risk factors before making a video call. Privacy is a huge concern when it comes to online video conferencing (Newman et al. 2009). The policies related to privacy of video conferencing are broad, therefore it enables to store enormous number of data and information that may include messages, files, recordings, documents, videos, and others.

Risks can be both hardware or software-related. Authors have provided a brief on Hardware and software-related risks to get a clear view of the vulnerabilities.

2.1 Hardware Risk

The hardware component used by the patient during this electronic healthcare transaction like the camera, speaker, etc. of the end-devices may remain under the control of adversary even after the completion of the electronic transaction. The web camera is one such device that provides the user with a window to the world (Vijayalakshmi and Arockiam 2018). This component is most vulnerable as it captures videos and still images and if any adversary has access to it, they may use it in some unfair way (Rajabai and Sivanantham 2020). The device encryption is most important while using online tools and camera for live communication. Other components like speakers are also vulnerable (Dhanvijay and Patil 2019) as in online meeting the adversary may capture private conversation of the authenticated users. Encryption of hardware components is thus of utmost importance as in case of live communication, streaming over camera, speaker, etc. could easily be tracked and captured (Pal et al. 2019).

2.2 Software Risk

Privacy is a serious concern. Policies related to confidentiality of video conferencing (Joseph et al. 2009) are broad therefore permitting it to collect and store wide range of data that may include documents that are shared over screen, cloud recordings, files, messages, videos, and others. For example, in online healthcare system, Voice over the Internet Protocol (VoIP) systems (Chong and Matthews 2004) play an important role in e-healthcare system. VoIP includes different software applications such as Skype, Adobe Connect Now, ooVoo, etc. for telerehabilitation (TR) therapy (Chong and Matthews 2004). It also allows communication between patients and therapists with both voice and video teleconferencing using Internet connection instead of regular phone calls. Many questions have been raised by people from different fields like information technologists and other healthcare entities regarding privacy policies and other security applications. The Health Insurance Portability and Accountability Act of 1996 (HIPAA) is a federal law for the creation of national standards to protect sensitive data of patient's health related information from getting disclosed without consent of the patient and his knowledge also compliance with these protocols.

3 Literature Survey on Recent Vulnerabilities/Attacks

Due to the severe spread of coronavirus, every person is facing global containment that is leading people to communicate through online mode. But this method of communicating through internet to avoid contamination can be dangerous when it comes to sharing data through telecommunication or video communication. In order to use online medium for communication such as Zoom, Google Duo, Microsoft Teams, other online medium privacy is to be maintained to safeguard valuable information. Many people are unaware of the vulnerabilities and risks related to online communications. Therefore, to bring awareness regarding the vulnerabilities and attacks of these online medium of communication, authors have done literature survey on significant security protocols that would provide a brief overview of the breaches related to security.

3.1 Zooming into Video Conferencing Privacy and Security Threats

Kagan et al. (2020) have mentioned about the malicious use of information in the form of facial images, usernames, recorded audio and videos, personal information, etc. in video conferencing. Moreover, video conferencing software is much more susceptible for unpaid users as it is an unencrypted communication and therefore allows execution of malware software at the participant's system. If a malicious user gains access for any video conferencing meeting the following malicious usage may be seen: (i) Collection of samples of facial image, voice, and shared personal data over the meeting. (ii) Usage of deepfake tools that may help in hiding the identity of a person and allow him to join meetings by using other's identity. The collected personal data of participants can be used to compromise safety.

3.2 Face Recognition and Privacy in the Age of Augmented Reality

Acuisti et al. (2014) have proposed a system that can identify which students are strolling through the campus with the help of facial recognition by collecting facial images from Facebook. In their paper, authors have also enlisted and explained about different privacy risks over online meetings that include Cyberbullying, Information

Leakage, Malware Attacks, Phishing Attack, Face Recognition Attack, Data Breach, Fake Avatars, and Zoom-bombing Campaign.

3.3 Coronavirus (COVID-19)—'Zoom' Application Boon or Bane

In another study made by Chawla (2020), the popularity of Zoom online video conferencing software and its vulnerabilities have been discussed in detail. According to his study, cybersecurity cases had increased by 82.5% as more and more people are working online due to pandemic and lockdown. He has focused on different Zoom-bombing attacks that took place where an uninvited person having meeting details had logged into the online meeting and had posted some random, disrupting images and/or pornographic contents. He also mentioned that more than 500,000 Zoom accounts have been sold to hacker's forum and some unethical websites. In addition to this, there are other attacks called zoomraids where mass zoom-bombing happened and the attendees were harassed and abused. With data mining capabilities of zoom, some of the hackers got access to LinkedIn accounts of the attendees. Due to these vulnerabilities some of the countries across the world had banned zoom for any kind of online meeting, conference, or any medical prognosis.

3.4 Facebook Spying on Instagram Users Through Cameras, Lawsuit Alleges

In an article, Robert Burnson (Facebook 2021) mentioned about how Facebook was sued for spying other applications through cameras. The incident took place in New Jersey where Britney Conditi, a user of Instagram was spied on. Facebook was accused and suspected for intentional spying and collecting valuable information on the users. This fact was denied by Facebook.

3.5 Risk and Remedies of E-Governance Systems

Another risk in that of government information that consists of all the data of the citizens. Roy and Karforma (2011) in their paper had mentioned about the attacks on E-Governance system. The most vulnerable attack is the attack over government scope as it consists of public information. In this paper, authors have discussed about attacks that affected E-Governance systems that consists of (i) Malicious Website, (ii) Violation of Citizen's Privacy through the use of Cookies, (iii) Citizen impersonation,

(iv) Spamming and Flaming, (v) Teardrop, (vi) Intranet associated threats, (vii) Risk associated with malicious code.

From the survey discussed, in this section, it can be concluded that online video conferencing is very risky and vulnerable if proper security protocol is not followed.

The following section discusses about some of the security protocols that have been proposed in recent times and are of prime importance.

4 Literature Survey on Recent Security Protocols

As each one of us are experiencing a global containment, we are bound to consult or communicate over the internet to maintain social distancing and save ourselves from getting contaminated by this lethal virus (COVID-19). In order to use online medium for communication such as Zoom, Microsoft Teams, etc., privacy is to be maintained to safeguard valuable information. To bring awareness about the secure usage of these online tools, authors have done literature survey on significant security protocols that are given in the following subsection.

4.1 A Privacy-Preserving Cryptosystem for IoT E-healthcare

In this paper, Hamza et al. (2020) have proposed an IoT-based Symmetric block encryption cryptosystem with fast and secure probabilistic chaos-based image cryptosystem to guarantee confidentiality of extracted keyframes of Wireless Capsule Endoscopy. It is based on confusion and diffusion operations and can prevent exhaustive, differential, and statistical attacks.

4.2 A Joint Resource-Aware and Medical Data Security Framework for Wearable Healthcare Systems

In another paper, Pirbhulal et al. (2019) proposed a Biometric-region security framework for resource-constrained wearable health monitoring systems by extracting heart beat from ECG signals. Analysis has been done that biometric features based on time-domain play an important part in enhancing security of IoMT-based medical applications. It works on bio-keys generation mechanism.

4.3 Secure Surveillance Mechanism for a Medical Healthcare System with Enabled IoT (Sensors) by Intelligently Recorded Video Summary into the Server and Keyframes Image Encryption

Khan et al. (2020) have discussed in their paper about the two-fold aspect that includes a well-organized keyframe extraction mechanism. With these extracted keyframes, the final decision of pre-occurred activities will be taken for high security. To create and show complex new chaos behavior, Cosine-transform-based chaotic sequence have been used as non-linear transform.

4.4 Hybrid Security Techniques to Protect Sensitive Data in E-healthcare Systems

Vijayalakshmi and Arockiam (2018) has discussed about the hybrid security techniques that include Data Obfuscation and Encryption Techniques in their paper to ensure data confidentiality and protection of sensitive data in electronic healthcare system.

4.5 Towards Seamless Authentication for Zoom-Based Online Teaching and Meeting

In another paper, Mohanty and Yaqub (2020) had discussed about the problems related to Zoom bombing and how it can be prevented Photo Response Non-Uniformity (PRNU) based camera authentication and others.

4.6 Blind Signatures Based Secured E-Healthcare System Discusses About the Blind Signature and Cloud Service Provider

Vora et al. (2018) in their paper had proposed a blind signature and cloud service provider built for the security of electronic healthcare system. It provides a detailed view of all the threat models related to e-healthcare system.

4.7 G. Secure and Fine-Grained Access Control on E-Healthcare Records in Mobile Cloud Computing

According to the paper, the authors, Liu et al. (2018) have provided a brief idea about the Electronic Health Record (EHR) Security and have proposed a Fine-grained EHR access control scheme in which offline cipher-texts can be generated by the owner even before knowing about the EHR data and access policies.

5 Conclusion

In this paper, the authors have proposed a survey on recent vulnerabilities/attacks and on the existing security protocols that will help in designing a secured audio and video conferencing system through wired and wireless networks with control and command of all the resources with the actual user only. The authors have successfully maintained a logfile in a secured manner to note down the access and release of resources during the audio and video conference.

5.1 Knowledge Gained

The authors had done a detailed study on the existing security protocols that will help in proposing a secured audio and video conferencing system through wired and wireless network with control and command of all the resources with the actual user only. Authors have successfully studied the risk factors and protocols and maintained a logfile in a secure manner to note down the safety measures to access and release of resources during the audio and video conferencing.

5.2 Future Direction

The research work will proceed further by de-escalating the risk factors for larger benefits of the society. As the future scope of this research survey, the authors will propose an enhanced security model to ensure the integrity of the electronic healthcare transaction system.

Acknowledgements The authors would like to convey their heartiest thanks to the reviewers for their comments and insight.

References

Acquisti A, Gross R, Stutzman FD (2014) Face recognition and privacy in the age of augmented reality. J Privacy Confid 6(2):1

Alam MM, Malik H, Khan MI, Pardy T, Kuusik A, Le Moullec Y (2018) A survey on the roles of communication technologies in IoT-based personalized healthcare applications. IEEE Access 6:36611–36631

Celio MA, Mastroleo NR, DiGuiseppi G, Barnett NP, Colby SM, Kahler CW, Operario D, Suffoletto B, Monti PM (2017) Using video conferencing to deliver a brief motivational intervention for alcohol and sex risk to emergency department patients: a proof-of-concept pilot study. Addict Res Theory 25(4):318–325

Chawla A (2020) Coronavirus (COVID-19)—'Zoom' application boon or bane. Available at: SSRN 3606716

Chong HM, Matthews HS (2004) Comparative analysis of traditional telephone and voice-over-Internet protocol (VoIP) systems. In: IEEE international symposium on electronics and the environment, 2004. Conference record. 2004. IEEE, pp 106–111

Dhanvijay MM, Patil SC (2019) Internet of Things: a survey of enabling technologies in healthcare and its applications. Comput Netw 153:113–131

Facebook (2021) Facebook spying on Instagram users through cameras, Lawsuit Alleges. https://gadgets.ndtv.com/apps/news/facebook-spying-on-instagram-users-through-cameras-lawsuit-alleges-2297332. Accessed 21 Oct 2020

Hamza R, Yan Z, Muhammad K, Bellavista P, Titouna F (2020) A privacy-preserving cryptosystem for IoT E-healthcare. Inf Sci 527:493–510

Joseph A, Tang H, Zhang L, Skelly PA (2009) U.S. Patent No. 7,577,131. U.S. Patent and Trademark Office, Washington, DC

Kagan D, Alpert GF, Fire M (2020) Zooming into video conferencing privacy and security threats. arXiv preprint arXiv:2007.01059

Khan J, Li JP, Ahamad B, Parveen S, Haq AU, Khan GA, Sangaiah AK (2020) SMSH: secure surveillance mechanism on smart healthcare IoT system with probabilistic image encryption. IEEE Access 8:15747–15767

Khomiakova T (2007) Information technology clusters in India. Trans Stud Rev 14(2):355–378

Ko H, Jung J, Kim J, Shim SW (2004) Cross-cultural differences in perceived risk of online shopping. J Interact Advert 4(2):20–29

Liu Y, Zhang Y, Ling J, Liu Z (2018) Secure and fine-grained access control on e-healthcare records in mobile cloud computing. Future Gener Comput Syst 78:1020–1026

Mohanty M, Yaqub W (2020) Towards seamless authentication for Zoom-based online teaching and meeting. arXiv preprint arXiv:2005.10553.

Newman C, Martin E, McGarry DE, Cashin A (2009) Survey of a videoconference community of professional development for rural and urban nurses

Pal S, Hitchens M, Varadharajan V, Rabehaja T (2019) Policy-based access control for constrained healthcare resources in the context of the Internet of Things. J Netw Comput Appl 139:57–74

Pirbhulal S, Samuel OW, Wu W, Sangaiah AK, Li G (2019) A joint resource-aware and medical data security framework for wearable healthcare systems. Future Gener Comput Syst 95:382–391

Rajabai CP, Sivanantham S (2020) Analysis of hardware implementations of deblocking filter for video codecs. Int J Mater Prod Technol 60(2–4):214–235

Rousmaniere T, Abbass A, Frederickson J, Henning I, Taubner S (2014) Videoconference for psychotherapy training and supervision: two case examples. Am J Psychother 68(2):231–250

Roy A, Karforma S (2011) Risk and remedies of E-governance systems. Orient J Comput Sci Technol (OJCST) 4(02):329–339

Tsai HH, Tsai YF, Wang HH, Chang YC, Chu HH (2010) Videoconference program enhances social support, loneliness, and depressive status of elderly nursing home residents. Aging Mental Health 14(8):947–954

Vijayalakshmi AV, Arockiam L (2018) Hybrid security techniques to protect sensitive data in E-healthcare systems. In: 2018 international conference on smart systems and inventive technology (ICSSIT). IEEE, pp 39–43

Vora J, DevMurari P, Tanwar S, Tyagi S, Kumar N, Obaidat MS (2018) Blind signatures based secured e-healthcare system. In: 2018 international conference on computer, information and telecommunication systems (CITS). IEEE, pp 1–5

A Survey on Current Trends in Human Action Recognition

Bibhas Das and Anirban Saha

Abstract Human action recognition is a challenging area of research in the field of computer vision due to its complex analytical structure. Researches have been carried out in this field over the past few years. Now, as it has become possible to recognize human action successfully, the researchers are trying to make the recognition system real time in nature. But due to its complex video analysis, it has not been possible for the researchers to make it real time completely. Though some algorithms had been developed that will successfully recognize human action with the minimum delay possible in order to make the recognition system almost real time in nature. In this work, we have compared some of the successful human action recognition methodologies along with the recent trends to accomplish the task in negligible time delay.

Keywords Action recognition · Human motion · Recognition model · Real-time human action · Convolution neural network · Machine instance learning · Optical flow · Auto encoder

1 Introduction

Human action recognition is an area of study in the field of computer vision which aims to analyze video or image sequence in order to classify different actions performed by human that are detected in the given video or image sequence. In other words, it aims to track, understand, and analyze human movements that is continuously captured by sensors.

Human action recognition is an interdisciplinary challenging field having grand applications with social, commercial, and educational benefits (Kale and Patil 2016) which includes visual surveillance system, robotics, human computer interaction, etc.

B. Das (✉)
Adamas University, Barasat, Kolkata 700126, India

A. Saha
Indian Institute of Technology, Patna 801106, India
e-mail: anirban.saha@ieee.org

M. Mukherjee et al. (eds.), *Advances in Medical Physics and Healthcare Engineering*, Lecture Notes in Bioengineering, https://doi.org/10.1007/978-981-33-6915-3_44

The main challenge lies in how to design an effective human action representation that is sufficiently descriptive while computationally efficient. Because of complexity and uncertainty in human action recognition, consistent accurate action identification is a challenging task.

Human action recognition system is based on systematic approach of understanding and analyzing the motion of humans in captured content. It comprises of the fields which includes video processing, machine vision, artificial intelligence, etc. Some of the premier applications of the human action recognition system are discussed below.

Surveillance: Today different highly secured areas of any organization requires 24×7 human monitoring system. On a general case, it is observed that only after a mishap has occurred, a concerned person regrets for not analyzing the situations that had led to the mishap. In this cases, the human action recognition-based surveillance system can analyze the event online and give a appropriate result using predefined human motion and behavioral analysis which can have the real-time processing capability. This has a high potential application in military, security, and commercial domain.

Robotics: In recent time, robotics is one of the major area of concern. Researchers are in the verge of developing advanced robotic system that can mimic almost every human activity as well as human intelligence. In this emerging field, modeling of human action or activity plays an important role. This modeling can be critical in some cases where it is necessary for the robotic system to conclude some decision based on the result of this model. So, in this case, the accuracy of the model plays a vital role.

Sports Analysis: It is widely used by the sports persons and the team committee members to understand and analyze the pattern of different players across the world. Most of the sports analysis are being done manually till date which sometimes lead to some unavoidable miscalculations. So some research committees are trying hard to automate this analysis system. In order to do so, human action recognition technique is highly important.

There exists varied applications having various representation of human motion along with different recognition model. Human action recognition is a general term, and it is the application that decides duration of the movement of body along with the parts involved. Human to computer interaction generally involves only hand movement, whereas complicated application requires whole body movement such as in sports. Human motion is divided into gestures, activity, action, interaction, and group activity depending on the complexity. Approach of 2D representation is in stick figure or kinematic, whereas 3D representation is defined by shape model, image model, and kinematics. Normal recognition requires single-layered approach, whereas complex recognition requires multi-layered approach.

Human action recognition involves analysis over a range of image frames in order to arrive at a particular conclusion. It is unable to conclude a particular action by processing a single frame. Due to this analysis over multiple image frames, a short latency is inherent in every such models which is proportional to the constant number of continuous image frames that is taken into consideration to detect a particular action in a given model.

This paper discusses various frameworks of human action recognition system that had proved to be persistent in recent modeling of the required systems.

2 Action Recognition Methods

In this section, a brief survey of some of the concepts proposed by different research team working in the field of human action recognition is discussed. All the methods discussed in this section have been taken from article Dhamsania and Ratanpara (2016) and verified accordingly. This will provide a clear idea about the techniques that has been explored in the field of human action recognition which are not real time in nature.

2.1 Method 1

In the approach proposed in article Antic et al. (2013), multiple instance learning is utilized for subsequent action classification. Features such as trajectory, HOG, HOF, and MBH are calculated, and bag of feature encoding techniques are used followed by SVM classifier to accomplish the desired goal. Model sketch for this method is provided in Fig. 1.

It was implemented on the dataset entitled Hollywood2 and was successful to provide an accuracy of 57.42% and 59.80% for full sequence and combined sequence classifier, respectively. The limitation of this technique is its failure when full body motion is not clearly visible.

2.2 Method 2

The framework proposed in article Nguyen and Yoshitaka (2014) uses three-layer convolutional neural network along with independent subspace analysis and principal component analysis for recognizing human interaction from segmented and unsegmented videos. Model sketch for this method is provided in Fig. 2.

It was implemented on the dataset named UT-Interaction and proved to be one of the best technique by giving an accuracy of 90–93% when used over segmented videos and 85–90% when used over unsegmented videos. But spatial and temporal localization of the recognized activities are not possible using this approach.

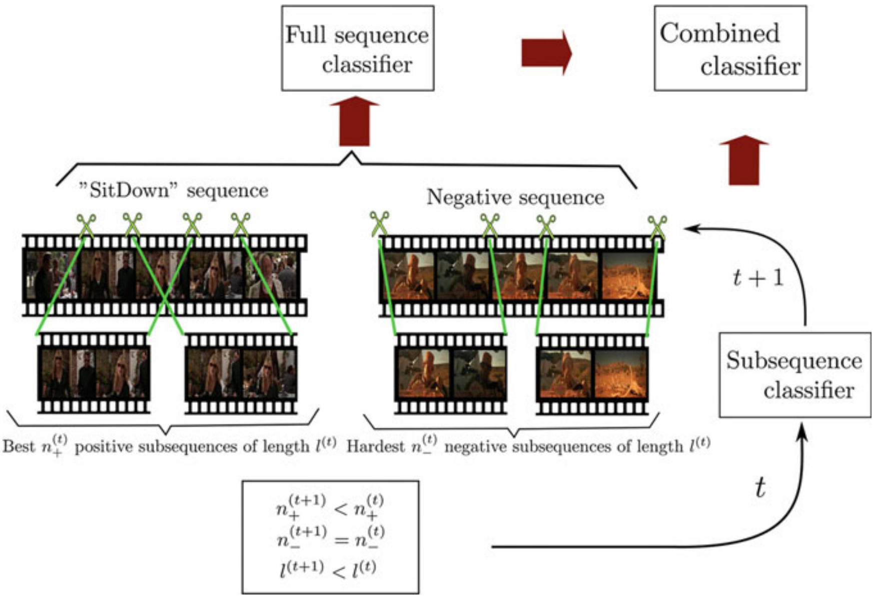

Fig. 1 Method 1 sketch analysis (Antic et al. 2013)

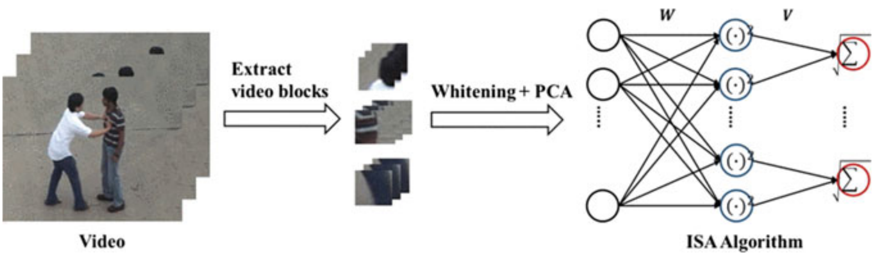

Fig. 2 Method 2 sketch analysis (Nguyen and Yoshitaka 2014)

2.3 Method 3

The method described in article Kong et al. (2014) uses two main models which are termed as attribute model and interaction model. Besides this model, an extra layer of data-driven phrase (DDP) technique is applied on the training data. Model sketch for this method is provided in Fig. 3.

This method was tested on BIT-Interaction, UT-Interaction, and collective activity datasets and provided the accuracy of 90.63, 91.67, and 82.54% on the respective datasets. In this method, there is a need to manually label attributes in each video and specify connectivity between attributes and phrases. Moreover, it does not consider

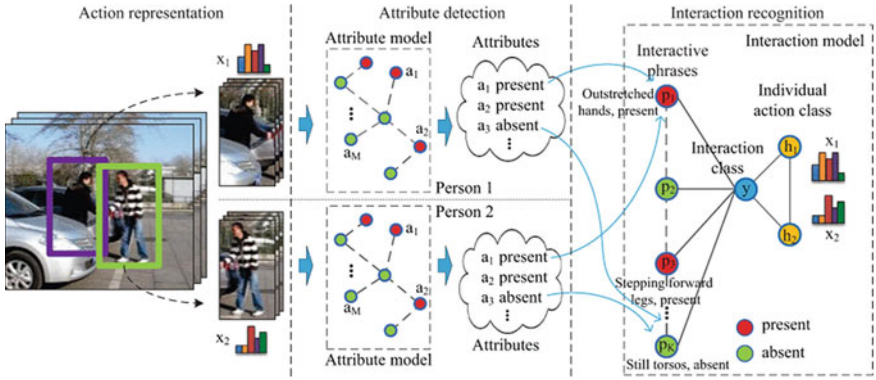

Fig. 3 Method 3 sketch analysis (Kong et al. 2014)

temporal dependencies in phrases and attributes, and due to this, the system may get confused between different types of interaction.

2.4 Method 4

The approach described in article Zhang et al. (2014) demonstrate a flow that detects the optical flow field of motion salient pixels from the region of interest followed by the computation of self-similarity matrix along with the usage of Fischer encoding technique. Then, using the computed motion interchange pattern, a support vector machine is trained to achieve the desired goal. Model sketch for this method is provided in Fig. 4.

But this process gave a very low accuracy of 50.1% when tested on TV human interaction dataset.

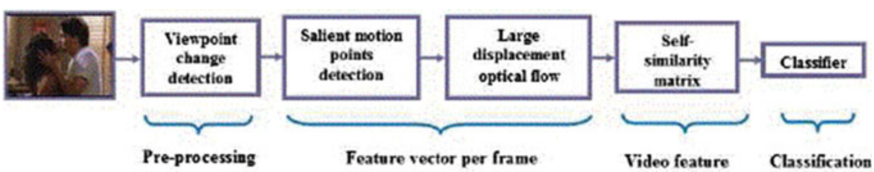

Fig. 4 Method 4 sketch analysis (Zhang et al. 2014)

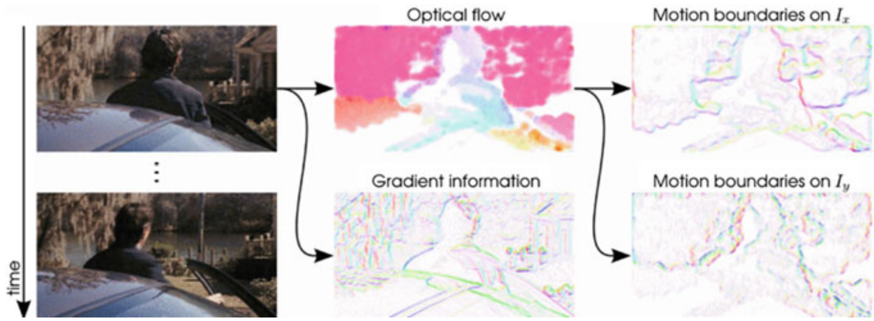

Fig. 5 Method 5 sketch analysis (Wang et al. 2011)

2.5 Method 5

The technique used in article Wang et al. (2011) for human action recognition utilizes dense trajectories with the computation of features which included optical flow, trajectory, HOG, HOF, and MBH followed by the generation of codebook with the help of bag of features concept. Then, a SVM is trained which is used for further classification. Model sketch for this method is provided in Fig. 5.

It had resulted providing a comparatively low accuracy of 58.3% when implemented on a dataset Hollywood2.

2.6 Method 6

The method that is proposed in article Marín-Jiménez and de la Blanca (2013) firstly detects the region of interest that consists the upper body of the actor. Then, the optical flow between interest regions of successive frame is calculated. After this calculation is done, the pyramid of accumulated histogram of optical flow descriptor is computed. Then, for classification purpose, the concept of bag-SVM is utilized. Model sketch for this method is provided in Fig. 6.

This approach is not completely validated but it provided a low accuracy of 46.3% during its testing phase on TV human interaction dataset.

Fig. 6 Method 6 sketch analysis (Marín-Jiménez and de la Blanca 2013)

2.7 Method 7

In the framework described in article Yun et al. (2012), classification of human interaction is carried out using body pose features. For this, joint features of skeleton are extracted using the skeleton features extraction method, and the concept of MIL is also used. Model sketch for this method is provided in Fig. 7.

The framework is tested for the videos from specific viewpoint and gave the accuracy of 87.3% when applied on RGBD videos captured using Microsoft Kinect Sensors.

3 Real-Time Action Recognition Methods

Present day research on real-time human action recognition aims to reduce the recognition latency to such a extent that it becomes almost negligible for a human eye to detect (without compromising the considerable accuracy). Recent research result in this domain validates that the researchers are successful in accomplishing the desired goal. Recent systems with built-in real-time human action recognition module recognizes the action within a fraction of second.

In this section, we will be discussing about the most recent technology that had provided successful results in the more precise domain of real-time human action recognition. To make the model behave like a real-time model, these methodologies will process a very small number of continuous image frames in order to classify a particular action performed by humans. The number of frames considered is so less that it becomes impossible for a human to detect the delay.

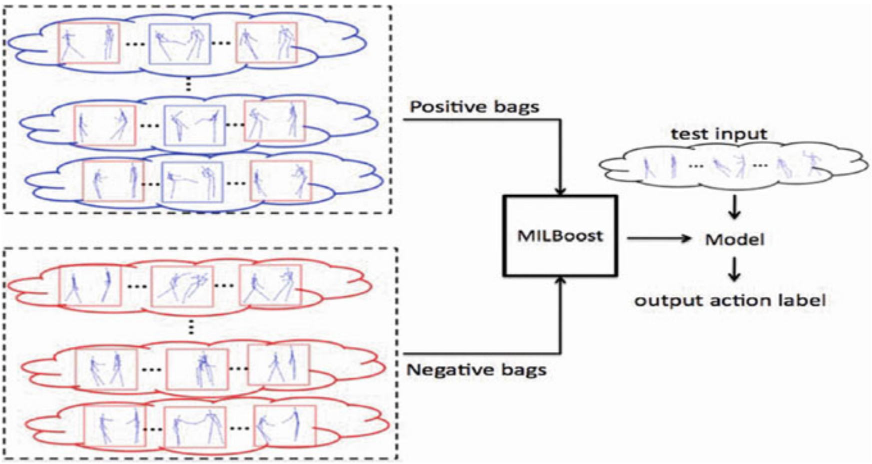

Fig. 7 Method 7 sketch analysis (Yun et al. 2012)

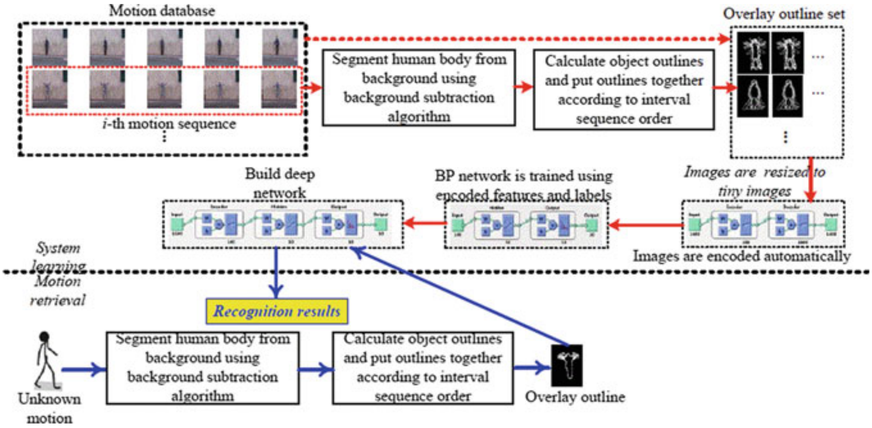

Fig. 8 Method 8 sketch analysis (Xiao and Si 2017)

3.1 Method 8

The methodology described in article Xiao and Si (2017) uses a deep neural network for its benefit. During the training phase, the foreground objects are extracted from the labeled dataset, and the outlines are calculated which is then combined together to build a set of overlay images. Based on these set of overlay images, an auto encoder along with a pattern recognition neural network is trained sequentially. Now, these two components are combined to construct a deep neural network which is then utilized for classification. Model sketch for this method is provided in Fig. 8.

This process provided an average accuracy of 96% and has a small requirement for training time and network size.

3.2 Method 9

The model structure stated in article Li et al. (2016) consisted of several phases. The first phase is adaptive temporal sampling in which the three largest gradients are selected whose corresponding frame indices are used to partition the depth sequence. The second phase is depth motion mapping which is calculated by projecting depth map sequences onto three orthogonal cartesian plane, and the absolute difference of the sequential projected sequences is computed. The third phase is dimensionality reduction by using the concept of principal component analysis. The last phase is classification where the l2-CRC classifier is trained and utilized for the purpose. Model sketch for this method is provided in Fig. 9.

This model proved to be efficient as it provided an accuracy of over 97% when tested over MSR-Action3D dataset.

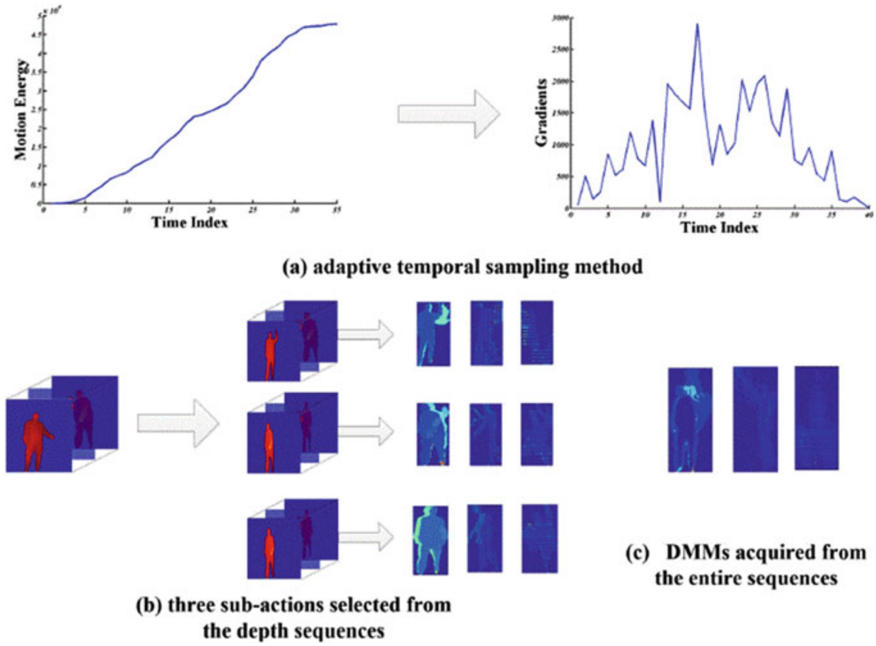

Fig. 9 Method 9 sketch analysis (Li et al. 2016)

3.3 Method 10

The approach proposed in article Talha et al. (2018) is fast, view-invariant, and good for early action recognition that also consists of several stages. First the skeleton extraction stage is encountered by the target object. Then, the output of this stage is preprocessed by Savitzky-Golay filter. Now, the skeletal image is broken into five parts and termed as B_1, B_2, B_3, B_4, and B_5 for right arm, left arm, right leg, left leg, and spine, respectively. Then, the body directional velocity (BDV) feature is extracted for each body parts and are concatenated. Now, a hidden Markov model (HMM) with the state-output distribution of Gaussian mixture model (GMM) is used for classification purpose. Model sketch for this method is provided in Fig. 10.

This approach provided an overall accuracy of 92.90%, 90.32%, and 91.10% when implemented on MSRAction3D, Florence3D, and UTKinect datasets, respectively.

4 Conclusion

In this work, we have become familiar with different latest technologies that are widely used for accomplishing the critical tasks of human action recognition. The discussed methodologies involves normal human action recognition as well as the

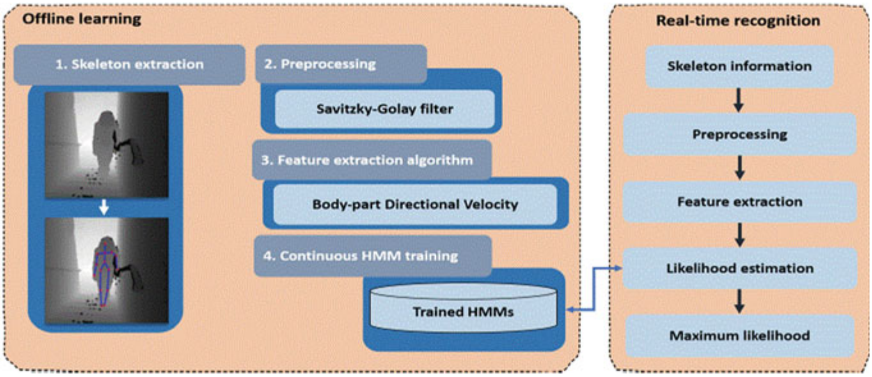

Fig. 10 Method 10 sketch analysis (Talha et al. 2018)

real-time methods for optimal cases. Along with these methodologies, we have also seen the small delay proportionality for the existing real-time human action recognition methodologies. The future work will include the concept to reduce this small delay proportionality to its optimal state by processing the frame-level information of a given video sequence and conclude the action from the present frame information considering the conclusions from the previous frames.

References

Antic B, Milbich T, Ommer B (2013) Less is more: video trimming for action recognition. In: 2013 IEEE international conference on computer vision workshops, Dec 2013, pp 515–521

Dhamsania CJ, Ratanpara TV (2016) A survey on human action recognition from videos. In: 2016 online international conference on green engineering and technologies (IC-GET), Nov 2016, pp 1–5

Kale GV, Patil VH (2016) A study of vision based human motion recognition and analysis. CoRR, abs/1608.06761

Kong Y, Jia Y, Fu Y (2014) Interactive phrases: semantic descriptions for human interaction recognition. IEEE Trans Pattern Anal Mach Intell 36(9):1775–1788

Li Y, Lu Q, Luo W (2016) Adaptive temporal sampling for real-time human action recognition. In: 2016 IEEE advanced information management, communicates, electronic and automation control conference (IMCEC), Oct 2016, pp 1306–1310

Marín-Jiménez MJ, de la Blanca NP (2013) Human interaction recognition by motion decoupling. In: Sanches JM, Micó L, Cardoso JS (eds) Pattern recognition and image analysis. Springer, Berlin, Heidelberg, pp 374–381

Nguyen N, Yoshitaka A (2014) Human interaction recognition using independent subspace analysis algorithm. In: 2014 IEEE international symposium on multimedia, Dec 2014, pp 40–46

Talha SAW, Hammouche M, Ghorbel E, Fleury A, Ambellouis S (2018) Features and classification schemes for view-invariant and real-time human action recognition. IEEE Trans Cogn Dev Syst 10(4):894–902

Wang H, Klser A, Schmid C, Liu C (2011) Action recognition by dense trajectories. CVPR 2011:3169–3176

Xiao Q, Si Y (2017) Human action recognition using autoencoder. In: 2017 3rd IEEE international conference on computer and communications (ICCC), Dec 2017, pp 1672–1675

Yun K, Honorio J, Chattopadhyay D, Berg TL, Samaras D (2012) Two-person interaction detection using body-pose features and multiple instance learning. In: 2012 IEEE Computer Society conference on computer vision and pattern recognition workshops, June 2012, pp 28–35

Zhang B, Yan Y, Conci N, Sebe N (2014) You talkin' to me?: recognizing complex human interactions in unconstrained videos. In: Proceedings of the 22Nd ACM international conference on multimedia, MM '14, New York, NY, USA, 2014. ACM, pp 821–824

Sarcasm Detection on Twitter Data Using R and Python

V. Haripriya, Poornima G. Patil, and T. V. Anil Kumar

Abstract A challenging task in Opinion Mining is to detect sarcasm. Sarcasm is a way of telling things in a positive way where the intended meaning is negative. Sarcastic texts lead to wrong classification of data due to the usage of positive words to convey negative emotions. It is important to detect sarcasm on social media data because there is no face-to-face conversation happening to understand the context. When this data is taken for sentiment analysis and decision-making process it leads to wrong inferences. The proposed work classifies the dataset into sarcastic and non-sarcastic using machine learning algorithms and the same has been implemented using R and Python for finding the difference in accuracy. The dataset has been collected from Twitter. Naïve Bayes algorithm is used for the classification. The result obtained from sarcasm detection on social media data will be helpful in areas such as sentiment analysis, natural language processing, opinion mining, business-related decision making, and so on. The result of the proposed method classified the given data into sarcastic and non-sarcastic with an accuracy of 0.91 and 0.88 using R and Python respectively.

Keywords Opinion mining · Sarcasm detection · Sentiment analysis · Naïve Bayes

1 Introduction

The word Sarcasm is derived from the Latin word which means "to tear flesh", and it has been called "hostility disguised as humor" and generally used to make fun of others by some people (Teh et al. 2018). Presence of sarcasm can completely change the meaning of a sentence. Hence it is important to identify the sarcasm in opinion mining and sentiment analysis. Sarcasm is considered to be an important aspect in the reviews because of the absence of face-to-face conversation. Since the growth of internet usage is getting higher over time and the volume of data

V. Haripriya (✉) · P. G. Patil
Visvesvaraya Technological University, Belgaum 590018, India

T. V. Anil Kumar
LEAD College of Management, Palakkad 678009, India

M. Mukherjee et al. (eds.), *Advances in Medical Physics and Healthcare Engineering*, Lecture Notes in Bioengineering, https://doi.org/10.1007/978-981-33-6915-3_45

generation is huge, the process of data analysis becomes a tedious task. Sarcasm leads to an additional complication in the text analysis process. Social media sites act as a platform for the users to express their views and opinions on various topics and events. When a customer tweets “Great multipurpose phone! Can be used as a phone and as a hot iron as well”, a review taken from a branded mobile contains positive sentiment words but the review is actually negative as it being mocked for over-heating. This results in the review to be wrongly classified into positive sentiment which will directly or indirectly affect the decision making for business development. This is why detection of sarcasm is important. Selecting and describing a set of features for identifying sarcasm at a linguistic level, especially in short texts created in social media such as Twitter postings or “tweets” is being followed widely. In the context of text classification, sarcasm detection is an important factor since it has many implications on various fields such as health, sales, politics, and many more (Sarsam et al. 2020). Sarcasm has a major effect on Sentiment analysis. But most of the research works ignored sarcasm detection due to its difficulty in finding. Numerous researches are being done in order to detect sarcasm with the help of the usage of words and various features in text data. There are also methods where models are built in order to extract sentiments and contextual information from the data. Supervised and Unsupervised approaches can be used for detecting sarcasm. Researches have been done using a lexicon-based, rule-based approach, corpus-based approach, statistical-based approach, and various machine learning approaches. The proposed work uses Naïve Bayes classification, a machine learning approach to detect sarcasm in tweets.

2 Literature Survey

Numerous studies and researches had been conducted on Sentiment Analysis. It was during the early 1990s that the research was started in the field of sentiment analysis. The term sentiment analysis along with opinion mining was first introduced in the year 2003 by Dave et al. (2003) during this time, the work was very much limited only to subjective detection, sentiment adjectives, and interpretation of metaphors and within 15 years the research interests in this area have increased manifold (Pang and Lee 2008; Kumar and Teeja 2012). Some remarkable studies mentioned that sarcasm in a sentence by conflict and contrast of sentiment polarity (Camp 2012; Riloff et al. 2013; Joshi et al. 2017). Kumar and Garg (2019) suggested that detection of sarcasm in natural language text is a well-accepted problem in the area of sentiment analysis.

Parveen and Pandey (2016) discussed the extraction process of sentiment from Twitter and they have analyzed the tweets to provide predictions on business intelligence using Naïve Bayes algorithm. Authors have used Hadoop Framework and worked on movie data from Twitter. The reviews of movies have been classified as positive, negative, and neutral sentiments. The proposed work proves that performance of the Naive Bayes algorithm increases by converting the emoticons into its equivalent word. A novel approach has been used (Khan et al. 2014) to classify the tweets into positive, negative, and neutral feelings using emoticon classifier, Bag-of-words, and SentiWordnet classifier and obtained increased classification accuracy. Authors (Samonte et al. 2018; Farías et al. 2018) mentioned Naive Bayes, Maximum Entropy, and Support Vector Machine are commonly used as the machine learning algorithms for the detection of sarcasm. Affective and structural features are employed (Mukherjee and Bala 2017) to predict irony with conventional machine learning classifiers such as Decision Tree, SVM, and Naïve Bayes. In a follow-up study by Farías et al. (2016) have used a knowledge-based k-NN classifier with a feature set that could capture a broad range of linguistic phenomena namely structural and emotional. Apart from machine learning algorithm, many research works are done using Deep learning networks. Saha et al. (2017) used Naïve Bayes and Support Vector Machine (SVM) classifiers to classify the data for sarcasm detection and also aim to differentiate between the accuracy, precision, recall, and F-score of Naïve Bayes and SVM classifier. Zhang et al. (2011) classified sentiment using Naïve Bayes and SVM for restaurant reviews written in Cantonese. The highest accuracy reported was 95.67% using Naïve Bayes. Kiilu et al. (2018) developed an approach for detecting and classifying hateful speech that uses content produced by self-identifying hateful communities from Twitter. Results from their experiments showed that Naive Bayes classifier achieved significantly better performance than existing methods in hate speech detection algorithms. The work is done by Van Hee et al. (2018) used a combination of lexical, semantic, and syntactic features and were implemented using Support Vector Machine Classifier and results showed that it outperformed Long short-term memory, deep neural network approaches. Potamias et al. (2020) employed advanced deep learning methodologies to tackle the problem of identifying the Figurative language forms. The performance was measured using the devised hybrid neural architecture and experimented with various datasets and contrasted with other appropriate state-of-the-art methodologies and systems. Irsoy and Cardie (2014) applied the deep Recurrent Neural Network (RNN) to the task of opinion expression extraction formulated as a token-level sequence labeling task. Experimental results show that deep, narrow RNNs outperform traditional shallow, wide RNNs with the same number of parameters.

Sarcasm detection becomes difficult without having adequate knowledge of the "context" of the situation, the particular topic, and the environment (Kumar and Garg 2019). Numerous researches are being done in order to detect sarcasm with the help of usage of the words and various features in text data. There are also methods where models are built in order to extract sentiments and contextual information from the data. Re-searches have been taken place using lexicon-based, rule-based approach, corpus-based approach, statistical-based approach, and various machine learning approaches. The recent work concentrates more on Deep learning approaches (Eke et al. 2020).

Though many researches have been done on Sarcasm detection, a comparison of accuracy level and the time required to complete the process using various tools like R and Python have not been done so far. Thereby the proposed work implemented

Naive Bayes algorithm for the dataset using R and Python. Moreover, this work helps researchers to get an idea of the steps involved in the sarcasm detection process.

3 Methodology

3.1 Data Collection and Preprocessing

The dataset has been collected from Twitter using Twitter API. The collected data is noisy and it cannot be directly fed into the classifier as it will affect the working of the classification algorithm. RE (Regular Expressions) and NLTK (Natural Language Tool Kit) packages in Python were used to clean the data by removing new lines and tabs, punctuations, hashtagged words, emoticons, and emojis and the stop words. In total 1992 preprocessed tweets have been parsed into the system.

3.2 Training and Testing Phase

The collected tweets were divided into training and testing set. In the proposed work the dataset has been split into 70:30 ratio. The purpose of the training dataset is to provide the algorithm with "ground truth" data whereas the test dataset is used to check how well the algorithm was trained with the provided training dataset.

3.3 Implementation

The proposed work used Naïve Bayes approach since it is one among the well-known classification algorithms and it works based on Bayes' Theorem. This algorithm makes use of conditional probability to predict the likelihood of future occurrence of events based on their historical information.

Bayes' Theorem is mentioned as:

$$P(A|B) = P(A)P(B|A)P(B) \tag{1}$$

The implementation has been done using R programming and Python to check the difference in accuracy. Various libraries namely Readxl, tm, wordcloud, E1071, gmodels, and naiveBayes have included in R studio whereas Nltk and stopwords were used for implementation using python.

Fig. 1 Classification of sarcastic and non-sarcastic tweets

```
> table(tweet$sarcasm)

   0    1
1018  974
>
```

```
Total Observations in Table:  1192


             | actual
   predicted |         0 |         1 | Row Total |
-------------|-----------|-----------|-----------|
           0 |       547 |        48 |       595 |
             |     0.910 |     0.081 |           |
-------------|-----------|-----------|-----------|
           1 |        54 |       543 |       597 |
             |     0.090 |     0.919 |           |
-------------|-----------|-----------|-----------|
Column Total |       601 |       591 |      1192 |
             |     0.504 |     0.496 |           |
-------------|-----------|-----------|-----------|


> #accuracy is 0.91
```

Fig. 2 Evaluation of model performance

4 Results and Discussion

4.1 Implementation Using R

Naïve Bayes approach is used as the classification algorithm and with the support of various libraries the model has been implemented using R Studio. The given data has been classified as sarcastic and non-sarcastic tweets where the value 0 indicates non-sarcastic and the value 1 represents sarcastic and the same has been depicted in Fig. 1 and the performance of the model has been evaluated and the results obtained are represented in Fig. 2 respectively.

4.2 Implementation Using Python

Dataset has been passed to the Naïve Bayes approach to check whether the given data is sarcastic or non-sarcastic. Nltk and stopwords were used for implementation using python. MultinominalNB has been used for the classification with discrete features

```
In [29]: df.head(5)
Out[29]:
```

	Tweets	is_sarcastic
0	I love working midnights tweet	1
1	I hate when I buy a bag of air and there's chi...	1
2	my grandad always sounds so ill when i speak t...	0
3	I realize I'm annoying to everyone, so I won't...	0
4	I love when I find these dudes on vine!! #Foll...	1

Fig. 3 Classification of sarcastic and non-sarcastic tweets

```
Out[8]: MultinomialNB(alpha=1.0, class_prior=None, fit_prior=True)

In [9]: from sklearn.metrics import accuracy_score

        test_data = vectorizer.transform(X_test)
        y_predict = model.predict(test_data)

In [10]: print(accuracy_score(y_test, y_predict))

         0.8822055137844611
```

Fig. 4 Evaluation of model performance

such as word counts for classifying the text. Training and testing data has been split in the ratio of 70:30 where 70% of data has been passed for training the model whereas 30% of data has been passed for testing the model. Tweets have been classified as sarcastic and non-sarcastic and are represented in Fig. 3 and the accuracy obtained was 0.88 and it is depicted in Fig. 4.

5 Conclusion

Sarcasm detection is considered as the challenging factor in sentiment analysis since it gives a gap between the intended meaning and the literal meaning of the sentences. This ambiguity poses challenges to the industries in making proper decisions. By doing sentiment analysis on the social media data, that gives a tremendous change in their way of making decisions. R and Python are open-source and widely used in the analytical process. Statistical analysis is the major purpose of using R whereas data science is the core idea of Python. Python is considered as the most robust language than R. However, R has more built-in analysis for summary statistics and Python works on the basis of packages. The main implications of the proposed work are to help to take decisions based on the reviews or comments written on social media platforms. As future research semantic tools can be used to detect sarcasm and an ontology model can be created to classify the texts accurately by reducing the problem of wrong classification of texts.

References

Camp E (2012) Sarcasm, pretense, and the semantics/pragmatics distinction. Noûs 46(4):587–634

Dave K, Lawrence S, Pennock DM (2003) Mining the peanut gallery: opinion extraction and semantic classification of product reviews. In: Proceedings of the 12th international conference on World Wide Web, pp 519–528

Eke CI, Norman AA, Shuib L, Nweke HF (2020) Sarcasm identification in textual data: systematic review, research challenges and open directions. Artif Intell Rev 53(6):4215–4258

Farías DIH, Patti V, Rosso P (2016) Irony detection in Twitter: the role of affective content. ACM Trans Internet Technol (TOIT) 16(3):1–24

Farías DIH, Montes-y-Gómez M, Escalante HJ, Rosso P, Patti VA (2018) Knowledge-based weighted KNN for detecting irony in Twitter. In: Mexican international conference on artificial intelligence. Springer, Cham, pp 194–206

Irsoy O, Cardie C (2014) Opinion mining with deep recurrent neural networks. In: Proceedings of the 2014 conference on empirical methods in natural language processing (EMNLP), pp 720–728

Joshi A, Bhattacharyya P, Carman MJ (2017) Automatic sarcasm detection: a survey. ACM Comput Surv (CSUR) 50(5):1–22

Khan FH, Qamar U, Javed MY (2014) Sentiview: a visual sentiment analysis framework. In: International conference on information society (i-Society 2014), pp 291–296. IEEE

Kiilu KK, Okeyo G, Rimiru R, Ogada K (2018) Using Naïve Bayes algorithm in detection of hate tweets. Int J Sci Res Publ 8(3)

Kumar A, Garg G (2019) Empirical study of shallow and deep learning models for sarcasm detection using context in benchmark datasets. J Ambient Intell Hum Comput 1–16

Kumar A, Teeja MS (2012) Sentiment analysis: a perspective on its past, present and future. Int J Intell Syst Appl 4(10):1

Mukherjee S, Bala PK (2017) Detecting sarcasm in customer tweets: an NLP based approach. Ind Manag Data Syst 117(6):1109–1126

Pang B, Lee L (2008) Opinion mining and sentiment analysis. Found Trends Inf Retr 2(1–2):1–135

Parveen H, Pandey S (2016) Sentiment analysis on Twitter Data-set using Naive Bayes algorithm. In: 2016 2nd international conference on applied and theoretical computing and communication technology (ICATCCT). IEEE, pp 416–419

Potamias RA, Siolas G, Stafylopatis AG (2020) A transformer-based approach to irony and sarcasm detection. Neural Comput Appl 1–12

Riloff E, Qadir A, Surve P, De Silva L, Gilbert N, Huang R (2013) Sarcasm as contrast between a positive sentiment and negative situation. In: Proceedings of the 2013 conference on empirical methods in natural language processing, pp 704–714

Saha S, Yadav J, Ranjan P (2017) Proposed approach for sarcasm detection in Twitter. Indian J Sci Technol 10(25):1–8

Samonte MJC, Dollete CJT, Capanas PMM, Flores MLC, Soriano CB (2018) Sentence-level sarcasm detection in English and Filipino tweets. In: Proceedings of the 4th international conference on industrial and business engineering, pp 181–186

Sarsam SM, Al-Samarraie H, Alzahrani AI, Wright B (2020) Sarcasm detection using machine learning algorithms in Twitter: a systematic review. Int J Market Res 1470785320921779

Teh PL, Ooi PB, Chan NN, Chuah YK (2018) A comparative study of the effectiveness of sentiment tools and human coding in sarcasm detection. J Syst Inf Technol

Van Hee C, Lefever E, Hoste V (2018) Exploring the fine-grained analysis and automatic detection of irony on Twitter. Lang Resour Eval 52(3):707–731

Zhang Z, Ye Q, Zhang Z, Li Y (2011) Sentiment classification of Internet restaurant reviews written in Cantonese. Expert Syst Appl 38(6):7674–7682

Automatic Smart Parking One-Sided Free Slot Booking Using Internet of Things (IoT)

Anjan Bandyopadhyay, Saptashwa Misra, Debolina Nath, and Vaskar Sarkar

Abstract Nowadays, Internet of Things (IoT) plays a major role everywhere in our daily lives. IoT can interconnect everything within a few and transfer data over a network without any human intervention. So, in this paper, we will introduce a smart car parking technology that can solve many problems regarding the parking issue as well as update the status of the car every day using IoT and the cloud platform. In cloud platforms, we can store the information about the cars when the cars enter the parking zone. The information combined with the details of the car can find out the parking lots in the commercial places in cities. In this paper, we have focused on two major directions- one is the allocation of appropriate location in a parking zone based on the preferences of the car to reduce search time, fuel consumption as well as reduce the carbon footprint of the atmosphere and the other is to store the information into the cloud platform and easily can access that information and maintain the security of the information using blockchain technology.

Keywords Internet of things (IoT) · Cloud computing · Smart parking system (SPS)

S. Misra · D. Nath
Department of Computer Science & Engineering, Amity University, Kolkata, India

A. Bandyopadhyay · V. Sarkar (✉)
Department of Mathematics, School of Basic and Applied Sciences, Adamas University, Kolkata, India

M. Mukherjee et al. (eds.), *Advances in Medical Physics and Healthcare Engineering*, Lecture Notes in Bioengineering, https://doi.org/10.1007/978-981-33-6915-3_46

1 Introduction

Searching for a suitable place to park the car is a tedious task for the drivers in the urban scenario especially during rush time and peak hours. Surveys have highlighted the fact that a lot of time is wasted in finding a parking slot which could otherwise be utilized for productive work. Moreover, this becomes a major cause for traffic jams and constricts road spaces for vehicular movement. Further, it is seen that there is an unnecessary wastage of fuel which could have been saved if the driver did not have the roam with the car in search of a parking slot. This consequently leads to an additional vehicular emission that contributes to the rising level of pollution in the urban environments. This issue can be resolved by smart parking technologies supported by IOT (internet of things).

Although by definition the Internet of Things (IoT) has existed since the post 2nd World War era, the term 'IoT' was first introduced by Kevin Ashton in the year 1999 cited in Young (1964). IoT provides a vision where devices become smart and behave alive through sensing, computing, and communicating by embedded small devices which interact with remote objects or persons through connectivity. As this technology evolves, it promises to connect with a network of all of the adjacent things and to communicate with fewer people. The connections are established in everyday life with devices such as transceivers, sensors, actuators, microcontrollers and so on. IoT technology is growing in different sectors of smart applications, but we have not yet discovered the limitations. These can be appropriately manufactured with a few processors. The gadgets are also associated with the use of a large number of important breakthroughs such as GPS, Wi-Fi, BT/BTLE, RFID, VoLTE, 5G, LTE, etc. acquiring more than half of the IoT sector. All these advances have their points of interests, however from these breakthroughs a few common points of interests can be determined. Here it is pertinent to mention that Cloud platform serves as a perfect co-partner to IOT as it acts as the storing platform from where accessing data from remote locations can be done easily. On one hand, by using the essentially unlimited capabilities and assets of Cloud, IoT can address its innovative solutions, including capacity, training, and vitality as seen in Smith (unpublished). Once again, cloud can also extend its compass to manage real substances in a more dynamic and disseminated way using IoT. Basically, the cloud is the middle of the road between things and applications, so that each one of the complexities and functionalities essential to the application is covered.

Our proposed smart parking system is based on allocation of parking spaces to the users on the basis of strict preferences provides by them. The main theme of our parking system is to allocate the preferred parking slot present in the parking area nearest to the user's destination, thus relieving the user from the cumbersome task of finding a slot for parking. The users give their preferences, prior to travel, through their IoT devices to the mechanism designer. The collected information from the users is sent to the cloud via the IoT devices such as smart phone and then referenced based algorithm is running and give the appropriate solution for the car parking. Every user gives their true information regarding lot and the car information to the mechanism designer which will be authentified by the use of blockchain technology. The mechanism designer distributes the information through the mobile app and the normal user gets that information and gives the preferred lot of the parking. Thus, it creates a centralized system controlling all the allocations based on preference and maintaining authenticated data regarding the vehicles and their users. Since the data is being maintained in the cloud, these can be accessed from anywhere whenever they are required for any kind of verification and security checks. This enhances the user's ability to check the status/availability of parking spaces prior to travel. The challenge here is to make the best possible use of existing resources to reduce the search time and traffic. A few existing parking systems that use artificial intelligence to gather information use sensors such as video sensors in a parking system, but they are expensive. So, our goal is to develop a model with lower cost and higher performance as aimed in Kaufman (1995) and Yorozu et al. (1987).

In our paper, we will be discussing this preference-based allocation in two phases-firstly, without the involvement of monetary transactions (i.e. a system of free slot booking) and secondly, with the use of monetary transactions, in which the allocation of the most preferred parking slot will be made to the highest bidder. In the first case, a preference-based allocator algorithm (based on Game Theory) will be applied which will make the most suitable allocations of the parking slots to the cars. In the latter, we will take taken into consideration the parking slots which are high in demand and propose a money-based allocation of the parking slots based on VCG mechanism as portrayed in Mi et al. (2014). The most preferred slot will be allotted to the highest bidder at the bid price of the second-highest bidder as per Vickey's Second price auction theory, which will be discussed in detail further in our paper. Thus, in both scenarios, the allotment is done based on the fixed preferences by the users.

The remainder of the paper is organized as follows: in Sect. 2 we have discussed some prior work in the area of literature review. In Sect. 3 we have discussed the system model and formulation of the problem. In Sect. 4, proposed mechanism has been discussed followed by the conclusion and references.

2 Literature Review

In recent years, everywhere around the globe, the manufacturing of cars is increasing daily leading to great demand for innovative parking systems with maximum advantages and trying to attenuate the disadvantages.

Ultrasonic sensors were employed in paper Park et al. (2008) by the employment of multiple echo function to detect the sides of the important parking environments. The paper Delot et al. (2009) allocates parking spaces using reservation protocol in vehicular impromptu networks (VANET) very efficiently which end up in less competition among the vehicles. In Panja et al. (2011), wireless sensors were accustomed to tracking vacant spaces within the parking lots using the strength of the signal.

In some urban environments, finding parking spaces will be a significant hassle for drivers. In Kokolaki et al. (2011) an application has been wont to find the open parking slots which were looked into with a competitive outlook and treated with a game-theoretic framework.

Within the paper Ilc and Dobnikar (2011), Gravitational Law is employed for locating complex cluster shapes which might automatically determine the number of clusters.

Through smarter pricing for parking, the proper level of parking availability is often achieved by periodically adjusting meter and garage to match demand which may be done through smarter pricing for parking referred to as “demand-responsive pricing”. This may encourage people to park in spaces (blocks and garages) which don’t seem to be being employed enough, helping to free congested areas during busy times as seen in http://sfpark.org/.

In Fraifer and Fernström (2016), it is highlighted that every cosmopolitan city across the globe is affected by traffic jams, leading to frustration of the drivers especially after they are attempting to find a parking zone. As a result of this, interest in this area has become important for scientists and researchers. Solving problems like reducing drivers’ frustration and stress by saving time and fuel, and reducing gas emissions, which successively, will affect levels of pollution have gained huge importance. Recent investigations have created an environment within which most of the fashionable statistics indicate shocking findings regarding the wastage of gasoline while they rummage around for parking places. Usually, such a system relies on counting what number of cars have entered the park and calculating the difference between this figure and therefore the maximum number of parking spaces to estimate the number of spaces available. In Li et al. (2017) stress was given to lower the maintenance costs of the smart parking system. In the past, smart parking system based on visual detection method was expensive because complex expensive appliances were to be used to receive light of different intensities. They designed a unique way of smart parking solution which was UAV-aided.

The Parking Guidance system is an “operating system” which is considered as one of the most intelligent transportation system. This operating system can assist the traffic management department to manage traffic flow efficiently, avoid traffic jam, and help the traveler by providing relevant information as seen in Fang et al. (2017).

In the paper Saleem et al. (2019), some investigations were done on certain papers related to IoT on the same topic. Different models augmented with sensors, integrating cloud and mobile application were presented, which ultimately led to a wise parking system which not only saved time, energy, and fuel but also reduced carbon footprint. The quick development in miniaturization and robustness of processors, sensor together with machine learning increased the potential of smart parking paving way for future researchers to look into parking issues for both indoor and outdoor parking slots.

In Das (2019), a parking system, comprising hardware and software modules was introduced. A Raspberry Pi device coupled with sensors and cameras was used along with python modules for data management. Here, three main cases were taken into consideration-firstly, when cars were parked correctly, the second had error-correction, and therefore in the third case error correction was needed in case of involvement of multiple cars. This especially applicable in areas like in hospitals, companies, airports, malls, and other busy places. The system was easily affordable because of the low cost of the hardware.

In the paper Farag et al. (2019), MATLAB software was used for image processing and experiments were performed which paved a way to a wise parking system.

Smart parking if implemented intelligently will end in the reduction of search time for parking, reduction of traffic congestion resulting in building up a smart city giving relief to the user.

3 System Model and Problem Formulation

In our model we have considered n number of cars and m number of parking slots present in a bounded parking area. The number of cars will be represented as $C = \{c_1, c_2, \ldots, c_n\}$ and the number parking lots represented as $P = \{p_1, p_2, \ldots, p_n\}$, where both C and P are finite sets. Here each car gives their preferences of the slots available in the preferred parking lot nearest to the location of the car or its destination and each can prebook the parking slots, if available, before reaching the destination. The user will be able to view the parking slots present in the parking area through the mobile app and can give the preference according to his/her choice. In this case, some priority will be given to the people of old-age, people with physical disabilities, medical personnel, expectant mothers, etc. In case the parking slots are completely occupied and there is no more slot available, the user can give the preferences for the parking slots of the next nearest parking area.

In the case where monetary exchanges will be involved in the allocation of the preferred parking slots, all users will also be required to provide the bid value for the slot they want to occupy in the parking area. This bid will be compared with the other bid values made by the other users so that the allocation of the most preferred slot can be made to the highest bidder.

For example, if there are three cars c_1, c_2, c_3 which give their preferences on the three parking lots p_1, p_2, p_3, the possible total ordering could be:

(1) $p_3 \succ_{c_1} p_1 \succ_{c_1} p_2$
(2) $p_2 \succ_{c_2} p_1 \succ_{c_2} p_3$
(3) $p_2 \succ_{c3} p_3 \succ_{c_3} p_1$

c_1	p_3	p_1	p_2
c_2	p_2	p_1	p_3
c_3	p_2	p_3	p_1

This information when obtained from the users along with other documents of the cars, the data is passed on to the cloud database. But before passing the obtained data to the cloud, the data will have to be authenticated. The authentication of documents will be done using the block chain technique. If the user is found to give false details, the data will not be accepted. After authenticating, only the true data will be passed to the cloud platform and it will be stored. Since the documents are stored in the cloud, these can be accessed from anywhere whenever required. Hence the centralized system can be implemented for both the storage od data as well as allocation of space in the parking area based on strict preferences given by the cars. Thus, the two major directions of our paper as mentioned earlier are being successfully dealt with in our system model.

Now the allocations of the parking slots will be done according to the mechanism that we have proposed in the following section. It will discuss in both monetary and non-monetary phases as mentioned earlier in the paper.

4 Proposed Mechanism

Proposed mechanism 1: Allocation without involving monetary transactions (Non-monetized system).

The proposed algorithm is called Preference Based Slot Allocator (PBSA). According to our designed mechanism, it is presumed that every car is assigned a parking slot, if available. During the execution phase, this can be done by randomly assigning a parking slot to a car/user. This will ensure that before running of our algorithm every car has a pre-allotted parking slot. PBSA then reallocates the car its parking slots such that every car either retains the slot that was allocated initially or attains a better slot according to the preferences that were given by them by the process of mutual exchanges. As the algorithm runs, a cycle is generated that keeps allotting the slots to the cars according to their preferences. On completion of this matching algorithm, the cars will be allotted the best possible slots according to their provided preferences.

Pseudocode

```
Input: C= ( c1, c2, c3,………cn )
Input: PS= ( p1, p2, p3,……….pm)
Input: pref = (pref1,pref2,pref3…..prefm)
Begin
//function 1 → preference generation
do {  for each ci belonging to C
for i=1 to n
{   for j=1 to m
    Enter the preference }
}   Generate the preference matrix
//function 2→ generation of car-parking slot pair
do {
for each ci belonging to C
      assign a random slot to each ci
//repeat for n cars
}
Function 3 → Formation of allocation cycle
Create a digraph DG with preference, random allotted slot and car
Detect cycle in DG and store the car and slot in datastructure DS
for all (ci , pj)
 do{
store the car and the allotted slot
store the new car-parking slot pair
remove the allocated car-slot pair
}end for
Update the preference matrix
 repeat
until no. of cars is null
main routine
{   Call Function 1
     Call Function 2
     Call Function 3
}
End
```

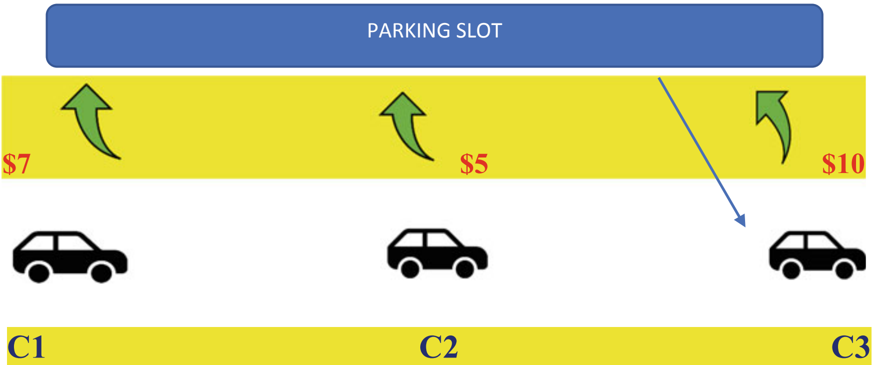

Fig. 1 Diagrammatic representation of allocation of parking slot to the car on the basis of Second Price Auction Theory

Proposed mechanism 2: Allocation involving monetary transactions (Monetized system).

In this case, the proposed mechanism is based on the VCG theory and Vickrey's Second Price Auction Theory. This will be applied to parking slots experiencing high demand. The cars here will be paying in order to occupy the parking slot of their choice. If multiple cars are opting for a certain slot, then an auction system is proposed, the winner of which will be allotted the slot at a price less then the maximum bid value. This will have a two-fold advantage—firstly, the allocation carried out aptly and secondly, the users stay at a profit as they are required to pay a value which is less compared to what they had actually offered to occupy the slot. According to the mechanism, after auction, the car will be allotted the slot at the price offered by the second-highest bidder of the auction.

Illustrative Example: Fig. 1 shows the detailed functioning of the proposed mechanism. Suppose c_1, c_2 and c_3 are the cars which opt to occupy parking slot s_1. Since s_1 can be allotted to any one of them therefore an auction is set up where each of them offers their own bid values. As shown in Figs. 1 and 2, c_1 bids \$7, c_2 bids \$5 dollar and c_3 bids \$10, respectively. So according to the proposed mechanism, the parking slot s_1 is allotted to c_3 since c_3 is the highest bidder. But c_3 will be getting the slot at \$7, which is the second-highest bid value. Hence this mechanism will be successfully allotting the parking slots via auctions.

5 Conclusion

With the rise in the number of transportation vehicles in moderate to highly populated cities, there is a consequent pressure on the car users or drivers to get a free parking slot in the rush hours and this directly and indirectly raises several issues like environmental pollution, time wastage, and unnecessary traffic congestion. Thus, a

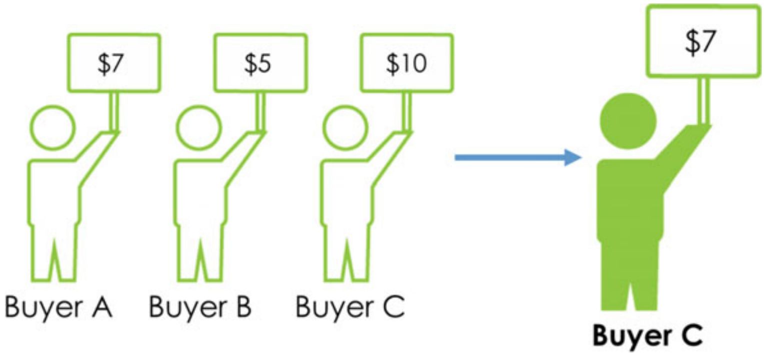

Fig. 2 Diagrammatic representation of the participating bidders and the winning bidder on the basis of Second Price Auction Theory

proper smart car parking slot allocation process is in high demand for almost all metropolitan as well as cosmopolitan cities. This paper will give us an opportunity to study the smart parking system where every car owner can give their preference of the parking slot. Thus the parking area will be allocated efficiently. This will reduce the consumption of the fuel and minimize vehicular emission that causes air pollution and will also save the cost as well as store the documents in cloud. Whenever any document will be needed they can download the documents anytime and anywhere.

References

Das S (2019) A novel parking management system, for smart cities, to save fuel, time, and money. In: 2019 IEEE 9th annual computing and communication workshop and conference (CCWC), Las Vegas, NV, USA, 2019, pp 0950–0954. https://doi.org/10.1109/ccwc.2019.8666537

Delot T, Cenerario N, Ilarri S, Lecomte S (2009) A cooperative reservation protocol for parking spaces in vehicular ad hoc networks. In: Proceedings of the 6th international conference on mobile technology, application and systems, Nice, France, Sept 2009

Fang J, Ma A, Fan H, Cai M, Song S (2017) Research on smart parking guidance and parking recommendation algorithm. In: 2017 8th IEEE international conference on software engineering and service science (ICSESS), Beijing, 2017, pp 209–212. https://doi.org/10.1109/icsess.2017.8342898

Farag MS, Mohie El Din MM, El Shenbary HA (2019) Parking entrance control using license plate detection and recognition. Indones J Electr Eng Comput Sci 15(1):476–483. ISSN: 2502-475. https://doi.org/10.11591/ijeecs.v15.i1

Fraifer M, Fernström M (2016) Investigation of Smart Parking Systems and their technologies. In: Thirty seventh international conference on information systems, Dublin 2016

Ilc N, Dobnikar A (2011) Gravitational clustering of the self-organizing map. In: International conference on adaptive and natural computing algorithms (ICANNGA) 2011: adaptive and natural computing algorithms, pp 11–20

Kaufman CJ (1995) Rocky Mountain Research Lab., Boulder, CO, private communication

Kokolaki E, Karaliopoulos M, Stavrakakis I (2011) Value of information exposed: wireless networking solutions to the parking search problem. In Proceedings of 8th international conference on wireless on-demand network systems and services (WONS), Bardonecchia, Italy, Jan 2011

Li X, Chuah MC, Bhattacharya S (2017) UAV assisted smart parking solution. In: 2017 international conference on unmanned aircraft systems (ICUAS)

Mi Z, Zhang M, Xiong Z (2014) A VCG mechanism based storage allocation strategy in cloud computing environment. J Commun 9(12)

Panja B, Schneider B, Meharia P (2011) Wirelessly sensing open parking spaces: accounting and management of parking facility. In: AMCIS 2011 proceedings, 2011

Park W, Kim B, Seo D, Kim D, Lee K (2008) Parking space detection using ultrasonic sensor in parking assistance system. In: IEEE intelligent vehicles symposium, Eindhoven, The Netherlands, June 2008

Saleem AA, Siddiqui HUR, Shafique R, Haider A, Javed MA (2019) A review on smart IoT based parking system. In: Conference: a review on smart IOT based parking system, Malaysia, Dec 2019

Smith B (unpublished) An approach to graphs of linear forms (unpublished work style)

http://sfpark.org/

Yorozu Y, Hirano M, Oka K, Tagawa Y (1987) Electron spectroscopy studies on magneto-optical media and plastic substrate interfaces (translation Journals style). IEEE Transl J Magn Jpn 2:740–741 [Dig. 9th Annu. Conf. Magnetics Japan, 1982, p 301]

Young GO (1964) Synthetic structure of industrial plastics (book style with paper title and editor). In: Peters J (ed) Plastics, vol 3, 2nd edn. McGraw-Hill, New York, pp 15–64

Understanding the Components of EMT Proteome and Their Regulations to Identify Biomarkers for Cancer Prognosis

Sanmitra Ghosh and Saptarshi Chatterjee

Abstract Epithelial–mesenchymal transition is a physiologic program contributing to embryonic development and organ fibrosis in normal individuals. At the same time, it also constitutes a major aspect of pathogenesis of progressive epithelial tumors when deregulated. Regulated by a battery of transcription factors, tumor cells exhibit EMT characterized by several epithelial as well as mesenchymal protein markers. The proteins involved in transcription regulation can further be regulated by tumor microenvironment and molecules like microRNAs. In this review, we present a comprehensive information regarding types of EMT and the proteome characterizing EMT pathway in carcinogenesis followed by identification of factors that regulate expression of EMT markers and hence cancer progression. Characterization of such molecular programmers of EMT may help us to identify biomarkers for early diagnosis and prognosis of malignancy.

Keywords Epithelial-mesenchymal transition · EMT-TFs · Hypoxia · microRNA

1 Introduction

Epithelial–mesenchymal transition is a tightly regulated cellular mechanism playing crucial roles in organogenesis during embryonic development, and during wound healing or tissue regeneration (Jolly et al. 2016). EMT permits a polarized epithelial cell that normally interacts with a basement membrane through its basal surface to undergo trans-differentiation to attain a mesenchymal phenotype characterized by elevated migratory capacity, invasiveness, increased resistance to apoptosis, and an amplification of ECM components (Kalluri and Neilson 2003; Kalluri and Weinberg 2009). This primary mesenchyme generated by EMT has the potential to undergo MET to generate secondary epithelia in course of constructing the three-dimensional structure of internal organs. The completion of an EMT is signaled by degradation of underlying basement membrane together with generation of a mesenchymal cell

S. Ghosh (✉) · S. Chatterjee
Department of Microbiology, School of Life Science and Biotechnology, Adamas University, Kolkata, West Bengal, India
e-mail: sanmitra.ghosh@adamasuniversity.ac.in

M. Mukherjee et al. (eds.), *Advances in Medical Physics and Healthcare Engineering*, Lecture Notes in Bioengineering, https://doi.org/10.1007/978-981-33-6915-3_47

that can drift away from the epithelial layer in which it originated (Kalluri and Weinberg 2009). Epithelium in transition lose polarity, adherens junctions, tight junctions, desmosomes, and cytokeratin intermediate filaments in order to rearrange their F-actin stress fibers and express filopodia and lamellopodia. This phenotypic conversion requires the molecular reprogramming of epithelium with new biochemical commands (Nistico et al. 2012).

2 Types of EMT

Broadly, EMT can be developmental or pathological. Developmental EMT involves the entire epithelial tissue where cells that will undergo EMT are specified through coordination of cell–cell, cell-ECM, and soluble signals. In this form of EMT, the degradation of the basement membrane is followed by cell ingression and morphogenesis of the retained epithelial cells to close the gap while the fully detached cell undergoes phenotypic mesenchymal shift. On the contrary, commencement of EMT program in pathological conditions can occur in a disorganized and more cell-autonomous fashion (Nistico et al. 2012). EMTs are embodied in three distinct biological settings (Types 1, 2 and 3) with distinctively different functional consequences (Fig. 1).

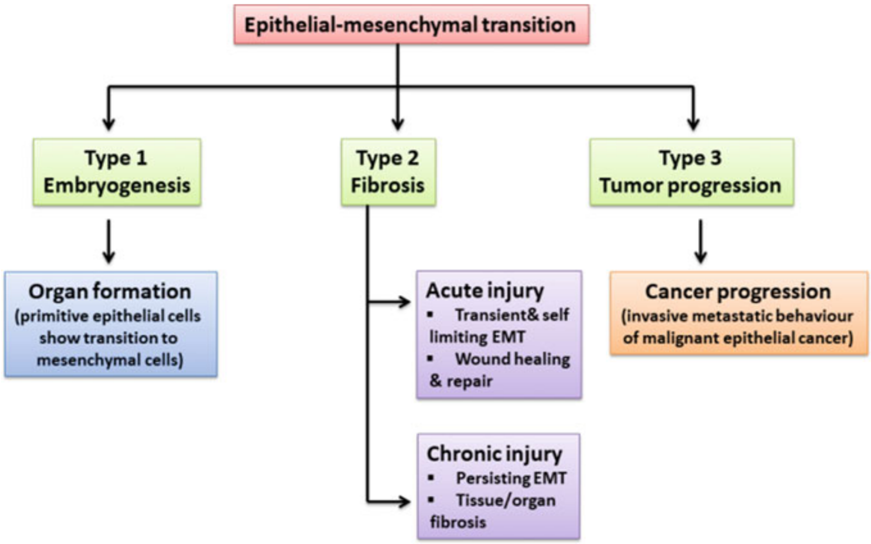

Fig. 1 Features of three types of EMT

2.1 Physiologic

Developmental or physiologic EMT can be functionally categorized further into two types: (i) Type 1 EMT associated with implantation, embryo formation and placenta formation, as well as organ developments and (ii) Type 2 EMT associated with wound healing, tissue regeneration, and organ fibrosis. During specific steps of embryogenesis and organ development, the cells within certain epithelia exhibit phenotypic plasticity and thus can move back and forth between epithelial and mesenchymal states via the processes of EMT and MET (Fig. 2) (Lee et al. 2006).

Type 1: Type 1 EMTs are ordered to produce different types of cells sharing common mesenchymal phenotypes. EMT in embryonic development generally occurs in an immunologically privileged setting with reduced inflammatory responses. Type 1 EMT does not cause fibrosis or induces any invasive phenotype, but can generate mesenchymal cells (primary mesenchyme) with capacity to subsequently undergo a MET to generate secondary epithelia. MET is essential for implantation as well as somitogenesis during gastrulation.

Gastrulation: During embryonic morphogenesis, a fertilized egg undergoes **gastrulation** that ultimately leads to generation of all tissue types of the body. Underlying this multi-step process are programmed changes dictated by specific expression of proteins associated with cell migration and differentiation (Hay 1990; Thiery and Sleeman 2006). At the biochemical level, the EMT associated with gastrulation is dependent on and orchestrated by canonical Wnt signaling (Skromne and Stern 2001;

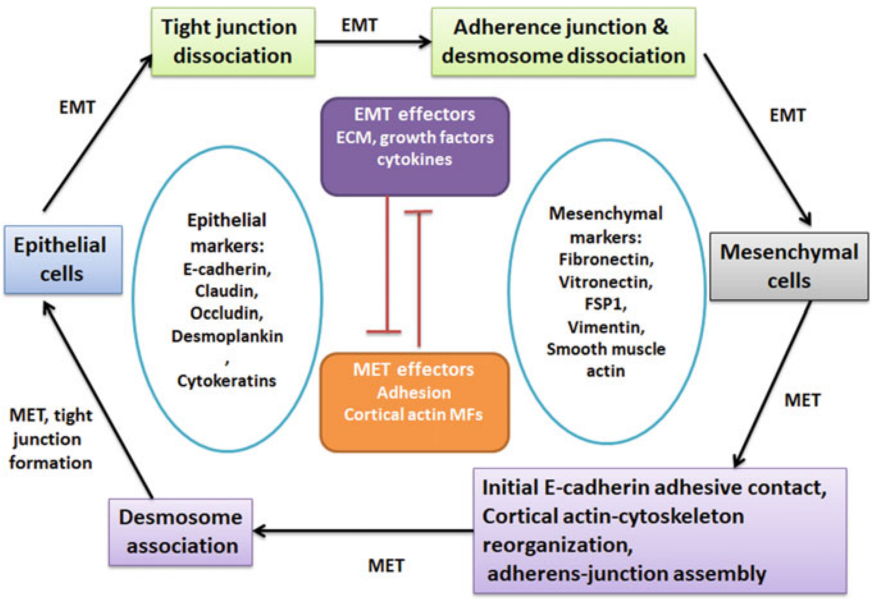

Fig. 2 Different stages of EMT and its reverse process MET

Liu et al. 1999). Upon completion of the development of epithelial tissues, the epithelial cells typically exert tissue-specific function, while the mesenchymal cells in such tissue play a supporting role (Jolly et al. 2016).

Neural crest formation: During embryonic development, an EMT involving the epithelial cells of the neuroectoderm gives rise to migratory neural crest cells that eventually disperse to different parts of the embryo and differentiate into diverse cell types, notably the melanocytes that provide pigment to the skin (Duband and Thiery 1982). In conjunction with EMT, MET is essential for localization of many cells in the adult tissue. EMT characteristic of neural crest is triggered by signaling pathways mediated by Wnts, FGFs, BMPs, c-Myc, and Msx-1 (Liem et al. 2000; Karafiat et al. 2007). It is interesting to note that cell adhesion molecules E-cadherin and N-cadherin need to be repressed in order for neural crest EMT to occur (Thiery 2003).

Type 2: Second type of EMTs initiates as component of a repair-associated event for tissue reconstruction following trauma and inflammatory injury. However, unlike type 1 EMTs, type 2 EMTs are associated with inflammation and cease once inflammation is attenuated, as is seen during wound healing and tissue regeneration. In the setting of organ fibrosis, type 2 EMTs may continue to respond to the enduring inflammation, leading eventually to organ destruction.

Organ fibrosis: Organ fibrosis is observed in the epithelial tissues of kidney, liver, lung, and intestine mediated by inflammatory cells and fibroblasts that release a variety of inflammatory signals as well as components of a complex ECM that includes collagens, laminins, elastin, and tenacins (Kalluri and Weinberg 2009; Potenta et al. 2008; Zeisberg et al. 2007). Under chronic inflammatory stress during wound healing and organ fibrosis, the epithelial cells progress to various extents through an EMT, creating the notion of a metastable "partial EMTs" where epithelial markers continue to be expressed but new mesenchymal markers have already been acquired. Eventually, these cells negotiate their way through the underlying basement membrane and accumulate in the interstitium of the tissue, where they ultimately gain a fully fibroblastic phenotype (Okada et al. 1996). A canonical process showing the role of partial EMT in development is the branching morphogenesis of the trachea and mammary gland—a mechanism that enables the repeated splitting of a tubular epithelial structure to generate a ductal tree where the growing tubule maintains cell–cell adhesion with neighbors, express P-cadherin together with transient display of mesenchymal features like loss of apico-basal polarity and increased migration in response to extracellular signals like FGF (Micalizzi et al. 2010; Welch-Reardon et al. 2014; Leopold et al. 2012; Leroy and Mostov 2007; Hudson et al. 2009; Niessen et al. 2008). Endothelial cells associated with the microvasculature can also lead to the formation of mesenchymal cells in course of fibrosis by an analogous process known as EndMT orchestrated by molecular regulators of EMT (Potenta et al. 2008). EndMT contributes to the organization of the endocardial cushion and the heart valves during embryogenesis, cardiac fibrosis associated with post-ischemic injury of the heart, and also in kidney fibrosis (Zavadil and Bottinger 2005).

2.2 Pathologic

Pathologic or **type 3 EMT** is characteristic of neoplastic cells that have previously undergone genetic and epigenetic alterations, typically in genes favoring clonal outgrowth and development of localized tumors. It is noteworthy that cancer cells may pass through EMTs to differing extents, with some cells retaining many epithelial traits while acquiring some mesenchymal ones and other cells shedding all vestiges of their epithelial origin and becoming fully mesenchymal. Despite immense attention, there is still uncertainty in identifying the specific signals that induce type 3 EMTs in carcinoma cells. An EMT mark the initiation step of metastatic cascade and MET completes the process on the other hand where the circulating tumor cells (CTCs) during seeding regain their epithelial characteristics and form secondary tumors or macrometastases (Yang and Weinberg 2008; Thiery 2002; Fidler and Poste 2008). While transitioning between the epithelial and mesenchymal phenotypes, cells can also attain a hybrid E/M (i.e., partial or intermediate EMT) phenotype in which the cells possess mixed epithelial (e.g., adhesion) and mesenchymal (e.g., migration) properties, thereby allowing collective cell migration, as seen during migration of multicellular aggregates in the ECM and clusters of CTCs in bloodstream of breast, lung, colon, brain and prostate cancer patients (Christiansen and Rajasekaran 2006; Lecharpentier et al. 2011; Hou et al. 2011; Armstrong et al. 2011; Al-Hajj et al. 2003; O'Brien et al. 2007; Singh et al. 2004). If these clusters reach the bloodstream intact, they can give rise to clusters of CTCs. Cells in the CTC clusters co-express epithelial and mesenchymal markers, can exit the bloodstream more efficiently, are apoptosis-resistant with the capacity of self-renewal and can be up to 50 times more metastatic than individually migrating CTCs with complete EMT phenotype (Yu et al. 2013; Joosse et al. 2015; Aceto et al. 2014). Cells co-expressing E and M markers can be present in the bloodstream of breast, lung, colon, and prostate cancer patients as clusters of CTCs with a median level of three cells per cluster, also referred to as "micro-emboli", and can be apoptosis-resistant correlating with poor prognosis in patients (Lecharpentier et al. 2011; Hou et al. 2011; Armstrong et al. 2011; Al-Hajj et al. 2003; Yu et al. 2013; Joosse et al. 2015; Aceto et al. 2014). However, CTC clusters need not essentially contain only the hybrid E/M cells, and there may be admixtures of E and M cells in a single cluster. Also some of these clusters may contain leukocytes as well as platelets and megakaryocytes implicating cellular heterogeneity of primary tumors. Therefore, EMT-MET reversibility characteristic of type 3 EMT enables solid tumors, over 90% of which are epithelial in nature, to disseminate and colonize distant organs (Christiansen and Rajasekaran 2006).

The tendency of disseminated cancer cells to undergo MET highlights the importance of local microenvironments that they encounter following extravasation into the parenchyma of a distant organ and where the heterotypic signals characteristic of primary tumor that were responsible for inducing the EMT in the first place were absent (Jechlinger et al. 2002; Bissell et al. 2002). Such deliberation indicates that induction of an EMT is likely to be a centrally important mechanism for the progression of carcinomas to a metastatic stage whereas MET is probably instrumental for colonization process.

3 Operating Principles and Inducers of EMT

EMT is a rapidly expanding field particularly, in the domain of tumor biology. The operating principles, proteome components and mechanistic underpinnings that operate in cancer and are pertinent in this synthesis, have been elaborated below.

3.1 Operating Principles of EMT

Epithelial cells can undergo EMT under the influence of multiplex signaling pathways such as TGFβ, EGF, HGF, Notch, FGF, Wnt, and IGF, and mechanical factors such as ECM density (Thiery and Sleeman 2006; Kumar et al. 2014). These signals usually activate one of the EMT-inducing transcription factors (EMT-TFs)—Twist1, Snai1, Snai2 (Slug), Zeb1, Zeb2 (Sip1), Brachyury, Goosecoid, SIX1, and PRRX1—that directly or indirectly repress E-cadherin, the hallmark of epithelial phenotype. Conversely, EMT can be inhibited by p53, MET-TFs such as GRHL2 and ELF5, and microRNA families such as miR-200 and miR-34 (Craene and Berx 2013).

In many carcinomas, these signals congregate on a central EMT regulatory network composed of two interlinked mutually inhibitory feedback loops—miR-34/Snail and miR-200/Zeb. The epithelial phenotype corresponds to high levels of miR-200 and miR-34, whereas the mesenchymal phenotype corresponds to high levels of Zeb and Snail. EMT-inducing signals such as TGFβ, EGF, HGF, and Notch activate Zeb and Snail, and p53 activates miR-200 and miR-34 (Craene and Berx 2013; Park et al. 2008; Burk et al. 2008; Bracken et al. 2008).

3.2 EMT Proteome

EMT proteome reflects a fundamental change in proteins gained, maintained, or lost with the conversion of epiblasts to primary mesenchyme, secondary epithelium to fibroblasts, or in the transition of tumor epithelia to metastatic cells (Carver et al. 2001; Ip and Gridley 2002; Zavadil et al. 2001; Ramaswamy et al. 2003). The signaling pathways act in consortia to stimulate EMT-TFs that repress expression of cardinal epithelial genes enhancing the expression of mesenchymal markers. Common epithelial markers for EMT comprise E-cadherin, β-catenin, cytokeratins, desmoplakin while prominent mesenchymal markers include N-cadherin, vimentin, fibronectin together with EMT-TFs (Grant and Kyprianou 2013). The much-studied

EMT-TFs belong to a number of gene families: (i) the Snail homolog superfamily of zinc-finger proteins (Snai1, Snai2), (ii) those with basic helix-loop-helix motifs (bHLH) (TCF3, TCF4, Twist1, and Twist2) and the Zeb family (Zeb1, Zeb2) that recognize E-box elements in target promoters (Diaz-Martin et al. 2014).

The dynamics of EMT proteome can be explained with the example of Snail superfamily of zinc-finger proteins has two evolutionary branches, one for Scratch and the other for Snail and Slug. These proteins recognize an E-box binding motif on the promoter for E-cadherin (among others) in competition with the basic helix-loop-helix protein SIP1. Ras/MAPK activates Snail while TGF-β regulates Smad-dependent pathways to engage SIP1 and Snail (Nieto 2002; Peinado et al. 2003). Subsequently, E-cadherin, cytokeratin, muc-1, and desmoplakin are repressed, while fibroblast-specific protein-1 (FSP1), fibronectin, vimentin, and Rho are increased (Nieto 2002). Repression of E-cadherin by Snail proteins frees up more cytoplasmic β-catenin, which is co-imported with LEF to the nucleus to be strongly associated with EMT (Kim et al. 2002). Ets transcription factors regulate EMT in the heart (Lie-Venema et al. 2003). One of the more interesting proteins found in the EMT proteome of fibroblast is FSP1, also known as S100A4 that can be induced in exposure to TGF-β and EGF (Strutz et al. 1995; Okada et al. 1997). Members of the S100 superfamily have been implicated in cytoskeletal-membrane interactions, calcium signal transduction, and cellular growth and differentiation (Barraclough 1998). In the presence of calcium, FSP1 may sequester p53 from the APC ubiquitination pathway, perhaps raising levels of free β-catenin (Grigorian et al. 2001). The expression of FSP1 indicates the potential presence of a molecular program determining fibroblast phenotype.

3.3 Mechanisms of EMT in Cancer Cells

The complete spectrum of signaling agents contributing to EMTs of carcinoma cells is yet to be deciphered. EMT can be easily affianced by a combination of cytokines associated with proteolytic dismantling of basement membranes by metalloproteinases or membrane assembly inhibitors (Zeisberg et al. 2002). In many carcinomas, EMT-inducing signals emanating from the tumor-associated stroma, notably HGF, EGF, PDGF, and TGF-β, facilitates EMT by binding epithelial receptors with ligand-inducible intrinsic kinase activity (Morali et al. 2001; Strutz et al. 2002). These EMT-inducers lead to the functional activation of a series of EMT-TFs, notably Snail, Slug, Zeb1, Twist, Goosecoid, and FOXC2 in cancer cells (Jechlinger et al. 2002; Medici et al. 2008; Kokudo et al. 2008). The actual execution of EMT program in tumor cells depends on a series of intracellular signaling networks involving ERK, MAPK, PI3K, Akt, Smads, RhoB, β-catenin, LEF, Ras, and c-Fos as well as cell surface proteins like β4 integrins, α5β1 integrin, and αVβ6 integrin (Tse and Kalluri 2007). Activation of EMT programs is also facilitated by the disruption of cell–cell adherens junctions and the cell-ECM adhesions mediated by integrins (Weinberg 2008; Taki et al. 2006). While TGF-β is considered prototypical in EMT induction, overexpression of epithelial EGF receptors in the EMT microenvironment is essential for completing the conversion (Strutz et al. 1995; Derynck and Zhang 2003). IGF-II directs the redistribution of β-catenins from the cell surface to the nucleus and facilitates the intracellular degradation of E-cadherin, while FGF-2 and TGF-β are required for the expression of MMP-2 and MMP-9 to assist in basement membrane degradation (Morali et al. 2001; Strutz et al. 2002). Combinations of growth factors/cytokines are generally present in most areas of tissue injury. It is difficult to assign priorities but each of them may contribute a unique inducement toward the transition.

TGF-β-induced EMT can serve as a positive regulator of tumor progression and metastasis through two signaling pathways (Bierie and Moses 2006): (a) Smad-mediated signaling induced by TGF-β activate EMT and enhance cellular motility via the ALK-5 receptor (Roberts et al. 2006). (b) p38 MAPK and RhoA mediate an autocrine TGF-β-induced EMT that requires integrin β1-mediated signaling and the activation of latent TGF-β by αVβ6 integrin (Bhowmick et al. 2001). TGF-β-induced EMT is augmented by ECM molecule Fibulin-5, Ras and Raf promoting invasiveness of cancer cells (Lee et al. 2008). The connection between inflammation and EMT was bridged when COX-2 also found to enhance TGF-β-induced EMT through a PGE_2-dependent mechanism (Neil et al. 2008). TGF-β is the most potent inducer of Snail factors' transcription, which of all EMT-TFs repress E-cadherin expression directly besides that of cadherin-16 and HNF-1β, (Boutet et al. 2007). Snails can also act as trans-activator of transcription of vimentin and α-SMA indirectly as well as pro-inflammatory mediators (IL-1, IL-6 and IL-8) (Boutet et al. 2006). In a tumor microenvironment, Snail can be activated through a number of pathways, including HIF1, HIF2, and Notch in response to hypoxia as well as NF-κB and TGF-β in response to inflammation (Zhang et al. 2013). IGFR has been shown to induce EMT through upregulation of NF-κB, Zeb and Snail and also by activating latent TGF-β1 (Graham et al. 2008). HIF-1α, the exemplary central mediator of aggressive, mesenchymal phenotypes in hypoxic and inflammatory environments, has been shown to induce IL-8, VEGF, and Twist1 expression, and thus EMT. VEGF-A, a noteworthy downstream molecule in HIF-1α regulatory pathway, is thought to contribute to EMT by promoting nuclear localization of Snail1 (Mak et al. 2010).

Sequestration of β-catenin in the cytoplasm is important for the preservation of epithelial features of cancer cells, and acquisition of the mesenchymal phenotype correlates with the movement of β-catenin to the nucleus, where it becomes part of Tcf/LEF complexes (Gottardi et al. 2001). The nuclear import of LEF proteins with Smad3 or β-catenin from the cytoplasm is being considered as one of several key molecular steps in EMT (Kim et al. 2002; Attisano et al. 2002). β-catenin phosphorylation by glycogen synthase kinase-3β (GSK-3β) or p53 activation of APC-dependent pathways leads to direct loss of free β-catenin through ubiquitation (Aberle et al. 1997). Wnt-1, IGF-II, Ras, Src kinase and ILK all stabilize cytoplasmic levels of β-catenin with suppression of E-cadherin to facilitate EMT (Kim et al. 2002; Bhowmick et al. 2001; Li et al. 2003). Smad3 activation by TGF-β family members can also activate LEF-1 in the absence of β-catenin (Attisano et al. 2002; Li et al. 2003; He 2003). E-cadherin expression levels vary dramatically in different human tumors, and an inverse relationship between levels of E-cadherin and patient survival has been documented. Loss of E-cadherin promotes Wnt signaling and is associated with high levels of SNAIL in the nucleus (Blanco et al. 2002). SIP1 represses E-cadherin expression and binds, along with SNAIL, to the E-cadherin promoter in an overlapping fashion (Putte et al. 2003).

Noncoding microRNAs are also components of the cellular signaling circuitry implicated in the EMT program where they present oncogenic or tumor-suppressive roles in cancer progression (Xia and Hui 2012). For instance, miR-221/222 induces tumor cell migration and invasion by suppressing expression of TRPS1 which in turn represses Zeb2 while miR-21 facilitates TGF-β-induced EMT (Zavadil et al. 2007). MicroRNAs like miR-200 family and miR-205 directly regulate expression of ZEB family of EMT drivers while members of miR-520/373 family and miR-302/miR-372/miR-106 family control expression of TGFBR2 and RhoC and thereby can accelerate reprogramming and stem cell pluripotency by inhibiting EMT and enhancing MET programs (Li et al. 2011; Keklikoglou et al. 2012). Therefore, blocking oncogenic microRNAs or introducing tumor-suppressive microRNAs represent potent therapeutic strategies against tumor progression.

3.4 Tumor Hypoxia and EMT

The capability to acclimatize to the microenvironment is possibly an initial survival strategy availed by the cancer cells to adverse conditions existing within the primary tumor and in metastatic microenvironments (Morton et al. 1993). Hypoxia is one of the most universal microenvironments for multi-pathophysiologic processes including tumorigenesis. HIF-1α is a master regulator of majority of cancer-associated transcriptional changes (Cantor and Sabatini 2012). HIF-1α can transactivate a wide range of target genes that includes several EMT regulators like Twist, Snail, Zeb1, Sip1, E47/TCF3, CTGF, and LOX through hypoxia-responsive element (Erler et al. 2006; Sun et al. 2009). Besides, hypoxia is also reported to activate a number of EMT-signaling pathways like Notch, TGFβ, NFκβ, MAPK, PI3K/AKT and WNT/β-catenin signaling pathways that triggers expression of the EMT-TFs in a number of cancers like prostate, breast and ovarian cancer (Chen et al. 2010; Sahlgren et al. 2008).

3.5 MicroRNAs and EMT

MicroRNAs have emerged as important controller in majority of cancers with many of them being involved in important developmental processes such as differentiation and EMT (Wiklund et al. 2011). Expression signatures of such microRNAs are often highly tissue-specific, stable and detectable in body fluids and therefore have been proposed by several reports to be useful in classifying tumor subtype and origin and also in predicting prognosis (Metias et al. 2009). Recently, several independent studies have shown a central role of miR-200 family and miR-205 in EMT vis-a-vis in tumor invasion and metastasis (Park et al. 2008; Burk et al. 2008; Li et al. 2011).

The miR-200 family comprises five members (miR-200a, -200b, -200c, -141 and -429) that are expressed as two genomic clusters, miR-200b-200a-429 and miR-200c-141, located on human chromosomes 1p36.33 and 12p12.31, respectively (Mongroo and Rustgi 2010). The members of miR-200 family and miR-205 are key determinants of the epithelial phenotype by directly targeting Zeb1/2, Snail and Slug which function as transcriptional repressors of E-cadherin and other genes central to adhesion and epithelial polarity, namely, P-cadherin, Occludin, Claudin 7, etc. (Park et al. 2008; Aigner et al. 2007). Adding to the complexity of the EMT regulatory program is the recent discovery of the self-reinforcing regulatory loop wherein the transcriptional repressors like Zeb1/2 and Slug specifically interact with the E /Z-boxes in the promoter regions of these microRNAs and suppress their transcription, leading to amplification of EMT (Burk et al. 2008; Bracken et al. 2008). The expression level of all five members of miR-200 family was demonstrated to be significantly reduced in cells following TGFβ-mediated EMT. Conversely, ectopic expression of the miR-200 microRNAs in mesenchymal cells promoted mesenchymal to epithelial transition. In addition, inhibition of miR-200 induces mesenchymal-like spindle cell morphology, accompanied by an increase in Zeb1 and Slug expression and cell migration in breast and prostate cancers (Liu et al. 2014). Overexpression of the miR-200 members individually or in separate clusters suppressed EMT by downregulating Zeb1/2 and upregulating E-cadherin expression in murine mammary tumor cells (Park et al. 2008; Li et al. 2011). Despite constituting same family miR 200, the five members can be categorized into two functional groups (miR-200b/200c/429 and miR-200a/141) based on two factors: (i) their seed sequences differ at one position from the other, and (iii) each group could target different or the same sets of genes (Liu et al. 2013).

4 Conclusion

Accumulating evidence in recent years implicates EMT to be a critical process correlating with the dissolution of epithelial integrity, increased migration along with acquisition of invasiveness and metastatic potential of cancer cells. Most pathways controlling EMT-like behavior in cancer cells can be linked to specific changes in the tumor microenvironment. Tumor cells eventually acclimatize to a nutrient-indigent, hypoxic surrounding by increasing their metabolic rate and activating alternative means to adjust to hypoxia. Identification of EMT markers like the transcriptional regulators and effector molecules that promote invasion, migration and metastatic properties of cancer will be useful to understand the pathway of disease progression. At the same time, characterization of features of tumor microenvironment and microRNAs that actively participate in molecular reprogramming of EMT pathway may provide biomarkers of clinical relevance for early diagnosis and prognosis of malignancy.

Acknowledgements We duly acknowledge the Honorable Chancellor, Adamas University, Kolkata, India for providing us the infrastructure and facilities.

References

Aberle H, Bauer A, Stappert J, Kispert A, Kemler R (1997) beta-catenin is a target for the ubiquitin-proteasome pathway. EMBO J 16(13):3797–3804

Aceto N, Bardia A, Miyamoto DT, Donaldson MC, Wittner BS, Spencer JA, Yu M, Pely A, Engstrom A, Zhu H, Brannigan BW, Kapur R, Stott SL, Shioda T, Ramaswamy S, Ting DT, Lin CP, Toner M, Haber DA, Maheswaran S (2014) Circulating tumor cell clusters are oligoclonal precursors of breast cancer metastasis. Cell 158(5):1110–1122

Aigner K, Dampier B, Descovich L, Mikula M, Sultan A, Schreiber M, Mikulits W, Brabletz T, Strand D, Obrist P, Sommergruber W, Schweifer N, Wernitznig A, Beug H, Foisner R, Eger A (2007) The transcription factor ZEB1 (deltaEF1) promotes tumour cell dedifferentiation by repressing master regulators of epithelial polarity. Oncogene 26(49):6979–6988

Al-Hajj M, Wicha MS, Benito-Hernandez A, Morrison SJ, Clarke MF (2003) Prospective identification of tumorigenic breast cancer cells. Proc Natl Acad Sci U S A 100(7):3983–3988

Armstrong AJ, Marengo MS, Oltean S, Kemeny G, Bitting RL, Turnbull JD, Herold CI, Marcom PK, George DJ, Garcia-Blanco MA (2011) Circulating tumor cells from patients with advanced prostate and breast cancer display both epithelial and mesenchymal markers. Mol Cancer Res 9(8):997–1007

Attisano L, Wrana JL (2002) Signal transduction by the TGF-beta superfamily. Science 296(5573):1646–1647

Barraclough R (1998) Calcium-binding protein S100A4 in health and disease. Biochim Biophys Acta (BBA) Mol Cell Res 1448(2):190–199

Bhowmick NA, Zent R, Ghiassi M, McDonnell M, Moses HL (2001) Integrin beta 1 signaling is necessary for transforming growth factor-beta activation of p38MAPK and epithelial plasticity. J Biol Chem 276(50):46707–46713

Bierie B, Moses HL (2006) TGFβ: the molecular Jekyll and Hyde of cancer. Nat Rev Cancer 6(7):506–520

Bissell MJ, Radisky DC, Rizki A, Weaver VM, Petersen OW (2002) The organizing principle: microenvironmental influences in the normal and malignant breast. Differentiation 70(9–10):537–546

Blanco MJ, Moreno-Bueno G, Sarrio D, Locascio A, Cano A, Palacios J, Nieto MA (2002) Correlation of Snail expression with histological grade and lymph node status in breast carcinomas. Oncogene 21(20):3241–3246

Boutet A, De Frutos CA, Maxwell PH, Mayol MJ, Romero J, Nieto MA (2006) Snail activation disrupts tissue homeostasis and induces fibrosis in the adult kidney. EMBO J 25(23):5603–5613

Boutet A, Esteban MA, Maxwell PH, Nieto MA (2007) Reactivation of Snail genes in renal fibrosis and carcinomas: a process of reversed embryogenesis? Cell Cycle 6(6):638–642

Bracken CP, Gregory PA, Kolesnikoff N, Bert AG, Wang J, Shannon MF, Goodall GJ (2008) A double-negative feedback loop between ZEB1-SIP1 and the microRNA-200 family regulates epithelial-mesenchymal transition. Cancer Res 68(19):7846–7854

Burk U, Schubert J, Wellner U, Schmalhofer O, Vincan E, Spaderna S, Brabletz T (2008) A reciprocal repression between ZEB1 and members of the miR-200 family promotes EMT and invasion in cancer cells. EMBO Rep 9(6):582–589

Cantor JR, Sabatini DM (2012) Cancer cell metabolism: one hallmark, many faces. Cancer Discov 2(10):881–898

Carver EA, Jiang R, Lan Y, Oram KF, Gridley T (2001) The mouse snail gene encodes a key regulator of the epithelial-mesenchymal transition. Mol Cell Biol 21(23):8184–8188

Chen J, Imanaka N, Chen J, Griffin JD (2010) Hypoxia potentiates Notch signaling in breast cancer leading to decreased E-cadherin expression and increased cell migration and invasion. Br J Cancer 102(2):351–360

Christiansen JJ, Rajasekaran AK (2006) Reassessing epithelial to mesenchymal transition as a prerequisite for carcinoma invasion and metastasis. Cancer Res 66(17):8319–8326

De Craene B, Berx G (2013) Regulatory networks defining EMT during cancer initiation and progression. Nat Rev Cancer 13(2):97–110

Derynck R, Zhang YE (2003) Smad-dependent and Smad-independent pathways in TGF-β family signalling. Nature 425(6958):577–584

Diaz-Martin J, Diaz-Lopez A, Moreno-Bueno G, Castilla MA, Rosa-Rosa JM, Cano A, Palacios J (2014) A core microRNA signature associated with inducers of the epithelial-to-mesenchymal transition. J Pathol 232(3):319–329

Duband JL, Thiery JP (1982) Appearance and distribution of fibronectin during chick embryo gastrulation and neurulation. Dev Biol 94(2):337–350

Erler JT, Bennewith KL, Nicolau M, Dornhöfer N, Kong C, Le QT, Chi JT, Jeffrey SS, Giaccia AJ (2006) Lysyl oxidase is essential for hypoxia-induced metastasis. Nature 440(7088):1222–1226

Fidler IJ, Poste G (2008) The seed and soil hypothesis revisited. Lancet Oncol 9(8):808

Gottardi CJ, Wong E, Gumbiner BM (2001) E-cadherin suppresses cellular transformation by inhibiting beta-catenin signaling in an adhesion-independent manner. J Cell Biol 153(5):1049–1060

Graham TR, Zhau HE, Odero-Marah VA, Osunkoya AO, Kimbro KS, Tighiouart M, Liu T, Simons JW, O'Regan RM (2008) Insulin-like growth factor-I-dependent up-regulation of ZEB1 drives epithelial-to-mesenchymal transition in human prostate cancer cells. Cancer Res 68(7):2479–2488

Grant CM, Kyprianou N (2013) Epithelial mesenchymal transition (EMT) in prostate growth and tumor progression. Transl Androl Urol 2(3):202–211

Grigorian M, Andresen S, Tulchinsky E, Kriajevska M, Carlberg C, Kruse C, Cohn M, Ambartsumian N, Christensen A, Selivanova G, Lukanidin E (2001) Tumor Suppressor p53 Protein Is a New Target for the Metastasis-associated Mts1/S100A4 Protein FUNCTIONAL CONSEQUENCES OF THEIR INTERACTION. J Biol Chem 276(25):22699–22708

Hay ED (1990) Role of cell-matrix contacts in cell migration and epithelial–mesenchymal transformation. Cell Differ Dev 32(3):367–375

He X (2003) A Wnt-Wnt situation. Dev Cell 4(6):791–797

Hou JM, Krebs M, Ward T, Sloane R, Priest L, Hughes A, Clack G, Ranson M, Blackhall F, Dive C (2011) Circulating tumor cells as a window on metastasis biology in lung cancer. Am J Pathol 178(3):989–996

Howe EN, Cochrane DR, Richer JK (2011) Targets of miR-200c mediate suppression of cell motility and anoikis resistance. Breast Cancer Res 13(2):R45

Hudson LG, Newkirk KM, Chandler HL, Choi C, Fossey SL, Parent AE, Kusewitt DF (2009) Cutaneous wound reepithelialization is compromised in mice lacking functional Slug (Snai2). J Dermatol Sci, 56(1):19–26

Ip YT, Gridley T (2002) Cell movements during gastrulation: snail dependent and independent pathways. Curr Opin Genet Dev 12(4):423–429

Jechlinger M, Grunert S, Beug H (2002) Mechanisms in epithelial plasticity and metastasis: insights from 3D cultures and expression profiling. J Mammary Gland Biol Neoplasia 7(4):415–432

Jolly MK, Boareto M, Huang B, Dongya J, Mingyang L, Eshel B-J, Onuchic JN, Herbert L (2016) Implications of the hybrid epithelial/mesenchymal phenotype in metastasis. Front Oncol 5:155

Joosse SA, Gorges TM, Pantel K (2015) Biology, detection, and clinical implications of circulating tumor cells. EMBO Mol Med 7(1):1–11

Kalluri R, Neilson EG (2003) Epithelial–mesenchymal transition and its implications for fibrosis. J Clin Invest 112(12):1776–1784

Kalluri R, Weinberg RA (2009) The basics of epithelial–mesenchymal transition. J Clin Invest 119(6):1420–1428

Karafiat V, Dvorakova M, Pajer P, Cermak V, Dvorak M (2007) Melanocyte fate in neural crest is triggered by Myb proteins through activation of c-kit. Cell Mol Life Sci 64(22):2975–2984
Keklikoglou I, Koerner C, Schmidt C, Zhang JD, Heckmann D, Shavinskaya A, Allgayer H, Gückel B, Fehm T, Schneeweiss A, Sahin O, Wiemann S, Tschulena U (2012) MicroRNA-520/373 family functions as a tumor suppressor in estrogen receptor negative breast cancer by targeting NF-kappaB and TGF-beta signaling pathways. Oncogene 31(37):4150–4163
Kim K, Lu Z, Hay LZ (2002) Direct evidence for a role of beta-catenin/LEF-1 signaling pathway in induction of EMT. Cell Biol Int 26(5):463–476
Kokudo T, Suzuki Y, Yoshimatsu Y, Yamazaki T, Watabe T, Miyazono K (2008) Snail is required for TGFβ-induced endothelial–mesenchymal transition of embryonic stem cell-derived endothelial cells. J Cell Sci 121(20):3317–3324
Kumar S, Das A, Sen S (2014) Extracellular matrix density promotes EMT by weakening cell–cell adhesions. Mol Biosyst 10(4):838–850
Lecharpentier A, Vielh P, Perez-Moreno P, Planchard D, Soria JC, Farace F(2011) Detection of circulating tumour cells with a hybrid (epithelial/mesenchymal) phenotype in patients with metastatic non-small cell lung cancer. Br J Cancer 105(9):1338–1341
Lee JM, Dedhar S, Kalluri R, Thompson EW (2006) The epithelial–mesenchymal transition: new insights in signaling, development, and disease. J Cell Biol 172(7):973–981
Lee YH, Albig AR, Regner M, Schiemann BJ, Schiemann WP (2008) Fibulin-5 initiates epithelial–mesenchymal transition (EMT) and enhances EMT induced by TGF-beta in mammary epithelial cells via a MMP-dependent mechanism. Carcinogenesis 29(12):2243–2251
Leopold PL, Vincent J, Wang H (2012) A comparison of epithelial-to-mesenchymal transition and re-epithelialization. Semin Cancer Biol 22(5–6):471–483
Leroy P, Mostov KE (2007) Slug is required for cell survival during partial epithelial–mesenchymal transition of HGF-induced tubulogenesis. Mol Biol Cell 18(5):1943–1952
Liem KF, Jessell TM, Briscoe J (2000) Regulation of the neural patterning activity of sonic hedgehog by secreted BMP inhibitors expressed by notochord and somites. Development 127(22):4855–4866
Lie-Venema H, Gittenberger-de Groot AC, van Empel LJ, Boot MJ, Kerkdijk H, de Kant E, DeRuiter MC (2003) Ets-1 and Ets-2 transcription factors are essential for normal coronary and myocardial development in chicken embryos. Circ Res 92(7):749–756
Liu P, Wakamiya M, Shea MJ, Albrecht U, Behringer RR, Bradley A (1999) Requirement for Wnt3 in vertebrate axis formation. Nat Genet 22(4):361–365
Liu YN, Yin JJ, Abou-Kheir W, Hynes PG, Casey OM, Fang L, Yi M, Stephens RM, Seng V, Sheppard-Tillman H, Martin P, Kelly K (2013) MiR-1 and miR-200 inhibit EMT via Slug-dependent and tumorigenesis via Slug-independent mechanisms. Oncogene, 32(3):296–306
Liu Y, Li X, Roslan S, Johnstone CN, Wright JA, Bracken CP, Anderson M, Bert AG, Selth LA, Anderson RL, Goodall GJ, Gregory PA, Khew-Goodall Y (2014) MiR-200 can repress breast cancer metastasis through ZEB1-independent but moesin-dependent pathways. Oncogene 33(31):4077–4088
Li Y, Yang J, Dai C, Wu C, Liu Y (2003) Role for integrin-linked kinase in mediating tubular epithelial to mesenchymal transition and renal interstitial fibrogenesis. J Clin Invest 112(4):503–516
Li Z, Yang CS, Nakashima K, Rana TM (2011) Small RNA-mediated regulation of iPS cell generation. EMBO J 30(5):823–834
Mak P, Leav I, Pursell B, Bae D, Yang X, Taglienti CA, Gouvin LM, Sharma VM, Mercurio AM (2010) ERbeta impedes prostate cancer EMT by destabilizing HIF-1alpha and inhibiting VEGF-mediated snail nuclear localization: implications for Gleason grading. Cancer Cell 17(4):319–332
Medici D, Hay ED, Olsen BR (2008) Snail and Slug promote epithelial–mesenchymal transition through beta-catenin-T-cell factor-4-dependent expression of transforming growth factor-beta3. Mol Biol Cell 19(11):4875–4887
Metias SM, Lianidou E, Yousef GM (2009) MicroRNAs in clinical oncology: at the crossroads between promises and problems. J Clin Pathol 62(9):771–776

Micalizzi DS, Farabaugh SM, Ford HL (2010) Epithelial–mesenchymal transition in cancer: parallels between normal development and tumor progression. J Mammary Gland Biol Neoplasia 15(2):117–134

Mongroo PS, Rustgi AK (2010) The role of the miR-200 family in epithelial–mesenchymal transition. Cancer Biol Ther 10(3):219–222

Morali OG, Delmas V, Moore R, Jeanney C, Thiery JP, Larue L (2001) IGF-II induces rapid β-catenin relocation to the nucleus during epithelium to mesenchyme transition. Oncogene 20(36):4942–4950

Morton RA, Ewing CM, Nagafuchi A, Tsukita S, Isaacs WB (1993) Reduction of E-cadherin levels and deletion of the alpha-catenin gene in human prostate cancer cells. Cancer Res 53(15):3585–3590

Neil JR, Johnson KM, Nemenoff RA, Schiemann WP (2008) Cox-2 inactivates Smad signaling and enhances EMT stimulated by TGF-beta through a PGE2-dependent mechanisms. Carcinogenesis 29(11):2227–2235

Niessen K, Fu Y, Chang L, Hoodless PA, McFadden D, Karsan A (2008) Slug is a direct Notch target required for initiation of cardiac cushion cellularization. J Cell Biol 182(2):315–325

Nieto MA (2002) The snail superfamily of zinc-finger transcription factors. Nat Rev Mol Cell Biol 3(3):155–166

Nistico P, Bissell MJ, Radisky DC (2012) Epithelial-mesenchymal transition: general principles and pathological relevance with special emphasis on the role of matrix metalloproteinases. Cold Spring Harb Perspect Biol 4(2)

O’Brien CA, Pollett A, Gallinger S, Dick JE (2007) A human colon cancer cell capable of initiating tumour growth in immunodeficient mice. Nature 445(7123):106–110

Okada H, Strutz F, Danoff TM, Kalluri R, Neilson EG (1996) Possible mechanisms of renal fibrosis. Contrib Nephrol 118:147–154

Okada H, Danoff TM, Kalluri R, Neilson EG (1997) Early role of Fsp1 in epithelial–mesenchymal transformation. Am J Physiol-Renal Physiol 273(4):F563–F574

Park SM, Gaur AB, Lengyel E, Peter ME (2008) The miR-200 family determines the epithelial phenotype of cancer cells by targeting the E-cadherin repressors ZEB1 and ZEB2. Genes Dev 22(7):894–907

Peinado H, Quintanilla M, Cano A (2003) Transforming growth factor beta-1 induces snail transcription factor in epithelial cell lines: mechanisms for epithelial mesenchymal transitions. J Biol Chem 278(23):21113–21123

Potenta S, Zeisberg E, Kalluri R (2008) The role of endothelial-to-mesenchymal transition in cancer progression. Br J Cancer 99(9):1375–1379

Ramaswamy S, Ross KN, Lander ES, Golub TR (2003) A molecular signature of metastasis in primary solid tumors. Nat Genet 33(1):49–54

Roberts AB, Tian F, Byfield SD, Stuelten C, Ooshima A, Saika S, Flanders KC (2006) Smad3 is key to TGF-β-mediated epithelial-to-mesenchymal transition, fibrosis, tumor suppression and metastasis. Cytokine Growth Factor Rev 17(1–2):19–27

Sahlgren C, Gustafsson MV, Jin S, Poellinger L, Lendahl U (2008) Notch signaling mediates hypoxia-induced tumor cell migration and invasion. Proc Natl Acad Sci U S A 105(17):6392–6397

Singh SK, Hawkins C, Clarke ID, Squire JA, Bayani J, Hide T, Henkelman RM, Cusimano MD, Dirks PB (2004) Identification of human brain tumour initiating cells. Nature 432(7015):396–401

Skromne I, Stern CD (2001) Interactions between Wnt and Vg1 signalling pathways initiate primitive streak formation in the chick embryo. Development 128(15):2915–2927

Strutz F, Okada H, Lo CW, Danoff T, Carone RL, Tomaszewski JE, Neilson EG (1995) Identification and characterization of a fibroblast marker: FSP1. J Cell Biol 130(2):393–405

Strutz F, Zeisberg M, Ziyadeh FN, Yang CQ, Kalluri R, Müller GA, Neilson EG, Renziehausen A, Sisic Z (2002) Role of basic fibroblast growth factor-2 in epithelial–mesenchymal transformation. Kidney Int 61(5):1714–1728

Sun S, Ning X, Zhang Y, Lu Y, Nie Y, Han S, Liu L, Du R, Xia L, He L, Fan D (2009) Hypoxia-inducible factor-1alpha induces Twist expression in tubular epithelial cells subjected to hypoxia, leading to epithelial-to-mesenchymal transition. Kidney Int 75(12):1278–1287

Taki M, Verschueren K, Yokoyama K, Nagayama M, Kamata N (2006) Involvement of Ets-1 transcription factor in inducing matrix metalloproteinase-2 expression by epithelial–mesenchymal transition in human squamous carcinoma cells. Int J Oncol 28(2):487–496

Thiery JP (2002) Epithelial–mesenchymal transitions in tumour progression. Nat Rev Cancer 2(6):442–454

Thiery JP (2003) Epithelial–mesenchymal transitions in development and pathologies. Curr Opin Cell Biol 15(6):740–746

Thiery JP, Sleeman JP (2006) Complex networks orchestrate epithelial–mesenchymal transitions. Nat Rev Mol Cell Biol 7(2):131–142

Tse JC, Kalluri R (2007) Mechanisms of metastasis: epithelial-to-mesenchymal transition and contribution of tumor microenvironment. J Cell Biochem 101(4):816–829

Van de Putte T, Maruhashi M, Francis A, Nelles L, Kondoh H, Huylebroeck D, Higashi Y (2003) Mice lacking ZFHX1B, the gene that codes for Smad-interacting protein-1, reveal a role for multiple neural crest cell defects in the etiology of Hirschsprung disease-mental retardation syndrome. Am J Hum Genet 72(2):465–470

Weinberg RA (2008) Twisted epithelial–mesenchymal transition blocks senescence. Nat Cell Biol 10(9):1021–1023

Welch-Reardon KM, Ehsan SM, Wang K, Wu N, Newman AC, Ashley RL, Fong H, George SC, Edwards RA, Hughes CCW (2014) Angiogenic sprouting is regulated by endothelial cell expression of Slug. J Cell Sci 127(Pt 9):2017–2028

Wiklund ED, Bramsen JB, Hulf T, Dyrskjøt L, Ramanathan R, Hansen TB, Villadsen SB, Gao S, Ostenfeld MS, Borre M, Peter ME, Ørntoft TF, Kjems J, Clark SJ (2011) Coordinated epigenetic repression of the miR-200 family and miR-205 in invasive bladder cancer. Int J Cancer 128(6):1327–1334

Xia H, Hui KM (2012) MicroRNAs involved in regulating epithelial-mesenchymal transition and cancer stem cells as molecular targets for cancer therapeutics. Cancer Gene Ther 19(11):723–730

Yang J, Weinberg RA (2008) Epithelial-mesenchymal transition: at the crossroads of development and tumor metastasis. Dev Cell 14(6):818–829

Yu M, Bardia A, Wittner BS, Stott SL, Smas ME, Ting DT, Isakoff SJ, Ciciliano JC, Wells MN, Shah AM, Concannon KF, Donaldson MC, Sequist LV, Brachtel E, Sgroi D, Baselga J, Ramaswamy S, Toner M, Haber DA, Maheswaran S (2013) Circulating breast tumor cells exhibit dynamic changes in epithelial and mesenchymal composition. Science 339(6119):580–584

Zavadil J, Bitzer M, Liang D, Yang YC, Massimi A, Kneitz S, Piek E, Bottinger EP (2001) Genetic programs of epithelial cell plasticity directed by transforming growth factor-beta. Proc Natl Acad Sci U S A 98(12):6686–6691

Zavadil J, Bottinger EP (2005) TGF-beta and epithelial-to-mesenchymal transitions. Oncogene 24(37):5764–5774

Zavadil J, Narasimhan M, Blumenberg M, Schneider RJ (2007) Transforming growth factor-beta and microRNA:mRNA regulatory networks in epithelial plasticity. Cells Tissues Organs 185(1–3):157–161

Zeisberg M, Maeshima Y, Mosterman B, Kalluri R (2002) Renal fibrosis: extracellular matrix microenvironment regulates migratory behavior of activated tubular epithelial cells. Am J Pathol 160(6):2001–2008

Zeisberg EM, Tarnavski O, Zeisberg M, Dorfman AL, McMullen JR, Gustafsson E, Chandraker A, Yuan X, Pu WT, Roberts AB, Neilson EG, Sayegh MH, Izumo S, Kalluri R (2007) Endothelial-to-mesenchymal transition contributes to cardiac fibrosis. Nat Med 13(8):952–961

Zhang L, Huang G, Li X, Zhang Y, Jiang Y, Shen J, Liu J, Wang Q, Zhu J, Feng X, Dong J, Qian C (2013) Hypoxia induces epithelial-mesenchymal transition via activation of SNAI1 by hypoxia-inducible factor -1alpha in hepatocellular carcinoma. BMC Cancer 13:108

Challenges Against DENV3 Vaccines: A Bioinformatic Approach

Souvik Maiti, Kuntal Pal, and Srijan Haldar

Abstract Dengue virus (DENV) causes significant mortality as well as co-morbidity in tropical and subtropical countries, causing huge number of infections every year. Dengue can cause a different disease, starting from mild flu-like symptoms, to severe DENV hemorrhagic fever and Dengue shock syndrome (DSS). Although in case of other flaviviruses like yellow fever and Japanese encephalitis viruses live attenuated vaccines have been developed none of the DENV vaccines are available till now however the different types of vaccine are under clinical trial including recombinant subunit, live attenuated, DNA, inactivated, and viral vectored vaccine, etc. In this study, we have focused on the challenges against the DENV3 vaccine. Our data reveals that the B-cell epitope region located in the variable regions of DENV3 genome which may cause a vital challenge in vaccine development.

Keywords Dengue · Vaccines · B-cell epitopes · DENV3

1 Introduction

Dengue virus, a RNA virus, member of the genus Flavivirus of the family (includes four different serotypes DEN-1, DEN-2, DEN-3, and DEN-4) causes approximately 390 million infections that lead to 25,000 deaths per year (Bhatt et al. 2013). Clinical syndrome caused by DENV infection is benign in most patients however can be fatal in a small proportion due to haemorrhage and fluid leakage that lead to systemic shock and multiorgan failure (Murphy and Whitehead 2011). The enzymatic response is marshal by way of the RNA-based RNA polymerase (RdRp) pursuit of the viral NS5 protein, in association with the viral protease/helicase NS3, different viral NS proteins, and possibly host factors (Henchal and Putnak 1990; Guzman et al. 2010) (see Fig. 1). The newly synthesized RNA pertains to the capsid (C) protein through a

S. Maiti · K. Pal (✉) · S. Haldar (✉)
Biotechnology Department, Adamas University, Kolkata, India
e-mail: kuntal.pal@adamsuniversity.ac.in

S. Haldar
e-mail: srijan.haldar@adamsuniversity.ac.in

M. Mukherjee et al. (eds.), *Advances in Medical Physics and Healthcare Engineering*, Lecture Notes in Bioengineering, https://doi.org/10.1007/978-981-33-6915-3_48

Fig. 1 Structural organization of viral genome

technique nevertheless unrevealed. Furin-mediated proteolysis of prM fusion causes of the E homodimerization rearrangement that leads to generation of viral particles (Ge and Zhou 2014). After mRNA translation, convoluted membranes and vesicle applications were generated due to virus-induced hypertrophy of intracellular membranes. Flavivirus RNA synthesis takes place in adjoining interrelation with cellular membranes within the vesicle programs in so-referred to as viral replication complexes. The operation is set approximately along with the synthesis of a poor strand RNA, which serves as a template for the amplification of additional tremendous strand genomic RNA. After host cell invasion through receptor mediated endocytosis fusion of viral and vesicular membranes allow to deliver of the genomic RNA into the cytoplasm. Over last two decades, several initiatives has been taken to develop a tetravalent DENV vaccine (Liu et al. 2016). None of the DENV vaccines is available till now however several trails have been already done which include live attenuated, inactivated, DNA vaccines, and viral vectored vaccines. However recent phase III live attenuated DENV vaccine efficacy trials showed mixed efficacy in some populations (Guy and Jackson 2016). The DENV mediated Ab responses have been well studied for many years (Halstead et al. 1983; Rothman 2011; Zompi and Harris 2013). A newly exposed individual to DENV showed an IgM-specific primary antibody response which is followed by a durable IgG response. Different type if IgG antibodies are generated initially which includes serotype cross-reactive neutralizing antibodies serotype cross-reactive non-neutralizing antibodies, and serotype-specific neutralizing antibodies (Torresi et al. 2017). However, none of these antibodies are able to protect individuals for more than a year (Torresi et al. 2017; Liu et al. 2016). Due to presence of different serotypes, it is more difficult to develop a single vaccine although there is huge similarity lies between all four serotypes. In this article, we have searched for the conserved nature of linear B-cell epitopes in DENV1 and DENV3 virus. DENV Genome polyprotein sequences were taken from UniProt database for all serotypes and sequence alignment was performed in the Clustal-W on MEGA6 platform. Aligned sequence of DENV 1-4 were rendered using ESPript3.0 server for identification of conserved mutation. With the help of IEDB B-cell epitope prediction database we have identified the possible epitope and the search their location in the genome. Our data showed liner bell epitopes are positioned in the non-conserved region of ORF in DENV3 which may indicate the higher fatality case of DENV 3 with respect to others.

2 Result

2.1 *Polyprotein Sequence Analysis of Dengue Virus Serotypes Reveals a Major Variations in Membrane Protein Region*

Polyprotein sequence of dengue serotypes for DENV1 (strain Nauru/West Pac/1974; strain Brazil/97-11/1997; strain Singapore/S275/1990; strain Thailand/AHF 82-80/1980), DENV2 (strain Puerto Rico/PR159-S1/1969; strain Thailand/NGS-C/1944; isolate Thailand/0168/1979; strain Thailand/16681/1984; strain Peru/IQT2913/1996; strain Jamaica/1409/1983; strain 16681-PDK53), DENV3 (strain Martinique/1243/1999; strain Philippines/H87/1956; strain Sri Lanka/1266/2000; strain Singapore/8120/1995; strain China/80-2/1980) and DENV4 (strain Thailand/0476/1997; strain Singapore/8976/1995; strain Dominica/814669/1981; strain Thailand/0348/1991; strain Philippines/H241/1956) were analyzed by alignment using clustal omega (https://www.ebi.ac.uk/Tools/msa/clustalo/). The alignments were further rendered using ESPript3. The alignment data for DENV1-4 reveals several regions with conserved and non-conserved mutations. Major variations among serotypes sequence were seen for DENV1 and DENV3. Several important reverse charge mutations in Envelope domain of DENV1 like E475R, K483E) were identified. Similar, sequence variability were also seen in DENV2-4 with highest rate of mutational change in DENV3. The regions were highlighted in Fig. 1. The non-conserved mutational changes are important to analyze as they are important characteristics of RNA viruses to adopt in a new host environment. The spontaneous mutations identified in this dengue virus serotypes may have a role in host-immunomodulation and adaptability. Mutational variations may be an outcome of polymerase fidelity rates, replication mechanism with changes in proofreading activities, and loses in function of post-replicative repair.

2.2 *B-Cell Epitope Prediction in DENV1 and DENV3*

The higher sequence variability in polyprotein sequence of DENV1 (strain Nauru/West Pac/1974) and DENV3 (strain Martinique/1243/1999) were further analyzed using epitope prediction online software (http://tools.iedb.org/bcell/). The online software predicted multiple epitopes in both polyprotein sequences with 20-25 amino acid in length. The predicted B-cell epitopes were then superimposed on sequence alignment in order to check their position with respect to mutation prone regions. The sequence of epitopes identified with their residual position in polyprotein has been shown in Tables 1 and 2. The analysis shows that the distribution of predicted epitopes in DENV3 spans more across the polyprotein proteome of dengue virus compared to DENV1. Epitope identified in DENV1 falls in region of Envelope

Table 1 Predicted epitope peptide sequences of DENV1 polyprotein against B cell

	Peptide sequences	Size
1	QRKKTGRPSFNMLKRARNRVSTVSQLAKRFSKGLLSGQG	39
2	FLDLPLPWTSGASTSQETWNRQDLL	25
3	VSGILAQGKKMIRPQPMEHKYSWKSWGKA	29
4	GGPISQHNYRPGYFTQTAGPWHLG	24
5	QKKKQRSGVLWDTPSPPEVERAVLD	25
6	RLEPSWASVKKDLISYGGGWRFQGSWNAG	29
7	AIAQAKASQEGPLPEIEDEVF	21
8	PEGIIPALFEPEREKSAAIDGEYRLRGE	28
9	KDLGIGHAAAENHHHAAMLDVDL	23
10	NPTVDGIVAIDLDPVVYDAKF	21
11	RQLNQLSKSEFNTYKRSGIIEVDRSE	26
12	TPFGQQRVFKEKVDTRTPKAKRGTA	25
13	GKVRKDIPQWEPSKGWNDWQQVPFCSH	27
14	WVPTSRTTWSIHAHHQWMTTE	21
15	IGNENYLDFMTSMKRFKNESDPEG	24

Table 2 Predicted epitope peptide sequences of DENV3 polyprotein against B cell

	Peptide sequences	Size
1	FLDLPLPWTSGASTSQETWNRQDLL	25
2	VSGILAQGKKMIRPQPMEHKYSWKSWGKA	29
3	GGPISQHNYRPGYFTQTAGPWHLG	24
4	QKKKQRSGVLWDTPSPPEVERAVLD	25
5	RLEPSWASVKKDLISYGGGWRFQGSWNAG	29
6	AIAQAKASQEGPLPEIEDEVF	21
7	PEGIIPALFEPEREKSAAIDGEYRLRGE	28
8	KDLGIGHAAAENHHHAAMLDVDL	23
9	NPTVDGIVAIDLDPVVYDAKF	21
10	RQLNQLSKSEFNTYKRSGIIEVDRSE	26
11	TPFGQQRVFKEKVDTRTPKAKRGTA	25
12	GKVRKDIPQWEPSKGWNDWQQVPFCSH	27
13	WVPTSRTTWSIHAHHQWMTTE	21
14	IGNENYLDFMTSMKRFKNESDPEG	24

protein, NS1, Serine protease subunits of NS2B and NS3, NS4A, and RNA-directed-RNA-polymerase but largely occupied by conserved residues (Supplementary Documents). However, the predicted epitopes for DENV3 were observed in capsid protein, NSP1, serine protease subunit of NSP3, NSP4B and RNA-directed-RNA-polymerase regions filled with non-conserved residues as shown in Fig. 2. The epitope prediction study and its comparison with sequence alignments of serotypes depict the role of genomic and proteomic variants of dengue virus in higher infectivity among population of different regions on earth. The study also indicates that DENV3 adaptability in variable host environment not only related to immune-suppression mechanism but also involved with modification in replication machinery (Fig. 3).

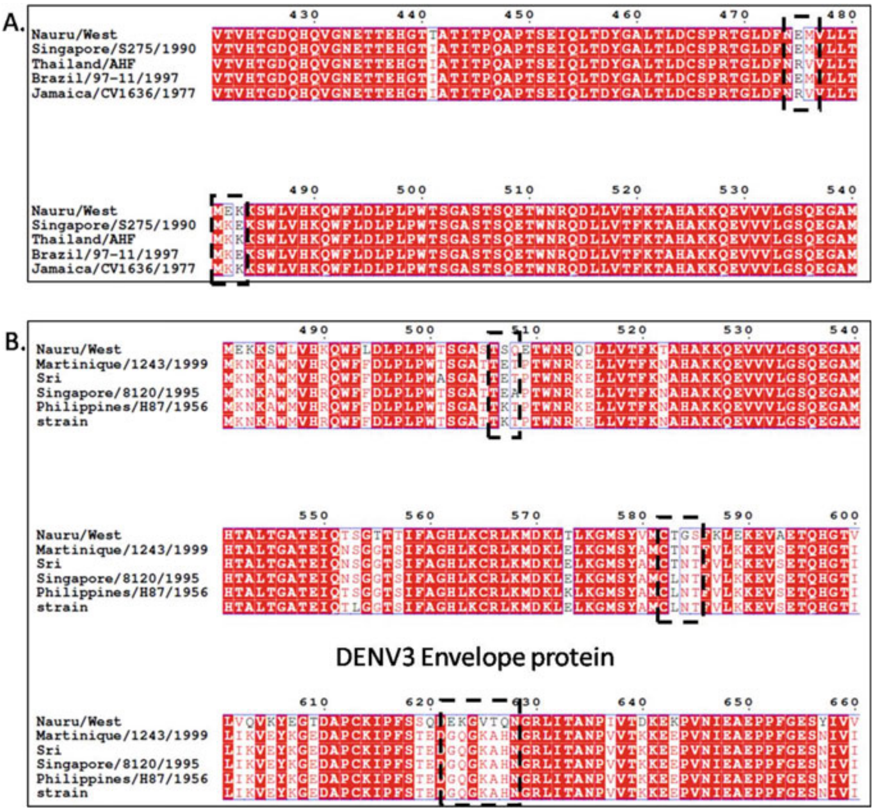

Fig. 2 Conserved and variable regions among the different serotypes of **a** DENV1 envelope protein, **b** DENV3 envelope protein. The red highlighted regions are conserved and the non highlighted regions show the amino acid variability. The black letters indicated the amino acid change in that region

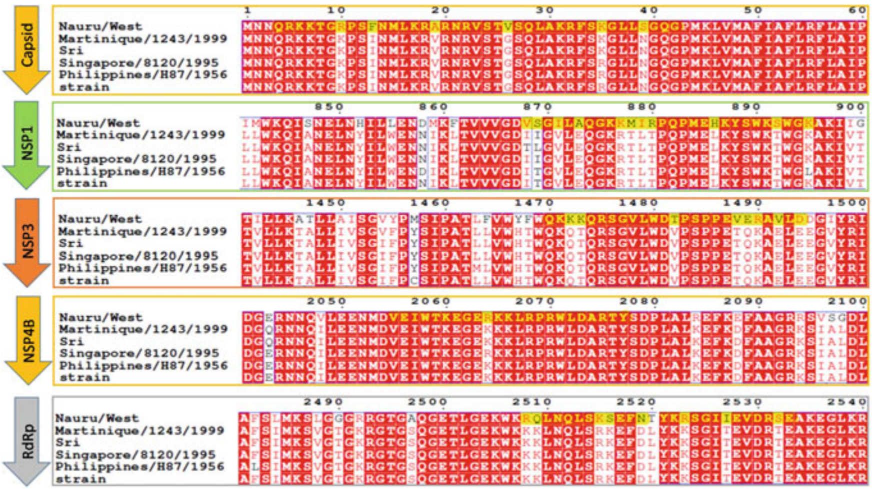

Fig. 3 Location of epitopes within polyprotein of DENV3. Yellow marked region shows the predicted epitope location

3 Discussion

Dengue is one of the most common mosquito-transmitted infections caused by dengue virus (DENV) worldwide (Swaminathan and Khanna 2017). Genome and proteome of this virus were studied with a great detail of structure-function relationship (Carlin and Shresta 2017; Perera and Kuhn 2019). Attempts were made to develop the vaccine against this virus but met with failures. Here we are reporting a small analysis of polyprotein sequence of dengue virus from 27 different serotypes belong to four different classes of dengue virus (DENV). We further compared the sequence alignment with predicted B-cell epitopes to illustrate the role of genomic and proteome variability in survival mechanisms by evading immune system of the body. DENV3 polyprotein based predicted epitopes show huge number of non-conserved mutations directly affects the elicitation of immune cells against this particular strain of virus. Further, large number of non-conserved mutation in NS4B represent the adaptability of protein in suppressing the cellular anti-viral state by inhibits interferon (IFN)-induced host STAT1 phosphorylation. The mutations in RNA-dependent-RNA-polymerase may be responsible for introducing additional mutation by reducing proofreading activity.

Conflict of interest Authors have no conflict of interest.

References

Bhatt S, Gething PW, Brady OJ, Messina JP, Farlow AW, Moyes CL, Drake JM, Brownstein JS, Hoen AG, Sankoh O, Myers MF, George DB, Jaenisch T, Wint GRW, Simmons CP, Scott TW, Farrar JJ, Hay SI (2013) The global distribution and burden of dengue. Nature (London) Annu Rev 496:504–507

Carlin AF, Shresta S (2017) Genome-wide approaches to unraveling host–virus interactions in Dengue and Zika infections. Curr Opin Virol 34:29–38

Ge P, Zhou H (2014) Chaperone fusion proteins aid entropy-driven maturation of class II viral fusion proteins. Trends Microbiol 22(2):100–106

Guy B, Jackson N (2016) Dengue vaccine: hypotheses to understand CYD-TDV-induced protection. Nat Rev Microbiol 14:45–54

Guzman MG, Halstead SB, Artsob H, Buchy P, Farrar J, Gubler DJ, Hunsperger E, Kroeger A, Margolis HS, Martínez E, Nathan MB, Pelegrino JL, Simmons C, Yoksan S, Peeling RW (2010) Dengue: a continuing global threat. Nat Rev Microbiol 8(Suppl):S7–S16

Halstead SB, Rojanasuphot S, Sangkawibha N (1983) Original antigenic sin in dengue. Am J Trop Med Hyg 32:154–156

Henchal EA, Putnak JR (1990) The dengue viruses. Clin Microbiol Rev 3:376–396

Liu Y, Liu J, Cheng G (2016) Vaccines and immunization strategies for dengue prevention. Emerg Microbes Infect 5(7):e77

Murphy BR, Whitehead SS (2011) Immune response to dengue virus and prospects for a vaccine. Annu Rev Immunol 29:587–619

Perera R, Kuhn RJ (2019) Structural proteomics of dengue virus. Curr Opin Microbiol 11(4):369–377

Rothman AL (2011) Immunity to dengue virus: a tale of original antigenic sin and tropical cytokine storms. Nat Rev Immunol 11:532–543

Swaminathan S, Khanna N (2017) Dengue vaccine development: global and Indian scenarios. Int J Infect Dis 84S:S80–S86

Torresi J, Ebert G, Pellegrini M (2017) Vaccines licensed and in clinical trials for the prevention of dengue. Hum Vaccin Immunother 13(5):1059–1072

Zompi S, Harris E (2013) Original antigenic sin in dengue revisited. Proc Natl Acad Sci USA 110:8761–8762

Real-Time Watermarking of Medical Images and Secure Transmission Through Steganography

Ajay Biswas, Pabak Indu, and Souvik Bhattacharyya

Abstract Medical images and reports are highly confidential information and should not be leaked, or modified in any circumstances. Healthcare organizations constantly face cyber-attacks with the motive of stealing medical information for their personal gains, and during the COVID-19 pandemic, the attacks have almost doubled. Encrypting medical information and transmitting them over a secure channel ensures the confidentiality of information, however, can be stolen and decrypted later. Also, most of the health organization lacks in terms of security and privacy of their patient's information. A real-time watermarking and steganography protocol can mitigate the aftermath of a cyber-attack by hiding confidential reports into useless looking files such as log files and user manuals as soon the reports are generated. We propose a secure steganographic medical report system that can hide medical reports as well as identify fake ones. The system uses real-time watermarking during report generation which prevents any kind of modification; thereafter, these data are transmitted/stored using a secure steganography protocol. Finally, the data is retrieved by doctors or health workers after stego-extraction and watermark verification.

Keywords Features · Medical images · Steganography · Verification · Watermarking

1 Introduction

Digital watermarking is the process of marking digital multimedia such as images and videos by their owner to protect content and to claim ownership. Watermark is of two types: visible watermark and invisible watermark. A visible watermark is placed to warn users from stealing content and is directly placed over the multimedia in a suitable position with desirable transparency or visibility. Invisible watermarking on

A. Biswas (✉) · S. Bhattacharyya
Department of Computer Science and Engineering, University Institute of Technology, the University of Burdwan, Burdwan, WB 713104, India

P. Indu
Adamas University, Kolkata, WB 700126, India

M. Mukherjee et al. (eds.), *Advances in Medical Physics and Healthcare Engineering*, Lecture Notes in Bioengineering, https://doi.org/10.1007/978-981-33-6915-3_49

the other hand does not warn its users nor does it reveal its pretense. An invisible watermark is placed over multimedia using steganography. Steganography is the process of hiding information into a medium such as texts, images, videos, and images (Anderson and Petitcolas 1998).

A medical image of a person's organ or body part contains vital information about his/her health condition and shouldn't be disclosed against the patient's will. Securing medical images has always been a challenging task. They are stolen by hackers to get personal details of a person and later to dupe them by trapping them into fake medical treatments and insurance schemes. Not only medical images are susceptible to stealing but are also prone to modification and tampering (Cox et al. 1999).

Watermarking medical images to protect them from modification is quite new, and only a few researches have been conducted in this regard. Zain and Fauzi (2006) propose a medical watermarking system that provides tamper detection and recovery. Their proposed technique uses a secret key and a public chaotic mixing algorithm to embed and recover a tampered image. In another watermarking scheme, proposed by Puech and Rodrigues (2004) provides a crypto-watermarking method that uses private and public key ciphering. Eswaraiah and Reddy (2015) proposed a novel medical image watermarking technique that can detect tampering inside the region of interest (ROI) and recover the original region of interest. In another research by Parah et al. (2017), provided a discrete cosine transform (DCT)-based watermarking scheme for e-healthcare which can resist singular as well as hybrid attacks.

The rest of the paper is organized as below. In Sect. 2, we propose a client–server based real-time digital watermarking scheme. Section 3 provides results and analysis, and finally, Sect. 4 concludes our paper.

2 Proposed Method

Real-time watermarking images ensure better security and reliability over conventional watermarking. This is because a remote server is involved in the process, without its approval, the watermark verification or validation will not succeed. Our proposed architecture uses a remote server to communicate securely to its senders and store certain features in the database that will be later used in verification. The communication, image storage, and retrieval are done through steganography. Figure 1 provides the entire flowchart of the proposed system. Here, Alice has taken a medical image and wants to watermark it. He extracts features from the image and sends it to the remote server. The remote server verifies the sender and stores the features into the database. After storage, the server sends a unique identification number (ID) to the sender which will be later user in the watermark verification. Later, Alice watermarks the image with a unique ID. Now Alice can use this image as per his needs or sends it to someone else using steganography. Bob has received the stego image from Alice, and he performs stego-extraction to get back the watermarked image. He then sends the extracted unique ID and features to the remote

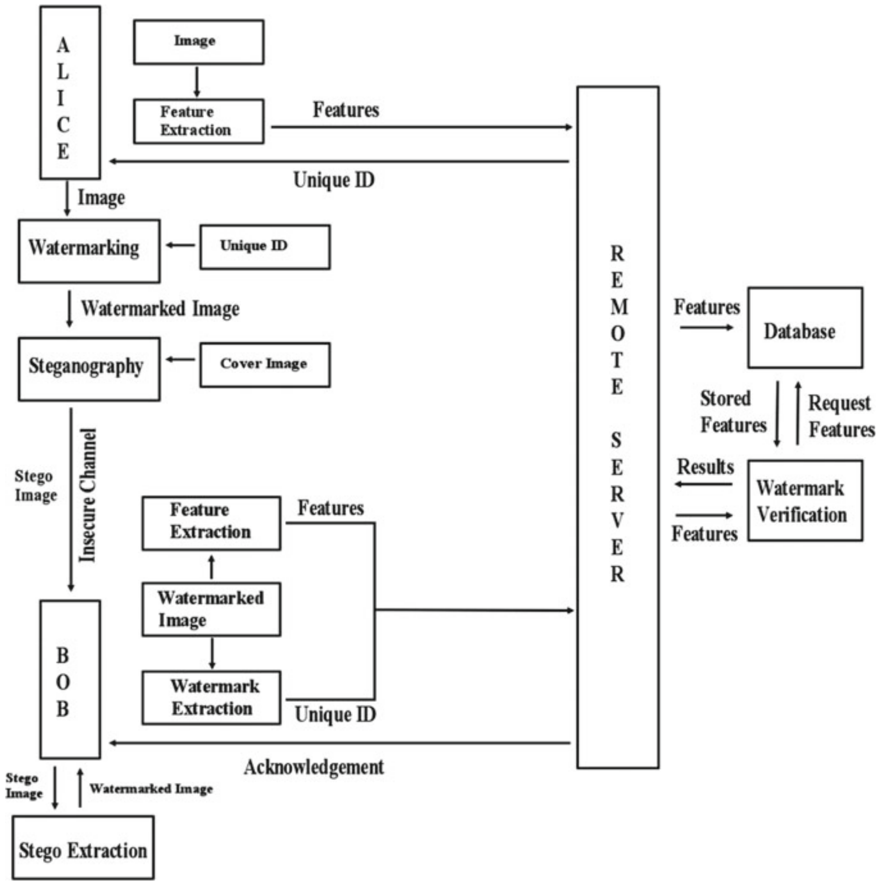

Fig. 1 Proposed real-time watermarking technique flowchart

server where it gets verified. If the verification is successful, the server sends back an acknowledgment. After receiving the acknowledgment Bob can safely assume that the image, he received is genuine.

The watermarking process is divided into two sub-processes, Sect. 2.1 describes the watermarking algorithm in detail, and Sect. 2.2 provides details of the watermark validation process.

2.1 The Watermarking Algorithm

The watermarking algorithm requires both server and client to be present. The key idea of this phase is to watermark a medical image so that gets to be treated as a genuine image. If an attacker tries to modify the image, he/she will have to incorporate some change into the image and will result in the generation of a different feature set. As the server stores the feature set, the attacker's image will be rejected by the system during the verification. Algorithm 1 provides a detailed explanation of the watermarking process.

Algorithm 1 Watermarking Algorithm

	Input: Image *I* **Output**: Watermarked Image *W* **Data**: Feature Matrix *M*
1	Identify the watermarking region *b* in *I*
2	Extract features of *I* excluding *b* and store in matrix *M*
3	Use steganography to hide *M* and send it to the remote server using channel *C*
4	Server verifies the sender and stores M in the database
5	Server sends back a unique identifier *U* which can uniquely identify *M,* securely using steganography
6	Watermark *U* on the region *b*
7	Generate the resultant image *W* after watermarking
8	End

2.2 The Watermark Verification Algorithm

Similar to the watermarking algorithm, the watermark verification algorithm requires the presence of both client and server. Algorithm 2 describes the watermark verification phase in detail. During verification, sometimes the genuine image may not produce the same features as that generated in the verification phase. It may happen if the image undergoes compression or incorporates noise. To avoid this problem, the features have to be tested against machine learning models.

Algorithm 2 Watermark Verification Algorithm

	Input: Watermarked Image *W* **Output:** A Boolean determining the verification status **Data:** Feature Matrix *M,* Trained Dataset *T*
1	Identify the watermark region *b* in *W*
2	Extract features of *W* excluding *b* and store in the matrix *M'*
3	Extract the unique identifier *U* from *W*
4	Use steganography to hide M' and *U* and sends them to the remote server using channel C'
5	Server verifies the sender and retrieves *M* from the database using *U*

(continued)

(continued)

Server matches M' with M
If $M = M'$ then
Return *True*
Else
If $M \approx M'$ then
Test M' against trained Dataset T
If *Passed*(M') then
Return *True*
Else
Return *False*
Else
Return *False*
End

3 Results and Analysis

The testing was performed using two machines, one of them acted as a server and the other as a client. The client machine contained the medical images which were later watermarked. Three different kinds of feature sets were used in the process, namely mean feature set, standard deviation feature set, and subtractive pixel adjacency matrix (SPAM) (Pevny et al. 2010) feature set. The mean and the standard deviation feature sets were generated by taking an 8×8-pixel block and applying mean and standard deviation, respectively. The SPAM686 feature set generates 686-second-order Markov-based features (Pevny and Fridrich 2007) of an image and is used to detect spatial domain steganography. The features generated from the SPAM686 can detect small changes in the spatial domain; therefore, it can be used to distinguish fake images from real ones. Figure 2 provides a comparison of “c4880h_s1” (Stegmann 2002) image with the images generated in three different scenarios.

After the watermarking stage, the images can be sent secretly using steganography. Table 1 provides the performance analysis of the least significant bit (LSB) (Bhattacharyya 2011; Chandramouli and Memon 2001) steganography with a hidden and visible watermark. The hidden watermarking was also performed using LSB steganography. Since the watermarking stage does not depend upon the steganography stage, the watermarked image should not affect the performance of steganography. Figure 3 shows the comparison of cover and stego image of “Lena 512×512” with “c4880h_s1 128×128” as cover image. The stego image was generated with peak signal-to-noise ratio (PSNR) of 54.16 dB.

To distinguish fake watermarked images from genuine watermarked images that were subjected to salt-and-pepper noise of density 0.01 and 0.001, the remote server

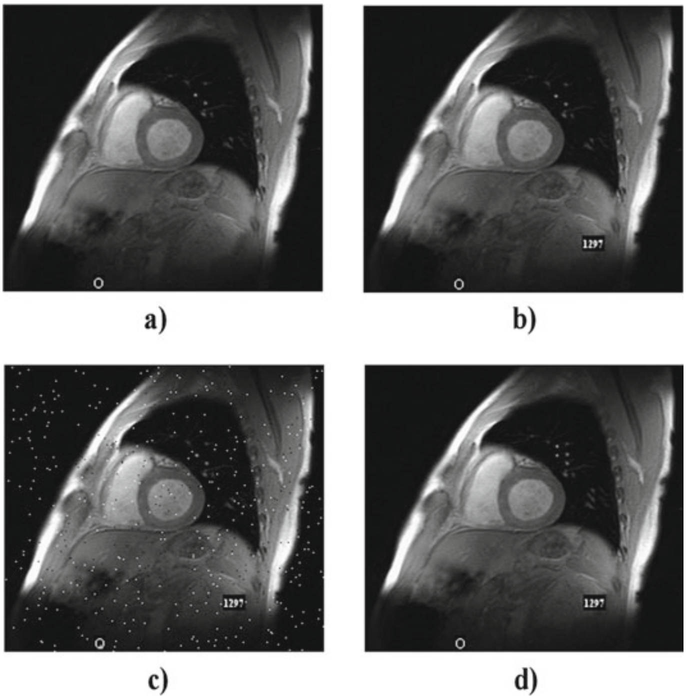

Fig. 2 **a** Original image; **b** watermarked image; **c** invisible watermarked image subjected to salt-and-pepper noise of density 0.01; **d** fake watermarked image

was trained and tested with 200 images from the Bossbase (Bas et al. 2011) using tenfolds cross-validated support vector machine (SVM) classifier (Ryu et al. 2008), 100 of each genuine and fake image. Figures 4, 5, and 6 provide receiver operating characteristics (ROC) curve for identifying fake images using mean, standard deviation, and SPAM features, respectively. Out of the three types of feature sets, the mean features provided better results. Both mean and standard deviation features provided better results when the noise was high; however, the SPAM features provided better results when the noise was low.

4 Conclusion

On analyzing results from Table 1, we can conclude that the proposed architecture does not affect the performance of steganography and kind of steganography can be incorporated until and unless the watermark is recoverable after stego-extraction. Also, we can see that the performance of both visible watermarked image and invisible watermarked image is similar; hence, any type of watermarking technique can be incorporated with the proposed architecture.

Table 1 Experimental results of LSB steganography over visible and invisible watermarked images

Cover image	Watermark type	Payload (bytes)	PSNR (dB)
Lena	No watermark	5174	59.12
	No watermark	17,462	53.87
	Invisible	5174	59.13
	Invisible	17,462	53.86
	Visible	5174	59.13
	Visible	17,462	53.87
Cameraman	No watermark	5174	59.14
	No watermark	17,462	53.87
	Invisible	5174	59.15
	Invisible	17,462	53.87
	Visible	5174	59.14
	Visible	17,462	53.87
Mandril	No watermark	5174	59.14
	No watermark	17,462	53.87
	Invisible	5174	59.14
	Invisible	17,462	53.87
	Visible	5174	59.14
	Visible	17,462	53.87

Fig. 3 **a** Invisible watermarked image; **b** cover Lena; **c** stego Lena

The proposed architecture provides a modular approach to validate and transmit medical images securely that give it an edge over current watermarking algorithms. In the future, testing will be performed with better steganography and watermarking algorithms with a variety of image formats. We will also work with other image distortion types.

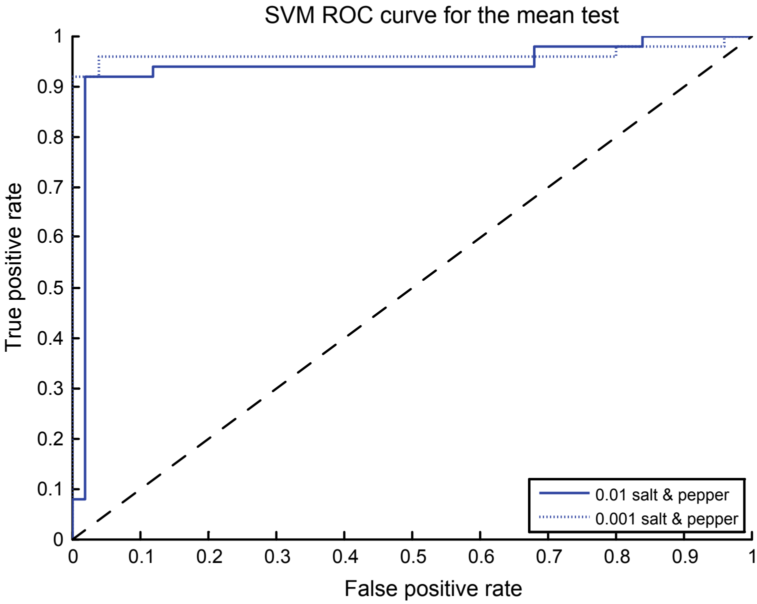

Fig. 4 ROC curve to distinguish fake images and noisy images using mean features and classification through SVM

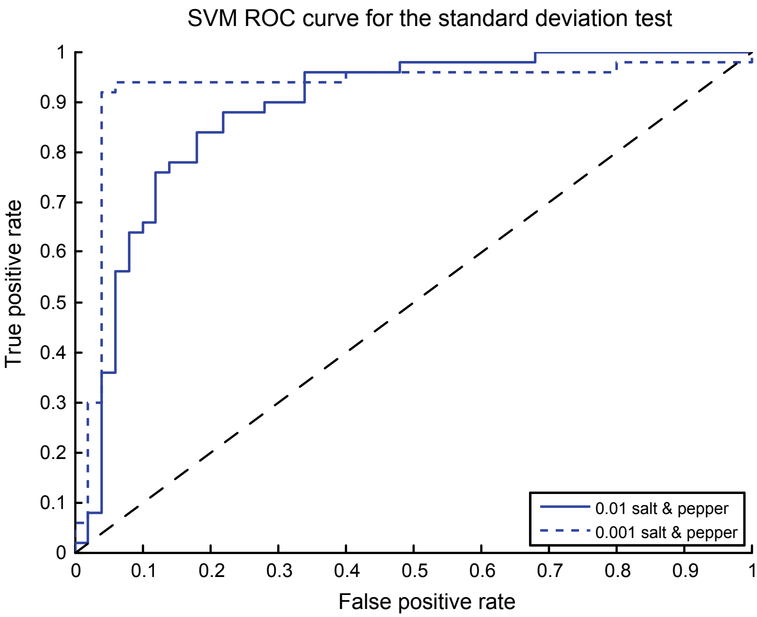

Fig. 5 ROC curve to distinguish fake images and noisy images using standard deviation features and classification through SVM

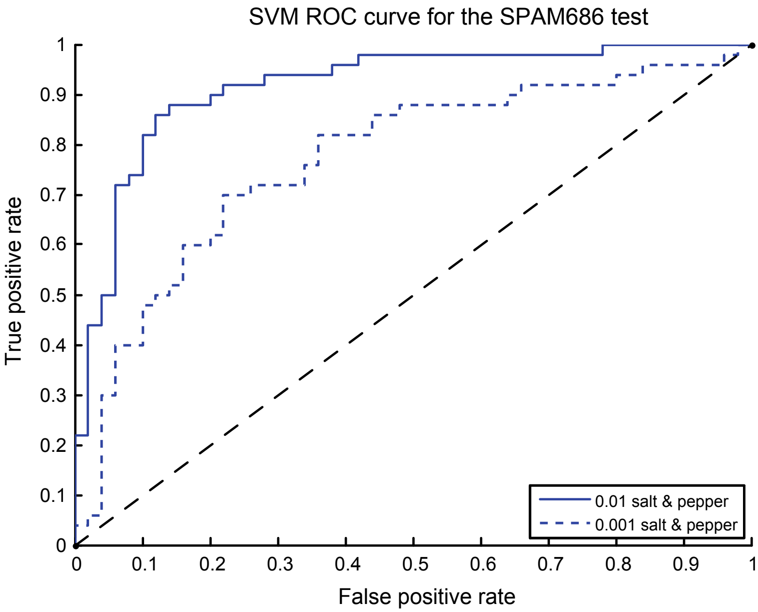

Fig. 6 ROC curve to distinguish fake images and noisy images using spam features and classification through SVM

References

Anderson RJ, Petitcolas FAP (1998) On the limits of steganography. IEEE J Sel Areas Commun 16(4):474–481

Bas P, Filler T, Pevný T (2011) "Break our steganographic system": the ins and outs of organizing BOSS. In: International workshop on information hiding. Springer, Berlin, Heidelberg, pp 59–70

Bhattacharyya S (2011) A survey of steganography and steganalysis technique in image, text, audio and video as cover carrier. J Global Res Comput Sci 2(4)

Chandramouli R, Memon N (2001) Analysis of LSB based image steganography techniques. In: Proceedings 2001 international conference on image processing (Cat. No. 01CH37205), vol 3. IEEE, pp 1019–1022

Cox IJ, Miller ML, Linnartz JMG, Kalker T (1999) A review of watermarking principles and practices. Digit Signal Process Multimed Syst 461–482

Eswaraiah R, Reddy ES (2015) Robust medical image watermarking technique for accurate detection of tampers inside region of interest and recovering original region of interest. IET Image Process 9(8):615–625

Parah SA, Sheikh JA, Ahad F, Loan NA, Bhat GM (2017) Information hiding in medical images: a robust medical image watermarking system for E-healthcare. Multimed Tools Appl 76(8):10599–10633

Pevny T, Fridrich J (2007) Merging Markov and DCT features for multi-class JPEG steganalysis. In: Security, steganography, and watermarking of multimedia contents IX, vol 6505. International Society for Optics and Photonics, p 650503

Pevny T, Bas P, Fridrich J (2010) Steganalysis by subtractive pixel adjacency matrix. IEEE Trans Inf Forens Secur 5(2):215–224

Puech W, Rodrigues JM (2004) A new crypto-watermarking method for medical images safe transfer. In: 2004 12th European signal processing conference. IEEE, pp 1481–1484

Ryu S-J, Lee H-Y, Cho I-W, Lee H-K (2008) Document forgery detection with SVM classifier and image quality measures. In: Pacific-Rim conference on multimedia. Springer, Berlin, Heidelberg, pp 486–495

Stegmann MB (2002) An annotated dataset of 14 cardiac MR images. Technical report, Informatics and Mathematical Modelling, Technical University of Denmark

Zain JM, Fauzi ARM (2006) Medical image watermarking with tamper detection and recovery. In: 2006 international conference of the IEEE engineering in medicine and biology society. IEEE, pp 3270–3273

A Review of Brain-Computer Interface

Dabosmita Paul, Moumita Mukherjee, and Ashish Bakshi

Abstract A brain-computer interface (BCI) is an equipment and programming interchanges framework that allows Brain movement alone to control PCs or outer gadgets. The main objective of BCI research is to give corresponding abilities to seriously handicapped individuals who are entirely deadened or locked by neuromuscular issues, for example, amyotrophic lateral sclerosis, chronic stroke, tetraplegia, stroke, and spinal cord injury. Here, we review the cutting edge of BCIs, looking at the various advances that structure a standard BCI: signal obtaining, reprocessing or signal upgrade, include extraction, arrangement, and the control interface. We talk about their preferences, disadvantages, and most recent advances, and we review the various advances detailed in the analytical writing to plan each progression of a BCI. Initially, the survey inspects the neuroimaging modalities utilized in the signal obtaining step, each of which monitors an alternate practical Brain action, for example, electrical, attractive, or metabolic movement. After that, the survey talks about various electrophysiological control signals that decide user's aims, which can be identified in mind action. At last, the survey gives a discussion of different BCI applications that control the scope of gadgets.

Keywords Brain–computer interface (BCI) · Neuroimaging · Application of sensor system

1 Introduction

The historical backdrop of brain-computer interfaces (BCI) begins with Hans Berger's revelation of the electrical activity of the human brain and the advancement of electroencephalography (EEG). In 1924 Berger was the first to record human

D. Paul · A. Bakshi
Mendel University, Brno, Czech Republic

M. Mukherjee (✉)
Adamas University, Kolkata, India
e-mail: moumita.mukherjee@adamasuniversity.ac.in

M. Mukherjee et al. (eds.), *Advances in Medical Physics and Healthcare Engineering*, Lecture Notes in Bioengineering, https://doi.org/10.1007/978-981-33-6915-3_50

brain movement by methods for EEG. Berger had the option to recognize the oscillatory activity, for example, Berger's wave or the alpha wave (8–13 Hz), by investigating EEG (Straebel and Thoben 2014).UCLA Professor Jacques Vidal instituted the expression "BCI" and created the principal peer-investigated distributions on this point (Vidal 1973). A brain-computer interface (BCI), likewise suggested to a mind-machine interface (BMI), is an equipment and programming interchanges framework that empowers people to cooperate with their environmental factors, without the overtone of peripheral nerves and muscles, by using control signals produced from electroencephalographic movement. A BCI is a human-made reasoning framework that can perceive a specific arrangement of examples in mind signals following five sequential stages: signal securing, preprocessing or signal upgrade, include extraction, characterization, and the control interface (Khalid et al. 2009). A BCI is a human-made reasoning framework that can perceive a specific arrangement of examples in mind signals following five sequential stages: signal securing, preprocessing or signal upgrade, include extraction, characterization, and the control interface (Bashashati et al. 2007). However, this setting has gone through radical change during the most recent twenty years of BCI research. The quantity of articles distributed for neural interface innovation has expanded exponentially over the previous decade (Konrad and Shanks 2010). From recent research about Using brain-computer interfaces and the study of employing social research methods, and they found 73 Publication, 71 studies address the user's viewpoint. A few examinations stretch out to thought of other BCI partners, for example, clinical innovation specialists, parental figures, or medical services experts. Most of the investigations utilize quantitative techniques. Repeating subjects over the examinations analyzed were general user supposition toward BCI, focal specialized or social issues revealed, demands/requests made by a user of the innovation, the potential/eventual fate of BCIs, and moral parts of BCIs (Kögel et al. 2019). NeuroSky-empowered arrangements convey extraordinary experiences into body and brain well-being and health that can inspire individuals to settle on a better way of life decisions (EEG - ECG- Biosensors 2020). More extensive relevance of BCIs requires more noteworthy convenience, which thus implies diminishing time spent on planning, preparing and alignment (Blankertz 2010). BCI research is a moderately youthful multidisciplinary field incorporating specialists from neuroscience, physiology, brain science, designing, software engineering, restoration, and other specialized and medical care disciplines. Thus, disregarding some remarkable advances, a specific language still cannot seem to develop, and existing BCI advances shift, which makes their examination troublesome and, in result, hinders the exploration. The people group of BCI scientists has, in this manner, focused on the need to set up an overall structure for the BCI plan (Mason and Birch 2003; Wolpaw et al. 2000).

2 Structure and Measurement Process of Brain

In the human body, brain plays an essential and crucial role. The human brain has mainly three parts: cerebrum, cerebellum, and brainstem. The cerebrum includes the cortex, and it is composed by the right and left cerebral hemispheres, each of which is subdivided into four lobes: frontal, parietal, temporal and occipital. The frontal lobe is associated with motor learning, language, planning, problem-solving, reasoning, memory, personality, and emotions. The primary motor cortex located in this lobe is associated with motor activity for planning and executing movements. The left side of the body is controlled by the right hemisphere controls and the left hemisphere controls, the right side of the body.

3 Classification of Brain-Computer Interface

According to Lotte et al. (2015), Wolpaw et al. (2002), Coyle et al. (2007), BCI could be classified as dependability, invasiveness, Synchronization and Source in Fig. 1. Some contradictories review is Presented between dependent, independent and Exogenous and Endogenous BCI. Thess categorized are briefed as follow.

3.1 Synchronous and Asynchronous BCI

Synchronous BCI is a cue built system which is controlled to a predefined time frame while an asynchronous BCI is a "self-paced" system which controls independently of a cue impetus. When the user interaction with the procedure is done at a certain period, then it could be called Synchronous BCI (Cao et al. 2017). Generally, the

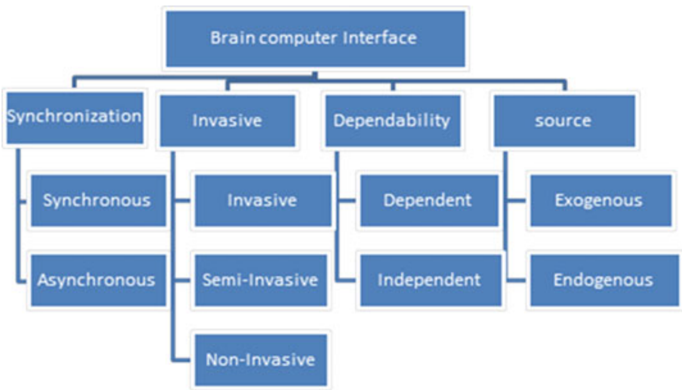

Fig. 1 Classification of brain–computer interface

system has to execute the subject to relate with it at a certain period. However, the system cannot be able to collect the subject signals. Instead, in asynchronous BCI (Nagel and Spüler 2019), also named as "self-paced" the subject can accomplish its mental responsibilities at any period, and the system will respond to person's mental actions. Thus, the subject is free to have a person action at any period.

3.2 Invasive, Semi-invasive and Non-invasive BCI

BCI is categorized as invasive, non-invasive, and semi-invasive according to the method of the brain action is measured.

Invasive BCI. The microelectrodes are imbedded in the brain, under the skull, through neurosurgery. In invasive BCI, there are two types of units: single unit and multiple unit. Single units detect the signal from a signal area of brain cell, and multiple units detect the signal from various locations of brain cell. In this procedure, the quality of the signal is highest, but there have several problems like the body reacts with a foreign object and builds the scar around the electrodes which can be the cause of deterioration in the signal. However, neurosurgery can be a risky and expensive Procedure, So the target of invasive BCI (Waldert 2016; Ball et al. 2009) is mainly for Blind and paralyzed patients.

Semi-invasive BCI. In this procedure, the electrodes are sited on the exposed surface of the brain to measure electrical activity for cerebral cortex using Electrocardiography. As it is called a semi-invasive, it still requires a craniotomy to implant the electrodes. It is only used when surgery is the need for any medical reasons. In this case, the electrodes may be placed outside the dura mater (epidural) or under the dura mater (subdural) (Ko et al. 2019). For cognitive studies, the procedure is beneficial because the strip or grid electrodes cover the broad area of the cortex (for 4–256 electrodes). It gives very high spatial resolution and single fidelity, resistance to noise, lower clinical risk, and robustness over long recording period, high amplitude. The Patient tried to perform imagery task for hand, mouth and tongue and the BCI system with the ability to classify the imagery task for ECoGsingle session (Mesgarani and Chang 2012).

Non-invasive BCI. Generally in non-invasive BCI, the signals can be received without any implant in the skull. There are several non-invasive techniques use to study the brain, Where EEG is most commonly used because of the cost and hardware portability. On the other hand, MEG, PET, MRI, NIRS are also used as a non-invasive BCIs; In this case, the signals could be in low quality; However non-invasive BCIs are still Preferable due to avoiding surgery (Waldert 2016; Cincotti 2008).

3.3 Dependent and Non-independent BCI

Dependent BCI. However, Dependent BCI requires a certain level of motor control from the subject to do things more efficiently as Playing video games and moving a wheelchair (Brainloop 2020).

Independent BCI. This type of signal control BCI does not require any power from the users with several disabilities. In this case, motor control is needed for independent BCI (Brainloop 2020).

3.4 Exogenous and Endogenous BCI

Exogenous BCI. BCI, which uses the neuron activity elicited in the brain by an external stimulus such as VEPs or auditory evoked potentials, is called Exogenons BCI. Exogenous systems do not need extensive training to control signals, SSVEPs and P300, can be easily and quickly set up that can control the signals. Moreover, the signal controls can be recognized with only one EEG channel and can achieve the highest information transfer rate of up to 60 bits/min.

Endogenous BCI. Endogenous BCI is built on self-regulation of brain rhythms and potentials without exterior stimulation. Over and done with neurofeedback training, the operators learn to produce specific brain patterns which may be interpreted by the BCI such as variations in the sensorimotor rhythms or the SCPs. The benefit of an endogenous BCI is that the user can control the BCI at free will and move a pointer to any point in a two-dimensional space, while an exogenous BCI may limit the user to the choices presented. Also, endogenous BCI is especially useful for users with advanced stages of ALS or whose sensory organs are affected (Han et al. 2019).

Dependent means that the BCI does require some control over peripheral nerves and muscles (e.g., eye gaze control) (Vilimek and Zander 2009), whether independent BCI solely relies on brain activity. Endogenous means the BCI is based only on spontaneously generated brain patterns (e.g., motor imagery) whereas exogenous means the BCI is based on brain responses to external stimulus (e.g., P300). by definition, endogenous BCI are necessarily independent. But, exogenous BCI can be either independent or dependent.

4 Neuroimaging Methods of Brain-Computer Interface

BCIs use mind signs to accumulate data on client aims. With that impact, BCIs dependent an account stage that estimates mind movement and makes an interpretation of the data into manageable electrical signs. Two sorts of cerebrum exercises might be observed: (a) electrophysiological (Wikipedia 2020) and (b) hemodynamic (Wikipedia 2020). Electroencephalography, magnetoencephalography, electrocorticography, and electrical signal acquisition in single neurons measure the Electrophysiological activity. Electrophysiological action is created by electro-compound transmitters trading data between the neurons. The neurons produce ionic flows which stream inside and across neuronal congregations. The vast assortment of current pathways can be improved as a dipole directing current from a source to a sink from side to side the dendritic trunk. These intracellular flows are known as essential flows. Protection of electric charges implies that the vital flows are encased by extracellular flow streams, which are known as auxiliary ebbs and flows (Baillet et al. 2001). The hemodynamic reaction is a cycle where the blood discharges glucose to active neurons at a more prominent rate than in the territory of inert neurons. The glucose and oxygen conveyed through the circulation system bring about an overflow of oxyhaemoglobin in the veins of the occupied territory, and a recognizable difference in the nearby proportion of oxyhaemoglobin to deoxyhaemoglobin (Laureys et al. 2015). Non-intrusive methodologies have effectively been utilized by harshly and somewhat deadened patients to reacquire essential types of correspondence and to control neuroprostheses and wheelchairs (Cincotti 2008; Paul et al. 2019; Müller-Putz and Pfurtscheller 2008; Sellers et al. 2010).

Regardless of the exceptional utility of non-intrusive methodologies in BCI applications, engine recuperation has been restricted, due to the requirement for mind signals with a higher goal. Obtrusive chronicle techniques, for example, electrocorticography or intracortical neuron recording were presented, with an end goal to improve the nature of mind signals observed by BCIs. Most scientists concur that development rebuilding through prostheses with products degrees of opportunity must be accomplished through an invasive approach (Lebedev and Nicolelis 2006; Luo et al. 2007). Maybe, the fate of nanotechnologies that may create nano-locators to be embedded idly in the cerebrum may give a precise answer for the issues of obtrusive long-haul applications. Second, a connection between the microelectrode and outer equipment that utilizes remote innovation is expected to lessen the dangers of the disease. Remote transmission of neuronal signs has just been tried in creatures. Also, third, nonstop pressure brought about by stopping and unplugging the chronicle framework may prompt tissue harm or framework disappointment.

Each neuroimaging methodology is clarified underneath. Initially, electrophysiological strategies, for example, electroencephalography, electrocorticography, magnetoencephalography, and electrical sign securing in single neurons will be talked. Besides, metabolic techniques, for example, sound, attractive reverberation and close infrared spectroscopy will be portrayed. At long last, practical imaging modalities are recorded in Table 1, alongside data identified with movement estimated, worldly and spatial goals, well-being, and compactness.

Method	Measurement technic	Resolution of (temporal and spatial)	Portability
EEG	Electrical	~0.05 s ~10 mm	Non-invasive
ECoG	Electrical	~0.003 s ~1 mm ~0.5 mm (LFP)	Invasive
Intracortical neuron recording	Electrical	~0.003 s ~0.1 mm (MUA) ~0.5 mm (SAU)	Invasive
MEG	Magnetic	~0.05 s ~5 mm	Non-Invasive
fMRI	Metabolic	~1 s ~1 mm	Non-Invasive
NIRS	Metabolic	~1 s ~5 mm	Non-Invasive

4.1 Electroencephalography (EEG)

In 1875, Richard Caton (1842–1926), a doctor rehearsing in Liverpool, introduced his discoveries about electrical wonders of the uncovered cerebral halves of the globe of bunnies and monkeys in the British Medical Journal. In 1890, Polish physiologist Adolf Beck distributed an examination of the unconstrained electrical movement of the cerebrum of hares and canines that included musical motions adjusted by light. Beck began probes the electrical mind movement of creatures. Beck put cathodes straightforwardly on the outside of the cerebrum to test for tangible incitement. His perception of fluctuating mind action prompted the finish of cerebrum waves (Coenen et al. 2014).

Electroencephalography (EEG) is an electrophysiological checking strategy to record the electrical activity of the cerebrum. It is regularly non-invasive, with the anodes set along the scalp, albeit intrusive terminals are here and there utilized, as in electrocorticography, now and then called intracranial EEG. EEG estimates electric mind action brought about by the progression of electric flows for the duration of synaptic excitations of the dendrites in the neurons and is incredibly delicate with the impacts of auxiliary flows (Baillet et al. 2001). These cathodes are typically made of silver chloride (AgCl) (Sinclair et al. 2007).

Medical Use. Brain damage for injury, brain tumor, stroke, encephalopathy, encephalitis, sleep disorders.

Wave	Range of frequency (Hz)	Amplitude	State of mind	Reference
ALPHA	8–13	30–50	Relaxed awareness	Lutzenberger et al. 1995)
BETA	12–30	5–30	Active thinking, active attention, alert	Pfurtscheller and Neuper 2001)
THETA	4–8	More than 20	Emotion stress, drowsiness, and sleep in adults	Kübler et al. May 2001; ScienceDirect 2020; Aftanas and Golocheikine 2001; Fernández 1995; Caplan et al. 2001; Klimesch 2001)
GAMMA	Above 31	Less than 5	Mechanism of consciousness	Luo et al. 2007; Coenen et al. 2014; Sinclair et al. 2007; Lutzenberger et al. 1995; Anand 1961)
DELTA	Up to 4	High amplitude (20–200)	Deep sleep	Kübler et al. 2001)

The EEG signal is estimated as the possible contrast after some time between sign or dynamic terminal and reference anode. An additional third terminal, known as the ground cathode, is utilized to gauge the differential voltage between the dynamic and the reference focuses. The insignificant setup for EEG estimation subsequently comprises of one dynamic, one reference, and one ground terminal. Multi-channel arrangements can include up to 128 or 256 active electrodes (Teplan 2002). Electrode-scalp makes contact impedance should be between 1 kΩ and ten kΩ to record an accurate signal (Usakli 2010).

Alpha rhythms. These rhythms are found over the occipital area in mind. This frequency exists in the 8–12 Hz go. Their adequacy increments when the eyes close and the body unwinds, and they weaken when the eyes open and mental exertion is made. These rhythms basically reflect visual preparing in the occipital cerebrum locale and may likewise be identified with the memory mind work (Klimesch 1997).

Beta rhythms. This rhythm state stays between the 12 and 30 Hz frequency, is recorded in the frontal and focal areas of the cerebrum, and is related to engine exercises. Beta rhythms are desynchronized during genuine development or engine symbolism. Beta waves are portrayed by their even dispersion when there is no engine movement. Nevertheless, if there should be an occurrence of dynamic development, the beta waves weaken, and their balanced dispersion changes (ScienceDirect Topic 2020).

Theta waves exist in the 4–8 Hz go. In an ordinary wakeful grown-up, just a limited quantity of theta frequencies can be recorded. A more significant measure of theta frequencies can be found in little youngsters, more seasoned kids, and grown-ups in tired, thoughtful or rest states (Kopell et al. 2000).

Gamma rhythms. Generally, this type of rhythms has a place with the repetition go from 30 to 100 Hz. The presence of gamma waves in the cerebrum movement of a dependable grown-up is identified with specific engine capacities or recognitions, among others. A few analyses have uncovered a relationship in typical people between engine exercises and gamma waves during maximal muscle constriction (ScienceDirect Topics 2020). Likewise, a few examinations have given proof to the function of gamma movement in the view of both visual and hear-able boosts. Gamma rhythms are less regularly utilized in EEG-based BCI frameworks, since relics, for example, electromyography (EMG) or electrooculography (EOG) are probably going to influence them (Kopell et al. 2000).

The delta band lies under 4 Hz, and the plentifulness of delta signals recognized in children diminishes as they age. Delta rhythms usually are just seen in grown-ups in a profound rest state and are strange in adults in a wakeful state. A lot of delta act in alert grown-ups is odd and is identified with neurological illnesses because of low repetition; it is anything but difficult to mistake delta waves for antiquity signals, which are brought about by the enormous muscles of the neck or jaw (Kübler et al. 2001).

4.2 Electrocardiography (ECoG)

ECoG was spearheaded in the mid-1950s by Wilder Penfield and Herbert Jasper, neurosurgeons at the Montreal Neurological Institute. The two created ECoG as a component of their notable Montreal strategy, a careful convention used to treat patients with extreme epilepsy. The cortical possibilities recorded by ECoG were utilized to recognize epileptogenic zones—locales of the cortex that create epileptic seizures. These zones would then be precisely taken out from the cortex during resectioning, hence pulverizing the mind tissue where epileptic seizures had started. Penfield and Jasper likewise utilized electrical incitement during ECoG accounts in patients going through epilepsy medical procedure under nearby sedation (Kuruvilla and Flink 2003). ECoG is a method that estimates electrical action in the cerebral cortex by methods for anodes put straightforwardly on the outside of the mind. Contrasted with EEG, ECoG gives higher worldly and spatial goal just as higher amplitudes and a lower weakness to antiques, for example, squints and eye development (Hill et al. 2012). The outcomes demonstrated that subdural terminals could give stable signs more than a while. In any case, the drawn-out security of the characters gained by ECoG is as of now indistinct. Later tests with monkeys have indicated that ECoG can perform at an elevated level for a considerable length of time with no float inexactness or recalibration (Chang et al. 2010).

4.3 Intracortical Neuron Recording

Intracortical neuron recording is a neuroimaging technic that demonstrated the subdural terminals which could give stable signs more than a while. In any case, the drawn-out security of the characters gained by ECoG is as of now indistinct. Later tests with monkeys have indicated that ECoG can perform at an elevated level for a considerable length of time with no float inexactness or recalibration Three signs can be acquired by intracortical neuron recording: single-unit action (SUA), multi-unit movement (MUA), and nearby field possibilities (LFPs) (Waldert et al. Dec. 2009). Intracortical neuron recording gives a lot higher spatial and transient goal than EEG recording. Henceforth the intracortical signs might be simpler to use than EEG signals. In any case, signal quality might be influenced by the response of cerebral tissue to the embedded chronicle microelectrode and by changes in the affectability of the microelectrode, which might be continuously harmed through the span of days and years (Polikov et al. 2005). The client can generally adjust to these moderate changes in the general affectability of the microelectrode, without the requirement for explicit retraining. By and by, periodic recalibrations of terminal affectability might be essential (Lauer et al. 2000).

Concerning the use of intracortical neuron recording in BCI frameworks, microelectrode exhibits,(Maynard et al. 1997) for example, the Utah Intracortical Electrode Array (UIEA) have been accounted for as a reasonable method for giving synchronous and corresponding control of countless outer gadgets.

4.4 MEG

MEG is a non-obtrusive imaging procedure that enlists the mind's attractive action by methods for acceptance. MEG gauges the intracellular flows moving through dendrites which produce fields that are quantifiable outside of the head (Waldert et al. 2009). The neurophysiological cycles that have MEG signals are indistinguishable from those who produce EEG signals. By the by, while EEG is amazingly touchy to auxiliary current sources, MEG is more delicate to those of essential flows (Baillet et al. 2001). The upside of MEG is that attractive fields are less twisted by the skull and scalp than electric fields (ScienceDirect Topics 2020). Magnetic fields are distinguished by superconducting quantum impedances gadgets, which are incredibly delicate to attractive aggravations delivered by neural action (Babiloni et al. 2009). MEG-based BCIs, when contrasted with EEG-based BCIs, are still at a beginning phase.

4.5 fMRI

fMRI is a non-intrusive neuroimaging procedure which distinguishes changes in nearby cerebral blood volume, cerebral bloodstream and oxygenation levels during neural initiation by methods for electromagnetic fields. fMRI is, for the most part, performed utilizing MRI scanners which apply electromagnetic fields of solidarity in the request for 3 T or 7 T. The principle bit of leeway of the utilization of fMRI is high space goal. Thus, fMRI has been applied for confining dynamic areas inside the mind (deCharms et al. 2004). fMRI seems unsatisfactory for quick correspondence in BCI frameworks and is profoundly powerless to head movement antiquities. In BCI frameworks, fMRI is ordinarily used to quantify the Blood Oxygen Level Dependent (BOLD) during neuronal enactment (Lee et al. 2009). The utilization of fMRI in BCI innovation is generally later. Prior to the development of ongoing fMRI, mind action recording by fMRI has customarily taken quite a while. The information gained by fMRI strategies was handled disconnected, and the outcomes just opened up following a few hours or even days (Weiskopf 2007). The data move rate in fMRI-based BCIs is somewhere in the range of 0.60 and 1.20 pieces/min (Ward and Mazaheri 2008).

4.6 NIRS

NIRS is an optical spectroscopy technique that utilizes infrared light to portray noninvasively gained vacillations in cerebral digestion during neural movement. Infrared light infiltrates the skull to a profundity of around 1–3 cm underneath its surface, where the force of the lessened light permits changes in oxyhaemoglobin and deoxyhaemoglobin focuses on being estimated. Because of shallow light infiltration in mind, this optical neuroimaging method is restricted to the external cortical layer. Along these lines to fMRI, one of the significant constraints of NIRS is the idea of the hemodynamic reaction, since vascular changes happen a specific number of seconds after its related neural action. The spatial goal of NIRS is meagre, in the request for 1 cm (Coyle et al. 2007).

A NIRS framework comprises of a light source, an electronic driving gadget, a light indicator, signal handling devices, and an account gadget. The light source is an infrared producing diode (IRED) set in direct contact with the scalp. The electronic driving gadget is an electronic circuit that controls the IRED to balance the light. The light locator is a photodiode put directly close to the light source. The sign handling gadgets are enhancers and channels that cycle the electrical flag and lessen the clamor because of the surrounding light. The account gadget is a PC or whatever another device that digitalizes, stores, and shows the electrical. Significant quality signals and commotion decrease, particularly foundation clamor initiated by head movements, are significant prerequisites progressively BCI frameworks. Hair obstacle can be overwhelmed by brushing the hair out of the photons’ way by methods for hair gel and clasps. The commotion can be decreased mostly by bandpass separating, moving averaging, and Wiener sifting. These classes of calculations typically neglect to eliminate sudden spike-like commotion created by head movement (Taga et al. 2007; Izzetoglu et al. 2005). Even though NIRS is moderately new estimation methodology, NIRS vows to be a robust neuroimaging methodology for future martialness to BCIs (Coyle et al. 2004).

5 Brain Control Signals Categorization

The determination of a BCI is to understand user aims by means of monitoring Brain activity. Brain signals encompass numerous simultaneous phenomena associated with cognitive tasks. Most of them are still inexplicable, and their origins are unknown. However, the physiological phenomena of more or fewer brain signals have been decoded in such technique that people may learn to modify them at will, to enable the BCI systems to understand their intentions. These signals are regarded as potential control signals in BCIs (Ramadan and Vasilakos 2016).

Various studies have described a vast cluster of brain signals that might serve as control signals in BCI systems. However, only those control signals active in current BCI systems will be discussed as slow cortical potentials, visual evoked potentials, P300 evoked potentials and sensorimotor rhythms. All the signal controls are listed in Fig. 2. Along with some of their main features (Wolpaw et al. 2002).

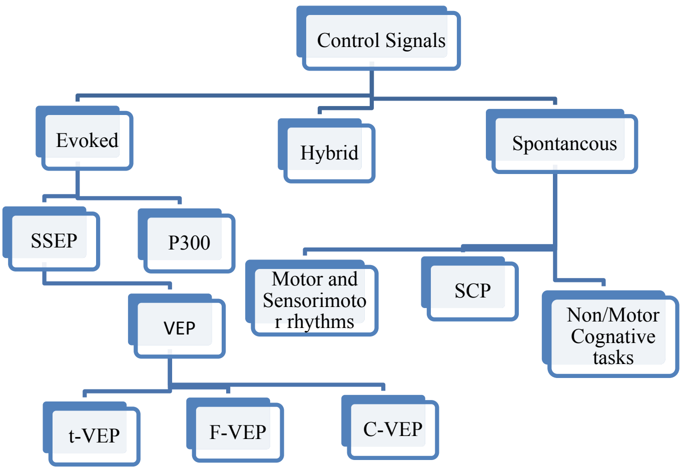

Fig. 2 Classification of control signals

5.1 Evoked

Evoked signals are known as Visual Evoked Signal (VEP). These signals are generated unconsciously by the user who receives external stimulations. The furthermost renowned evoked signals are steady-state evoked potentials (SSEPs) and P300. Evoked signals can be determined by the external stimulus, which could be painful, gauche and strenuous for the user.

Steady-State Evoked Potentials (SSEPs). SSEP signals are brain signals that are generated when the user recognizes intermittent stimulation such as trembling image, restrained sound, and even when the user feel some vibrations. Generally, the EEG signals power in the brain will increase to reach the stimulus frequency. Therefore, based on the feeling process, signals at different brain areas are observed. Various types of SSEP signals are distinguished, such as steady-state visual potentials (SSVEPs) and somatosensory SSEP or auditory SSEP. SSVEP is usually used in many applications (İşcan and Nikulin 2018).

SSVEPs signals are triggered by usually repetitive visual stimulations. The visual stimulation such image trembling generates SSVEP at the optical cortex that has the same frequency of the trembling image (generally between 6 and 30 Hz). SSVEP could be categorized based on the type of modulation into time modulated VEP (t-VEP) BCIs, frequency-modulated VEP (f-VEP) BCIs, and pseudorandom code modulated VEP (c-VEP) (Wang et al. 2006). In t-VEP, the flash sequences of the altered targets to altered stimulus should be orthogonal or near orthogonal individuals to ensure reliable identification of the target. T-VEP has a low information transfer rate which is almost less than 30bits/min. Though there is no requisite for user training. f-VEP depends on flashing each target with a unique frequency; this produces evoked responses with a similar frequency (Bin et al. 2009). f-VEP has a high information transmission rate; in general (30–60 bits/min).f-VEP does not need any kind of training. Finally, c-VEP uses pseudorandom sequences that regulate the duration of ON and OFF. At this point, the information transfer rate is very high, in which it could be more than 100 bits/min. Nevertheless, the user has to be trained first. One of the similar application of the SSVEP is the graphical user interface with some buttons on it where the respective button has a particular frequency. While the user focuses on one of the buttons, the brain generates the equivalent frequency that can be used, for illustration, to control the button click (Lutzenberger et al. 1995; Drislane et al. 2007).

P300. It is an EEG signal that appears after almost 300 ms when the subject is exposed to the infrequent or surprising task. This signal is usually generated through “odd-ball” paradigm where the user is requested to attend a random sequence of stimuli with one is less frequent than the others. When this rare stimulus is relevant to the subject, it triggers the P300 EEG signals. Again P300 does not require any subject training; however, it requires repetitive stimuli which might lead to tiring and inconsistency to the subject (Arvaneh et al. 2019).

5.2 Hybrid Signals

Hybrid signals mean that a combination of brain generated signals is used for control. Therefore, instead of only one type of signals is measured and used in the BCI system, a hybrid of signals is utilized. The primary purpose behind using two or more types of brain signals as input to a BCI system is the reliability and to avoid the disadvantages of each kind of signals. The reader is also referred to (Hong and Khan 2017) for more information on some of these systems.

5.3 Spontaneous Signals

In spontaneous signals, users are voluntary without any external stimulations generate Signals. Most of the distinguished spontaneous signals are the Slow Cortical Potentials (SCP), Motor and sensorimotor rhythms, and Non-motor cognitive tasks (Mcfarland et al. 2005).

Motor and Sensorimotor rhythms. Motor and sensorimotor rhythms are those rhythms related to motor actions such as any movement of body parts. These types of rhythms generated from the motor cortex with frequency bands located at μ ($\simeq$8–13 Hz) and β ($\simeq$13–30 Hz). These rhythms amplitude could be controlled by the user. Generally, one of two different methods of these sensorimotor rhythms is control of by the operant conditioning and motor imagery (Yuan and He 2014).

Motor imagery. The user's motor intention into control signals through motor imagery states is the translation of motor imagery. For instance, the left-hand movement may generate EEG signals accompany within the μ and β rhythms, (μ 8–12 Hz) and (β 18–26 Hz) decrease in specific motor cortex area. Different applications could be used according to the motor imagery rhythms such as controlling a mouse or playing a computer game. With new Artificial Intelligence techniques, the subject might not need any training; however, it is always better to have some training before using motor imagery systems (Pfurtscheller and Neuper 2001).

Slow Cortical Potentials (SCP). EEG signal with a frequency below 1 Hz belongs to SCP. This kind of low-frequency potential can be detected in the frontal and central parts of the cortex; because of this, the upper cortical dendrites perceive the depolarization level shift of the lower frequency. SCP is an activity of shallow frequency, which may be last from milliseconds to several seconds in cortical activity because of its prolonged vibration, which can be positive or negative. Using operant condition, user can control the generation of such a signal (Hinterberger 2004). Thus, the user has to be more train than the required for motor rhythms. Currently, SCP replaced by Motor and sensorimotor rhythms by many researchers.

Non-motor cognitive tasks. Non-motor cognitive tasks can be described by the cognitive functions which are used to drive the BCI. With non-motor cognitive tasks, many of the functions could be performed, such as visual counting, music imagination, mathematical computation and mental rotation (Faller 2014).

6 Features Extraction

Feature extraction represents the unique properties of BCI technology. Several methods for feature extraction have been studied in the twenty-first century. Features and location are the appropriate two sections which are the base of neuroscientific funding. There are many linear and nonlinear methods that have been reported for feature extraction in BCIs, and they are shown in Fig. 3. Multiples features can be taken out from numerous channels and from multiple time segments before being sequenced into a single feature vector. One of the major complications in BCI design is choosing relevant features from the vast number of possible features (Vega-Escobar et al. 2015).

6.1 PAC (Principal Component Analysis)

Principal Component Analysis is known as a statistically linear transformation feature extraction method (Kottaimalai et al. 2013). In PAC, a set of possible correlated observations which transformed into a set of uncorrelated variables. From this analysis method, an optimal representation of data can be determined in terms of minimal mean square-error. Linear transformation generates the statistical variance, which allows PCA to separate the brain signal into a different component with valuable noise and dimension reduction method (Spüler et al. 2012). PCA requires that commodity which is uncorrelated with EEG signal. PCA has also been engaged, in imperative to diminish feature space dimensionality (Lin and Hsieh 2009).

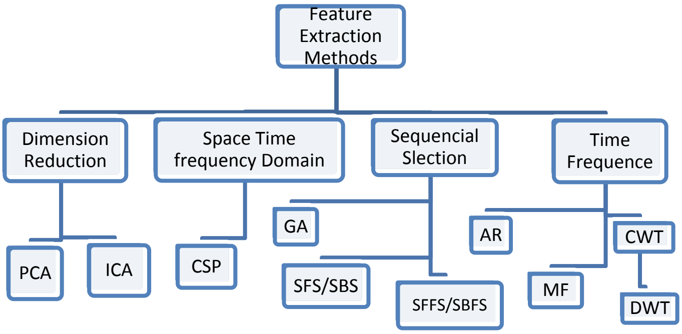

Fig. 3 Different methods of feature extraction

6.2 ICA (Independent Component Analysis)

ICA is a statistical procedure in which a set of hybrid signal slips into a different commodity. In ICA mutual statistical independence of underlying source is assumed. ICA is mainly used as a preprocessing tool before the feature extraction step in order to remove commodity in BCI systems./it is also known as a powerful and robust tool for commodity removal in signal analysis. ICA can be modified to categorize EEG signals by employing Brage's rule (Lee et al. 1999a).

6.3 CSP (Common Spatial Pattern)

Common spatial pattern method can be shown as a multi-channel EEG signal into a subspace, where the discrimination between classes is emphasized, and the similarities are lessened. This feature extraction method intentionally makes the subsequent classification much more effective, by scheming a spatial filter that transforms the input data which is obsessed by the output data with an ideal variance for the subsequent discrimination (Ramoser et al. 2000). CSP can analyze the multi-channel data belonging to 2-class problems (Grosse-Wentrup and Buss 2008).CSP increases the precision of synchronous BCIs, where it is allowed to send signals throughout a certain predefined time period. Nevertheless, CSP does not offer the same enhancement in asynchronous BCIs due to the nonstationary possessions of EEG signals. Similarly, the performance of CSP is affected by the spatial resolution, because of some electrode locations which offer more Preferential information for some specific brain activities. Because of these reasons, several methods improving the original CSP feature extraction method have been projected to increase the performance of wavelet common spatial pattern, common spatio-spectral pattern, and common sparse spectral spatial pattern (Mousavi et al. 2011).

6.4 GA (Genetic Algorithm)

Genetic algorithm is improvement procedure which proves a particular set of features is the most efficient or not. GA is used as an automatic method to extract an ideal set of a similar quality in BCI research. It is a metaheuristic inspired by Charles Darwin's theory of natural evolution (ScienceDirect Topics 2020). This GA Procedure algorithm starts with Initial Population, which is a set of individuals information and then evaluation of individuals information optimum population or a maximum number of interaction in individuals which determines by selection, crossover and mutation. As a final point, the fitness of the new community is evaluated (Seno et al. 2008). When a suitable solution is reached, or the disproportionate number of generations has been produced, the Algorithm is terminated. Else, another iteration of the Algorithm is made.

6.5 AR (Autoregressive Components)

AR spectral estimation is a method for demonstrating signals. AR are models of EEG signal as the output chance signal of a linear period invariant filter, where the input was white noise with a mean of zero and a specific variance of σ^2. The goal of the AR procedure is to find the filter coefficients; meanwhile, it is assumed that different thinking actions will produce dissimilar filter coefficients. The filter coefficients were used as the structures of the signal. However, AR performs poorly when the signal is not stationary (Foldesova and Lanczos 2000). The nonstationary nature of EEG signals, of a multivariate adaptive AR model, has been proposed to design more effective online BCI systems (Wang et al. 2010).

6.6 MF (Matched Filtering)

MF is a feature extraction method that efforts to detect a specific pattern on the basis of its matches with prearranged known signals or templates. The purpose of the user is revealed by means of the association between the unknown EEG signals and the set of templates. Each template signifies the intention of the user. A higher association would imply better matching between the template and the user's preference. MF has been proven particularly useful for the detection of waveforms with dependable temporal characteristics and used MF for the identification of user purposes by μ-rhythms (Lee et al. 1999b).

6.7 WT (Wavelet Transform)

WT is a mathematical tool extensively used for extracting information from many different kinds of data, such as audio or image data, among other things. WT is particularly apposite when signals are not stationary, because it provides a flexible way of representing the time–frequency of a signal. According to the Heisenberg uncertainty principle, it is difficult to measure the signal in both time and frequency domains simultaneously, i.e., increasing accuracy in time domain leads to decrease in accuracy in the frequency domain, and vice-versa. The time–frequency domain combines the time and frequency domain analyses. They represent the distribution of the signal energy in the time–frequency plane (t-fplane). Time–frequency analysis is beneficial in clarifying rhythmic information in EEG signals. Wavelets are functions of variable frequency and limited period that allow simultaneous study of the signal in together the time and the frequency domain, in contrast to other modalities of signal analysis such as Fourier transform (FT). Short-term Fourier transform (STFT) was projected to overcome this limitation of the Fourier analysis. Continuous wavelet transform (CWT) is definite as the complication of the signal $x(t)$ with the wavelet function $\psi s{,}\tau(t)$ (Samar et al. 1999)

$$\omega(s,\tau) = \int_{-\infty}^{\infty} x(t)\varphi^{*}_{s,\tau}(t)\mathrm{d}t \tag{1}$$

$\omega(s, \tau)$ is the wavelet coefficient of corresponds to the frequency related to the scale s and time τ of the wavelet function $\psi s, \tau(t)$, and the symbol "*" can be expressed as the complex conjugation.

The wavelet function $\psi s, \tau(t)$ is a dilated and shifted version of a mother wavelet $\psi(t)$:

$$\varphi_{s,\tau}(t) = \frac{1}{\sqrt{s}}\varphi\left(\frac{t-T}{s}\right) \tag{2}$$

A mother wavelet can take multiples shapes, but it continuously mollifies the following condition:

$$\int_{-\infty}^{\infty} \varphi(t) = \mathrm{d}t = 0 \tag{3}$$

The CWT defined in Eq. (3) is actually a kind of template matching, like a matched filter in which the cross modification between the signal and a predefined waveform is calculated (Demiralp et al. 1999). The CWT introduces a lot of severance and complexity since it contains the study of a signal at in height number of frequencies via several dilations and instable of the mother wavelet. Discrete wavelet transform (DWT) was presented to decrease this redundancy and complexity. The DWT translates and opens the mother wavelet in specific discrete values only. The bi-scale wavelet has been employed effectively for designing an asynchronous BCI based on detection of imaginary movement in the 1–4 Hz frequency range. Also, the Daubechies wavelet, a very well-known mother wavelet, has been used for the classification of SCPs (Hinterberger et al. 2003).

7 BCI Technology

Any research field to be advanced, it requires two things which are a killer application and advanced technology. This segment briefly reviews some of the current BCI technologies in terms of hardware and software. The hardware devices are used to capture the signals either through invasive or non-invasive methods. However, BCI software platforms through intelligent algorithms are responsible for preprocessing and analyzing the signals provided by the hardware as well as generating the control commends for the external environment (Gonfalonieri 2018).

7.1 Hardware BCI Technology

As can be seen in the previous sections, there are different signals to be recorded out of the brain. In addition, there are a number of channels that are recorded as well; these channels differ based on the type of signals to be measured. For instance, EEG deals with 8–64 channels, ECoG works with 32–192 channels, and the single-unit recording might work with 100–300 channels. Therefore, there is no yet a generic device or a platform that can handle all of the brain signals at once. Nevertheless, since BCI is dealing with human as well as animals brains, different regularity organization around the world including Ministry of Health, Labor, and Welfare (MHLW) in Japan, Food and Drug Administration (FDA) in the US, and European Commission (CE) in Europe allowing only specific devices for safety reasons. Therefore, laboratories and researchers around the world might implement their own tools to do their experimentations (Wilson et al. 2012a).

7.2 Software BCI Technology

This segment briefly reviews some of the current BCI platforms and tools that are available and used in research. The review tries to identify the key points, development language, and operating system of each device. However, the BCI requires many of the algorithms for signal acquisition, artifact removal, feature extraction, classification, and post-processing to be included in the tool. Table 7 summarizes the major BCI platforms and tools in terms of their programming languages, supported platforms, and characteristics. The reader is stimulated to read the survey for more details on some of these platforms (Wilson et al. 2012b).

8 Conclusion

The article has reviewed the development from brain-computer interface in its early days and the evolution of it through the last two decades. Through successfully implying different neuroimages techniques like EEG, fMRI and MEG, NIRS, invasive modalities, it has a different level of breakthroughs in these times.

Different wide ranges of signaling features are tested in BCI. Started from signal processing and pattern recognition it has developed a lot and gone furthermore from its starting. More efficient signal processing, reduced user training time widespread the use and again study of BCI.

In current days the BCI stretched its wing toward different daily life works of disabled people, for example, word processing, browsing, wheelchair control, simple environmental control, etc. But there are still some serious problems yet to be sorted out. First and for most the pros and cons of different signal acquisition, more animal and human trial are needed. Secondly, investigation of how it deals with tissue damage, the formation of infections, There are few more concerns like the neurotropic materials for the electrodes which promote neuronal growth, wireless transmission of neuronal signals, the betterment of encoding electrophysiological and metabolic signals are still to be done.

A steady increasing trend emphasizing EEG and movement disorder in BCI is observed, whereas still, it does not get enough emphasis as it should get. Problems like drug-resistant epilepsy can be cured through BCI technology in the near future. BCI is an excellent platform for real-time applications of artificial intelligence and machine learning. It is an application in the field of epilepsy surgery, and localization of seizures has lagged behind, but the transition is unavoidable. In a word, BCI shows the first ray of hope that in the near future, it will become widespread in different general areas and facilitate not only disabled people but also the general population.

References

Aftanas LI, Golocheikine SA (2001) Human anterior and frontal midline theta and lower alpha reflect emotionally positive state and internalized attention: high-resolution EEG investigation of meditation. Neurosci Lett 310(1):57–60. https://doi.org/10.1016/s0304-3940(01)02094-8

Anand BK et al (1961) Some aspects of electroencephalographic studies in Yogis. ScienceDirect. https://www.sciencedirect.com/science/article/pii/0013469461900153. Accessed 9 Sept 2020

Arvaneh M, Robertson IH, Ward TE (2019) A P300-based brain-computer interface for improving attention. Front Hum Neurosci 12. https://doi.org/10.3389/fnhum.2018.00524

Babiloni C, Pizzella V, Gratta CD, Ferretti A, Romani GL (2009) Fundamentals of electroencefalography, magnetoencefalography, and functional magnetic resonance imaging. Int Rev Neurobiol 86:67–80. https://doi.org/10.1016/S0074-7742(09)86005-4

Baillet S, Mosher JC, Leahy RM (2001) Electromagnetic brain mapping. IEEE Signal Process Mag 18(6):14–30. https://doi.org/10.1109/79.962275

Ball T, Kern M, Mutschler I, Aertsen A, Schulze-Bonhage A (2009) Signal quality of simultaneously recorded invasive and non-invasive EEG. NeuroImage 46(3):708–716. https://doi.org/10.1016/j.neuroimage.2009.02.028

Bashashati A, Fatourechi M, Ward RK, Birch GE (2007) A survey of signal processing algorithms in brain-computer interfaces based on electrical brain signals. J Neural Eng 4(2):R32-57. https://doi.org/10.1088/1741-2560/4/2/R03

Bin G, Gao X, Wang Y, Hong B, Gao S (2009) VEP-based brain-computer interfaces: time, frequency, and code modulations [Research Frontier]. IEEE Comput Intell Mag 4(4):22–26. https://doi.org/10.1109/MCI.2009.934562

Blankertz B et al (2010) The Berlin brain-computer interface: non-medical uses of BCI technology. Front Neurosci 4:198. https://doi.org/10.3389/fnins.2010.00198

Brainloop. https://aksioma.org/brainloop/bci_dependent.html. Accessed 04 Nov 2020

Cao L, Xia B, Maysam O, Li J, Xie H, Birbaumer N (2017) A synchronous motor imagery based neural physiological paradigm for brain computer interface speller. Front Hum Neurosci 11. https://doi.org/10.3389/fnhum.2017.00274

Caplan JB, Madsen JR, Raghavachari S, Kahana MJ (2001) Distinct patterns of brain oscillations underlie two basic parameters of human maze learning. J Neurophysiol 86(1):368–380. https://doi.org/10.1152/jn.2001.86.1.368

Chang EF, Rieger JW, Johnson K, Berger MS, Barbaro NM, Knight RT (2010) Categorical speech representation in human superior temporal gyrus. Nat Neurosci 13(11):1428–1432. https://doi.org/10.1038/nn.2641

Cincotti F et al (2008) Non-invasive brain-computer interface system: towards its application as assistive technology. Brain Res Bull 75(6):796–803. https://doi.org/10.1016/j.brainresbull.2008.01.007

Coenen A, Fine E, Zayachkivska O (2014) Adolf Beck: a forgotten pioneer in electroencephalography. J Hist Neurosci 23(3):276–286. https://doi.org/10.1080/0964704X.2013.867600

Coyle S, Ward T, Markham C, McDarby G (2004) On the suitability of near-infrared (NIR) systems for next-generation brain-computer interfaces. Physiol Meas 25(4):815–822. https://doi.org/10.1088/0967-3334/25/4/003

Coyle SM, Ward TE, Markham CM (2007) Brain-computer interface using a simplified functional near-infrared spectroscopy system. J. Neural Eng 4(3):219–226. https://doi.org/10.1088/1741-2560/4/3/007

de Charms RC, Christoff K, Glover GH, Pauly JM, Whitfield S, Gabrieli JDE (2004) Learned regulation of spatially localized brain activation using real-time fMRI. NeuroImage 21(1):436–443. https://doi.org/10.1016/j.neuroimage.2003.08.041

Demiralp T, Yordanova J, Kolev V, Ademoglu A, Devrim M, Samar VJ (1999) Time-frequency analysis of single-sweep event-related potentials by means of fast wavelet transform. Brain Lang. 66(1):129–145. https://doi.org/10.1006/brln.1998.2028

Drislane FW (2007) Visual evoked potentials. In: Blum AS, Rutkove SB (eds) the clinical neurophysiology primer. Humana Press, Totowa, pp 461–473

EEG–ECG–Biosensors. https://neurosky.com/. Accessed 7 Sept 2020

Faller J et al (2014) Non-motor tasks improve adaptive brain-computer interface performance in users with severe motor impairment. Front Neurosci 8. https://doi.org/10.3389/fnins.2014.00320

Fernández T et al (1995) EEG activation patterns during the performance of tasks involving different components of mental calculation. Electroencephalogr Clin Neurophysiol 94(3):175–182. https://doi.org/10.1016/0013-4694(94)00262-j

Foldesova K, Lanczos T (2000) The evaluation of hydraulic effects of different pumping rates in the polluted aquifer by numerical modeling. WIT Trans Ecol Environ 41

Gonfalonieri A (2018) A beginner's guide to brain-computer interface and convolutional neural networks. Towards Data Science. https://towardsdatascience.com/a-beginners-guide-to-brain-computer-interface-and-convolutional-neural-networks-9f35bd4af948. Accessed 5 Nov 2020

Grosse-Wentrup M, Buss M (2008) Multiclass common spatial patterns and information theoretic feature extraction. IEEE Trans Biomed Eng 55(8):1991–2000. https://doi.org/10.1109/TBME.2008.921154

Han C-H, Kim Y-W, Kim DY, Kim SH, Nenadic Z, Im C-H (2019) Electroencephalography-based endogenous brain–computer interface for online communication with a completely locked-in patient. J NeuroEng Rehabil 16(1):18. https://doi.org/10.1186/s12984-019-0493-0

Hill NJ et al (2012) Recording human electrocorticographic (ECoG) signals for neuroscientific research and real-time functional cortical mapping. J Vis Exp JoVE 64. https://doi.org/10.3791/3993

Hinterberger T, Kübler A, Kaiser J, Neumann N, Birbaumer N (2003) A brain-computer interface (BCI) for the locked-in: comparison of different EEG classifications for the thought translation

device. Clin Neurophysiol Off J Int Fed Clin Neurophysiol 114(3):416–425. https://doi.org/10.1016/s1388-2457(02)00411-x
Hinterberger T et al (2004) Brain-computer communication and slow cortical potentials. IEEE Trans Biomed Eng 51(6):1011–1018. https://doi.org/10.1109/TBME.2004.827067
Hong K-S, Khan MJ (2017) Hybrid brain–computer interface techniques for improved classification accuracy and increased number of commands: a review. Front Neurorobotics 11. https://doi.org/10.3389/fnbot.2017.00035
İşcan Z, Nikulin VV (2018) Steady state visual evoked potential (SSVEP) based brain-computer interface (BCI) performance under different perturbations. https://journals.plos.org/plosone/article?id=https://doi.org/10.1371/journal.pone.0191673. Accessed 4 Nov 2020
Izzetoglu M, Devaraj A, Bunce S, Onaral B (2005) Motion artifact cancellation in NIR spectroscopy using Wiener filtering. IEEE Trans Biomed Eng 52(5):934–938. https://doi.org/10.1109/TBME.2005.845243
Khalid MB, Rao NI, Rizwan-i-Haque I, Munir S, Tahir F (2009) Towards a brain computer interface using wavelet transform with averaged and time segmented adapted wavelets. In: 2nd international conference on computer, control and communication, Feb 2009, pp. 1–4. https://doi.org/10.1109/IC4.2009.4909189
Klimesch W (1997) EEG-alpha rhythms and memory processes. Int J Psychophysiol Off J Int Organ Psychophysiol 26(1–3):319–340. https://doi.org/10.1016/s0167-8760(97)00773-3
Klimesch W et al (2001) Theta synchronization during episodic retrieval: neural correlates of conscious awareness. Brain Res Cogn Brain Res 12(1):33–38. https://doi.org/10.1016/s0926-6410(01)00024-6
Ko W, Jeon E, Lee J, Suk H (2019) Semi-supervised deep adversarial learning for brain-computer interface. In: 2019 7th international winter conference on brain-computer interface (BCI), Feb 2019, pp 1–4. https://doi.org/10.1109/IWW-BCI.2019.8737345
Kögel J, Schmid JR, Jox RJ, Friedrich O (2019) Using brain-computer interfaces: a scoping review of studies employing social research methods. BMC Med Ethics 20(1):18. https://doi.org/10.1186/s12910-019-0354-1
Konrad P, Shanks T (2010) Implantable brain computer interface: challenges to neurotechnology translation. Neurobiol Dis 38(3):369–375. https://doi.org/10.1016/j.nbd.2009.12.007
Kopell N, Ermentrout GB, Whittington MA, Traub RD (2000) Gamma rhythms and beta rhythms have different synchronization properties. Proc Natl Acad Sci 97(4):1867–1872. https://doi.org/10.1073/pnas.97.4.1867
Kottaimalai R, Rajasekaran MP, Selvam V, Kannapiran B (2013) EEG signal classification using principal component analysis with neural network in brain computer interface applications. In: 2013 IEEE international conference on emerging trends in computing, communication and nanotechnology (ICECCN), Mar 2013, pp 227–231. https://doi.org/10.1109/ICE-CCN.2013.6528498
Kübler A, Kotchoubey B, Kaiser J, Wolpaw JR, Birbaumer N (2001) Brain-computer communication: unlocking the locked in. Psychol Bull 127(3):358–375. https://doi.org/10.1037/0033-2909.127.3.358
Kuruvilla A, Flink R (2003) Intraoperative electrocorticography in epilepsy surgery: useful or not? Seizure—Eur J Epilepsy 12(8):577–584. https://doi.org/10.1016/S1059-1311(03)00095-5
Lauer RT, Peckham PH, Kilgore KL, Heetderks WJ (2000) Applications of cortical signals to neuroprosthetic control: a critical review. IEEE Trans Rehabil Eng Publ IEEE Eng Med Biol Soc 8(2):205–208. https://doi.org/10.1109/86.847817
Laureys S, Gosseries O, Tononi G (2015) The neurology of consciousness: cognitive neuroscience and neuropathology. Academic, New York
Lebedev MA, Nicolelis MAL (2006) Brain-machine interfaces: past, present and future. Trends Neurosci 29(9):536–546. https://doi.org/10.1016/j.tins.2006.07.004
Lee T-W, Lewicki MS, Girolami M, Sejnowski TJ (1999a) Blind source separation of more sources than mixtures using overcomplete representations. IEEE Signal Process. Lett. 6(4):87–90. https://doi.org/10.1109/97.752062

Lee TW, Girolami M, Sejnowski TJ (1999b) Independent component analysis using an extended infomax algorithm for mixed subgaussian and supergaussian sources. Neural Comput. 11(2):417–441. https://doi.org/10.1162/089976699300016719

Lee J-H, Ryu J, Jolesz FA, Cho Z-H, Yoo S-S (2009) Brain-machine interface via real-time fMRI: preliminary study on thought-controlled robotic arm. Neurosci Lett 450(1):1–6. https://doi.org/10.1016/j.neulet.2008.11.024

Lin C-J, Hsieh M-H (2009) Classification of mental task from EEG data using neural networks based on particle swarm optimization. Neurocomputing 72(4):1121–1130. https://doi.org/10.1016/j.neucom.2008.02.017

Lotte F, Bougrain L, Clerc M (2015) Electroencephalography (EEG)-based brain-computer interfaces. In: Wiley encyclopedia of electrical and electronics engineering. Wiley, Hoboken, pp 1–20

Luo P, Xie G, Jiang Z (2007) The progress in researches on biocompatibility for direct brain-machine interface. J Biomed Eng 24(6):1416–1418

Lutzenberger W, Pulvermüller F, Elbert T, Birbaumer N (1995) Visual stimulation alters local 40-Hz responses in humans: an EEG-study. Neurosci Lett 183(1–2):39–42. https://doi.org/10.1016/0304-3940(94)11109-v

Mason SG, Birch GE (2003) A general framework for brain-computer interface design. IEEE Trans Neural Syst Rehabil Eng Publ. IEEE Eng Med Biol Soc 11(1):70–85. https://doi.org/10.1109/TNSRE.2003.810426

Maynard EM, Nordhausen CT, Normann RA (1997) The Utah intracortical electrode array: a recording structure for potential brain-computer interfaces. Electroencephalogr Clin Neurophysiol 102(3):228–239. https://doi.org/10.1016/s0013-4694(96)95176-0

Mcfarland D, Sarnacki W, Vaughan T, Wolpaw J (2005) Brain-computer interface (BCI) operation: signal and noise during early training sessions. Clin Neurophysiol Off J Int Fed Clin Neurophysiol 116:56–62. https://doi.org/10.1016/j.clinph.2004.07.004

Mesgarani and Chang (2012) Selective cortical representation of attended speaker in multi-talker speech perception. Nature. https://www.nature.com/articles/nature11020. Accessed 4 Nov 2020

Mousavi EA, Maller JJ, Fitzgerald PB, Lithgow BJ (2011) Wavelet common spatial pattern in asynchronous offline brain computer interfaces. Biomed Signal Process Control 6(2):121–128. https://doi.org/10.1016/j.bspc.2010.08.003

Müller-Putz GR, Pfurtscheller G (2008) Control of an electrical prosthesis with an SSVEP-based BCI. IEEE Trans Biomed Eng 55(1):361–364. https://doi.org/10.1109/TBME.2007.897815

Nagel S, Spüler M (2019) Asynchronous non-invasive high-speed BCI speller with robust non-control state detection. Sci Rep 9(1), Art no. 1. https://doi.org/10.1038/s41598-019-44645-x

Paul D, Mukherjee M, Mukherjee M, Dey M, Bhattacharya A (2019) Automation of wheelchair using brain computer interface (BCI) technique. AIP Conf Proc 2072(1):020004. https://doi.org/10.1063/1.5090244

Pfurtscheller G, Neuper C (2001) Motor imagery and direct brain-computer communication. Proc IEEE 89(7):1123–1134. https://doi.org/10.1109/5.939829

Polikov VS, Tresco PA, Reichert WM (2005) Response of brain tissue to chronically implanted neural electrodes. J Neurosci Methods 148(1):1–18. https://doi.org/10.1016/j.jneumeth.2005.08.015

Ramadan R, Vasilakos A (2016) Brain computer interface: control signals review. Neurocomputing 223. https://doi.org/10.1016/j.neucom.2016.10.024

Ramoser H, Muller-Gerking J, Pfurtscheller G (2000) Optimal spatial filtering of single trial EEG during imagined hand movement. IEEE Trans Rehabil Eng 8(4):441–446. https://doi.org/10.1109/86.895946

Sinclair CM, Gasper MC, Blum AS (2007) Basic electronics in clinical neurophysiology. In: Blum AS, Rutkove SB (eds) The clinical neurophysiology primer. Humana Press, Totowa, pp 3–18

Samar VJ, Bopardikar A, Rao R, Swartz K (1999) Wavelet analysis of neuroelectric waveforms: a conceptual tutorial. Brain Lang. 66(1):7–60. https://doi.org/10.1006/brln.1998.2024

Sellers EW, Vaughan TM, Wolpaw JR (2010) A brain-computer interface for long-term independent home use. Amyotroph. Lateral Scler. Off Publ World Fed Neurol Res Group Mot Neuron Dis 11(5):449–455. https://doi.org/10.3109/17482961003777470

ScienceDirect Topics (2020) Beta rhythm—an overview. https://www.sciencedirect.com/topics/immunology-and-microbiology/beta-rhythm. Accessed 4 Nov 2020

ScienceDirect Topics (2020) Gamma Rhythm—an overview. https://www.sciencedirect.com/topics/medicine-and-dentistry/gamma-rhythm. Accessed 4 Nov 2020

ScienceDirect Topics (2020) Genetic algorithm—an overview. https://www.sciencedirect.com/topics/engineering/genetic-algorithm. Accessed 4 Nov 2020

Seno BD, Matteucci M, Mainardi L (2008) A genetic algorithm for automatic feature extraction in P300 detection. In: 2008 IEEE international joint conference on neural networks. IEEE World Congress on Computational Intelligence, June 2008, pp 3145–3152. https://doi.org/10.1109/IJCNN.2008.4634243

Spüler M, Rosenstiel W, Bogdan M (2012) Principal component based covariate shift adaption to reduce non-stationarity in a MEG-based brain-computer interface. EURASIP J Adv Signal Process 2012(1):129. https://doi.org/10.1186/1687-6180-2012-129

Straebel V, Thoben W (2014) Alvin Lucier's music for solo performer: experimental music beyond sonification. Organised Sound 19(1):17–29. https://doi.org/10.1017/S135577181300037X

Taga G, Homae F, Watanabe H (2007) Effects of source-detector distance of near infrared spectroscopy on the measurement of the cortical hemodynamic response in infants. NeuroImage 38(3):452–460. https://doi.org/10.1016/j.neuroimage.2007.07.050

Teplan M (2002) Fundamentals of EEG measurement. Meas Sci Rev 2:11

Usakli AB (2010) Improvement of EEG signal acquisition: an electrical aspect for state of the art of front end. Comput Intell Neurosci 630649. https://doi.org/10.1155/2010/630649

Vega-Escobar L, Castro-Ospina AE, Duque-Muñoz L (2015) Feature extraction schemes for BCI systems. In: 2015 20th symposium on signal processing, images and computer vision (STSIVA), Sept 2015, pp 1–6. https://doi.org/10.1109/STSIVA.2015.7330455

Vidal JJ (1973) Toward direct brain-computer communication. Annu Rev Biophys Bioeng 2(1):157–180. https://doi.org/10.1146/annurev.bb.02.060173.001105

Vilimek R, Zander TO (2009) BC(eye): combining eye-gaze input with brain-computer interaction. In: Universal access in human-computer interaction. Intelligent and ubiquitous interaction environments, Berlin, Heidelberg, pp 593–602. https://doi.org/10.1007/978-3-642-02710-9_66

Waldert S (2016) Invasive versus non-invasive neuronal signals for brain-machine interfaces: will one prevail? Front Neurosci 10. https://doi.org/10.3389/fnins.2016.00295

Waldert S, Pistohl T, Braun C, Ball T, Aertsen A, Mehring C (2009) A review on directional information in neural signals for brain-machine interfaces. J Physiol Paris 103(3–5):244–254. https://doi.org/10.1016/j.jphysparis.2009.08.007

Wang Y, Wang R, Gao X, Hong B, Gao S (2006) A practical VEP-based brain-computer interface. IEEE Trans Neural Syst Rehabil Eng Publ IEEE Eng Med Biol Soc 14(2):234–239. https://doi.org/10.1109/TNSRE.2006.875576

Wang J, Xu G, Wang L, Zhang H (2010) Feature extraction of brain-computer interface based on improved multivariate adaptive autoregressive models. In: 2010 3rd international conference on biomedical engineering and informatics, vol 2, pp 895–898. https://doi.org/10.1109/BMEI.2010.5639885

Ward BD, Mazaheri Y (2008) Information transfer rate in fMRI experiments measured using mutual information theory. J Neurosci Methods 167(1):22–30. https://doi.org/10.1016/j.jneumeth.2007.06.027

Weiskopf N et al (2007) Real-time functional magnetic resonance imaging: methods and applications. Magn Reson Imaging 25(6):989–1003. https://doi.org/10.1016/j.mri.2007.02.007

Wikipedia (2020) Electrophysiology. 28 Aug 2020. Accessed 07 Sept 2020. [Online]. Available: https://en.wikipedia.org/w/index.php?title=Electrophysiology&oldid=975471801

Wikipedia (2020) Hemodynamics, 06 Sept 2020, Accessed 07 Sept 2020. [Online]. Available: https://en.wikipedia.org/w/index.php?title=Hemodynamics&oldid=977100597

Wilson JA, Guger C, Schalk G (2012a) BCI hardware and software. Oxford University Press, Oxford

Wilson A, Guger C, Schalk G (2012b) BCI Hardware and software. Brain-Comput Interfaces Princ Pract. https://doi.org/10.1093/acprof:oso/9780195388855.003.0009

Wolpaw JR et al (2000) Brain-computer interface technology: a review of the first international meeting. IEEE Trans Rehabil Eng Publ IEEE Eng Med Biol Soc 8(2):164–173. https://doi.org/10.1109/tre.2000.847807

Wolpaw JR, Birbaumer N, McFarland DJ, Pfurtscheller G, Vaughan TM (2002) Brain-computer interfaces for communication and control. Clin Neurophysiol Off J Int Fed Clin Neurophysiol 113(6):767–791. https://doi.org/10.1016/s1388-2457(02)00057-3

Yuan H, He B (2014) Brain-computer interfaces using sensorimotor rhythms: current state and future perspectives. IEEE Trans Biomed Eng 61(5):1425–1435. https://doi.org/10.1109/TBME.2014.2312397

Entropy of DNA Sequences as Similarity Index for Various SARS-CoV-2 Virus Strains

Satarupa Biswas and Bimal Kumar Sarkar

Abstract In this work, we have described the analysis of digitized sequences of genetic information by means of the notions of entropy. The occurrence of a particular pattern in the genetic sequence is paid special attention. The occurrence of genetic word is expressed in a density manner. The occurrence frequency of the *q*-gram genetic word of interest is determined with the help of finite impulse response (FIR) type filter along the sequence. It is in turn, used for the determination of horizontal correlations, i.e., correlations between the word along the sequence. We use the probability distribution of the genetic word occurrence as the input for the calculation of entropy in the sequence. The sequence entropy is further used for principal component analysis (PCA) to determine the similarity/dissimilarity between the biological sequences. We have considered seven human corona virus sequences. Entropy-based similarity study for SARS-CoV-2 strains is presented in this paper.

Keywords Sequences · Genetic information · FIR filter · Entropy · PCA · Corona virus

1 Introduction

The entropy of amino acid sequences in DNA of an organism can be considered as the measure of diversity of proteins. The higher the value of entropy, the greater the possibility of variation in the information content coded by the nucleic acid (Hasegawa and Yano 1975). This theory is utilized in the present study to understand the variation in the genetic sequences of different novel corona viruses that have infected people across the world leading to one of the world's biggest pandemics. The pandemic itself highlights the importance of tracking the dynamics of viral transmission in real-time. Moreover, as the virus mutates frequently, each sequence is studied and compared with others to understand the variation of information that is transmitted

S. Biswas · B. K. Sarkar (✉)
Department of Physics, Adamas University, Kolkata, India
e-mail: bks@physics.org.in

M. Mukherjee et al. (eds.), *Advances in Medical Physics and Healthcare Engineering*, Lecture Notes in Bioengineering, https://doi.org/10.1007/978-981-33-6915-3_51

from one species to the other. Hyper-variable genomic hotspot for the novel coronavirus SARS-CoV-2 has already been identified by Wen et al. (2020). Likewise, the similarities in the genetic code would also provide important information in understanding the virus and its prevention.

Corona virus molecule has a single-stranded, positive-sense RNA genome of length of approximately 27–32 kilobases (kb). The genome sizes of HCoV-229E and HCoV-NL63 are approximately 27.5 kb, and it is more than 30 kb for HCoV-OC43 and HCoV-HKU1. It possesses the RNA harbors a 50-cap structure and a 30-polyadenylate tail which enable to play a role of messenger RNA (mRNA) (Zhou et al. 2020; de Wit et al. 2016; Wu et al. 2020; Su et al. 2016; Perlman and Netland 2009; Lu et al. 2020a; Fehr and Perlman 2015; Masters 2006).

This study presents identification and analysis of regions of similarity in SARS-CoV genetic sequence (Ge et al. 2013; Chinese SARS Molecular Epidemiology Consortium 2004; Raj et al. 2013). According to information theory, individuality of a species can be aggregates that propagate information from past to future. The Shannon Entropy is considered as a measure for the order/disorder state of nucleotide sequences of the DNA (Schmitt and Herzel 1997). The information in a genetic code is comprised of an alphabetic sequence of the four letters A, C, G, and T, which symbolizes the four nucleotides, namely, adenine (A), cytosine (C), guanine (G) and thymine (T). The sequences have been recognized for most of the SARS-CoV-2 genes and are accessible in computer-readable form. The probability of occurrence of a combination of a group of symbols in a sequence is the measure of order in a sequence. An alignment-free approach of DNA sequence analysis, n-mer/word frequency estimation, is attempted in this work.

2 Methodology

Our method is based on the observation through a sliding "counter "of width W over DNA sequence (Saha and Sarkar 2020). A certain number of q-grams called bins are set in the counter. As there are only four letters in the DNA alphabet, viz., $\{A, C, G, T\}$ the number of all combinations of q-grams in a DNA sequence is 4^q.

Definition 1 (*q-gram of sequence*) Given a sequence 'seq', when a window of length q slides over the characters of 'seq', its q-grams are formed. For a sequence 'seq, there are $|\text{seq}| - (q - 1)$ q-grams.

The number of all possible q-grams or called as "bin" is 4^q. Bins can be arranged in lexicographic order, and b_i is used to denote the ith bin in this order. All the possible bins are denoted as:

$$B_q = \{b_1, b_2, \ldots, b_{4^q}\}$$

Example 1 One-gram bins are $B_1 = \{A, C, G, T\}$, consisting 4 bins. Two-gram bins are $B_2 = \{$AA, AC, AG, AT, CA, CC, CG, CT, GA, GC, GG, GT, TA, TC, TG, TT$\}$, consisting 16 bins.

Definition 2 (*Bin signature*) For a sequence, the q-gram bin signature, S_j is a mapping with the bin b_j $\left(b_j \in B_q\right)$ where ith bit in S_j, is corresponding to the presence or absence of b_j. For a sequence 'seq, there are $|\text{seq}| - \left(\left|b_j\right| - 1\right)$ bits in S_j.

Example 2 Consider a sequence, $S =$ "AACTCG". Its two-grams ($q = 2$) signature in the sequence is $S_2 = [0\ 1\ 0\ 0\ 0]$.

Definition 3 (*Filter*) A sequence $x[n]$ is filtered through mapping of the sequence into output sequence $y[n]$ via a weighted window b by means of the convolution summation as

$$y[n] = \sum_{i=0}^{k} b_i x[n - i] \tag{1}$$

b is independent of $x[n]$ and $y[n]$, where n is the time index. $y[n]$ is the response of the filter to input signal $x[n]$. The filter is finite impulse response (FIR) digital filter. The term digital filter arises because it operates on discrete-time signals. Finite impulse response arises because the filter output is computed as a weighted, finite term sum, of past and present (Fig. 1).

Example 3 Weighted filter output of S_A with the weighted window $\beta = [0.2\ 0.1\ 0.3\ 0.4]$ is as follows:

$$S_A = \left[1\ 1\ 0\ 0\ 0\ 0\right]$$

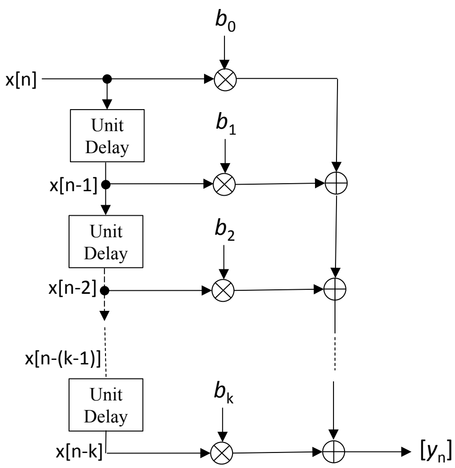

Fig. 1 Block diagram of finite impulse response (FIR) digital filter

$$y_A[n] = \sum_{0}^{3} \beta_k S_A[n-k] \quad \text{with}\, \beta_0 = 0.2,\ \beta_1 = 0.1,\ \beta_2 = 0.3,\ \beta_3 = 0.4$$
$$\Rightarrow y_A[n] = \beta_0 S_A[n] + \beta_1 S_A[n-1] + \beta_2 S_A[n-2] + \beta_3 S_A[n-3]$$

$y_A = [0.2\ 0.3\ 0.4\ 0.7\ 0.4\ 0]$; Similarly for other nucleotide viz., C, G, T, the output is obtained as,

$$y_C = [0.2\ 0.0\ 0.2\ 0.1\ 0.5\ 0.5]; \quad y_G = [0.0\ 0.0\ 0.0\ 0.0\ 0.0\ 0.2];$$
$$y_T = [0.0\ 0.0\ 0.0\ 0.2\ 0.1\ 0.3].$$

For nucleotide density calculation, evenly distributed window of unit value is considered. As explained, the output of the convolution summation represents the nucleotide density along the sequence. The detail algorithms for bin construction, bin signature, filter operation is displayed in Algorithms 1, 2, and 3, respectively.

Algorithm 1: Bin Construction
Input: q - length of bin **Output:** set of bins $B_q = \{b_1, b_2, \ldots\ldots b_{4^q}\}$

0 ← bincount;
4^q ← n;
cell(1,n) ← bin;
for first = 1:4 **do**
    for qth = 1:4 **do**
    convert integer to nucleotide character ([first … qth]) ← binq;
    bincount = bincount + 1;
    binq ← bin{bincount};
    end
end
bin ← B_q

Algorithm 2: Bin Signature
Input: Sequence (seq), bin (b) **Output:** Bin Signature

m ← length (*seq*);
nbin ← length (*b*);
for *i* ← *1….m - (nbin - 1)* **do**
    if *seq* (*i : i+nbin-1*) = *b* **then**
        signature (i) = 1
    else
        signature (i) = 0
end
signature ← *Bin Signature*

Algorithm 3 Filter
Input: *BinSignature*, *window* **Output:** *filter*

$w \leftarrow$ length (*window*);
*window = 1/w*array of ones(1,w)*;
$0 \leftarrow sum$
for $i \leftarrow 1$.... length (*window*) **do**
make array of zeros with length of i -1 $\leftarrow$ *zero*
*sum=sum+window (i) * array[zeros BinSignature(1:(length(BinSignature)-(i-1)))]*
end
filter $\leftarrow$ *sum*

3 Sequence Analysis

The filter output is taken as a density distribution for DNA sequences. The density distribution is based on q-gram word density, which in turn is considered for the determination of Shannon Entropy as

$$y_i = -\sum_{j=1}^{q} p_{ij} \log p_{ij} \tag{2}$$

where p_{ij} is the probability of appearance of the jth genetic letter at ith position in the genetic sequence. Further, we want to find a similarity/dissimilarity measure between two entropy distributions $\rho_i = (y_{i1}, y_{i2}, \ldots, y_{\mathrm{in}})$ and $\rho_j = (y_{j1}, y_{j2},\ldots,y_{jn})$. We construct the data matrix D comprising elements $[\rho_1, \rho_2, \ldots, \rho_m]'$, where m is the number of sequences. Principal Component Analyses (PCA) is used to estimate scores between density distributions such that it reduces multidimensional data sets to lower dimensions with the consistent original data matrix (Novembre and Stephens 2008).

We determine the dissimilarity between two sequences from the scores in the first three principal components by computing the Euclidean distance between pairs of density distributions in the m-by-n data matrix D. Rows of D correspond to sequence (observations) and columns correspond to position index in the sequence (variables). Thus, Euclidean distance X is a row vector of length $m(m - 1)/2$, corresponding to pairs of observations in D. The distances are arranged in the order (2, 1), (3, 1), …, (m, 1), (3, 2), …, (m, 2), …, (m, $m - 1$). X is used as a dissimilarity matrix in clustering or multidimensional scaling. An unweighted pair group method with arithmetic mean (UPGMA) is employed on PC scores for the construction of a phylogenetic tree (Yu et al. 2010). UPGMA uses a local objective function to construct a rooted bifurcating tree.

4 Results and Discussions

The nucleotide density distribution was obtained through FIR filter. We have calculated the density distribution for one-, two-, three-, gram nucleotide for different species. Secondly, we have calculated entropy distributions $\rho_i = (y_{i1}, y_{i2}, \ldots, y_{\text{in}})$ and $\rho_j = (y_{j1}, y_{j2}, \ldots, y_{jn})$. The variation of entropy with position for all other sequences are calculated for the above three combinations. The entropy values were found to be minimum for mono-mer density distributions in individual sequences while increasing linearly for di-mers and codons respectively. Observations based on the position of the *n*-mers in sequences of SARS-CoV-2 DNA reveals significant minimum entropy regions for codons. Figure 1 shows the heat map of entropy calculated over 29,000 bases for 7 DNA sequences. Similar analysis profile for mono-mers and di-mers does not show overlapping regions for different sequences. This suggests that codons are more effective in transferring information through different species. Codon bias has been reported for HIV 1 virus (Grantham et al. 1981). Therefore, it can be inferred that in various novel coronavirus strains, the codons at specific positions are the highest bias representing minimum entropy and hence carry the maximum information. Further studies with the sequences of these loci can be useful genetic engineering for developing vaccines or taking control over the spread of the second wave of the pandemic.

We have chosen seven SARS Corona virus sequences (SARS-COV) from various countries. The details of the organism are presented in Table 1.

Based on FIR filtering, firstly the nucleotide density distribution is generated. We have calculated the density distribution for one-, two-, three-, gram nucleotide for different species. Secondly, we have calculated entropy distributions $\rho_i = (y_{i1}, y_{i2}, \ldots, y_{\text{in}})$ and $\rho_j = (y_{j1}, y_{j2}, \ldots, y_{jn})$. Figure 2 displays the spatial variation of the entropy along the SARS-COV sequence for seven species.

In fact, it is inconvenient to realize all the entropy variation in 2D graphical representation. For example, the organism HKU1 shows the positions where it possesses the minima in entropy values. Some are demonstrated at the positions, around 7400, 10,000, 23,000, etc. the Amsterdam strain, NL63 has shown minima at around 7300, 8000, etc. But other strains exhibit their entropy representation in a crowded manner.

Table 1 SARS-COV strains with their complete genome sequence, accession no. and source

Sequence No.	Strain	Accession No.	Place
1	Wuhan-Hu-1	MN908947	Wuhan
2	CV7	DQ898174	Canada
3	MERS-CoV/C1272	MH734115	Kenya
4	HCoV-OC43	KU131570	UK/London
5	NL63	DQ445912	Amsterdam
6	HCoV_229E	MN306046	Seattle/USA
7	HKU1	MH940245	Thailand

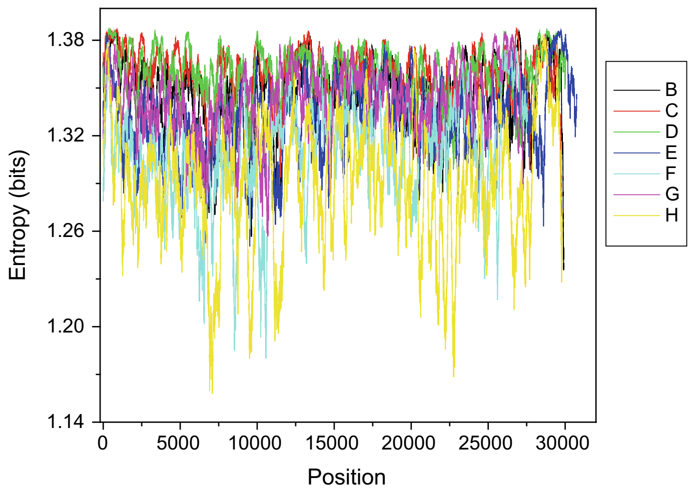

Fig. 2 Entropy profile of seven SARS-COV sequences. Entropy is calculated based on single nucleotide distribution. Sequences are: B: Wuhan-Hu-1; C CV7; D: MERS-CoV/C1272; E: HCoV-OC43; F: NL63; G: HCoV_229E; H: HKU1 (see Table 1)

It is difficult to understand the variation for them differentially. Rather it is more comprehensive to show the entropy variation for all sequences (total 7) in a single panel. It has been shown in Fig. 3

The present work intends to assess the variability and complexity at each nucleotide site with the calculation of entropy for each positions using the Shannon entropy formula, Eq. (2). The low entropy regions around 7400 and 9000 position are common to all 7 sequences (Fig. 3). Entropy (Y_i) is an important parameter for the understanding of sequential stability. Y_i becomes maximal when all symbols occur at equal probability. On the other hand, Y_i becomes the least if one symbol occurs at probability 1 and in that case the other symbols will be forbidden. It means that lower the value of entropy the site is more stable without much complexity. Under

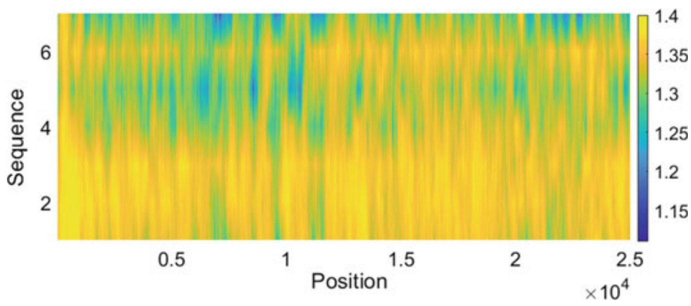

Fig. 3 Entropy profile of 7 SARS-COV sequences. Entropy is calculated based on single nucleotide distribution. Sequences are represented as number starting from 1 to 7 (see Table 1)

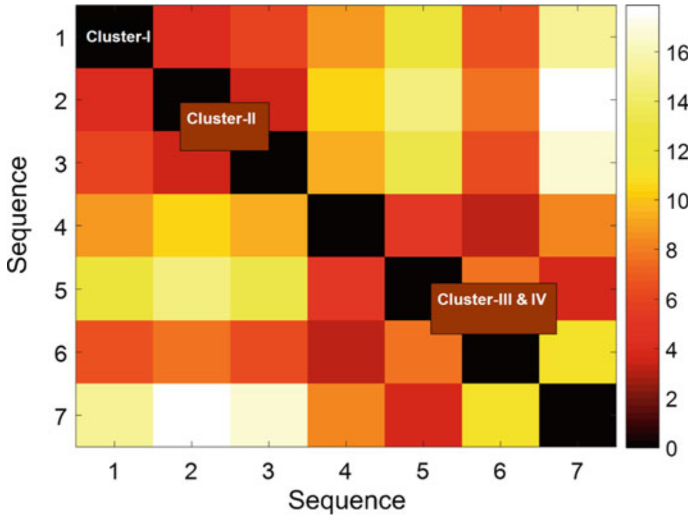

Fig. 4 Dissimilarity matrix for 7 SARS-COV sequences

this assumption, the zone around the site 7400 and 9000 position are most stable for all strain/ species. It may find a good structural relationship between the regions of low entropy and the secondary structure of proteins which include α-helix, β-sheets and loops regions.

Strain no. 4–7 (HCoV-OC43; F: NL63; G: HCoV_229E; H: HKU1) show the stability with lower entropy around 8, 9, 11, 12 K site position. But this behavior is not exhibited in case of the strains numbers 1–3 (Wuhan-Hu-1; C CV7; D: MERS-CoV/C1272). If one can go through these strains, as a whole, it is noticed that the entropy is increasing or in turn the complexity is more. It is an indication of evolutionary development among the SARS-COV strains. Based on site entropy we prepared the dissimilarity matrix for the sequences (Fig. 4).

The dissimilarity matrix demonstrates the existence of 4 different clusters. One can see that the SARS-COV sequences in a cluster show less dissimilarity among themselves. In other way to mean that the sequences have much similarity residing in a cluster (Chan et al. 2020). The COVID sequence appearing in cluster I is typically from Wuhan, China. The Wuhan virus genome sequence examination found β-CoV strain (Lu et al. 2020b). The Wuhan novel β-CoV revealed 88% similarity with the sequence of two bat-derived SARS-COV, bat-SL-CoVZC45 and it was named “SARS-CoV-2” by the International Virus Classification Commission. The genome of SARS-CoV-2 sequence has the similarity with a typical CoVs. It encompasses more than ten open reading frames (ORFs). The first ORFs cover about two-thirds of viral RNA, which get translated into two large polyproteins, pp1a and pp1ab. These proteins assist to form the viral replicase transcriptase complex (Fehr and Perlman 2015). The remaining one-third of viral RNA take part in translation of four structural proteins: spike (S), envelope (E), nucleocapsid (N) and membrane (M) proteins (Knoops et al. 2008).

Cluster-II comprising of two strains CV7, MERS-CoV, belong to β-CoV genera, which also includes SARS-CoV-2 strain as placed singly in cluster-I. Two HCoVs of strains HCoV-229E and HCoV-OC43 being placed in the mixed Cluster of III and IV, are the members of β-CoV genera. From the cluster presentation (Fig. 6), it will be understood that they belong to cluster-III. Remaining two strains, NL63 and HKU1 are placed in cluster IV.

Phylogenic relation among the strains is represented in Fig. 5. We obtain the phylogenetic tree of the data set based on unweighted pair group method with arithmetic mean (UPGMA) on PC scores. Phylogenetic tree analysis clearly shows the relationship among all COVID strains under each cluster. We further sub-cluster in each cluster based on their genetic distance (GD). We have considered PC score to determine the dissimilarity or genetic distance between two organisms.

Explicitly the COVID strains are placed in a cluster description (Fig. 6). The scores are determined in the principal component analysis. Three principal components are taken into consideration. Each strain is represented as state point by scatter plot in the three PC space. Cluster presentation is well in agreement with phylogenic relations. Wuhan-Hu-1 strain is well isolated from all other strains. It belongs to cluster-I. Each of the other three clusters possess two-member strain. Cluster-II comprises of two strains CV7 and MERS-CoV belonging to β-CoV genera (encircled with blue color ellipse in Fig. 6). Already it is mentioned in the previous section that the strains HCoV-229E and HCoV-OC43 exist in Cluster of III. It is displayed by two

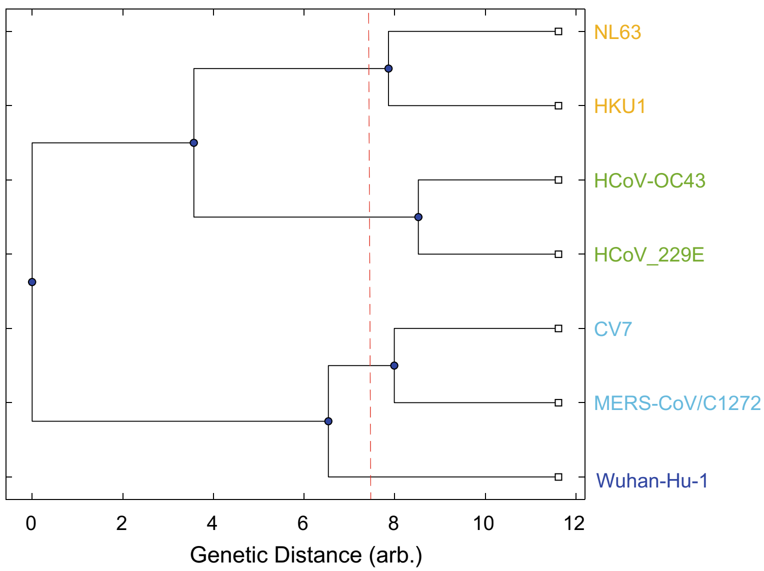

Fig. 5 The phylogenetic tree of 7 SARS-COV sequences

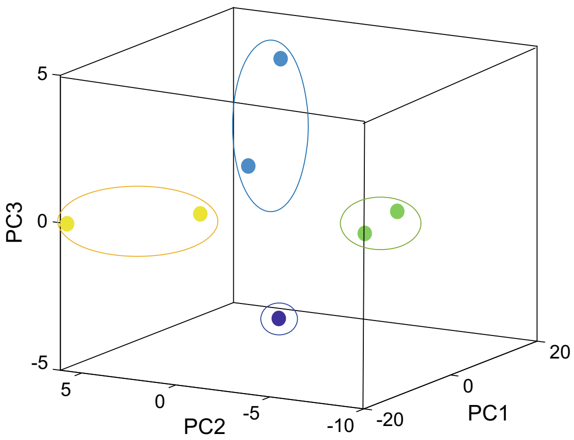

Fig. 6 Scatter plot PC values for 7 SARS-COV sequences: Cluster-I (Wuhan-Hu-1) is encircled with deep blue color). Cluster-II (CV7 and MERS-CoV) is encircled with light blue color. Cluster-III (HCoV-229E and HCoV-OC43) is encircled with green color. Cluster-IV (NL63 and HKU1) is encircled with yellow color.

state points encircled in green colored ellipse. Remaining pair of strains, NL63 and HKU1 are placed in cluster IV which is marked by yellow colored ellipse.

5 Conclusions

Entropy-based methods have been shown to be more accurate than other approaches. The entropy has been used to select SARS-COV genome regions for stability zone detection. Even though a great deal of genetic variation is generally found, the present entropy calculation is sufficient to observe low informational complexity regions, which are representation of the conserved sites of the sequence. The low entropy regions are related to important functional domains in the proteins of these viruses. Based on entropy calculations seven SARS-COV genomes have been phylogenically described. The clusters of the genome formation is well understood.

Acknowledgements The authors are thankful to the Department of Physics, Adamas University for providing computational facility. The authors acknowledge the collection of sequence data from NCBI gene bank.

References

Chan JF-W, Yuan S, Kok K-H, Wang K-K, Chu H (2020) A familial cluster of pneumonia associated with the 2019 novel coronavirus indicating person-to-person transmission: a study of a family cluster. Lancet 395(10223):514–523

Chinese SARS Molecular Epidemiology Consortium (2004) Chinese molecular evolution of the SARS coronavirus during the course of the SARS epidemic in China. Science 303:1666–1669

de Wit E, van Doremalen N, Falzarano D et al (2016) SARS and MERS: recent insights into emerging coronaviruses. Nat Rev Microbiol 14:523–534

Fehr AR, Perlman S (2015) Coronaviruses: an overview of their replication and pathogenesis. Methods Mol Biol 1282:1–23

Ge XY, Li JL, Yang XL et al (2013) Isolation and characterization of a bat SARS-like coronavirus that uses the ACE2 receptor. Nature 503:535–538

Grantham R, Gautier C, Gouy M, Jacobzone M, Mercier R (1981) Codon catalog usage is a genome strategy modulated for gene expressivity. Nucl Acids Res 9(1):213–213

Hasegawa M, Yano TA (1975) The genetic code and the entropy of protein. Math Biosci 24(1–2):169–182

Knoops K, Kikkert M, Worm SH et al (2008) SARS-coronavirus replication is supported by a reticulovesicular network of modified endoplasmic reticulum. PLoS Biol 6:e226

Lu R, Zhao X, Li J et al (2020a) Genomic characterisation and epidemiology of 2019 novel coronavirus: implications for virus origins and receptor binding. Lancet 395(10224):565–574

Lu R, Zhao X, Li J, Niu P, Yang B, Wu H (2020b) Genomic characterisation and epidemiology of 2019 novel coronavirus: implications for virus origins and receptor binding. Lancet 395(10224):565–574

Masters PS (2006) The molecular biology of coronaviruses. Adv Virus Res 66:193–292

Novembre J, Stephens M (2008) Interpreting principal component analyses of spatial population genetic variation. Nat Genet 40:646–649

Perlman S, Netland J (2009) Coronaviruses post-SARS: update on replication and pathogenesis. Nat Rev Microbiol 7:439–450

Raj VS, Mou H, Smits SL et al (2013) Dipeptidyl peptidase 4 is a functional receptor for the emerging human coronavirus-EMC. Nature 495:251–254

Saha P, Sarkar BK (2020) Entropy based analysis of genetic information. J Phys Conf Ser 1579(1):012003

Schmitt AO, Herzel H (1997) Estimating the entropy of DNA sequences. J Theor Biol 188(3):369–377

Su S, Wong G, Shi W et al (2016) Epidemiology, genetic recombination, and pathogenesis of coronaviruses. Trends Microbiol 24:490–502

Wen F, Yu H, Guo J, Li Y, Luo K, Huang S (2020) Identification of the hyper-variable genomic hotspot for the novel coronavirus SARS-CoV-2. J Infect 80(60):671–693

Wu JT, Leung K, Leung GM (2020) Nowcasting and forecasting the potential domestic and international spread of the 2019-nCoV outbreak originating in Wuhan, China: a modelling study. Lancet 395(10225):689–697

Yu JF, Wang JH, Sun X (2010) Analysis of similarities/dissimilarities of DNA sequences based on a novel graphical representation. Commun Math Comput Chem 63:493–512

Zhou P, Yang XL, Wang XG et al (2020) A pneumonia outbreak associated with a new coronavirus of probable bat origin. Nature 579:270–273

A Review of an Energy-Efficient Routing Algorithm for Wireless Body Area Networks Using Machine Learning

P. Arivubrakan, G. R. Kanagachidambaresan, and Dinesh Bhatia

Abstract The Wireless Body Area Network (WBAN) having sensors and actuators are embedded into the human body to communicate via wearable devices in a wireless environment. Humans can wear devices into the body with various limitations. The healthcare industry plays a vital role in the WBAN to communicate and monitor the patients as a technology-based service. The sensor nodes are capable of transmitting into the human body efficiently. The nodes are communicated via wireless with the other sensors embedded in the human body. The tiny nodes having multipath communication in WBAN. In this paper, WBAN infrastructure and architecture, transmission technologies for body area networks, limitations, and energy-efficient constraints for different aspects of the routing algorithm using machine learning techniques are illustrated. It describes the energy-efficient routing protocol of WBAN is presented in this paper. Finally, as a source of motivation towards the future development of research incorporating machine learning into the supervised learning algorithms into WBAN is also provided.

Keywords WBAN · Energy efficient · Machine learning

1 Introduction

The Wireless sensor networks are basics for the WBAN to define the standard communication between the devices in a multipath environment with low power wearable devices, The Communication standard protocol is the IEEE 802.15.6 is for sending and receiving the messages in the low power devices. The tiny sensor nodes are inserted in and around the body to have a variety of applications in the field of healthcare-related sectors for monitoring the activity of the patients to avoid the death

P. Arivubrakan · G. R. Kanagachidambaresan
Department of Computer Science and Engineering, Vel Tech Rangarajan Dr, Sagunthala R&D Institute of Science and Technology, Avadi, Chennai 600062, India
e-mail: arivubrakan@veltech.edu.in

D. Bhatia (✉)
Department of Biomedical Engineering, North Eastern Hill University, Shillong, Meghalaya 793022, India

M. Mukherjee et al. (eds.), *Advances in Medical Physics and Healthcare Engineering*, Lecture Notes in Bioengineering, https://doi.org/10.1007/978-981-33-6915-3_52

rate. The WBAN consists of a number of few sensor nodes as in the form of wearable devices and is set with a broadcasting interface. It further periodically monitors the patients natural signals such as electroencephalogram (EEG), Electrocardiogram (ECG) signals, various blood pressure, insulins, heart rate, body temperature and automatically transmits these data to the nearby surroundings or closest to the health center where the doctors will take the immediate decision after observing all of this information via a remote monitoring system. It allows us to keep track of the alert signals of a human body and provides continuous real-time feedback on the recovery process. The specific characteristics of the WBAN sensors are capable of monitoring the sensing heart bit rate, the temperature of the human, beat rate, and other important physiological parameters. These sensors are transferring the health condition of the patients about the current situations to the doctors Abbasi et al. (2014), Ahmad et al. (2014a), Ahourai et al. (2009), Xiong et al. (2009), Yang and Yang (2006). The Doctors periodically keep track of the records about the patients either through the web or video. The final output of the WBAN is to minimize the death rate and monitor the entire activity of the patients. A WBAN connects the sensor/device to PDA and finally transfers the information via the internet through the wireless communication channel and the self-determining body nodes by using a middle controller, known as Body Node Coordinator (BNC) or destination node as a sink. The information from the BNC to be used for various applications such as the military sector, health-care system, etc. (Fig. 1).

The WBAN has various metrics to establish the Quality of Service (QoS) in wireless sensor network applications. QoS in WSN cannot be directly implied to WBAN since QoS depends on the sensitivity of the applications and the nature of transported data. Hence, depending on the applications, QoS is different in WBAN. The critical patients monitoring systems require the fastest release of information to the doctors for quick recovery and save humans. Traditionally, QoS includes

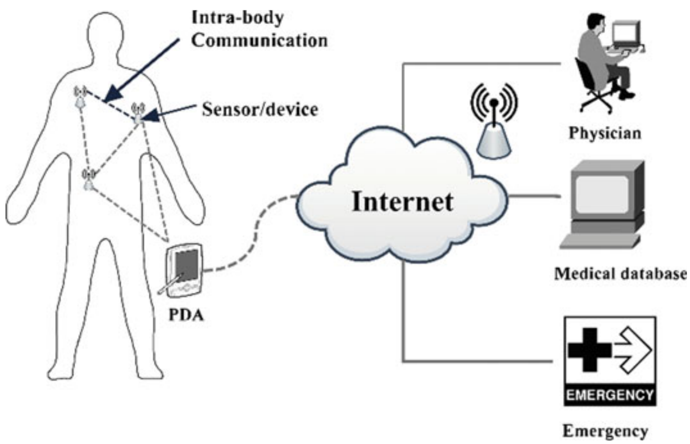

Fig. 1 WBAN infrastructure

Table 1 Comparison of WSN and WBAN

Comparison criteria	WSN	WBAN
Scale	Meter/kilometer	Meter/kilometer
Topology	Static/dynamic	Static/dynamic
Node replacement	Easy	Difficult
Node size	Small size preferred	Should be small
Energy scavenging	Solar, wind	Motion, body heat
Nodes deployment	High	Low
Energy demand	Large	Less

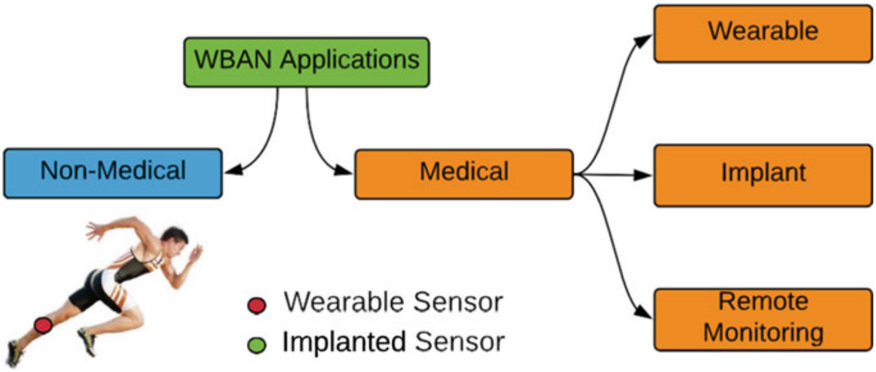

Fig. 2 WBAN applications

latency, transmission power, reliability, and bandwidth reservation to support QoS in WBAN, the following factors need to be considered Cavallari et al. (2014), Javaid et al. (2013), Latre et al. (2011), Movassaghi et al. (2014), Ullah et al. (2012), Yazaki and Matsunaga (2008), Zhang and Sawchuk (2009). The energy-efficient routing is the major factor for the delivery of the data in and around the human body. Power plays a major role in communication and transmission (Table 1).

The various applications of WBAN are medical and non-medical. The medical applications are used in WBAN for good results. Two sensors are available in the medical field. The wearable sensors for the monitoring of the activity of the patients. A small sensor network consists of a large number of nodes and each of these nodes uses the routing protocols to establish the communications to share their data or limited resources to enable the transmission (Fig. 2).

2 Routing Protocols in WBANs

The routing protocol is the best way of finding the shortest path among the multiple nodes of the communication networking system. The routing protocol is the set of rules to establish the best communication with the standard regulations. The entire network for the communication of the wearable devices depends on the protocol. The constraints of the wearable networking for the implanted networks to exhibit the sensor requirements. The Wearable device of the nodes of the requirements can change from the various applications. The allocation of the resources and the harvesting of the energy are the two constraints in the WBAN networks. In WBAN, nodes carry a large number of data endlessly. In WBAN have the priority-based networking standards are limited?

2.1 Network Lifetime

The Network lifetime of a WBAN is the routing constraint for the path establishment from the beginning to the end position Abbasi et al. (2014) Cavallari et al. (2014), Javaid et al. (2013), Movassaghi et al. (2014), Zhou and Hou (2010) and Zhou et al. (2008). For example, the patient's devices are sending the information to the doctors, while at the time of the transmission due to the network is significantly damaged. The network lifetime is expressed as network exhaustion time. Since the change of the battery and increase the charging capacity is not feasible in implant health care devices used in WBANs, The lifetime of the network plays an important role in WBAN when compare to the WSN.

2.2 Resource Constraints

The limited number of the resources of the WBANs will use tiny sensor nodes that perform its functionalities. The WBANs nodes are prone to frequent failure due to limited battery power, storage capacity, and bandwidth limitations, which lead to poor QoS Cavallari et al. (2014), Javaid et al. (2013), Ullah et al. (2012), Xiong et al. (2009), Yang and Yang (2006), Zhou and Hou (2010). Temperature awareness: Rise in temperature is an important issue in WBANs, which is mostly unconsidered in Wireless Sensor Networks. Improvident temperature rise may even cause serious tissue damage which seems to be harmful to the human body. So, the routing protocol should be temperature sensitive which not only detects the temperature rise but also prevents the overheating problem (Fig. 3).

3 Energy-Efficient Routing

Energy consumption in WBAN is an important metric for all battery-powered sensor nodes. In WBANs the available energy sources of nodes are a very primitive factor that determines the usefulness of the network systems. Since the nodes replacement

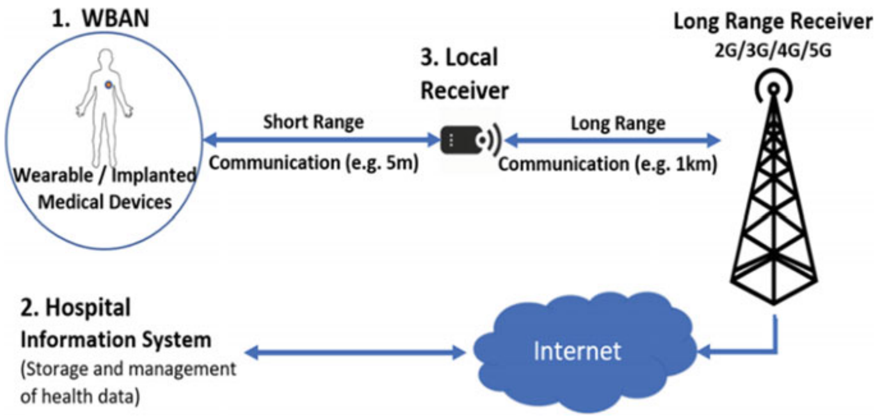

Fig. 3 WBAN communication

at the time of transmission of the patient data is very difficult. So, effective energy utilization is one of the most threatening issues to enable the network successfully.

Thus energy efficiency is the most primitive requirement when designing a routing protocol in WBANs. Some of the energy-efficient routing protocols are explained below. One of the methods to achieve energy efficiency is to perform energy-efficient routing. The factors of the energy-efficient routing protocols in WBAN such as temperature, link, routing matrix, mobility, etc. Ahmad et al. (2014a), Javaid et al. (2013), Latre et al. (2011), Movassaghi et al. (2014), Yang and Yang (2006), Yazaki and Matsunaga (2008), Zhou et al. (2008).

Tang et al. (2005) introduced an energy-efficient and thermal-aware routing protocol for WBANs to minimize the data loss and also reducing the node temperature as well as decreasing the delay.

M-ATTEMPT has four different phases of operation: initialization phase, routing phase, scheduling phase, and data transmission phase. In the initialization phase, all nodes broadcast a packet and this packet includes the sink ID and position. Single-hop communication is used for critical data delivery and normal data delivery multi-hop communication is used. A route with less hop count is selected during the routing phase. If more than two routes are available, a node with less energy consumption to the sink is selected. The proposed protocol introduces a threshold to control the temperature rise. If any node's temperature rises beyond the threshold, the route to the neighboring node will break. This protocol re-route the data if the temperature is above the threshold, without occurring the link break and this process is called the link-hot spot detection. The sink node creates a Time Division Multiple Access (TDMA) schedule for all root nodes in the scheduling phase, while the root nodes send their data to the sink node during the data transmission phase. This protocol provides a high network lifetime Cavallari et al. (2014), Javaid et al. (2013), Latre et al. (2011), Ullah et al. (2012), Xiong et al. (2009), Yang and Yang (2006), Zhou et al. (2008).

An energy-efficient protocol named Distance Aware Relaying Energy efficient (DARE) (Tauqir et al. 2013) to monitor the biological status of patients. This protocol tries to reduce the energy consumption of the monitoring sensors by providing the facility of deploying relay nodes which in turn, helps to reduce the communication distance. For decreasing the energy consumption, the sensors create a link with the sink utilizing an on-body relay, attached to the chest of each patient. The attached body relay retains greater energy resources as compared to other body sensors. It offers a greater packet delivery ratio, longer network lifetime, and better stability period, but it has a high propagation delay.

Ahmed et al. (2014) introduced a routing protocol called Link Aware and Energy Efficient scheme for Body Area Network (LAEEBA). In LAEEBA, a path with a minimum number of hops is selected for transmission. Direct communication is used for emergency data and multi-hop is used for normal data delivery. It consists of the initialization phase, next-hop selection phase, routing phase, energy consumption phase, and path-loss selection phase. Here nodes with minimum energy and minimum distance from the sink will be selected as forwarding nodes. When a node receives all the information from other nodes, the forwarder node transmits the data to the sink. In subject to the operating frequency band, high losses may occur according to the communication protocol adopted for nodes. The path loss model can be selected by using the distance between the node and sink.

Nadeem et al. (2013) introduced energy and power-efficient routing protocol model for WBANs. Stable Increased-throughput Multi-hop Protocol for Link Efficiency in wireless body area networks (SIMPLE) protocol has three phases of operation: initial phase, selection of next-hop, and scheduling. At the initial phase, the sink will send a packet that contains information about the location of the sink, packet ID, location, residual energy. In the selection of the next-hop phase, a new forwarder node is selected in each round based on the cost function. The cost function depends on residual energy and distance to the sink. Here the parameter residual energy is used to balance the energy consumption between the sensor nodes. This protocol ensures minimum energy consumption, increased throughput, and longer network lifetime. In the scheduling phase forwarder node allocate Time Division Multiple Access (TDMA) slots for its root nodes.

Ahmed et al. (2015) introduced a protocol called Cooperative Link Aware and Energy Efficient scheme for Body Area Network (Co-LAEEBA). In this, relay nodes are utilized for cooperation which allows a source node to utilize more than one link at a time. Three advanced nodes act as cooperative nodes. Normal nodes forward packets to the cooperative node in each round. Incoming and outgoing data flow at each node must be equal. The path selection depends on the varying distance between the nodes if the body is in motion. It is an advanced version of LAEEBA.

Javaid et al. (2015) proposed a new energy-efficient routing protocol called iMproved Stable Increased-throughput Multi-hop Protocol for Link Efficiency in wireless body area networks (iM-SIMPLE) in which the operation is carried out in three phases; Initial phase, selection of next-hop, and scheduling. At the initial phase, the sink will send a packet that contains information about the location of the sink, and also sensor nodes send their packet with their ID, location, residual energy.

In the selection of the next-hop phase, a new forwarder is selected in each round. The sink calculates the cost function based on residual energy and distance of nodes to the sink. Based on the calculated cost function, those nodes with minimum cost function will select as a forwarder node. In the scheduling phase, the forwarder node will allocate a Time Division Multiple Access (TDMA) slots for its root nodes. Also, mobility support (arm mobility) is considered in this protocol. This protocol utilizes a linear mathematical model for reducing energy consumption.

The energy consumption is the large scale of the nodes in WBAN that occurs during radio frequency communication, sensing, and data processing of the devices. The Routing metrics play an important role to make effective communication among sensor nodes and increase the lifetime of a WBAN. Energy efficiency is the most important primitive requirement in case of designing a routing path for a better quality of service (Kanagachidambaresan and Chitra 2015; Maheswar et al. 2019; Malathy et al. 2020; Jayarajan et al. 2019; Kanagachidambaresan et al. 2011).

4 Machine Learning Algorithms

Machine learning is the application of intelligence to learn the systems without programmed explicitly. In WBAN, the doctors can access the data uses the patient information for further process. So, machine learning algorithms are very helpful for body area networks. The doctors can learn from history that is already available in devices. The 3 types of machine learning algorithms are supervised learning, unsupervised learning, and reinforcement learning. Machine learning aims to learn from the computers automatically as similar in WBAN the information from the patient is automatically transferred to the doctors without human intervention. In this WBAN, we are looking into supervised learning in which we can teach or train the machine using various data which is well labeled, after that, the machine is provided with a new set of data so that the learning algorithm analyses the given training data sets and produces a correct outcome from labeled data.

4.1 Linear Regression

A regression problem is when the output variable is a real value, such as “dollars” or “weight”. Supervised learning deals with or learns with “labeled” data. The linear regression is used to approximate values such as house prizes based on a continuous variable(s). Here, we establish a relationship between independent and dependent variables by fitting the best line. This best fit line is known as the regression line and represented by a linear equation $Y = a * X + b$. The best way to understand linear regression is to relive this experience of childhood. Let us say, you ask a child in fifth grade to arrange people in his class by increasing order of weight, without asking them their weights! What do you think the child will do? He/she would likely look (visually analyze) at the height and build of people and arrange them using a combination of these visible parameters. This is a linear regression in real life! The child has figured out that height and build would be correlated to weight by a relationship, which looks like the equation above.

In this equation:

- Y—Dependent variable
- a—Slope
- X—Independent variable
- b—Intercept.

These coefficients a and b are derived based on minimizing the sum of squared difference of distance between data points and regression line.

Look at the below example. Here we have identified the best fit line having linear equation $y = 0.2811x + 13.9$. Now using this equation, we can find the weight, knowing the height of a person.

Linear Regression is mainly of two types: Simple Linear Regression and Multiple Linear Regression. Simple Linear Regression is characterized by one independent variable. And, Multiple Linear Regression (as the name suggests) is characterized by multiple (more than 1) independent variables. While finding the best fit line, you can fit a polynomial or curvilinear regression. And these are known as polynomial or curvilinear regression.

5 Conclusion

In this context, the importance of developing energy-efficient routing by using the machine learning algorithm in WBAN is illustrated with the survey. Reducing the energy constraints in the WBAN provides a review of suitable machine learning algorithms for better performance and attain the maximum throughput. The frequent replacement of the WBAN leads to the maximum loss so, in this paper, they explained energy-efficient routing algorithms within the domain of the medical sector. In this survey, a review of current research in WBANs, recent literature on different energy-efficient research challenges in terms of routing are provided. In this paper, it is essential to incorporate the WBAN architectures and limitations to address the recent challenges efficiently by using machine learning.

References

Abbasi UF, Awang A, Hamid NH (2014) A cross-layer opportunistic mac/routing protocol to improve reliability in WBAN. In: 2014 Asia-Pacific conference on communications (APCC). IEEE, pp 36–41

Ahmad A, Nadeem J, Zahoor AK, Muhammad I, Mohammed A (2014a) iA-MAC: improved adaptive medium access control protocol for wireless body area networks. In: 14th international symposium on communications and information technologies (ISCIT), IEEE, pp 156–160

Ahmed S, Javaid N, Akbar M, Iqbal A, Khan Z, Qasim U (2014b) Laeeba: link aware and energy-efficient scheme for body area networks. IEEE 28th international conference on advanced information networking and applications. IEEE, pp 435–440

Ahmed S, Javaid N, Yousaf S, Ahmad A, Sandhu M, Imran M, Khan Z, Alrajeh N (2015) Co-laeeba: cooperative link aware and energy-efficient protocol for wireless body area networks. Comput Hum Behav 51:1205–1215

Ahourai F, Mahmoud T, Mehran J, Saber M (2009) A thermal-aware shortest hop routing algorithm for in vivo biomedical sensor networks. In: Sixth international conference on information technology: new generations, 2009. ITNG'09. IEEE, pp 1612–1613

Cavallari R, Martelli F, Rosini R, Buratti C, Verdone R (2014) A survey on wireless body area networks: technologies and design challenges. IEEE Commun Surv Tutor 16(3):1635–1657

Javaid N, Abbas Z, Fareed M, Khan Z, Alrajeh N (2013) *M*-attempt: a new energy-efficient routing protocol for wireless body area sensor networks. Proc Comput Sci 19:224–231

Javaid N, Ahmad A, Nadeem Q, Imran M, Haider N (2015) iM-SIMPLE: improved stable increased-throughput multi-hop link efficient routing protocol for wireless body area networks. Comput Hum Behav 51:1003–1011

Jayarajan P, Maheswar R, Kanagachidambaresan GR (2019) Modified energy minimization scheme using queue threshold based on priority queueing model. Clust Comput 22(S5):12111–12118. https://doi.org/10.1007/s10586-017-1564-2

Kanagachidambaresan GR, Chitra A (2015) Fail-Safe fault-tolerant mechanism for wireless body sensor network (WBSN). Wirel Pers Commun 80(1):247–260. https://doi.org/10.1007/s11277-014-2006-6

Kanagachidambaresan GR, Sarma Dhulipala VR, Vanusha D, Udhaya MS (2011) Matlab based modelling of body sensor network using ZigBee protocol. In: Das VV, Thankachan N (eds) Computational intelligence and information technology, vol 250. Springer, Berlin, pp 773–776

Latre B, Braem B, Moerman I, Blondia C, Demeester P (2011) A survey on wireless body area networks. Wireless Netw 17(1):1–18

Maheswar R, Kanagachidambaresan GR, Jayaparvathy R, Thampi SM (eds) (2019) Body area network challenges and solutions. Springer International Publishing, Cham

Malathy S, Rastogi R, Maheswar R, Kanagachidambaresan GR, Sundararajan TVP, Vigneswaran D (2020) A novel energy-efficient framework (NEEF) for the wireless body sensor network. J Supercomput 76(8):6010–6025. https://doi.org/10.1007/s11227-019-03107-x

Movassaghi S, Abolhasan M, Lipman J, Smith D, Jamalipour A (2014) Wireless body area networks: A survey. IEEE Commun Surv Tutor 16(3):1658–1686

Nadeem Q, Javaid N, Mohammad S, Khan M, Sarfraz S, Gull M (2013) Simple: stable increased-throughput multi-hop protocol for link efficiency in wireless body area networks. In: 2013 eighth international conference on broadband and wireless computing, communication and applications (BWCCA). IEEE, pp 221–226

Tang Q, Naveen T, Gupta SKS, Schwiebert L (2005) TARA: thermal aware routing algorithm for implanted sensor networks. In: International conference on distributed computing in sensor systems. Springer, Berlin, pp 206–217

Tauqir A, Javaid N, Akram S, Rao A, Mohammad S (2013) Distance aware relaying energy-efficient: dare to monitor patients in multi-hop body area sensor networks. In: Eighth international conference on broadband and wireless computing, communication and applications (BWCCA). IEEE, pp 206–213

Ullah S, Higgins H, Braem B, Latre B, Blondia C, Moerman I, Saleem S, Rahman Z, Kwak KS (2012) A comprehensive survey of wireless body area networks. J Med Syst 36(3):1065–1094

Xiong N, Vasilakos AV, Yang LT, Song L, Pan Y, Kannan, R., Li, Y (2009) Comparative analysis of quality of service and memory usage for adaptive failure detectors in healthcare systems. IEEE J Sel Area Commun 27(4):495–509

Yang G-Z, Yang G (2006) Body sensor networks. Springer, London

Yazaki S, Matsunaga T (2008) A proposal of the abnormal condition detection system for elderly people using a wireless wearable biosensor. In: 2008 SICE annual conference. IEEE, pp 2234–2238

Zhang M, Sawchuk A (2009) A customizable framework of body area sensor network for rehabilitation. In: International symposium on applied sciences in biomedical and communication technologies (ISABEL), pp 1–6

Zhou H-Y, Hou K-M (2010) Pervasive cardiac monitoring system for remote continuous heart care. In: 2010 4th international conference on bioinformatics and biomedical engineering. IEEE, pp 1–4

Zhou G, Lu J, Wan C, Yarvis MD, Stankovic, JA, Bodyqos (2008) Adaptive and radio-agnostic QoS for body sensor networks. In: IEEE INFOCOM 2008—the 27th conference on computer communications, pp 565–573

PKL Electricity-An Observations

Md. Afzol Hossain, Md. Ohiduzzaman, Rajia Sultana, Rajada Khatun, Shirin Akter, K. A. Khan, and Mehedi Hasan

Abstract A study on PKL electricity has been performed by the authors. The pH, current, and voltage have been measured by the calibrated pH meter, voltmeter and amperemeter. The variation pH of the PKL extract with the variation of time duration has been studied. It is shown that pH increases with the increase of time duration during electricity generation. It is also studied the variation of Current and voltage with the variation of pH. It is found that Current and Voltage decreases with the increase of pH of the PKL extract. Finally, it has been studied the variation of current and voltage with the variation of time duration. It is found that current and voltage decreases with the time duration which is feasible and viable. Mobile phone and some LED lights have been used for practical utilizations.

Keywords Electric power · Mobile technology · Off-grid region · AAS · PKL cell · Cell voltage

Md. A. Hossain
Department of Chemistry, University of Dhaka, Dhaka 1000, Bangladesh

Md. Ohiduzzaman
Department of Physics, Jashore University of Science and Technology, Jashore 7408, Bangladesh
e-mail: ohid@just.edu.bd

R. Sultana
Primeasia University, Dhaka, Bangladesh

R. Khatun · S. Akter
Medical Physics Division, Atomic Energy Centre, Dhaka 1000, Bangladesh

K. A. Khan (✉)
Department of Physics, Jagannath University, Dhaka 1100, Bangladesh

M. Hasan
Department of EEE, City University, Dhaka, Bangladesh

M. Mukherjee et al. (eds.), *Advances in Medical Physics and Healthcare Engineering*, Lecture Notes in Bioengineering, https://doi.org/10.1007/978-981-33-6915-3_53

1 Introduction

The PKL (Pathor Kuchi Leaf) power system is effective in both the day and night even in the rainy season. It is mentioned that the scientific name of the PKL is *Bryophillum Pinnatum* Leaf. The PKL electricity is more effective in night than day light because of the presence of malic acid in PKL leaf. It is also pointed out that the PKL consists of some weak organic acids including citric acid, iso-citric acid, and malic acid. PKL electricity generation system can give the importance to meet the energy needs in rural inaccessible off-grid areas of Bangladesh. In this study, a range of electrical and physico-chemical parameters have been explored after fabrication of electrochemical cell for mobile technology. Mobile technology is the most attractive communication technology to contact each other all over the world (Khan et al. 2016a, b, 2017, 2018; Hasan and Khan 2018). It is found that the utilization of the mobile phone is very effective, feasible, and viable technology to both the on-grid and off-grid people in Bangladesh (Khan et al. 2015, 2016c, d; Alam Khan 1998). At present everybody wants to use mobile phone to contact at home and abroad (Hamid 2013; Hamid et al. 2016; Khan 2009; Khan and Arafat 2010; Khan and Bosu 2010). But it needs electricity for recharging and hence it depends on electricity. But at the off-grid areas as there is no electricity the people of that region can cultivate PKL in their unused land so as to generate electricity for mobile charging (Khan and Hossain 2010; Shuva Paul et al. 2012; Khan et al. 2013a, b). Therefore, it is very urgent to study both the chemical parameters and electrical performances of the PKL electrochemical cell during the application in mobile phone (Akter et al. 2017; Khan 1999, 2008; Khan and Paul 2013). A Galvanic cell produces electrical energy from spontaneous redox reaction (the chemical reaction which involves both the reduction and oxidation reaction simultaneously) taking place within the cell. In 1800, Alessandro Volta invented his Voltaic cell which was exclusively out of non-biological material to challenge Galvanie's animal electricity theory in favor of his own metal–metal contract electricity theory (Ruhane et al. 2017). The cell invented by Volta was the first electrical battery. In common usages, the word "battery" has come to include a single Galvanic cell, but a battery properly consists of manifold cells (Khan 1999, 2008; Khan and Paul 2013; Ruhane et al. 2017; Khan et al. 2016). The branch of Chemistry that deals with the relationship between electricity (flow of electrons) and chemical reactions associated with Electrochemistry, which involves the reactions involving the transfer of electrons (reduction and oxidation), spontaneous reactions, non-spontaneous reactions (in electrolytic or electroplating cells). Oxidation–reduction or redox reactions take place in electrochemical cells. There are two types of electrochemical cells. Spontaneous reactions occur in galvanic (voltaic) cells; non-spontaneous reactions occur in electrolytic cells. Both types of cells contain electrodes where the oxidation and reduction reactions occur (Hasan et al. 2017).

2 Methods and Materials

Algorithm of the Total System
The algorithm of the PKL electricity in mobile technology is summarized below:

Design → Fabrication → Electricity generation → Application in Mobile phone (Load).

2.1 *Chemical Reaction in Half Cells*

The standard hydrogen half-cell reaction: $2H^{+}_{(aq)} + 2e^{-} \rightarrow H_2(g)$. The half-cell reactions of a Daniel cell: The overall reaction: $Zn + Cu^{2+} \rightarrow Zn^{2+} + Cu$. Half-cell (anode) reaction at Zn electrode: $Zn \rightarrow Zn^{2+} + 2e^{-}$, Where, Zn is a sacrificial element and it is being dissolved as Zn^{2+} in electrolyte solution losing electrons in Zn electrode. Half-cell (cathode) reaction at Cu electrode: $Cu^{2+} + 2e^{-} \rightarrow Cu$, Where, Cu^{2+} from electrolyte solution gains electrons from the cathode.

2.2 *PKL Electrochemical Cell*

PKL Extract Preparación
The PKL was collected from the field. Then it was blended by a blender machine with different ratios of the water. Thereafter a mixture, containing paste and water with different proportion, will have to be prepared. This mixture can be used directly for electricity production. However, this juice can be filtered out to get the clean juice for the use of electricity generation. Figure 1 illustrates the flow diagram of

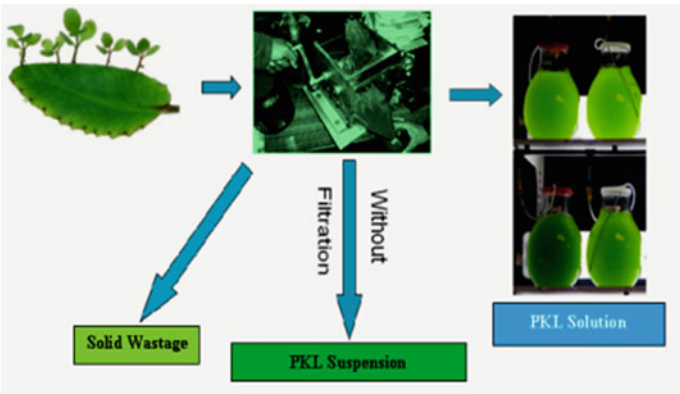

Fig. 1 PKL juice preparation process

preparation process of juice. After blending the juice is pouring and reserved in a plastic container or pot (Hamid et al. 2016). This juice can be reserved/preserved for long time.

Construction of a PKL Battery

PKL Cell is one type of voltaic cell in which the electrolyte is PKL juice. A PKL unit cell (Fig. 2a) can produce only 1.1 V which is not sufficient to meet the practical utilization. Therefore, in order to meet the practical application of PKL cells are assembled in module and panel (Fig. 2b).

Electrode Preparation

For production of electricity we need to make the electrodes (Fig. 3) for the cell. We need two half cells for the production of electricity. One is zinc plate and the other is copper plate. Zinc plate acts as negative plate or negative terminal and copper plate acts as positive plate or positive terminal.

2.3 Constituents of Pathor Kuchi Leaf (PKL)

Which are significant for PKL cell, are mainly fatty acids and minerals. Fatty acids fraction includes palmitic acid (89.3%), stearic acid (10.7%), traces of others acids. Plant also contains HCN (hydrocyanic acid), oxalic acid, citric acid, isocitric acid, oxaloacetate, malic acid, and succinic acid. The plant is rich in vitamins and amino acids such as ascorbic acid, riboflavin, thiamine, niacin, pyridoxine, glycine, cysteine, casein hydrolysate, glutamic acid, protein hydrolysate, methionine, tyrosine, phenylalanine (Khan and Bosu 2010).

2.4 Energy Source

The energy for the PKL battery comes from the electrochemical change in the zinc (or other metal) when it dissolves in PKL juice (Khan 2013). The zinc is oxidized inside the cell, exchanging some of its electrons with the acid and metal ions in order to reach a lower energy state, and the energy released provides the power.

2.5 Methods

Different instruments were used in the present research work to study the different electro-chemical properties of PKL Cell in Mobile Cell Technology.

Figure 4a–d shows the application of PKL Electricity in Mobile Technology. It demonstrates the practical utilization of the PKL electricity is in mobile phone

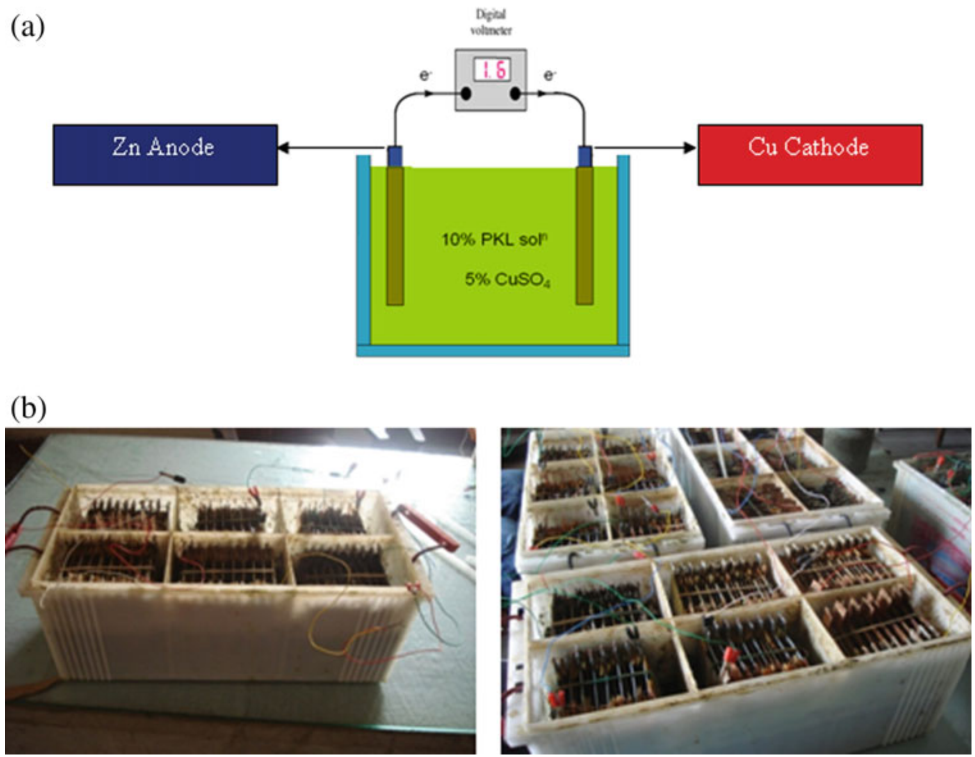

Fig. 2 **a** A schematic diagram of a PKL unit cell. **b** Experimental set-up of PKL electric module and panel

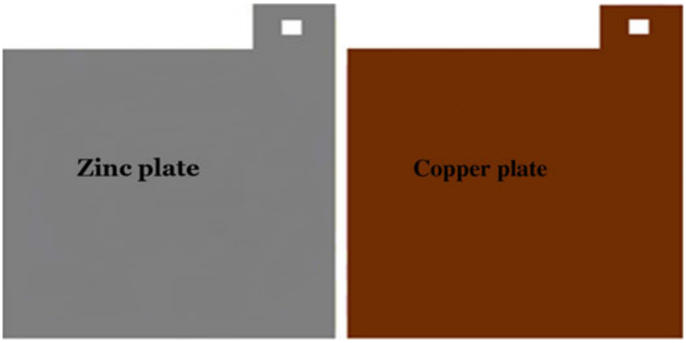

Fig. 3 Preparation of zinc plates and copper plates for use in the production of electricity from PKL cell

Fig. 4 **a** at night **b** at day time **c** a man is charging a mobile **d** PKL lamp for night time

technology during day and at night (Fig. 4a, b). It shows a professor of Physics of Dhaka University, Bangladesh is charging a Mobile phone with the PKL electricity (Fig. 4c). PKL lamp is used during night time for functioning the mobile phone.

3 Analysis: Theory of Measurement of pH of the Solution of PKL Electrochemical Cell

Figure 5a, b shows the variation of pH with the variation of time duration.

Chemical Reactions in the PKL Cell

The reduction processes are:

$$Cu^{2+} + 2e^- \rightarrow Cu$$
$$2H^+ + 2e^- \rightarrow H_2\uparrow$$

And the oxidation process is

$$2Zn - 4e^- \rightarrow 2Zn^{2+}$$

The Nernst equation (Akter et al. 2017) for the above reactions is given below:

$$E_{Cu^{2+}|Cu} = E^0_{Cu^{2+}|Cu} - \frac{0.0591}{n} \log \frac{1}{[Cu^{2+}]} \tag{1}$$

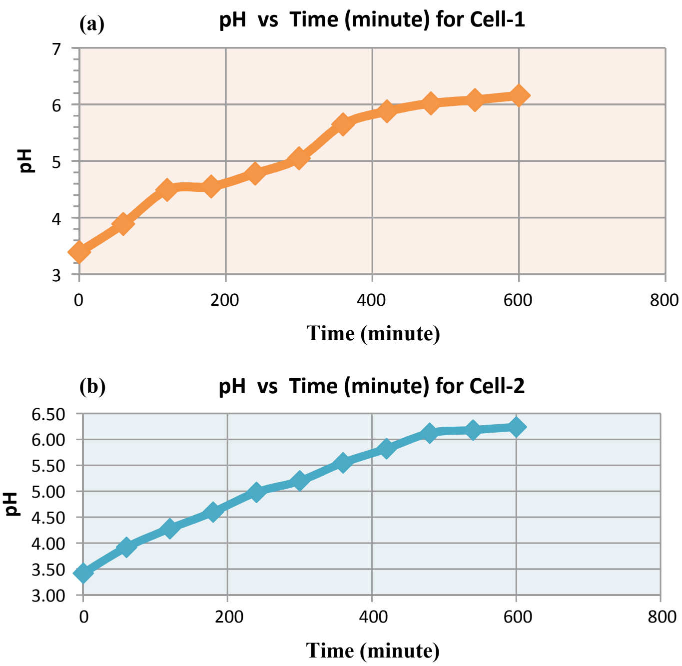

Fig. 5 **a** pH-time duration (minute) for cell-1. **b** pH–time duration (minute) for cell-2

$$E_{2H^+|H_2} = E^0_{2H^+|H_2} - \frac{0.0591}{n} \log \frac{1}{[H^+]^2} \quad (2)$$

$$E_{Zn^{2+}|Zn} = E^0_{Zn^{2+}|Zn} - \frac{0.0591}{n} \log \frac{1}{[Zn^{2+}]^2} \quad (3)$$

*In this study, two batteries were used in parallel so as to increase the current flow and a 3 W LED bulb was used in load.

*The ammeter used had the highest range 5.00 A but the above range was written as 5.00 A.

4 Results and Discussion

Figure 5 a, b shows how the pH of a PKL cell reduces. At first, the pH was minimum that is for cell-1 this was 3.37 and for cell-6 it was 3.40 and after a certain time they were 6.16 and 6.24 respectively.

Thus we may propose that the weak organic acids presence in PKL extract dissociates slowly and in presence of secondary salt ($CuSO_4 \cdot 5H_2O$) the dissociation increases.

$$\text{R-COOH}_{(aq)} \leftrightarrow \text{R-COO}^-_{(aq)} + \text{H}^+_{(aq)} \leftrightarrows$$
$$\text{R-COOH}^{\text{secondary salt}}_{(aq)}\text{R-COO}^-_{(aq)} + \text{H}^+_{(aq)}$$

The potential and current both were measured with VOM. Here, the potential and current decreases significantly with time. We studied several types of PKL cells where the composition of PKL juice was changed which were responsible for this decreasing. In cell-2, 3, 4 we used 40%, 40%, and 0% PKL sap with 5%, 0%, 5% secondary salt ($CuSO_4 \cdot 5H_2O$) respectively. It can be designated that the current and potential were high for the cell-2, 8 but for cell-3 and-4 both of them were very low of not reasonable. Again, if we compare cell-2 with cell-4, it can be revealed that the potential and current was steady more time for cell-2 comparing to cell-4. This may be due to the presence of both Cu^{2+} ion from the secondary salt and H^+ ion from the PKL sap.

Figure 6a, b represents the discharge of a PKL cell and a motor bike battery (secondary battery). Here the potential and current both were compared with the PKL cell and the motor bike battery. The potential and current decreases steadily in secondary storage battery but in case PKL battery this decreases sharply. This may arise due to the lower concentration of electrolytes or the fast reaction rate in PKL cell because the initial potential and current was as same as the storage battery. Moreover there is no separator or salt bridge in between the electrodes so there may take place the local action. To prevent this unwanted losing we may use the separator and the current density can be increased by increasing the concentration of secondary salt

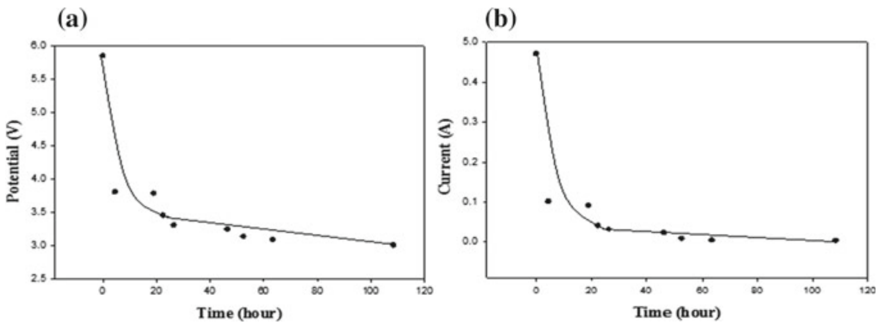

Fig. 6 **a** Voltage–time (h) curve. **b** Current–time (h) curve

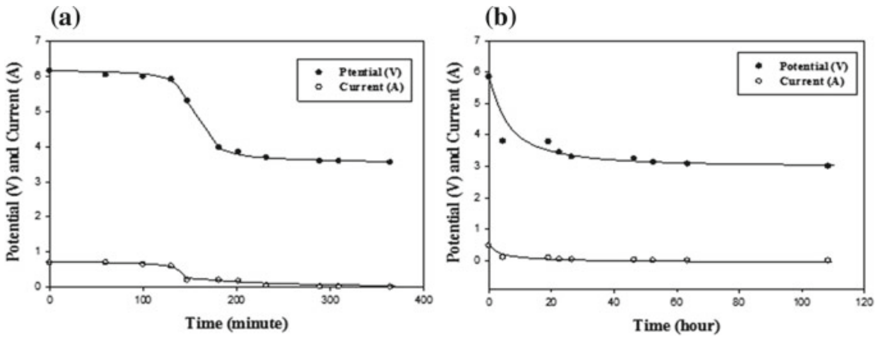

Fig. 7 **a** Voltage and time duration. **b**: Voltage and time duration

and PKL sap. However, from the experimental data and graphical representation we can say that as the concentration of Cu^{2+} and pH decreases with time the potential and current flow decreases following a curvature.

It is shown that the load current (I_L), short circuit current (I_{sc}), load voltage (V_L) and open circuit voltage (V_{oc}) have been measured by calibrated multimeter (Fig. 7). It is also shown that in Figs. 8, 9 and 10 the pH of the PKL extract has been measured.

5 Conclusion

- The utilization of PKL electricity for mobile technology is easy and simple.
- PKL electricity can help to setup the small mobile charge centre for the betterment of the people those who are living at the off-grid areas.
- Any people can setup this technology easily.
- Anyone can earn 8–10 $ per day by setting-up a mobile charging center using PKL electricity.
- Any handicapped person can setup a mobile charge center.

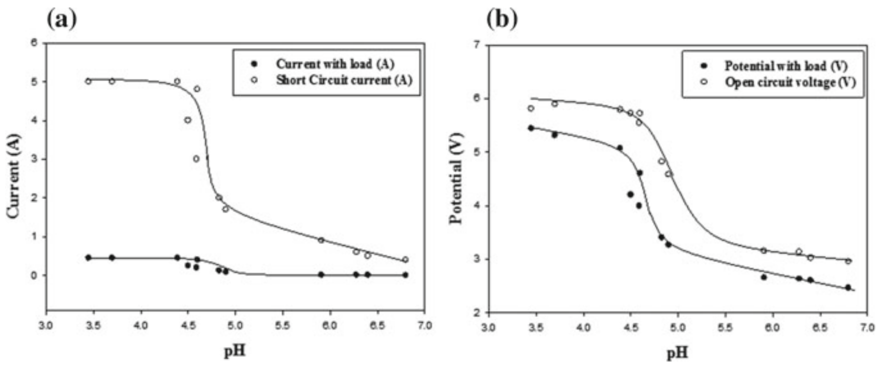

Fig. 8 **a** Current discharging of a PKL cell with pH. **b** Potential discharging of a PKL cell with pH

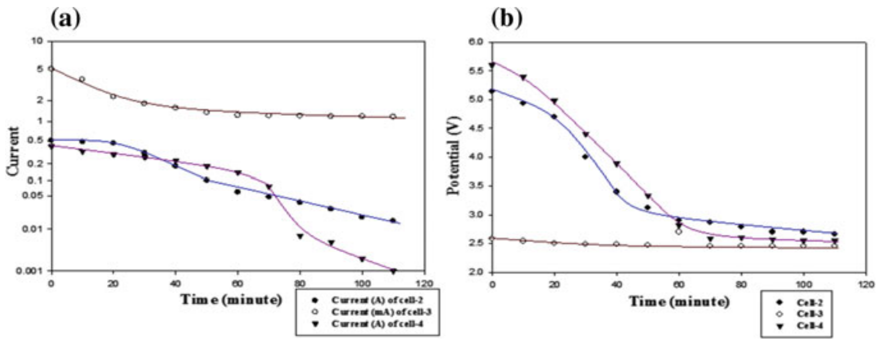

Fig. 9 **a** Variation of current (A) with time. **b** Variation of potential (V) with time

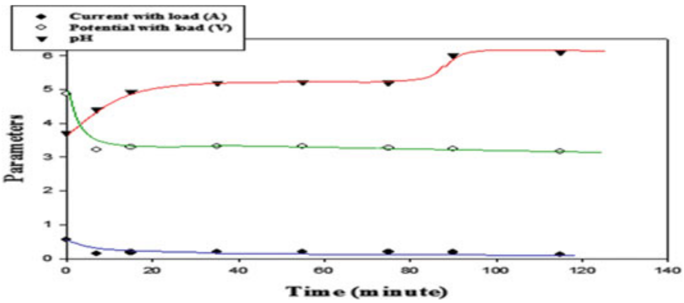

Fig. 10 Variation of voltage (V), current (A), and pH with the variation of time duration (minute) of cell-6

- The cultivation of PKL for electricity generation is very easy.
- There is no need for extra care to cultivate PKL.
- The unused land like coastal areas, hilly areas, both sides of the road, forest areas are sufficient for cultivation of PKL for electricity production.
- The internal resistance of the PKL cell depends on the Physical Characteristics of the PKL extract. The internal resistance becomes lower for smaller granular size of the of the PKL extract.
- The internal resistance was increased at the contact point of electrodes and wires. So that it should be maintained with proper connection of electrodes.
- The internal resistance of a PKL cell also depends on temperature.
- The voltage regulation of the PKL cell is low.

Acknowledgements The authors are grateful to the PKL electricity research group named Md. Ibrahim Khan, Dr. M. A. Latif, Md. Mahfuz Alam, Md. Abdullah Al Momin, Md. Moiful Alam, Mr. Rashed, Mr. Mamun, Dr. Md. Sajjad Hossain, Md. Asrafusjaman Rubel, Dr. Fakrul Islam, Dr. Bapy Guh, Dr. Jesmin Sultana, and Prof. Dr. Mesbah Uddin Ahmed for their valuable suggestions and whole-hearted cooperation during research work.

Conflict of Interest Statement On behalf of all the authors, the corresponding author declares that we don't have any conflict of interest.

Funding This work is self-funded.

References

Akter T, Bhuiyan MH, Khan KA, Khan MH (2017) Impact of photo electrode thickness and annealing temperature on natural dye sensitized solar cell. Ms. Ref. no.: SETA-D-16-00324R2

Alam Khan MK (1998) Copper oxide coating for use in linear solar Fresnel reflecting concentrating collector. Renewa Energy Int J WREN (World Renew Energy Netw), UK, RE: 12.97/859

Hamid MR (2013) Characterization of a battery cell fueled by bryophyllum Pinnatum sap. Int J Sci Eng Re 4(3). ISSN 2229-5518

Hamid MR, Yusuf A, Abdul Wadud AM, Rahaman MM (2016) Design and performance test of a prototype of a 12 volt DC battery fueled by bryophyllum Pinnatum sap and improvement of its characteristics. Int J Electron Electr Eng 4(5)

Hasan M, Khan KA (2018) Dynamic model of bryophyllum Pinnatum leaf fueled BPL cell: a possible alternate source of electricity at the off-grid region in Bangladesh. Microsyst Technol. Manuscript number, MITE-D-18-00800R1. Springer. https://doi.org/10.1007/s00542-018-4149-y. Print ISSN: 0946-7076. Online ISSN: 1432-1858. First Online: 28 Sept 2018

Hasan M, Hassan L, Haque S, Rahman M, Khan KA (2017) A study to analyze the self-discharge characteristics of bryophyllum Pinnatum leaf fueled BPL test cell. IJRET 6(12)

Khan KA (1999) Technical note "copper oxide coatings for use in a linear solar Fresnel reflecting concentrating collector. J Renew Energy 17(4):603–608. Pergamon. Publication date 1999/8/1

Khan KA (2008) Electricity generation form Pathor Kuchi Leaf (PKL). Publication date 2008/12/31. Patent number BD 1004907

Khan KA (2009) Electricity generation form Pathor Kuchi Leaf (*Bryophyllum pinnatum*). Int J Sustain Agril Tech 5(4):146–152

Khan KA, Arafat ME (2010) Development of Portable PKL (Pathor Kuchi Leaf) Lantern. Int J SOC Dev Inf Syst 1(1):15–20

Khan KA, Bosu R (2010) Performance study on PKL electricity for using DC fan. Int J SOC Dev Inf Syst 1(1):27–30

Khan KA, Hossain MI (2010) PKL electricity for switching on the television and radio. Int J SOC Dev Inf Syst 1(1):31–36

Khan KA, Paul S (2013) A analytical study on electrochemistry for PKL (Pathor Kuchi Leaf) electricity generation system. IEEE, Publication date 2013/5/21, conference—Energytech. IEEE, pp 1–6

Khan KA, Paul S, Zobayer A, Hossain SS (2013a) A study on solar photovoltaic conversion. Int J Sci Eng Res 4(3). ISSN 2229-5518

Khan KA, Paul S, Adibullah M, Alam MF, Sifat SM, Yousufe MR (2013b) Performance analysis of BPL/PKL electricity module. Int J Sci Eng Res 4(3). ISSN 2229-5518

Khan MKA, Rahman MS, Das T, Ahmed MN, Saha KN, Paul S (2015) Investigation on parameters performance of Zn/Cu electrodes of PKL, AVL, Tomato and Lemon juice based electrochemical cells: a comparative study. In: 2015 3rd international conference on electrical information and communication technology (EICT). IEEE, pp 1–6

Khan KA, Rahman A, Rahman MS, Tahsin A, Jubyer KM, Paul S (2016a) Performance analysis of electrical parameters of PKL electricity (an experimental analysis on discharge rates, capacity and discharge time, pulse performance and cycle life and deep discharge of Pathor Kuchi Leaf (PKL) electricity cell). In: Innovative smart grid technologies-Asia (ISGT-Asia). IEEE, pp 540–544

Khan MKA, Paul S, Rahman MS, Kundu RK, Hasan MM, Moniruzzaman M, Mamun MA (2016b) A study of performance analysis of PKL electricity generation parameters: (an experimental analysis on voltage regulation, capacity and energy efficiency of Pathor Kuchi Leaf (PKL) electricity cell). In: IEEE 7th Power India international conference (PIICON). IEEE, pp 1–6

Khan KA, Rahman A, Rahman MS, Tahsin A, Jubyer KM, Paul S (2016c) Performance analysis of electrical parameters of PKL electricity (an experimental analysis on discharge rates, capacity and discharge time, pulse performance and cycle life and deep discharge of Pathor Kuchi Leaf (PKL) electricity cell). In: Innovative smart grid technologies-Asia (ISGT-Asia). IEEE, pp 540–544

Khan MKA, Paul S, Rahman MS, Kundu RK, Hasan MM, Moniruzzaman M, Al Mamun M (2016d) A study of performance analysis of PKL electricity generation parameters: (an experimental analysis on voltage regulation, capacity and energy efficiency of Pathor Kuchi Leaf (PKL) electricity cell). In: 7th power India international conference (PIICON). IEEE, pp. 1–6

Khan KA, Hassan L, Obaydullah AKM, Azharul Islam SM, Mamun MA, Akter T, Hasan M, Alam MS, Ibrahim M, Rahman MM, Shahjahan M (2017) Bioelectricity: a new approach to provide the electrical power from vegetative and fruits at off-grid region. Microsyst Technol 24(3). Springer, Manuscript number: 2018 MITE-D-17-00623R2. Received: 14 Aug 2017/Accepted: 3 Feb 2018. Impact Factor: 1.195. ISSN: 0946-7076 (Print) 1432-1858 (Online). https://doi.org/10.1007/s00542-018-3808-3

Khan KA, Bhuyan MS, Mamun MA, Ibrahim M, Hassan L, Wadud MA (2018) Organic electricity from Zn/Cu–PKL electrochemical cell. In: Contemporary advances in innovative and applicable information technology. Advances in intelligent systems and computing, vol 812, Springer. ISBN: 978-981-13-1539-8. https://doi.org/10.1007/978-981-13-1540-4

Khan KA, Alam MS, Mamun MA, Saime MA, Kamal MM (2016) Studies on electrochemistry for Pathor Kuchi Leaf power system. J Agric Environ 12(1):37–42

Paul S, Khan KA, Islam KA, Islam B, Reza MA (2012) Modeling of a biomass energy based (BPL) generating power plant and its features in comparison with other generating plants. IPCBEE 44 @ (2012). IACSIT Press, Singapore. https://doi.org/10.7763/IPCBEE.2012.V44.3

Ruhane TA, Islam MT, Rahaman MS, Bhuiyan MMH, Islam JMM, Newaz MK, Khan KA, Khan MA (2017) Photo current enhancement of natural dye sensitized solar cell by optimizing dye extraction and its loading period. Opt Int J Light Electr Opt 149:174–183

A Study on Electrochemical Characterizations of *Bryophyllum pinnatum* Leaf Electricity

Kamrul Alam Khan, Md. Siddikur Rahman, Md. Nafeez Rahman, Saleh Ahmad Khan, Md. Tarikul Islam Juel, and Mohua Islam Nirjhar

Abstract This paper presents an experimental study on electrochemical properties of *Bryophyllum pinnatum* Leaf (BPL)/PKL battery in terms of equilibrium constant of cell reaction, gas evolved from cell and observed voltage and current variation with respect to the change of composition of fueled solution of PKL cell. It is found that (compare to a lead–acid battery of same rating used in motorbike) voltage and current decrease sharply due to the lower concentration of electrolyte and fast reaction rate in PKL sap. The current density can be expanded by putting salt bridge/separator to increase the reaction rate between secondary salt and PKL sap. Additionally, it is identified that a low amount of H_2 gas can be extracted as by-product during electricity production from PKL battery. The rapid decrease in charge is improved through secondary salt in PKL juice. Additionally, the presence and amount of H_2 gas are identified to check the scale of risk for flammability associated with PKL/BPL battery compared to conventional lead–acid batteries. At instance, the work is significantly important for the low-income people who require a minimum amount of electricity to change their state of living.

Keywords Pathor Kuchi Leaf (PKL) · Electrochemistry · Green energy · Biomass energy

1 Introduction

According to energy vision 2013 energy transitions, 520 quadrillion BTU of energy was used globally in 2010 (energy vision 2013). According to the report of the national petroleum council, the time period in between 2000 and 2030 the annual

K. A. Khan (✉)
Department of Physics, Jagannath University, Dhaka, Bangladesh

Md. S. Rahman · S. A. Khan · Md. T. I. Juel · M. I. Nirjhar
Department of Electrical and Electronic Engineering, American International University, Dhaka, Bangladesh

Md. N. Rahman
Department of Solar Energy Engineering, Dalarna University, Falun, Sweden

M. Mukherjee et al. (eds.), *Advances in Medical Physics and Healthcare Engineering*, Lecture Notes in Bioengineering, https://doi.org/10.1007/978-981-33-6915-3_54

average global energy demand growth would be change (from 1.5 to 2.5%, respectively) (Energy Demand 2007). Continuous growth of population will keep a key driver position for increasing demand along with socio-economic development (Singh and Singh 2012). Moreover, with the advancement of the electric power generation, transmission and distribution system, smart grid is facing numerous security threats which destabilize the power system by attacking the power system (Ni et al. 2017; Ni and Paul 2019; Paul et al. 2016; Paul and Ni 2017, 2018). Due to lack of grid electricity, renewable energy can be a very trustworthy solution to provide backup service during the restoration of those failed zones and hence come the electricity generation from Pathor Kuchi Leaf (PKL).

Electricity generation from Pathor Kuchi Leaf (PKL) is a new type of biomass energy source, which is an additional energy source in the list of renewable energy. Biomass energy as electricity source is familiar and popular nowadays in Bangladesh (Hasan and Alam 2016). The acidity of PKL is responsible for the electricity production via electrochemical process. One of the major reasons of this invention (Khan and Alam 2008) is to ensure that poor people can get electricity for doing necessary daily works which are low cost and environment friendly. Most of the people are living under the poverty line at countryside area. This invention is a new milestone for electricity generation of Bangladesh. A number of papers have been discussed on *Bryophyllumpinnatum* Leaf (BPL) or Pathor Kuchi Leaf (PKL) regarding different aspects. The authors of these papers (Khan and Paul 2013; Khan and Alam 2017; Mamun 2017) provide a brief introduction about BPL or PKL, analyze the chemistry of PKL battery, discuss design mechanism of PKL quasi voltaic battery, provide the reason behind the green electricity generation from BPL or PKL and discuss the efficiency of BPL battery. The authors of this paper (Khan et al. 2014) are tried to discuss unit cell of BPL, the process of electricity production and public desire about this cell in Bangladesh. In this paper (Khan et al. 2016a), the authors are discussed on voltage regulation, the capacity of BPL and energy efficiency of BPL. The author of this paper (Paul et al. 2012), discussed about the discharge rates of BPL battery, capacity and discharge time of BPL battery, pulse performance of BPL battery, cycle life and deep discharge of BPL battery. In this paper (Khan et al. 2012), the authors are analyzed ideal characteristics of BPL battery and discussed the overview of BPL power plant. The authors of this paper (Khan et al. 2013) discussed and analyzed about a hybrid model of BPL electricity module and solar photovoltaic module at different operational conditions. In this paper (Khan et al. 2016b), authors are addressed about discharged rates, capacity and discharge time, pulse performance, cycle life and deep discharge of BPL battery. The latest investigations of BPL battery are related to pH behavior and cell potential (Rahman et al. 2018). Beside these, electrochemical characterizations study is conducted on lithium-ion battery electrodes (Geng et al. 2018), anode material for sodium-ion rechargeable batteries (Fiore et al. 2018) in recent years. Another most recent study (Pan et al. 2019) found about electrochemical characterizations of anodes for high-capacity lithium-ion batteries. Most of the existing literature, rarely considered the characterization of the PKL electricity generation module by calculating equilibrium constant, identifying the hydrogen gas from observation and analyzing the *V–I* characteristics. Investigating these electrochemical parameters will eventually help the future studies to do more deep analysis in this area.

Motivated by the literature, we investigate the characteristics of the PKL electricity generation module for calculation of equilibrium constant, identify the hydrogen gas from the observation, and analyze the voltage and current characteristics.

The rest of the paper is organized as follows: Sect. 2 presents a brief discussion about the theoretical study of the construction about BPL/PKL cell or battery. Section 3 presents the overall scenario of this research. Section 4 presents the description about equilibrium constant estimation from BPL cell reaction, H_2 gas identification from BPL battery and voltage, current estimation from BPL battery. Section 5 represents the numerical results. Section 6 presents the discussion about the numerical results. Finally, the conclusive remarks and future scopes are presented in Sect. 7.

2 Methods and Materials

Any electrochemical cell consists of basically two parts such as electrodes and electrolyte. The electrodes are named as anode and cathode; the electrolytes include ionic solution of acids, base salt or the paste of ionic substance. PKL cell is one type of electrochemical cell. Thus, some experiments have conducted using various PKL cells. Here, the variation was performed by modifying the electrodes by plating on anode, charging the composition of electrolytes. In PKL cell, the electrolyte used was the sap of PKL with the addition of secondary salt ($CuSO_4 \cdot 5H_2O$). However, the optimization of PKL juice was done by changing the amount (in percentage, %) of PKL sap in different PKL cells. Again, the anode was modified by electroplating on iron sheet by Zn. Each type of electrodes was connected it selves by series, and anodes and cathodes were arranged by parallel in each cell. A PKL battery consists of six PKL cells connected in series in each plastic shell. Number of anodes in each cell was varied by two or three but not the cathode. Cu wire was used to connect the electrodes and the cells (Fig. 1).

3 Overall Block Diagram

Start process by theoretical calculation of equilibrium constant estimation from experimented raw data. Obtained numerical results for one unit cell (equilibrium constant). H_2 gas identification by observing physical characteristics (testless, odorless, burns with pop sound) through basic experiment. Voltage and current are measured by volt-ohm multimeter (VOM) to observe the changes with time. End process by evaluating the significance of obtained numerical values toward the objectives (Fig. 2).

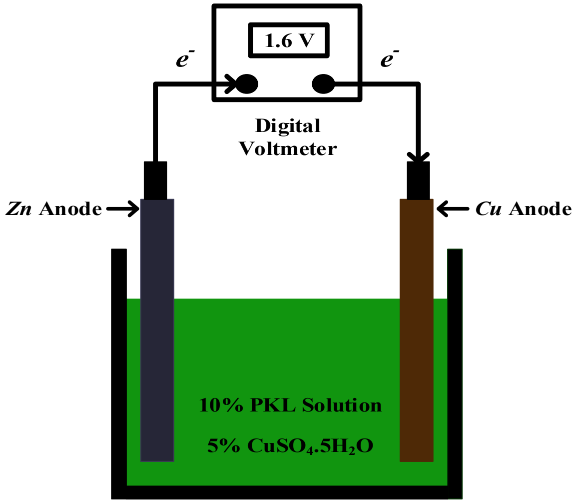

Fig. 1 An experimental setup of a unit PKL cell

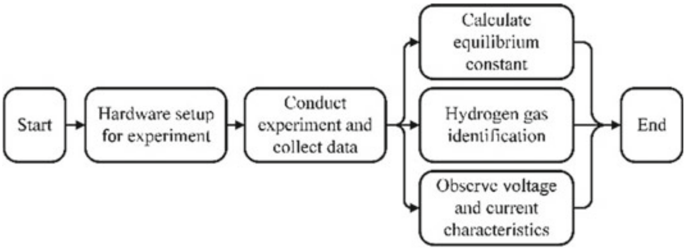

Fig. 2 An overall diagram of the electrochemical characterizations process

4 Problem Formulation

4.1 Case I: Equilibrium Constant Estimation from BPL Cell Reaction

Equilibrium constant defines as the ratio of the equilibrium concentrations of the products raised to the power of their stoichiometric coefficients to the equilibrium concentrations of the reactants raised to the power of their stoichiometric coefficients. Consider the following reversible reaction

$$aA + bB \leftrightarrow cC + dD \tag{1}$$

where $[A]$, $[B]$, $[C]$ and $[D]$ indicate the equilibrium concentration of A, B, C and D, respectively. Here, all equilibrium concentration is measured in molarity. a, b, c and d symbolize the number of moles of all equilibrium concentration used in Eq. (1).

Produced current from a battery can be used to do work, e.g., to run an electric motor. To derive a chemical reaction between electrical energy and the maximum amount of work ($W_{\max}$) obtainable from the battery, principle of thermodynamics is needed to be employed. The maximum amount of work obtainable from the battery defines as the product of the amount of charge flowing per mole and the maximum potential difference ($E_{\max}$) through which is transferred. Mathematically, it is expressed as follows:

$$W_{\max} = -nFE_{\max} \tag{2}$$

In Eq. (2), the number of moles of transferred electrons is symbolized by 'n' and which is equivalent to the valence of the ion participating in the chemical reaction of battery, the Faraday's constant is symbolized by 'F,' and the electromotive force (EMF) of the battery is symbolized by 'E.'

So, the input work is as follows:

$$W_{\max} = -nFE_{\max} \tag{3}$$

And the output work is as follows:

$$W = -nFE \tag{4}$$

Therefore, the maximum amount of work ($W_{\max}$) is equivalent to the free energy (ΔG) which is known from the thermodynamics, mathematically which is as follows:

$$W_{\max} = \Delta G \tag{5}$$

Therefore, from Eqs. (3) and (5), we can write,

$$\Delta G = -nFE_{\max} \tag{6}$$

Again in equilibrium, Gibbs free energy is as follows:

$$\Delta G = -2.303RT \ln K \tag{7}$$

$$\Delta G = -2.303RT \log K \tag{8}$$

From Eqs. (6) and (8), we can write\

$$\begin{aligned}
&\Delta G = -nFE_{\max} = -2.303RT \log K \\
&\Rightarrow \log K = \frac{-nFE_{\max}}{-2.303RT} \\
&\Rightarrow K = \text{anti log}\left[\frac{nFE_{\max}}{2.303RT}\right]
\end{aligned} \tag{9}$$

4.2 Case II: H_2 Gas Identification from BPL Battery

PKL juice contains many organic acids. The value of pH with 10% PKL juice solution is around 4.2. The reduction process of H^+ will be continued because of the acidity, and the reducing agent is Zn metal (anode). H^+ ion converts into H_2 gas by the redox process and evolved from the solution phase. The overall considered process is as follows:

$$\begin{aligned}
&\mathrm{Zn} \rightarrow \mathrm{Zn}^{2+} + 2\mathrm{e}^- \text{ (chemical reaction in anode)} \\
&\mathrm{H}^+ + \mathrm{e}^- \rightarrow \mathrm{H} \text{ (chemical reaction in cathode)} \\
&\mathrm{H} + \mathrm{H} \rightarrow \mathrm{H}_2 \uparrow \text{ (evolved from cathode)}
\end{aligned}$$

Because of the electromotive force (EMF) of the battery, the emerged gas (e.g., H_2) should be identified by the redox process. However, a simple test can be used to detect hydrogen.

Hydrogen blazes clearly. When hydrogen blazes, its blue flame comes to visible but it is rare, and it does not infect the atmosphere. If hydrogen gas is found inside the container, the flame will be quickly sucked into the container. During this, a 'pop' sound is created. This 'pop' sound of the hydrogen gas is combusting rapidly, and the pressures are equalizing inside and outside of the container. The pop sound is occurred like as a miniature explosion. The hydrogen unites with air oxygen and produces water molecule at the blazes of hydrogen. This process is shown as follows:

$$\mathrm{H}_{2(\mathrm{g})} + \frac{1}{2} O_{2(\mathrm{g})} \rightarrow \mathrm{H}_2 O_{(\mathrm{g})} \Delta\mathrm{H} = -285.85 \text{ kJ mol}^{-1}$$

Produced H_2 gas cannot escape during the experiment because the PKL battery is well covered. A long tube is used to collect the produced H_2 gas. Therefore, the tube is connected with a jar which contains water, and because of this, the collection of the produced H_2 gas into test tube safely. It is mandatory that no air can stay in tube that is why tube is filled with water. A rubber cork is used to cover the test tube when the test tube is filled with the H_2 gas.

4.3 Case III: Potential and Current Estimation from BPL Battery

During the oxidation process of a chemical reaction, every metal has a tendency to join into the solution and hence produces the solution pressure (SP) but at the same time and during the reduction process, the ionic molecule has tendency to deposit on the electrode surface as well as hence produces the osmic pressure (OP). Therefore, oxidation occurs when the value of solution pressure is greater than the value of osmic pressure, and on the other hand, reduction occurs when the value of solution pressure is less than the value of osmic pressure. In an electrochemical cell, oxidation occurs at anode and reduction occurs at cathode. In PKL battery, Zn plate is used as an anode, Cu plate is used as a cathode, and PKL juice is used as the electrolyte with a secondary salt ($CuSO_4 \cdot 5H_2O$). Thus, the ionic reactant molecules (e.g., H^+ and Cu^{2+}) are present on the solution, and the overall chemical reaction is shown as follows:

$$Zn_{(s)} + Cu^{2+}(aq) + H^{+}(aq) \rightarrow Zn^{2+}(aq) + Cu_{(s)} + H_{2(g)} \uparrow \tag{10}$$

Analysis of the chemical reaction states that the concentration of Zn^{2+} increases while the concentration of Cu^{2+} and H^+ decreases with time because of the reason behind this Zn^{2+} acts as an electron donor, and Cu^{2+} and H^+ act as the electron acceptor, and hence, the current and potential are decreased gradually. This is because the electron acceptors accept electrons by reduction process. The reduction processes are as follows:

$$Cu^{2+} + 2e^{-} \rightarrow Cu \tag{11}$$

$$2H^{+} + 2e^{-} \rightarrow H_2 \uparrow \tag{12}$$

And the oxidation process is as follows

$$2Zn - 4e^{-} \rightarrow 2Zn^{2+} \tag{13}$$

The Nernst equation for the above reactions is given as follows:

$$E_{Cu^{2+}|Cu} = E^{o}Cu^{2+}|Cu - \frac{0.0591}{n}\log\left[\frac{1}{Cu^{2+}}\right] \tag{14}$$

$$E_{2H^{+}|H_2} = E^{o}2H^{+}|H_2 - \frac{0.0591}{n}\log\frac{1}{\left[H^{+}\right]^{2}} \tag{15}$$

$$E_{Zn^{2+}|Zn} = E^{o}Zn^{2+}|Zn - \frac{0.0591}{n}\log\frac{1}{\left[Zn^{2+}\right]^{2}} \tag{16}$$

5 Numerical Results

5.1 Case I: Experimental Data and Calculation of Equilibrium Constant for One-Unit Cell

In Table 1, T represents room temperature (K), $E'_{\max}$ represents maximum potential of PKL cell, $E_{\max}$ represents average potential of PKL cell, n represents number of electron transferred, F represents Faraday constant (96,500 C), and R represents gas constant (8.314 J K^{-1} mol^{-1}). To calculate equilibrium constant for one-unit cell, we can use the following equation:

$$K = \text{anti}\log\left[\frac{nFE_{\max}}{2.303RT}\right]$$

where n represents number of moles of electrons transferred in cell reactions, F represents faraday constant (96,485 C), E_{max} represents maximum potential of PKL cell, R represents gas constant (8.314 J K^{-1} mol^{-1}), and T represents room temperature (measured in K). Putting the value of n, F, $E_{\max}$, R and T into above equation for cell number 10. So,

$$K = \text{anti}\log\left[\frac{nFE_{\max}}{2.303RT}\right]$$

$$\Rightarrow K = \text{anti}\ \log\left[\frac{4 \times 96500 \times 1.027}{2.303 \times 8.314 \times 301}\right]$$

$$\Rightarrow K = 6.03 \times 10^{68}$$

Table 1 Observed data during measurement of equilibrium constant

Cell number	Investigated parameters				
	T	$E'_{\max}$	$E_{\max}$	n	Equilibrium constant (K)
1	301	5.89	0.982	4	5.88×10^{65}
2	301	6.12	1.020	4	2.09×10^{68}
3	301	4.93	0.822	2[a]	3.39×10^{27}
4	301	6.25	1.042	2[b]	7.76×10^{34}
5	301	6.34	1.057	4	6.16×10^{70}
6	301	5.31	0.885	4	1.86×10^{59}

[a]PKL cell is fueled with only PKL juice
[b]Cell is fueled with only secondary salt

Table 2 Observations during the identification of hydrogen gas

Number	Observed physical characteristics	
	Properties	Observations
1	Taste	Taste less
2	Odor	Odorless
3	Color	Colorless
4	Burning capability	Burns with pop sound

5.2 *Case II: Observations of Hydrogen Gas Identification*

After observed some physical characteristics and visual perception, the radiated gas has been identified. Physical characteristics are like color, test, odor, and the burning capability and observed physical characteristics are given in Table 2. Disconnect the connection in between test tube and PKL battery, and the light is being splinted. At the end of the burning, the splint has been placed onto the top portion of the test tube and creating a 'popping' sound.

5.3 *Case III: Current and Voltage Observations of BPL Battery*

The measurements were collected from the voltmeter which state that the potential difference between its two half-cells of reaction's cell. In general, cell potential is also known as cell voltage, E_{cell}. In experiment, the cell potential is measured in two ways. They are open-circuit potential and potential with load. The potential is measured by a multimeter. Electrons flow from the oxidation half-cell to the reduction half-cell or in other words from the anode to the cathode. In terms of $E^o{}_{cell}$ of the oxidation–reduction reaction, the electrons flow in opposite from the more positive half-reaction to the more negative half-reaction. In this study, flow of electron (current) was measured by following two ways. They were short-circuit current and current with load. The short-circuit current is the current when the circuit is open and when the circuit is closed with a connection of electrical instrument is the current with load. The current was measured by using a multimeter in Ampere (A) unit.

During experiment, we observed and collected data of current with load, short-circuit current, potential with load and open-circuit voltage for cell no. 1, 2, 3, 4 and 6. For better understanding, we plotted the value of current and potential against time for cell no. 1, 2, 3, 4 and 6 which are represented in Figs. 3, 4, 5, 6 and 7.

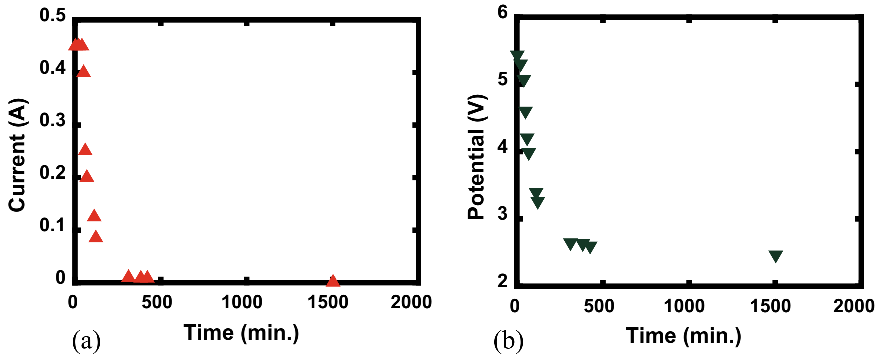

Fig. 3 **a**, **b** Variation of current and voltage with time, respectively, (cell-01)

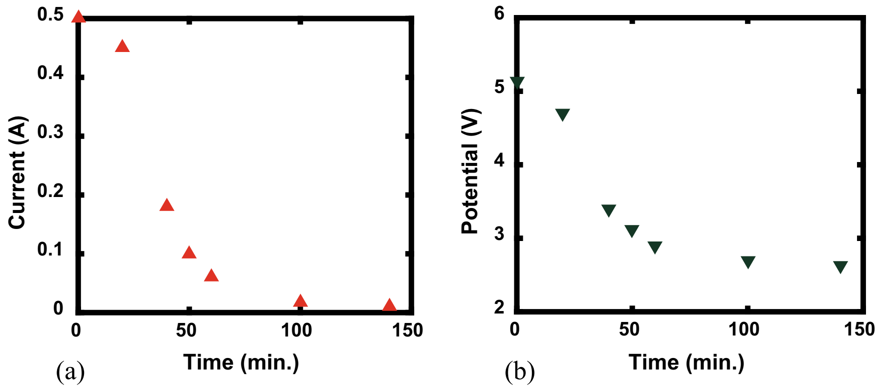

Fig. 4 **a**, **b** Variation of current and voltage with time, respectively, (cell-02)

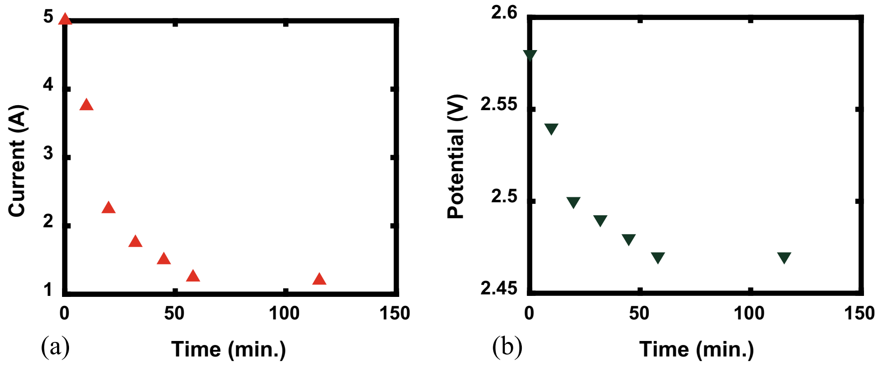

Fig. 5 **a**, **b** Variation of current and voltage with time, respectively, (cell-03)

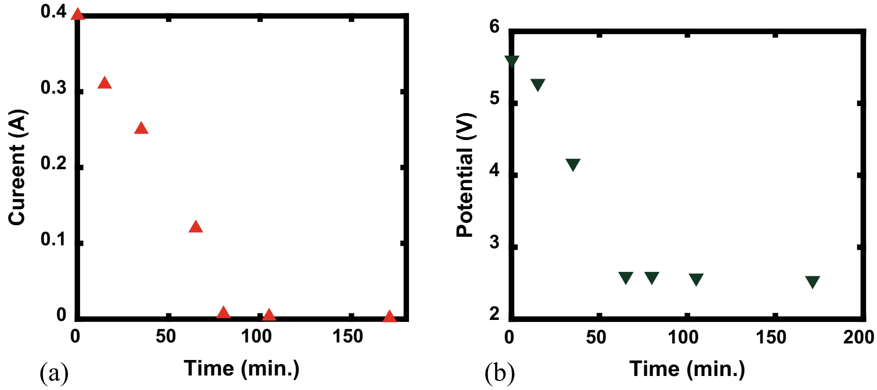

Fig. 6 **a**, **b** Variation of current and voltage with time, respectively, (cell-04)

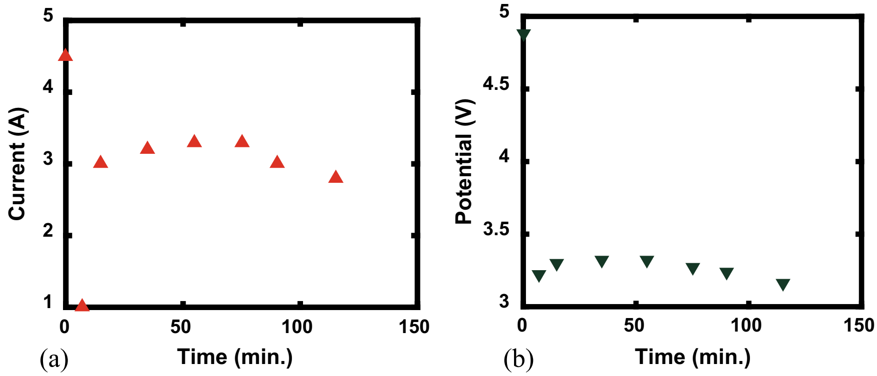

Fig. 7 **a**, **b** Variation of current and voltage with time, respectively, (cell-06)

6 Discussion

6.1 Case I: Discussion About Equilibrium Constant of BPL Cell Reaction

The reaction which has taken place is known as the ionic reaction in where charged ions may produce and consume at the same time. The concentration of the product ions and the reactant ions increases very fast and decreases, respectively, and synchronously. The equilibrium constant was calculated from the maximum potential, which was observed initially. It has been monitored that both reactant ions (e.g., H^+ and Cu^{2+}) are found in cell no. 3 and 4. From this discussion, it can be decided that when both the reactant ions are present, then the forward reaction is higher. This is because of both the Cu^{2+} and H^+ ions reduce synchronously to provide solid copper and hydrogen gas, and for the zinc plate, oxidation occurs very frequently. Again $CuSO_4 \cdot 5H_2O$ acts as a secondary salt in the chemical reaction, and hence, the presence of this secondary salt enhances the ionization of weak organic acids present in PKL juice.

6.2 Case II: H_2 Gas Identification from BPL Battery

Experimentally, it was found that the gas evolved was hydrogen. Hydrogen gas evolved from the cell was due to the reduction of H^+ ion to $H_2(g)$. The pH of the 10% PKL solution was 4.2. After mixing the 10% of secondary salt ($CuSO_4 \cdot 5H_2O$), the pH of the 10% PKL solution became 3.8. So, the amount of evolved gas was very much low. Therefore, it is an obvious that during electricity production from the PKL, hydrogen gas can be extracted as a by-product during PKL electricity generation.

6.3 Case III: Current and Potential Observation from BPL Battery

The potential and current both were measured with volt-ohm-milliammeter (also known as multimeter) (VOM). Here, the potential and current have been decreased significantly with time (represented in figure). We have studied several types of PKL cell where the composition of PKL juice was changed which are main responsible factor for this decreasing. In cell no. 2, 3 and 4, we have used 40%, 40% and 0% PKL sap with 5%, 0% and 5% secondary salt ($CuSO_4 \cdot 5H_2O$), respectively. According to Figs. 3, 4, 5, 6 and 7, it can be concluded that the current and potential were high for the cell no. 02 but cell no. 03 and 04 both were very low. Again, if we compare cell no. 02 with cell no. 04, it can be revealed that the potential and current were steady more time for cell no. 02. This might be occurring due to the presence of both Cu^{2+} ion from the secondary salt and H^+ ion from the PKL sap. Figures 8 and 9 represent variation of current and voltage with time for the discharge of a PKL cell and motor bike battery (secondary battery). Observations have been shown that current and voltage decreases steadily in secondary storage battery but in case of PKL battery, the scenario is different—current and potential decreases sharply. This may rise due to the lower concentration of electrolyte of the fast reaction rate in PKL cell because the initial current and voltage was same as the secondary storage battery. Moreover, there is no separator or salt bridge in between the electrodes so there may take place the local action. To prevent this unwanted losing, we may use the separator, and the current density can be increased by increasing the connection of secondary slat and PKL sap. From the experiment, it can be concluded that the concentration of Cu^{2+} and pH decreases with time similarly as current and potential also which are following a curvature.

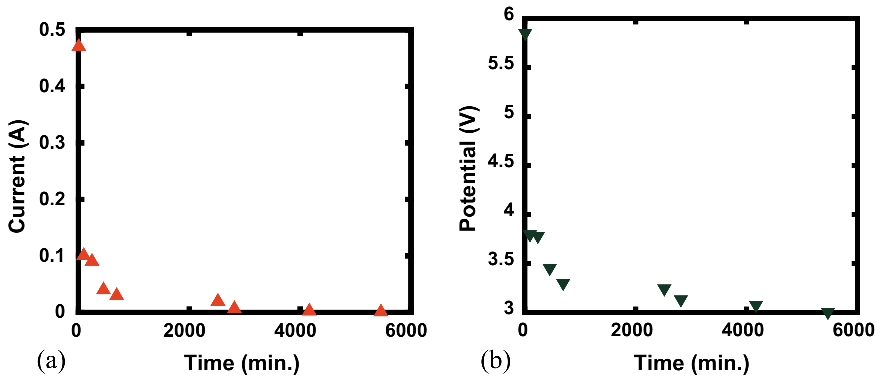

Fig. 8 **a**, **b** Variation of current and voltage with time, respectively, (for discharging of a PKL cell)

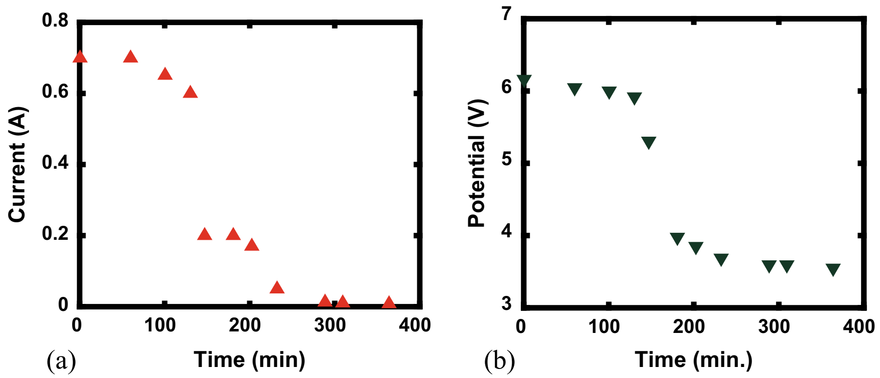

Fig. 9 **a**, **b** Variation of current and voltage with time, respectively, (for discharging of a motor bike battery)

7 Conclusion

The fundamental aim of this study was to analyze and observe the ionization phenomena of weak organic acid in PKL sap and identify the characteristics of voltage and current change in different cells over a long period of time, significance of putting salt bridge to eradicate fast reaction between electrodes of PKL cell. Potential and current both were measured in volt-ohm multimeter (VOM). Ionization phenomena were identified by measuring equilibrium constant in individual cell. Hydrogen gas was identified by physical properties of Hydrogen through practical experiment. Comparable same-rated lead–acid storage (motorbike battery) was tested to observe the current and voltage curve over time with the PKL battery current and voltage curve to identify the reason of fast decrease in curve/fast reaction in weak organic acids of PKL. Finally, some vital solutions were found to utilize PKL battery more effectively. However, PKL cell is needed to be investigated more, and further study can be continued considering these matters: UV visible and atomic absorption spectrophotometric analysis. The future works along this direction can be feasibility of integrating as a renewable energy source.

Acknowledgements The authors are grateful to M. Shamsul Islam, Mohammad Al Mamun, M. Ibrahim, Mehedi Hasan, Dr. A. Latif, Dr. Fakrul Islam, and Dr. Bappy Guha for their cooperation during the research work.

Conflict of Interest Statement On behalf of all the authors, the corresponding author declares that we do not have any conflict of interest.

Funding This work is self-funded.

References

Energy Demand (2007) Facing the hard truths about energy, p 34

Energy Vision (2013) Energy transitions: past and future. World Economic Forum, p 7

Fiore M, Longoni G, Santangelo S, Pantò F, Stelitano S, Frontera P, Antonucci P, Ruffo R (2018) Electrochemical characterization of highly abundant, low cost iron (III) oxide as anode material for sodium-ion rechargeable batteries. Electrochim Acta 269:367–377. https://doi.org/10.1016/j.electacta.2018.02.161

Geng L, Denecke ME, Foley SB, Dong H, Qi Z, Koenig GM Jr (2018) Electrochemical characterization of lithium cobalt oxide within aqueous flow suspensions as an indicator of rate capability in lithium-ion battery electrodes. Electrochim Acta 281:822–830. https://doi.org/10.1016/j.electacta.2018.06.037

Hasan M, Alam K (2016) Bryophyllum pinnatum leaf fueled cell: an alternate way of supplying electricity at the off-grid areas in Bangladesh. Paper present at the 4th international conference on the development in the in renewable energy technology (ICDRET), Bangladesh, 7–9 Jan 2016

Khan MKA (2008) Electricity Generation from Pathor Kuchi Leaf (PKL). BD Patent 1 004 907, 31 Dec 2008

Khan M, Alam K (2017) Performance of electricity generation from bryophyllum leaf for practical utilisation. Paper presented at the APS April meeting abstracts. Washington, DC, 28–31 Jan 2017

Khan MKA, Paul S (2013) A analytical study on electrochemistry for PKL (Pathor Kuchi Leaf) electricity generation system. Paper presented at the conference of IEEE Energy Tech, Cleveland, Ohio, 21–23 May 2013

Khan MK, Alam S, Paul SR, Zishan MA, Mahmud S (2012) Design of a hybrid model of BPL electricity module and solar photovoltaic cell. Int J Sci Eng Res 3(12):1–4

Khan KA, Paul S, Adibullah M, Alam MF, Sifat SM, Yousufe MR (2013) Performance analysis of BPL/PKL electricity module. Int J Sci Eng Res 4(3):1–4

Khan KA, Bakshi MH, Mahmud AA (2014) Bryophyllum pinnatum leaf (BPL) is an eternal source of renewable electrical energy for future world. Am J Phys Chem 3(5):77–83. https://doi.org/10.11648/j.ajpc.20140305.15

Khan MKA, Paul S, Rahman MS, Kundu RK, Hasan MM, Moniruzzaman M, Mamun MA (2016a) A study of performance analysis of PKL electricity generation parameters: an experimental analysis on voltage regulation, capacity and energy efficiency of Pathor Kuchi Leaf (PKL) electricity cell. Paper present at the conference of IEEE 7th power India international conference (PIICON). Bikaner, Rajasthan, 25–27 Nov 2016

Khan KA, Rahman A, Rahman MS, Tahsin A, Jubyer KM, Paul S (2016b) Performance analysis of electrical parameters of PKL electricity: an experimental analysis on discharge rates, capacity and discharge time, pulse performance and cycle life & deep discharge of Pathor Kuchi Leaf (PKL) electricity cell. Paper present at the IEEE innovative smart grid technologies-Asia (ISGT-Asia), Melbourne, 28 Nov–1 Dec 2016

Mamun MA, Khan MI, Sarker MH, Khan KA, Shajahan M, Khan KA (2017) A study on the performance and electrochemistry of Bryophyllum pinnatum leaf (BPL) electrochemical cell. Paper presented at the APS April meeting abstracts. Washington, DC, 28–31 Jan 2017

Ni Z, Paul S (2019) A multistage game in smart grid security: a reinforcement learning solution. IEEE Trans Neural Netw Learn Syst. https://doi.org/10.1109/TNNLS.2018.2885530

Ni Z, Paul S, Zhong X, Wei Q (2017) A reinforcement learning approach for sequential decision-making process of attacks in smart grid. Paper present at the IEEE symposium series on computational intelligence (SSCI), Hawaii, 27 Nov–1 Dec 2017

Pan K, Zou F, Canova M, Zhu Y, Kim J-H (2019) Systematic electrochemical characterizations of Si and SiO anodes for high-capacity Li–Ion batteries. J Power Sources 413:20–28. https://doi.org/10.1016/j.jpowsour.2018.12.010

Paul S, Ni Z (2017) Vulnerability analysis for simultaneous attack in smart grid security. Paper present at the IEEE power & energy society innovative smart grid technologies conference (ISGT), Washington, DC, 23–26 Apr 2017

Paul S, Ni Z (2018) A study of linear programming and reinforcement learning for one-shot game in smart grid security. Paper present at the international joint conference on neural networks (IJCNN), Rio, 8–13 July 2018

Paul S, Khan KA, Islam KA, Islam B, Reza MA (2012) Modeling of a biomass energy based (BPL) generating power plant and its features in comparison with other generating plants. Paper present at the 2nd international conference of environment and BioScience (IPCBEE), 44(3):12–16. https://doi.org/10.7763/IPCBEE.2012.V44.3

Paul S, Parajuli A, Barzegaran MR, Rahman A (2016) Cyber physical renewable energy microgrid: a novel approach to make the power system reliable, resilient and secure. Paper present at the IEEE innovative smart grid technologies-Asia (ISGT-Asia), Melbourne, 28 Nov–1 Dec 2016

Rahman MN, Rahman MS, Saha KN, Paul S, Khan MKA, Hazari MR (2018) Experimental investigations in pH behavior and cell potential of Bryophyllum pinnatum solution. Paper present at the grand renewable energy proceedings Japan council for renewable energy. Pacifico Yokohama, 17–22 June 2018

Singh BR, and Singh O (2012) Global trends of fossil fuel reserves and climate change in the 21st century. Intech

In Silico Molecular Docking and in Vitro Analysis of Eugenol as Free Radical Scavenger in Patients with Dengue Infection

Moumita Paul, Sourav Misra, Goutam Patra, Sourav Datta, Bibhuti Saha, and Sumi Mukhopadhyay

Abstract Infection by the Dengue virus (DENV) threatens global public health due to its high prevalence and the lack of effective treatments. Oxidative and cytotoxic damage plays an important role in Dengue pathogenesis and may serve as an important target for treatment. DENV infection activates Keap1/Nrf2 signaling pathway that leads to transcription of downstream antioxidant and detoxification genes such as HMOX-1, SOD2, NQO1, etc. In this study, both the molecular docking technique and In-Vitro experiments were performed to show potentiality of Eugenol as an activator of Keap1/Nrf2 signaling pathway. The molecular docking work concludes that Eugenol can actually induce Keap1/Nrf2 signaling pathway with a significant change in negative Firedock Global-Energy value, AScore value and as well as experimentally, Eugenol demonstrated promising antioxidant potential and free radical (RNS) scavenging activity.

Keywords Keap1/Nrf2 · RNS · DENV · Eugenol · DPPH · PatchDock · FireDock · BioVia discovery studio · Global-energy value · ArgusLab · AScore value

1 Introduction

Dengue-infection is a mosquito-borne viral infection spreading rapidly throughout the world, particularly in tropical or subtropical countries (Mapalagamage et al. 2018). Dengue-virus belongs to the family-Flaviviridae and genus-Flavivirus and might cause dengue-infection. According to WHO guidelines in 2009, Dengue infection has been classified based on their symptoms: Dengue-without warning-sign

M. Paul · S. Misra · G. Patra · S. Datta · S. Mukhopadhyay (✉)
Department of Laboratory Medicine, School of Tropical Medicine, Government of West Bengal, 108, C. R. Avenue, Kolkata, West Bengal 700073, India

B. Saha
Department of Tropical Medicine, Department of Health and Family Welfare, School of Tropical Medicine, Government of West Bengal, 108, C. R. Avenue, Kolkata, West Bengal 700073, India

M. Mukherjee et al. (eds.), *Advances in Medical Physics and Healthcare Engineering*, Lecture Notes in Bioengineering, https://doi.org/10.1007/978-981-33-6915-3_55

(DWOWS) (Nausea, Vomiting, Aches, and pain leucopenia), Dengue-with warning-signs (DWWS) (Abdominal pain or tenderness, persistent vomiting, clinical-fluid-accumulation, Mucosal-bleeding, Restlessness) and Severe-dengue (SD) (Severe plasma-leakage, Severe bleeding). A current model calculates 390 million belongings each year, with ninety-six million cases manifesting with a minimum of some clinical displays. As per WHO, the South-East Asia and Western Pacific regions square measure extremely endemic for this sickness (Ahmad et al. 2018). In India, Kolkata is a hyperendemic region and has witnessed many Dengue epidemics in current years. So far, dengue infection remains the number one pathological state, in Asian nations and around the world (World Health Organization 2011).

Viral infections usually cause the enhanced expression of proinflammatory cytokines. Reactive-Oxygen and Nitrogen-species (i.e. ROS, RNS) are generated in the monocytes, macrophages, and many other resistant cells in viral infections. However excessive secretion of ROS, RNS makes the inequity between these peroxidant and antioxidants leading oxidative-stress which may cause many deleterious effects on the host. Damages induced by oxidative-stresses and changes into redox status are being identified in some patients with Dengue infection which suggests the crucial role of oxidative-stress in Dengue pathogenesis (Chaturvedi and Nagar 2009). NO is one such extremely reactive molecule and considered as major peroxidant in the body which can spread through cells. The enzyme NO synthase produces NO. Peroxynitrite is also harmful when it is there in high concentration, oxidizing genetic material, lipids, and oxidizing and nitrating proteins thus peroxynitrite enhances oxidative stresses (Chaturvedi and Nagar 2009). Defense against such excessive free radical accumulation and reticence of the RNS is important cytoprotective mechanisms that are regulated and controlled by the activation of Keap1/Nrf2 signaling pathway (Olagnier et al. 2014). Keap1-Nrf2 signaling cascade is the key controller pathway against prolonged oxidative stresses. Nrf2 (nuclear factor E2-related factor 2) belongs to family of leucine zipper transcription protein factors. It binds with Maf-Proteins to the regulatory promoter region of downstream Nrf2 targeted genes and enhances expression of >200 oxidative stress-related genes to protect the cell from oxidative stress-induced damages (Barrera-Rodríguez 2018; Kansanen et al. 2013; Leung et al. 2019). The transactivation of Nrf2 targeted genes within the cell is strictly regulated and maintained at its basal level by Keap1, a cytoplasmic adaptor protein molecule of the Cullin3 based E3- ligase complex (David et al. 2017). The 605-residue human Nrf2 protein is composed of seven Nrf2-ECH homology (Neh1–7) domains all that have distinct functions. The N-terminal Neh2 domain mediates interaction with C-terminal portion of Keap1 that tightly regulates the permanency of Nrf2 (Tonelli et al. 2018). Keap1 (Kelch-like ECH-associated protein 1) contains five domains of which the C terminal portion of Keap1or the Kelch domain interacts with Neh2 domain. The other domains of Keap1 namely BTB domain and IVR help in homo dimerization of Keap1 and interacting with Cullin3 (Taguchi et al. 2011). Neh2 domain is bound to Kelch domain in homeostasis. Keap1 protein moderates Cul3 E3 complex for ubiquitination, which leads to continuous ubiquitination and destruction of Nrf2 during non-stressed conditions (Tong et al. 2006). This kind of quenching interaction keeps up lower basal expression of Nrf2 mediated cytoprotective gene transcription. However, when cell experiences oxidative stress, Keap1 gets inactivated and the poly-ubiquitination of Nrf2 is halted and newly synthesized Nrf2 proteins bypass Keap1 mediated degradation resulting in accumulation of the Nrf2 in cytoplasm. Consequently, Nrf2 gets accessed into nucleus, transcribes downstream Nrf2 targeted genes like SOD2, HMOX1, etc. (Theodore et al. 2008).

Thus the administration of antioxidant molecules to Dengue infected patients may limit virus-mediated cell damage and restrict the patient to go into severe conditions. Any phytochemical that has potent antioxidant activity and proved to be less toxic to human body can be employed in Dengue pathogenesis. Eugenol, a very common natural phytochemical suffice all our requirements to study its beneficial role in Dengue-induced oxidative stress and in future it may open up novel treatment methods for Dengue-associated diseases. Eugenol (4-allyl-2-methoxy phenol (EUG)) a hydrocarbon is present as yellow viscous oil (de Araújo Lopes et al. 2018). This is an associate with aromatic and phenolic compound from the category of phenylpropanoids (Barboza et al. 2018). It is a key component of cloves and found in bay leaves and all spices (Barboza et al. 2018; Ghofran et al. 2019). This is utilized in food industry (Nagababu et al. 2010)) as a preservative compound, appreciated due to its inhibitor property (Zhang et al. 2009). Eugenol shows numerous biological activities like bactericide, (Xu et al. 2016) antifungal (Chami et al. 2005; Gayoso et al. 2005) antiallergic (Kim et al. 1998; Corrêa et al. 2008) properties. Eugenol conjointly has medication, chemoprotective effects furthermore it has antioxidant-activity (Yogalakshmi et al. 2010) credited due to the existence of the phenolic cluster in its structure. For that reason, Eugenol has attracted several researchers. Numerous studies also opine that Eugenol has bioactive terpenes that inhibit ROS production in human neutrophil. Eugenol is a helpful pain reliever, and has antioxidant-activity. Taken together the current study aims to investigate the effectiveness of Eugenol (if any) in Dengue infection.

2 Materials and Methods

2.1 In-Silico Analysis

Protein preparation: The X-ray Crystallographic structure of Keap1-Neh2 complex (PDB ID 3ZGC) was obtained from the Protein Data Bank (PDB) at a resolution of 2.2 Å. Water molecules, ligands, and other hetero atoms were removed from protein complex and obtained the C-terminal Kelch domain (A and B chain) of Keap1 and the Neh domain (C chain) of Nrf2 separately by using Biovia Discovery Studio client software.

Ligand Preparation: The 3D structure of Eugenol was obtained and downloaded from the PUBCHEM database. The proteins and ligand were saved as PDB format for further analysis.

Automatic Docking: The computational molecular docking was accomplished by PatchDock server. Protein-small ligand platform of PatchDock was employed for docking by using clustering Root-Mean-Square-Deviation (RMSD) value of 4.0 (Chaturvedi et al. 2016). Neh domain of Nrf2 was docked against Kelch domain of Keap1 and Eugenol was docked against Kelch domain followed by docking of Neh domain against Kelch-Eugenol complex domain in separate pair of docking analysis. In both analyses, the complexes were sorted based on their PatchDock scores produced by the server. Further, PatchDock score refinement was accomplished by using FireDock server. The most stable conformations of desired protein–protein and the protein–ligand complexes were selected based on highest negative Global Energy (GE) value given by the FireDock server. Further validation was done by implementing flexible algorithm with ArgusLab 4.0.1 Docking Engine. The grid box was generated for assortment and formation of the dynamic binding pocket where the ligand could actually bind using grid resolution of 0.40 Å. Docking calculation was performed using AScore scoring function and the complexes that were best docked were chosen depending on the least AScore calculated by ArgusLab (Chikhi and Bensegueni 2008). The conformations of the complexes were envisaged by Discovery Studio software for further analysis.

2.2 *In-Vitro Experiments*

Chemicals: The subsequent compounds used for inhibitor activities, obtained from Sigma-Aldrich: Eugenol (4-allyl-2-methoxyphenol), Ascorbic acid. DPPH was purchased from Himedia. Ethanol was purchased from Merck. Griess chemical agent was purchased from Sigma. NO colorimetric assay kit from Cayman, subsequent experimental procedures were applied to guage the radical scavenging activity of Eugenol.

Study Population: Enrolled 37 Dengue patients at Calcutta School of Tropical Medicine from July 2019 to October 2019 after obtaining their consent. They were confirmed by both Dengue-NS1/IgM ELISA, and RT-PCR. They are classified into Dengue-without warning-sign (DWOWS), Dengue-with warning-signs (DWWS) according to WHO 2009 criteria through their symptoms. We had also enrolled 15 Healthy Donors (HD) with no history of illness in the past 3 months.

Serum separation and processing: Venous blood was collected from all patients and healthy. Five ml of blood were collected by venipuncture into a germ-free clot-activated tube and blood was separated by centrifugation process at 2000 RPM for ten minutes, stored in -20 °C temperature and clear serum were used for experiments.

DPPH assay: To assess the antioxidant potential of Eugenol, DPPH assay based on the methods of Brand-Williams et al. with small modification (Szerlauth et al. 2019) was used. Diphenyl-1-picrylhydrazyl (DPPH) has a radical-scavenger effect and has the ability to donate hydrogen, especially those with a phenolic cluster in their structure. This method is based on electron transport. It produces a purple ethanolic solution. Free radical molecules are decreased by the antioxidant molecules, producing yellowish ethanolic solution. Different concentrations (1.5–5.5 μg/ml) of Eugenol and Ascorbic acid (standard) were used, mixed with equivolume of DPPH solution. Optical density was measured at 492 nm after 30 min incubation at room temperature. The radical scavenging activity was calculated in percentage from the following formula: % scavenging [DPPH] = [(A0 − A1)/A0] × 100**.**Where A0 was the absorbance of the control and A1 was the absorbance of the samples. IC50 value was interpolated from the standard graph.

Serum Nitrite and Nitrate measurement: Reactive-nitrogen**-**species were determined by estimating the stable merchandise of nitrite and nitrate. Total nitrite + nitrate was considered by utilizing a nitrate and nitrite colorimetric-assay**-**kit (Cayman, USA) in the serum sample, following the manufacturer's directions. This assay determine nitrite + nitrate depending on the enzymatic translation of nitrate to nitrite by nitrate reductase enzyme. The reaction following a quantitative chemical analysis detection of nitrite by Griess reaction supported by the diazotization-reaction within which acidified NO_2^- produces a nitrosating agent that reacts with sulphanilic acid to yield the anion particle. This particle is then combined to N-(1-naphthyl) ethylenediamine making deep purple chromophoric chemical group spin off that absorbs light-wavelength at 540 nm.

Statistical Analysis: All analysis was performed using Graph-Pad Prism statistics software (Graph-Pad-Software-Inc., San-Diego, CA, USA). As the numeric variables had nonparametric distribution, One-way ANOVA with Kruskal–Wallis tests was used to differentiate more groups, respectively. Mann–Whitney test was used to compare two groups. For Mean ± SEM values, we used descriptive statistics. Differences with p values smaller than 0.05 were considered to be statistically significant.

3 Results

In-Silico Results: To find the potentiality of Eugenol as an antioxidant molecule and whether it could enhance the Keap1/Nrf2 pathway, two different sets of analysis on molecular docking were done. The first set of docking analysis showed Neh domain of Nrf2 docked against Kelch domain of Keap1 protein via PatchDock server. The docking result shows FireDock GE value of −48.90 with 10 conventional Hydrogen-bonding (SER363, ASN382, SER508, GLN530, TYR572, SER602, ASN387, GLY574, GLY386 of Keap1), 3 salt bridges (ARG380, ARG415, ARG483 of Keap1), 3 electrostatic interactions (ARG415 of Keap1, GLU78, GLU79 of Nrf2) and 2 hydrophobic interactions (GLU82, THR80, GLY81 of Nrf2)—a sum total of 18 Non-bonding interactions (Table 1). In the other set of docking analysis, Eugenol was docked against Kelch domain of Keap1 and the most stable Keap1-Eugenol complex structure was chosen on the basis of highest negative Firedock GE value. Then, Neh domain of Nrf2 was docked against Keap1-Eugenol complex via PatchDock server. The docking result shows decreased FireDock GE value of -38.04 with 2 conventional Hydrogen bonding (ASN382, TYR572 of Keap1), 1 Salt bridge (ARG380 of Keap1) and 4 electrostatic interactions (ARG380, ARG483 of Keap1, and GLU78 of Nrf2)—a total of 7 Non-bonding interactions (Table 2) demonstrating Eugenol prevents Keap1 to bind Nrf2 and thus bypassing proteasomal destruction of Nrf2. ArgusLab flexible docking analysis also shows similar kind of results. Nrf2 when docked against Keap1 best Ligand Pose energy of −5.80586 kcal/mol was obtained and when Nrf2 docked against Keap1-Eugenol complex best Ligand Pose energy of −5.53895 kcal/mol was obtained.

Study Population: Dengue-patients were classified into DWOWS, DWWS as per 2009 WHO guidelines. They were categorized according to their symptoms and the result of the biochemical test.

Table 1 Amino acids involved in non-bonding interactions in Nrf2-Keap1 docked complex (obtained from Discovery Studo software)

Neh2 Domain of Nrf2 interacting with Kelch Domain of Keap1	
Bond Donor to bond acceptor	Type of bond
1. keap1:ARG380:NH1—nrf2:GLU82:OE1	Salt bridge
2. keap1:ARG415:NH2—nrf2:GLU79:OE2	Salt bridge
3. keap1:ARG483:NH1—nrf2:GLU79:OE1	Salt bridge
4. keap1:ARG415:NH1—nrf2:ASP77:OD2	Electrostatic
5. keap1:ARG415:NH1—nrf2:GLU79:OE1	Electrostatic
6. keap1:SER363:OG—nrf2:GLU82:OE2	Conventional hydrogen bond
7. keap1:ASN382:ND2—nrf2:GLU82:OE1	Conventional hydrogen bond
8. keap1:SER508:OG—nrf2:GLU79:OE2	Conventional hydrogen bond
9. keap1:GLN530:NE2—nrf2:GLU78:O	Conventional hydrogen bond
10. keap1:GLN530:NE2—nrf2:GLU78:OE1	Conventional hydrogen bond
11. keap1:TYR572:OH—nrf2:GLU78:OE2	Conventional hydrogen bond
12. keap1:SER602:OG—nrf2:THR80:O	Conventional hydrogen bond
13. keap1:ASN387:N—nrf2:GLY76:O	Conventional hydrogen bond
14. keap1:GLY574:CA—nrf2:GLU78:OE1	Conventional hydrogen bond
15. keap1:GLY386:CA—nrf2:GLY76:O	Conventional hydrogen bond
16. nrf2:GLU78:C,O;GLU79:N—keap1:TYR525	Electrostatic
17. nrf2:GLU82:OE2—keap1:TYR334	Hydrophobic
18. nrf2:THR80:C,O;GLY81:N—keap1:TYR572	Hydrophobic

Table 2 Amino acids involved in non-bonding interactions when Nrf2 docked against Keap1-Eugenol complex (obtained from Discovery Studio software)

Neh2 Domain interacting with Kelch Domain in presence of Eugenol	
Bond Donor to Bond acceptor	Type of bond
1. keap1:ARG380:NH2—nrf2:GLU82:OE2	Salt bridge
2. keap1:ARG380:NH1—nrf2:GLU82:OE1	Electrostatic
3. keap1:ARG483:NH1—nrf2:GLU78:OE2	Electrostatic
4. keap1:ARG483:NH2—nrf2:GLU78:OE1	Electrostatic
5. keap1:ASN382:ND2—nrf2:GLU82:OE1	Conventional hydrogen bond
6. keap1:TYR572:OH—nrf2:GLU79:OE1	Conventional hydrogen bond
7. nrf2:GLU78:OE1—keap1:TYR525	Electrostatic

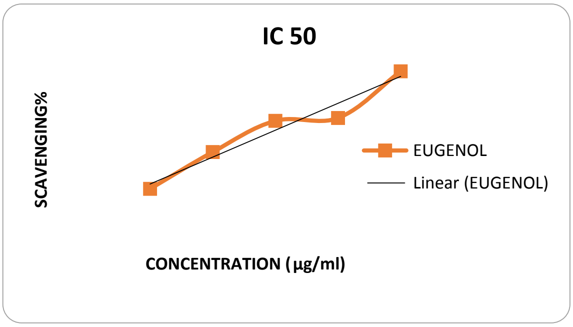

Fig. 1 Determination of IC 50 of Eugenol

DPPH Assay: The antioxidant property of Eugenol was determined by using DPPH scavenging assay followed by gross IC50 value determination. The IC50 of Eugenol was 3.02 µg/ml. A standard curve was prepared using ascorbic acid in different concentrations. The DPPH—scavenging capacity, was calculated from the graph through linear regression (R2 = 0.941). Thus Eugenol's ability to sequester free radicals within the DPPH solution was obtained (Fig. 1).

3.1 Determination of Nitrite and Nitrate Level

High concentration of nitrite and nitrate was observed in the patients with DWWS (57.25 ± 5.9 µM) compared with patients with DWOWS (42.71 ± 5.5 µM) and HD (23.56 ± 2.6 µM) (Fig. 2). Though there was no significant difference between patients with DWWS and DWOWS ($p = 0.3077$). The level of nitrite + nitrate level is significantly higher in DWWS than HD ($p = 0.0340$).

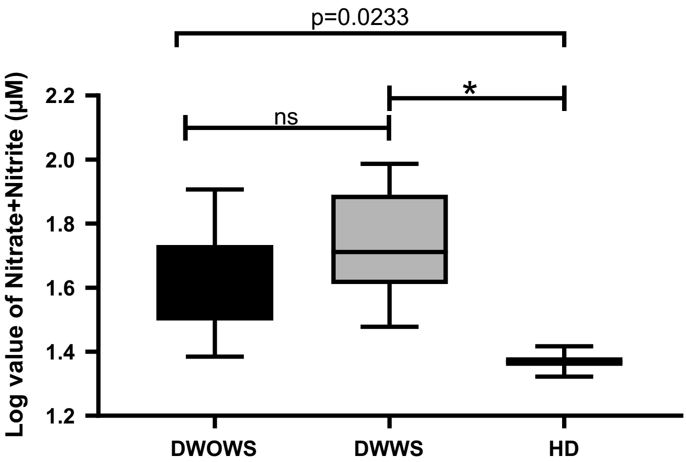

Fig. 2 Nitrite and Nitrate values in serum samples (μM of NO_2^- and NO_3^-) of patients with Dengue without warning sign (DWOWS, $n = 19$), Dengue with Warning sign (DWWS, $n = 18$), and Healthy Donors (HD, $n = 15$) measured by Griess reaction. Results were expressed by the median value using the box plot. Symbols (*) represent statistically significant differences ($p = 0.0340$) between DWWS and HD. Nitrite and Nitrate level is comparatively higher in DWWS ($p = 0.0233$) than DWOWS and HD. One-way ANOVA with Kruskal–Wallis test was done for comparing different study categories and Dunn's multiple comparisons test was done for repeated measures

3.2 Determination of Nitrite and Nitrate level After Eugenol Treatment

From Figs. 1 and 2, the antioxidant property of Eugenol was obtained and additionally high nitrite + nitrate level was found in patients with Dengue with warning signs. Further following Srejayar and Rao.et.al protocol the RNS quenching ability of Eugenol was investigated. Serum samples containing high nitrite + nitrate level were treated with/without Eugenol for 150 min, room temperature, subsequent to which Griess reagent was added and Optical Density was measured at 546 nm after 30 min incubation (Fig. 3).

Interestingly, very low amounts of nitrite and nitrate were obtained in the eugenol treated serum of dengue infected patients (28.37 ± 4.9 μM) as compared to samples without eugenol treatment (59.14 ± 5.9 μM). Thus, 2.1 fold reduced nitrite and nitrate were obtained in the serum of dengue patients when it was treated with eugenol.

4 Discussion

Dengue infection is one of the fastest spreading viral infections, threatening the whole world. Its cure and treatment have become a major concern. In this respect, the current

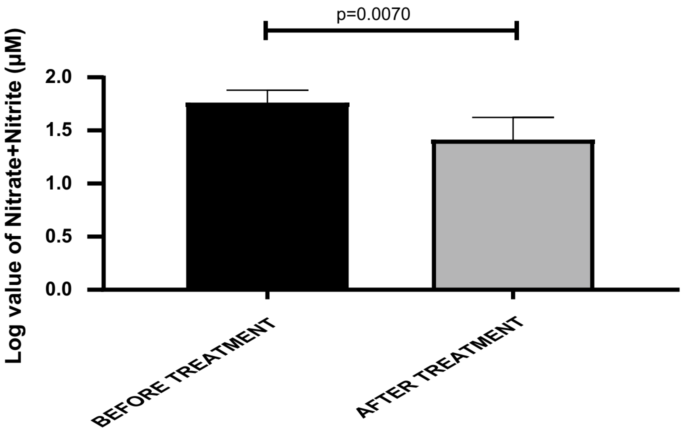

Fig. 3 Nitrite and nitrate value of patients with dengue infection before Eugenol treatment and after Eugenol treatment. Results were expressed, using Mann–Whitney test. Nitrite and Nitrate level is significantly reduced ($p = 0.0070$) after Eugenol treatment

study tried to find out a natural cure for dengue pathogenesis and found Eugenol to be a potent candidate for our studies. Eugenol was demonstrated to modulate the antioxidative Keap1-Nrf2 pathway through In Silico studies and could results in reduction in the free radical accumulation during Dengue infection through in vitro serum analysis. In this investigation, In Silico studies showed a reduction in free energies as well as diminution in the number of non- bonding interactions. Though the changes obtained in the free energy by the docking engines may seem very little and insignificant but all these changes are moderated by only a single molecule of Eugenol. Decreasing the number of non-bonding interactions inbetween Keap1 and Nrf2 is evident that Eugenol binds with Keap1 in the same interacting domain where Nrf2 binds. The lowering in the negative FireDock GE value as well as AScore pose energy value indicates that Keap1 cannot bind Nrf2 so firmly that it can act as an adaptor protein molecule for the Cul3 E3 ligase as long as Eugenol is bound to it. This propounds that newly synthesized Nrf2 can then bypass Keap1 mediated proteasomal degradation pathway which might lead to summoning up of Nrf2 in the cytosol followed by translocation into nucleus where it can induce transcription of oxidative stress-related genes (Fig. 4).

Eugenol, a compound, containing phenolic resin clusters, exhibits antioxidant-property by ending radical species through the loss of atom. In step with the results of our study, Eugenol had the foremost powerful antioxidant-activity. Nitric oxide is an essential chemical moderator, generated by neurons, macrophages, endothelial cells etc., and is implicated in many physiological processes. NO produced in macrophages and epithelial cells acts as an important molecule in the regulation of the diameter of blood vessels, inhibiting WBC adhesion and platelet aggregation. A balanced quantity of NO in the body is essential to maintain vital metabolic activities, a decreased or increased level, however may be deleterious to health. Figure 2,

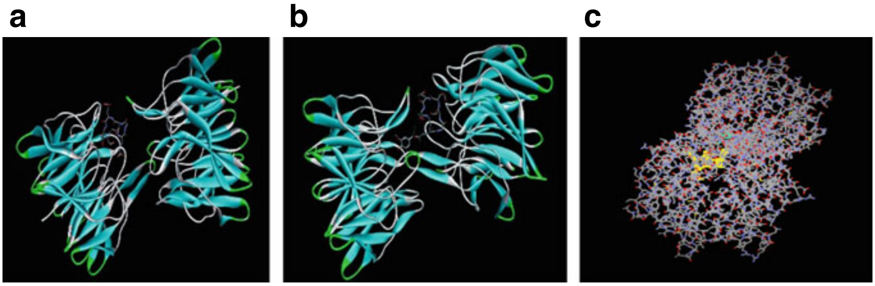

Fig. 4 **a** Neh domain interacting with Kelch domain. **b** Neh domain interacting with Eugenol-Kelch complex (Discovery Studio visualization). **c** Neh domain interacting with Eugenol-Kelch complex (ArgusLab visualization)

demonstrated, higher concentration of Reactive Nitrogen species (nitrite + nitrate) in Dengue with warning sign. In the acute phase of Dengue infection, the amount of Reactive-Nitrogen-Species remains high in infection, causing major pathophysiological effects. Therefore, the RNS quenching ability of Eugenol was next investigated, Fig. 3 demonstrated the amount of nitrite + nitrate, which is drastically reduced after Eugenol treatment. This may be caused by occurrence of antioxidant properties in the Eugenol, which competes with oxygen, doing a reaction with nitric oxide and thereby blocking the formation of nitrite and nitrate. This, therefore, demonstrates the usefulness of Eugenol in Dengue infection.

5 Conclusion

Thus, In-Silico analysis concludes that Keap1 cannot bind Nrf2 to that extend so that it can degrade Nrf2 by Proteasomal pathway as long as Eugenol is bound to Keap1. So, Keap1-Nrf2 pathway can be modulated in presence of Eugenol which ultimately leads to cytoprotection during oxidative stress. We conclude from the above discussion that Eugenol has an antioxidant activity by scavenging the free Reactive-Nitrogen-Species. Eugenol thus could be a possible drug candidate for treating Dengue infections. However, our conclusions must be verified in a larger study population.

References

Ahmad MH, Ibrahim MI, Mohamed Z, Ismail N, Abdullah MA, Shueb RH, Shafei MN (2018) The sensitivity, specificity and accuracy of warning signs in predicting severe dengue, the severe dengue prevalence and its associated factors. Int J Environ Res Public Health 15(9)

Barboza JN, da Silva Maia Bezerra Filho C, Silva RO, Medeiros JVR, de Sousa DP (2018) An overview on the anti-inflammatory potential and antioxidant profile of Eugenol. Oxid Med Cell Longev 2018:3957262. https://doi.org/10.1155/2018/3957262. PMID: 30425782; PMCID: PMC6217746

Barrera-Rodríguez R (2018) Importance of the Keap1-Nrf2 pathway in NSCLC: is it a possible biomarker? Biomed Rep 9(5):375–382

Chami F, Chami N, Bennis S, Bouchikhi T, Remmal A (2005) Oregano and clove essential oils induce surface alteration of Saccharomyces cerevisiae. Phytother Res 19(5):405–408

Chaturvedi UC, Nagar R (2009) Nitric oxide in dengue and dengue haemorrhagic fever: necessity or nuisance? FEMS Immunol Med Microbiol 56(1):9–24

Chaturvedi I, Sinha S, Chaudhary PP (2016) A molecular docking study to understand the interaction between anti-cancerous compounds and 12bp DNA sequences: poly (dA-dT) 12 and poly (dG-dC) 12. J Sci 1(4)

Chikhi A, Bensegueni A (2008) Docking efficiency comparison of Surflex, a commercial package and Arguslab, a licensable freeware. J Comput Sci Syst Biol 1(01):081–086

Corrêa MFP, Melo GO, Costa SS (2008) Substâncias de origem vegetal potencialmente úteis na terapia da Asma. Rev Bras Farm 18:785–797

David JA, Rifkin WJ, Rabbani PS, Ceradini DJ (2017) The Nrf2/Keap1/ARE pathway and oxidative stress as a therapeutic target in type II diabetes mellitus. J Diab Res 2017:4826724. https://doi.org/10.1155/2017/4826724. Epub 2017 Aug 20. PMID: 28913364; PMCID: PMC5585663

de Araújo Lopes A, da Fonseca FN, Rocha TM, de Freitas LB, Araújo EVO, Wong DVT, Júnior RCPL, Leal LKAM (2018) Eugenol as a promising molecule for the treatment of dermatitis: antioxidant and anti-inflammatory activities and its nanoformulation. Oxid Med Cell Longev 2018:8194849. https://doi.org/10.1155/2018/8194849. PMID: 30647816; PMCID: PMC6311755

Gayoso CW, Lima EO, Olivera VT et al (2005) Sensitivity of fungi isolated from onychomycosis to Eugenia cariophyllata essential oil and eugenol. Fitoterapia 76:247–249

Ghofran O, Safari T, Shahraki MR (2019) Effects of eugenol on pain response to the formalin test and plasma antioxidant activity in high fructose drinking water in male rats. Int J Prev Med 10

Kansanen E, Kuosmanen SM, Leinonen H, Levonen AL (2013) The Keap1-Nrf2 pathway: mechanisms of activation and dysregulation in cancer. Redox Biol 1(1):45–49

Kim HM, Lee EH, Hong SH et al (1998) Effect of Syzygium aromaticum extract on immediate hypersensitivity in rats. J Ethnopharmacol 60(2):125–131

Leung CH, Zhang JT, Yang GJ, Liu H, Han QB, Ma DL (2019) Emerging screening approaches in the development of Nrf2–Keap1 protein-protein interaction inhibitors. Int J Mol Sci 20(18):4445

Mapalagamage M, Handunnetti S, Premawansa G, Thillainathan S, Fernando T, Kanapathippillai K, Wickremasinghe R, De Silva AD, Premawansa S (2018) Is total serum nitrite and nitrate (NO_x) level in dengue patients a potential prognostic marker of dengue hemorrhagic fever? In: Disease markers

Nagababu, E., Rifkind, J. M., Boindala, S., & Nakka, L. (2010). Assessment of antioxidant activity of eugenol in vitro and in vivo. In: Free radicals and antioxidant protocols. Humana Press, pp 165–180

Olagnier D, Peri S, Steel C, van Montfoort N, Chiang C et al (2014) Cellular oxidative stress response controls the antiviral and apoptotic programs in dengue virus-infected dendritic cells. PLoS Pathog 10(12):e1004566. https://doi.org/10.1371/journal.ppat.1004566

Szerlauth A, Muráth S, Viski S, Szilagyi I (2019) Radical scavenging activity of plant extracts from improved processing. Heliyon 5(11):e02763

Taguchi K, Motohashi H, Yamamoto M (2011) Molecular mechanisms of the Keap1-Nrf2 pathway in stress response and cancer evolution. Genes Cells 16:123–140

Theodore M, Kawai Y, Yang J, Kleshchenko Y, Reddy SP, Villalta F, Arinze IJ (2008) Multiple nuclear localization signals function in the nuclear import of the transcription factor Nrf2. J Biol Chem 283:8984–8994

Tonelli C, Chio IIC, Tuveson DA (2018) Transcriptional regulation by Nrf2. Antioxid Redox Signal 29(17):1727–1745

Tong KI, Katoh Y, Kusunoki H, Itoh K, Tanaka T, Yamamoto M (2006) Keap1 recruits Neh2 through binding to ETGE and DLG motifs: characterization of the two-site molecular recognition model. Mol Cell Biol 26:2887–2900

World Health Organization (2011) Comprehensive guidelines for prevention and control of dengue and dengue haemorrhagic fever. Revised and expanded edition. WHO Regional Office for South-East Asia, New Delhi, India

Xu JG, Liu T, Hu QP, Cao XM (2016) Chemical composition, antibacterial properties and mechanism of action of essential oil from clove buds against staphylococcus aureus. Molecules 21(9):1194–1206

Yogalakshmi B, Viswanathan P, Anuradha CV (2010) Investigation of antioxidant, anti-inflammatory and DNA protective properties of eugenol in thioacetamide-induced liver injury in rats. Toxicology 268(3):204–212

Zhang H, Chen X, He JJ (2009) Pharmacological action of clove oil and its application in oral care products. Oral Care Ind 19:23–24

Author Index

M. Mukherjee et al. (eds.), *Advances in Medical Physics and Healthcare Engineering*, Lecture Notes in Bioengineering, https://doi.org/10.1007/978-981-33-6915-3